

CERN-ACC-Note-2020-0002
Version v1.0
Geneva, February 14, 2020



The Large Hadron-Electron Collider at the HL-LHC

LHeC Study Group



To be submitted to J.Phys. G

LHeC Study Group

P. Agostini¹, H. Aksakal², H. Alan³, S. Alekhin^{4,5}, P. P. Allport⁶, N. Andari⁷, K. D. J. Andre^{8,9}, D. Angal-Kalinin^{10,11}, S. Antusch¹², L. Aperio Bella¹³, L. Apolinario¹⁴, R. Apsimon^{15,11}, A. Apyan¹⁶, G. Arduini⁹, V. Ari¹⁷, A. Armbruster⁹, N. Armesto¹, B. Auchmann⁹, K. Aulenbacher^{18,19}, G. Azuelos²⁰, S. Backovic²¹, I. Bailey^{15,11}, S. Bailey²², F. Balli⁷, S. Behera²³, O. Behnke²⁴, I. Ben-Zvi²⁵, J. Bernauer²⁶, S. Bertolucci^{9,27}, S. S. Biswal²⁸, J. Blümlein²⁴, A. Bogacz²⁹, M. Bonvini³⁰, M. Boonekamp³¹, F. Bordry⁹, G. R. Boroun³², L. Bottura⁹, S. Bousson⁷, A. O. Bouzas³³, C. Bracco⁹, J. Bracinik⁶, D. Britzger³⁴, S. J. Brodsky³⁵, C. Bruni⁷, O. Brüning⁹, H. Burkhardt⁹, I. T. Cakir³⁶, O. Cakir¹⁷, R. Calaga⁹, A. Caldwell³⁴, A. Caliskan³⁷, S. Camarda⁹, N. C. Catalan-Lasheras⁹, K. Cassou³⁸, J. Cepila³⁹, V. Cetinkaya¹⁷, V. Chetvertkova⁹, B. Cole⁴⁰, B. Coleppa⁴¹, J. G. Contreras³⁹, A. Cooper-Sarkar²², E. Cormier⁴², A. S. Cornell⁴³, R. Corsini⁹, E. Cruz-Alaniz⁸, D. Curtin⁴⁴, M. D'Onofrio⁸, E. Daly²⁹, A. Das⁴⁵, S. P. Das⁴⁶, L. Dassa⁹, J. De Blas⁴⁷, L. Delle Rose⁴⁸, H. Denizli⁴⁹, K. S. Deshpande⁵⁰, D. Douglas²⁹, L. Duarte⁵¹, K. Dupraz^{38,52}, S. Dutta⁵³, A. V. Efremov⁵⁴, R. Eichhorn⁵⁵, K. J. Eskola³, E. G. Ferreira¹, O. Fischer⁵⁶, O. Flores-Sánchez⁵⁷, S. Forte^{58,59}, A. Gaddi⁹, J. Gao⁶⁰, T. Gehrman⁶¹, F. Gerigk⁹, A. Gilbert⁶², F. Giuli²², A. Glazov²⁴, R. M. Godbole⁶³, B. Goddard⁹, V. Gonçalves⁶⁴, G. A. Gonzalez-Sprinberg⁵¹, A. Goyal⁶⁵, J. Grames²⁹, E. Granados⁹, A. Grassellino⁶⁶, Y. O. Gunaydin⁶⁷, Y. Guo⁶⁸, V. Guzey⁶⁹, C. Gwenlan²², A. Hammad¹², C. C. Han^{70,71}, L. Harland-Lang²², F. Haug⁹, F. Hautmann²², D. Hayden⁷², J. Heßler³⁴, I. Helenius³, J. Henry²⁹, J. Hernandez-Sanchez⁵⁷, H. Hesari⁷³, T. J. Hobbs⁷⁴, N. Hod⁷⁵, G. H. Hoffstaetter⁵⁵, B. Holzer⁹, C. G. Honorato⁵⁷, B. Hounsell^{8,11,38}, N. Hu³⁸, F. Hug^{18,19}, A. Huss⁹, A. Hutton²⁹, R. Islam²³, S. Iwamoto⁷⁶, S. Jana⁵⁶, M. Jansova⁷⁷, E. Jensen⁹, T. Jones⁸, J. Jowett⁹, W. Kaabi³⁸, M. Kado³⁰, D. A. Kalinin^{10,11}, H. Karadeniz⁷⁸, U. Kaya⁷⁹, R. A. Khalek⁸⁰, H. Khanpour⁷³, M. Klein⁸, S. Klein⁸¹, U. Klein⁸, M. Köksal⁸², M. Korostelev²², P. Kostka⁸, M. Krelina⁸³, J. Kretzschmar⁸, S. Kuday¹⁷, G. Kulipanov⁸⁴, M. Kumar⁸⁵, M. Kuze⁸⁶, T. Lappi³, F. Larios³³, A. Latina⁹, P. Laycock²⁵, G. Lei⁸⁷, E. Levitchev⁸⁴, A. Levy⁸⁸, R. Li⁸⁹, X. Li⁶⁰, H. Liang⁶⁰, M. Lindner⁵⁶, V. Litvinenko^{25,90}, M. Liu⁶⁸, T. Liu⁹¹, W. Liu⁹², Y. Liu⁹³, S. Liuti⁹⁴, E. Lobodzinska²⁴, D. Longuevergne³⁸, X. Luo⁹⁵, W. Ma⁶⁰, M. Machado⁹⁶, S. Mandal⁹⁷, F. Marhauser²⁹, C. Marquet⁹⁸, A. Martens³⁸, R. Martin⁹, S. Marzani^{99,100}, J. McFayden⁹, P. Mcintosh¹⁰, B. Mellado⁸⁵, F. Meot⁵⁵, A. Milanese⁹, J. G. Milhano¹⁴, B. Militsin^{10,11}, M. Mitra¹⁰¹, S. Moch²⁴, S. Mondal¹⁰², S. Moretti¹⁰³, A. Morreale⁹⁰, P. Nadolsky⁷⁴, M. M. Najafabadi⁷³, F. Navarra¹⁰⁴, Z. Nergiz⁹, P. Newman⁶, J. Niehues¹⁰⁵, E. W. Nissen⁹, M. Nowakowski¹⁰⁶, N. Okada¹⁰⁷, G. Olivier³⁸, F. Olness⁷⁴, G. Olry³⁸, J. A. Osborne⁹, A. Ozansoy¹⁷, R. Pan¹⁰⁸, B. Parker²⁵, M. Patra¹⁰⁹, H. Paukkunen³, Y. Peinaud³⁸, D. Pellegrini⁹, G. Perez-Segurana^{15,11}, D. Perini⁹, L. Perrot³⁸, N. Pietralla¹¹⁰, B. Pire⁹⁸, R. Placakyte¹¹¹, M. Poelker²⁹, R. Polifka¹¹², A. Pollini^{27,113}, P. Poulou²³, G. Pownall²², Y. A. Pupkov⁸⁴, F. S. Queiroz¹¹⁴, K. Rabbertz¹¹⁵, V. Radescu¹¹⁶, R. Rahaman¹¹⁷, N. Raicevic¹¹⁸, P. Ratoff^{15,11}, D. Raut¹¹⁹, S. Raychaudhuri¹⁰⁹, J. Repond¹²⁰, R. Rimmer²⁹, L. Rinolfi⁹, W. Rodejohann⁵⁶, J. Rojo⁸⁰, A. Rosado⁵⁷, X. Ruan⁸⁵, S. Russenschuck⁹, M. Sahin¹²¹, C. A. Salgado¹, O. A. Sampayo¹²², K. R. Santosh¹⁰¹, K. Satendra²³, N. Satyanarayan¹²³, B. Schenke²⁵, K. Schirm⁹, H. Schopper⁹, M. Schott¹⁹, D. Schulte⁹, C. Schwanenberger²⁴, A. Senol⁴⁹, A. Seryi²⁹, S. Setiniyaz^{15,11}, L. Shang¹²⁴, X. Shen⁸⁹, N. Shipman⁹, N. Sinha¹²⁵, W. Slominski¹²⁶, S. Smith^{10,11}, C. Solans⁹, M. Song¹²⁷, H. Spiesberger¹⁹, J. Stanyard⁹, A. Starostenko⁸⁴, A. Stasto¹²⁸, A. Stocchi³⁸, M. Strikman¹²⁸, M. J. Stuart⁹, S. Sultansoy⁷⁹, H. Sun⁹⁵, M. Sutton¹²⁹, L. Szymanowski¹³⁰, D. Tapia-Takaki¹³¹, M. Tanaka⁸⁶, Y. Tang¹³², A. T. Tasci¹³³, A. T. Ten-Kate⁹, P. Thonet⁹, R. Tomas-Garcia⁹, D. Tommasini⁹, D. Trbojevic^{25,55}, M. Trott¹³⁴, I. Tsurin⁸, A. Tudora⁹, K. Tywoniuk¹³⁵, C. Vallerand³⁸, A. Valloni⁹, D. Verney³⁸, E. Vilella⁸, D. Walker⁴⁷, S. Wallon³⁸, B. Wang⁸⁹, K. Wang¹³⁶, K. Wang¹³⁷, X. Wang⁹⁵, Z. S. Wang¹³⁸, H. Wei¹³⁹, C. Welsch^{8,11}, G. Willering⁹, P. Williams^{10,11}, D. Wollmann⁹, C. Xiaohao¹³, T. Xu¹⁴⁰, C. E. Yaguna¹⁴¹, Y. Yamazaki¹⁴², H. Yang⁸¹, A. Yilmaz⁷⁸, P. Yock¹⁴³, C. Yue⁶⁸, S. G. Zadeh¹⁴⁴, O. Zenaiev⁹, C. Zhang¹⁴⁵, J. Zhang¹⁴⁶, R. Zhang⁶⁰, Z. Zhang³⁸, G. Zhu⁸⁹, S. Zhu¹²⁴, F. Zimmermann⁹

F. Zomer³⁸, J. Zurita^{147,148}, P. Zurita¹⁴⁹

- ¹ Universidade de Santiago de Compostela (USC), Santiago de Compostela, Spain
- ² Nigde Universitesi, Nigde, Turkey
- ³ University of Jyvaskyla, Jyvaskyla, Finland
- ⁴ Universität Hamburg, Hamburg, Germany
- ⁵ Institute of High Energy Physics (IHEP), Protvino, Russia
- ⁶ University of Birmingham, Birmingham, United Kingdom
- ⁷ Université Paris-Saclay, Saint-Aubin, France
- ⁸ University of Liverpool, Liverpool, United Kingdom
- ⁹ European Organization for Nuclear Research (CERN), Genève, Switzerland
- ¹⁰ Science & Technology Facilities Council (STFC) - Daresbury Laboratory, Daresbury, United Kingdom
- ¹¹ Cockcroft Institute of Accelerator Science and Technology, Daresbury, United Kingdom
- ¹² Universität Basel, Basel, Switzerland
- ¹³ Chinese Academy of Sciences - Institute of High Energy Physics (IHEP), Beijing, China
- ¹⁴ Laboratório de Instrumentação e Física Experimental de Partículas (LIP), Lisbon, Portugal
- ¹⁵ University of Lancaster, Lancaster, United Kingdom
- ¹⁶ A. Alikhanian National Laboratory (AANL), Yerevan, Armenia
- ¹⁷ Ankara University, Ankara, Turkey
- ¹⁸ Johannes Gutenberg University Mainz (JGU) - PRISMA Cluster of Excellence, Mainz, Germany
- ¹⁹ Johannes Gutenberg-Universität Mainz (JGU), Mainz, Germany
- ²⁰ Université de Montréal, Montreal, Canada
- ²¹ University of Montenegro, Podgorica, Montenegro
- ²² University of Oxford, Oxford, United Kingdom
- ²³ Indian Institute of Technology, North, Guwahati, Guwahati
- ²⁴ Deutsches Elektronen-Synchrotron (DESY), Hamburg, Germany
- ²⁵ Brookhaven National Laboratory (BNL), Upton, USA
- ²⁶ Massachusetts Institute of Technology (MIT), Cambridge, USA
- ²⁷ Università di Bologna, Bologna, Italy
- ²⁸ Ravenshaw University, Cuttack, India
- ²⁹ Thomas Jefferson National Accelerator Facility (Jefferson Lab), Newport News, USA
- ³⁰ Istituto Nazionale di Fisica Nucleare (INFN) - Sezione di Roma, Rome, Italy
- ³¹ Commissariat à l’Energie Atomique (CEA) - Institut de Recherche sur les Lois Fondamentales de l’Univers (IRFU), Gif-sur-Yvette, France
- ³² Razi University, Kermanshah, Iran
- ³³ Centro de Investigación y Estudios Avanzados (CINVESTAV), San Pedro, Mexico
- ³⁴ Max-Planck-Institut für Physik - Werner-Heisenberg-Institut, Munich, Germany
- ³⁵ SLAC National Accelerator Laboratory, Menlo Park, USA
- ³⁶ Ankara Nuclear Research and Training Center, Ankara, Turkey
- ³⁷ Gumushane University, Gumushane, Turkey
- ³⁸ Université Paris-Saclay, CNRS/IN2P3, IJCLab, Orsay, France
- ³⁹ Inst. of Technological Investigations, Prague, Czech Republic
- ⁴⁰ Columbia University, New York, USA
- ⁴¹ Indian Institute of Technology (IIT), Gandhinagar, India
- ⁴² Centre Lasers Intenses et Applications (CELIA), Bordeaux, France
- ⁴³ University of Johannesburg (UJ), Johannesburg, South Africa
- ⁴⁴ University of Toronto, Toronto, Canada
- ⁴⁵ Osaka University, Osaka, Japan

- 46 Universidad de los Andes, Santiago, Columbia
- 47 Durham University - Institute for Particle Physics Phenomenology, Durham, United Kingdom
- 48 Istituto Nazionale di Fisica Nucleare (INFN) - Sezione di Firenze, Firenze, Italy
- 49 Abant Izzet Baysal University, Golkoy Kampusu, Turkey
- 50 University of Maryland, College Park, USA
- 51 Universidad de la Republica - Instituto de Fisica Facultad de Ciencias (IFFC), Montevideo, Uruguay
- 52 Université Paris-Sud, Orsay, France
- 53 Sri Guru Tegh Badadur Khalsa College, Delhi, India
- 54 Joint Institute for Nuclear Research (JINR), Dubna, Russia
- 55 Cornell University, Ithaca, USA
- 56 Max-Planck-Institut für Kernphysik, Heidelberg, Germany
- 57 Benemerita Universidad Autonoma de Puebla (BUAP), Puebla, Mexico
- 58 Università degli Studi di Milano, Milano, Italy
- 59 Istituto Nazionale di Fisica Nucleare (INFN) - Sezione di Milano, Milano, Italy
- 60 University of Science and Technology of China (USTC), Hefei, China
- 61 Universität Zürich, Zurich, Switzerland
- 62 Northwestern University, Evanston, USA
- 63 Indian Institute of Science (IISc), Bangalore, India
- 64 Universidade Federal de Pelotas (UFPel), Pelotas, Brazil
- 65 University of Delhi, Delhi, India
- 66 Fermi National Accelerator Laboratory (FNAL), Batavia, USA
- 67 University of Iowa, Iowa City, USA
- 68 Liaoning Normal University (LNNU), Dalian, China
- 69 Petersburg Nuclear Physics Institute (PNPI), Petersburg, Russia
- 70 University of Tokyo, Tokyo, Japan
- 71 Kavli Institute for the Physics and Mathematics of the Universe (KIPMU), Kashiwa, Japan
- 72 Michigan State University, East Lansing, USA
- 73 Institute for Research in Fundamental Sciences (IPM), Tehran, Iran
- 74 Southern Methodist University, Dallas, USA
- 75 Weizmann Institute of Science, Rehovot, Israel
- 76 Università degli Studi di Padova, Padua, Italy
- 77 Université de Strasbourg, Strasbourg, France
- 78 Giresun University, Giresun, Turkey
- 79 TOBB University of Economic and Technology (TOBB ETU), Ankara, Turkey
- 80 Vrije University, Amsterdam, Netherlands
- 81 Lawrence Berkeley National Laboratory (LBNL), Berkeley, USA
- 82 Cumhuriyet Univ., Alsancak, Turkey
- 83 Universidad Tecnica Federico Santa Maria, Valparaiso, Chile
- 84 Siberian Branch of Russian Academy of Science - Budker Institute of Nuclear Physics (BINP), Novosibirsk, Russia
- 85 University of the Witwatersrand, Johannesburg, South Africa
- 86 Tokyo Institute of Technology, Tokyo, Japan
- 87 Tsinghua University, Beijing, China
- 88 Tel-Aviv University, Tel Aviv, Israel
- 89 Hangzhou University (HZU), Hangzhou, China
- 90 Stony Brook University, Stony Brook, USA
- 91 Xiamen University (XMU), Xiamen, China
- 92 University College London, London, United Kingdom

- 93 Henan Institute of Science and Technology (HIST), Xinxiang, China
- 94 University of Virginia, Charlottesville, USA
- 95 Dalian University of Technology (DLUT), Dalian, China
- 96 Universidade Federal do Rio Grande do Sul (UFRGS), Porto Alegre, Brazil
- 97 Institute of Physics, Bhubaneswar, India
- 98 Laboratoire Leprince-Ringuet (LLR), Palaiseau, France
- 99 Università degli Studi di Genova, Genova, Italy
- 100 Istituto Nazionale di Fisica Nucleare (INFN) - Sezione di Genova, Genova, Italy
- 101 Harish-Chandra Research Institute (HRI), Allahabad, India
- 102 University of Helsinki, Helsinki, Finland
- 103 University of Southampton, Southampton, United Kingdom
- 104 Universidade de Sao Paulo (USP), Sao, Paolo
- 105 Universität Aachen, Aachen, Germany
- 106 Universidad de los Andes, Carrera, Colombia
- 107 The University of Alabama, Tuscaloosa, USA
- 108 Zhejiang Institute of Modern Physics (ZIMP), Hangzhou, China
- 109 Tata Institute of Fundamental Research (TIFR), Mumbai, India
- 110 Technische Universität Darmstadt, Darmstadt, Germany
- 111 Homeday GmbH Berlin, Berlin, Germany
- 112 Charles University, Prague, Czech Republic
- 113 Istituto Nazionale di Fisica Nucleare (INFN) - Sezione di Bologna, Bologna, Italy
- 114 Univ. Federal do Rio Grande do Norte, Natal, Brazil
- 115 Karlsruher Institut für Technologie (KIT), Karlsruhe, Germany
- 116 IBM Deutschland R&D, GmbH, Urbar, Germany
- 117 Indian Institute of Science Education and Research (IISER), Kolkata, India
- 118 Univ. of Montenegro, Podgorica, YUOGSLAVIA
- 119 University of Delaware, Newark, USA
- 120 Argonne National Laboratory, Argonne, USA
- 121 Usak University, Usak, Turkey
- 122 National University of Mar del Plata, ???, Argentina
- 123 Oklahoma State University (OSU), Stillwater, USA
- 124 Peking University (PKU), Beijing, China
- 125 Institute of Mathematical Sciences (IMSc), Chennai, India
- 126 Jagiellonian University, Cracow, Poland
- 127 Anhui University (AHU), Hefei, China
- 128 Pennsylvania State University (PSU), University Park, USA
- 129 University of Sussex, Sussex, United Kingdom
- 130 Narodowe Centrum Badań Jądrowych (NCBJ), Warsaw, Poland
- 131 Kansas State University, Manhattan, USA
- 132 Korea Institute for Advanced Study (KIAS), Cheongryangri-dong, Korea
- 133 Kastamonu University, Kastamonu, Turkey
- 134 Københavns, Universitet - Niels Bohr Institutet (NBI), Copenhagen
- 135 University of Bergen, Bergen, Norway
- 136 Zhejiang University (ZJU), Hangzhou, China
- 137 Wuhan University (WHU), Wuhan, China
- 138 Asia Pacific Center for Theoretical Physics (APCTP), Pohang, Korea
- 139 University of California (UC), Riverside, USA
- 140 Hebrew University of Jerusalem - Racah Inst. of Physics, Jerusalem, Israel
- 141 Universidad Pedagógica y Tecnológica de Colombia, Tunja, Colombia

¹⁴² Kobe University, Kobe, Japan

¹⁴³ , Auckland, New Zealand

¹⁴⁴ Universität Rostock, Rostock, Germany

¹⁴⁵ National Center for Theoretical Sciences (NCTS), Hsinchu, Taiwan

¹⁴⁶ Nankai University (NKU), Tianjin, China

¹⁴⁷ Karlsruher Institut für Technologie (KIT) - Institut für Theoretische Teilchenphysik (TTP),
Karlsruhe, Germany

¹⁴⁸ Karlsruher Institut für Technologie (KIT) - Institut für Kernphysik (IKP), Karlsruhe, Ger-
many

¹⁴⁹ Universität, Regensburg, Regensburg

Abstract

The Large Hadron electron Collider, LHeC, is the means to move deep inelastic physics following HERA to the energy frontier of particle physics as it is being exploited by the HL-LHC. The paper presents a thorough update of the initial LHeC Conceptual Design Report (CDR) published in 2012. It comprises new results on the far reaching physics programme on parton structure, QCD dynamics, electroweak and top physics. It is shown how LHeC will open a new chapter of nuclear particle physics by extending the kinematic range in lepton-nucleus scattering by several orders of magnitude. Owing to an enhanced luminosity goal, the high centre of mass energy and the cleanliness of the neutral and charged current final states, the LHeC has a very remarkable Higgs programme and a promising potential to discover new physics beyond the Standard Model. The design is for concurrent LHeC and HL-LHC operation which paves the way for transforming the LHC in its final phase of operation to a high precision Higgs and electroweak physics facility with also a much increased range to explore new physics up to 100 TeV mass, as is demonstrated in a separate chapter. Building on the CDR, the paper presents a detailed updated design of the energy recovery electron linac (ERL) including new lattice, magnet, SRF technology and interaction region designs. A lower energy, high current ERL facility, PERLE at Orsay, is described which uses the basic LHeC configuration parameters, a 3-turn racetrack, the source, and cryo-module designs, enabling it to serve as a development facility assisting the design and anticipated operation of the LHeC. The electron accelerator frequency is now chosen to be 801.58 MHz and the first 5-cell Niobium cavity is presented which has reached a Q_0 of $3 \cdot 10^{10}$ exceeding the design goal. An updated detector design, including a forward hadron tagger, is presented as a base for the acceptance, resolution and calibration goals which arise from the Higgs and PDF physics programme. The detector is shown to require an installation time of two years which is commensurate with typical LHC shutdown durations. The paper comprises a brief report of the LHeC international advisory committee with recommendations on the next steps to be made in preparing the possible endorsement of the LHeC as part of the LHC project. While the paper is dedicated to the LHeC, it also presents novel results on the FCC-eh which is designed to utilise the same ERL technology, or a relocated LHeC depending on future developments of the energy frontier collider landscape.

Preface

This paper represents the updated design study of the Large Hadron-electron Collider, the LHeC, a TeV energy scale electron-hadron (eh) collider which may come into operation during the third decade of the lifetime of the Large Hadron Collider (LHC) at CERN. It is an account, accompanied by numerous papers in the literature, for many years of study and development, guided by an International Advisory Committee (IAC) which was charged by the CERN Directorate to advise on the directions of energy frontier electron-hadron physics at CERN. End of 2019 the IAC summarised its observations and recommendations in a brief report to the DG of CERN, which is here reproduced as an Appendix.

The paper outlines a unique, far reaching physics programme, a design concept for a new generation collider detector, together with a novel configuration of the intense, high energy electron beam. This study builds on the previous, detailed LHeC Conceptual Design Report (CDR), which was published eight years ago [1]. It surpasses the initial study in essential characteristics: i) the depth of the physics programme, owing to the insight obtained mainly with the LHC, and ii) the luminosity prospect, for enabling a novel Higgs facility to be built and the prospects to search for and discover new physics to be strengthened. It builds on recent and forthcoming progress of modern technology, due to major advances especially of the superconducting RF technology and as well new detector techniques.

Unlike in 2012, there has now a decision been taken to configure the LHeC as an electron linac-proton or nucleus ring configuration, which leaves the ring-ring option [1] as a backup. In ep , the high instantaneous luminosity of about $10^{34} \text{ cm}^{-2}\text{s}^{-1}$ may be achieved with the electron accelerator built as an energy recovery linac (ERL) and because the brightness of the LHC exceeds early expectations by far, not least through the upgrade of the LHC to its high luminosity version, the HL-LHC [2, 3]. For $e\text{Pb}$ collisions, the corresponding per nucleon instantaneous luminosity would be about $10^{33} \text{ cm}^{-2}\text{s}^{-1}$. The LHeC is designed to operate concurrently with the LHC. It thus represents a unique opportunity to advance particle physics by building on the singular investments which CERN and its global partners have made into the LHC facility.

Extending much beyond the CDR, a configuration has newly been designed for a low energy ERL facility, termed PERLE [4], which is moving ahead to be built at Orsay by an international collaboration. The major parameters of PERLE have been taken from the LHeC, such as the 3-turn configuration, source, the 802 MHz frequency and cavity-cryomodule technology, in order to make PERLE a suitable facility for the development of LHeC ERL technology and the accumulation of operating experience prior to and later in parallel with the LHeC. In addition, the PERLE facility has a striking low energy physics programme, industrial applications and will be an enabler for ERL technology as the first facility to operate in the 10 MW power regime.

While the 2012 CDR focussed the physics discussion on the genuine physics of deep inelastic

37 scattering (DIS) leading much beyond HERA, the focus here is shifted to the challenges posed
38 by the LHC. It is demonstrated that DIS at the LHeC can play a crucial role in sustaining
39 and enriching the LHC programme, a consequence of the results obtained at the LHC, i.e.
40 the discovery of the Higgs boson, the non-observation of supersymmetry (SUSY) or other non
41 Standard Model (SM) exotic particles and, not least, the unexpected realisation of the huge
42 potential of the LHC for discovery through precision measurements in the strong and electroweak
43 sectors. It thus was felt time to summarise the recent seven years of LHeC development, also
44 in support of the current discussions on the future of particle physics, especially at the energy
45 frontier. Both for the LHeC [5–7] and PERLE [8], documents were submitted for consideration
46 to the European Strategy for Particle Physics Update.

47 The LHeC has something of a one in our lifetime opportunity for substantial progress in particle
48 physics. It comprises, with a linac shorter than the pioneering two-mile linac at SLAC, a most
49 ambitious and exciting physics programme, the introduction of novel accelerator technology
50 and the complete exploitation of the unique values of and spendings into the LHC. It requires
51 probably less courage than that of Pief Panowsky and colleagues half a century ago. Finally,
52 not least, one may realise that the power LHeC needed without the energy recovery technique
53 is beyond 1 GW. It so appears to be a significant step towards green accelerator technology,
54 a major general desire and requirement of our times. This paper aims at substantiating these
55 statements in the various chapters following.

Contents

Preface	1
1 Introduction	8
1.1 The Context	8
1.1.1 Particle Physics - an unfinished Area of Fundamental Science	8
1.1.2 Deep Inelastic Scattering and HERA	9
1.2 The Paper	11
1.2.1 The LHeC Physics Programme	11
1.2.2 The Accelerator	12
1.2.3 PERLE	13
1.2.4 The Detector	14
2 LHeC Configuration and Parameters	16
2.1 Introduction	16
2.2 Cost Estimate, Default Configuration and Staging	17
2.3 Configuration Parameters	18
2.4 Luminosity	19
2.4.1 Electron-Proton Collisions	20
2.4.2 Electron-Ion Collisions	21
2.5 Linac Parameters	22
2.6 Operation Schedule	22
3 Precision Standard Model Physics with LHeC	25
3.1 Resolving the Parton Substructure of the Proton	25
3.1.1 Open Questions on the QCD of PDFs	25
3.1.2 PDFs and the LHC	26
3.1.3 Parton Distributions and DIS	29
3.1.4 HERA PDFs	31
3.1.5 Simulated LHeC Data Sets	34
3.1.6 Expectations on PDFs from the LHeC	35
3.1.7 Heavy Quarks	46
3.2 Pushing the limits of QCD with high precision measurements	50
3.2.1 Determination of the strong coupling constant	51
3.2.2 New QCD Dynamics at Small x	59
3.2.3 Low x and the Longitudinal Structure Function F_L	65
3.2.4 Disentangling non-linear QCD dynamics at the LHeC	71
3.2.5 The 3D Structure of the Proton	76
3.2.6 Inclusive diffraction	82
3.2.7 Light-Front Holography and Superconformal Algebra	90

3.3	Electroweak Physics	94
3.3.1	Electroweak effects in inclusive NC and CC DIS cross sections	94
3.3.2	Methodology of a combined EW and QCD fit	95
3.3.3	Weak boson masses M_W and M_Z	96
3.3.4	Further mass determinations	98
3.3.5	Weak Neutral Current Couplings	99
3.3.6	The neutral current ρ_{NC} and κ_{NC} parameters	100
3.3.7	The effective weak mixing angle $\sin^2 \theta_{\text{W}}^{\text{eff},\ell}$	101
3.3.8	Electroweak effects in charged-current scattering	103
3.3.9	Direct W and Z production and Anomalous Triple Gauge Couplings . . .	103
3.3.10	Radiation Amplitude Zero	107
3.3.11	Conclusion	108
3.4	Top Quark Physics	108
3.4.1	Wtq Couplings	109
3.4.2	FCNC Top Quark Couplings	111
3.4.3	Other Top Quark Property Measurements and Searches for New Physics .	112
3.4.4	Summary Top Quark Physics	112
4	Nuclear Particle Physics with Electron-Ion Scattering at the LHeC	114
4.1	Introduction	114
4.2	Nuclear Parton Densities	116
4.2.1	Pseudodata	117
4.2.2	Nuclear gluon PDFs in a global-fit context	119
4.2.3	nPDFs from DIS on a single nucleus	121
4.3	Nuclear diffraction	126
4.3.1	Exclusive vector meson diffraction	126
4.3.2	Inclusive diffraction on nuclei	131
4.4	New Dynamics at Small x with Nuclear Targets	133
4.5	Collective effects in dense environments – the ‘ridge’	134
4.6	Novel QCD Nuclear Phenomena at the LHeC	134
5	Higgs Physics with LHeC	138
5.1	Signal Strength and Couplings	138
5.1.1	Introduction	138
5.1.2	Higgs Production in Deep Inelastic Scattering	139
5.1.3	Kinematics of Higgs Production	139
5.1.4	Cross Sections and Rates	141
5.1.5	Higgs Signal Strength Measurements	142
5.1.6	Higgs Decay into Bottom and Charm Quarks	144
5.1.7	Higgs Decay into WW	149
5.1.8	Accessing Further Decay Channels	152
5.1.9	Systematic and Theoretical Errors	153
5.1.10	Higgs Coupling Analyses	155
5.1.11	Parton Distributions	157
5.2	Measuring the Top-quark–Higgs Yukawa Coupling	158
5.3	Higgs Decay into Invisible Particles	163
6	Searches for Physics Beyond the Standard Model	166
6.1	Introduction	166
6.2	Extensions of the SM Higgs Sector	166

6.2.1	Modifications of the Top-Higgs interaction	167
6.2.2	Charged scalars	167
6.2.3	Neutral scalars	168
6.2.4	Modifications of Higgs self-couplings	169
6.2.5	Exotic Higgs boson decays	170
6.3	Searches for supersymmetry	170
6.3.1	Search for the SUSY Electroweak Sector: prompt signatures	171
6.3.2	Search for the SUSY Electroweak Sector: long-lived particles	172
6.3.3	R-parity violating signatures	173
6.4	Feebly Interacting Particles	174
6.4.1	Searches for heavy neutrinos	174
6.4.2	Fermion triplets in type III seesaw	175
6.4.3	Dark photons	175
6.4.4	Axion-like particles	176
6.5	Anomalous Gauge Couplings	177
6.6	Theories with heavy resonances	178
6.6.1	Leptoquarks	178
6.6.2	Vector-like quarks	179
6.6.3	Excited fermions (ν^*, e^*, u^*)	179
6.6.4	Colour octet leptons	180
6.6.5	Electric precursor to QCD	180
6.7	Summary and conclusion	181
7	Influence of the LHeC on Physics at the HL-LHC	183
7.1	Precision Electroweak Measurements at the HL-LHC	183
7.1.1	The effective weak mixing angle	183
7.1.2	The W -boson mass	185
7.1.3	Impact on electroweak precision tests	187
7.2	Higgs Physics	190
7.2.1	Impact of LHeC data on Higgs cross section predictions at the LHC . . .	190
7.2.2	Higgs Couplings from a simultaneous analysis of pp and ep collision data	191
7.3	Further precision Standard Model measurements at the HL-LHC	194
7.4	High Mass Searches at the LHC	198
7.4.1	Strongly-produced supersymmetric particles	198
7.4.2	Contact interactions	198
7.5	Heavy Ion Physics with eA Input	199
8	The Electron Energy Recovery Linac	204
8.1	Introduction – Design Goals	204
8.2	The ERL Configuration of the LHeC	206
8.2.1	Baseline Design – Lattice Architecture	206
8.2.2	30 GeV ERL Options	214
8.2.3	Component Summary	215
8.3	Electron-Ion Collisions	215
8.4	Beam-Beam Interactions	216
8.4.1	Effect on the electron	217
8.4.2	Effect on the proton	219
8.5	Arc Magnets	219
8.5.1	Dipole magnets	219
8.5.2	Quadrupole magnets	221

8.6	LINAC and SRF	222
8.6.1	Choice of Frequency	223
8.6.2	Cavity Prototype	224
8.6.3	Cavity-Cryomodule	227
8.6.4	Electron sources and injectors	230
8.6.5	Compensation of Synchrotron Radiation Losses	234
8.6.6	LINAC Configuration and Infrastructure	235
8.7	Interaction Region	236
8.7.1	Layout	236
8.7.2	Proton Optics	238
8.7.3	Electron Optics	245
8.7.4	Interaction Region Magnet Design	253
8.8	Civil Engineering	257
8.8.1	Placement and Geology	257
8.8.2	Underground infrastructure	259
8.8.3	Construction Methods	260
8.8.4	Civil Engineering for FCC-eh	261
8.8.5	Cost estimates	264
8.8.6	Spoil management	265
9	Technology of ERL and PERLE	266
9.1	Energy Recovery Linac Technology - Status and Prospects	266
9.1.1	ERL Applications	266
9.1.2	Challenges	266
9.1.3	ERL Landscape	269
9.2	The ERL Facility PERLE	270
9.2.1	Configuration	271
9.2.2	Importance of PERLE towards the LHeC	271
9.2.3	PERLE Layout and Beam Parameters	272
9.2.4	PERLE Lattice	273
9.2.5	The Site	275
9.2.6	Staging Strategy and Time Schedule	275
9.2.7	Concluding Remark	277
10	Experimentation at the LHeC	278
10.1	Introduction	278
10.2	Overview of Main Detector Elements	280
10.3	Inner Tracking	281
10.4	Calorimetry	284
10.5	Muon Detector	285
10.6	Forward and Backward Detectors	288
10.6.1	Zero-Degree (Neutron) Calorimeter	289
10.7	Detector Installation and Infrastructure	292
10.8	Detector Design for a Low Energy FCC-eh	295
11	Conclusion	298
A	Statement of the International Advisory Committee	301

Chapter 1

Introduction

1.1 The Context

1.1.1 Particle Physics - an unfinished Area of Fundamental Science

Despite the striking success of the Standard Model, it has been recognised to have major deficiencies. These may be summarised in various ways. Some major questions concern the:

- **Higgs boson** Is the electroweak scale stabilised by new particles, interactions, symmetries? Is the Higgs boson discovered in 2012 the SM Higgs boson, what is its potential? Do more Higgs bosons exist as are predicted for example in SUSY?
- **Elementary Particles** The SM has 61 discovered particles (12 leptons, 36 quarks, 12 mediators, 1 H boson). Are these too many or too few? Do right handed neutrinos exist? Why are there 3 families? What makes leptons and quarks different? Do leptoquarks exist, is there further substructure?
- **Strong Interactions** What is the meaning of the ADS/CFT relation and of SUSY in strong interactions? Do axions, odderons, instantons exist? How is confinement explained and how do partons hadronise? How can the Quark Gluon Plasma state be described in Quantum Chromodynamics? What is the true parton dynamics and structure of proton and nuclei at different levels of resolution?
- **GUT** Is there a genuine, grand unification of the interactions at high scales, would this include gravitation? What is the real value of the strong coupling constant, is lattice correct in this respect?
- **Neutrinos** Do Majorana neutrinos exist, is there CP violation in the neutrino sector, is the proton stable?

These (and others) are known and persistent questions in Particle Physics. They are intimately related and any future strategic programme should not be confined to only one or a few of these. The field is far from being understood, despite the phenomenological success of the $SU_L(2) \times U(1) \times SU_c(3)$ gauge field theory termed the Standard Model. Attempts to declare its end [9], despite their perhaps stimulating irritation, may possibly be compared with Kelvin's prediction about the future which comprised precision only as all principal questions had already been solved, back in around 1900. The question is not why to end particle physics but how to

86 proceed. The answer is not hidden in philosophy but requires new, better, affordable experi-
87 ments. Indeed the situation is special as expressed by Guido Altarelli a few years ago: *It is now*
88 *less unconceivable that no new physics will show up at the LHC. . . We expected complexity and*
89 *instead we have found a maximum of simplicity. The possibility that the Standard model holds*
90 *well beyond the electroweak scale must now be seriously considered [10].* This is reminiscent of
91 the time before 1969, prior to anything like a Standard Model, when gauge theory was just for
92 theorists, while a series of new accelerators, such as the 2 mile electron linac at Stanford or the
93 SPS at CERN were planned which caused a complete change of the paradigm of particle physics.

94 Major challenges for particle physics also comprise basic puzzles on the Universe, especially
95 on the nature of Dark Matter. Ingenuitive theoretical hypotheses, such as on the existence of
96 extra dimensions, on SUSY, of un-particles or the embedding in higher gauge groups, like E8,
97 are a strong motivation to develop high energy physics rigorously further. In this endeavour
98 a substantial increase of precision, the conservation of diversity and a broadening of kinematic
99 coverage is a necessity, which may turn out to be of fundamental importance. The strategic
100 question in this context, therefore, is not just which new collider should be built next, as one
101 often hears, but how we may challenge the current and incomplete knowledge best. A realistic
102 step to progress requires to build a new e^+e^- collider, preferentially in Asia, and to complement
103 the LHC in the thirties with an electron ERL to synchronously operate pp with ep at the LHC,
104 the topic of this paper.

105 One may call these machines first technology generation colliders as their technology has been
106 proven to principally work [11]. Beyond these times there is a long-term future reaching to the
107 year 2050 and much beyond, of a second, further generation of hadron, lepton and electron-
108 hadron colliders, which is not considered in the present paper ¹. For CERN a joint design study
109 has recently been published of a future circular collider (FCC) accelerator complex [12–14], which
110 would provide a corresponding base. A similar prospect is being discussed in China [15, 16].

111 A new collider for CERN at the level of $\mathcal{O}(10)$ GSF cost should have the potential to change
112 the paradigm of particle physics with direct, high energy discoveries in the 10 TeV mass range.
113 This may only be achieved with the FCC-hh including an eh experiment. The FCC-hh accesses
114 physics to several hundred TeV, assisted by a qualitatively new level of QCD/DIS input. It
115 is the only collider to measure the Higgs potential as its major goal and thus may not fail.
116 It reaches rare H decays, high scales and, when combined with ep , it measures the SM Higgs
117 couplings to below percent precision. There is a huge, fundamental program on electroweak
118 and strong interactions, flavour and heavy ions. It is CERN's unique opportunity to build on
119 the ongoing LHC program, for many decades ahead. The FCC-hh requires high field dipoles.
120 A strongly supported magnet R+D program shall find an affordable, high field solution, to be
121 selected in the early thirties, and not this time. The size of the FCC-hh, in any case, requires
122 this to be established as a global enterprise. The LHeC can be understood as a very important
123 step towards this major new facility, both in terms of physics and technology.

124 1.1.2 Deep Inelastic Scattering and HERA

125 The field of deep inelastic lepton-hadron scattering (DIS) [17] was born with the discovery [18, 19]
126 of partons [20, 21] about 50 years ago. It readily contributed fundamental insight, for example
127 on the development of QCD with the confirmation of fractional quark charges and of asymptotic

¹There are a few exceptions when studies are presented not only for the LHeC but also the ep version of the Future Circular Collider, the FCC-eh, which uses, seen from today, the same ERL technology and possibly hardware as is currently under development for the LHeC.

128 freedom or with the spectacular finding that the right handed weak isospin charge of the electron
 129 was zero [22] which established the Glashow-Weinberg-Salam model of leptons [23] as the base
 130 of the united electroweak theory. The quest to reach higher energies in accelerator based particle
 131 physics led to generations of colliders, with HERA [24] as the so far only electron-proton collider.

132 HERA collided electrons (and positrons) of about 27.6 GeV energy, E_e , off protons of 920 GeV
 133 energy, E_p , achieving a centre of mass energy of $\sqrt{s} = 2\sqrt{E_e E_p}$ of about 320 GeV. It therefore
 134 extended the kinematic range covered by fixed target experiments by two orders of magnitude
 135 in Bjorken x and in four-momentum transfer squared, Q^2 , with its limit $Q_{max}^2 = s$. HERA
 136 had a unique collider physics programme and success [25]. It was built in less than a decade
 137 and it operated for 16 years. Together with the Tevatron and LEP, HERA was pivotal to the
 138 development of the Standard Model. It established QCD as the correct description of proton
 139 substructure and parton dynamics down to 10^{-19} m. It demonstrated electroweak theory to
 140 hold in the newly accessed range, especially with the measurement of neutral and charged
 141 current ep scattering cross sections beyond $Q^2 \sim M_{W,Z}^2$ and with the proof of electroweak
 142 interference at high scales through the measurement of the interference structure functions $F_2^{\gamma Z}$
 143 and $xF_3^{\gamma Z}$. The HERA collider has been the basis of the physics of parton distributions, not only
 144 in providing the genuine base to measure longitudinal gluon, valence, light and heavy sea quark
 145 momentum distributions, but as well in supporting the foundation of the theory of unintegrated,
 146 diffractive, photon, neutron PDFs through a series of corresponding measurements. It discovered
 147 the rise of the parton distributions towards small momentum fractions x supporting early QCD
 148 expectations on the asymptotic behaviour of the structure functions [26]. Like the $p\bar{p}$ and e^+e^-
 149 colliders exploring the Fermi scale of a few hundred GeV energy, determined by the vacuum
 150 expectation value of the Higgs field, $v = 1/\sqrt{\sqrt{2}G_F} = 2M_W/g \simeq 246$ GeV, HERA showed that
 151 there was no SUSY or other exotic particle with reasonable couplings existing at Fermi energies.

152 HERA established electron-proton scattering as an integral part of modern high energy particle
 153 physics. It demonstrated the richness of DIS physics, and the feasibility of constructing and
 154 operating energy frontier ep colliders. What did we learn to take into a next higher energy ep
 155 collider design? Perhaps there were three lessons about

- 156 • *the need for higher energy*, for three reasons: i) to make charged currents a real, precision
 157 part of ep physics, for instance for the complete unfolding of the flavour composition of
 158 the sea and valence quarks, ii) to produce heavier mass particles (Higgs, top, exotics) with
 159 favourable cross sections and iii) in order to discover or disprove the existence of gluon
 160 saturation for which one needs to measure at lower $x \propto Q^2/s$ than HERA could;
- 161 • *the need for much higher luminosity*: the first almost ten years of HERA provided just a
 162 hundred pb^{-1} . As a consequence, HERA could not accurately access the high x region,
 163 and it was inefficient and short of statistics in resolving puzzling event fluctuations;
- 164 • *the complexity of the interaction region* when a bent electron beam caused synchrotron
 165 radiation while the opposite proton beam generated quite some halo background through
 166 beam-gas and beam-wall proton-ion interactions.

167 Based on these and further lessons, the LHeC design has been pursued recognising that the
 168 LHC is the only base to realise a TeV energy scale electron-hadron collider in the accessible
 169 future. It offers highly energetic, intense hadron beams, a long time perspective and a unique
 170 infrastructure and expertise, i.e. everything required for an energy frontier DIS physics and
 171 innovative accelerator programme.

172 **1.2 The Paper**

173 **1.2.1 The LHeC Physics Programme**

174 This paper presents a design concept of the LHeC, using a 50 GeV energy electron beam to
 175 be scattered off the LHC hadron beams (proton and ion) in concurrent operation. Its main
 176 characteristics are presented in **Chapter 2**. The instantaneous luminosity is designed to exceed
 177 that of HERA, which achieved a few times $10^{31} \text{ cm}^{-2}\text{s}^{-1}$, by a factor of several hundreds. The
 178 kinematic range nominally is extended by a factor of about 15, but in fact by a larger amount
 179 because of the hugely increased luminosity which is required to explore the maximum Q^2 and
 180 large $x \leq 1$ regions, which was a major deficiency of HERA. The coverage of the Q^2, x plane
 by previous and future DIS experiments is illustrated in Fig. 1.1.

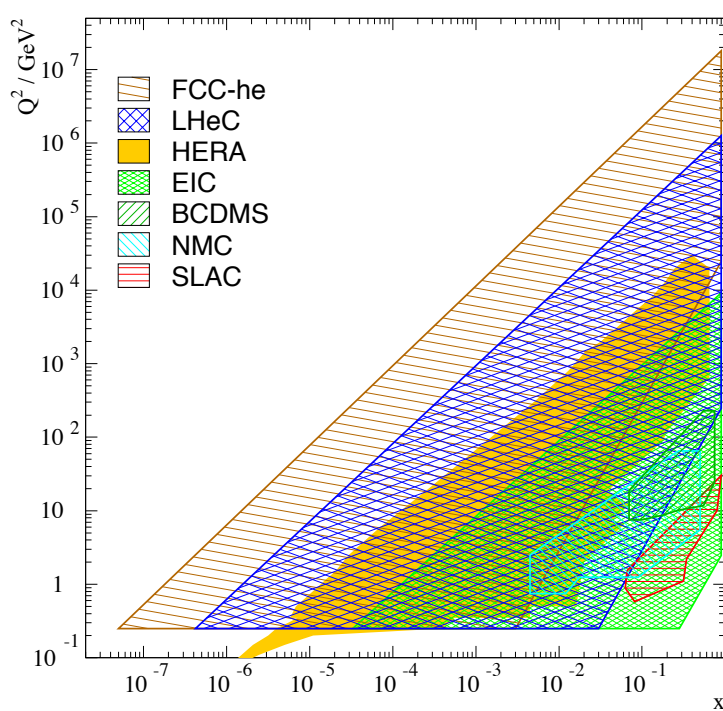


Figure 1.1: Coverage of the kinematic plane in DIS by some initial fixed target experiments with electrons (SLAC) and muons (NMS,BCDMS), by the future electron ion collider (EIC,green), HERA (yellow), the LHeC (blue) and the FCC-eh (brown). The low Q^2 region for the colliders is here limited to about 0.2 GeV^2 , which is covered by the central detectors, roughly and perhaps using low electron beam data. Electron taggers may extend this to even lower Q^2 . The high Q^2 limit is given by the line of inelasticity $y = 1$. Approximate limitations of acceptance at medium x , low Q^2 are drawn using polar angle limits of $\eta = -\ln \tan \theta/2$ of 4, 5, 6 for the EIC, LHeC, and FCC-eh, respectively. Since these lines are given by $x = \exp \eta \cdot \sqrt{Q^2}/2E_p$, it is clear that largest x values at low Q^2 are covered by the EIC (green area bottom, right).

181

182 The LHeC would provide a major extension of the kinematics as is adequate for a physics
 183 programme of the next DIS generation. For the LHC, the ep/A detector would be the fifth
 184 major experiment. Centred around different kinematic regions, a number of major themes
 185 would be developed as are discussed in quite some detail in this paper:

- 186 • Based on the unique hadron beams of the LHC and employing a point-like probe, the
187 LHeC would represent the world’s cleanest, high resolution microscope for exploring the
188 substructure of and dynamics inside matter, which may be termed the Hubble telescope for
189 the smallest dimensions. It would clarify the dynamics of parton interactions at small x as
190 is necessary for any future hadron collider, including the HL- LHC. The LHeC would chal-
191 lenge the SM to utmost precision in electroweak interactions, diffractive and top physics
192 (c.f. Chapter 3):
- 193 • The LHeC extends the kinematic range in lepton-nucleus scattering by nearly four orders
194 of magnitude. It so will transform nuclear particle physics completely, by establishing a
195 QCD base for Quark Gluon Plasma (QGP) phenomena and resolving the hitherto hidden
196 parton dynamics and substructure of nuclei (c.f. Chapter 4);
- 197 • The clean DIS final state in neutral and charged current scattering enables a high precision
198 Higgs physics programme with the LHeC. This delivers unique insight especially into the
199 $H - WW$ and $H - bb/cc$ couplings (c.f. Chapter 5);
- 200 • As a new, unique, luminous TeV scale collider, the LHeC has an outstanding opportunity
201 to discover new physics, such as in the exotic Higgs, dark matter, heavy neutrino and QCD
202 areas, which is presented in Chapter 6;
- 203 • With concurrent ep and pp operation, the LHeC would transform the LHC into a 3-
204 beam, twin-collider of greatly improved potential (c.f. Chapter 7). Through ultra-precise
205 strong and electroweak interaction measurements, the ep results would make the HL-
206 LHC complex a much more powerful search and measurement laboratory than current
207 expectations based on pp only could possibly entail. The joint pp/ep LHC facility can
208 become a Higgs factory of unprecedented impact as it challenges and complements what
209 e^+e^- promises.

210 The development of particle physics including and leading beyond DIS, the future of CERN, the
211 exploitation of the unprecedented LHC investments, the culture of accelerator art, all make the
212 LHeC a project of singular interest with the advantage of being realistic in terms of technology,
213 time and budget constraints.

214 1.2.2 The Accelerator

215 The LHeC should provide an intense, high energy electron beam to collide with the LHC.
216 The intensity is gauged through the integrated luminosity goal of $\mathcal{O}(1)\text{ab}^{-1}$. The electron
217 beam energy is chosen to achieve a TeV energy collision and enable competitive searches and
218 Higgs boson measurements. A cost-physics-energy evaluation is presented here which points
219 to choosing $E_e \geq 50\text{ GeV}$ as the default value. The wall plug power of the default design [1]
220 had been constrained to 100 MW. In that configuration two super-conducting linacs, opposite
221 to each other, accelerate the passing electrons by 8.3 GeV to 10 GeV each. This leads to a final
222 electron beam energy of about 50 GeV in a 3-turn racetrack configuration. For measuring at
223 very low Q^2 and/or determining F_L , see below, the electron beam energy may be reduced to
224 a minimum of perhaps 20 GeV. For maximising the acceptance at large Bjorken x , the proton
225 beam energy, E_p , may be reduced to 1 TeV about. If the ERL may be combined in the further
226 future with the double energy HE-LHC [27], E_p could reach 14 TeV. One therefore considers a
227 DIS scattering complex with an energy range between $\sqrt{s} \simeq 300$ to 1800 GeV. It thus covers
228 an energy range from HERA to the TeV region, at hugely increased luminosity and much more
229 sophisticated experimental techniques.

230 The ERL beam configuration is located inside the LHC ring but outside its tunnel, which
231 minimises any interference with the main hadron beam infrastructure. The electron accelerator
232 may thus be built independently, to a considerable extent, of the status of operation of the
233 proton machine.

234 The chosen energy of 50 GeV leads to a circumference U of the electron racetrack of 5.4 km,
235 smaller than the SPS. This length is a fraction $1/n$ of the LHC circumference, for $n = 5$, as
236 is required for the e and p matching of bunch patterns. It is chosen also in order to limit the
237 energy loss in the last return arc and as a result of a cost optimisation between the fractions of
238 the circumference covered by SRF and by return arcs. That configuration is adopted also as the
239 default for the FCC-he.

240 For the LHC, the ERL would be tangential to IP2 which, according to the current plans, is
241 taken by the ALICE detector until the first long shutdown following the three year pause of
242 the LHC operation for upgrading the luminosity performance and detectors. This shutdown
243 is termed LS4 and is scheduled to start in 2031. For FCC-he the preferred position is IP L
244 for geological reasons mainly, and the time of operation fully depending on the progress with
245 FCC-hh, beginning at the earliest in 2050.

246 The LHeC operation is transparent to the LHC collider experiments owing to the low lepton
247 bunch charge and resulting small beam-beam tune shift experienced by the protons. The LHeC
248 is thus designed to run simultaneously with pp (or pA or AA) collisions with a dedicated final
249 operation of a few years.

250 The paper presents in considerable detail the design of the LHeC (c.f. Chapter 8), i.e. the optics
251 and lattice, components, magnets, as well as designs of the linac and interaction region besides
252 special topics such as the prospects for electron-ion scattering, positron-proton operation and
253 a novel analysis of beam-beam interaction effects. With the more ambitious luminosity goal, a
254 new lattice for the new default energy of 50 GeV, with progress on the IR design, a novel analysis
255 of the civil engineering work and especially the production and successful test [28] of the first SC
256 cavity, at the newly chosen default frequency of 801.58 MHz, this report considerably extends
257 beyond the initial CDR. Large progress has been made in the development of superconducting,
258 high gradient cavities with quality factors beyond 10^{10} . This will enable the exploitation of ERLs
259 in high-energy physics colliders, with the LHeC as the prime example, while considerations are
260 also brought forward for future e^+e^- colliders [29].

261 1.2.3 PERLE

262 The status and challenges of ERLs are summarised in Chapter 9. This also presents the design,
263 status and prospects for the ERL development facility PERLE. The major parameters of PERLE
264 have been taken from the LHeC, such as the 3-turn configuration, source, frequency and cavity-
265 cryomodule technology, in order to make PERLE a suitable facility for the development of LHeC
266 ERL technology and the accumulation of operating experience prior to and later in parallel with
267 the LHeC. An international collaboration has been invited to build PERLE at Orsay. With
268 the design goals of 500 MeV electron energy obtained in three passes through two cryo-modules
269 and of 20 mA, corresponding to 500 nC charge at 40 MHz bunch frequency, PERLE is set to
270 become the first ERL facility to operate at 10 MW power. Following its CDR [4] and a paper
271 submitted to the European strategy [8], work is directed to build a first dressed cavity and to
272 release a TDR by 2021. Besides its interest in accelerator and ERL technology, PERLE is also
273 of importance for pursuing a low energy physics programme, see [4], and for several possible
274 industrial applications. It also serves as a local hub for the education of accelerator physicists

275 at a place, previously called Linear Accelerator Laboratory (LAL), which has long been at the
276 forefront of accelerator design and operation.

277 The realisation of the ERL for the LHeC at CERN represents a unique opportunity not only for
278 physics and technology but as well for a next and the current generation of accelerator physi-
279 cists, engineers and technicians to realise an ambitious collider project while the plans for very
280 expensive next machines may take shape. Similarly, this holds for a new generation of detector
281 experts, as the design of the upgrade of the general purpose detectors (GPDs) at the LHC is
282 reaching completion and the question increasingly posed about opportunities for new collider
283 detector construction to not lose the expertise nor the infrastructure for building trackers,
284 calorimeters and alike. The LHeC offers the opportunity for a novel 4π particle physics detector
285 design, construction and operation. As a linac-ring accelerator, it may serve one detector of a
286 size smaller than CMS and larger than H1.

287 1.2.4 The Detector

288 Chapter 10 on the detector relies to a large extent on the very detailed write-up on the kinematics,
289 design considerations, and realisation of a detector for the LHeC as was presented in the CDR [1].
290 In the previous report one finds detailed studies not only on the central detector and its magnets,
291 a central solenoid for momentum measurements and an extended dipole for ensuring head-on ep
292 collisions, but as well on the forward (p and n) and backward (e and γ) tagging devices. The
293 work on the detector as presented here was focussed on an optimisation of the performance and
294 on the scaling of the design towards higher proton beam energies. It presents a new, consistent
295 design and summaries of the essential characteristics in support of many physics analyses this
296 paper entails.

297 The most demanding performance requirements arise from the ep Higgs measurement pro-
298 gramme, especially the large acceptance and high precision desirable for heavy flavour tagging
299 and the wish to resolve the hadronic final states completely. This has been influenced by the
300 acceptance ambitions and the technology progress of the HL-LHC detector upgrades, a key ex-
301 ample being the high granularity and low material prospects of HV-CMOS Silicon technology,
302 which is here sketched also.

303 Therefore we have now completed two studies of design: previously, of a rather conventional de-
304 tector with limited cost and, here, of a more ambitious device. Both of these, perhaps, extremes
305 appear realisable. This regards also the installation. The paper presents a brief description of
306 the installation of the LHeC detector at IP2 with the result that it may proceed within two
307 years, including the dismantling of the then residing detector. This calls for modularity and
308 pre-mounting of detector elements on the surface, as was done for CMS too. It will be for the
309 LHeC detector Collaboration, to be established with and for the approval of the project, to
310 design the detector according to its understanding and technical capabilities.

311 Subsequently follow the chapters as mentioned above: Chapter 2 summarises the LHeC charac-
312 teristics. Chapter 3 presents key topics on how the SM will be developed and tested through
313 high precision measurements in the PDF, strong, electroweak and top physics sector, with a
314 section on novel QCD phenomena to be found. Ample space is given to the question of parton
315 saturation at small x . Chapter 4 presents the unique potential of the LHeC to advance nuclear
316 particle physics with its far reaching, luminous electron-ion scattering programme. Chapter 5
317 presents a detailed analysis of the opportunity for precision SM Higgs boson physics with CC

318 and NC ep scattering. Chapter 6 is a description of the striking variety of opportunities to
319 discover physics beyond the Standard Model with the LHeC, including non-SM Higgs physics,
320 right-handed neutrinos, physics of the dark sector or heavy resonances. Chapter 7 describes the
321 interplay of ep and pp physics, i.e. the necessity to have the LHeC in order to fully exploit the
322 search and measurement potential of the LHC facility. Chapter 8 presents the update of the
323 CDR on the ERL configuration with many novel results as on the lattice and interaction region
324 design, besides new specifications of components. It also presents the very encouraging results of
325 the first LHeC 802 MHz cavity. Chapter 9 is devoted, first, to the status and challenges of energy
326 recovery based accelerators and, second, to the description of the PERLE facility, between its
327 CDR and a forthcoming TDR. Chapter 10 describes the update of the detector study towards an
328 optimum configuration in terms of acceptance and performance. Chapter 11 presents a summary
329 of the paper including a time line for realising the LHeC to operate with the LHC.

Chapter 2

LHeC Configuration and Parameters

2.1 Introduction

The Conceptual Design Report (CDR) of the LHeC was published in 2012 [1]. The CDR default configuration uses a 60 GeV energy electron beam derived from a racetrack, three-turn, intense energy recovery linac (ERL) achieving a cms energy of $\sqrt{s} = 1.3 \text{ TeV}$, where $s = 4E_p E_e$ is determined by the electron and proton beam energies, E_e and E_p . In 2012, the Higgs boson, H , was discovered which has become a central topic of current and future high energy physics. The Higgs production cross section in charged current (CC) deep inelastic scattering (DIS) at the LHeC is roughly 100 fb. The Large Hadron Collider has so far not led to the discovery of any exotic phenomenon. This forces searches to be pursued, in pp but as well in ep , with the highest achievable precision in order to access a maximum range of phase space and possibly rare channels. The DIS cross section at large x roughly behaves like $(1-x)^3/Q^4$, demanding very high luminosities for exploiting the unknown regions of Bjorken x near 1 and very high Q^2 , the negative four-momentum transfer squared between the electron and the proton. For the current update of the design of the LHeC this has set a luminosity goal about an order of magnitude higher than the $10^{33} \text{ cm}^{-2}\text{s}^{-1}$ which had been adopted for the CDR. There arises the potential, as described subsequently in this paper, to transform the LHC into a high precision electroweak, Higgs and top quark physics facility.

The ep Higgs production cross section rises approximately with E_e . New physics may be related to the heaviest known elementary particle, the top quark, the ep production cross section of which rises more strongly than linearly with E_e in the LHeC kinematic range as that is not very far from the $t\bar{t}$ threshold. Searches for heavy neutrinos, SUSY particles, etc. are the more promising the higher the energy is. The region of deep inelastic scattering and pQCD requires that Q^2 be larger than $M_p^2 \simeq 1 \text{ GeV}^2$. Access with DIS to very low Bjorken x requires high energies because of $x = Q^2/s$, for inelasticity $y = 1$. In DIS, one needs $Q^2 > M_p^2 \simeq 1 \text{ GeV}^2$. Physics therefore requires a maximally large energy. However, cost and effort set realistic limits such that twice the HERA electron beam energy, of about 27 GeV, appeared as a reasonable and affordable target value.

In the CDR [1] the default electron energy was chosen to be 60 GeV. This can be achieved with an ERL circumference of 1/3 of that of the LHC. Recently, the cost was estimated in quite some detail [30], comparing also with other accelerator projects. Aiming at a cost optimisation and providing an option for a staged installation, the cost estimate lead to defining a new default configuration of $E_e = 50 \text{ GeV}$ with the option of starting in an initial phase with a beam energy

364 of $E_e = 30$ GeV and a circumference of 5.4 km which is 1/5 of the LHC length. Lowering
 365 E_e is also advantageous for mastering the synchrotron radiation challenges in the interaction
 366 region. Naturally, the decision on E_e is not taken now. This paper comprises studies with
 367 different energy configurations, mainly $E_e = 50$ and 60 GeV, which are close in their centre of
 368 mass energy values of 1.2 and 1.3 TeV, respectively.

369 Up to beam energies of about 60 GeV, the ERL cost is dominated by the cost for the supercon-
 370 ducting RF of the linacs. Up to this energy the ERL cost scales approximately linearly with the
 371 beam energy. Above this energy the return arcs represent the main contribution to the cost and
 372 to the ERL cost scaling is no longer linear. Given the non-linear dependence of the cost on E_e ,
 373 for energies larger than about 60 GeV, significantly larger electron beam energy values may only
 374 be justified by overriding arguments, such as, for example, the existence of leptoquarks ¹. Higher
 375 values of \sqrt{s} are also provided with enlarged proton beam energies by the High Energy LHC
 376 ($E_p = 13.5$ TeV) [27] and the FCC-hh [14] with E_p between 20 and possibly 75 TeV, depending
 377 on the dipole magnet technology.

378 2.2 Cost Estimate, Default Configuration and Staging

379 In 2018 a detailed cost estimate was carried out [30] following the guidance and practice of
 380 CERN accelerator studies. The assumptions were also compared with the DESY XFEL cost.
 381 The result was that for the 60 GeV configuration about half of the total cost was due to the two
 382 SC linacs. The cost of the arcs decreases more strongly than linearly with decreasing energy,
 383 about $\propto E^4$ for synchrotron radiation losses and $\propto E^3$ when emittance dilution is required to be
 384 avoided [31]. It was therefore considered to set a new default of 50 GeV with a circumference of
 385 1/5 of that of the LHC, see Sect. 2.3, compared to 1/3 for 60 GeV. Furthermore, an initial phase
 386 at 30 GeV was considered, within the 1/5 configuration but with only partially equipped linacs.
 387 The HERA electron beam energy was 27 GeV. The main results, taken from [30] are reproduced
 388 in Tab. 2.1.

389 The choice of a default of 50 GeV at 1/5 of the LHC circumference results, as displayed, in
 390 a total cost of 1,075 MCHF for the initial 30 GeV configuration and an additional, upgrade
 391 cost to 50 GeV of 296 MCHF. If one restricted the LHeC to a non-upgradeable 30 GeV only
 392 configuration one would, still in a triple racetrack configuration, come to roughly a 1 km long
 393 structure with two linacs of about 500 m length, probably in a single linac tunnel configuration.
 394 The cost of this version of the LHeC is roughly 800 MSF, i.e. about half the 60 GeV estimated
 395 cost. However, this would essentially reduce the LHeC to a QCD and electroweak machine, still
 396 very powerful but accepting substantial losses in its Higgs, top and BSM programme.

397 A detailed study was made on the cost of the civil engineering, which is also discussed subse-
 398 quently. This concerned a comparison of the 1/3 vs the 1/5 LHC circumference versions, and
 399 the FCC-eh. The result is illustrated in Fig. 2.1. It shows that the CE cost for the 1/5 version is
 400 about a quarter of the total cost. The reduction from 1/3 to 1/5 economises about 100 MCHF.

401 Choices of the final energy will be made later. They depend not only on a budget but also on the
 402 future development of particle physics at large. For example, it may turn out that, for some years

¹If these existed with a mass of say $M = 1.5$ TeV this would require, at the LHC with $E_p = 7$ TeV, to
 choose E_e to be larger than 90 GeV, and to pay for it. Leptoquarks would be produced by ep fusion and appear as
 resonances, much like the Z boson in e^+e^- and would therefore fix E_e (given certain E_p which at the FCC exceeds
 7 TeV). The genuine DIS kinematics, however, is spacelike, the exchanged four-momentum squared $q^2 = -Q^2$
 being negative, which implies that the choice of the energies is less constrained than in an e^+e^- collider aiming
 at the study of the Z or H bosons.

Component	CDR 2012 (60 GeV)	Stage 1 (30 GeV)	Default (50 GeV)
SRF System	805	402	670
SRF R+D and Prototyping	31	31	31
Injector	40	40	40
Arc Magnets and Vacuum	215	103	103
SC IR Magnets	105	105	105
Source and Dump System	5	5	5
Cryogenic Infrastructure	100	41	69
General Infrastructure and Installation	69	58	58
Civil Engineering	386	289	289
Total Cost	1756	1075	1371

Table 2.1: Summary of cost estimates, in MCHF, from [30]. The 60 GeV configuration is built with a 9 km triple racetrack configuration as was considered in the CDR [1]. It is taken as the default configuration for FCC-eh, with an additional CE cost of 40 MCHF due to the larger depth on point L (FCC) as compared to IP2 (LHC). Both the 30 and the 50 GeV assume a 5.4 km configuration, i.e. the 30 GeV is assumed to be a first stage of LHeC upgradeable to 50 GeV ERL. Whenever a choice was to be made on estimates, in [30] the conservative number was chosen.

403 into the future, the community may not find the $\mathcal{O}(10)$ GCHF required to build any of the e^+e^-
404 colliders currently considered. Then the only way to improve on the Higgs measurements beyond
405 HL-LHC substantially is the high energy (50 – 60 GeV), high luminosity ($\int L = 1 \text{ ab}^{-1}$) LHeC.
406 Obviously, physics and cost are intimately related. Based on such considerations, but also taking
407 into account technical constraints as resulting from the amount of synchrotron radiation losses
408 in the interaction region and the arcs, we have chosen 50 GeV in a 1/5 of U(LHC) configuration
409 as the new default. This economises about 400 MCHF as compared to the CDR configuration.

410 If the LHeC ERL were built, it may later be transferred, with some reconfiguration and upgrades,
411 to the FCC to serve as the FCC-eh. The FCC-eh has its own location, L, for the ERL which
412 requires a new accelerator tunnel. It has been decided to keep the 60 GeV configuration for the
413 FCC, as described in the recently published CDR of the FCC [14]. The LHeC ERL configuration
414 may also be used as a top-up injector for the Z and possibly WW phase of the FCC-e should
415 the FCC-ee indeed precede the FCC-hh/eh phase.

416 2.3 Configuration Parameters

417 A possible transition from the 60 GeV to the 50 GeV configuration of the LHeC was already
418 envisaged in 2018, as considered in the paper submitted to the European Strategy [6]. The
419 machine layout shown in that paper is reproduced in Fig. 2.2. It is a rough sketch illustrating
420 the reduction from a 60 GeV to a 50 GeV configuration, which results not only in a reduction of
421 capital costs, as discussed above, but also of effort.

422 The ERL configuration has been recently revisited [31] considering its dependence on the electron
423 beam energy. Applying a dimension scaling which preserves the emittance dilution, the results
424 have been obtained as are summarised in Tab. 2.2. The 1/5 configuration is chosen as the new
425 LHeC default while the CDR on the LHeC from 2012 and the recent CDR on FCC-eh have used
426 the 1/3 configuration. The energy and configuration may be decided as physics, cost and effort
427 dictate, once a decision is taken.

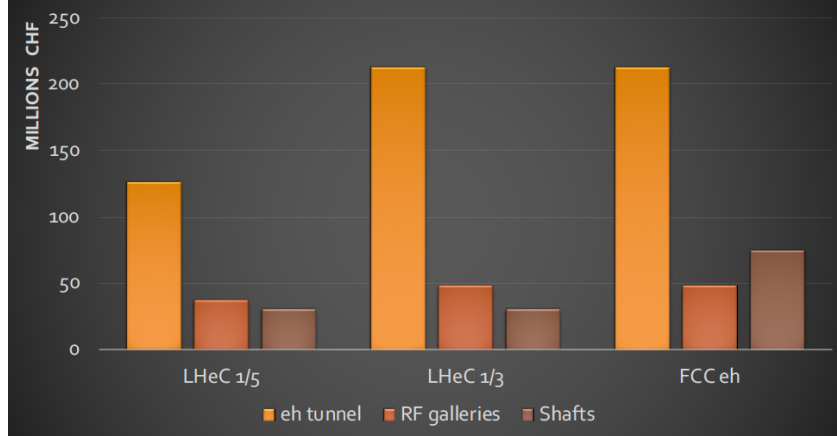


Figure 2.1: Cost estimate for the civil engineering work for the tunnel, rf galleries and shafts for the LHeC at 1/5 of the LHC circumference (left), at 1/3 (middle) and the FCC-eh (right). The unit costs and percentages are consistent with FCC and CLIC unit prices. The estimate is considered reliable to 30%. The cost estimates include: Site investigations: 2%, Preliminary design, tender documents and project changes: 12% and the Contractors profit: 3%. Surface site work is not included, which for LHeC exists with IP2.

Parameter	Unit	LHeC option			
		1/3 LHC	1/4 LHC	1/5 LHC	1/6 LHC
Circumference	m	9000	6750	5332	4500
Arc radius	$m \cdot 2\pi$	1058	737	536	427
Linac length	$m \cdot 2$	1025	909	829	758
Spreader and recombiner length	$m \cdot 4$	76	76	76	76
Electron energy	GeV	61.1	54.2	49.1	45.2

Table 2.2: Scaling of the electron beam energy, linac and further accelerator element dimensions with the choice of the total circumference in units $1/n$ of the LHC circumference. For comparison, the CERN SPS has a circumference of 6.9 km, only somewhat larger than 1/4 of that of the LHC.

428 2.4 Luminosity

429 The luminosity L for the LHeC in its linac-ring configuration is determined as

$$L = \frac{N_e N_p n_p f_{rev} \gamma_p}{4\pi \epsilon_p \beta^*} \cdot \prod_{i=1}^3 H_i, \quad (2.1)$$

430 where $N_{e(p)}$ is the number of electrons (protons) per bunch, n_p the number of proton bunches
431 in the LHC, f_{rev} the revolution frequency in the LHC [the bunch spacing in a batch is given
432 by Δ , equal to 25 ns for protons in the LHC] and γ_p the relativistic factor E_p/M_p of the proton
433 beam. Further, ϵ_p denotes the normalised proton transverse beam emittance and β^* the proton
434 beta function at the IP, assumed to be equal in x and y . The luminosity is moderated by the
435 hourglass factor, $H_1 = H_{geo} \simeq 0.9$, the pinch or beam-beam correction factor, $H_2 = H_{b-b} \simeq 1.3$,
436 and the filling factor $H_3 = H_{coll} \simeq 0.8$, should an ion clearing gap in the electron beam be
437 required. This justifies taking the product of these factors. As the product is close to unity, the
438 factors are not listed for simplicity in the subsequent tables.

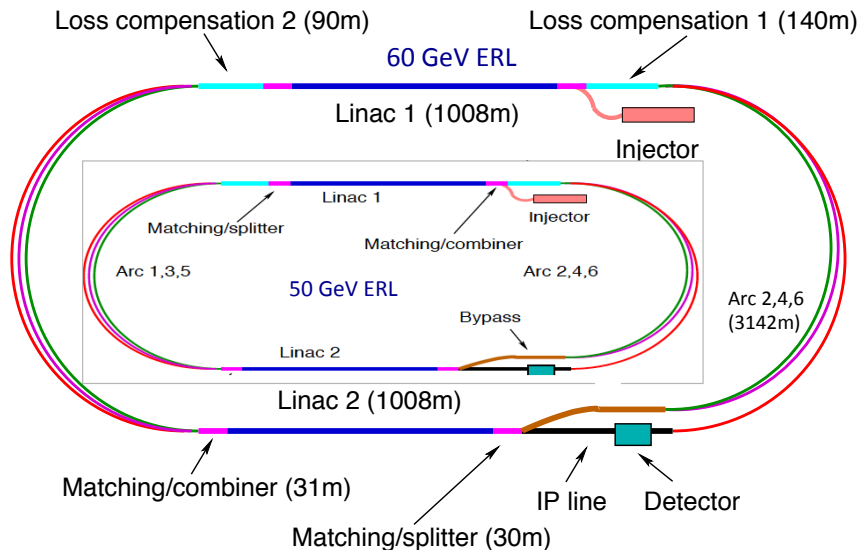


Figure 2.2: Schematic view of the three-turn LHeC configuration with two oppositely positioned electron linacs and three arcs housed in the same tunnel. Two configurations are shown: Outer: Default $E_e = 60$ GeV with linacs of about 1 km length and 1 km arc radius leading to an ERL circumference of about 9 km, or 1/3 of the LHC length. Inner: Sketch for $E_e = 50$ GeV with linacs of about 0.8 km length and 0.55 km arc radius leading to an ERL circumference of 5.4 km, or 1/5 of the LHC length, which is smaller than the size of the SPS. The 1/5 circumference configuration is flexible: it entails the possibility to stage the project as funds of physics dictate by using only partially equipped linacs, and it also permits upgrading to somewhat higher energies if one admits increased synchrotron power losses and operates at higher gradients.

439 The electron beam current is given as

$$I_e = eN_e f, \quad (2.2)$$

440 where f is the bunch frequency $1/\Delta$. The current for the LHeC is limited by the charge delivery
 441 of the source. In the new default design we have $I_e = 20$ mA which results from a charge of
 442 500 pC for the bunch frequency of 40 MHz. It is one of the tasks of the PERLE facility to
 443 investigate the stability of the 3-turn ERL configuration in view of the challenge for each cavity
 444 to hold the sixfold current due to the simultaneous acceleration and deceleration of bunches at
 445 three different beam energies each.

446 2.4.1 Electron-Proton Collisions

447 The design parameters of the luminosity were recently provided in a note describing the FCC-eh
 448 configuration [32], including the LHeC. Tab. 2.3 represents an update comprising in addition
 449 the initial 30 GeV configuration and the lower energy version of the FCC-hh based on the LHC
 450 magnets². For the LHeC, as noted above, we assume $E_e = 50$ GeV while for FCC-eh we retain
 451 60 GeV. Since the source limits the electron current, the peak luminosity may be taken not to

² The low energy FCC-pp collider, as of today, uses a 6 T LHC magnet in a 100 km tunnel. If, sometime in the coming decades, high field magnets become available based on HTS technology, then a 20 TeV proton beam energy may even be achievable in the LHC tunnel. To this extent the low energy FCC considered here and an HTS based HE-LHC would be comparable options in terms of their energy reach.

452 depend on E_e . Studies of the interaction region design, presented in this paper, show that one
 453 may be confident of reaching a β^* of 10 cm but it will be a challenge to reach even smaller values.
 454 Similarly, it will be quite a challenge to operate with a current much beyond 20 mA. That has
 455 nevertheless been considered [33] for a possible dedicated LHeC operation mode for a few years
 following the pp operation program.

Parameter	Unit	LHeC				FCC-eh	
		CDR	Run 5	Run 6	Dedicated	$E_p=20$ TeV	$E_p=50$ TeV
E_e	GeV	60	30	50	50	60	60
N_p	10^{11}	1.7	2.2	2.2	2.2	1	1
ϵ_p	μm	3.7	2.5	2.5	2.5	2.2	2.2
I_e	mA	6.4	15	20	50	20	20
N_e	10^9	1	2.3	3.1	7.8	3.1	3.1
β^*	cm	10	10	7	7	12	15
Luminosity	$10^{33} \text{ cm}^{-2}\text{s}^{-1}$	1	5	9	23	8	15

Table 2.3: Summary of luminosity parameter values for the LHeC and FCC-eh. Left: CDR from 2012; Middle: LHeC in three stages, an initial run, possibly during Run 5 of the LHC, the 50 GeV operation during Run 6, both concurrently with the LHC, and a final, dedicated, stand-alone ep phase; Right: FCC-eh with a 20 and a 50 TeV proton beam, in synchronous operation.

456

457 The peak luminosity values exceed those at HERA by 2–3 orders of magnitude. The operation
 458 of HERA in its first, extended running period, 1992-2000, provided an integrated luminosity
 459 of about 0.1 fb^{-1} for the collider experiments H1 and ZEUS. This may now be expected to be
 460 taken in a day of initial LHeC operation.

461 2.4.2 Electron-Ion Collisions

462 The design parameters and luminosity were also provided recently [32] for collisions of electrons
 463 and lead nuclei (fully stripped $^{208}\text{Pb}^{82+}$ ions). Tab. 2.4 is an update of the numbers presented
 464 there for consistency with the Run 6 LHeC configuration in Tab. 2.3 and with the addition
 465 of parameters corresponding to the $E_p = 20$ TeV FCC-hh configuration. Further discussion of
 466 this operating mode and motivations for the parameter choices in this table are provided in
 467 Section 8.3.

468 One can expect the average luminosity during fills to be about 50% of the peak in Tab. 2.4
 469 and we assume an overall operational efficiency of 50%. Then, a year of eA operation, possibly
 470 composed by combining shorter periods of operation, would have the potential to provide an
 471 integrated data set of about 5 (25) fb^{-1} for the LHeC (FCC-eh), respectively. This exceeds
 472 the HERA electron-proton luminosity value by about tenfold for the LHeC and much more at
 473 FCC-eh while the fixed target nuclear DIS experiment kinematics is extended by 3 – 4 orders of
 474 magnitude. These energy frontier electron-ion configurations therefore have the unique potential
 475 to radically modify our present view of nuclear structure and parton dynamics. This is discussed
 476 in Chapter 4.

Parameter	Unit	LHeC	FCC-eh ($E_p=20$ TeV)	FCC-eh ($E_p=50$ TeV)
Ion energy E_{Pb}	PeV	0.574	1.64	4.1
Ion energy/nucleon E_{Pb}/A	TeV	2.76	7.88	19.7
Electron beam energy E_e	GeV	50	60	60
Electron-nucleon CMS $\sqrt{s_{eN}}$	TeV	0.74	1.4	2.2
Bunch spacing	ns	50	100	100
Number of bunches		1200	2072	2072
Ions per bunch	10^8	1.8	1.8	1.8
Normalised emittance ϵ_n	μm	1.5	1.5	1.5
Electrons per bunch	10^9	6.2	6.2	6.2
Electron current	mA	20	20	20
IP beta function β_A^*	cm	10	10	15
e-N Luminosity	$10^{32}\text{cm}^{-2}\text{s}^{-1}$	7	14	35

Table 2.4: Baseline parameters of future electron-ion collider configurations based on the electron ERL, in concurrent eA and AA operation mode with the LHC and the two versions of a future hadron collider at CERN. Following established convention in this field, the luminosity quoted, at the start of a fill, is the *electron-nucleon* luminosity which is a factor A larger than the usual (i.e. electron-nucleus) luminosity.

477 2.5 Linac Parameters

478 The brief summary of the main LHeC characteristics here concludes with a table of the main
479 ERL parameters for the new default electron energy of 50 GeV, Tab. 2.5, which are discussed in detail in Chapter 8.

Parameter	Unit	Value
Frequency	MHz	801.58
Bunch charge	pC	499
Bunch spacing	ns	24.95
Electron current	mA	20
Injector energy	MeV	500
Gradient	MV/m	19.73
Cavity length, active	m	0.918
Cavity length, flange-to-flange	m	1.5
Cavities per cryomodule		4
Length of cryomodule	m	7
Acceleration per cryomodule	MeV	72.45
Total number of cryomodules		112
Acceleration energy per pass	GeV	8.1

Table 2.5: Basic LHeC ERL characteristics for the default configuration using two such linacs located opposite to each other in a racetrack of 5.4 km length. Each linac is passed three times for acceleration and three times for deceleration.

480

481 2.6 Operation Schedule

482 The LHeC parameters are determined to be compatible with a parasitic operation with the
483 nominal HL-LHC proton-proton operation. This implies limiting the electron bunch current to

484 sufficiently small values so that the proton beam-beam parameter remains small enough to be
485 negligible for the proton beam dynamics.

486 Assuming a ten year construction period for the LHeC after approval of the project and a
487 required installation window of two years for the LHeC detector, the earliest realistic operation
488 period for the LHeC coincides with the LHC Run 5 period in 2032 and with a detector installation
489 during LS4 which is currently scheduled during 2030 and would need to be extended by one year
490 to 2031. The baseline HL-LHC operation mode assumes 160 days of proton operation, 20 days
491 of ion operation and 20 days of machine development time for the Run4 period, amounting to
492 a total of 200 operation days per year. After the Run4 period the HL-LHC does at the moment
493 not consider ion operation and assumes 190 days for proton operation. The HL-LHC project
494 assumes an overall machine efficiency of 54 % (e.g. fraction of scheduled operation time spent in
495 physics production) and we assume that the ERL does not contribute to significant additional
496 downtime for the operation. Assuming an initial 15 mA of electron beam current, a β^* of 10 cm
497 and HL-LHC proton beam parameters, the LHeC reaches a peak luminosity of $0.5 \cdot 10^{34} \text{cm}^{-2} \text{s}^{-1}$.
498 Assuming further a proton beam lifetime of 16.7 hours, a proton fill length of 11.7 hours and an
499 average proton beam turnaround time of 4 hours, the LHeC can reach in this configuration an
500 annual integrated luminosity of 20fb^{-1} .

501 For the evaluation of the physics potential it is important to note that the Run5 initial ep
502 operation period may accumulate about 50fb^{-1} of integrated luminosity. This is the hundredfold
503 value which H1 (or ZEUS) took over a HERA lifetime of 15 years. As one may expect, for details
504 see Chapter 3, such a huge DIS luminosity is ample for pursuing basically the complete QCD
505 programme. In particular, the LHeC would deliver on time for the HL-LHC precision analyses
506 the external, precise PDFs and with just a fraction of the 50fb^{-1} the secrets of low x parton
507 dynamics would unfold. Higher ep luminosity is necessary for ultimate precision and for the top,
508 BSM and the Higgs programme of the LHeC to be of competitive value.

509 For the Run6 period of the HL-LHC, the last of the HL-LHC operation periods, we assume
510 that the number of machine development sessions for the LHC can be suppressed, providing
511 an increase in the operation time for physics production from 190 days to 200 days per year.
512 Furthermore, we assume that the electron beam parameters can be slightly further pushed.
513 Assuming a β^* reduced to 7 cm, an electron beam current of up to 25 mA and still nominal
514 HL-LHC proton beam parameters, the LHeC reaches a peak performance of $1.2 \cdot 10^{34} \text{cm}^{-2} \text{s}^{-1}$
515 and an annual integrated luminosity of 50fb^{-1} . This would add up to an integrated luminosity
516 of a few hundred fb^{-1} , a strong base for top, BSM and Higgs physics at the LHeC.

517 Beyond the HL-LHC exploitation period, the electron beam parameters could be further pushed
518 in dedicated ep operation, when the requirement of a parasitic operation to the HL-LHC proton-
519 proton operation may no longer be imposed. The proton beam lifetime without proton-proton
520 collisions would be significantly larger than in the HL-LHC configuration. In the following we
521 assume a proton beam lifetime of 100 hours and a proton beam efficiency of 60 % without proton-
522 proton beam collisions. The electron beam current in this configuration would only be limited
523 by the electron beam dynamics and the SRF beam current limit. Assuming that electron beam
524 currents of up to 50 mA, the LHeC would reach a peak luminosity of $2.4 \cdot 10^{34} \text{cm}^{-2} \text{s}^{-1}$ and an
525 annual integrated luminosity of up to 180fb^{-1} . Table 2.6 summarises the LHeC configurations
526 over these three periods of operation.

527 Depending on the years available for a dedicated final operation (or through an extension of
528 the pp LHC run, currently not planned but interesting for collecting 4 instead of 3ab^{-1} to, for
529 example, observe di-Higgs production at the LHC), a total luminosity of 1ab^{-1} could be available
530 for the LHeC. This would double the precision of Higgs couplings measured in ep as compared to

Parameter	Unit	Run 5 Period	Run 6 Period	Dedicated
Brightness $N_p/(\gamma\epsilon_p)$	10^{17}m^{-1}	2.2/2.5	2.2/2.5	2.2/2.5
Electron beam current	mA	15	25	50?
Proton β^*	m	0.1	0.7	0.7
Peak luminosity	$10^{34}\text{cm}^{-2}\text{s}^{-1}$	0.5	1.2	2.4
Proton beam lifetime	h	16.7	16.7	100
Fill duration	h	11.7	11.7	21
Turnaround time	h	4	4	3
Overall efficiency	%	54	54	60
Physics time / year	days	160	180	185
Annual integrated lumi.	fb^{-1}	20	50	180

Table 2.6: The LHeC performance levels during different operation modes.

531 the default HL-LHC run period with ep added as described. It would also significantly enlarge
532 the potential to observe or/and quantify rare and new physics phenomena. Obviously such
533 considerations are subject to the grand developments at CERN. A period with most interesting
534 physics and on-site operation activity could be particularly welcome for narrowing a possible
535 large time gap between the LHC and its grand successor, the FCC-hh. One may, however, be
536 interested in ending LHC on time. It thus is important for the LHeC project to recognise its
537 particular value as an asset of the HL-LHC, and on its own, with even less than the ultimate
538 luminosity, albeit values which had been dreamt of at HERA.

Chapter 3

Precision Standard Model Physics with LHeC

3.1 Resolving the Parton Substructure of the Proton

3.1.1 Open Questions on the QCD of PDFs

The LHeC provides the opportunity to push our Standard Model (SM) measurements to unprecedented precision. This will allow stringent searches for deviations from the SM predictions which may signal the presence of undiscovered channels involving physics beyond the SM (BSM).

While direct production of BSM physics may be limited by the centre-of-mass (CoM) energy (\sqrt{s}) of the machine, indirect precision measurements can probe scales many times larger than the CoM energy; this is an area where the LHeC excels. While the LHeC can directly probe the TeV scale, it offers the most promising avenue to search for BSM physics signals at multi-TeV scales, gathering clues as how to design the next-generation of accelerator experiments such as the FCC program.

An essential step in advancing this precision program is improving our knowledge of the Parton Distribution Functions (PDFs). For many precision measurements and *standard-candle* observables, a dominant systematic limitation on our sensitivity to the highest energy scales is the PDF uncertainty, as well as uncertainties on a number of related hadron structure observables. PDF uncertainty reductions therefore have the potential to greatly extend the sensitivity of collider-based BSM physics searches, both in terms of the interaction strengths and effective masses of hypothetical degrees-of-freedom. For this reason, the LHeC can be expected to have a sizeable impact on BSM searches, both through possible direct sensitivity to various conjectured BSM processes, as well as by helping to relieve PDF limitations of BSM searches at the HL-LHC and other facilities.

Aside from impacts on BSM searches, explorations of PDFs at the LHeC would be instrumental in disentangling many fundamental issues in QCD and the structure of hadrons and nuclei, for which many open questions remain. For example, the detailed flavour structure of the nucleon remains imperfectly determined, with very large uncertainties in the magnitude and shape of the proton's strangeness content as well as the exact nature of flavour-symmetry breaking in the light-quark sea (e.g. the behaviour of the PDF ratio \bar{d}/\bar{u}) being representative examples. The precision and kinematic reach of the LHeC will allow it to significantly clarify these issues, as

570 well as related ones that must be addressed in the push for high-precision nucleon PDFs, such as
571 the nature and size of quark-level charge-symmetry violation [34]. The very high luminosity of
572 the LHeC and the comparative phenomenological *cleanliness* of the lepton-nucleon DIS process
573 could also play a pivotal role in unraveling some of the systematic tensions among data sets
574 fitted in modern PDF analyses, which can be an impediment to higher PDF precision.

575 In another instance, the increased energy and luminosity of the LHeC will also enable explo-
576 rations of extreme regions in the kinematic (x, Q) plane to study new QCD phenomena. These
577 include the rise of the proton's inclusive DIS structure function F_2^p at low x , which may suggest
578 the onset of parton saturation and point to new contributions which are not included in the
579 DGLAP framework of leading-twist linear evolution equations. Here, the LHeC can offer us a
580 glimpse of the high-density regime of QCD where we can study collective effects and test/refine
581 our theoretical resummation tools.

582 The measurement of heavy-quark production at the LHeC will be especially important to im-
583 prove our knowledge of the gluon, strange, charm and bottom PDFs. The challenge is that the
584 computation of heavy-quark production in the framework of perturbative QCD is complicated
585 due to the presence of several large scales like the heavy-quark masses, m_Q , the transverse mo-
586 mentum, p_T , of the produced quarks, and the momentum transfer, Q^2 . In this case, the large
587 kinematic reach of the LHeC will be extremely advantageous as the span from the low-energy
588 *decoupling* region into the high-energy *asymptotic* region will allow improved understanding of
589 the treatment of mass in perturbative QCD calculations.

590 We point out that analogous questions to these (and others) apply to nuclear PDFs, for which
591 experimental constraints are far more limited at the present time. While the question of LHeC
592 impacts on the nuclear PDFs will be addressed in Chapter 4, we stress that improved knowl-
593 edge of nuclear-medium effects and nuclear PDFs that LHeC might furnish could substantially
594 improve free-nucleon PDFs, for which contemporary attempts to separate the PDF flavour
595 dependence often involve measurements on nuclear targets. Also, when measuring more com-
596 plicated hadronic final states, the LHeC might also provide information sensitive to the PDFs
597 of other hadrons, including the lighter mesons, which would shed light on aspects of QCD.

598 In this Section, we will explore specific processes by which the LHeC can significantly improve
599 our determination of PDFs.

600 **3.1.2 PDFs and the LHC**

601 **Prospects with the HL-LHC**

602 The particle physics community is busy preparing for the extensive precision and discovery
603 physics programme that will come from Run III of the LHC and, most significantly, for the
604 major upgrade beginning in the mid-2020s, the High-Luminosity LHC (HL-LHC). Here, protons
605 will be collided with an instantaneous luminosity a factor of five greater than at the LHC and
606 will accumulate up to ten times more data, resulting in an integrated luminosity of around
607 $\mathcal{L} = 3 \text{ ab}^{-1}$ for both the ATLAS and CMS detectors, and 300 fb^{-1} for LHCb. In this context,
608 a precise determination of PDFs is an essential ingredient for the success of the HL-LHC and
609 conversely, the HL-LHC itself offers a significant opportunity to improve our understanding of
610 proton structure.

611 In Ref. [35] the HL-LHC potential to constrain PDFs was analysed in detail, focussing on SM
612 processes that are expected to have the most impact at higher x . In particular, projections for

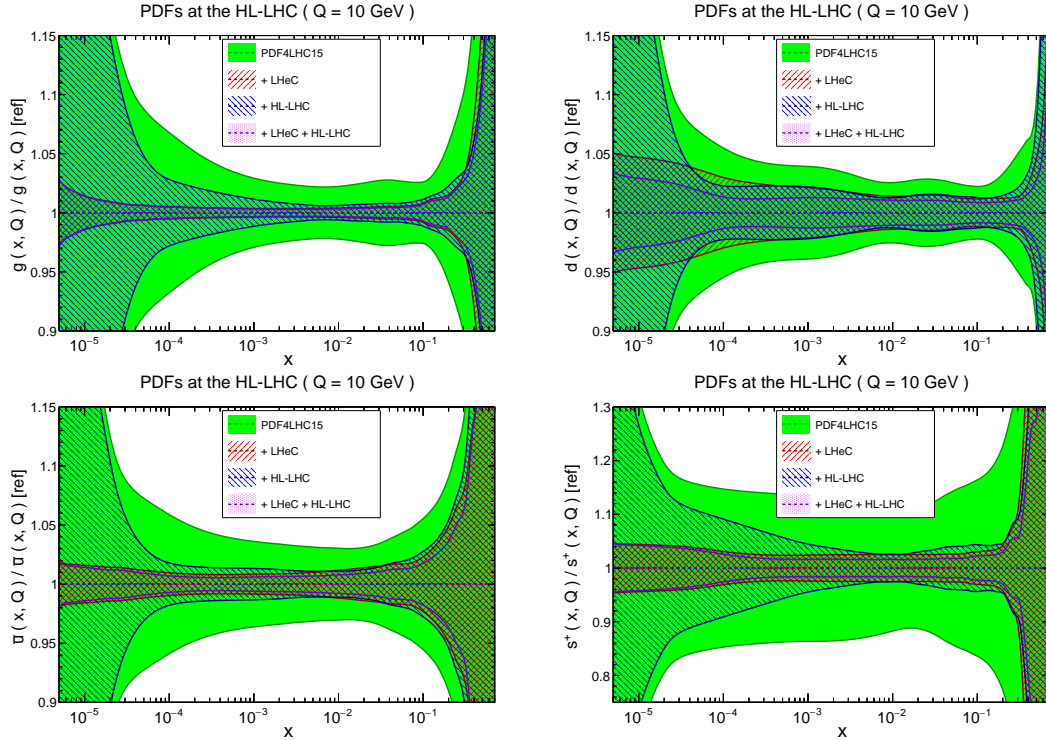


Figure 3.1: Impact of LHeC on the $1\text{-}\sigma$ relative PDF uncertainties of the gluon, down quark, anti-up quark and strangeness distributions, with respect to the PDF4LHC15 baseline set. Results for the LHeC, HL-LHC and to their combination are shown.

613 the production of top quark pairs, inclusive jets, forward W + charm quark and direct photons,
 614 as well as forward and high-mass Drell-Yan and the Z boson p_{\perp} distribution were included.
 615 It was found that PDF uncertainties on LHC processes can be reduced by a factor between
 616 two and five, depending on the specific flavour combination and on the assumptions about the
 617 experimental systematic uncertainties.

618 It is of course important to compare these constraints with those expected to come from the
 619 LHeC itself, as well as those coming from a combined PDF fit to the HL-LHC and LHeC
 620 datasets; this was studied in [36]. The basic procedure consists in generating HL-LHC and LHeC
 621 pseudodata with the PDF4LHC15 set [37] and then applying Hessian PDF profiling [38, 39], in
 622 other words a simplified version of a full refit, to this baseline to assess the expected impact of
 623 the data. While the HL-LHC datasets are described above, for the LHeC pseudodata correspond
 624 to the most recent publicly available official LHeC projections, see Section 3.1.5, for electron
 625 and positron neutral-current (NC) and charged-current (CC) scattering. As well as inclusive
 626 data at different beam energies ($E_p = 1, 7$ TeV), charm and bottom heavy quark NC and charm
 627 production in e^-p CC scattering are included.

628 In Fig. 3.1 we show the expected impact of the HL-LHC, LHeC and their combination on the
 629 PDF uncertainties of the gluon, down quark, anti-up quark and strangeness distributions. We
 630 can see that at low x the LHeC data place in general by far the strongest constraint, in particular
 631 for the gluon, as expected from its greatly extended coverage at small x . At intermediate x the
 632 impact of the HL-LHC and LHeC are more comparable in size, but nonetheless the LHeC is
 633 generally expected to have a larger impact. At higher x the constraints are again comparable in
 634 size, with the HL-LHC resulting in a somewhat larger reduction in the gluon and strangeness
 635 uncertainty, while the LHeC has a somewhat larger impact for the down and anti-up quark

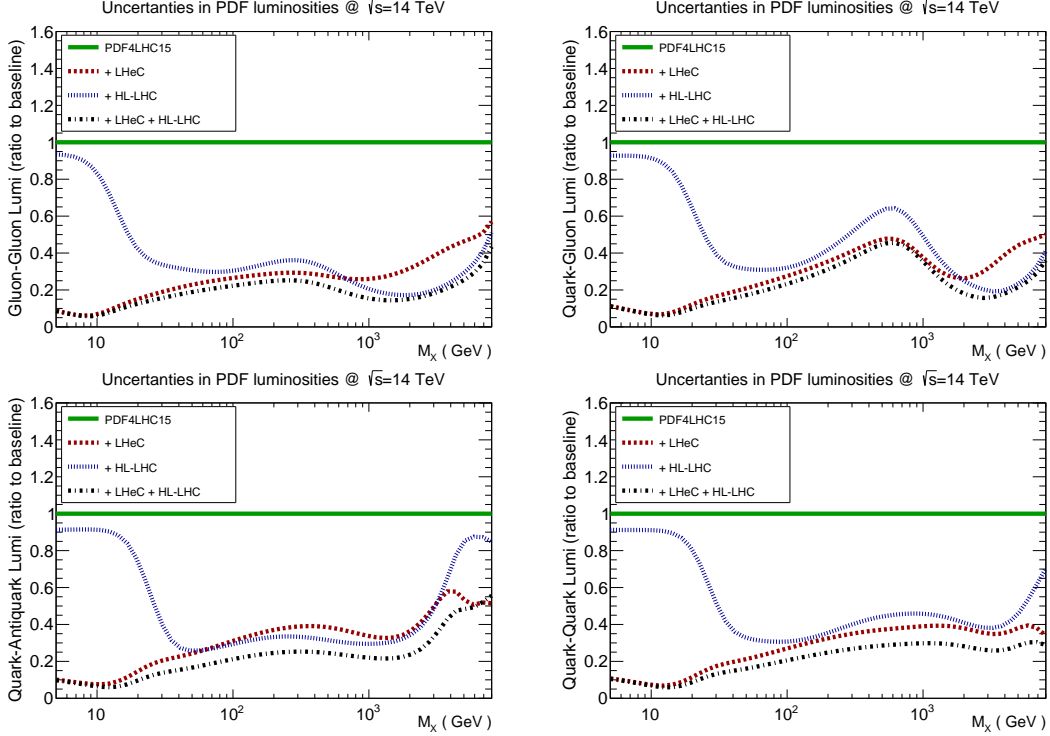


Figure 3.2: Impact of LHeC, HL-LHC and combined LHeC + HL-LHC pseudodata on the uncertainties of the gluon-gluon, quark-gluon, quark-antiquark and quark-quark luminosities, with respect to the PDF4LHC15 baseline set. In this comparison we display the relative reduction of the PDF uncertainty in the luminosities compared to the baseline.

636 distributions. Thus, the combination of both HL-LHC and LHeC pseudodata nicely illustrate
 637 a clear and significant reduction in PDF uncertainties over a very wide range of x , improving
 638 upon the constraints from the individual datasets in a non-negligible way.

639 In Fig. 3.2 we show the impact on the gluon-gluon, quark-gluon, quark-antiquark and quark-
 640 quark partonic luminosities. Some clear trends are evident from this comparison, consistent with
 641 the results from the individual PDFs. We can in particular observe that at low mass the LHeC
 642 places the dominant constraint, while at intermediate masses the LHeC and HL-LHC constraints
 643 are comparable in size, and at high mass the stronger constraint on the gluon-gluon and quark-
 644 gluon luminosities comes from the HL-LHC, with the LHeC dominating for the quark-quark
 645 and quark-antiquark luminosities. As in the case of the PDFs, for the partonic luminosities
 646 the combination of the HL-LHC and LHeC constraints leads to a clear reduction in the PDF
 647 uncertainties in comparison to the individual cases, by up to an order of magnitude over a wide
 648 range of invariant masses, M_X , of the produced final state.

649 In summary, our results demonstrate that while the HL-LHC alone is expected to have a sizeable
 650 impact on PDF constraints, the LHeC can improve our current precision on PDFs significantly
 651 in comparison to this, in particular at low to intermediate x . Moreover, the combination of
 652 both the LHeC and HL-LHC pseudodata leads to a significantly superior PDF error reduction
 653 in comparison to the two facilities individually. Further details, including LHeC-only studies as
 654 well as an investigation of the impact of the PDF baseline on the uncertainty projections, can
 655 be found in [36].

656 **PDF Sensitivity: Comparing LHC and LHeC**

657 While the experimental reach of each facility in the $\{x, Q^2\}$ kinematic plane provides a useful
 658 comparison, there are more factors to consider – especially when we are striving for ultra-high
 659 precision measurements.

660 One measure that provides a dimension beyond the $\{x, Q^2\}$ plane is the *sensitivity*; this is a
 661 combination of the correlation coefficient times a scaled residual [40, 41]. In Fig. 3.3 we display
 662 this sensitivity for a sample PDF flavour. This gives us an extra dimension of information
 compared a simple $\{x, Q^2\}$ map and provides a measure of the impact of the data. In particular,

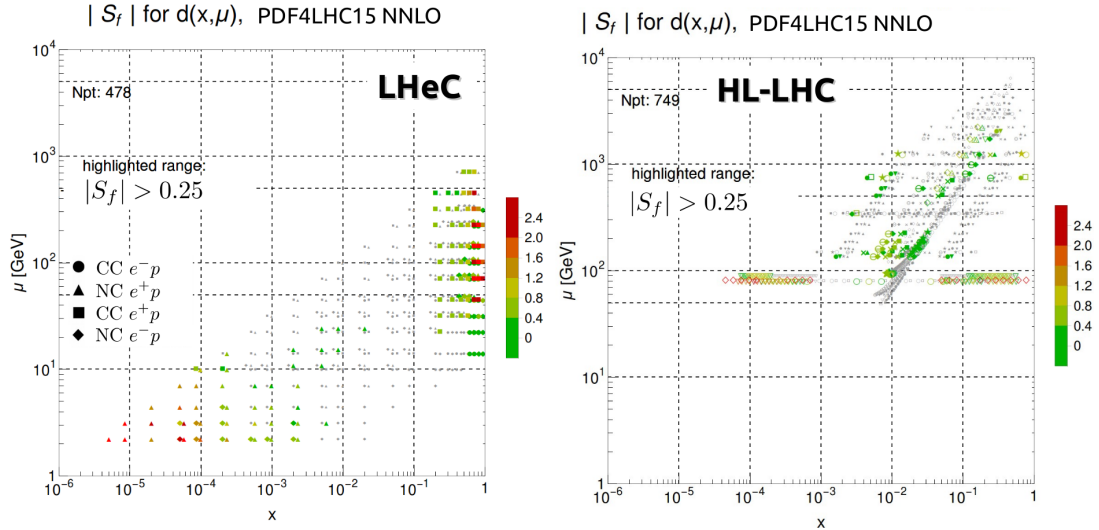


Figure 3.3: Sensitivity for a sample flavour $\{d(x, Q)\}$ in the $\{x, Q^2\}$ kinematic plane for the LHeC (left) and the HL-LHC (right) calculated with pseudodata [41]. We observe the LHeC is particularly sensitive in both the high and low x regions, and the HL-LHC covers the intermediate x region out to large Q scales.

663 we observe the LHeC provides strong sensitivity in the high- x region (which is important for
 664 BSM searches), and also in the low- x region (which is relevant for saturation). The HL-LHC
 665 provides constraints coming from W/Z production ($Q \sim M_{W/Z}$) as well as from jets at high
 666 Q scales. The combination of these measurements can provide very strong constraints on the
 667 various PDF flavours across the broad $\{x, Q^2\}$ kinematic plane.

669 In conclusion, while the kinematic $\{x, Q^2\}$ plots provide a valuable overview, we must be cau-
 670 tion to consider other *dimensions* to ascertain the complementary aspects when comparing the
 671 separate facilities.

672 **3.1.3 Parton Distributions and DIS**

673 The momentum distributions of partons inside the proton, $xP(x, Q^2)$, must be determined from
 674 experiment. The most reliable base so far have been the HERA data. They provide, with certain
 675 assumptions, kinematics and luminosity limitations, a first DIS-only based set of PDFs, which
 676 will be briefly summarised below. The LHC uses Drell-Yan and other data to obtain constrains
 677 on PDFs as has been introduced above. All of these use the HERA data also. It is one of the
 678 important principal goals and opportunities of the LHeC to provide a complete data set which
 679 has the strength to replace all previous data and thus will offer novel tests of QCD, of data

680 consistency, of improved searches for new particles at high mass - possibly non-resonant, etc. It
681 will open a thoroughly new phase of parton distribution physics. This is detailed subsequently.

682 The most suited process to obtain an unbiased determination of the quark and gluon distri-
683 butions is inclusive deep inelastic NC and CC scattering. The LHeC will cover a hitherto not
684 accessible kinematic region, see Fig. 1.1 in the Introduction to this paper. This spans, as will
685 be detailed below, almost six orders of magnitude in x and Q^2 and makes full use of the weak
686 interactions in NC and CC, thus enabling a complete separation of flavour contributions which
687 is impossible with data on F_2 alone as are typically obtained in fixed target experiments. The
688 US EIC misses the low x region and the high Q^2 by about one (two) order(s) of magnitude as
689 compared to HERA (LHeC). It thus cannot solve the problem of non-DGLAP evolution and it
690 cannot reliably separate different flavours, nor access the top fraction of the proton's momentum.

691 *PDFs* have two meanings in that i) they represent a probability view on the substructure of
692 the proton, or similarly of other hadrons, at a given distance $1/\sqrt{Q^2}$, and ii) they describe,
693 supposedly universally through cross section factorisation theorems [42], the hard scattering
694 processes involving partons. In his referee report on the LHeC CDR, in 2012, Guido Altarelli
695 noted on the factorisation theorem in QCD for hadron colliders that: *many people still advance*
696 *doubts. Actually this question could be studied experimentally, in that the LHeC, with its im-*
697 *proved precision, could put bounds on the allowed amount of possible factorisation violations*
698 *(e.g. by measuring in DIS the gluon at large x and then comparing with jet production at large*
699 *p_T in hadron colliders). This question was addressed also in a previous LHeC paper [43]. It*
700 *receives extra emphasis because in the relevant kinematic region at the LHC both new physics*
701 *and violations of factorisation may be superimposed. This requires very high luminosity in ep in*
702 *order to distinguish valence from sea quarks, up from down flavours and the gluon from quarks*
703 *at high x .*

704 The determination of PDFs in DIS is: i) theoretically cleanest; ii) free of colour interactions in the
705 initial or final state; iii) it enables a prescribed selection of Q^2 and iv) allows the determination
706 of the kinematics externally to the intrinsic scattering process. It also clearly distinguishes the
707 NC from CC probes of proton structure.

708 Beyond these principal advantages of DIS, the PDF programme of the LHeC is of unprecedented
709 depth for the following reasons:

- 710 • it will resolve the partonic structure of the proton (and nuclei, Chapter 4) for the first time
711 completely, i.e. determine $P = u_v, d_v, u, d, s, c, b$ and the top and gluon momentum
712 distributions through NC and CC cross section and direct heavy quark measurements in
713 a huge kinematic range, from below $x = 10^{-6}$ to $x = 0.9$ and in Q^2 from below the DIS
714 region to nearly $Q^2 = 4E_e E_p = 1.4 \cdot 10^6 \text{ GeV}^2$;
- 715 • a thousand-fold increase of the HERA luminosity, unprecedented precision from new de-
716 tector technology and the redundant evaluation of the event kinematics from the lepton
717 and hadron final state components will lead to extremely large precision. Also, technically
718 important, to the fixation of the various PDF analysis parameters from the LHeC data
719 themselves;
- 720 • because at high energy the CC cross section becomes as large as the NC one, no other
721 data will be required, besides dedicated measurements of the strange, charm and bottom
722 quark densities with impact parameter tags. This means that there is no influence from
723 higher twists, hadronisation nor nuclear uncertainties, and no other experiment needed,
724 i.e. the LHeC will indeed provide a unique and complete base for PDFs, for predictions,
725 discovery and novel tests of theory.

726 Given the impressive theoretical progress on pQCD, one will have these PDFs available to at
727 least [44] N³LO. This is important to reduce scale uncertainties but as well for a coherent
728 analysis, for example of Higgs production at the LHC which has already been calculated to
729 N³LO. For QCD, this will resolve many open issues (and probably create new ones) such as on
730 the correct value of α_s , discussed below, the question on the persistence (or not) of linear parton
731 evolution at small x and, as mentioned, it will also decisively test whether factorisation holds or
732 not between DIS and Drell-Yan scattering. The way to do PDF analyses with ep collider data
733 has been paved over decades with HERA, as is next briefly illustrated.

734 3.1.4 HERA PDFs

735 HERA PDFs are determined by QCD fits to HERA data [45] with combined inputs from the
736 H1 and ZEUS experiments. The fits use information from both $e^\pm p$ neutral current (NC) and
737 charged current (CC) scattering up to high Q^2 30,000 GeV². The lower- Q^2 NC data constrain
738 the low- x sea-quark distributions and, through their precisely measured Q^2 variations,] also
739 the gluon distribution. The difference between the NC e^+p and e^-p cross sections at high Q^2 ,
740 together with the high- Q^2 CC data, constrain the valence distributions. Data from different
741 centre-of-mass energies give information on the longitudinal structure function F_L and hence
742 further constrain the gluon distribution (see also the discussion on F_L at the LHeC below). The
743 precision of the HERA combined data is below 1.5% over the Q^2 range of $3 < Q^2 < 500$ GeV²
744 and remains below 3% up to $Q^2 = 3000$ GeV².

745 The evolution equations of QCD yield the PDFs at any value of Q^2 given that they are param-
746 eterised as functions of x at an initial scale Q_0^2 . The evolved PDFs are then convoluted with
747 QCD-calculable coefficient functions to predict the DIS structure functions and thus to give
748 predictions for the DIS cross sections at the measured values of Q^2 . These are then confronted
749 with the data through a χ^2 fit, which determines the PDF parameters. The QCD analysis is
750 performed at LO, NLO and NNLO and the latest version is the HERAPDF2.0 family [45]

751 The QCD analysis uses the *xFitter* framework [46–48]. The DGLAP evolution of the PDFs is
752 done using QCDNUM [49]. The light-quark coefficient functions are also calculated using QCD-
753 NUM. The contributions of heavy quarks are calculated in the general-mass variable-flavour-
754 number (GMVFN) scheme of Refs. [50, 51]. The renormalisation and factorisation scales for
755 the DIS processes are taken as $\mu_r = \mu_f = \sqrt{Q^2}$. The program MINUIT [52] is used for the
756 χ^2 minimisation. Experimental uncertainties are determined using the Hessian method with
757 $\Delta\chi^2 = 1$.

758 In the HERAPDF analysis, the starting scale is chosen to be $Q_0^2 = 1.9$ GeV² such that it is
759 below the charm mass threshold m_c^2 . The heavy quark masses are chosen to be $m_c = 1.43$ GeV
760 and $m_b = 4.5$ GeV, following the results of an analysis of the HERA combined charm and
761 beauty data. The strong coupling constant is fixed to $\alpha_S(M_Z) = 0.118$. A minimum Q^2 cut
762 $Q_{min}^2 \geq 3.5$ GeV² is imposed on the HERA data. All these assumptions are varied in the
763 evaluation of model uncertainties on the final fit.

764 The quark distributions at the initial scale are represented by the generic form

$$xq_i(x) = A_i x^{B_i} (1-x)^{C_i} P_i(x), \quad (3.1)$$

765 where i specifies the flavour of the quark distribution and $P_i(x) = (1 + D_i x + E_i x^2)$. The param-
766 eterised quark distributions, xq_i , are chosen to be the valence quark distributions (xu_v , xd_v)
767 and the light anti-quark distributions ($x\bar{u}$, $x\bar{d}$). The gluon distribution is parameterised with

768 the more flexible form $xg(x) = A_g x^{B_g} (1-x)^{C_g} P_g(x) - A'_g x^{B'_g} (1-x)^{C'_g}$. The parameters A_{u_v}
769 and A_{d_v} are fixed using the quark counting rule and A_g using the momentum sum rule. The
770 normalisation and slope parameters, A and B , of \bar{u} and \bar{d} are set equal such that $x\bar{u} = x\bar{d}$ at
771 $x \rightarrow 0$. The strange quark PDF $x\bar{s}$ is set as a fixed fraction $r_s = 0.67$ of the $x\bar{d}$ PDF. This
772 fraction is varied in the determination of model uncertainties. By default it is assumed that
773 $xs = x\bar{s}$. The D, E and F terms in the polynomial expansion $P_i(x)$ are used only if required
774 by the data, following the procedure described in Ref. [47]. This leads to two additional terms,
775 $P_{u_v}(x) = 1 + E_{u_v} x^2$ and $P_{\bar{u}} = 1 + D_{\bar{u}} x$. Alternative parameterisations are used in the evaluation
776 of a parameterisation uncertainty. These variations include: introducing extra parameters $D,$
777 E for each quark distribution; the removal of primed gluon parameters; and the relaxation of
778 assumptions about the low- x sea. These fits provide alternative extracted PDFs with similar
779 fit χ^2 . The maximum deviation from the central PDF at each value of x is taken as an enve-
780 lope and added in quadrature with the experimental and model uncertainties to give the total
781 uncertainty. Full details on the fit methodology are given in [45].

782 The results of the HERAPDF analysis are shown for the HERAPDF2.0NNLO PDF set, display-
783 ing experimental, model and parameterisation uncertainties separately, in Fig. 3.4 and compared
784 to other PDFs (using total uncertainties) in Fig. 3.5. Note that the HERAPDF differs from
785 other PDF sets in that; i) it represents a fit to a consistent data set with small correlated system-
786 atic uncertainties such that χ^2 tolerance of unity may be used for 68 % uncertainties; ii) it uses
787 data on a proton target such that no heavy target corrections are needed and the assumption
788 of strong isospin invariance, $d_{proton} = u_{neutron}$, is not required; iii) the kinematic region is such
that no cuts need be made for higher twist effects at low Q^2 and high x .

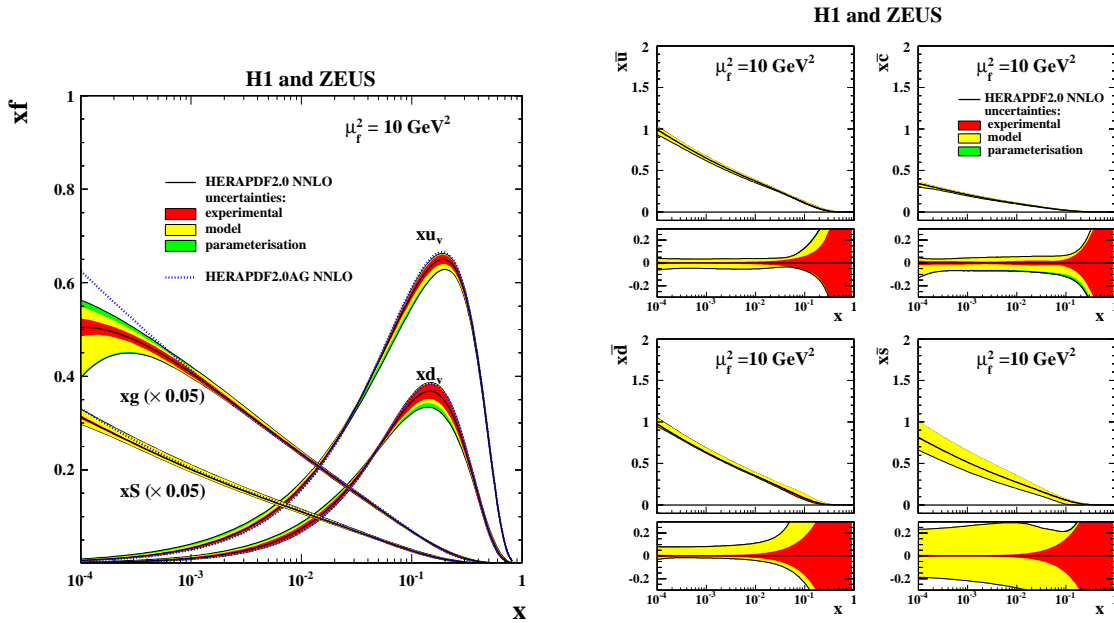


Figure 3.4: Left: HERAPDF2.0NNLO PDFs for valence, gluon and total sea, showing experimental, model and parameterisation uncertainties separately, at factorisation scale $\mu_f = 10 \text{ GeV}^2$. An alternative (AG) PDF with no negative term to the gluon parameterisation is also shown. Right: HERAPDF2.0NNLO PDFs for the Sea, $x\bar{u}, x\bar{d}, x\bar{c}, x\bar{s}$ showing experimental, model and parameterisation uncertainties separately, at factorisation scale $\mu_f = 10 \text{ GeV}^2$. Fractional uncertainties are shown below the plots.

789

790 More recently NNLO predictions for inclusive jet and dijet production in DIS have been com-

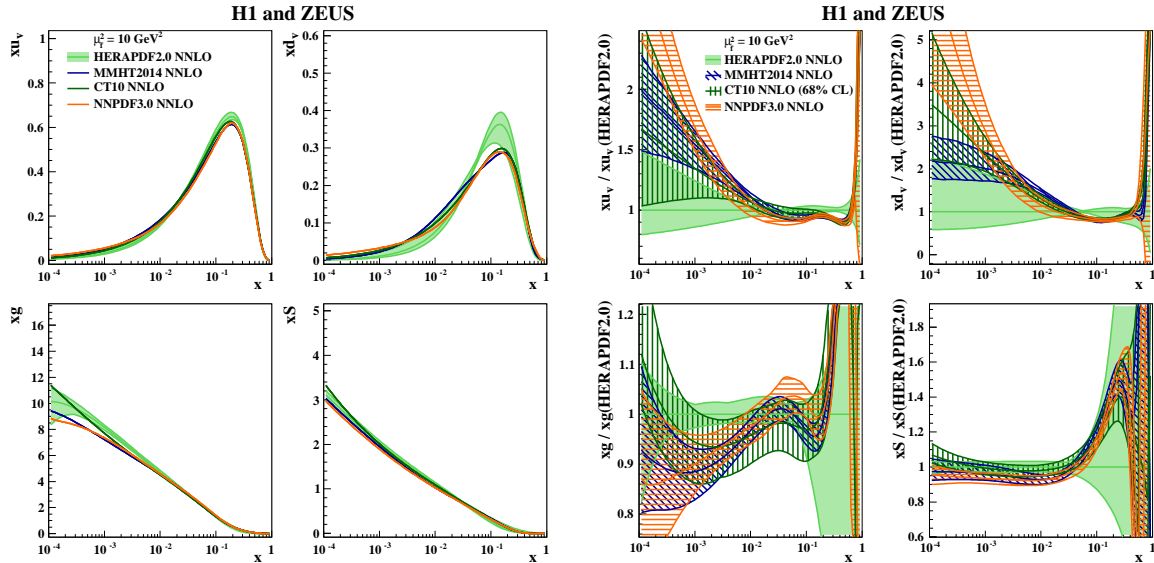


Figure 3.5: The HERAPDF2.0 NNLO PDFs for valence, gluon and total sea compared to other NNLO PDF sets MMHT14, CT10, NNPDF3.0, at factorisation scale $\mu_f = 10 \text{ GeV}^2$. Left; PDFs: right; ratios of PDFs to the HERAPDF. Total uncertainties are shown for the HERAPDFs in both the left and right hand side plots, whereas total uncertainties for the MMHT, CT and NNPDF PDFs are only shown on the right hand side plots.

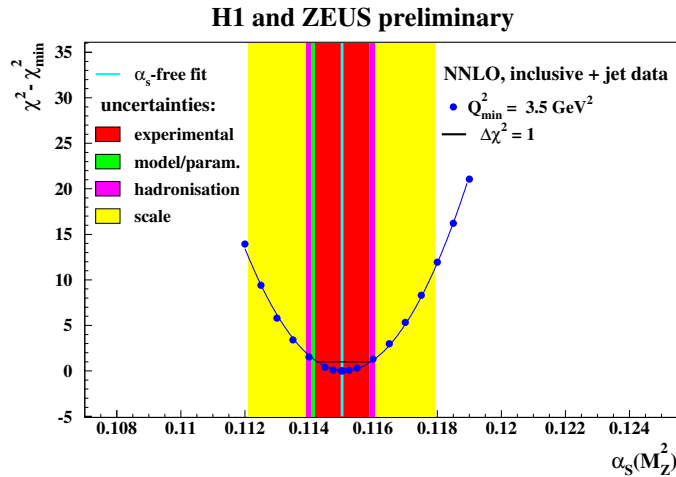


Figure 3.6: $\Delta\chi^2 = \chi^2 - \chi_{\min}^2$ vs. $\alpha_S(M_Z)$ for HERAPDF2.0 Jets NNLO (prel.) fits with fixed $\alpha_S(M_Z)$.

791 pleted and HERA jet data have been included in the HERAPDF2.0 NNLOJets preliminary anal-
792 ysis [53]. These data do not have much impact on the PDFs if a fixed value of $\alpha_S(M_Z) = 0.118$
793 is used; however, they indicate that a lower value of $\alpha_S(M_Z) = 0.115$ is preferred at NNLO, see
794 Fig. 3.6. Note that HERAPDFs are standardly issued with a series of fixed values of $\alpha_S(M_Z)$
795 so that this change can be readily accommodated. The result on α_s agrees with an early mea-
796 surement by H1 [54] based on inclusive H1 and BCDMS data, in which a very special PDF
797 parameterisation was introduced in order to enhance the sensitivity to α_s . This underlines the
798 importance of precisely measuring the strong coupling, which the LHeC can do (see below). It
799 has long been emphasised [55] that the value of α_s may be lower than the long time canonical
800 0.118, at least in DIS, which has to be resolved, in view also of the lattice results - for a discussion
801 see Ref. [56].

802 **3.1.5 Simulated LHeC Data Sets**

803 The systematic uncertainties of the DIS cross sections have a number of sources, which can be
 804 classified as uncorrelated and correlated across bin boundaries. For the NC case, the uncorre-
 805 lated sources, apart from event statistics, are a global efficiency uncertainty, due for example to
 806 tracking or electron identification errors, as well as uncertainties due to photo-production back-
 807 ground, calorimeter noise and radiative corrections. The correlated uncertainties result from
 808 imperfect electromagnetic and hadronic energy scale and angle calibrations. In the classic ep
 809 kinematic reconstruction methods used here, the scattered electron energy E'_e and polar angle
 810 θ_e , complemented by the energy of the hadronic final state E_h can be employed to determine
 811 Q^2 and x in a redundant way.

812 Briefly, Q^2 is best determined with the electron kinematics and x is calculated from $y = Q^2/sx$.
 813 At large y the inelasticity is essentially measured with the electron energy $y_e \simeq 1 - E'_e/E_e$. At low
 814 y the relation $y_h = E_h \sin^2(\theta_h/2)/E_e$ is used to provide a measurement of the inelasticity with
 815 the hadronic final state energy E_h and angle θ_h , resulting in $\delta y_h/y_h \simeq \delta E_h/E_h$ to good approx-
 816 imation. There have been various refined methods proposed to determine the DIS kinematics,
 817 such as the double angle method or the so-called sigma method. For the initial estimate of the
 818 cross section uncertainty behaviour as functions of Q^2 and x , however, the simplest method
 819 using Q_e^2, y_e at large y and Q_e^2, y_h at low y is transparent and accurate to better than a factor
 820 of two. In much of the phase space, moreover, it is rather the uncorrelated efficiency or further
 821 specific errors than the kinematic correlations, which dominate the cross section measurement
 822 precision.

823 The assumptions used in the simulation of pseudodata are summarised in Table 3.1. The proce-
 824 dure was gauged with full H1 Monte Carlo simulations and the assumptions are corresponding
 825 to H1's achievements with an improvement where justified by at most a factor of two. Using a
 826 numerical procedure [57] the scale uncertainties were transformed to kinematics-dependent cor-
 related cross section uncertainties caused by imperfect measurements of E'_e , θ_e and E_h . These

Source of uncertainty	Uncertainty
Scattered electron energy scale $\Delta E'_e/E'_e$	0.1 %
Scattered electron polar angle	0.1 mrad
Hadronic energy scale $\Delta E_h/E_h$	0.5 %
Radiative corrections	0.3 %
Photoproduction background (only $y > 0.5$)	1 %
Global efficiency error	0.5 %

Table 3.1: Assumptions used in the simulation of the NC cross sections on the size of uncertainties from various sources. The top three are uncertainties on the calibrations which are transported to provide correlated systematic cross section errors. The lower three values are uncertainties of the cross section caused by various sources.

827 data uncertainties were imposed for all data sets, NC and CC, as are subsequently listed and
 828 described.
 829

830 The design of the LHeC assumes that it operates with the LHC in the high luminosity phase,
 831 following LS4 at the earliest. As detailed in Chapter 2, it is assumed there will be an initial
 832 phase, during which LHeC may collect 50 fb^{-1} of data. This may begin with a sample of 5 fb^{-1} .
 833 Such values are very high when compared with HERA, corresponding to the hundred(ten)-fold
 834 of luminosity which H1 collected in its about 15 years lifetime. The total luminosity may reach
 835 about 1 ab^{-1} . The bulk of the data is likely to be taken with electrons, possibly at large negative

836 helicity P_e , because this configuration maximises the number of Higgs bosons one can produce
837 at the LHeC: e^- couples to W^- which interacts primarily with an up-quark and the CC cross
838 section is proportional to $(1 - P_e)$. However, for electroweak physics there is a strong interest
839 to vary the polarisation and charge. With a linac source, the generation of an intense positron
840 beam is very challenging and will not be able to compete with the electron intensity. Finally, a
841 dataset has also been produced with reduced proton beam energy which enlarges the acceptance
towards large x at smaller Q^2 . The full list of sets is provided in Tab. 3.2. It is instructive to see

Parameter	Unit	Data set								
		D1	D2	D3	D4	D5	D6	D7	D8	D9
Proton beam energy	TeV	7	7	7	7	1	7	7	7	7
Lepton charge		-1	-1	-1	-1	-1	+1	+1	-1	-1
Longitudinal lepton polarisation		-0.8	-0.8	0	-0.8	0	0	0	+0.8	+0.8
Integrated luminosity	fb ⁻¹	5	50	50	1000	1	1	10	10	50

Table 3.2: Summary of characteristic parameters of data sets used to simulate neutral and charged current e^\pm cross section data, for a lepton beam energy of $E_e = 50$ GeV.

842
843 how the variation of the beam energy changes the kinematics and enables coverage of various
844 regions. The highest energies obviously give access to the smallest x at a given Q^2 , and to the
845 maximum Q^2 at fixed x . This is illustrated with the kinematic plane and iso-energy and iso-angle
846 lines, see Fig. 3.7. The coverage changes considerably if the energies are lowered. This is clear
847 from Fig. 3.8 which shows the kinematic plane choosing the about minimum energies the LHeC
848 could operate with. There are striking changes one may note which are related to kinematics,
849 see Ref. [57]. One can see that the line of $\theta_e = 179^\circ$ now corresponds to $Q^2 \simeq 1$ GeV² which
850 is due to lowering E_e as compared to the maximum energy case, Fig. 3.7. Similarly, comparing
851 the two figures one finds that the lower Q^2 , larger x region becomes much easier accessible with
852 lower energies, in this case solely owing to the reduction of E_p from 7 to 1 TeV. It is interesting
853 to note that with 1 fb⁻¹ of data, the LHeC, when operating at these low energies, would permit
854 a complete repetition of the HERA programme, within not many days of data taking.

855 The coverage of the kinematic plane is illustrated in the plot of the x, Q^2 bin centers of data
856 points used in simulations, see Fig. 3.9 [36]. The very high luminosity enables a full coverage of
857 high Bjorken- x , very close to $x = 1$, which was impossible for HERA to achieve as the DIS NC
858 and CC cross sections decrease proportional to some power of $(1 - x)$ when x approaches 1 as
859 has long been established with Regge counting [58–60].

860 It has been a prime goal, leading much beyond previous PDF studies, to understand the im-
861 portance of these varying conditions for measuring PDFs with the LHeC. This holds especially
862 for the question about what can be expected from the initial LHeC operation period, which is
863 of highest interest for the LHC analyses during the HL-LHC period. Some special data sets of
864 lowered electron energy have also been produced in order to evaluate the potential to measure
865 F_L , as is discussed below in this paper. These data sets have not been included in the analyses
866 which are presented in the following.

867 3.1.6 Expectations on PDFs from the LHeC

868 In this section, PDF constraints from the full simulation of LHeC inclusive NC and CC cross
869 section measurements are investigated. Given the expected timeline for the HL-LHC and the
870 potential timescale for LHeC operation, it is of utmost importance that the LHeC can deliver

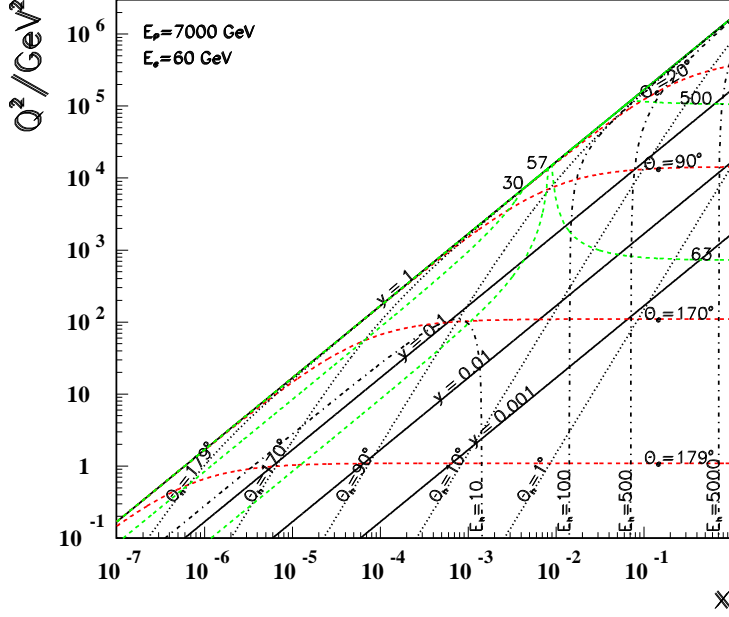


Figure 3.7: Kinematic plane covered with the maximum beam energies at LHeC. Red dashed: Lines of constant scattered electron polar angle. Note that low Q^2 is measured with electrons scattered into the backward region, highest Q^2 is reached with Rutherford backscattering; Black dotted: lines of constant angle of the hadronic final state; Black solid: Lines of constant inelasticity $y = Q^2/sx$; Green dashed: Lines of constant scattered electron energy E'_e . Most of the central region is covered by what is termed the kinematic peak, where $E'_e \simeq E_e$. The small x region is accessed with small energies E'_e below E_e while the very forward, high Q^2 electrons carry TeV energies; Black dashed-dotted: lines of constant hadronic final state energy E_h . Note that the very forward, large x region sees very high hadronic energy deposits too.

871 PDFs of transformative precision on a short timescale, in order to be useful within the lifetime
872 of the HL-LHC. Therefore, particular attention is paid to the constraints that are possible from
873 the first 50 fb^{-1} of electron-proton data (corresponding to the first 3 years of LHeC operation,
874 labelled dataset **D2** in Tab. 3.2). This is referred to as “LHeC 1st run” in the following text
875 (though note that sufficient data to provide precision measurements of s, c, b will also be accumu-
876 lated during this period). The expectations for the “LHeC full inclusive” dataset, corresponding
877 to the combination of datasets (**D4+D5+D7+D8**) are also presented. While this full combi-
878 nation is likely to be achievable only after the expected end of HL-LHC operation, it would be
879 valuable for re-analysis or re-interpretation of LHC data, and for further-future hadron colliders.

880 To assess the importance of different operating conditions, the impact of datasets with: differing
881 amounts of integrated luminosity (**D1, D4**); positrons (**D6, D7**); and with different polarisation
882 states for the leptons (**D3, D8**) are also considered.

883 Additional dedicated studies of the impact of s, c, b data on the PDFs are also presented, based
884 on a small amount (10 fb^{-1}) of e^-p simulated data. Additional PDF constraints that would be
885 provided by a measurement of F_L and ep jet measurements are not yet considered.

886 For the QCD analyses presented in this section, the xFitter [61] framework has been used, with
887 settings based on the HERAPDF QCD fit analysis [45], described above, but with some differing
888 or relaxed assumptions as detailed below.

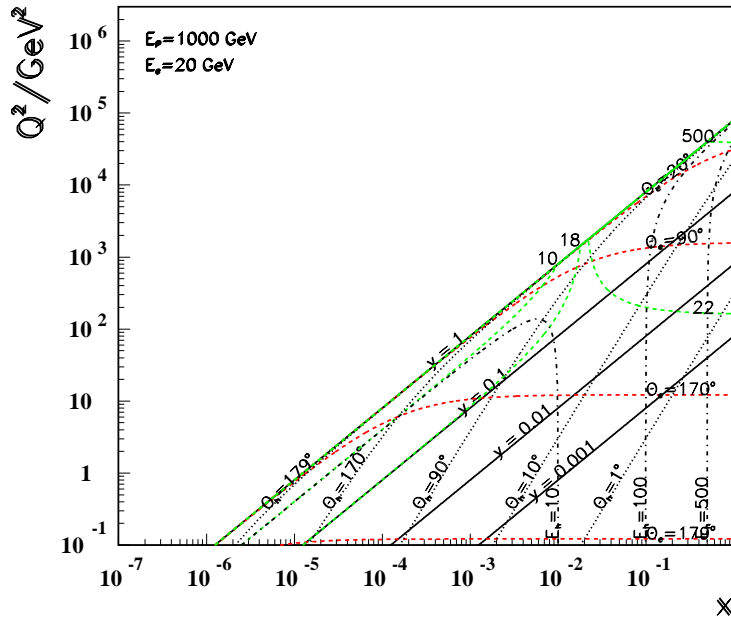


Figure 3.8: Kinematic plane covered with the minimum beam energies at LHeC. The meaning of the curves is the same as in the previous figure. This coverage is very similar to that by HERA as the energies are about the same.

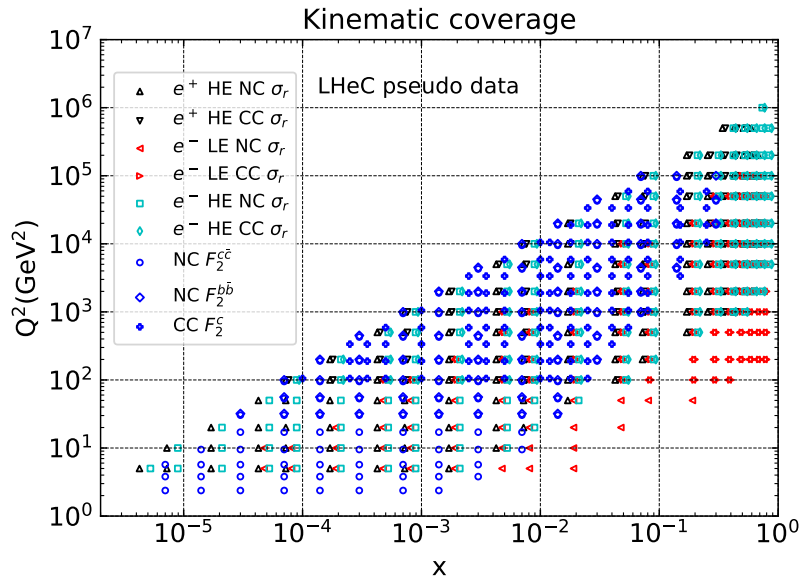


Figure 3.9: Illustration of the x, Q^2 values of simulated cross section and heavy quark density data used in LHeC studies. The red points illustrate the gain in acceptance towards large x at fixed Q^2 when E_p is lowered, see text.

889 Fit Procedure

890 The simulated input data sets, and assumed systematic uncertainties, are detailed above. NLO
 891 QCD fits have been performed (and cross checked at NNLO QCD), in order to study the effects

892 of the simulated LHeC data on the knowledge of PDFs. The present analysis follows the HERA
 893 QCD fit procedure, with a minimum Q^2 cut of 3.5 GeV^2 and a starting scale $Q_0^2 = 1.9 \text{ GeV}^2$,
 894 chosen to be below the charm mass threshold. The fits are extended to the lowest x for illu-
 895 stration, even though at such low- x values non-linear effects are expected to appear, eventually
 896 altering the evolution laws, see Sec. 3.2.4.

897 The parameterised PDFs are the valence distributions xu_v and xd_v , the gluon distribution xg ,
 898 and the $x\bar{U}$ and $x\bar{D}$ distributions, where $x\bar{U} = x\bar{u}$, $x\bar{D} = x\bar{d} + x\bar{s}$. This ansatz is natural to the
 899 extent that the NC and CC inclusive cross sections determine the sums of up and down quark
 900 distributions, and their antiquark distributions, as the four independent sets of PDFs, which
 901 may be transformed to the ones chosen if one assumes $u_v = U - \bar{U}$ and $d_v = D - \bar{D}$, i.e. the
 902 equality of anti- and sea quark distributions of given flavour.

903 The following standard functional form is used to parameterise them

$$xf(x) = Ax^B(1-x)^C(1+Dx+Ex^2), \quad (3.2)$$

904 where the normalisation parameters (A_{uv}, A_{dv}, A_g) are constrained by quark counting and mo-
 905 mentum sum rules. For the majority of the QCD fits presented, the strange quark distribution
 906 at the starting scale is assumed to be a constant fraction of \bar{D} , $x\bar{s} = f_s x\bar{D}$, with a value of
 907 $f_s = 0.4$, as chosen for the HERAPDF2.0 parameterisation [45]. This assumption is relaxed for
 908 the fits including simulated s, c, b data.

909 The parameterisation chosen is close but not identical to that used for HERAPDF2.0. Specifi-
 910 cally, the following parameters are set free: $B_g, C_g, D_g, B_{uv}, C_{uv}, E_{uv}, B_{dv}, C_{dv}, A_{\bar{U}}, B_{\bar{U}},$
 911 $C_{\bar{U}}, A_{\bar{D}}, B_{\bar{D}}, C_{\bar{D}}$. This is a total of 14 free parameters in the main fit. Note that the B
 912 parameters for u_v and d_v , and the A and B parameters for \bar{U} and \bar{D} are fitted independently, such
 913 that the up and down valence and sea quark distributions become totally uncorrelated in the
 914 analysis. This is much more flexible than the HERAPDF2.0 parameterisation, which requires
 915 that $x\bar{u} \rightarrow x\bar{d}$ as $x \rightarrow 0$. The other main difference is that no negative gluon term has been
 916 included in the present analysis ¹.

917 The PDFs are evolved using DGLAP evolution equations at NLO in the $\overline{\text{MS}}$ scheme with the
 918 renormalisation and factorisation scales set to Q^2 using standard sets of parameters, and a
 919 value of $\alpha_s(M_Z) = 0.118$ is used. These choices, as well as the exact treatment of the heavy
 920 quark thresholds, have no significant influence on the estimates of the PDF uncertainties. The
 921 experimental uncertainties on the PDFs are determined using the $\Delta\chi^2 = 1$ criterion.

922 It is important to realise that it needs data to fix a parameterisation. With coherent DIS collider
 923 data sets, this can be achieved with a χ^2 saturation criterion: at HERA PDF parameters were
 924 only added when the χ^2 of the fit changed significantly. The resulting parameterisation will
 925 thus be different at LHeC than anticipated here. While the LHeC NC and CC real data, and
 926 the inclusion of further information, such as F_L , will almost certainly lead to a quite different
 927 parameterisation, it has been checked that with more flexible sets of parameters, very similar
 928 results on the PDF uncertainties are obtained.

929 It is finally to be noted that data of very high precision into the corners of phase space have
 930 a great potential, much larger than HERA had, to fix the parameterisation from data. For
 931 example, one can directly derive relations for how the valence quarks are determined with a set
 932 of NC and CC cross section data in a redundant way. One has, as is pointed out in the section

¹This choice is purely for aesthetic purposes, so that no distribution crosses the x -axis when presenting ratio plots. Analogous fits with a negative gluon term as used in the HERAPDF2.0 parameterisation have also been checked and found to have no substantive impact on the relative PDF uncertainties presented here.

933 on F_L , a redundant way to determine the gluon distribution at small x , from the Q^2 derivate
 934 of F_2 and from F_L . The question of whether the gluon goes negative at low x and small Q^2
 935 may then be settled by analysing these constraints and not with some fit peculiarity. Direct,
 936 precise determinations of s , c and b densities with impact parameter measurements will put the
 937 treatment of heavy flavours in these analyses on a new level, the poor f_s factor will disappear
 938 and the debate on the value of fixed and variable heavy flavour schemes will be settled. The
 939 prospects here presented are illustrations for a different era of PDF physics which will be richer
 940 and deeper than one may be able to now simulate.

941 Valence Quarks

942 Knowledge of the valence quark distributions, at both large and small x , is extremely limited,
 943 as is illustrated in Fig. 3.10 which compares the results of a variety of modern PDF sets. At
 944 high x , this has to do with the limited luminosity, challenging systematics rising $\propto 1/(1-x)$
 945 and with nuclear correction uncertainties and, at low x , with the smallness of the valence quark
 distributions as compared to the sea quarks.

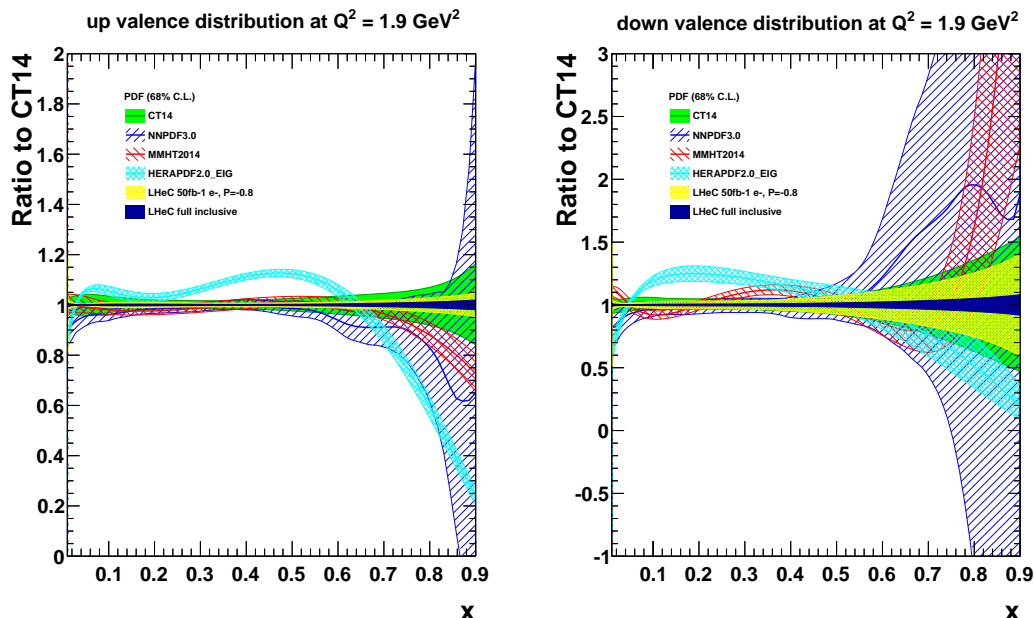


Figure 3.10: Valence quark distributions at $Q^2 = 1.9 \text{ GeV}^2$ as a function of Bjorken x , presented as the ratio to the CT14 central values. The yellow band corresponds to the “LHeC 1st Run” PDFs (**D2**), while the dark blue shows the “LHeC full inclusive” PDFs based on the data sets (**D4+D5+D7+D8**), as described in the text. Both LHeC PDFs shown are scaled to the central value of CT14.

946

947 The impressive improvement that can be expected from an LHeC is illustrated in the same
 948 Figure. Note that the central value for the LHeC PDF has been scaled in all cases to that
 949 of the CT14 PDF, for the purposes of illustrating the improvement to the uncertainties most
 950 clearly. The u valence quark distribution is better known than the d valence, since it enters
 951 with a four-fold weight in F_2 due to the electric quark charge ratio squared. Nevertheless, a
 952 substantial improvement in d_v is also visible, because the relative weight of d_v to u_v is changing
 953 favourably towards the down quark due to the influence of weak NC and CC interactions at high
 954 Q^2 where the LHeC is providing very accurate data. Note that the yellow band (corresponding
 955 to the first run of the LHeC) includes only electron, i.e. no positron, data. Note also that such a

956 determination is free from higher twist corrections, which plague all fixed target data, and from
 957 nuclear uncertainties as the $u - d$ distinction at LHeC is achieved in high luminosity, high Q^2
 958 ep scattering only.

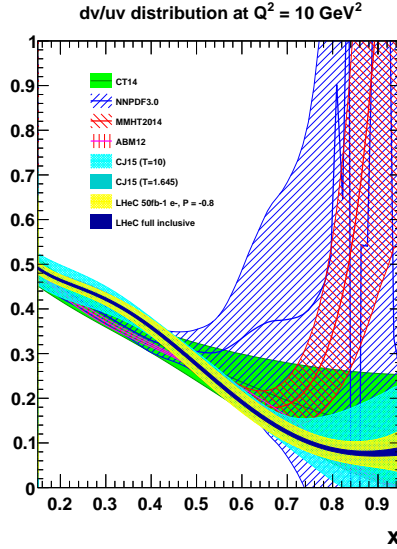


Figure 3.11: The d_v/u_v distribution at $Q^2 = 10 \text{ GeV}^2$ as a function of Bjorken x . The yellow band corresponds to the “LHeC 1st run” PDFs (**D2**), while the dark blue shows the “LHeC full inclusive” PDFs (**D4+D5+D7+D8**), as described in the text. Both LHeC PDFs shown are scaled to the central value of CT14.

959 The vast improvements compared to HERA constraints come from the much higher luminosity
 960 and extension in kinematic reach. Such precise determinations of the valence quark distributions
 961 at large x has strong implications for BSM searches at the LHC. In addition, the LHeC will
 962 eventually resolve the mystery of the d/u ratio at large x (shown in Fig. 3.11), where currently
 963 there are conflicting theoretical pictures, and where the constraints from previous data are
 964 inconclusive statistically and also suffer from large nuclear uncertainties. Access to valence
 965 quarks at low x can also be obtained from the $e^\pm p$ cross section differences, information which is
 966 present in the “LHeC full inclusive” PDF, but not in the “LHeC 1st run” PDF. As has already
 967 been illustrated in the CDR from 2012 [1] the sum of $2u_v + d_v$ may be measured directly with
 968 the NC γZ interference structure function $x F_3^{\gamma Z}$ down to $x \simeq 10^{-4}$ with very good precision,
 969 which also tests the equality of sea- and anti-quark densities.

970 Sea Quarks

971 Figure 3.12 shows the distributions of \bar{U} and \bar{D} for the present global and HERA pdf analyses
 972 and for the first and full LHeC run. The plots uses a normalisation to the central value of
 973 CT14. It is striking to see, note the logarithmic x scale, that the anti-quark distributions are
 974 unknown at small x , where they are large and at high x , where they are small. This will be
 975 changed completely with the sizeable very high precision determination for the LHeC PDF. This
 976 is obtained despite the relaxation of any assumptions, present in other determinations, which
 977 would force $\bar{u} \rightarrow \bar{d}$ as $x \rightarrow 0$. At smaller Q^2 in DIS one measures essentially $F_2 \propto 4\bar{U} + \bar{D}$. At
 978 HERA, thus one could not resolve the two parts, neither will that be possible at lower energy
 979 ep colliders. At the LHeC, however, the CC is measured very well down to x below 10^{-4} which
 980 enables this distinction, helped by the NC weak current part of the cross section.

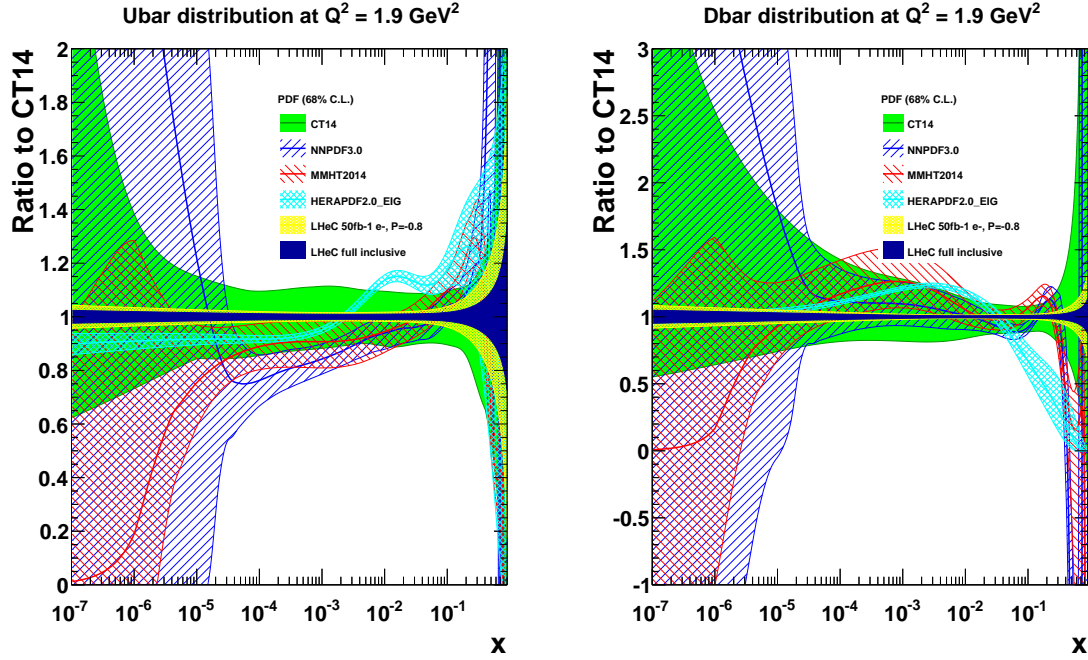


Figure 3.12: Sea quark distributions at $Q^2 = 1.9 \text{ GeV}^2$ as a function of Bjorken x , presented as the ratio to the CT14 central values. The yellow band corresponds to the “LHeC 1st run” PDFs (**D2**), while the dark blue shows the “LHeC full inclusive” PDFs (**D4+D5+D7+D8**), as described in the text. Both LHeC PDFs shown are scaled to the central value of CT14.

981 Gluon

982 The LHeC, with hugely increased precision and kinematic range of the most appropriate process
 983 (DIS) to explore $xg(x, Q^2)$, can pin down the gluon distribution much more accurately than
 984 the situation today. This primarily comes from the extension of range and precision in the
 985 measurement of $\partial F_2 / \partial \log Q^2$, which at small x is a measure of xg . The precision determination
 986 of the quark distributions, discussed previously, also strongly constrains xg . Further sensitivity
 987 arises with the high- y part of the NC cross section which is controlled by the longitudinal
 988 structure function as is discussed below.

989 The result for the gluon distribution from the LHeC inclusive NC and CC data is presented in
 990 Fig. 3.13, compared to several other modern PDF sets. On the left, the distribution is presented
 991 as a ratio to CT14, and is displayed on a log- x scale to highlight the small x region. On the
 992 right, the xg distribution is shown on a linear- x scale, accentuating the region of large x . The
 993 determination of xg is predicted to be radically improved with the LHeC NC and CC precision
 994 data, which extend down to lowest x values close to 10^{-6} and large $x \leq 0.8$.

995 Below $x \simeq 10^{-3}$, the HERA data have almost vanishing constraining power due to kinematic
 996 range limitations, as one needs a lever arm to determine the Q^2 derivative, and so the gluon
 997 is simply not determined at low x . With the LHeC, a precision of a few per cent at small x
 998 becomes possible. This has direct implications for the LHC: with the extension of the rapidity
 999 range to about 4 at the HL-LHC by ATLAS and CMS, Higgs physics will become small x physics
 1000 for which xg must be known as $gg \rightarrow H$ is the dominant production mechanism.

1001 While the analysis performed here has used standard DGLAP evolution, the precise measure-
 1002 ment of F_L at the LHeC (not yet included in the analysis presented here), in addition to F_2 ,

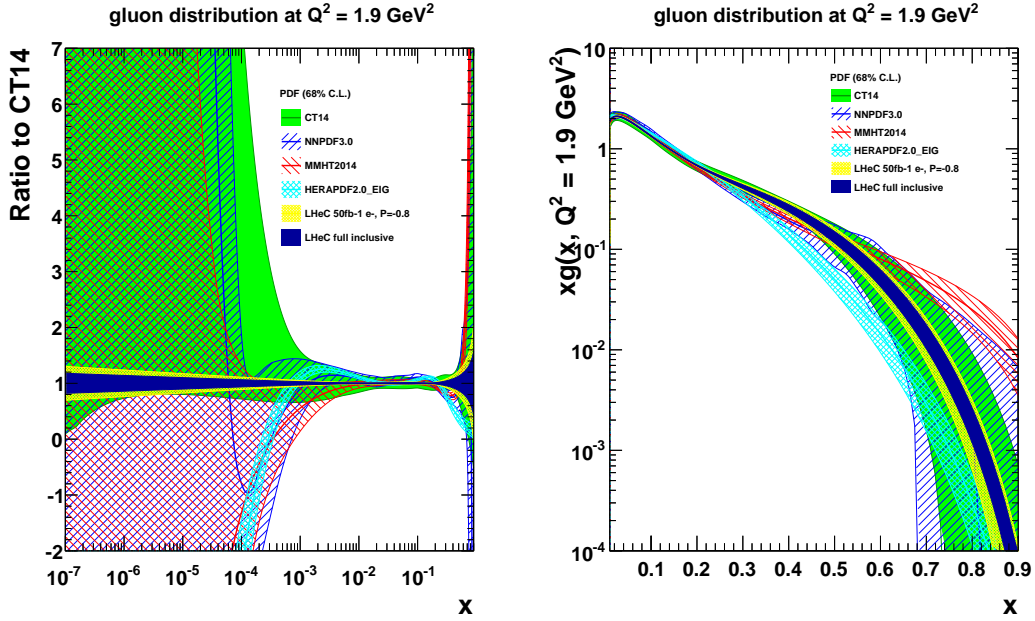


Figure 3.13: Gluon distribution at $Q^2 = 1.9 \text{ GeV}^2$ as a function of Bjorken x , highlighting (left) the low x and (right) the high x regions. The yellow band corresponds to the “LHeC 1st Run” PDFs (D2), while the dark blue shows the “LHeC full inclusive” PDFs (D4+D5+D7+D8), as described in the text. Both LHeC PDFs shown are scaled to the central value of CT14.

1003 can discover whether xg saturates, and whether the DGLAP equations need to be replaced by
 1004 non-linear parton evolution equations, as is also discussed in several Sections below.

1005 At large $x \geq 0.3$ the gluon distribution becomes very small and large variations appear in its
 1006 determination from different PDF groups, differing by orders of magnitude, which is related
 1007 to uncertainties on jet measurements, theoretical uncertainties, and the fact that HERA did
 1008 not have sufficient luminosity to cover the high x region where, moreover, the sensitivity to xg
 1009 diminishes, since the valence quark evolution is insensitive to it. For the LHeC, the sensitivity
 1010 at large x comes as part of the overall package: large luminosity allowing access to x values close
 1011 to 1, fully constrained quark distributions and strong constraints at small x which feed through
 1012 to large x via the momentum sum rule. The high precision illustrated will be crucial for BSM
 1013 searches at high scales. It is also important for testing QCD factorisation and scale choices, as
 1014 well as electroweak effects.

1015 It is worth noting that the uncertainties considered here are restricted to those related to the
 1016 genuine cross section measurement uncertainties. There are further uncertainties, for instance,
 1017 related to the difficulty of parameterising the PDFs and choosing the optimum solution in such
 1018 a fit analysis. These would also be considerably reduced with the LHeC extended data base as
 1019 was mentioned above. Moreover, the analysis presented here has not made use of the additional
 1020 information that can be provided at the LHeC in measurements of $F_2^{c,b}$ (see Sec 3.1.7) or F_L . The
 1021 large x situation can be expected to further improve by using LHeC jet data, providing further,
 1022 direct constraints at large x which, however, have not yet been studied in any comparable detail.

1023 The LHeC is the ideal laboratory to resolve all unknowns of the gluon density, which is the cause
 1024 for essentially all visible matter, and one of the particular secrets of particle physics for it cannot
 1025 directly be observed but is confined inside matter. It is obvious that resolving this puzzle is an
 1026 energy frontier DIS task and goal, including electron-ion scattering since the gluon inside heavy
 1027 matter is known even much less. Therefore, the special importance of this part of high energy

1028 PDF physics is not primarily related to the smallness of uncertainties: it is about a consistent
 1029 understanding and resolution of QCD at all regions of spatial and momentum dimensions which
 1030 the LHeC will explore, and later the FCC-eh too.

1031 Impact of Different Datasets

1032 It is informative to illustrate the transition of the PDF determination from the “LHeC 1st Run”
 1033 PDFs (including only dataset **D2**), through to the “LHeC full inclusive” PDFs (**D4+D5+D7**
 1034 **+D8**). Various intermediate PDF fits have been performed including subsets of the datasets
 1035 summarised in Tab.3.2. The results are illustrated in Figs.3.14 and 3.15, which show the
 1036 distributions of the: (a) u_v , (b) d_v , (c)–(d) gluon, and (e)–(f) sea quarks. In both Fig. 3.14 and
 1037 3.15, three of the bands are the same: the yellow shows the “LHeC 1st Run” PDF, the dark
 1038 blue shows the results of the “LHeC full inclusive” PDF, and the cyan is an identical PDF fit
 1039 including only the HERA II combined inclusive NC and CC data, rather than LHeC simulated
 1040 data.

1041 In Fig. 3.14 two further fits are also shown. The blue and the red, respectively, show the results
 1042 of a fit to LHeC simulated datasets with $5 \text{ fb}^{-1} e^-p$ (**D1**) and $1000 \text{ fb}^{-1} e^-p$ (**D4**). Therefore,
 1043 the transition from the blue \rightarrow yellow \rightarrow red, illustrates the impact of increasing the amount
 1044 of integrated luminosity of e^-p inclusive NC and CC data. The small and medium- x regions
 1045 are quickly constrained, even with only 5 fb^{-1} , corresponding to approximately the 1st year of
 1046 LHeC operation ². The high x region benefits from increased luminosity, though it is clear that
 1047 the vast majority of the gain, compared to the analogous HERA fit, comes already from the
 1048 first 50 fb^{-1} .

1049 Figure 3.15 illustrate the impact of adding positron data. The orange band shows the result of
 1050 adding 1 fb^{-1} of e^+p (**D2+D6**), while the green is the result of using 10 fb^{-1} of e^+p (**D2+D7**).
 1051 In both cases the positron data is added to the baseline “LHeC 1st run” dataset. Most of the
 1052 improvement with respect to the equivalent HERA fit has already been gained within the first
 1053 50 fb^{-1} , as mentioned above. Nevertheless, the addition of even a small amount of positrons
 1054 does bring benefit, most especially to the d -valence PDF, primarily due to the sensitivity gained
 1055 via the CC cross section.

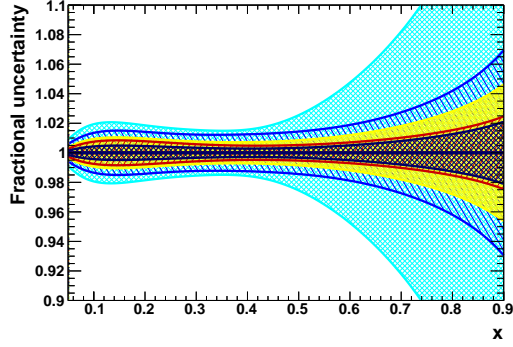
1056 PDF fits including LHeC simulated data with different electron-polarisations was also studied,
 1057 and found to have only a small impact on the PDF determination ³. While the impact for PDFs
 1058 is small, having datasets with both negatively and positively polarised leptons is important for
 1059 the electroweak programme of the LHeC as is described subsequently.

1060 Inclusion of Heavy Quark Measurements

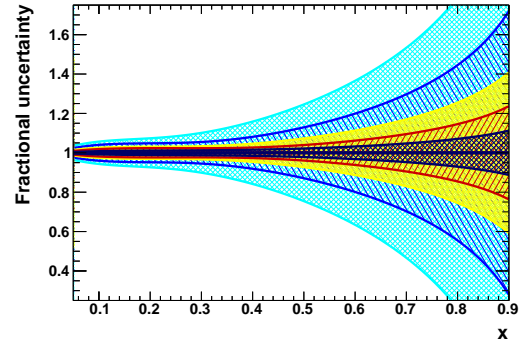
1061 As discussed in Sec 3.1.6, the inclusive NC and CC data determine the sums of the up and down
 1062 quark and antiquark distributions. In the studies presented so far, the parameterised PDFs are
 1063 the 4 quark distributions $xu_v, xd_v, x\bar{U}, x\bar{D}$ and g (a $4 + 1$ parameterisation), with the strange
 1064 assumed to be a constant fraction of $x\bar{D} = x\bar{d} + x\bar{s}$. The addition of exclusive measurements, for
 1065 example of the strange density and of $F_2^{c,b}$ will allow individual quark flavours to be determined.
 1066 In this section, a short study is presented which highlights these constraints. For all fits presented

²Note that HERA experiments, H1 and ZEUS, together collected about 1 fb^{-1} of integrated luminosity, divided between e^-p and e^+p datasets

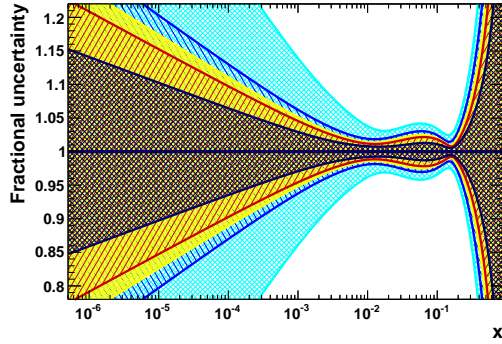
³What impact there is comes primarily from the overall increase (decrease) in inclusive CC cross section for negatively (positively) polarised electrons.



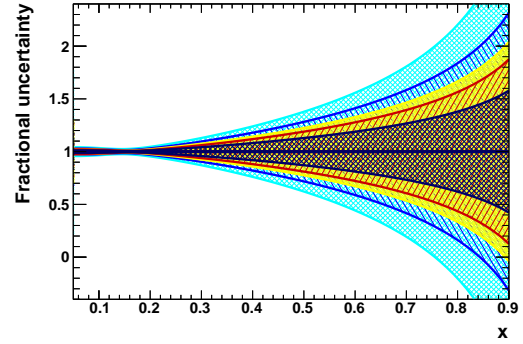
(a) u -valence distribution.



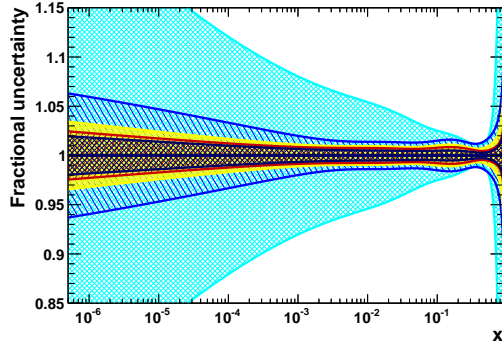
(b) d -valence distribution.



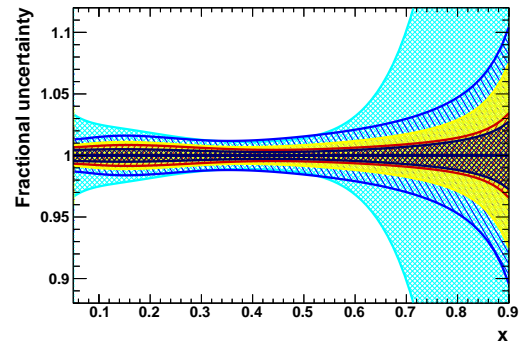
(c) Gluon distribution ($\log_{10} x$ scale).



(d) Gluon distribution (linear x scale).

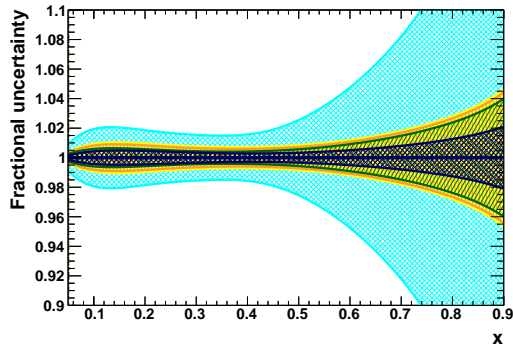


(e) Sea quark distribution ($\log_{10} x$ scale).

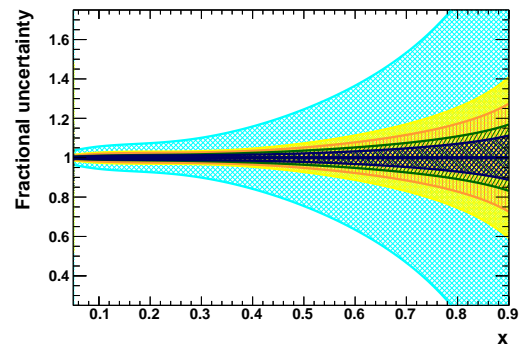


(f) Sea quark distribution (linear x scale).

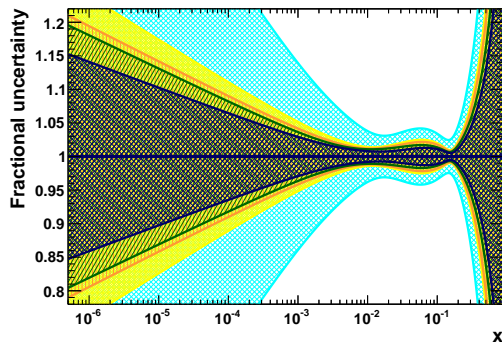
Figure 3.14: PDF distributions at $Q^2 = 1.9 \text{ GeV}^2$ as a function of Bjorken x , illustrating the impact of different amounts of integrated luminosity. The blue, yellow and red bands correspond to LHeC PDFs using electron-only NC and CC inclusive measurements with $5, 50$ and 1000 fb^{-1} , respectively. The yellow is the same as the “LHeC 1st run” PDF. For comparison, the dark blue band shows the results of the “LHeC full inclusive” PDF, while the cyan band corresponds to a completely analogous fit including only the full HERA II combined inclusive data. Note that this, unlike the LHeC, extends everywhere beyond the narrow limits of the y scale of the plots.



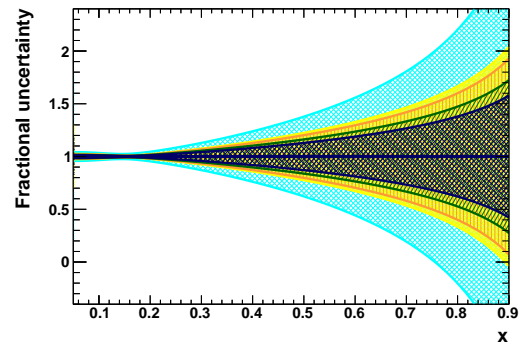
(a) u -valence distribution.



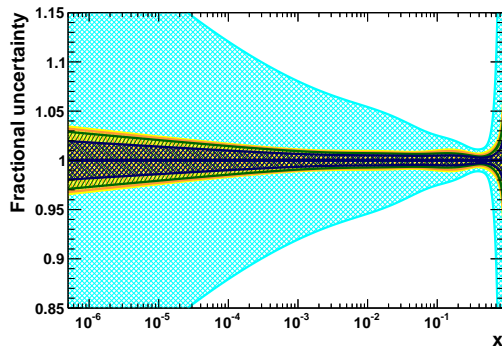
(b) d -valence distribution.



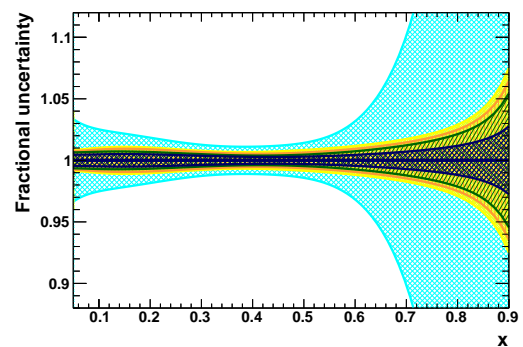
(c) Gluon distribution ($\log_{10} x$ scale).



(d) Gluon distribution (linear x scale).



(e) Sea quark distribution ($\log_{10} x$ scale).



(f) Sea quark distribution (linear x scale).

Figure 3.15: PDF distributions at $Q^2 = 1.9 \text{ GeV}^2$ as a function of Bjorken x , illustrating the impact of including positron data. The cyan, yellow and dark blue bands are as for Fig. 3.14. The orange band corresponds to a fit with 1 fb^{-1} of inclusive NC and CC positron-proton data, in addition to 50 fb^{-1} of electron-proton data (D2+D6), while the green band is similar, but with 10 fb^{-1} of positron-proton data (D2+D7).

1067 in this section, the \bar{d} and \bar{s} are treated separately, so that a total of 5 quark distributions are
 1068 parameterised ($xu_v, xd_v, x\bar{U}, x\bar{d}, x\bar{s}$) as well as g (i.e. a 5 + 1 parameterisation), and the total
 1069 number of free parameters becomes 17. Results are shown in Fig. 3.16.

1070 The impact on the PDFs when treating the \bar{d} and \bar{s} separately is illustrated by comparing the
 1071 yellow (which corresponds to the 4 + 1 “LHeC full inclusive” PDF shown previously) to the
 1072 cyan, which shows a fit including the same inclusive LHeC simulated data, but using the more
 1073 flexible 5 + 1 fit. The uncertainties, especially on the \bar{d} and \bar{s} distributions themselves (bottom
 1074 in Fig. 3.16) become substantially larger, demonstrating that the inclusive data alone does
 1075 not have the flavour separating power to determine the individual distributions very precisely.
 1076 The red bands in the same figure shows what happens to the PDF uncertainties when an LHeC
 1077 measurement of the \bar{s} quark density is included, assuming 10 fb^{-1} of e^-p data. The uncertainties
 1078 on the separate \bar{d} and \bar{s} PDFs become comparable again to the more constrained 4 + 1 fit. Note
 1079 that the assumption $s = \bar{s}$ has been imposed for this study. However, if a measurement of
 1080 the s -quark density from e^+p data were also available, then the s and \bar{s} distributions could be
 1081 separately and precisely determined.

1082 Fig. 3.16 also shows the results for a fit which, on top of the inclusive NC and CC and strange
 1083 data, additionally includes LHeC measurements of F_2^c and F_2^b from simulated e^-p data with an
 1084 assumed integrated luminosity of 10 fb^{-1} . The impact is mainly observed in the gluon PDFs
 1085 (top left and top right), where the uncertainties are substantially reduced and become roughly
 1086 comparable to (at low x) and substantially better than (at high x) the fits using only inclusive
 1087 data.

1088 The complete provision of NC, CC and tagged s , c and b data thus resolves the partonic sub-
 1089 structure of the proton completely. This holds similarly for the nuclear parton distributions
 1090 presented below. Indeed, the LHeC is the cleanest microscope for resolving the dynamics and
 1091 structure of matter which may be built during the coming decade.

1092 3.1.7 Heavy Quarks

1093 Heavy Quarks: Strange

1094 The determination of the strange PDF has generated significant controversy in the literature
 1095 for more than a decade. The older fixed-target neutrino DIS measurements typically prefer a
 1096 strange PDF that is roughly half of the up and down sea distribution; $\kappa = (s + \bar{s})/(\bar{u} + \bar{d}) \sim 0.5$,
 1097 while recent measurements from the LHC suggest a larger strange quark distribution. The LHeC
 1098 provides the opportunity to resolve many of these outstanding issues and greatly improved the
 1099 precision of $s(x)$. The strange quark provides a significant contribution to *standard candle*
 1100 measurements such as W/Z production, and influences the W mass determination.

1101 The high precision measurements of the inclusive W and Z boson cross section at the LHC
 1102 provide new constraints on the strange quark density in the low- x regime. One of the earlier
 1103 LHC analyses to study the strange quark PDF used the ATLAS inclusive W/Z data [64, 65].
 1104 In contrast to the results from the fixed-target experiments, the LHC analysis suggested the
 1105 strange quark could be as large, or larger, than the up and down sea quarks (\bar{u} and \bar{d}). This
 1106 observation was supported by analysis of the ATLAS $W + c$ data [66]

1107 However, the CMS $W + c$ data [67] favor a somewhat smaller strangeness. Since the analysis
 1108 of the $W + c$ data involve assumptions on charm jet fragmentation and hadronisation, it is

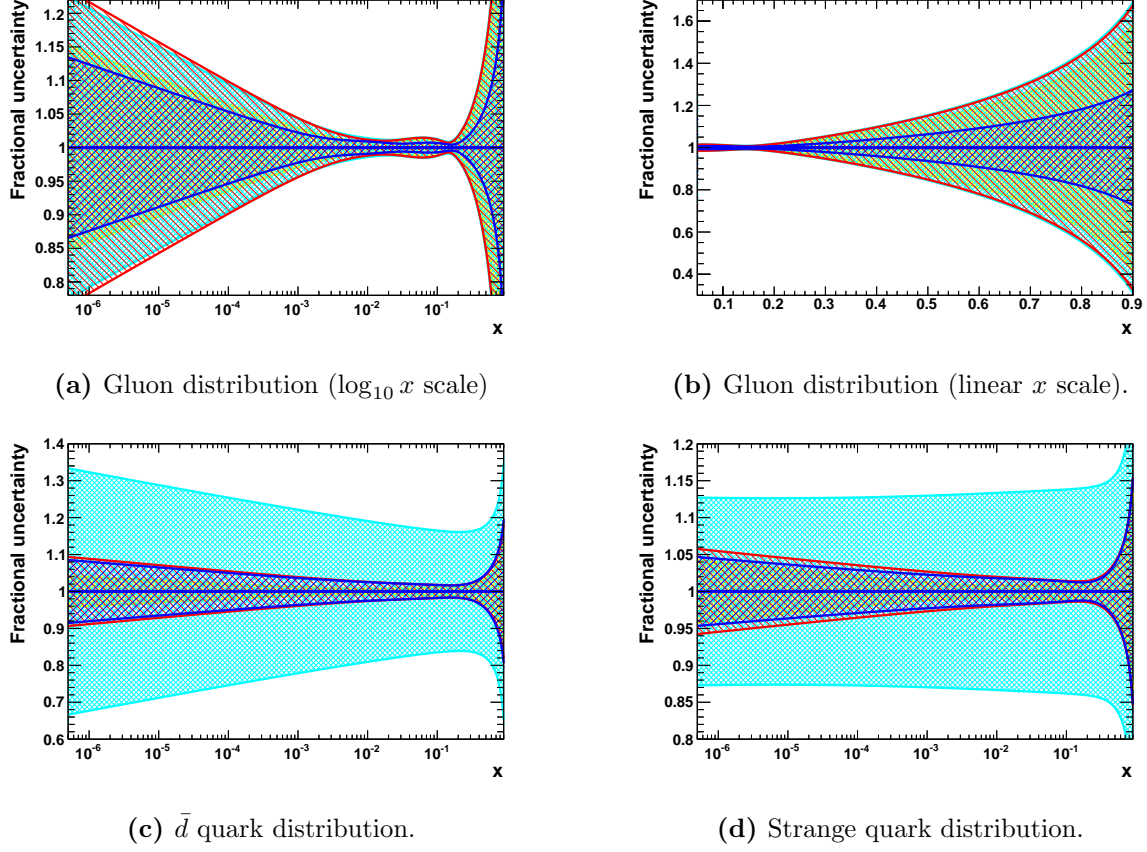


Figure 3.16: PDF distributions at $Q^2 = 1.9 \text{ GeV}^2$ as a function of Bjorken x , illustrating the impact of inclusion of s, c, b data. See the text for more details.

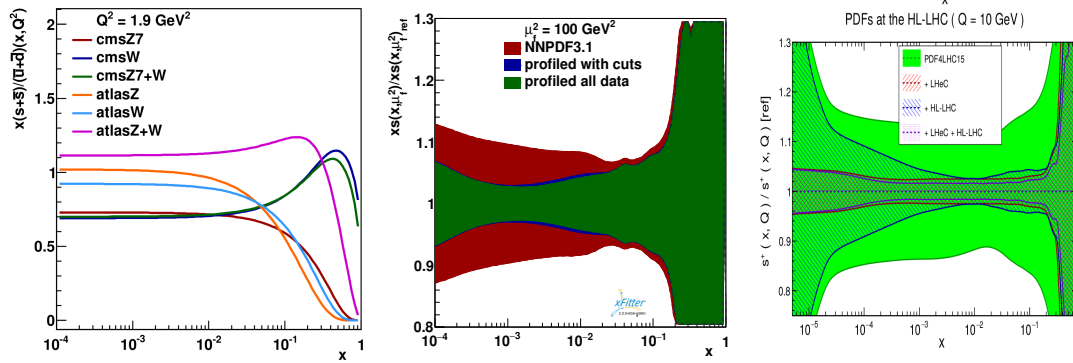


Figure 3.17: a) The fits to the PDF ratio $(s + \bar{s})/(\bar{u} + \bar{d})$ for various subsets of the ATLAS and CMS W and Z data sets from Ref. [62]. b) Constraints on the strange quark PDF using charged-current production of charm at the LHeC from Ref. [63]. c) Constraints on the strange quark PDF from Ref. [36].

1109 interesting to investigate if this disagreement is present for the inclusive Drell-Yan (DY) data of
 1110 ATLAS and CMS.

1111 A combined analysis was done by performing a parton distribution function analysis in NNLO
 1112 QCD using the inclusive deep inelastic scattering data from HERA jointly with the ATLAS and
 1113 CMS inclusive Drell-Yan data [62]. This study found that while there was no tension between
 1114 the HERA data and the LHC data, or between the LHC data sets, the LHC data support

1115 unsuppressed strangeness in the proton at low x at both low and high scales. The result is
 1116 dominated by the ATLAS data but is not in contradiction with the CMS data. Figure 3.17-a
 1117 displays the preferred value of the ratio $(s + \bar{s})/(\bar{u} + \bar{d})$ for the individual measurements.

1118 The LHeC has the potential to significantly improve the precision of the strange quark PDF,
 1119 and this may provide additional insight into the above analyses. To investigate this possibility,
 1120 the xFitter collaboration used LHeC pseudodata for charged current production of charm final
 1121 states to constrain the initial strange quark PDF; at leading-order, the subprocess is $Ws \rightarrow c$.
 1122 Additionally, the charged current process allows us to use the electron and positron beams to
 1123 separately probe the strange and anti-strange PDFs individually; this provides another level of
 1124 flavour discrimination.

1125 This study found that the LHeC can provide strong constraints on the strange-quark PDF,
 1126 especially in the previously unexplored small- x region. Figure 3.17-b displays the improved
 1127 constraints on the strange PDF using the LHeC pseudodata for the charged current charm
 1128 production channel ($sg \rightarrow Wc$) as obtained using xFitter profiling tools [63]. A large reduction
 1129 of uncertainties is observed also when restricting the input data (profiled with cuts, Fig. 3.17-b)
 1130 to the kinematic range where the differences between the different heavy flavour schemes (VFNS
 1131 and FFNS) are not larger than the present PDF uncertainties, indicating that the obtained PDF
 1132 constraints are stable and independent of the particular heavy-flavour scheme. A reduction of
 1133 the strange-PDF uncertainties influences the W/Z production, and thus the Higgs production;
 1134 hence, the LHeC CC DIS charm production data represent a valuable addition for the future
 1135 global PDF fits.

1136 A separate study [36] also looked at constraints on $s(x)$ using a variety of channels. The results
 1137 of the improved PDF limits are displayed in Fig. 3.17-c which shows the constraints from the
 1138 LHeC, the HL-LHC, and the combination.

1139 In summary, we find that CC DIS charm production at the LHeC can provide strong constraints
 1140 on the strange PDF which are complementary to the current data sets. As the PDF uncertainty is
 1141 the dominant factor for many precision analyses, a reduction of these uncertainties will allow for
 1142 more accurate predictions which can be used to constrain both SM and BSM physics processes.

1143 Heavy Quarks: Charm & Bottom

1144 The production of heavy quarks at HERA (charm and bottom) was an especially interesting
 1145 process as the quark mass introduced a new scale ($m_{c,b}$) which was neither heavy or light. Such
 1146 multi-scale problems are particularly difficult, and numerous techniques were developed to cope
 1147 with this challenging problem [68–77].

1148 At the LHeC, the increased centre-of-mass energy allows us to extend to very large Q^2 values.
 1149 Thus, the LHeC can comprehensively explore the *asymptotic* high energy limit where $m_{c,b}^2/Q^2 \rightarrow$
 1150 0, as well as low energy *decoupling* region $m_{c,b}^2/Q^2 \sim 1$. In Fig. 3.18 we display the kinematic
 1151 reach of $F_2^{c\bar{c}}$ and $F_2^{b\bar{b}}$, and contrast this with the HERA combined data. The extended reach
 1152 is dramatic. These channels can also help improve the determination of the charm and bottom
 1153 quark masses and bring these uncertainties into the range of $\lesssim 10$ MeV.

1154 Additionally, the production of heavy quarks is closely tied to the gluon distribution via the
 1155 process $g \rightarrow Q\bar{Q}$, so improved heavy quark measurements can also contribute to reducing the
 1156 gluon uncertainty, see Fig. 3.19.

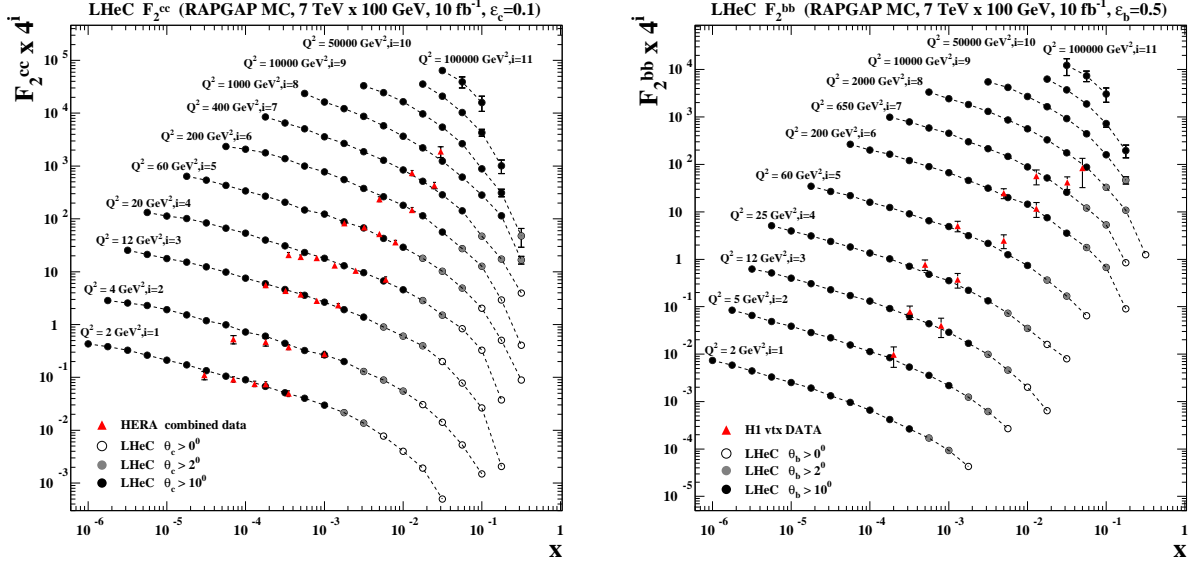


Figure 3.18: Heavy quark structure functions $F_2^{c\bar{c}}$ and $F_2^{b\bar{b}}$ showing the comparison of the HERA data to LHeC pseudodata.

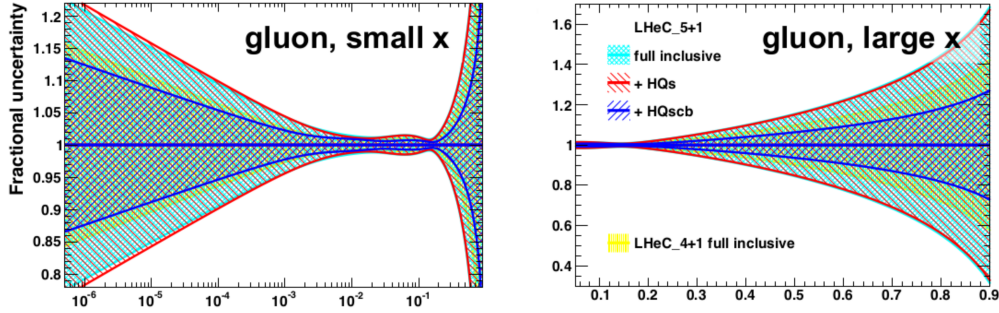


Figure 3.19: Impact of heavy quark production data on LHeC PDFs.

1157 Intrinsic Heavy Quark Phenomena

1158 One of the most interesting nonperturbative quantum field theoretic aspect of hadron light front
 1159 wavefunctions in QCD are the intrinsic heavy-quark Fock states [78–80]. Consider a heavy-quark
 1160 loop insertion to the proton’s self-energy. The heavy-quark loop can be attached by gluons to
 1161 just one valence quark. The cut of such diagrams yields the standard DGLAP gluon splitting
 1162 contribution to the proton’s heavy quark structure function. In this case, the heavy quarks are
 1163 produced at very small x . However, the heavy quark loop can also be attached to two or more
 1164 valence quarks in the proton self-energy. In the case of QED this is corresponds to the light-
 1165 by-light lepton loop insertion in an atomic wavefunction. In the case of QCD, the heavy quark
 1166 loop can be attached by three gluons to two or three valence quarks in the proton self-energy.
 1167 This is a non-Abelian insertion to the hadron’s self-energy. The cut of such diagrams gives the
 1168 *intrinsic* heavy-quark contribution to the proton’s light-front wavefunction. In the case of QCD,
 1169 the probability for an intrinsic heavy $Q\bar{Q}$ pair scales as $\frac{1}{M_Q^2}$; this is in contrast to heavy $\ell\bar{\ell}$ lepton
 1170 pairs in QED where the probability for heavy lepton pairs in an atomic wavefunction scales as
 1171 $\frac{1}{M_\ell^4}$. This difference in heavy-particle scaling in mass distinguishes Abelian from non-Abelian
 1172 theories.

1173 A basic property of hadronic light-front wavefunctions is that they have strong fall-off with the
1174 invariant mass of the Fock state. For example, the LFWFs of the colour-confining AdS/QCD
1175 models [81] $\mathcal{M}^2 = [\sum_i k_i^\mu]^2$ of the Fock state constituents. This means that the probability is
1176 maximised when the constituents have equal true rapidity, i.e. $x_i \propto (\vec{k}_{\perp i}^2 + m_i^2)^{1/2}$. Thus the
1177 heavy quarks carry most of the momentum in an intrinsic heavy quark Fock state. For example,
1178 the charm quark in the intrinsic charm Fock state $|uudc\bar{c}\rangle$ of a proton carries about 40 % of the
1179 proton's momentum: $x_c \sim 0.4$. After a high-energy collision, the co-moving constituents can
1180 then recombine to form the final state hadrons. along the proton. Thus, in a ep collision the
1181 comoving udc quarks from the $|uudc\bar{c}\rangle$ intrinsic 5-quark Fock state can recombine to a Λ_c , where
1182 $x_{\Lambda_c} = x_c + x_u + x_d \sim 0.5$. Similarly, the comoving dcc in the $|uudc\bar{c}\bar{c}\bar{c}\rangle$ intrinsic 7-quark Fock
1183 state can recombine to a $\Xi(ccd)^+$, with $x_{\Xi(ccd)} = x_c + x_c + x_d \sim 0.9$.

1184 Therefore, in the intrinsic heavy quark model the wavefunction of a hadron in QCD can be rep-
1185 resented as a superposition of Fock state fluctuations, e.g. $|n_V\rangle$, $|n_V g\rangle$, $|n_V Q\bar{Q}\rangle$, \dots components
1186 where $n_V \equiv dds$ for Σ^- , uud for proton, $\bar{u}d$ for π^- and $u\bar{d}$ for π^+ . Charm hadrons can be
1187 produced by coalescence in the wavefunctions of the moving hadron. Doubly-charmed hadrons
1188 require fluctuations such as $|n_V c\bar{c}\bar{c}\bar{c}\rangle$. The probability for these Fock state fluctuations to come
1189 on mass shell is inversely proportional to the square of the quark mass, $\mathcal{O}(m_Q^{-2n})$ where n is the
1190 number of $Q\bar{Q}$ pairs in the hadron. Thus the natural domain for heavy hadrons produced from
1191 heavy quark Fock states is $\vec{k}_{\perp Q}^2 \sim m_Q^2$ and high light-front momentum fraction x_Q [78, 79, 79, 80].
1192 For example, the rapidity regime for double-charm hadron production $y_{ccd} \sim 3$ at low energies is
1193 well within the kinematic experiment domain of a fixed target experiment such as SELEX at the
1194 Tevatron [82]. Note that the intrinsic heavy-quark mechanism can account for many previous
1195 observations of forward heavy hadron production single and double J/ψ production by pions ob-
1196 served at high $x_F > 0.4$ in the low energy fixed target NA3 experiment, the high x_F production
1197 of $pp \rightarrow \Lambda_c, +X$ and $pp \rightarrow \Lambda_b + X$ observed at the ISR; single and double $\Upsilon(b\bar{b})$ production, as
1198 well as *quadra-bottom* tetraquark $[bb\bar{b}\bar{b}]$ production observed recently by the AnDY experiment
1199 at RHIC [83]. In addition the EMC collaboration observed that the charm quark distribution
1200 in the proton at $x = 0.42$ and $Q^2 = 75 \text{ GeV}^2$ is 30 times larger than expected from DGLAP
1201 evolution. All of these experimental observations are naturally explained by the intrinsic heavy
1202 quark mechanism. The SELEX observation [82] of double charm baryons at high x_F reflects
1203 production from double intrinsic heavy quark Fock states of the baryon projectile. Similarly,
1204 the high x_F domain – which would be accessible at forward high x_F – is the natural production
1205 domain for heavy hadron production at the LHeC.

1206 The production of heavy hadrons based on intrinsic heavy quark Fock states is thus remarkable
1207 efficient and greatly extends the kinematic domain of the LHeC, e.g. for processes such as
1208 $\gamma^* b \rightarrow Z^0 b$. This is in contrast with the standard production cross sections based on gluon
1209 splitting, where only a small fraction of the incident momentum is effective in creating heavy
1210 hadrons.

1211 3.2 Pushing the limits of QCD with high precision measure- 1212 ments

1213 The straightforward and strikingly simple formalism of Quantum Chromodynamics (QCD) pro-
1214 vides a very successful description of strong interactions. Despite its undoubted success, the
1215 strong force remains one of the least known fundamental sectors of (particle) physics and many
1216 of its phenomena are known only with moderate or even poor precision, and several aspects still

1217 need to be explored, see the introductory Chapter 1.

1218 For an improved understanding of strong interactions and to answer a variety of those open
1219 questions additional measurements with highest precision have to be performed. At the LHeC,
1220 deep-inelastic electron-proton and lepton-nucleus reactions will extend tests of QCD phenomena
1221 to a new and yet unexplored domain up to the TeV scale and to x values as low as 10^{-6} , and
1222 QCD measurements can be performed with very high experimental precision. This is because
1223 the proton is a *strongly* bound system and in deep-inelastic scattering (DIS) the exchanged
1224 *colourless* photon (or Z) between the electron and the parton inside the proton acts as a neutral
1225 observer with respect to the phenomena of the strong force. In addition, the over-constrained
1226 kinematic system in DIS allows for precise (*in-situ*) calibrations of the detector to measure the
1227 kinematics of the scattered lepton, and, more importantly here, also the hadronic final state. In
1228 DIS, in many cases, the virtuality of the exchanged γ/Z boson often provides a reasonable scale
1229 to stabilise theoretical predictions.

1230 In this Section, selected topics of QCD studies at the LHeC are discussed.

1231 3.2.1 Determination of the strong coupling constant

1232 Quantum Chromodynamics (QCD) [84, 85] has been established as the theory of strong inter-
1233 actions within the Standard Model of particle physics. While there are manifold aspects both
1234 from the theoretical and from the experimental point-of-view, by far the most important pa-
1235 rameter of QCD is the coupling strength which is most commonly expressed at the mass of the
1236 Z boson, M_Z , as $\alpha_s(M_Z)$. Its (renormalisation) scale dependence is given by the QCD gauge
1237 group $SU(3)$ [86, 87]. Predictions for numerous processes in e^+e^- , pp or ep collisions are then
1238 commonly performed in the framework of perturbative QCD, and (the lack of) higher-order
1239 QCD corrections often represent limiting aspects for precision physics. Therefore, the deter-
1240 mination of the strong coupling constant $\alpha_s(M_Z)$ constitutes one of the most crucial tasks for
1241 future precision physics, while at the same time the study of the scale dependence of α_s provides
1242 an inevitable test of the validity of QCD as the theory of strong interactions and the portal for
1243 GUT theories.

1244 Different processes and methodologies can be considered for a determination of $\alpha_s(M_Z)$ (see e.g.
1245 reviews [88–90]). Since QCD is an asymptotically free theory, with free behaviour at high scales
1246 but confinement at low scales, a high sensitivity to the value of $\alpha_s(M_Z)$ is naturally obtained
1247 from low-scale measurements. However, the high-scale behaviour must then be calculated by
1248 solving the renormalisation group equation, which implies the strict validity of the theory and
1249 an excellent understanding of all subleading effects, such as the behaviour around quark-mass
1250 thresholds.

1251 Precision measurements at the LHeC offer the unique opportunity to exploit many of these
1252 aspects. Measurements of jet production cross sections or inclusive NC and CC DIS cross
1253 sections provide a high sensitivity to the value of $\alpha_s(M_Z)$, since these measurements can be
1254 performed at comparably low scales and with high experimental precision. At the same time,
1255 the LHeC provides the opportunity to test the running of the strong coupling constant over a
1256 large kinematic range. In this Section, the prospects for a determination of the strong coupling
1257 constant with inclusive jet cross sections and with inclusive NC/CC DIS cross sections are
1258 studied.

1259 **Strong coupling from inclusive jet cross sections**

1260 The measurement of inclusive jet or di-jet production cross sections in NC DIS provides a high
 1261 sensitivity to the strong coupling constant and to the gluon PDF of the proton. This is because
 1262 jet cross sections in NC DIS are measured in the Breit reference frame [91], where the virtual
 1263 boson γ^* or Z collides head-on with the struck parton from the proton and the outgoing jets are
 1264 required to have a non-zero transverse momentum in that reference frame. The leading order
 QCD diagrams are QCD Compton and boson-gluon fusion and are both $\mathcal{O}(\alpha_s)$, see Fig. 3.20.

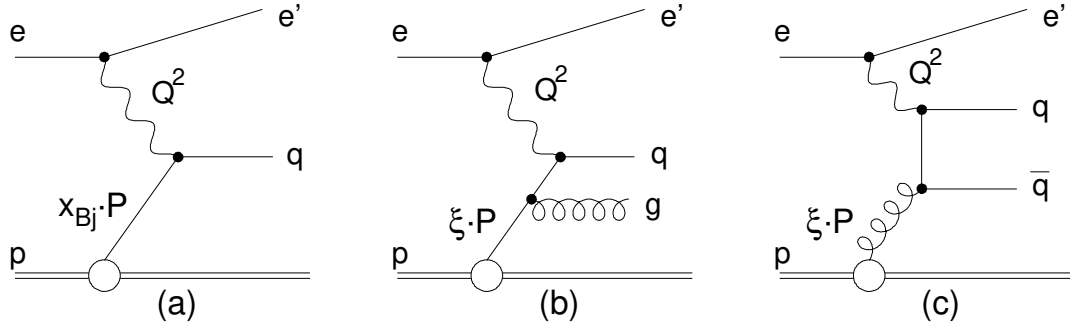


Figure 3.20: Leading order diagrams for inclusive DIS (a) and jet production (b,c) in the Breit frame (taken from Ref. [92]).

1265

1266 At HERA, jets are most commonly defined by the longitudinally invariant k_t jet algorithm [93]
 1267 with a distance parameter $R = 1.0$ [92, 94–110]. This provides an infrared safe jet definition
 1268 and the chosen distance parameter guarantees a small dependence on non-perturbative effects,
 1269 such as hadronisation. Differently than in pp at the LHC [111–114], jet algorithms at the LHeC
 1270 do not require any pile-up subtraction and any reduction of the dependence on minimum bias
 1271 or underlying event, due to the absence of such effects. Therefore, for this study we adopt the
 1272 choices made at HERA.

1273 In Fig. 3.21 the next-to-next-to-leading order QCD (NNLO) predictions [115, 116] for cross
 1274 sections for inclusive jet production in NC DIS as a function of the transverse momentum of the
 1275 jets in the Breit frame are displayed. The calculations are performed for an electron beam energy
 1276 of $E_e = 60$ GeV and include γ/Z and Z exchange terms and account for the electron polarisation
 1277 $P_e = -0.8$. The NC DIS kinematic range is set to $Q^2 > 4$ GeV². The calculations are performed
 1278 using the NNLOJET program [117] interfaced to the fastNLO (applfast) library [118–120].

1279 The kinematically accessible range in jet- P_T ranges over two orders of magnitude, $4 < P_T \lesssim$
 1280 400 GeV. The size of the cross section extends over many orders in magnitude, thus imposing
 1281 challenging demands on LHeC experimental conditions, triggers and DAQ bandwidth, calibra-
 1282 tion, and data processing capabilities. The scale uncertainty of the NNLO predictions is about
 1283 10% at low values of P_T and significantly decreases with increasing values of P_T . Future im-
 1284 proved predictions will further reduce these theoretical uncertainties.

1285 For the purpose of estimating the uncertainty of $\alpha_s(M_Z)$ in a determination from inclusive jet
 1286 cross sections at the LHeC, double-differential cross sections as a function of Q^2 and P_T with
 1287 a full set of experimental uncertainties are generated. Altogether 509 cross section values are
 1288 calculated in the kinematic range $8 < Q^2 < 500\,000$ GeV² and $4 < P_T < 512$ GeV, and the bin
 1289 grid is similar to the ones used by CMS, H1 or ZEUS [45, 111, 120, 121]. The various error sources
 1290 considered are summarised in Tab. 3.3. The uncertainties related to the reconstruction of the NC
 1291 DIS kinematic variables, Q^2 , y and x_{bj} , are similar to the estimates for the inclusive NC DIS cross

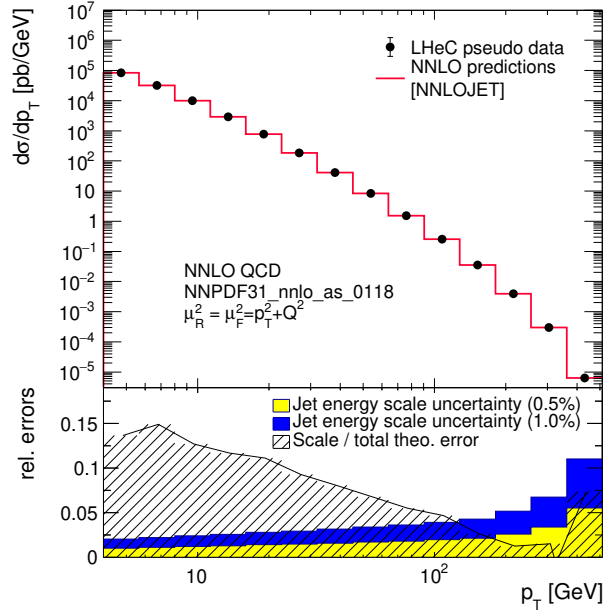


Figure 3.21: Inclusive jet cross sections calculated in NNLO QCD as a function of the jet transverse momentum in the Breit frame, p_T . The shaded area indicates NNLO scale uncertainties and the yellow band shows the estimated experimental jet energy scale uncertainty (JES) of 0.5%. The blue band shows a very conservative assumption on the JES of 1%.

1292 sections (see section 3.1.5). For the reconstruction of hadronic final state particles which are the
 1293 input to the jet algorithm, jet energy scale uncertainty (JES), calorimetric noise and the polar
 1294 angle uncertainty are considered. The size of the uncertainties is gauged with achieved values by
 1295 H1, ZEUS, ATLAS and CMS [101, 109, 122–124]. The size of the dominant JES one is assumed
 1296 to be 0.5% for reconstructed particles in the laboratory rest frame, yielding an uncertainty of
 1297 0.2–4.4% on the cross section after the boost to the Breit frame. A JES uncertainty of 0.5%
 1298 is well justified by improved calorimeters, since already H1 and ZEUS reported uncertainties
 1299 of 1% [101, 109, 122], and ATLAS and CMS achieved 1% over a wide range in P_T [123, 124],
 1300 albeit the presence of pile-up and the considerably more complicated definition of a reference
 1301 object for the in-situ calibration. The size of the JES uncertainty is also displayed in Fig. 3.21.
 1302 The calorimetric noise of ± 20 MeV on every calorimeter cluster, as reported by H1, yields an
 1303 uncertainty of up to 0.7% on the jet cross sections. A minimum size of the statistical uncertainty
 1304 of 0.15% is imposed for each cross section bin. An overall normalisation uncertainty of 1.0%
 1305 is assumed, which will be mainly dominated by the luminosity uncertainty. In addition, an
 1306 uncorrelated uncertainty component of 0.6% collects various smaller error sources, such as for
 1307 instance radiative corrections, unfolding or model uncertainties. Studies on the size and the
 1308 correlation model of these uncertainties are performed below.

1309 The value and uncertainty of $\alpha_s(M_Z)$ is obtained in a χ^2 -fit of NNLO predictions [115, 116] to
 1310 the simulated data with $\alpha_s(M_Z)$ being a free fit parameter. The methodology follows closely
 1311 analyses of HERA jet data [120, 121] and the χ^2 quantity is calculated from relative uncertainties,
 1312 i.e. those of the right column of Tab. 3.3. The predictions for the cross section σ account for
 1313 both α_s -dependent terms in the NNLO calculations, i.e. in the DGLAP operator and the hard
 1314 matrix elements, by using

$$\sigma = f_{\mu_0} \otimes P_{\mu_0 \rightarrow \mu_F}(\alpha_s(M_Z)) \otimes \hat{\sigma}(\alpha_s(M_Z), \mu), \quad (3.3)$$

Exp. uncertainty	Shift	Size on σ [%]
Statistics with 1 ab^{-1}	min. 0.15 %	0.15–5
Electron energy	0.1 %	0.02–0.62
Polar angle	2 mrad	0.02–0.48
Calorimeter noise	$\pm 20 \text{ MeV}$	0.01–0.74
Jet energy scale (JES)	0.5 %	0.2–4.4
Uncorrelated uncert.	0.6 %	0.6
Normalisation uncert.	1.0 %	1.0

Table 3.3: Anticipated uncertainties of inclusive jet cross section measurements at the LHeC.

1315 where f_{μ_0} are the PDFs at a scale of $\mu_0 = 30 \text{ GeV}$, and $P_{\mu_0 \rightarrow \mu_F}$ denotes the DGLAP operator,
1316 which is dependent on the value of $\alpha_s(M_Z)$. The α_s uncertainty is obtained by linear error
1317 propagation and is validated with a separate study of the $\Delta\chi^2 = 1$ criterion.

1318 In the fit of NNLO QCD predictions to the simulated double-differential LHeC inclusive jet cross
1319 sections an uncertainty of

$$\Delta\alpha_s(M_Z)(\text{jets}) = \pm 0.00013_{(\text{exp})} \pm 0.00010_{(\text{PDF})} \quad (3.4)$$

1320 is found. The PDF uncertainty is estimated from a PDF set obtained from LHeC inclusive DIS
1321 data (see Sec. 3.1.6). These uncertainties promise a determination of $\alpha_s(M_Z)$ with the highest
1322 precision and would represent a considerable reduction of the current world average value with
1323 a present uncertainty of ± 0.00110 [89].

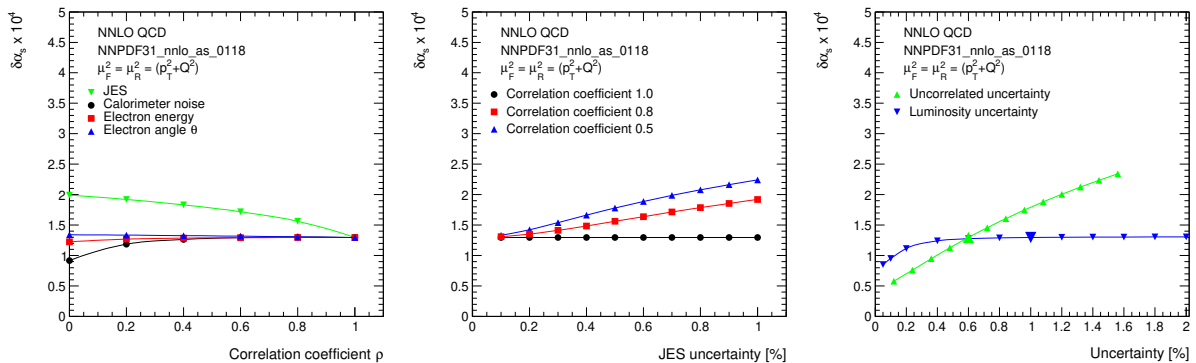


Figure 3.22: Studies of the size and correlations of experimental uncertainties impacting the uncertainty of $\alpha_s(M_Z)$. Left: Study of the value of the correlation coefficient ρ for different systematic uncertainties. Common systematic uncertainties are considered as fully correlated, $\rho = 1$. Middle: Size of the JES uncertainty for three different values of ρ_{JES} . Right: Impact of the uncorrelated and normalisation uncertainties on $\Delta\alpha_s(M_Z)$.

1324 The uncertainty of α_s is studied for different values of the experimental uncertainties for the
1325 inclusive jet cross section measurement and for different assumption on bin-to-bin correlations,
1326 expressed by the correlation coefficient ρ , of individual uncertainty sources, as shown in Fig. 3.22.
1327 It is observed that, even for quite conservative scenarios, $\alpha_s(M_Z)$ will be determined with an
1328 uncertainty smaller than 2%. For this, it is important to keep the size of the uncorrelated
1329 uncertainty or the uncorrelated components of other systematic uncertainties under good control.

1330 In the present formalism theoretical uncertainties from scale variations of the NNLO predictions
1331 amount to about $\Delta\alpha_s(M_Z) = 0.0035$ (NNLO). These can be reduced with suitable cuts in P_T

1332 or Q^2 to about $\Delta\alpha_s(M_Z) \approx 0.0010$. However, it is expected that improved predictions, e.g. with
 1333 resummed contributions or N³LO predictions will significantly reduce these uncertainties in the
 1334 future. Uncertainties on non-perturbative hadronisation effects will have to be considered as
 1335 well, but these will be under good control due to the measurements of charged particle spectra
 1336 at the LHeC and improved phenomenological models.

1337 **The running of the strong coupling**

1338 The dependence of the coupling strength as a function of the renormalisation scale μ_R is predicted
 1339 by QCD, which is often called the *running* of the strong coupling. Its study with experimental
 1340 data represents an important consistency and validity test of QCD. Using inclusive jet cross
 1341 sections the running of the strong coupling can be tested by determining the value of α_s at
 1342 different values of μ_R by grouping data points with similar values of μ_R and determining the
 1343 value of $\alpha_s(\mu_R)$ from these subsets of data points. The assumptions on the running of $\alpha_s(\mu_R)$
 1344 are then imposed only for the limited range of the chosen interval, and not to the full measured
 1345 interval as in the previous study. Here we set $\mu_R^2 = Q^2 + P_T^2$ ⁴. The experimental uncertainties
 1346 from the fits to subsets of the inclusive jet pseudodata are displayed in Fig. 3.23. These results
 1347 demonstrate a high sensitivity to α_s over two orders of magnitude in renormalisation scale up
 1348 to values of about $\mu_R \approx 500$ GeV. In the range $6 < \mu_R \lesssim 200$ GeV the experimental uncertainty
 1349 is found to be smaller than the expectation from the world average value [132]. This region is of
 1350 particular interest since it connects the precision determinations from lattice calculations [133]
 1351 or τ decay measurements [134], which are at low scales $\mathcal{O}(\text{GeV})$, to the measurements at the
 1352 Z pole [135] and to the applications to scales which are relevant for the LHC, e.g. for Higgs
 1353 or top-quark physics or high-mass searches. This kinematic region of scales $\mathcal{O}(10 \text{ GeV})$ cannot
 1354 be accessed by (HL-)LHC experiments because of limitations due to pile-up and underlying
 1355 event [136].

1356 **Strong coupling from inclusive DIS cross sections**

1357 Inclusive DIS cross sections are sensitive to $\alpha_s(M_Z)$ through higher-order QCD corrections,
 1358 contributions from the F_L structure function and the scale dependence of the cross section at
 1359 high x (*scaling violations*). The value of $\alpha_s(M_Z)$ can then be determined in a combined fit
 1360 of the PDFs and $\alpha_s(M_Z)$ [121]. While a simultaneous determination of $\alpha_s(M_Z)$ and PDFs is
 1361 not possible with HERA inclusive DIS data alone due to its limited precision and kinematic
 1362 coverage [45, 121], the large kinematic coverage, high precision and the integrated luminosity of
 1363 the LHeC data will allow for the first time such an α_s analysis.

1364 For the purpose of the determination of $\alpha_s(M_Z)$ from inclusive NC/CC DIS data, a combined
 1365 PDF+ α_s fit to the simulated data is performed, similar to the studies in Sec. 3.1. Other technical
 1366 details are outlined in Ref. [121]. In this fit, however, the numbers of free parameters of the
 1367 gluon parameterisation is increased, since the gluon PDF and $\alpha_s(M_Z)$ are highly correlated and

⁴ The choice of the scales follows a *conventional* scale setting procedure and uncertainties for the scale choice and for unknown higher order terms are estimated by varying the scales. Such variations are sensitive only to the terms which govern the behaviour of the running coupling, and may become unreliable due to renormalons [125]. An alternative way to fix the scales is provided by the Principle of Maximum Conformality (PMC) [126–130]. The PMC method was recently applied to predictions of event shape observables in $e^+e^- \rightarrow \text{hadrons}$ [131]. When applying the PMC method to observables in DIS, the alternative scale setting provides a profound alternative to verify the running of $\alpha_s(\mu_R)$. Such a procedure could be particularly relevant for DIS event shape observables, where the leading-order terms are insensitive to α_s and conventional scale choices may not be adequately related to the α_s -sensitive higher order QCD corrections.

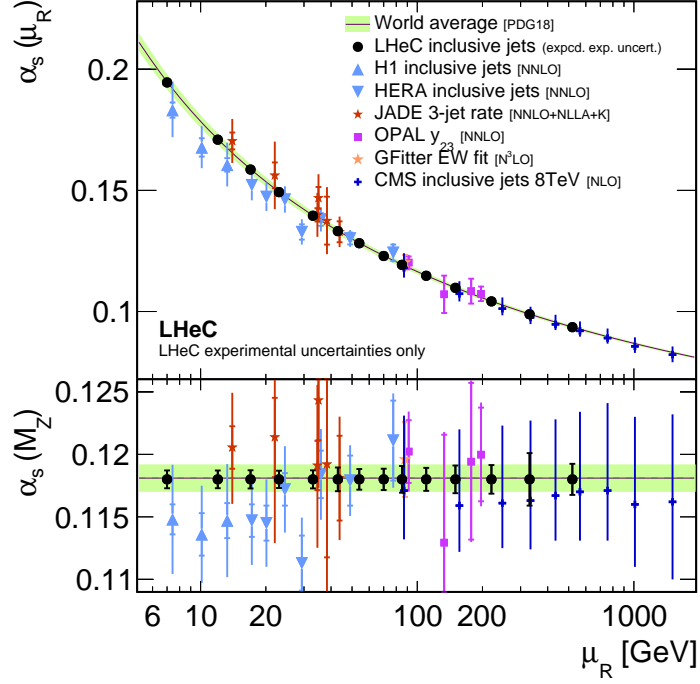


Figure 3.23: Uncertainties of $\alpha_s(M_Z)$ and corresponding $\alpha_s(\mu_R)$ in a determination of α_s using LHeC inclusive jet cross sections at different values of $\mu_R^2 = Q^2 + p_T^2$. Only experimental uncertainties are shown for LHeC and are compared with a number of presently available measurements and the world average value.

1368 LHeC data are sensitive to values down to $x < 10^{-5}$, which requires additional freedom for the
 1369 gluon parameterisation. The inclusive data are restricted to $Q^2 > 3.5 \text{ GeV}^2$ in order to avoid a
 1370 region where effects beyond fixed-order perturbation theory may become sizeable [45, 137].

1371 Exploiting the full LHeC inclusive NC/CC DIS data with $E_e = 50 \text{ GeV}$, the value of $\alpha_s(M_Z)$ can
 1372 be determined with an uncertainty $\Delta\alpha_s(M_Z) = \pm 0.00038$. With a more optimistic assumption
 1373 on the dominant uncorrelated uncertainty of $\delta\sigma_{(\text{uncor.})} = 0.25\%$, an uncertainty as small as

$$\Delta\alpha_s(M_Z)(\text{incl. DIS}) = \pm 0.00022_{(\text{exp+PDF})} \quad (3.5)$$

1374 is achieved. This would represent a considerable improvement over the present world average
 1375 value. Given these small uncertainties, theoretical uncertainties from missing higher orders or
 1376 heavy quark effects have to be considered in addition. In a dedicated study, the fit is repeated
 1377 with a reduced data set which can be accumulated already during a single year of operation ⁵,
 1378 corresponding to about $\mathcal{L} \sim 50 \text{ fb}^{-1}$. Already these data will be able to improve the world
 1379 average value. These studies are displayed in Fig. 3.24.

1380 Inclusive DIS and inclusive jet data

1381 The highest sensitivity to $\alpha_s(M_Z)$ and an optimal treatment of the PDFs is obtained by using
 1382 inclusive jet data together with inclusive NC/CC DIS data in a combined determination of
 1383 $\alpha_s(M_Z)$ and the PDFs. Jet data will provide an enhanced sensitivity to $\alpha_s(M_Z)$, while inclusive

⁵Two different assumptions are made. One fit is performed with only electron data corresponding to $\mathcal{L} \sim 50 \text{ fb}^{-1}$, and an alternative scenario considers further positron data corresponding to $\mathcal{L} \sim 1 \text{ fb}^{-1}$.

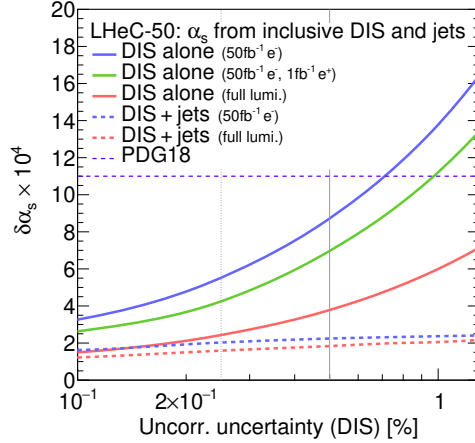


Figure 3.24: Uncertainties of $\alpha_s(M_Z)$ from simultaneous fits of $\alpha_s(M_Z)$ and PDFs to inclusive NC/CC DIS data as a function of the size of the uncorrelated uncertainty of the NC/CC DIS data. The full lines indicate the uncertainties obtained with different assumptions on the data taking scenario and integrated luminosity. The dashed lines indicate results where, additionally to the inclusive NC/CC DIS data, inclusive jet cross section data are considered.

1384 DIS data has the highest sensitivity to the determination of the PDFs. Furthermore, a consistent
 1385 theoretical QCD framework can be employed.

1386 For this study, the double-differential inclusive jet data as described above, and additionally
 1387 the inclusive NC/CC DIS data with $E_e = 50$ GeV as introduced in Sec. 3.1.5, are employed.
 1388 Besides the normalisation uncertainty, all sources of systematic uncertainties are considered as
 1389 uncorrelated between the two processes. A fit of NNLO QCD predictions to these data sets is
 1390 then performed, and $\alpha_s(M_Z)$ and the parameters of the PDFs are determined. The methodology
 1391 follows closely the methodology sketched in the previous study. Using inclusive jet and inclusive
 1392 DIS data in a single analysis, the value of $\alpha_s(M_Z)$ is determined with an uncertainty of

$$\Delta\alpha_s(M_Z)(\text{incl. DIS \& jets}) = \pm 0.00018_{(\text{exp+PDF})}. \quad (3.6)$$

1393 This result will improve the world average value considerably. However, theoretical uncertainties
 1394 are not included and new mathematical tools and an improved understanding of QCD will
 1395 be needed in order to achieve small values similar to the experimental ones. The dominant
 1396 sensitivity in this study arises from the jet data. This can be seen from Fig. 3.24, where
 1397 $\Delta\alpha_s(M_Z)$ changes only moderately with different assumptions imposed on the inclusive NC/CC
 1398 DIS data. Assumptions made for the uncertainties of the inclusive jet data have been studied
 1399 above, and these results can be translated easily to this PDF+ α_s fit.

1400 Discussion of $\alpha_s(M_Z)$ determinations at LHeC

1401 The expected values for $\alpha_s(M_Z)$ obtained from inclusive jets or from inclusive NC/CC DIS data
 1402 are compared in Fig. 3.25 with present determinations from global fits based on DIS data (called
 1403 *PDF fits*) and the world average value [89]. It is observed that LHeC will have the potential
 1404 to improve considerably the world average value. Already after one year of data taking, the
 1405 experimental uncertainties of the NC/CC DIS data are competitive with the world average
 1406 value. The measurement of jet cross sections will further improve that value (not shown).

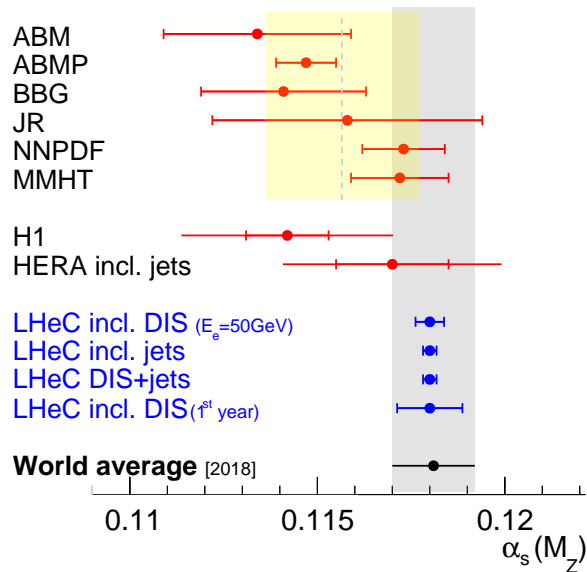


Figure 3.25: Summary of $\alpha_s(M_Z)$ values in comparison with present values.

1407 Furthermore, LHeC will be able to address a long standing puzzle. All α_s determinations from
 1408 global fits based on NC/CC DIS data find a lower value of $\alpha_s(M_Z)$ than determinations in the
 1409 lattice QCD framework, from τ decays or in a global electroweak fit. With the expected precision
 1410 from LHeC this discrepancy will be resolved.

1411 Strong coupling from other processes

1412 A detailed study for the determination of $\alpha_s(M_Z)$ from NC/CC DIS and from inclusive jet data
 1413 was presented in the previous paragraphs. However, a large number of additional processes
 1414 and observables that are measured at the LHeC can also be considered for a determination of
 1415 $\alpha_s(M_Z)$. Suitable observables or processes are di-jet and multi-jet production, heavy flavour
 1416 production, jets in photoproduction or event shape observables. These processes all exploit
 1417 the α_s dependence of the hard interaction. Using suitable predictions, also *softer* processes
 1418 can be exploited for an α_s determination. Examples could be jet shapes or other substructure
 1419 observables, or charged particle multiplicities.

1420 Since $\alpha_s(M_Z)$ is a parameter of a phenomenological model, the total uncertainty of $\alpha_s(M_Z)$ is
 1421 always a sum of experimental and theoretical uncertainties which are related to the definition of
 1422 the observable and to the applied model, e.g. hadronisation uncertainties, diagram removal/sub-
 1423 traction uncertainties or uncertainties from missing higher orders. Therefore, credible prospects
 1424 for the total uncertainty of $\alpha_s(M_Z)$ from other observables or processes are altogether difficult
 1425 to predict, even more since LHeC will explore a new kinematic regime that was previously
 1426 unmeasured.

1427 In a first approximation, for any process the sensitivity to $\alpha_s(M_Z)$ scales with the order n of α_s
 1428 in the leading-order diagram, α_s^n . The higher the power n the higher the sensitivity to $\alpha_s(M_Z)$.
 1429 Consequently, the experimental uncertainty of an α_s fit may reduce with increasing power n .
 1430 Already at HERA three-jet cross section were proven to have a high sensitivity to $\alpha_s(M_Z)$ albeit
 1431 their sizeable statistical uncertainties [92, 102]. At the LHeC, due to the higher \sqrt{s} and huge

1432 integrated luminosity, as well as the larger acceptance of the detector, three-, four- or five-jet
 1433 cross sections represent highly sensitive observables for a precise determination of $\alpha_s(M_Z)$, and
 1434 high experimental precision can be achieved. In these cases, fixed order pQCD predictions may
 1435 become limiting factors, since they are more complicated for large n .

1436 Di-jet observables are expected to yield a fairly similar experimental uncertainty than inclusive
 1437 jet cross sections, as studied in the previous paragraphs, since both have $n = 1$ at LO. How-
 1438 ever, their theoretical uncertainties may be smaller, since di-jet observables are less sensitive to
 1439 additional higher-order radiation, in particular at lower scales where $\alpha_s(\mu_R)$ is larger.

1440 Event shape observables in DIS exploit additional radiation in DIS events (see e.g. review [138]
 1441 or HERA measurements [139, 140]). Consequently, once measured at the LHeC the experi-
 1442 mental uncertainties of $\alpha_s(M_Z)$ from these observables are expected to become very similar
 1443 to that in Eq. (3.6), since both the event sample and the process is similar to the inclusive
 1444 jet cross sections⁶. However, different reconstruction techniques of the observables may yield
 1445 reduced experimental uncertainties, and the calculation of event shape observables allow for
 1446 the resummation of large logarithms, and steady theoretical advances promise small theoretical
 1447 uncertainties [141–147].

1448 Jet production cross sections in photoproduction represents a unique opportunity for another
 1449 precision determination of $\alpha_s(M_Z)$. Such measurements have been performed at HERA [148–
 1450 151]. The sizeable photoproduction cross section provides a huge event sample, which is statisti-
 1451 cally independent from NC DIS events, and already the leading-order predictions are sensitive
 1452 to $\alpha_s(M_Z)$ [152]. Also its running can be largely measured since the scale of the process is well
 1453 estimated by the transverse momentum of the jets $\mu_R \sim P_T^{\text{jet}}$. Limiting theoretical aspects are
 1454 due to the presence of a quasi-real photon and the poorly known photon PDF [153, 154].

1455 A different class of observables represent heavy flavour (HF) cross sections, which are discussed in
 1456 Sec. 3.1.7. Due to flavour conservation, these are commonly proportional to $\mathcal{O}(\alpha_s^1)$ at leading-
 1457 order. However, when considering inclusive HF cross sections above the heavy quark mass
 1458 threshold heavy quarks can be factorised into the PDFs, and the leading structure functions
 1459 $F_2^{c,b}$ are sensitive to α_s only beyond the LO approximation (see reviews [155, 156], recent HERA
 1460 measurements [157, 158] and references therein). The presence of the heavy quark mass as an
 1461 additional scale stabilises perturbative calculations, and reduced theoretical uncertainties are
 1462 expected.

1463 At the LHeC the structure of jets and the formation of hadrons can be studied with unprece-
 1464 dented precision. This is so because of the presence of a single hadron in the initial state.
 1465 Therefore, limiting effects like the underlying event or pile-up are absent or greatly diminished.
 1466 Precise measurements of jet shape observables, or the study of jet substructure observables [159],
 1467 are highly sensitive to the value of $\alpha_s(M_Z)$, because parton shower and hadronisation take place
 1468 at lower scales where the strong coupling becomes large and an increased sensitivity to $\alpha_s(M_Z)$
 1469 is attained [160, 161].

1470 Finally, also the determination of $\alpha_s(M_Z)$ from inclusive NC DIS cross sections can be improved.
 1471 For NC DIS the dominant sensitivity to α_s arises from the F_L structure function and from scaling
 1472 violations of F_2 at lower values of Q^2 but at very high values of x . Dedicated measurements of
 1473 these kinematic regions will further improve the experimental uncertainties from the estimated
 1474 values in Eq. (3.5).

⁶It shall be noted, that event shape observables in NC DIS can be defined in the laboratory rest frame or the Breit frame.

1475 3.2.2 New QCD Dynamics at Small x

1476 The LHeC machine will offer access to a completely novel kinematic regime of DIS characterised
 1477 by very small values of x . From the kinematical plane in (x, Q^2) depicted in Fig. 1.1, it is clear
 1478 that the LHeC will be able to probe Bjorken- x values as low as 10^{-6} for perturbative values of
 1479 Q^2 . At low values of x various phenomena may occur which go beyond the standard collinear
 1480 perturbative description based on DGLAP evolution. Since the seminal works of Balitsky, Fadin,
 1481 Kuraev and Lipatov [162–164] it has been known that, at large values of centre-of-mass energy
 1482 \sqrt{s} or, to be more precise, in the Regge limit, there are large logarithms of energy which need
 1483 to be resummed. Thus, even at low values of the strong coupling α_s , logarithms of energy $\ln s$
 1484 may be sufficiently large, such that terms like $(\alpha_s \ln s)^n$ will start to dominate the cross section.

1485 The calculation of scattering amplitudes in the high-energy limit and the resummation of
 1486 $(\alpha_s \ln s)^n$ series in the leading logarithmic order was performed in [162–164] and it resulted
 1487 in the famous BFKL evolution equation. This small x evolution equation, written for the so-
 1488 called gluon Green’s function or the unintegrated gluon density, is a differential equation in
 1489 $\ln 1/x$. An important property of this equation is that it keeps the transverse momenta un-
 1490 ordered along the gluon cascade. This has to be contrasted with DGLAP evolution which is
 1491 differential in the hard scale Q^2 and relies on the strong ordering in the transverse momenta of
 1492 the exchanged partons in the parton cascade. The solution to the BFKL equation is a gluon
 1493 density which grows sharply with decreasing x , as a power i.e. $\sim x^{-\omega_{IP}}$, where ω_{IP} is the hard
 1494 Pomeron intercept, and in the leading logarithmic approximation equals $\frac{N_c \alpha_s}{\pi} 4 \ln 2$, which gives
 1495 a value of about 0.5 for typical values of the strong coupling. The leading logarithmic (LLx)
 1496 result yielded a growth of the gluon density which was too steep for the experimental data at
 1497 HERA. The next-to-leading logarithmic (NLLx) calculation performed in the late 90s [165, 166]
 1498 resulted in large negative corrections to the LLx value of the hard Pomeron intercept and yielded
 1499 some instabilities in the cross section [167–171].

1500 The appearance of the large negative corrections at NLLx motivated the search for the appro-
 1501 priate resummation which would stabilize the result. It was understood very early that the
 1502 large corrections which appear in BFKL at NLLx are mostly due to the kinematics [172–174]
 1503 as well as DGLAP terms and the running of the strong coupling. First attempts at combining
 1504 the BFKL and DGLAP dynamics together with the proper kinematics [175] yielded encouraging
 1505 results, and allowed a description of HERA data on structure functions with good accuracy. The
 1506 complete resummation program was developed in a series of works [176–189]. In these works
 1507 the resummation for the gluon Green’s function and the splitting functions was developed.

1508 The low- x resummation was recently applied to the description of structure function data at
 1509 HERA using the methodology of NNPDF [190]. It was demonstrated that the resummed fits
 1510 provide a better description of the structure function data than the pure DGLAP based fits at
 1511 fixed NN order. In particular, it was shown that the χ^2 of the fits does not vary appreciably
 1512 when more small x data are included in the case of the fits which include the effects of the small- x
 1513 resummation. On the other hand, the fits based on NNLO DGLAP evolution exhibit a worsening
 1514 of their quality in the region of low x and low to moderate values of Q^2 . This indicates that
 1515 there is some tension in the fixed order fits based on DGLAP, and that resummation alleviates
 1516 it. In addition, it was shown that the description of the longitudinal structure function F_L
 1517 from HERA data is improved in the fits with the small x resummation. This analysis suggests
 1518 that the small x resummation effects are indeed visible in the HERA kinematic region. Such
 1519 effects will be strongly magnified at the LHeC, which probes values of x more than one order
 1520 of magnitude lower than HERA. The NNPDF group also performed simulation of the structure
 1521 functions F_2 and F_L with and without resummation in the LHeC range as well as for the next

1522 generation electron-hadron collider FCC-eh [190]. The predictions for the structure functions as
 1523 a function of x for fixed values of Q^2 are shown in Figs. 3.26.

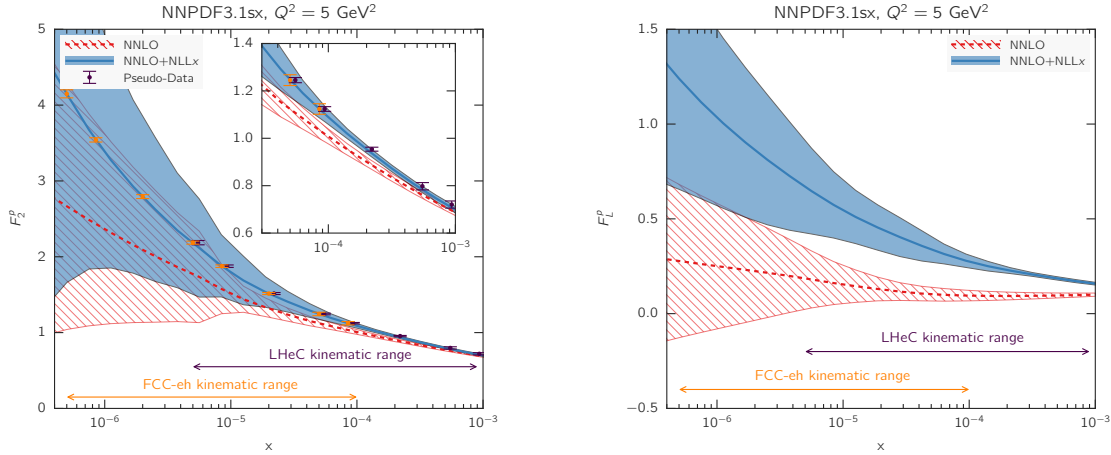


Figure 3.26: Predictions for the F_2 and F_L structure functions using the NNPDF3.1sx NNLO and NNLO+NLLx fits at $Q^2 = 5 \text{ GeV}^2$ for the kinematics of the LHeC and FCC-eh. In the case of F_2 , we also show the expected total experimental uncertainties based on the simulated pseudodata, assuming the NNLO+NLLx values as the central prediction. A small offset has been applied to the LHeC pseudodata as some of the values of x overlap with the FCC-eh pseudodata points. The inset in the left plot shows a magnified view in the kinematic region $x > 3 \times 10^{-5}$, corresponding to the reach of HERA data. Figure taken from Ref. [190].

1524 The simulations were done using APFEL [191] together with the HELL package [192] which
 1525 implements the small x resummation. From Fig. 3.26 it is clear that LHeC will have much
 1526 higher sensitivity to discriminate between fixed order and resummed scenarios than the HERA
 1527 collider, with even better discrimination at the FCC-eh. The differences between the central
 1528 values for the two predictions are of the order of 15% for the case of F_2 and this is much larger
 1529 than the projected error bar on the reduced cross section or structure function F_2 which could be
 1530 measured at LHeC. For comparison, the simulated pseudodata for F_2 are shown together with
 1531 the expected experimental uncertainties. The total uncertainties of the simulated pseudodata
 1532 are at the few percent level at most, and are therefore much smaller than the uncertainties
 1533 coming from the PDFs in most of the kinematic range.

1534 It is evident that fits to the LHeC data will have power to discriminate between the different
 1535 frameworks. In the right plot in Fig. 3.26, the predictions for the longitudinal structure function
 1536 are shown. We see that in the case of the F_L structure function, the differences between the
 1537 fixed order and resummed predictions are even larger, consistently over the entire range of x .
 1538 This indicates the importance of the measurement of the longitudinal structure function F_L
 1539 which can provide further vital constraints on the QCD dynamics in the low x region due to its
 1540 sensitivity to the gluon density in the proton.

1541 To further illustrate the power of a high energy DIS collider like the LHeC in exploring the
 1542 dynamics at low x , fits which include the simulated data were performed. The NNLO+NLLx
 1543 resummed calculation was used to obtain the simulated pseudodata, both for the LHeC, in a
 1544 scenario of a 60 GeV electron beam on a 7 TeV proton beam as well as in the case of the FCC-eh
 1545 scenario with a 50 TeV proton beam. All the experimental uncertainties for the pseudodata have
 1546 been added in quadrature. Next, fits were performed to the DIS HERA as well as LHeC and
 1547 FCC-eh pseudodata using the theory with and without the resummation at low x . Hadronic data

1548 like jet, DY or top, were not included for this analysis but, as demonstrated in [190], these data
 1549 do not have much of the constraining power at low x , and therefore the results of the analysis at
 1550 low x are independent of the additional non-DIS data sets. The quality of the fits characterised
 1551 by the χ^2 was markedly worse when the NNLO DGLAP framework was used to fit the HERA
 1552 data and the pseudodata from LHeC and/or FCC-eh than was the case with resummation. To be
 1553 precise, the χ^2 per degree of freedom for the HERA data set was equal to 1.22 for the NNLO fit,
 1554 and 1.07 for the resummed fit. For the case of the LHeC/FCC-eh the χ^2 per degree of freedom
 1555 was equal to 1.71/2.72 and 1.22/1.34 for NNLO and NNLO+resummation fits, respectively.
 1556 These results demonstrate the huge discriminatory power of the new DIS machines between
 1557 the DGLAP and resummed frameworks, and the large sensitivity to the low x region while
 1558 simultaneously probing low to moderate Q^2 values.

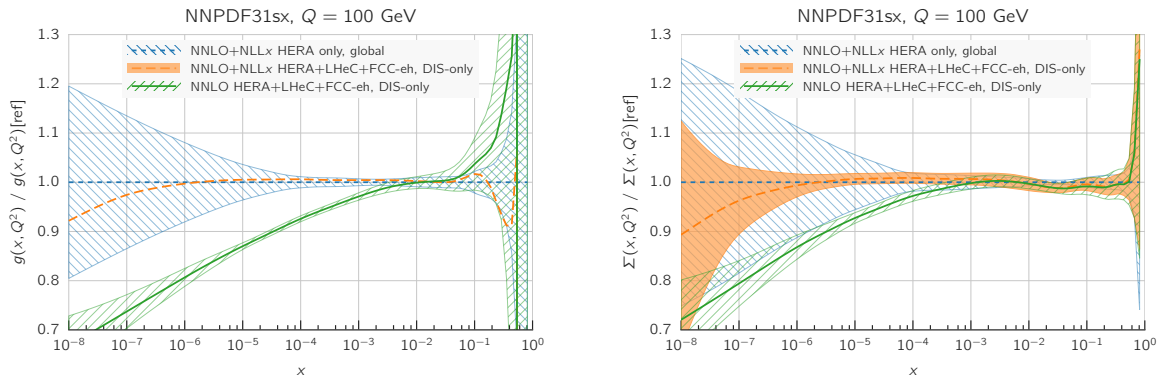


Figure 3.27: Comparison between the gluon (left plot) and the quark singlet (right plot) PDFs in the NNPDF3.1sx NNLO+NLLx fits without (blue hatched band) and with the LHeC+FCC-eh pseudodata (orange band) on inclusive structure functions. For completeness, we also show the results of the corresponding NNPDF3.1sx NNLO fit with LHeC+FCC-eh pseudodata (green hatched band). Figure taken from Ref. [190].

1559 In Fig. 3.27 the comparison of the gluon and quark distributions from the NNLO + NLLx
 1560 fits is shown at $Q = 100$ GeV as a function of x , with and without including the simulated
 1561 pseudodata from LHeC as well as FCC-eh. The large differences at large x are due to the
 1562 fact that only DIS data were included in the fits, and not the hadronic data. The central
 1563 values of the extracted PDFs using only HERA or using HERA and the simulated pseudodata
 1564 coincide with each other, but a large reduction in uncertainty is visible when the new data are
 1565 included. The uncertainties from the fits based on the HERA data only increase sharply already
 1566 at $x \sim 10^{-4}$. On the other hand, including the pseudodata from LHeC and/or FCC-eh can
 1567 extend this regime by order(s) of magnitude down in x . Furthermore, fits without resummation,
 1568 based only on NNLO DGLAP, were performed to the HERA data and the pseudodata. We see
 1569 that in this case the extracted gluon and singlet quark densities differ significantly from the fits
 1570 using the NNLO+NLLx. Already at $x = 10^{-4}$ the central values of the gluon differ by 10% and
 1571 at $x = 10^{-5}$, which is the LHeC regime, the central values for the gluon differ by 15%. This
 1572 difference is much larger than the precision with which the gluon can be extracted from the DIS
 1573 data, which is of the order of $\sim 1\%$.

1574 The presented analysis demonstrates that the fixed order prediction based on the DGLAP
 1575 evolution would likely fail to describe accurately the structure function data in the new DIS
 1576 machines and that in that regime new dynamics including resummation are mandatory for
 1577 quantitative predictions. Therefore, the LHeC machine has an unprecedented potential to pin
 1578 down the details of the QCD dynamics at low values of Bjorken x .

1580 The small- x region probed by the LHeC is also very important in the context of ultra-high energy
 1581 neutrino physics and astroparticle physics. Highly energetic neutrinos provide a unique window
 1582 into the Universe, due to their weak interaction with matter, for a review see for example [193].
 1583 They can travel long distances from distant sources, undeflected by the magnetic fields inside
 1584 and in between galaxies, and thus provide complementary information to cosmic rays, gamma
 1585 rays and gravitational wave signals. The IceCube observatory on Antarctica [194] is sensitive
 1586 to neutrinos with energies from 100 GeV up (above 10 GeV with the use of their Deep Core
 1587 detector). Knowledge about low- x physics becomes indispensable in two contexts: neutrino
 1588 interactions and neutrino production. At energies beyond the TeV scale the dominant part of the
 1589 cross section is due to the neutrino DIS CC and NC interaction with the hadronic targets [193].

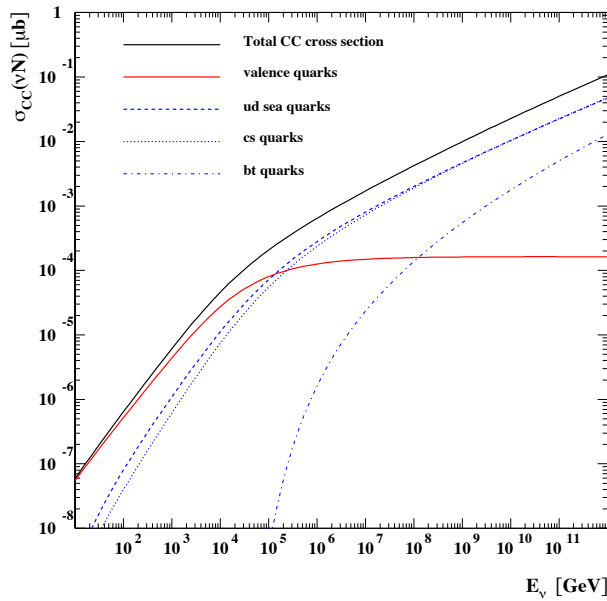


Figure 3.28: Charged current cross section for the neutrino - nucleon interaction on a isoscalar target as a function of neutrino energy. The total CC cross section is broken down into several contributions due to valence, up-down, strange-charm and bottom-top quarks. The calculation was based on Ref. [195].

1590 In Fig. 3.28 we show the charged current neutrino cross section as a function of the neutrino
 1591 energy for an isoscalar target (in the laboratory frame where the target is at rest), using a
 1592 calculation [195] based on the resummed model in [175]. We see that at energies below ~ 50 TeV
 1593 the cross section grows roughly linearly with energy, and in this region it is dominated by
 1594 contributions from the large- x valence region. Beyond that energy the neutrino cross section
 1595 grows slower, roughly as a power $\sim E_\nu^\lambda$ with $\lambda \simeq 0.3$. This high energy behaviour is totally
 1596 controlled by the small- x behaviour of the parton distributions. The dominance of the sea
 1597 contributions to the cross section is clearly seen in Fig. 3.28. To illustrate more precisely the
 1598 contributing values of x and Q^2 , in Fig. 3.29 we show the differential cross section for the CC
 1599 interaction $xQ^2 d\sigma^{CC}/dx dQ^2$ for a neutrino energy $E_\nu = 10^{11}$ GeV (in the frame where the
 1600 hadronic target is at rest). We see a clear peak of the cross section at roughly a value of
 1601 $Q^2 = M_W^2$ and an x value

$$x \simeq \frac{M_W^2}{2ME_\nu}, \quad (3.7)$$

which in this case is about 3×10^{-8} . We note that IceCube extracted the DIS cross section from

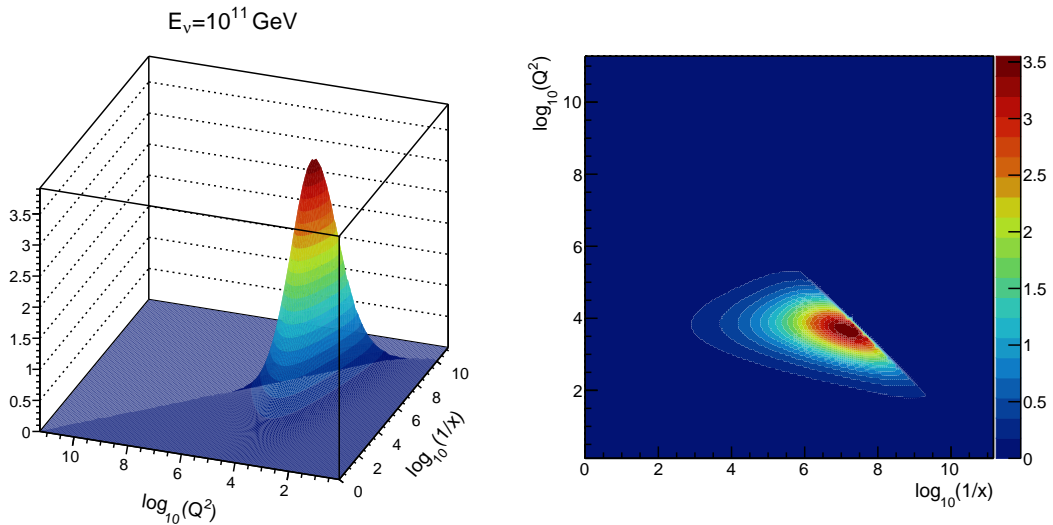


Figure 3.29: Differential charged current neutrino cross section $10^5 \cdot xQ^2 d\sigma^{CC}/dx dQ^2$ [nb] as a function of Q^2 and x for fixed neutrino energy $E_\nu = 10^{11}$ GeV. Left: surface plot; right: contour plot.

1602

1603 neutrino observations [196] in the region of neutrino energies 10 – 1000 TeV. The extraction
 1604 is consistent, within the large error bands, with the predictions based on the QCD, like those
 1605 illustrated in Fig. 3.28. It is important to note that the IceCube extraction is limited to these
 1606 energies by the statistics due to the steeply falling flux of neutrinos at high energy. We thus
 1607 see that the neutrino interaction cross section at high energies is sensitive to a region which is
 1608 currently completely unconstrained by existing precision DIS data.

1609

1610 Another instance where dynamics at low x are crucial for neutrino physics is in understand-
 1611 ing the mechanisms of ultra-high energy neutrino production. The neutrinos are produced in
 1612 interactions which involve hadrons, either in γp or in pp interactions. They emerge as decay
 1613 products of pions, kaons and charmed mesons, and possibly beauty mesons if the energy is high
 1614 enough [197]. For example, in the atmosphere neutrinos are produced in the interactions of the
 1615 highly energetic cosmic rays with nitrogen and oxygen nuclei. The lower energy part of the
 1616 atmospheric neutrino spectrum, up to about 100 TeV or so, is dominated by the decay of pions
 1617 and kaons. This is called the conventional atmospheric neutrino flux. Above that energy the
 1618 neutrino flux is dominated by the decay of the shorter-lived charmed mesons. Thus, this part of
 1619 the neutrino flux is called the prompt-neutrino flux. The reason why the prompt-neutrino flux
 1620 dominates at high energies is precisely related to the life-time of the intermediate mesons (and
 1621 also baryons like Λ_c). The longer lived pions and kaons have a high probability of interacting
 1622 before they decay, thus degrading their energy and leading to a steeply falling neutrino flux.
 1623 The cross section for the production of charmed mesons is smaller than that for pions and kaons,
 1624 but the charmed mesons D^\pm, D^0, D_s and baryon Λ_c live shorter than pions and kaons, and thus
 1625 decay prior to any interaction. Thus, at energies about 100 TeV the prompt neutrino flux will
 1626 dominate over the conventional atmospheric neutrino flux. Therefore, the knowledge of this part
 1627 of the spectrum is essential as it provides a background for the sought-after astrophysical neu-
 1628 trinos [198]. Charmed mesons in high energy hadron-hadron interactions are produced through
 1629 gluon-gluon fusion into $c\bar{c}$ pairs, where one gluon carries rather large x and the other one carries
 1630 very small x . Since the scales are small, of the order of the charm masses, the values of the
 1631 longitudinal momentum fractions involved are also very small and thus the knowledge of the
 parton distributions in this region is essential [199]. The predictions for the prompt neutrino

flux become extremely sensitive to the behaviour of the gluon distribution at low x (and low Q^2), where novel QCD phenomena like resummation as well as gluon saturation are likely to occur [200].

Finally, the low- x dynamics will become even more important at the HL-LHC and FCC hadron colliders. With increasing centre-of-mass energy, hadron colliders will probe values of x previously unconstrained by HERA data. It is evident that all the predictions in pp interactions at high energy will heavily rely on the PDF extrapolations to the small x region which carry large uncertainties. As discussed in detail in this Section, resummation will play an increasingly important role in the low x region of PDFs. A precision DIS machine is thus an indispensable tool for constraining the QCD dynamics at low x with great precision as well as for providing complementary information and independent measurements to hadronic colliders.

3.2.3 Low x and the Longitudinal Structure Function F_L

DIS Cross Section and the Challenge to Access F_L

The inclusive, deep inelastic electron-proton scattering cross section at low $Q^2 \ll M_Z^2$,

$$\frac{Q^4 x}{2\pi\alpha^2 Y_+} \cdot \frac{d^2\sigma}{dx dQ^2} = \sigma_r \simeq F_2(x, Q^2) - f(y) \cdot F_L(x, Q^2) = F_2 \cdot \left(1 - f(y) \frac{R}{1+R}\right) \quad (3.8)$$

is defined by two proton structure functions, F_2 and F_L , with $y = Q^2/sx$, $Y_+ = 1 + (1-y)^2$ and $f(y) = y^2/Y_+$. The cross section may also be expressed [201] as a sum of two contributions, $\sigma_r \propto (\sigma_T + \epsilon\sigma_L)$, referring to the transverse and longitudinal polarisation state of the exchanged boson, with ϵ characterising the ratio of the longitudinal to the transverse polarisation. The ratio of the longitudinal to transverse cross sections is termed

$$R(x, Q^2) = \frac{\sigma_L}{\sigma_T} = \frac{F_L}{F_2 - F_L}, \quad (3.9)$$

which is related to F_2 and F_L as given above. Due to the positivity of the cross sections $\sigma_{L,T}$ one observes that $F_L \leq F_2$. The reduced cross section σ_r , Eq. (3.8), is therefore a direct measure of F_2 , apart from a limited region of high y where a contribution of F_L may be sizeable. To leading order, for spin 1/2 particles, one expected $R = 0$. The initial measurements of R at SLAC [202, 203] showed that R was indeed small, $R \simeq 0.18$, which was taken as evidence for quarks to carry spin 1/2.

The task to measure F_L thus requires to precisely measure the inclusive DIS cross section near to $y = 1$ and to then disentangle the two structure functions by exploiting the $f(y) = y^2/Y_+$ variation which depends on x , Q^2 and s . By varying the centre-of-mass (cms) beam energy, s , one can disentangle F_2 and F_L obtaining independent measurements at each common, fixed point of x, Q^2 . This is particularly challenging not only because the F_L part is small, calling for utmost precision, but also because it requires to measure at high y . The inelasticity $y = 1 - E'/E_e$, however, is large only for scattered electron energies E'_e much smaller than the electron beam energy E_e , for example $E'_e = 2.7$ GeV for $y = 0.9$ at HERA⁷. In the region where E' is a few GeV only, the electron identification becomes a major problem and the electromagnetic ($\pi^0 \rightarrow \gamma\gamma$) and hadronic backgrounds, mainly from unrecognised photoproduction, rise strongly.

⁷The nominal electron beam energy E_e at the LHeC is doubled as compared to HERA. Ideally one would like to vary the proton beam energy in an F_L measurement at the LHeC, which yet would affect the hadron collider operation. In the present study it was therefore considered to lower E_e which may be done independently of the HL-LHC.

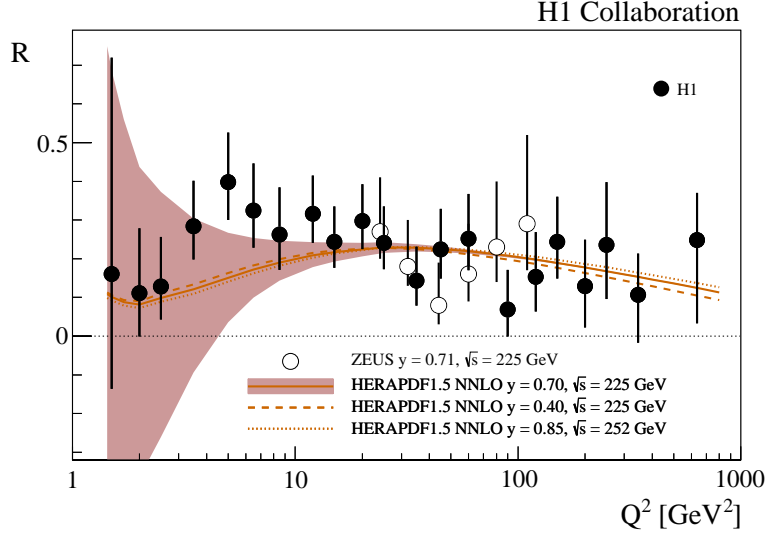


Figure 3.30: Measurement of the structure function ratio $R = F_L/(F_2 - F_L)$ by H1 (solid points) and ZEUS (open circles), from a variation of proton beam energy in the final half year of HERA operation. The curve represents an NNLO QCD fit analysis of the other HERA data. This becomes uncertain for Q^2 below 10 GeV^2 where the Q^2 dependence of F_2 at HERA does not permit an accurate determination of the gluon density which dominates the prediction on F_L .

1667 The history and achievements on F_L , the role of HERA and the prospects as sketched in the
 1668 CDR of the LHeC, were summarised in detail in [56]. The measurement of F_L at HERA [204]
 1669 was given very limited time and it collected about 5.9 and 12.2 pb^{-1} of data at reduced beam
 1670 energies which were analysed together with about 100 pb^{-1} at nominal HERA energies. The
 1671 result may well be illustrated with the data obtained on the ratio $R(x, Q^2)$ shown in Fig. 3.30.
 1672 To good approximation, $R(x, Q^2)$ is a constant which was determined as $R = 0.23 \pm 0.04$,
 1673 in good agreement with the SLAC values of $R \simeq 0.18$ despite the hugely extended kinematic
 1674 range. The rather small variation of R towards small x , at fixed $y = Q^2/sx$, may appear to be
 1675 astonishing as one observed F_2 to strongly rise towards low x . A constant R of e.g. 0.25 means
 1676 that $F_2 = (1 + R)F_L/R$ is five times larger than F_L , and that they rise together, as they have
 1677 a common origin, the rise of the gluon density. This can be understood in approximations to
 1678 the DGLAP expression of the Q^2 derivative of F_2 and the so-called Altarelli-Martinelli relation
 1679 of F_L to the parton densities [205, 206], see the discussion in Ref. [56]. The resulting H1 value
 1680 also obeyed the condition $R \leq 0.37$, which had been obtained in a rigorous attempt to derive
 1681 the dipole model for inelastic DIS [207].

1682 Parton Evolution at Low x

1683 Parton distributions are to be extracted from experiment as their x dependence and flavour
 1684 sharing are not predicted in QCD. They acquire a particular meaning through the theoretical
 1685 prescription of their kinematic evolution. PDFs, as they are frequently used for LHC analyses,
 1686 are predominantly defined through the now classic DGLAP formalism, in which the Q^2 depen-
 1687 dence of parton distributions is regulated by splitting functions while the DIS cross section,
 1688 determined by the structure functions, is calculable by folding the PDFs with coefficient func-
 1689 tions. Deep inelastic scattering is known to be the most suited process to extract PDFs from
 1690 the experiment, for which the HERA collider has so far delivered the most useful data. Through
 1691 factorisation theorems the PDFs are considered to be universal such that PDFs extracted in ep

1692 DIS shall be suited to describe for example Drell-Yan scattering cross sections in pp at the LHC.
 1693 This view has been formulated to third order pQCD already and been quite successful in the
 1694 interpretation of LHC measurements, which by themselves also constrain PDFs in parton-parton
 1695 scattering sub-processes.

1696 As commented in Sec. 3.2.2, the question has long been posed about the universal validity of
 1697 the DGLAP formalism, especially for the region of small Bjorken x where logarithms $\propto \ln(1/x)$
 1698 become very sizeable. This feature of the perturbation expansion is expected to significantly
 1699 modify the splitting functions. This in turn changes the theory underlying the physics of parton
 1700 distributions, and predictions for the LHC and its successor will correspondingly have to be
 1701 altered. This mechanism, for an equivalent Q^2 of a few GeV^2 , is illustrated in Fig. 3.31, taken
 1702 from Ref. [208]. It shows the x dependence of the gluon-gluon and the quark-gluon splitting
 1703 functions, P_{gg} and P_{qg} , calculated in DGLAP QCD. It is observed that at NNLO P_{gg} strongly
 1704 decreases towards small x , becoming smaller than P_{qg} for x below 10^{-4} . Resummation of
 1705 the large $\ln(1/x)$ terms, see Ref. [208], here performed to next-to-leading log x , restores the
 1706 dominance of the gg splitting over the qg one. Consequently, the gluon distribution in the
 resummed theory exceeds the one derived in pure DGLAP. While this observation has been

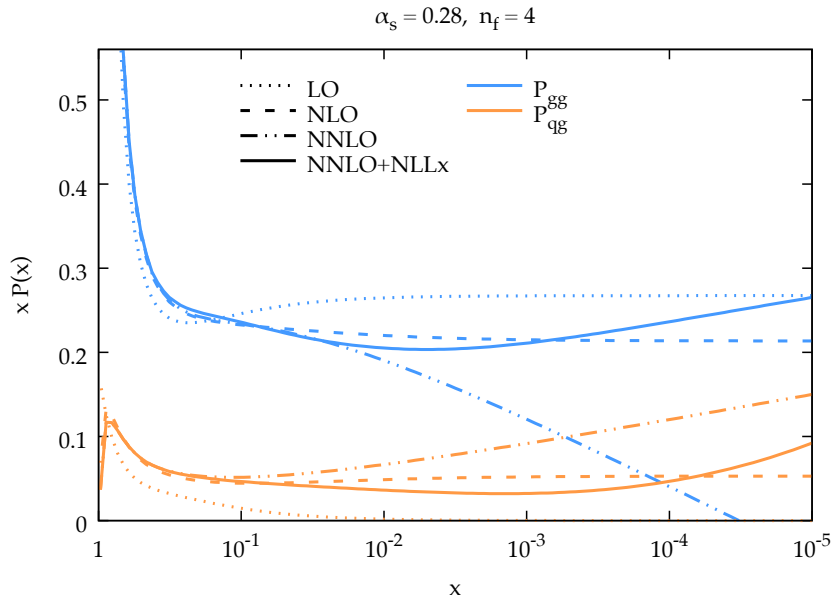


Figure 3.31: Calculation of splitting functions P_{gg} (top, blue) and P_{qg} (bottom, brown) in resummed NNLO (solid) as compared to non-resummed calculations at LO (dotted), NLO (dashed) and NNLO (dashed-dotted) as functions of x for $n_f = 4$ at a large value of α_s corresponding to a Q^2 of a few GeV^2 , from Ref. [208]. The resummed calculation is seen to restore the dominance of P_{gg} over P_{qg} as x becomes small (towards the right side), which is violated at NNLO.

1707 supported by the HERA data, it yet relies on limited kinematic coverage and precision. The
 1708 LHeC will examine this in detail, at a hugely extended range and is thus expected to resolve the
 1709 long known question about the validity of the BFKL evolution and the transition from DGLAP
 1710 to BFKL as x decreases while Q^2 remains large enough for pQCD to apply.
 1711

1712 Kinematics of Higgs Production at the HL-LHC

1713 The clarification of the evolution and the accurate and complete determination of the parton
1714 distributions is of direct importance for the LHC. This can be illustrated with the kinematics of
1715 Higgs production at HL-LHC which is dominated by gluon-gluon fusion. With the luminosity
1716 upgrade, the detector acceptance is being extended into the forward region to pseudorapidity
1717 values of $|\eta| = 4$, where $\eta = \ln \tan \theta/2$ is a very good approximation of the rapidity. In Drell-Yan
1718 scattering of two partons with Bjorken x values of $x_{1,2}$ these are related to the rapidity via the
1719 relation $x_{1,2} = \exp(\pm\eta) \cdot M/\sqrt{s}$ where $\sqrt{s} = 2E_p$ is the cms energy and M the mass of the
1720 produced particle. It is interesting to see that $\eta = \pm 4$ corresponds to $x_1 = 0.5$ and $x = 0.00016$
1721 for the SM Higgs boson of mass $M = 125$ GeV. Consequently, Higgs physics at the HL-LHC
1722 will depend on understanding PDFs at high x , a challenge resolved by the LHeC too, and on
1723 clarifying the evolution at small x . At the FCC-hh, in its 100 TeV energy version, the small x
1724 value for $\eta = 4$ will be as low as $2 \cdot 10^{-5}$. Both the laws of QCD and the resulting phenomenology
1725 of particle production at the HL-LHC and its successor demand to clarify the evolution of the
1726 parton contents at small x as a function of the resolution scale Q^2 . This concerns in particular
1727 the unambiguous, accurate determination of the gluon distribution, which dominates the small- x
1728 parton densities and as well the production of the Higgs boson in pp scattering.

1729 Indications for Resummation in H1 F_L Data

1730 The simultaneous measurement of the two structure functions F_2 and F_L is the cleanest way
1731 to establish new parton dynamics at low x . This holds because their independent constraints
1732 on the dominating gluon density at low x ought to lead to consistent results. In other words,
1733 one may constrain all partons with a complete PDF analysis of the inclusive cross section in
1734 the kinematic region where its F_L part is negligible and confront the F_L measurement with
1735 this result. A significant deviation from F_L data signals the necessity to introduce new, non-
1736 DGLAP physics in the theory of parton evolution, especially at small x . The salient value of the
1737 F_L structure function results from its inclusive character enabling a clean theoretical treatment
1738 as has early on been recognised [205, 206]. This procedure has recently been illustrated [208]
1739 using the H1 data on F_L [209] which are the only accurate data from HERA at smallest x . The
1740 result is shown in Fig. 3.32. One observes the trend described above: the resummed prediction
1741 is higher than the pure NNLO curve, and the description at smallest x , below $5 \cdot 10^{-4}$, appears
1742 to be improved. The difference between the two curves increases as x decreases. However, due
1743 to the peculiarity of the DIS kinematics, which relates x to Q^2/sy , one faces the difficulty of
1744 Q^2 decreasing with x at fixed s for large $y \geq 0.6$, which is the region of sensitivity to F_L . Thus
1745 one not only wishes to improve substantially the precision of the F_L data but also to increase
1746 substantially s in order to avoid the region of non-perturbative behaviour while testing theory
1747 at small x . This is the double and principal advantage which the LHeC offers - a much increased
1748 precision and more than a decade of extension of kinematic range.

1749 The Longitudinal Structure Function at the LHeC

1750 Following the method described above, inclusive cross section data have been simulated for
1751 $E_p = 7$ TeV and three electron beam energies E_e of 60, ~ 30 and 20 GeV. The assumed integrated
1752 luminosity values are 10, ~ 1 and 1 fb^{-1} , respectively. These are about a factor of a hundred
1753 larger than the corresponding H1 luminosities. At large y , the kinematics is best reconstructed
1754 using the scattered electron energy, E'_e , and polar angle, θ_e . The experimental methods to

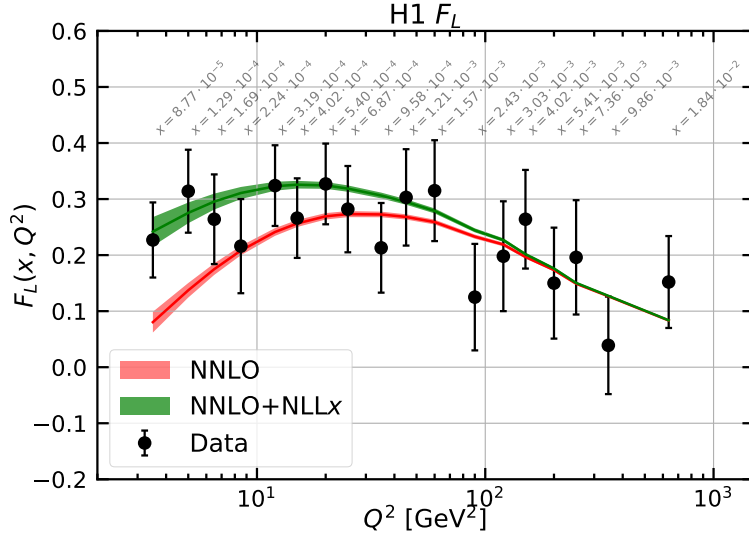


Figure 3.32: Measurement of the longitudinal structure function F_L , obtained as an average results over a number of x dependent points at fixed Q^2 , plotted vs Q^2 with the corresponding x values indicated in grey. Red curve: NNLO fit to the H1 cross section data; green curve: NNLO fit including NLLx resummation, from Ref. [208].

1755 calibrate the angular and energy measurements are described in [204]. For the present study
1756 similar results are assumed: for E'_e a scale uncertainty of 0.5% at small y (compared to 0.2%
1757 with H1) rising linearly to 1.2%, in the range of $y = 0.4$ to 0.9. For the polar angle, given
1758 the superior quality of the anticipated LHeC Silicon tracker as compared to the H1 tracker,
1759 it is assumed that θ_e may be calibrated to 0.2mrad, as compared to 0.5mrad at H1. The
1760 residual photo-production background contamination is assumed to be 0.5% at largest y , twice
1761 better than with H1. There is further an assumption made on the radiative corrections which
1762 are assumed to be uncertain to 1% and treated as a correlated error. The main challenge is to
1763 reduce the uncorrelated uncertainty, which here was varied between 0.2 and 0.5%. This is about
1764 ten to three times more accurate than the H1 result which may be a reasonable assumption: the
1765 hundred fold increase in statistics sets a totally different scale to the treatment of uncorrelated
1766 uncertainties, as from imperfect simulations, trigger efficiency or Monte Carlo statistics. It
1767 is very difficult to transport previous results to the modern and future conditions. It could,
1768 however, be an important fix point if one knows that the most precise measurement of Z boson
1769 production by ATLAS at the LHC had a total systematic error of just 0.5% [210].

1770 The method here used is that of a simple straight-line fit of $\sigma_r = F_2 - f(y)F_L$ (Eq. (3.8)), in
1771 which F_L is obtained as the slope of the $f(y)$ dependence⁸. The predictions for F_2 and F_L were
1772 obtained using LO formulae for the PDF set of MSTW 2008. In this method any common factor
1773 does not alter the absolute uncertainty of F_L . This also implies that the estimated absolute error
1774 on F_L is independent of whether F_L is larger or smaller than here assumed. For illustration,
1775 F_L was scaled by a factor of two. Since $f(y) \propto y^2$, the accuracy is optimised with a non-linear
1776 choice of lowered beam energies. The fit takes into account cross section uncertainties and their
1777 correlations, calculated numerically following [57], by considering each source separately and
1778 adding the results of the various correlated sources to one correlated systematic error which is
1779 added quadratically to the statistical and uncorrelated uncertainties to obtain one total error.

⁸Better results were achieved by H1 using a χ^2 minimisation technique, see Ref. [211], which for the rough estimate on the projected F_L uncertainty at the LHeC has not been considered.

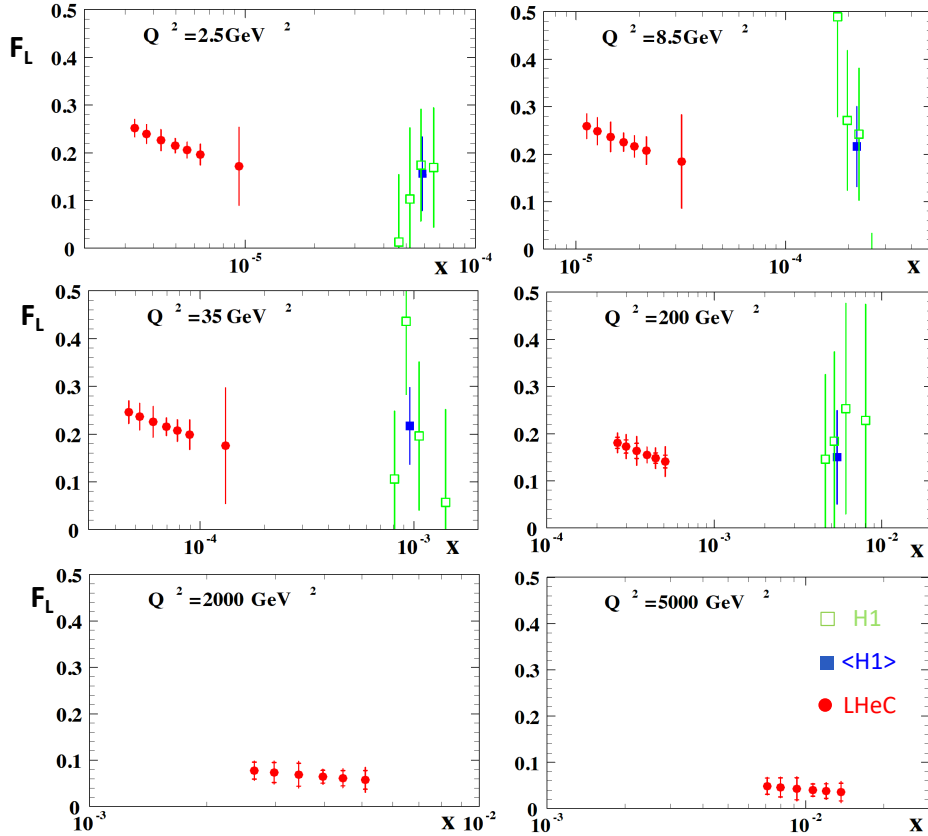


Figure 3.33: H1 measurement and LHeC simulation of data on the longitudinal structure function $F_L(x, Q^2)$. Green: Data by H1, for selected Q^2 intervals from Ref. [209]; Blue: Weighted average of the (green) data points at fixed Q^2 ; Red: Simulated data from an F_L measurement at the LHeC with varying beam energy, see text. The H1 error bars denote the total measurement uncertainty. The LHeC inner error bars represent the data statistics, visible only for $Q^2 \geq 200 \text{ GeV}^2$, while the outer error bars are the total uncertainty. Since the F_L measurement is sensitive only at high values of inelasticity, $y = Q^2/sx$, each Q^2 value is sensitive only to a certain limited interval of x values which increase with Q^2 . Thus each panel has a different x axis. The covered x range similarly varies with s , i.e. H1 x values are roughly twenty times larger at a given Q^2 . There are no H1 data for high Q^2 , beyond 1000 GeV^2 , see Ref. [209].

1780 The result is illustrated in Fig. 3.33 presenting the x -dependent results, for some selected Q^2
 1781 values, of both H1, with their average over x , and the prospect LHeC results. It reflects the
 1782 huge extension of kinematic range, towards low x and high Q^2 by the LHeC as compared to
 1783 HERA. It also illustrates the striking improvement in precision which the LHeC promises to
 1784 provide. The F_L measurement will cover an x range from $2 \cdot 10^{-6}$ to above $x = 0.01$. Surely,
 1785 when comparing with Fig. 3.32, one can safely expect that any non-DGLAP parton evolution
 1786 would be discovered with such data, in their combination with a very precise F_2 measurement.

1787 A few comments are in order on the variation of the different error components with the kine-
 1788 matics, essentially Q^2 since the whole F_L sensitivity is restricted to high y which in turn for each
 1789 Q^2 defines a not wide interval of x values covered. One observes in Fig. 3.33 that the precision
 1790 is spoiled towards large $x \propto 1/y$, see e.g. the result for $Q^2 = 8.5 \text{ GeV}^2$. The assumptions on
 1791 the integrated luminosity basically define a Q^2 range for the measurement. For example, the
 1792 statistical uncertainty for $Q^2 = 4.5 \text{ GeV}^2$ and $x = 10^{-5}$, a medium x value at this Q^2 interval,
 1793 is only 0.6 % (or 0.001 in absolute for $F_L = 0.22$). At $Q^2 = 2000 \text{ GeV}^2$ it rises to 21 % (or 0.012
 1794 for $F_L = 0.064$). One thus can perform the F_L measurement at the LHeC, with a focus on only

1795 small x , with much less luminosity than the 1 fb^{-1} here used. The relative size of the various
1796 systematic error sources also varies considerably, which is due to the kinematic relations between
1797 angles and energies and their dependence on x and Q^2 . This is detailed in [57]. It implies, for ex-
1798 ample, that the 0.2 mrad polar angle scale uncertainty becomes the dominant error at small Q^2 ,
1799 which is the backward region where the electron is scattered near the beam axis in the direction
1800 of the electron beam. For large Q^2 , however, the electron is more centrally scattered and the
1801 θ_e calibration requirement may be more relaxed. The E'_e scale uncertainty has a twice smaller
1802 effect than that due to the θ_e calibration at lowest Q^2 but becomes the dominant correlated
1803 systematic error source at high Q^2 . The here used overall assumptions on scale uncertainties
1804 are therefore only rough first approximations and would be replaced by kinematics and detector
1805 dependent requirements when this measurement may be pursued. These could also exploit the
1806 cross calibration opportunities which result from the redundant determination of the inclusive
1807 DIS scattering kinematics through both the electron and the hadronic final state. This had been
1808 noted very early at HERA times, see Ref. [212–214] and was worked out in considerable detail
1809 by both H1 and ZEUS using independent and different methods. A feature used by H1 in their
1810 F_L measurement includes a number of decays such as $\pi^0 \rightarrow \gamma\gamma$ and $J/\psi \rightarrow e^+e^-$ for calibrating
1811 the low energy measurement or $K_s^0 \rightarrow \pi^+\pi^-$ and $\Lambda \rightarrow p\pi$ for the determination of tracker scales,
1812 see Ref. [204].

1813 It is obvious that the prospect to measure F_L as presented here is striking. For nearly a decade,
1814 Guido Altarelli was a chief theory advisor to the development of the LHeC. In 2011, he publishes
1815 an article [211], in honour of Mario Greco, about *The Early Days of QCD (as seen from Rome)*
1816 in which he describes one of his main achievements [205], and persistent irritation, regarding
1817 the longitudinal structure function, F_L , and its measurement: *... The present data, recently*
1818 *obtained by the H1 experiment at DESY, are in agreement with our [!this] LO QCD prediction*
1819 *but the accuracy of the test is still far from being satisfactory for such a basic quantity.* The
1820 LHeC developments had not been rapid enough to let Guido see results of much higher quality
1821 on F_L with which the existence of departures from the DGLAP evolution, to high orders pQCD,
1822 may be expected to most safely be discovered.

1823 3.2.4 Disentangling non-linear QCD dynamics at the LHeC

1824 The LHeC will extend the kinematic reach of HERA at small- x by one order of magnitude in
1825 the perturbative regime $Q \gtrsim 1\text{ GeV}$ [1]. This extension will allow unprecedented tests of the
1826 strong interaction in this extreme region, where deviations from the linear DGLAP evolution are
1827 expected to appear. In particular, it has been argued that the strong growth of the gluon PDF
1828 at small- x should eventually lead to gluon recombination [215] to avoid violating the unitary
1829 bounds. The onset of such non-linear dynamics, also known as saturation, has been extensively
1830 searched but so far there is no conclusive evidence of its presence, at least within the HERA
1831 inclusive structure function measurements. In this context, the extended kinematic range of the
1832 LHeC provides unique avenues to explore the possible onset of non-linear QCD dynamics at
1833 small- x . The discovery of saturation, a radically new regime of QCD, would then represent an
1834 important milestone in our understanding of the strong interactions.

1835 The main challenge in disentangling saturation lies in the fact that non-linear corrections are
1836 expected to be moderate even at the LHeC, since they are small (if present at all) in the region
1837 covered by HERA. Therefore, great care needs to be employed in order to separate such effects
1838 from those of standard DGLAP linear evolution. Indeed, it is well known that HERA data at
1839 small- x in the perturbative region can be equally well described, at least at the qualitative level,
1840 both by PDF fits based on the DGLAP framework as well as by saturation-inspired models.

1841 However, rapid progress both in theory calculations and methodological developments have
1842 pushed QCD fits to a new level of sophistication, and recently it has been shown that subtle but
1843 clear evidence of BFKL resummation at small- x is present in HERA data, both for inclusive and
1844 for heavy quark structure functions [208, 216]. Such studies highlight how it should be possible
1845 to tell apart non-linear from linear dynamics using state-of-the-art fitting methods even if these
1846 are moderate, provided that they are within the LHeC reach.

1847 Here we want to assess the sensitivity of the LHeC to detect the possible onset of non-linear
1848 saturation dynamics. This study will be carried out by generalising a recent analysis [36] that
1849 quantified the impact of LHeC inclusive and semi-inclusive measurements on the PDF4LHC15
1850 PDFs [37, 217] by means of Hessian profiling [38]. There, the LHeC pseudodata was generated
1851 assuming that linear DGLAP evolution was valid in the entire LHeC kinematic range using
1852 the PDF4LHC15 set as input. To ascertain the possibility of pinning down saturation at the
1853 LHeC, here we have revisited this study but now generating the LHeC pseudodata by means of
1854 a saturation-inspired calculation. By monitoring the statistical significance of the tension that
1855 will be introduced (by construction) between the saturation pseudodata and the DGLAP theory
1856 assumed in the PDF fit, we aim to determine the likelihood of disentangling non-linear from
1857 linear evolution effects at the LHeC. See also [218] for previous related studies along the same
1858 direction.

1859 Analysis settings

1860 In this study we adopt the settings of [35, 36], to which we refer the interested reader for further
1861 details. In Ref. [36] the impact on the proton PDFs of inclusive and semi-inclusive neutral-
1862 current (NC) and charged current (CC) DIS structure functions from the LHeC was quantified.
1863 These results were then compared with the corresponding projections for the PDF sensitivity of
1864 the High-Luminosity upgrade of the LHC (HL-LHC). In the left panel of Fig. 3.34 we display
1865 the kinematic range in the (x, Q^2) plane of the LHeC pseudodata employed in that analysis,
1866 which illustrated how the LHeC can provide unique constraints on the behaviour of the quark
1867 and gluon PDFs in the very small- x region.

1868 Since non-linear dynamics are known to become sizeable only at small- x , for the present analysis
1869 it is sufficient to consider the NC e^-p inclusive scattering cross sections from proton beam en-
1870 ergies of $E_p = 7$ TeV and $E_p = 1$ TeV. In the right panel in Fig. 3.34 we show the bins in (x, Q^2)
1871 for which LHeC pseudodata for inclusive structure functions has been generated according to
1872 a saturation-based calculation. Specifically, we have adopted here the DGLAP-improved satu-
1873 ration model of Ref. [219], in which the scattering matrix is modelled through eikonal iteration
1874 of two gluon exchanges. This model was further extended to include heavy flavour in [220].
1875 The specific parameters that we use were taken from Fit 2 in [221], where parameterisations
1876 are provided that can be used for $x < 0.01$ and $Q^2 < 700$ GeV². These parameters were ex-
1877 tracted from a fit to the HERA legacy inclusive structure function measurements [45] restricted
1878 to $x < 0.01$ and $0.045 < Q^2 < 650$ GeV². In contrast to other saturation models, the one we
1879 assume here [221] provides a reasonable description for large Q^2 in the small x region, where it
1880 ensure a smooth transition to standard fixed-order perturbative results.

1881 Note that the above discussion refers only to the generated LHeC pseudodata: all other aspects of
1882 the QCD analysis of [36] are left unchanged. In particular, the PDF profiling will be carried out
1883 using theory calculations obtained by means of DGLAP evolution with the NNLO PDF4LHC15
1884 set (see also [222]), with heavy quark structure functions evaluated by means of the FONLL-
1885 B general-mass variable flavour number scheme [75]. In order to ensure consistency with the

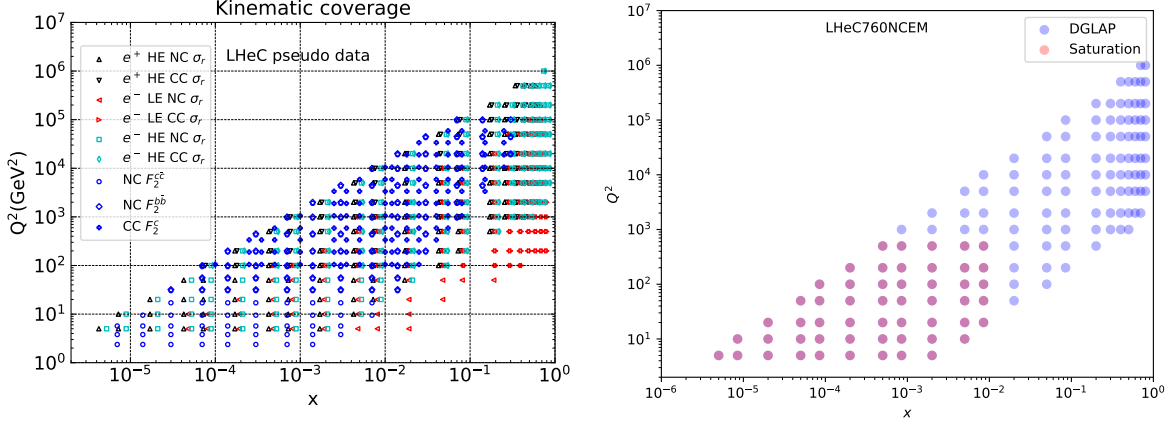


Figure 3.34: Left: the kinematic range in the (x, Q^2) plane of the LHeC pseudodata on inclusive and semi-inclusive DIS structure functions used in the PDF projections of [36]. Right: the kinematic coverage of the NC e^-p scattering pseudodata at the LHeC, where the blue (red) points indicate those bins for which DGLAP (saturation) predictions are available.

1886 PDF4LHC15 prior, here we will replace the DGLAP pseudodata by the saturation calculation
 1887 only in the kinematic region for $x \lesssim 10^{-4}$, rather than for all the bins indicated in red in
 1888 Fig. 3.34. The reason for this choice is that PDF4LHC15 already includes HERA data down to
 1889 $x \simeq 10^{-4}$ which is successfully described via the DGLAP framework, and therefore if we assume
 1890 departures from DGLAP in the LHeC pseudodata this should only be done for smaller values
 1891 of x .

1892 Results and discussion

1893 Using the analysis settings described above, we have carried out the profiling of PDF4LHC15
 1894 with the LHeC inclusive structure function pseudodata, which for $x \leq 10^{-4}$ ($x > 10^{-4}$) has
 1895 been generated using the GBW saturation (DGLAP) calculations, and compare them with the
 1896 results of the profiling where the pseudodata follows the DGLAP prediction. We have generated
 1897 $N_{\text{exp}} = 500$ independent sets LHeC pseudodata, each one characterised by different random
 1898 fluctuations (determined by the experimental uncertainties) around the underlying central value.

1899 To begin with, it is instructive to compare the data versus theory agreement, χ^2/n_{dat} , between
 1900 the pre-fit and post-fit calculations, in order to assess the differences between the DGLAP and
 1901 saturation cases. In the upper plots of Fig. 3.35 we show the distributions of pre-fit and post-fit
 1902 values of χ^2/n_{dat} for the $N_{\text{exp}} = 500$ sets of generated LHeC pseudodata. We compare the results
 1903 of the profiling of the LHeC pseudodata based on DGLAP calculations in the entire range of
 1904 x with those where the pseudodata is based on the saturation model in the region $x < 10^{-4}$.
 1905 Then in the bottom plot we compare of the post-fit χ^2 distributions between the two scenarios.
 1906 Note that in these three plots the ranges in the x axes are different.

1907 From this comparison we can observe that for the case where the pseudodata is generated using
 1908 a consistent DGLAP framework (PDF4LHC15) as the one adopted for the theory calculations
 1909 used in the fit, as expected the agreement is already good at the pre-fit level, and it is further
 1910 improved at the post-fit level. However the situation is rather different in the case where a
 1911 subset of the LHeC pseudodata is generated using a saturation model: at the pre-fit level the
 1912 agreement between theory and pseudodata is poor, with $\chi^2/n_{\text{dat}} \simeq 7$. The situation markedly

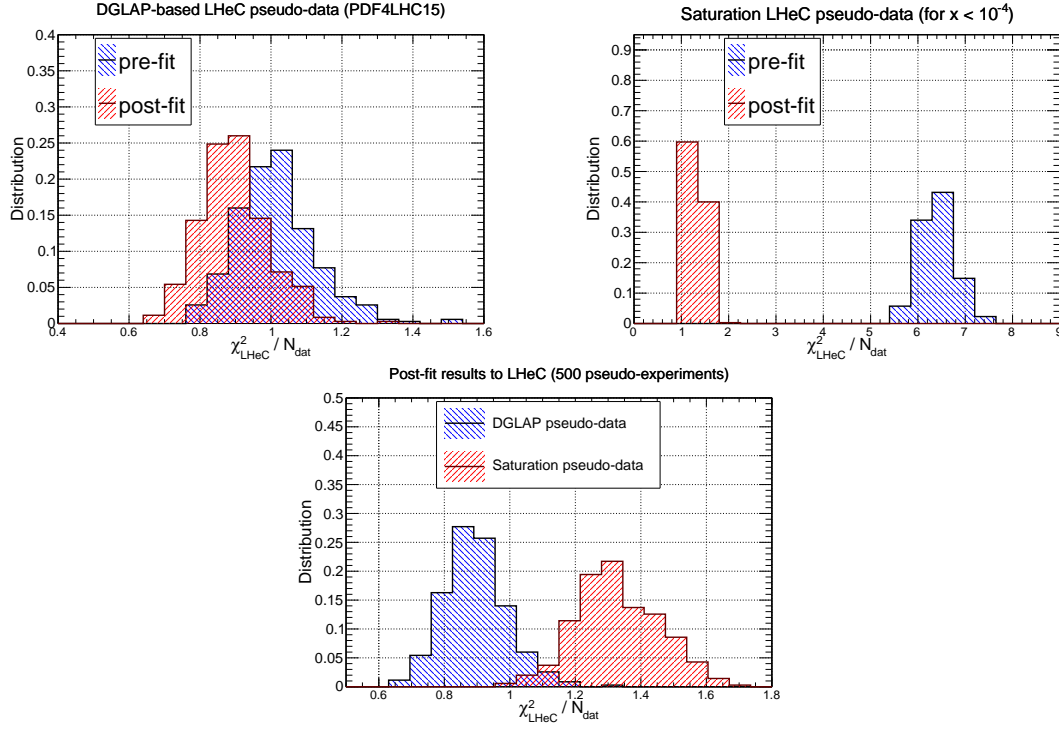


Figure 3.35: Upper plots: the distribution of pre-fit and post-fit values of χ^2/n_{dat} for the $N_{\text{exp}} = 500$ sets of generated LHeC pseudodata. We compare the results of the profiling of the LHeC pseudodata based on DGLAP calculations in the entire range of x (left) with those where the pseudodata is based on the saturation model in the region $x < 10^{-4}$ (right plot). Bottom plot: comparison of the post-fit χ^2/n_{dat} distributions between these two scenarios for the pseudodata generation.

1913 improves at the post-fit level, where now the χ^2/n_{dat} distributions peaks around 1.3. This result
 1914 implies that the DGLAP fit manages to absorb most of the differences in theory present in
 1915 the saturation pseudodata. This said, the DGLAP fit cannot entirely *fit away* the non-linear
 1916 corrections: as shown in the lower plot of Fig. 3.35, even at the post-fit level one can still tell
 1917 apart the χ^2/n_{dat} distributions between the two cases, with the DGLAP (saturation) pseudodata
 1918 peaking at around 0.9 (1.3). This comparison highlights that it is not possible for the DGLAP
 1919 fit to completely absorb the saturation effects into a PDF redefinition.

1920 In order to identify the origin of the worse agreement between theory predictions and LHeC
 1921 pseudodata in the saturation case, it is illustrative to take a closer look at the pulls defined as

$$P(x, Q^2) = \frac{\mathcal{F}_{\text{fit}}(x, Q^2) - \mathcal{F}_{\text{dat}}(x, Q^2)}{\delta_{\text{exp}}\mathcal{F}(x, Q^2)}, \quad (3.10)$$

1922 where \mathcal{F}_{fit} is the central value of the profiled results for the observable \mathcal{F} (in this case the reduced
 1923 neutral current DIS cross section), \mathcal{F}_{dat} is the corresponding central value of the pseudodata,
 1924 and $\delta_{\text{exp}}\mathcal{F}$ represents the associated total experimental uncertainty. In Fig. 3.36 we display the
 1925 pulls between the post-fit prediction and the central value of the LHeC pseudodata for different
 1926 bins in Q^2 . We compare the cases where the pseudodata has been generated using a consistent
 1927 theory calculation (DGLAP) with that based on the GBW saturation model.

1928 The comparisons in Fig. 3.36 show first of all that in the DGLAP case the pulls are $\mathcal{O}(1)$ in
 1929 the entire kinematical range. This is of course expected, given that the LHeC pseudodata is
 1930 generated using the same theory as the one subsequently used for the fit. In the case where
 1931 the pseudodata has been partially generated with the saturation calculation, on the other hand,

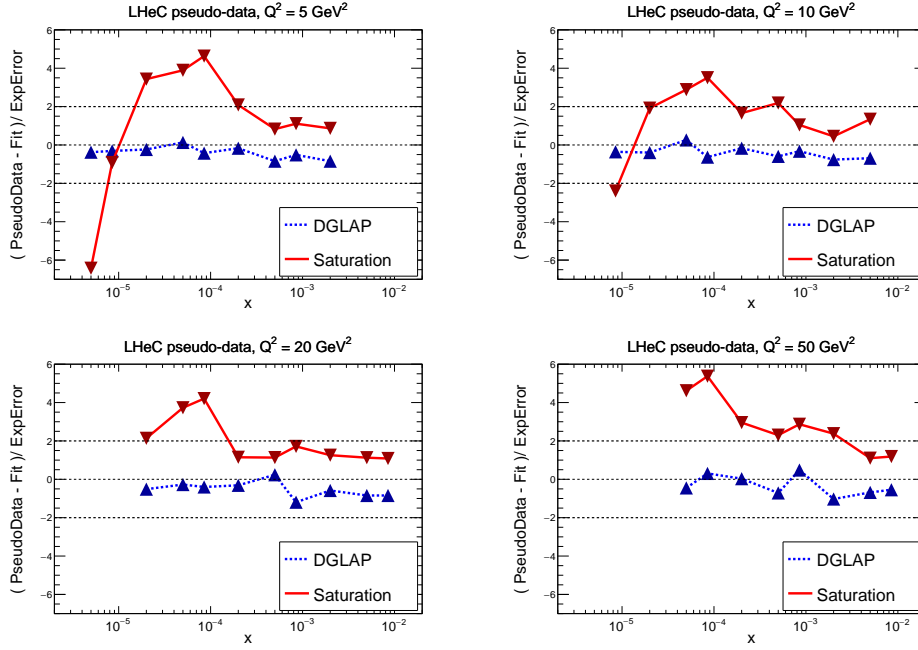


Figure 3.36: The pulls between the post-fit prediction and the central value of the LHeC pseudodata, Eq. (3.10), for four different bins in Q^2 . We compare the results of the profiling where the LHeC pseudodata has been generated using a consistent DGLAP theory with that partially based on the saturation calculations.

1932 one finds a systematic tension between the theory used for the fit (DGLAP) and the one used
 1933 to generate the pseudodata (saturation). Indeed, we find that at the smallest values of x the
 1934 theory prediction undershoots the data by a significant amount, while at higher x the opposite
 1935 behaviour takes place. One can also see that in the region $10^{-4} \lesssim x \lesssim 10^{-3}$ the fit overshoots
 1936 the pseudodata by a large amount.

1937 These comparisons highlight how a QCD fit to the saturation pseudodata is obtained as a
 1938 compromise between opposite trends: the theory wants to overshoot the data at very small x
 1939 and overshoot it at larger values of x . These tensions result in a distorted fit, explaining the
 1940 larger χ^2/n_{dat} values as compared to the DGLAP case. Such a behaviour can be partially traced
 1941 back by the different scaling in Q^2 between DGLAP and GBW: while a different x dependence
 1942 could eventually be absorbed into a change of the PDFs at the parameterisation scale Q_0 , this
 1943 is not possible with a Q^2 dependence.

1944 The pull analysis of Fig. 3.36 highlights how in order to tell apart linear from non-linear QCD
 1945 evolution effects at small- x it would be crucial to ensure a lever arm in Q^2 as large as possible
 1946 in the perturbative region. This way it becomes possible to disentangle the different scaling
 1947 in Q^2 for the two cases. The lack of a sufficiently large lever arm in Q^2 at HERA at small x
 1948 could explain in part why both frameworks are able to describe the same structure function
 1949 measurements at the qualitative level. Furthermore, we find that amplifying the significance
 1950 of these subtle effects can be achieved by monitoring the χ^2 behaviour in the Q^2 bins more
 1951 affected by the saturation corrections. The reason is that the total χ^2 , such as that reported
 1952 in Fig. 3.35, is somewhat less informative since the deviations at small- Q are washed out by
 1953 the good agreement between theory and pseudodata in the rest of the kinematical range of the
 1954 LHeC summarised in Fig. 3.34.

1955 To conclude this analysis, in Fig. 3.37 we display the comparison between the PDF4LHC15

1956 baseline with the results of the PDF profiling of the LHeC pseudodata for the gluon (left) and
 1957 quark singlet (right) for $Q = 10$ GeV. We show the cases where the pseudodata is generated
 1958 using DGLAP calculations and where it is partially based on the GBW saturation model (for
 1959 $x \lesssim 10^{-4}$). We find that the distortion induced by the mismatch between theory and pseudodata
 1960 in the saturation case is typically larger than the PDF uncertainties expected once the LHeC
 1961 constraints are taken into account. While of course in a realistic situation such a comparison
 1962 would not be possible, the results of Fig. 3.37 show that saturation-induced effects are expected
 1963 to be larger than the typical PDF errors in the LHeC era, and thus that it should be possible to
 1964 tell them apart using for example tools such as the pull analysis of Fig. 3.36 or other statistical
 1965 methods.

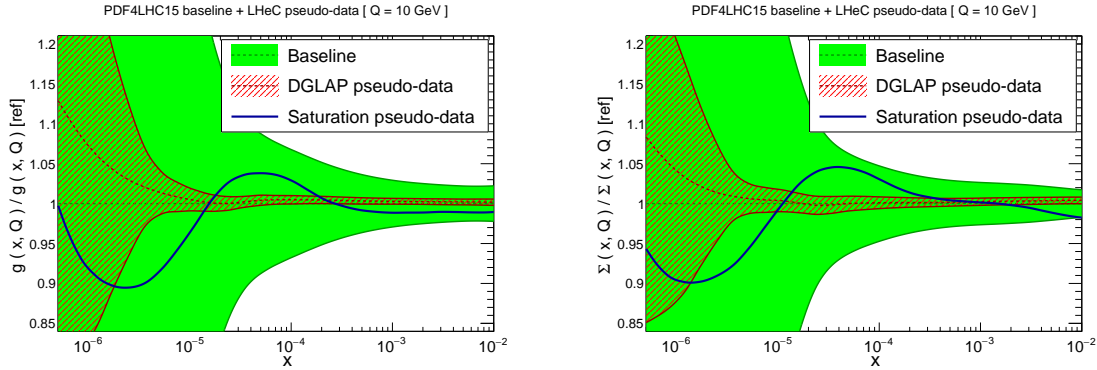


Figure 3.37: Comparison between the PDF4LHC15 baseline (green band) with the results of the profiling of the LHeC pseudodata for the gluon (left) and quark singlet (right) for $Q = 10$ GeV. We show the cases where the pseudodata is generated using DGLAP calculations (red hatched band) and where it is partially based on the GBW saturation model (blue curve).

1966 Summary

1967 Here we have assessed the feasibility of disentangling DGLAP evolution from non-linear effects at
 1968 the LHeC. By means of a QCD analysis where LHeC pseudodata is generated using a saturation
 1969 model, we have demonstrated that the LHeC should be possible to identify non-linear effects
 1970 with large statistical significance, provided their size is the one predicted by current calculations
 1971 such as the that of [221] that have been tuned to HERA data. A more refined analysis would
 1972 require to study whether or not small- x BFKL resummation effects can partially mask the
 1973 impact of non-linear dynamics, though this is unlikely since the main difference arises in their
 1974 Q^2 scaling. The discovery of non-linear dynamics would represent an important milestone for
 1975 the physics program of the LHeC, demonstrating the onset of a new gluon-dominated regime of
 1976 the strong interactions and paving the way for detailed studies of the properties of this new state
 1977 of matter. Such discovery would have also implications outside nuclear and particle physics, for
 1978 instance it would affect the theory predictions for the scattering of ultra-high energy neutrinos
 1979 with matter [223].

1980 3.2.5 The 3D Structure of the Proton

1981 As is evident from the discussion in the previous Sections, the LHeC machine will be able to
 1982 measure the collinear parton distribution functions with unprecedented accuracy in its extended
 1983 range of x and Q^2 . Thus, it will provide a new insight into the details of the one-dimensional

1984 structure of the proton and nuclei, including novel phenomena at low x . In addition to collinear
 1985 dynamics, the LHeC opens a new window into proton and nuclear structure by allowing a precise
 1986 investigation of the partonic structure in more than just the one dimension of the longitudinal
 1987 momentum. Precision DIS thus gives access to multidimensional aspects of hadron structure.
 1988 This can be achieved by accurately measuring processes with more exclusive final states like pro-
 1989 duction of jets, semi-inclusive production of hadrons and exclusive processes, in particular the
 1990 elastic diffractive production of vector mesons and deeply virtual Compton (DVCS) scattering.
 1991 These processes have the potential to provide information not only on the longitudinal distribu-
 1992 tion of partons in the proton or nucleus, but also on the dependence of the parton distribution
 1993 on transverse momenta and momentum transfer. Therefore, future, high precision DIS machines
 1994 like the LHeC or the Electron Ion Collider (EIC) in the US [224], open a unique window into
 1995 the details of the 3D structure of hadrons.

1996 The most general quantity that can be defined in QCD that would contain very detailed infor-
 1997 mation about the partonic content of the hadron, is the Wigner distribution [225]. This function
 1998 $W(x, \mathbf{k}, \mathbf{b})$ is a 1+4 dimensional function. One can think of it as the mother or master parton
 1999 distribution, from which lower-dimensional distributions can be obtained. In the definition of
 2000 the Wigner function, \mathbf{k} is the transverse momentum of the parton and \mathbf{b} is the 2-dimensional
 2001 impact parameter, which can be defined as a Fourier conjugate to the momentum transfer of
 2002 the process. The other, lower dimensional parton distributions can be obtained by integrating
 2003 out different variables. Thus, transverse momentum dependent (TMD) parton distributions
 2004 (or unintegrated parton distribution functions) $f_{\text{TMD}}(x, \mathbf{k})$ can be obtained by integrating out
 2005 the impact parameter \mathbf{b} in the Wigner function, while the generalised parton densities (GPD),
 2006 $f_{\text{GPD}}(x, \mathbf{b})$, can be obtained from the Wigner function through the integration over the trans-
 2007 verse momentum \mathbf{k} . In the regime of small x , or high energy, a suitable formalism is that of
 2008 the dipole picture [226–231], where the fundamental quantity which contains the details of the
 2009 partonic distribution is the dipole amplitude $N(x, \mathbf{r}, \mathbf{b})$. This object contains the dependence
 2010 on the impact parameter \mathbf{b} as well as another transverse size \mathbf{r} , the dipole size, which can be
 2011 related to the transverse momentum of the parton \mathbf{k} through a Fourier transform. The impor-
 2012 tant feature of the dipole amplitude is that it should obey the unitarity limit $N \leq 1$. The dipole
 2013 amplitude N within this formalism can be roughly interpreted as a Wigner function in the high
 2014 energy limit, as it contains information about the spatial distribution of the partons in addition
 2015 to the dependence on the longitudinal momentum fraction x .

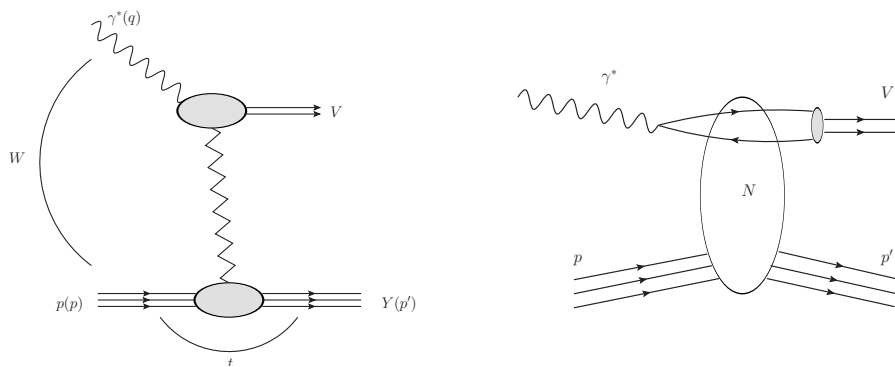


Figure 3.38: Left: diagram for the quasi-elastic production of the vector meson. Right: schematic illustration of the same process, quasi-elastic vector meson production, within the framework of the dipole picture. The initial virtual photon, fluctuates into a quark-antiquark pair which then scatters off the hadronic target and forms the vector meson. The details of the hadronic interaction of the dipole with the target are encoded in the dipole amplitude N .

2016 Detailed simulations of elastic J/ψ vector meson production were performed for the LHeC
 2017 kinematic region and beyond [1], using the formalism of the dipole picture. This particular
 2018 process is shown in Fig. 3.38, left plot. The proton is scattered elastically with momentum
 2019 transfer t , and the vector meson is produced, which is separated from the final state proton
 2020 by a rapidity gap. Of particular importance is the measurement of the t slope of this process,
 2021 since it can be related directly to the impact parameter distribution and is thus sensitive to the
 2022 transverse variation of the partonic density in the target. The first type of analysis like this,
 2023 in the context of elastic scattering, was performed by Amaldi and Schubert [232], where it was
 2024 demonstrated that the Fourier transform of the elastic cross section yields access to the impact
 2025 parameter profile of the scattering amplitude. This method can be used in the context of vector
 2026 meson scattering in DIS, where the transverse distribution of partons, in the perturbative regime,
 2027 can be extracted through the appropriate Fourier transform [233]. The additional advantage of
 2028 studying diffractive vector meson production is the fact that the partonic distributions can be
 2029 studied as a function of the hard scale in this process given by the mass of the vector meson M_V^2
 2030 in the photoproduction case or Q^2 (or more precisely a combination of Q^2 and M_V^2) in the case
 2031 of the diffractive DIS production of vector mesons, as well as the energy W of the photon-proton
 2032 system available in the process which is closely related to x .

2033 The differential cross section for elastic vector meson production can be expressed in the following
 2034 form:

$$\frac{d\sigma^{\gamma^* p \rightarrow J/\psi p}}{dt} = \frac{1}{16\pi} |\mathcal{A}(x, Q, \Delta)|^2, \quad (3.11)$$

2035 where the amplitude for the process of elastic diffractive vector meson production in the high
 2036 energy limit, in the dipole picture, is given by

$$\mathcal{A}(x, Q, \Delta) = \sum_{h\bar{h}} \int d^2\mathbf{r} \int dz \Psi_{h\bar{h}}^*(z, \mathbf{r}, Q) \mathcal{N}(x, \mathbf{r}, \Delta) \Psi_{h\bar{h}}^V(z, \mathbf{r}). \quad (3.12)$$

2037 In the above formula, $\Psi_{h\bar{h}}^*(z, \mathbf{r}, Q)$ is the photon wave function which describes the splitting
 2038 of the virtual photon γ^* into a $q\bar{q}$ pair. This wave function can be calculated in perturbative
 2039 QCD. The function $\Psi_{h\bar{h}}^V(z, \mathbf{r})$ is the wave function of the vector meson. Finally, $\mathcal{N}(x, \mathbf{r}, \Delta)$ is the
 2040 dipole amplitude which contains all the information about the interaction of the quark-antiquark
 2041 dipole with the target. The formula (3.12) can be interpreted as the process of fluctuation of the
 2042 virtual photon into a $q\bar{q}$ pair, which subsequently interacts with the target through the dipole
 2043 amplitude \mathcal{N} and then forms the vector meson, given by the amplitude Ψ^V , see Fig. 3.38, right
 2044 plot. The two integrals in the definition Eq. (3.12) are performed over the dipole size which is
 2045 denoted by \mathbf{r} , and z which is the longitudinal momentum fraction of the photon carried by the
 2046 quark. The scattering amplitude depends on the value of the momentum transfer Δ , which is
 2047 related to the Mandelstam variable $t = -\Delta^2$. The sum is performed over the helicity states of
 2048 the quark and antiquark.

2049 The dipole amplitude $\mathcal{N}(x, \mathbf{r}, \Delta)$ can be related to the dipole amplitude in coordinate space
 2050 through the appropriate Fourier transform

$$N(x, \mathbf{r}, \mathbf{b}) = \int d^2\Delta e^{i\Delta \cdot \mathbf{b}} \mathcal{N}(x, \mathbf{r}, \Delta). \quad (3.13)$$

2051 We stress that \mathbf{r} and \mathbf{b} are two different transverse sizes here. The dipole size \mathbf{r} is conjugate
 2052 to the transverse momentum of the partons \mathbf{k} , whereas the impact parameter is roughly the
 2053 distance between the centre of the scattering target to the centre-of-mass of the quark-antiquark
 2054 dipole and is related to the Fourier conjugate variable, the momentum transfer Δ .

2055 The dipole amplitude $N(x, \mathbf{r}, \mathbf{b})$ contains rich information about the dynamics of the hadronic
2056 interaction. It is a 5-dimensional function and it depends on the longitudinal momentum frac-
2057 tion, and two two-dimensional coordinates. The dependence on the longitudinal momentum
2058 fraction is obviously related to the evolution with the centre-of-mass energy of the process,
2059 while the dependence on \mathbf{b} provides information about the spatial distribution of the partons in
2060 the target. The dipole amplitude is related to the distribution of gluons in impact parameter
2061 space. The dipole amplitude has a nice property that its value should be bounded from above
2062 by the unitarity requirement $N \leq 1$. The complicated dependence on energy, dipole size and
2063 impact parameter of this amplitude can provide a unique insight into the dynamics of QCD,
2064 and on the approach to the dense partonic regime. Besides, from Eqs. (3.11),(3.12) and (3.13) it
2065 is evident that the information about the spatial distribution in impact parameter \mathbf{b} is related
2066 through the Fourier transform to the dependence of the cross section on the momentum transfer
2067 $t = -\Delta^2$.

2068 To see how the details of the distribution, and in particular the approach to unitarity, can
2069 be studied through the VM elastic production, calculations based on the dipole model were
2070 performed [234], and extended to energies which can be reached at the LHeC as well as the
2071 FCC-eh. The parameterisations used in the calculation were the so-called IP-Sat [235, 236]
2072 and b-CGC [237] models. In both cases the impact parameter dependence has to be modelled
2073 phenomenologically. In the IP-Sat model the dipole amplitude has the following form

$$N(x, \mathbf{r}, \mathbf{b}) = 1 - \exp \left[-\frac{\pi^2 r^2}{2N_c} \alpha_s(\mu^2) xg(x, \mu^2) T_G(b) \right], \quad (3.14)$$

2074 where $xg(x, \mu^2)$ is the collinear gluon density, evolved using LO DGLAP (without quarks), from
2075 an initial scale μ_0^2 up to the scale μ^2 set by the dipole size $\mu^2 = \frac{4}{r^2} + \mu_0^2$. $\alpha_s(\mu^2)$ is the strong
2076 coupling. The parameterisation of the gluon density at the initial scale μ_0^2 is given by

$$xg(x, \mu_0^2) = A_g x^{-\lambda_g} (1-x)^{5.6}, \quad (3.15)$$

2077 and the impact parameter profile for the gluon by

$$T_G(b) = \frac{1}{2\pi B_G} \exp(-b^2/2B_G). \quad (3.16)$$

An alternative parameterisation is given by the b-CGC model [237] which has the form

$$N(x, \mathbf{r}, \mathbf{b}) = \begin{cases} N_0 \left(\frac{rQ_s}{2} \right)^{2\gamma_{\text{eff}}} & \text{for } rQ_s \leq 2, \\ 1 - \exp(-\mathcal{A} \ln^2(\mathcal{B}rQ_s)) & \text{for } rQ_s > 2. \end{cases} \quad (3.17)$$

2078 Here the effective anomalous dimension γ_{eff} and the saturation scale Q_s of the proton explicitly
2079 depend on the impact parameter and are defined as

$$\begin{aligned} \gamma_{\text{eff}} &= \gamma_s + \frac{1}{\kappa \lambda \ln 1/x} \ln \left(\frac{2}{rQ_s} \right), \\ Q_s(x, b) &= \left(\frac{x_0}{x} \right)^{\lambda/2} \exp \left[-\frac{b^2}{4\gamma_s B_{\text{CGC}}} \right] \text{ GeV}, \end{aligned} \quad (3.18)$$

2080 where $\kappa = \chi''(\gamma_s)/\chi'(\gamma_s)$, with $\chi(\gamma)$ being the leading-logarithmic BFKL kernel eigenvalue
2081 function [164]. The parameters \mathcal{A} and \mathcal{B} in Eq.(3.17) are determined uniquely from the matching
2082 of the dipole amplitude and its logarithmic derivatives at the limiting value of $rq_s = 2$. The

2083 b-CGC model is constructed by smoothly interpolating between two analytically known limiting
 2084 cases [237], namely the solution of the BFKL equation in the vicinity of the saturation line for
 2085 small dipole sizes $r < 2/Q_s$, and the solution of the BK equation deep inside the saturation
 2086 region for large dipole sizes $r > 2/Q_s$.

2087 The parameters μ_0, A_g, λ_g of the IP-Sat model and $N_0, \gamma_s, x_0\lambda$ of the b-CGC model were fitted
 2088 to obtain the best description of the inclusive data for the structure function F_2 at HERA. The
 2089 slope parameters B_g and B_{CGC} , which control the b -dependence in both models, were fitted to
 2090 obtain the best description of elastic diffractive J/ψ production, in particular its t -dependence,
 2091 at small values of t .

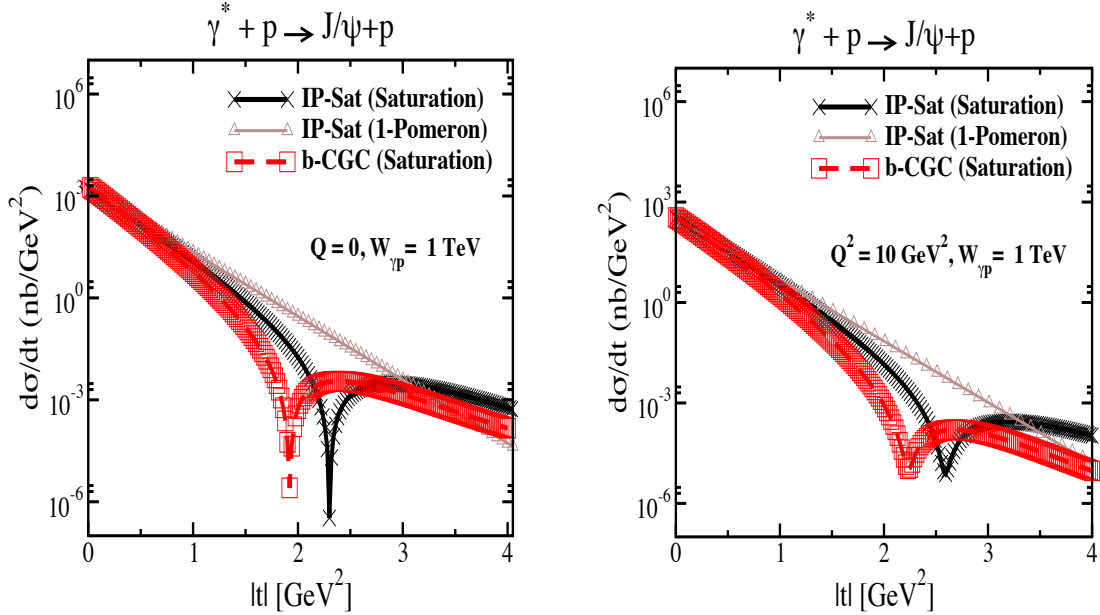


Figure 3.39: Differential cross section for the elastic J/ψ production as a function of $|t|$ within the IP-Sat (saturation), b-CGC and 1-Pomeron models at a fixed $W_{\gamma p} = 1$ TeV, which corresponds to the LHeC kinematics, and for two different values of photon virtuality $Q = 0$ and $Q^2 = 10$ GeV². The thickness of points includes the uncertainties associated with the freedom to choose different values for the charm quark mass within the range $m_c = 1.2 - 1.4$ GeV.

2092 In Figs. 3.39 and 3.40 we show the simulated differential cross section $d\sigma/dt$ as a function of $|t|$
 2093 and study its variation with energy and virtuality, and its model dependence. First, in Fig. 3.39
 2094 we show the differential cross section as a function of t for fixed energy $W = 1$ TeV, in the case of
 2095 the photoproduction of J/ψ (left plot) and for the case of DIS with $Q^2 = 10$ GeV² (right plot).
 2096 The energy W corresponds to the LHeC kinematics. There are three different calculations in
 2097 each plot, using the IP-sat model, the b-CGC model and the 1-Pomeron approximation. The
 2098 last one is obtained by keeping just the first non-trivial term in the expansion of the eikonalsed
 2099 formula of the IP-Sat amplitude (3.14). First, let us observe that all three models coincide
 2100 for very low values of t , where the dependence on t is exponential. This is because for low
 2101 $|t|$, relatively large values of impact parameter are probed in Eq. (3.12) where the amplitude
 2102 is small, and therefore the tail in impact parameter is Gaussian in all three cases. Since the
 2103 Fourier transform of the Gaussian in b is an exponential in t , the result at low t follows. On
 2104 the other hand, the three scenarios differ significantly for large values of $|t|$. In the case of the
 2105 1-Pomeron approximation the dependence is still exponential, without any dips, which is easily
 2106 understood since the impact parameter profile is perfectly Gaussian in this case. For the two
 2107 other scenarios, dips in $d\sigma/dt$ as a function in t emerge. They signal the departure from the

2108 Gaussian profile in b for small values of b where the system is dense. A similar pattern can be
 2109 observed when performing the Fourier transform of the Wood-Saxon distribution, which is the
 2110 typical distribution used for the description of the matter density in nuclei. When Q^2 is increased
 2111 the pattern of dips also changes. This is illustrated in Fig. 3.39. It is seen that the dips move to
 2112 higher values of $|t|$ for DIS than for photoproduction. This can be understood from the dipole
 2113 formula Eq. (3.12) which contains the integral over the dipole size. Larger values of Q^2 select
 2114 smaller values of dipole size r , where the amplitude is smaller and thus in the dilute regime,
 2115 where the profile in b is again Gaussian. On the other hand, small scales select large dipole sizes
 2116 for which the dipole amplitude is larger and thus the saturation effects more prominent, leading
 2117 to the distortion of the impact parameter profile and therefore to the emergence of dips in the
 2118 differential cross section $d\sigma/dt$ when studied as a function of t .

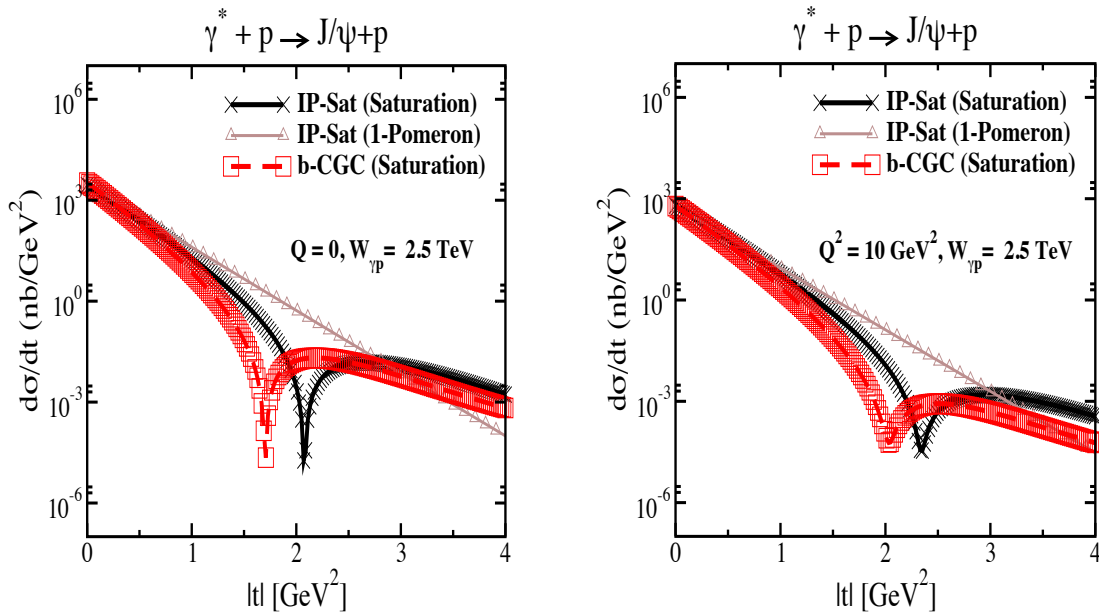


Figure 3.40: Differential cross section for elastic J/ψ production as a function of $|t|$ within the IP-Sat (saturation), b-CGC and 1-Pomeron models at a fixed $W\gamma p = 2.5$ TeV, which corresponds to the region that can be explored by FCC-eh, and for two different values of photon virtuality $Q = 0$ (left plot) and $Q^2 = 10$ GeV² (right plot). The thickness of points includes the uncertainties associated with the freedom to choose different values for the charm quark mass within the range $m_c = 1.2 - 1.4$ GeV .

2119 In the next Fig. 3.40 we show the same calculation but for higher energy $W = 2.5$ TeV, which
 2120 could be explored in the FCC-eh. In this case we see that the dips move to lower values of
 2121 $|t|$. This can be easily understood, as with increasing energy the dipole scattering amplitude
 2122 increases, and thus the dilute-dense boundary shifts to larger values of b , meaning that the
 2123 deviation from the exponential fall off occurs for smaller values of $|t|$. Similar studies [234]
 2124 show also the change of the position of the dips with the mass of the vector meson: for lighter
 2125 vector mesons like ρ, ω, ϕ the dips occur at smaller t than for the heavier vector mesons J/ψ
 2126 or Υ . We note that, of course, the positions of the dips depend crucially on the details of the
 2127 models, which are currently not constrained by the existing HERA data. We also note the
 2128 sizeable uncertainties due to the charm quark mass (the fits to inclusive HERA data from which
 2129 parameters of the models have been extracted are performed at each fixed value of the charm
 2130 mass that is then used to compute exclusive J/ψ production).

2131 We thus see that the precise measurement of the t -slope in the elastic production of vector mesons
 2132 at the LHeC, and its variation with x and scales, provide a unique opportunity to explore the

2133 transition between the dilute and dense partonic regimes. As mentioned earlier, elastic diffractive
 2134 production is one among several different measurements which can be performed to explore the
 2135 3D structure of the hadron. Another one is Deeply Virtual Compton Scattering which is a
 2136 process sensitive to the spatial distribution of quarks inside the hadron. Previous preliminary
 2137 analyses [1] indicate a huge potential of LHeC for the measurement of DVCS. Another example
 2138 of a process that could be studied at the LHeC, is diffractive exclusive dijet production. It
 2139 has been suggested [238] that this process is sensitive to the Wigner function, and that the
 2140 transverse momentum and spatial distribution of partons can be extracted by measuring this
 2141 process. The transverse momentum of jets would be sensitive to the transverse momentum of
 2142 the participating partons, whereas the momentum transfer of the elastically scattered proton
 2143 would give a handle on the impact parameter distribution of the partons in the target [239–241],
 2144 thus giving a possibility to extract information about the Wigner distribution.

2145 So far we have referred to coherent diffraction, i.e. to a scenario in which the proton remains
 2146 intact after the collision. There also exists incoherent diffraction, where the proton gets excited
 2147 into some state with the quantum numbers of the proton and separated from the rest of the
 2148 event by a large rapidity gap. In order to apply the dipole formalism to the incoherent case,
 2149 see Sec. 4.3.1 where the formulae applicable for both protons and nuclei are shown. Here one
 2150 must consider a more involved structure of the proton (e.g. as composed by a fixed [242–245]
 2151 or a growing number with $1/x$ of hot spots [246–248]). As discussed in Sec. 4.3.1, coherent
 2152 diffraction is sensitive to the gluon distribution in transverse space, while incoherent diffraction
 2153 is particularly sensitive to fluctuations of the gluon distribution. A prediction of the model with
 2154 a growing number of hot spots, both in models where this increasing number is implemented
 2155 by hand [246–248] and in those where it is dynamically generated [245] from a fixed number
 2156 at larger x , is that the ratio of incoherent to coherent diffraction will decrease with W , and
 2157 that this decrease is sensitive to the details of the distribution of hot spots. Thus, to the
 2158 fluctuations of the gluon distribution in transverse space. In order to check these ideas, both
 2159 the experimental capability to separate coherent from incoherent diffraction and a large lever
 2160 arm in W , as available at the LHeC, are required.

2161 3.2.6 Inclusive diffraction

2162 An important discovery of HERA was the observation of a large ($\sim 10\%$) fraction of diffractive
 2163 events in DIS [249, 250]. In these events the proton stays intact or dissociates into a state with
 2164 the proton quantum numbers, despite undergoing a violent, highly energetic collision, and is
 2165 separated from the rest of the produced particles by a large rapidity gap. In a series of ground-
 2166 breaking papers (see Ref. [251] for a review), the HERA experiments determined the deep
 2167 inelastic structure of the t -channel exchange in these events in the form of diffractive parton
 2168 densities.

2169 The precise measurement of diffraction in DIS is of great importance for our understanding of the
 2170 strong interaction. First, the mechanism through which a composite strongly interacting object
 2171 interacts perturbatively while keeping colour neutrality offers information about the confinement
 2172 mechanism. Second, diffraction is known to be highly sensitive to the low- x partonic content
 2173 of the proton and its evolution with energy and it therefore has considerable promise to reveal
 2174 deviations from standard linear evolution through higher twist effects or, eventually, non-linear
 2175 dynamics. Third, it allows checks of basic theory predictions such as the relation between
 2176 diffraction in ep scattering and nuclear shadowing [252]. Finally, the accurate extraction of
 2177 diffractive parton distribution functions facilitates tests of the range of validity of perturbative
 2178 factorisation [253–255]. The potential studies of inclusive diffraction that would be possible at

2179 the LHeC are presented here (see Ref. [256] for further details). They substantially extend the
 2180 kinematic coverage of the HERA analyses, leading to much more detailed tests of theoretical
 2181 ideas than have been possible hitherto. Although we work here at NLO of QCD, it is worth
 2182 noting that similar analyses in the HERA context have recently extended to NNLO [257].

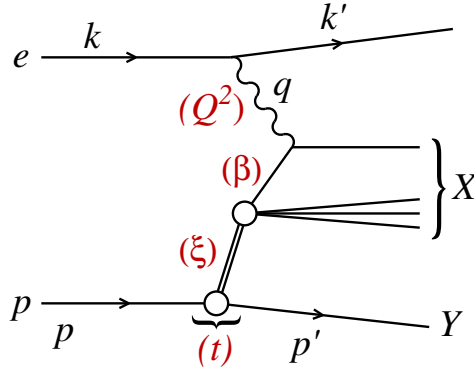


Figure 3.41: A diagram of a diffractive NC event in DIS together with the corresponding variables, in the one-photon exchange approximation. The large rapidity gap is between the system X and the scattered proton (or its low mass excitation) Y .

2183 In Fig. 3.41 we show a diagram depicting a neutral current diffractive deep inelastic event.
 2184 Charged currents could also be considered and were measured at HERA [258] but with large
 2185 statistical uncertainties and in a very restricted region of phase space. Although they could be
 2186 measured at both the LHeC and the FCC-eh with larger statistics and more extended kinematics,
 2187 in this first study we limit ourselves to neutral currents. The incoming electron or positron, with
 2188 four momentum k , scatters off the proton, with incoming four momentum p , and the interaction
 2189 proceeds through the exchange of a virtual photon with four-momentum q . The kinematic
 2190 variables for such an event include the standard deep inelastic variables

$$Q^2 = -q^2, \quad x = \frac{-q^2}{2p \cdot q}, \quad y = \frac{p \cdot q}{p \cdot k}, \quad (3.19)$$

2191 where Q^2 describes the photon virtuality, x is the Bjorken variable and y the inelasticity of the
 2192 process. In addition, the variables

$$s = (k + p)^2, \quad W^2 = (q + p)^2, \quad (3.20)$$

2193 are the electron-proton centre-of-mass energy squared and the photon-proton centre-of-mass
 2194 energy squared, respectively. A distinguishing feature of the diffractive event $ep \rightarrow eXY$ is the
 2195 presence of the large rapidity gap between the diffractive system, characterised by the invariant
 2196 mass M_X and the final proton (or its low-mass excitation) Y with four momentum p' . In
 2197 addition to the standard DIS variables listed above, diffractive events are also characterised by
 2198 an additional set of variables defined as

$$t = (p - p')^2, \quad \xi = \frac{Q^2 + M_X^2 - t}{Q^2 + W^2}, \quad \beta = \frac{Q^2}{Q^2 + M_X^2 - t}. \quad (3.21)$$

2199 In the above t is the squared four-momentum transfer at the proton vertex, ξ (alternatively
 2200 denoted by x_{IP}) can be interpreted as the momentum fraction of the *diffractive exchange* with
 2201 respect to the hadron, and β is the momentum fraction of the parton with respect to the
 2202 diffractive exchange. The two momentum fractions combine to give Bjorken- x , $x = \beta\xi$.

2203 The kinematic range in (β, Q^2, ξ) that we consider at the LHeC is restricted by the following
 2204 cuts:

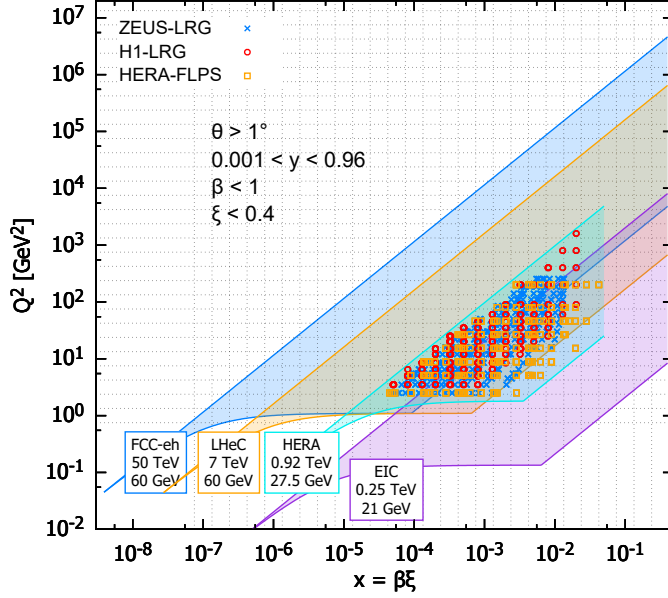


Figure 3.42: Kinematic phase space for inclusive diffraction in (x, Q^2) for the EIC (magenta region), the LHeC (orange region) and the FCC-eh (dark blue region) as compared with the HERA data (light blue region, ZEUS-LRG [259], H1-LRG [260], HERA-FLPS [261]). The acceptance limit for the electron in the detector design has been assumed to be 1° , and we take $\xi < 0.4$.

- 2205 • $Q^2 \geq 1.8 \text{ GeV}^2$: due to the fact that the initial distribution for the DGLAP evolution is
 2206 parameterised at $\mu_0^2 = 1.8 \text{ GeV}^2$. The renormalization and factorisation scales are taken
 2207 to be equal to Q^2 .
- 2208 • $\xi < 0.4$: constrained by physical and experimental limitations. This rather high ξ value is
 2209 an experimental challenge and physically enters the phase-space region where the Pomeron
 2210 contribution should become negligible compared with sub-leading exchanges. Within the
 2211 two-component model, see Eq. (3.26) below, at high ξ the cross section is dominated by
 2212 the secondary Reggeon contribution, which is poorly fixed by the HERA data. We present
 2213 this high ξ (> 0.1) region for illustrative purpose and for the sake of discussion of the fit
 2214 results below.

2215 In Fig. 3.42 the accessible kinematic range in (x, Q^2) is shown for three machines: HERA, LHeC
 2216 and FCC-eh. For the LHeC design the range in x is increased by a factor ~ 20 over HERA
 2217 and the maximum available Q^2 by a factor ~ 100 . The FCC-eh machine would further increase
 2218 this range with respect to LHeC by roughly one order of magnitude in both x and Q^2 . We
 2219 also show the EIC kinematic region for comparison. The three different machines are clearly
 2220 complementary in their kinematic coverage, with LHeC and EIC adding sensitivity at lower and
 2221 higher x than HERA, respectively.

2222 In Fig. 3.43 the phase space in (β, Q^2) is shown for fixed ξ for the LHeC. The LHeC machine
 2223 probes very small values of ξ , reaching 10^{-4} with a wide range of β . Of course, the ranges in
 2224 β and ξ are correlated since $x = \beta\xi$. Therefore, for small values of ξ only large values of β are
 2225 accessible while for large ξ the range in β extends to very small values.

2226 Diffractive cross sections in the neutral current case can be presented in the form of the reduced

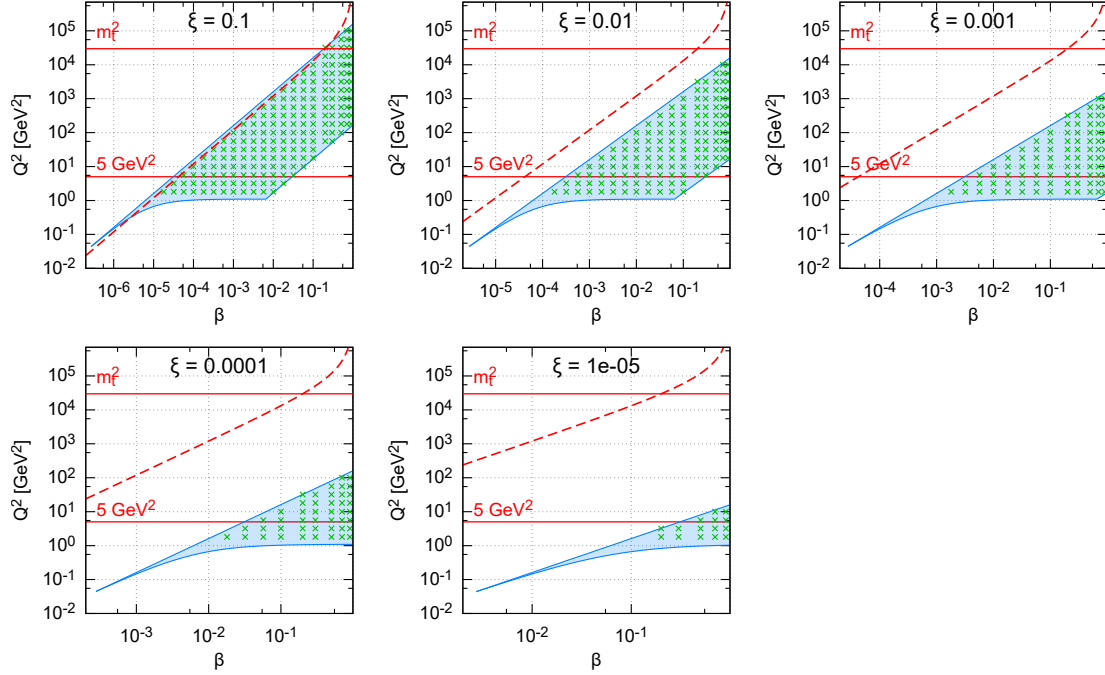


Figure 3.43: Kinematic phase space for inclusive diffraction in (β, Q^2) for fixed values of ξ for the LHeC design. The horizontal lines indicate correspondingly, $Q^2 = 5 \text{ GeV}^2$, the lowest data value for the DGLAP fit performed in this study and m_t^2 the 6-flavour threshold. The dashed line marks the kinematic limit for $t\bar{t}$ production.

2227 cross sections integrated over t [258]:

$$\frac{d^3\sigma^D}{d\xi d\beta dQ^2} = \frac{2\pi\alpha_{\text{em}}^2}{\beta Q^4} Y_+ \sigma_{\text{red}}^{\text{D}(3)}, \quad (3.22)$$

2228 where $Y_+ = 1 + (1-y)^2$ and the reduced cross sections can be expressed in terms of two diffractive
2229 structure functions F_2^{D} and F_L^{D} . In the one-photon approximation, the relations are

$$\sigma_{\text{red}}^{\text{D}(3)} = F_2^{\text{D}(3)}(\beta, \xi, Q^2) - \frac{y^2}{Y_+} F_L^{\text{D}(3)}(\beta, \xi, Q^2). \quad (3.23)$$

2230 In this analysis we neglect Z^0 exchange, though it should be included in future studies.

2231 Both $\sigma_{\text{red}}^{\text{D}(3)}$ and $\sigma_{\text{red}}^{\text{D}(4)}$ have been measured at the HERA collider [249, 250, 258–260, 262–265] and
2232 used to obtain QCD-inspired parameterisations.

2233 The standard perturbative QCD approach to diffractive cross sections is based on collinear
2234 factorisation [253–255]. It was demonstrated that, similarly to the inclusive DIS cross section,
2235 the diffractive cross section can be written, up to terms of order $\mathcal{O}(\Lambda^2/Q^2)$, where Λ is the
2236 hadronic scale, in a factorised form

$$d\sigma^{ep \rightarrow eXY}(\beta, \xi, Q^2, t) = \sum_i \int_{\beta}^1 dz d\hat{\sigma}^{ei} \left(\frac{\beta}{z}, Q^2 \right) f_i^{\text{D}}(z, \xi, Q^2, t), \quad (3.24)$$

2237 where the sum is performed over all parton flavours (gluon, d -quark, u -quark, etc.). The hard
2238 scattering partonic cross section $d\hat{\sigma}^{ei}$ can be computed perturbatively in QCD and is the same
2239 as in the inclusive deep inelastic scattering case. The long distance part f_i^{D} corresponds to the

2240 diffractive parton distribution functions, which can be interpreted as conditional probabilities
 2241 for partons in the proton, provided the proton is scattered into the final state system Y with
 2242 specified 4-momentum p' . They are evolved using the DGLAP evolution equations [266–269]
 2243 similarly to the inclusive case. The analogous formula for the t -integrated structure functions
 2244 reads

$$F_{2/L}^{\text{D}(3)}(\beta, \xi, Q^2) = \sum_i \int_{\beta}^1 \frac{dz}{z} C_{2/L,i} \left(\frac{\beta}{z} \right) f_i^{\text{D}(3)}(z, \xi, Q^2), \quad (3.25)$$

2245 where the coefficient functions $C_{2/L,i}$ are the same as in inclusive DIS.

2246 Fits to the diffractive structure functions usually [258, 264] parameterise the diffractive PDFs in
 2247 a two component model, which is a sum of two diffractive exchange contributions, \mathbb{P} and \mathbb{R} :

$$f_i^{\text{D}(4)}(z, \xi, Q^2, t) = f_{\mathbb{P}}^p(\xi, t) f_i^{\mathbb{P}}(z, Q^2) + f_{\mathbb{R}}^p(\xi, t) f_i^{\mathbb{R}}(z, Q^2). \quad (3.26)$$

2248 For both of these terms proton vertex factorisation is separately assumed, meaning that the
 2249 diffractive exchange can be interpreted as colourless objects called a *Pomeron* or a *Reggeon*
 2250 with parton distributions $f_i^{\mathbb{P},\mathbb{R}}(\beta, Q^2)$. The flux factors $f_{\mathbb{P},\mathbb{R}}^p(\xi, t)$ represent the probability
 2251 that a Pomeron/Reggeon with given values ξ, t couples to the proton. They are parameterised
 2252 using the form motivated by Regge theory,

$$f_{\mathbb{P},\mathbb{R}}^p(\xi, t) = A_{\mathbb{P},\mathbb{R}} \frac{e^{B_{\mathbb{P},\mathbb{R}} t}}{\xi^{2\alpha_{\mathbb{P},\mathbb{R}}(t)-1}}, \quad (3.27)$$

2253 with a linear trajectory $\alpha_{\mathbb{P},\mathbb{R}}(t) = \alpha_{\mathbb{P},\mathbb{R}}(0) + \alpha'_{\mathbb{P},\mathbb{R}} t$. The diffractive PDFs relevant to the
 2254 t -integrated cross sections read

$$f_i^{\text{D}(3)}(z, \xi, Q^2) = \phi_{\mathbb{P}}^p(\xi) f_i^{\mathbb{P}}(z, Q^2) + \phi_{\mathbb{R}}^p(\xi) f_i^{\mathbb{R}}(z, Q^2), \quad (3.28)$$

2255 with

$$\phi_{\mathbb{P},\mathbb{R}}^p(\xi) = \int dt f_{\mathbb{P},\mathbb{R}}^p(\xi, t). \quad (3.29)$$

2256 Note that, the notions of *Pomeron* and *Reggeon* used here to model hard diffraction in DIS are,
 2257 in principle, different from those describing the soft hadron-hadron interactions; in particular,
 2258 the parameters of the fluxes may be different.

2259 The diffractive parton distributions of the Pomeron at the initial scale $\mu_0^2 = 1.8 \text{ GeV}^2$ are
 2260 parameterised as

$$z f_i^{\mathbb{P}}(z, \mu_0^2) = A_i z^{B_i} (1-z)^{C_i}, \quad (3.30)$$

2261 where i is a gluon or a light quark and the momentum fraction $z = \beta$ in the case of quarks. In the
 2262 diffractive parameterisations the contributions of all the light quarks (anti-quarks) are assumed
 2263 to be equal. For the treatment of heavy flavours, a variable flavour number scheme (VFNS)
 2264 is adopted, where the charm and bottom quark DPDFs are generated radiatively via DGLAP
 2265 evolution, and no intrinsic heavy quark distributions are assumed. The structure functions are
 2266 calculated in a General-Mass Variable Flavour Number scheme (GM-VFNS) [270, 271] which
 2267 ensures a smooth transition of $F_{2,L}$ across the flavour thresholds by including $\mathcal{O}(m_h^2/Q^2)$ correc-
 2268 tions. The parton distributions for the Reggeon component are taken from a parameterisation
 2269 which was obtained from fits to the pion structure function [272, 273].

2270 In Eq. (3.26) the normalisation factors of fluxes, $A_{\mathbb{P},\mathbb{R}}$ and of DPDFs, A_i enter in the product.
 2271 To resolve the ambiguity we fix⁹ $A_{\mathbb{P}}$ and use $f_i^{\mathbb{R}}(z, Q^2)$ normalised to the pion structure function,
 2272 which results in A_i and $A_{\mathbb{R}}$ being well defined free fit parameters. For full details, see Ref. [256].

⁹Here, as in the HERA fits, $A_{\mathbb{P}}$ is fixed by normalizing $\phi_{\mathbb{P}}^p(0.003) = 1$.

2273 **Pseudodata for diffractive structure functions**

2274 The reduced cross sections are extrapolated using the ZEUS-SJ DPDFs. Following the scenario
 2275 of the ZEUS fit [264] we work within the VFNS scheme at NLO accuracy. The transition scales
 2276 for DGLAP evolution are fixed by the heavy quark masses, $\mu^2 = m_h^2$ and the structure functions
 2277 are calculated in the Thorne–Roberts GM-VFNS [274]. The Reggeon PDFs are taken from the
 2278 GRV pion set [273], the numerical parameters are taken from Tables 1 and 3 of Ref. [264], the
 2279 heavy quark masses are $m_c = 1.35$ GeV, $m_b = 4.3$ GeV, and $\alpha_s(M_Z^2) = 0.118$.

2280 The pseudodata were generated using the extrapolation of the fit to HERA data, which pro-
 2281 vides the central values, amended with a random Gaussian smearing with standard deviation
 2282 corresponding to the relative error δ . An uncorrelated 5% systematic error was assumed giving
 2283 a total uncertainty

$$\delta = \sqrt{\delta_{\text{sys}}^2 + \delta_{\text{stat}}^2}. \quad (3.31)$$

2284 The statistical error was computed assuming a very modest integrated luminosity of 2 fb^{-1} , see
 2285 Ref. [32, 33]. For the binning adopted in this study, the statistical uncertainties have a very
 2286 small effect on the uncertainties in the extracted DPDFs. Obviously, a much larger luminosity
 2287 would allow a denser binning that would result in smaller DPDF uncertainties.

2288 In Fig. 3.44 we show a subset of the simulated data for the diffractive reduced cross section $\xi\sigma_{\text{red}}$
 2289 as a function of β in selected bins of ξ and Q^2 for the LHeC. For the most part the errors are
 2290 very small, and are dominated by the systematics. The breaking of Regge factorisation evident
 2291 at large ξ comes from the large Reggeon contribution in that region, whose validity could be
 2292 further investigated at the LHeC.

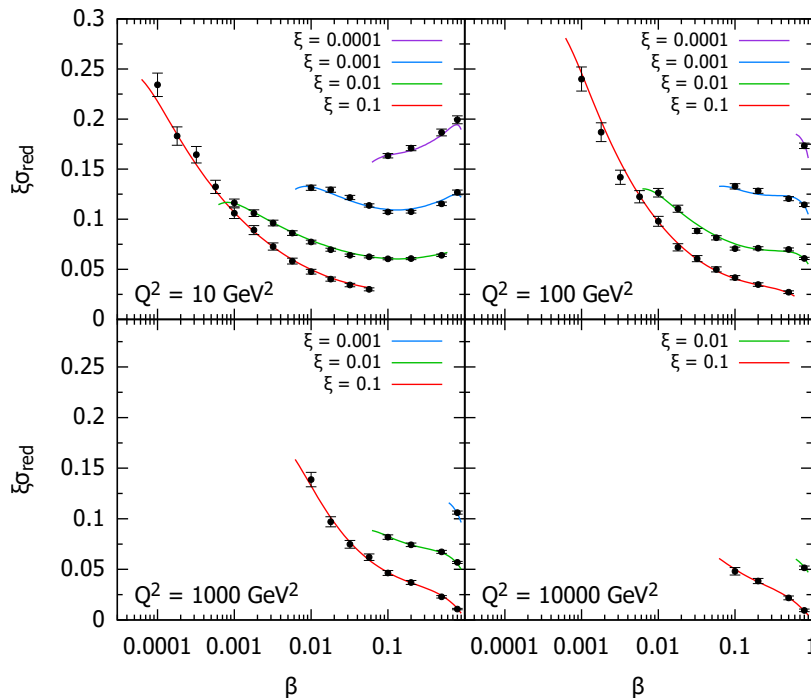


Figure 3.44: Selected subset of the simulated data for the diffractive reduced cross section as a function of β in bins of ξ and Q^2 for ep collisions at the LHeC. The curves for $\xi = 0.01, 0.001, 0.0001$ are shifted up by 0.04, 0.08, 0.12, respectively.

2293 **Potential for constraining diffractive PDFs at the LHeC and FCC-eh**

2294 With the aim of establishing the experimental precision with which DPDFs could be extracted
 2295 when LHeC data become available, we generate the central values of the pseudodata using the
 2296 central set of the ZEUS-SJ fit that are distributed according to a Gaussian with experimental
 2297 width given by Eq. (3.31), that also provides the uncertainty in the pseudodata. We then include
 2298 the pseudodata in a fit alongside the existing HERA data using the same functional form and,
 2299 as expected, obtain a $\chi^2/\text{ndf} \sim 1$, which demonstrates the consistency of the approach.

2300 To evaluate the experimental precision with which the DPDFs can be determined, several pseu-
 2301 dodata sets, corresponding to independent random error samples, were generated. Each pseudo-
 2302 data set was fitted separately. The minimal value of Q^2 for the data considered in the fits was set
 2303 to $Q_{\min}^2 = 5 \text{ GeV}^2$. The reason for this cut-off is to show the feasibility of the fits including just
 2304 the range in which standard twist-2 DGLAP evolution is expected to be trustable. At HERA,
 2305 the Q_{\min}^2 values giving acceptable DGLAP (twist-2) fits were 8 GeV^2 [258] and 5 GeV^2 [259] for
 2306 H1 and ZEUS, respectively. The maximum value of ξ was set by default to $\xi_{\max} = 0.1$, above
 2307 which the cross section starts to be dominated by the Reggeon exchange. The binning adopted
 2308 in this study corresponds roughly to 4 bins per order of magnitude in each of ξ, β, Q^2 . For
 2309 $Q_{\min}^2 = 5 \text{ GeV}^2$, $\xi_{\max} = 0.1$ and below the top threshold this results in 1229 and 1735 pseudo-
 2310 data points for the LHeC and FCC-eh, respectively. The top-quark region adds 17 points for the
 2311 LHeC and 255 for FCC-eh. Lowering Q_{\min}^2 down to 1.8 GeV^2 we get 1589 and 2171 pseudodata
 2312 points, while increasing ξ up to 0.32 adds around 180 points for both proposed machines.

2313 The potential for determination of the gluon DPDF was investigated by fitting the inclusive
 2314 diffractive DIS pseudodata with two models with different numbers of parameters, named S and
 2315 C (see Ref. [256]) with $\alpha_{IP,IR}(0)$ fixed, in order to focus on the shape of the Pomeron's PDFs. At
 2316 HERA, both S and C fits provide equally good descriptions of the data with $\chi^2/\text{ndf} = 1.19$ and
 2317 1.18, respectively, despite different gluon DPDF shapes. The LHeC pseudodata are much more
 2318 sensitive to gluons, resulting in χ^2/ndf values of 1.05 and 1.4 for the S and C fits, respectively.
 2319 This motivates the use of the larger number of parameters in the fit-S model, which we employ
 2320 in the following studies. It also shows clearly the potential of the LHeC and the FCC-eh to
 2321 better constrain the low- x gluon and, therefore, unravel eventual departures from standard
 2322 linear evolution.

2323 In Fig. 3.45 the diffractive gluon and quark distributions are shown for the LHeC and FCC-eh,
 2324 respectively, as a function of momentum fraction z for fixed scales $\mu^2 = 6, 20, 60, 200 \text{ GeV}^2$.
 2325 The bands labelled A, B, C denote fits to three statistically independent pseudodata replicas,
 2326 obtained from the same central values and statistical and systematic uncertainties. Hereafter the
 2327 uncertainty bands shown correspond to $\Delta\chi^2 = 2.7$ (90% CL). Also the extrapolated ZEUS-SJ
 2328 DPDFs are shown with error bands marked by the '/' hatched area. Note that the depicted
 2329 uncertainty bands come solely from experimental errors, neglecting theoretical sources, such as
 2330 fixed input parameters and parameterisation biases. The extrapolation beyond the reach of
 2331 LHeC/FCC-eh is marked in grey and the HERA kinematic limit is marked with the vertical
 2332 dotted line. The stability of the results with respect to the independent pseudodata replicas
 2333 used for the analysis is evident, so in the following only one will be employed. The low x DPDF
 2334 determination accuracy improves with respect to HERA by a factor of 5–7 for the LHeC and
 2335 10–15 for the FCC-eh and completely new kinematic regimes are accessed.

2336 For a better illustration of the precision, in Fig. 3.46 the relative uncertainties are shown for
 2337 parton distributions at different scales. The different bands show the variation with the upper
 2338 cut on the available ξ range, from 0.01 to 0.32. In the best constrained region of $z \simeq 0.1$,

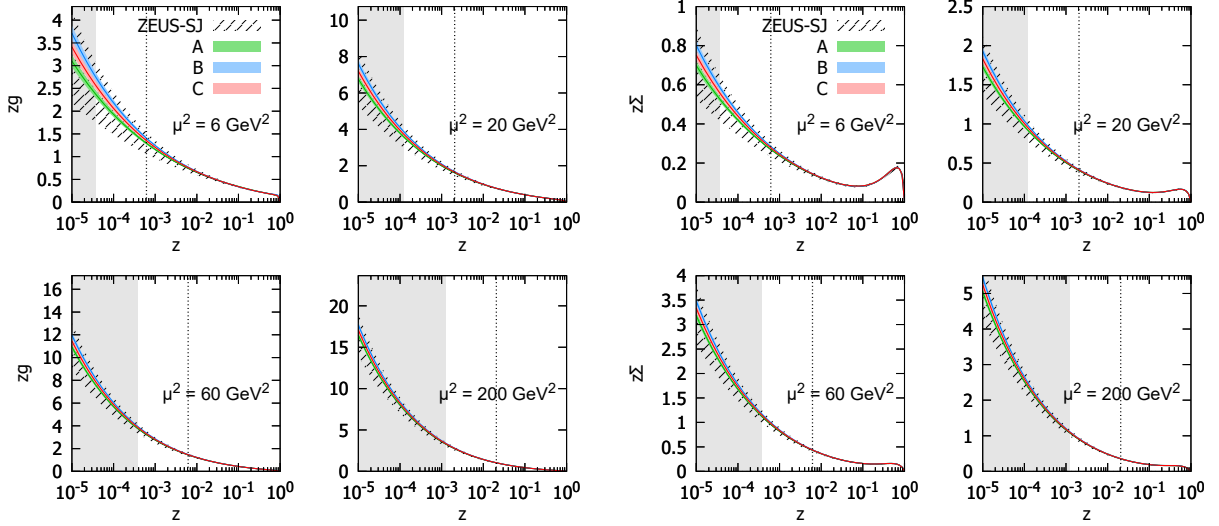


Figure 3.45: Diffractive PDFs for gluon and quark in the LHeC kinematics as a function of momentum fraction z for fixed values of scale μ^2 . Results of fits to three (A,B,C) pseudodata replicas are shown together with the experimental error bands. For comparison, the extrapolated ZEUS-SJ fit is also shown (black) with error bands marked with the hatched pattern. The vertical dotted lines indicate the HERA kinematic limit. The bands indicate only the experimental uncertainties.

2339 the precision reaches the 1% level. We observe only a modest improvement in the achievable
 2340 accuracy of the extracted DPDFs with the change of ξ by an order of magnitude from 0.01
 2341 to 0.1. An almost negligible effect is observed when further extending the ξ range up to 0.32.
 2342 This is encouraging, since the measurement for the very large values of ξ is challenging. It
 2343 reflects the dominance of the secondary Reggeon in this region. We stress again that only
 2344 experimental errors are included in our uncertainty bands. Neither theoretical uncertainties nor
 2345 the parameterisation biases are considered. For a detailed discussion of this and other aspects
 2346 of the fits, see Ref. [256].

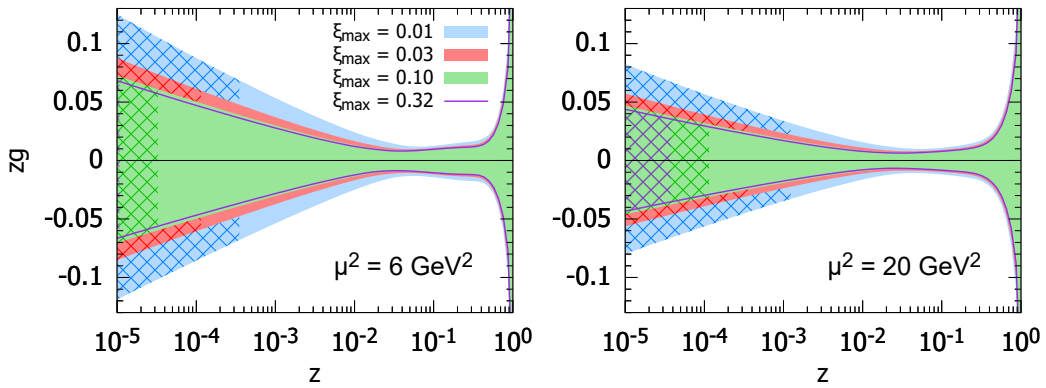


Figure 3.46: Relative uncertainties on the diffractive gluon PDFs for the LHeC kinematics. Two different choices of scales are considered $\mu^2 = 6$ and $\mu^2 = 20 \text{ GeV}^2$. The blue, red, green bands and magenta line correspond to different maximal values of $\xi = 0.01, 0.03, 0.1, 0.32$, respectively. The cross-hatched areas show kinematically excluded regions. The bands indicate only the experimental uncertainties, see the text.

2347 Factorisation tests using Hadronic Final States in Diffractive DIS

2348 The factorisation properties of diffractive DIS were a major topic of study at HERA [251] and
2349 are highly relevant to the interpretation of diffractive processes at the LHC [275]. A general theo-
2350 retical framework is provided by the proof [253] of a hard scattering collinear QCD factorisation
2351 theorem for semi-inclusive DIS scattering processes such as $ep \rightarrow epX$. This implies that the
2352 DPDFs extracted in fits to inclusive diffractive DIS may be used to predict perturbative cross
2353 sections for hadronic final state observables such as heavy flavour or jet production. Testing this
2354 factorisation pushes at the boundaries of applicability of perturbative QCD and will be a major
2355 topic of study at the LHeC.

2356 Tests of diffractive factorisation at HERA are strongly limited by the kinematics. The mass of
2357 the dissociation system X is limited to approximately $M_X < 30$ GeV, which implies for example
2358 that jet transverse momenta cannot be larger than about 15 GeV and more generally leaves very
2359 little phase space for any studies at perturbative scales. As well as restricting the kinematic range
2360 of studies, this restriction also implied large hadronisation and scale uncertainties in theoretical
2361 predictions, which in turn limit the precision with which tests can be made.

2362 The higher centre-of-mass energy of the LHeC opens up a completely new regime for diffractive
2363 hadronic final state observables in which masses and transverse momenta are larger and theo-
2364 retical uncertainties are correspondingly reduced. For example, M_X values in excess of 250 GeV
2365 are accessible, whilst remaining in the region $\xi < 0.05$ where the leading diffractive (pomeron)
2366 exchange dominates. The precision of tests is also improved by the development of techniques
2367 for NNLO calculations for diffractive jets [276].

2368 Fig. 3.47 shows a simulation of the expected diffractive jet cross section at the LHeC, assuming
2369 DPDFs extrapolated from H1 at HERA [258], using the NLOJET++ framework [277]. An
2370 integrated luminosity of 100 fb^{-1} is assumed and the kinematic range considered is $Q^2 > 2 \text{ GeV}^2$,
2371 $0.1 < y < 0.7$ and scattered electron angles larger than 1° . Jets are reconstructed using the k_T
2372 algorithm with $R = 1$. The statistical precision remains excellent up to jet transverse momenta
2373 of almost 50 GeV and the theoretical scale uncertainties (shaded bands) are substantially reduced
2374 compared with HERA measurements. Comparing a measurement of this sort of quality with
2375 predictions refined using DPDFs from inclusive LHeC data would clearly provide an exacting
2376 test of diffractive factorisation.

2377 Further interesting hadronic final state observables that were studied at HERA and could be
2378 extended at the LHeC include open charm production, thrust and other event shapes, charged
2379 particle multiplicities and energy flows. In addition, the LHeC opens up completely new chan-
2380 nels, notably diffractive beauty, W and Z production, the latter giving complementary sensitivity
2381 to the quark densities to that offered by inclusive diffraction.

2382 3.2.7 Light-Front Holography and Superconformal Algebra

2383 The LHeC has the potential of probing the high mass spectrum of QCD, such as the spectroscopy
2384 and structure of hadrons consisting of heavy quarks. Insights into this new domain of hadron
2385 physics can now be derived by new non-perturbative colour-confining methods based on light-
2386 front (LF) holography. A remarkable feature is universal Regge trajectories with universal
2387 slopes in both the principal quantum number n and internal orbital angular momentum L . A
2388 key feature is di-quark clustering and supersymmetric relations between the masses of meson,
2389 baryons, and tetraquarks. In addition the running coupling is determined at all scales, including
2390 the soft domain relevant to rescattering corrections to LHeC processes. The combination of

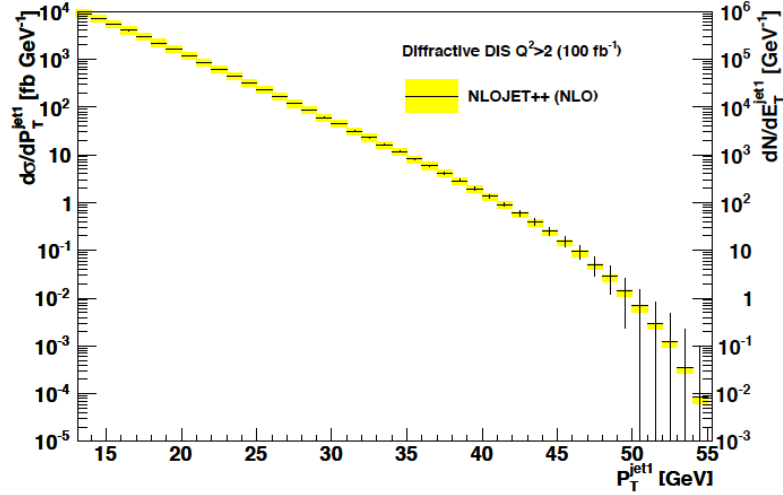


Figure 3.47: Simulated diffractive dijet cross section as a function of leading jet transverse momentum in the kinematic range $Q^2 > 2 \text{ GeV}^2$ and $0.1 < y < 0.7$, with scattered electron angles in excess of 1° . The error bars indicate predicted statistical uncertainties for a luminosity of 100 fb^{-1} . The coloured bands correspond to theoretical uncertainties when varying the renormalisation and factorisation scales by factors of 2.

2391 lightfront holography with superconformal algebra leads to the novel prediction that hadron
 2392 physics has supersymmetric properties in both spectroscopy and dynamics.

2393 Light-front holography and recent theoretical advances

2394 Five-dimensional AdS_5 space provides a geometrical representation of the conformal group.
 2395 Remarkably, AdS_5 is holographically dual to $3 + 1$ spacetime at fixed LF time τ [278]. A
 2396 colour-confining LF equation for mesons of arbitrary spin J can be derived from the holographic
 2397 mapping of the *soft-wall model* modification of AdS_5 space for the specific dilaton profile $e^{+\kappa^2 z^2}$,
 2398 where z is the fifth dimension variable of the five-dimensional AdS_5 space. A holographic
 2399 dictionary maps the fifth dimension z to the LF radial variable ζ , with $\zeta^2 = b_\perp^2(1 - x)$. The
 2400 same physics transformation maps the AdS_5 and $(3 + 1)$ LF expressions for electromagnetic and
 2401 gravitational form factors to each other [279].

2402 A key tool is the remarkable dAFF principle [280] which shows how a mass scale can appear in a
 2403 Hamiltonian and its equations of motion while retaining the conformal symmetry of the action.
 2404 When applying it to LF holography, a mass scale κ appears which determines universal Regge
 2405 slopes, and the hadron masses. The resulting *LF Schrödinger Equation* incorporates colour
 2406 confinement and other essential spectroscopic and dynamical features of hadron physics, includ-
 2407 ing Regge theory, the Veneziano formula [281], a massless pion for zero quark mass and linear
 2408 Regge trajectories with the universal slope in the radial quantum number n and the internal
 2409 orbital angular momentum L . The combination of LF dynamics, its holographic mapping to
 2410 AdS_5 space, and the dAFF procedure provides new insight into the physics underlying colour
 2411 confinement, the non-perturbative QCD coupling, and the QCD mass scale. The $q\bar{q}$ mesons and
 2412 their valence LFWFs are the eigensolutions of the frame-independent a relativistic bound-state
 2413 LF Schrödinger equation.

2414 The mesonic $q\bar{q}$ bound-state eigenvalues for massless quarks are $M^2(n, L, S) = 4\kappa^2(n + L + S/2)$.
 2415 This equation predicts that the pion eigenstate $n = L = S = 0$ is massless for zero quark mass.

2416 When quark masses are included in the LF kinetic energy $\sum_i \frac{k_{\perp i}^2 + m^2}{x_i}$, the spectroscopy of mesons
 2417 are predicted correctly, with equal slope in the principal quantum number n and the internal
 2418 orbital angular momentum L . A comprehensive review is given in Ref. [278].

2419 The QCD Running Coupling at all Scales from Light-Front Holography

2420 The QCD running coupling $\alpha_s(Q^2)$ sets the strength of the interactions of quarks and gluons
 2421 as a function of the momentum transfer Q (see Sec. 3.2.1). The dependence of the coupling
 2422 Q^2 is needed to describe hadronic interactions at both long and short distances [282]. It can
 2423 be defined [283] at all momentum scales from a perturbatively calculable observable, such as
 2424 the coupling $\alpha_s^{g_1}(Q^2)$, which is defined using the Bjorken sum rule [284], and determined from
 2425 the sum rule prediction at high Q^2 and, below, from its measurements [285–287]. At high Q^2 ,
 2426 such *effective charges* satisfy asymptotic freedom, obey the usual pQCD renormalisation group
 2427 equations, and can be related to each other without scale ambiguity by commensurate scale
 2428 relations [288].

2429 The high Q^2 dependence of $\alpha_s^{g_1}(Q^2)$ is predicted by pQCD. In the small Q^2 domain its functional
 2430 behaviour can be predicted by the dilaton $e^{+\kappa^2 z^2}$ soft-wall modification of the AdS₅ metric,
 2431 together with LF holography [289], as $\alpha_s^{g_1}(Q^2) = \pi e^{-Q^2/4\kappa^2}$. The parameter κ determines the
 2432 mass scale of hadrons and Regge slopes in the zero quark mass limit, and it was shown that it can
 2433 be connected to the mass scale Λ_s , which controls the evolution of the pQCD coupling [289–291].
 2434 Measurements of $\alpha_s^{g_1}(Q^2)$ [292,293] are remarkably consistent with this predicted Gaussian form,
 2435 and a fit gives $\kappa = 0.513 \pm 0.007$ GeV, see Fig. 3.48.

2436 The matching of the high and low Q^2 regimes of $\alpha_s^{g_1}(Q^2)$ determines a scale Q_0 , which sets the
 2437 interface between perturbative and non-perturbative hadron dynamics. This connection can be
 2438 done for any choice of renormalisation scheme and one obtains an effective QCD coupling at all
 2439 momenta. In the $\overline{\text{MS}}$ scheme one gets $Q_0 = 0.87 \pm 0.08$ GeV [294]. The corresponding value of
 2440 $\Lambda_{\overline{\text{MS}}}$ agrees well with the measured world average value and its value allows to compute hadron
 2441 masses using the AdS/QCD superconformal predictions for hadron spectroscopy. The value of
 2442 Q_0 can further be used to set the factorization scale for DGLAP evolution [267–269] or the ERBL
 2443 evolution of distribution amplitudes [295,296]. The use of the scale Q_0 to resolve the factorization
 2444 scale uncertainty in structure functions and fragmentation functions, in combination with the
 2445 scheme-independent *principle of maximum conformality* (PMC) [129] for setting renormalization
 2446 scales, can greatly improve the precision of pQCD predictions for collider phenomenology at
 2447 LHeC and HL-LHC.

2448 Superconformal Algebra and Hadron Physics with LHeC data

2449 If one generalises LF holography using *superconformal algebra* the resulting LF eigensolutions
 2450 yield a unified Regge spectroscopy of mesons, baryons and tetraquarks, including remark-
 2451 able supersymmetric relations between the masses of mesons and baryons of the same par-
 2452 ity¹⁰ [297,298]. This generalisation further predicts hadron dynamics, including vector meson
 2453 electroproduction, hadronic LFWFs, distribution amplitudes, form factors, and valence structure
 2454 functions [299,300]. Applications to the deuteron elastic form factors and structure functions
 2455 are given in Refs. [301,302]

¹⁰ QCD is not supersymmetrical in the usual sense, since the QCD Lagrangian is based on quark and gluonic fields, not squarks or gluinos. However, its hadronic eigensolutions conform to a representation of superconformal algebra, reflecting the underlying conformal symmetry of chiral QCD and its Pauli matrix representation.

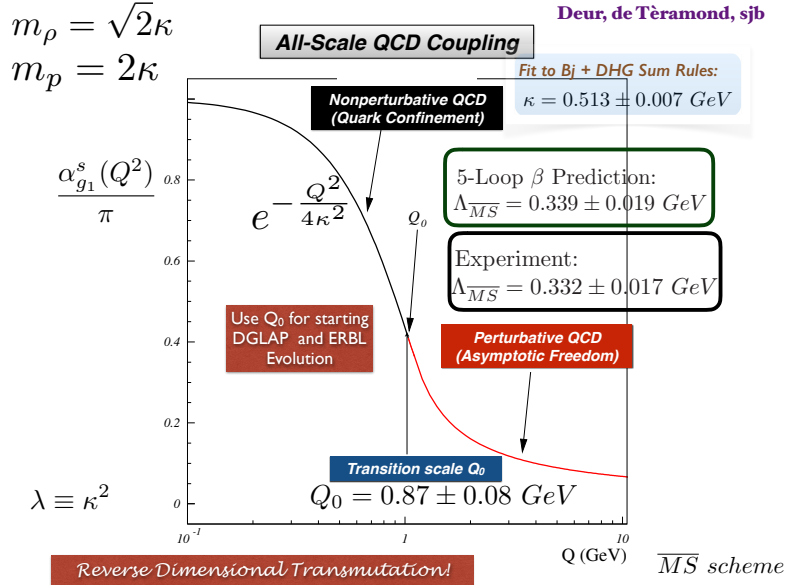


Figure 3.48: Prediction for the running coupling $\alpha_{g_1}^s(Q^2)$ at all scales. At lower Q^2 predictions are obtained from LF Holography and at higher Q^2 from perturbative QCD. The magnitude and derivative of the perturbative and non-perturbative coupling are matched at the scale Q_0 . This matching connects the perturbative scale $\Lambda_{\overline{MS}}$ to the non-perturbative scale κ which underlies the hadron mass scale.

2456 The eigensolutions of superconformal algebra predict the Regge spectroscopy of mesons, baryons,
 2457 and tetraquarks of the same parity and twist as equal-mass members of the same 4-plet repre-
 2458 sentation with a universal Regge slope [303–305]. A comparison with experiment is shown in
 2459 Fig. 3.49. The $q\bar{q}$ mesons with orbital angular momentum $L_M = L_B + 1$ have the same mass as
 their baryonic partners with orbital angular momentum L_B [303, 306].

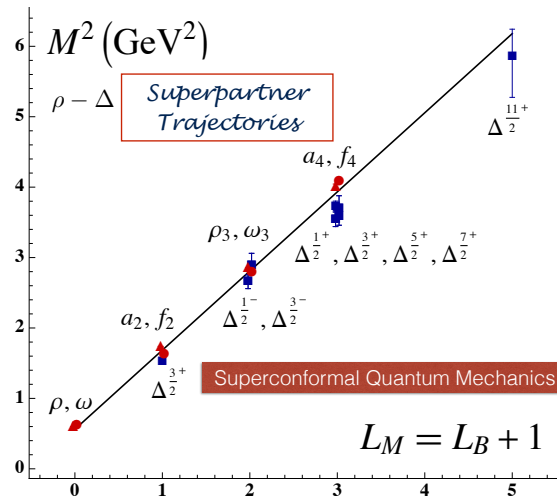


Figure 3.49: Comparison of the ρ/ω meson Regge trajectory with the $J = 3/2$ Δ baryon trajectory. Superconformal algebra predicts the mass degeneracy of the meson and baryon trajectories if one identifies a meson with internal orbital angular momentum L_M with its superpartner baryon with $L_M = L_B + 1$. See Refs. [303, 306].

2460 The predictions from LF holography and superconformal algebra can also be extended to mesons,
 2461 baryons, and tetraquarks with strange, charm and bottom quarks. Although conformal symme-
 2462 try is strongly broken by the heavy quark masses, the basic underlying supersymmetric mech-
 2463 anism, which transforms mesons to baryons (and baryons to tetraquarks), still holds and gives
 2464 remarkable mass degeneracy across the entire spectrum of light, heavy-light and double-heavy
 2465 hadrons.

2466 The 4-plet symmetry of quark-antiquark mesons, quark-diquark baryons, and diquark-antidiquark
 2467 tetraquarks are important predictions by superconformal algebra [294,297]. Recently the AnDY
 2468 experiment at RHIC has reported the observation of a state at 18 GeV which can be identified
 2469 with the $[bb][\bar{b}\bar{b}]$ tetraquark [83]. The states with heavy quarks such as the $[bb][\bar{b}\bar{b}]$ tetraquark
 2470 can be produced at the LHeC, especially at high x_F along the proton beam direction. New
 2471 measurements at the LHeC are therefore inevitable to manifest the superconformal nature of
 2472 hadronic bound states.

2473 3.3 Electroweak Physics

2474 With the discovery of the Standard Model (SM) Higgs boson at the CERN LHC experiments
 2475 and subsequent measurements of its properties, all fundamental parameters of the SM have now
 2476 been measured directly and with remarkable precision. To further establish the validity of the
 2477 theory of electroweak interactions [23,307–310], validate the mechanism of electroweak symmetry
 2478 breaking and the nature of the Higgs sector [311–313], new electroweak measurements have to
 2479 be performed at highest precision. Such high-precision measurements can be considered as a
 2480 portal to new physics, since non-SM contributions, as for instance loop-insertions, may cause
 2481 significant deviations for some precisely measurable and calculable observables. At the LHeC,
 2482 the greatly enlarged kinematic reach to higher mass scales in comparison to HERA [314–316]
 2483 and the large targeted luminosity will enable electroweak measurements in ep scattering with
 2484 higher precision than ever before.

2485 3.3.1 Electroweak effects in inclusive NC and CC DIS cross sections

2486 Electroweak NC interactions in inclusive $e^\pm p$ DIS are mediated by exchange of a virtual photon
 2487 (γ) or a Z boson in the t -channel, while CC DIS is mediated exclusively by W -boson exchange
 2488 as a purely *weak* process. Inclusive NC DIS cross sections are expressed in terms of generalised
 2489 structure functions \tilde{F}_2^\pm , $x\tilde{F}_3^\pm$ and \tilde{F}_L^\pm at EW leading order (LO) as

$$\frac{d^2\sigma^{\text{NC}}(e^\pm p)}{dx dQ^2} = \frac{2\pi\alpha^2}{xQ^4} \left[Y_+ \tilde{F}_2^\pm(x, Q^2) \mp Y_- x\tilde{F}_3^\pm(x, Q^2) - y^2 \tilde{F}_L^\pm(x, Q^2) \right], \quad (3.32)$$

where α denotes the fine structure constant. The terms $Y_\pm = 1 \pm (1-y)^2$, with $y = Q^2/sx$, describe the helicity dependence of the process. The generalised structure functions are separated into contributions from pure γ - and Z -exchange and their interference [89,317]:

$$\tilde{F}_2^\pm = F_2 - (g_V^e \pm P_e g_A^e) \varkappa_Z F_2^{\gamma Z} + [(g_V^e g_V^e + g_A^e g_A^e) \pm 2P_e g_V^e g_A^e] \varkappa_Z^2 F_2^Z, \quad (3.33)$$

$$\tilde{F}_3^\pm = -(g_A^e \pm P_e g_V^e) \varkappa_Z F_3^{\gamma Z} + [2g_V^e g_A^e \pm P_e (g_V^e g_V^e + g_A^e g_A^e)] \varkappa_Z^2 F_3^Z. \quad (3.34)$$

Similar expressions hold for \tilde{F}_L . In the naive quark-parton model, which corresponds to the LO QCD approximation, the structure functions are calculated as

$$[F_2, F_2^{\gamma Z}, F_2^Z] = x \sum_q [Q_q^2, 2Q_q g_V^q, g_V^q g_V^q + g_A^q g_A^q] \{q + \bar{q}\}, \quad (3.35)$$

$$x [F_3^{\gamma Z}, F_3^Z] = x \sum_q [2Q_q g_A^q, 2g_V^q g_A^q] \{q - \bar{q}\}, \quad (3.36)$$

representing two independent combinations of the quark and anti-quark momentum distributions, xq and $x\bar{q}$. In Eq. (3.34), the quantities g_V^f and g_A^f stand for the vector and axial-vector couplings of a fermion ($f = e$ or $f = q$ for electron or quark) to the Z boson, and the coefficient \varkappa_Z accounts for the Z -boson propagator including the normalisation of the weak couplings. Both parameters are fully calculable from the electroweak theory. The (effective) coupling parameters depend on the electric charge, Q_f and the third component of the weak-isospin, $I_{L,f}^3$. Using $\sin^2\theta_W = 1 - \frac{M_W^2}{M_Z^2}$, one can write

$$g_V^f = \sqrt{\rho_{\text{NC},f}} (I_{L,f}^3 - 2Q_f \kappa_{\text{NC},f} \sin^2\theta_W), \quad \text{and} \quad (3.37)$$

$$g_A^f = \sqrt{\rho_{\text{NC},f}} I_{L,f}^3 \quad \text{with } f = (e, u, d). \quad (3.38)$$

2490 The parameters $\rho_{\text{NC},f}$ and $\kappa_{\text{NC},f}$ are calculated as real parts of complex form factors which
 2491 include the higher-order loop corrections [318–320]. They contain non-leading flavour-specific
 2492 components.

2493 Predictions for CC DIS are written in terms of the CC structure functions W_2 , xW_3 and W_L and
 2494 higher-order electroweak effects are collected in two form factors $\rho_{\text{CC},eq}$ and $\rho_{\text{CC},e\bar{q}}$ [321, 322].

2495 In this study, the on-shell scheme is adopted for the calculation of higher-order corrections.
 2496 This means that the independent parameters are chosen as the fine structure constant α and
 2497 the masses of the weak bosons, the Higgs boson and the fermions. The weak mixing angle is
 2498 then fixed and G_F is a prediction, whose higher-order corrections are included in the well-known
 2499 correction factor Δr [323–325] (see discussion of further contributions in Ref. [89]).

2500 The predicted single-differential inclusive NC and CC DIS cross sections for polarised e^-p scat-
 2501 tering as a function of Q^2 are displayed in Fig. 3.50. For NC DIS and at higher Q^2 , electroweak
 2502 effects are important through γZ interference and pure Z -exchange terms and the polarisation
 2503 of the LHeC electron beam of $P_e = \pm 0.8$ will considerably alter the cross sections. For CC DIS,
 2504 the cross section scales linearly with P_e . Two different electron beam energies are displayed in
 2505 Fig. 3.50, and albeit the impact of a reduction from $E_e = 60$ to 50 GeV appears to be small,
 2506 a larger electron beam energy would yield higher precision for the measurement of electroweak
 2507 parameters, since these are predominantly sensitive to the cross sections at highest scales, as
 2508 will be shown in the following.

2509 3.3.2 Methodology of a combined EW and QCD fit

2510 A complete electroweak analysis of DIS data has to consider PDFs together with electroweak
 2511 parameters [327]. In this study, the uncertainties of electroweak parameters are obtained in
 2512 a combined fit of electroweak parameters and the PDFs, and the inclusive NC and CC DIS
 2513 pseudodata (see Sec. 3.2.6) are explored as input data. The PDFs are parameterised with 13
 2514 parameters at a starting scale Q_0^2 and NNLO DGLAP evolution is applied [49, 328]. In this
 2515 way, uncertainties from the PDFs are taken into account, which is very reasonable, since the

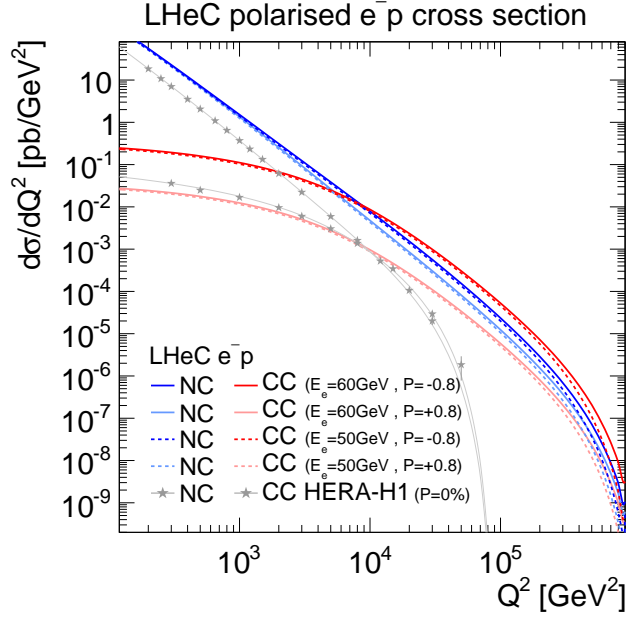


Figure 3.50: Single differential cross sections for polarised e^-p NC and CC DIS at LHeC for two different electron beam energies (E_e). Cross sections for longitudinal electron beam polarisations of $P_e = -0.8$ and $+0.8$ are displayed. For comparison also measurements at centre-of-mass energies of $\sqrt{s} = 920$ GeV by H1 at HERA for unpolarised ($P_e = 0\%$) electron beams are displayed [326].

2516 PDFs will predominantly be determined from those LHeC data in the future. The details of
 2517 the PDF fit are altogether fairly similar to the PDF fits outlined in Sec. 3.1. Noteworthy
 2518 differences are that additionally EW effects are included into the calculation by considering the
 2519 full set of 1-loop electroweak corrections [329], and the χ^2 quantity [101], which is input to the
 2520 minimisation and error propagation, is based on normal-distributed relative uncertainties. In
 2521 this way, a dependence on the actual size of the simulated cross sections is avoided. The size of
 2522 the pseudodata are therefore set equivalent to the predictions [330].

2523 3.3.3 Weak boson masses M_W and M_Z

The expected uncertainties for a determination of the weak boson masses, M_W and M_Z , are determined in the PDF+EW-fit, where one of the masses is determined together with the PDFs, while the other mass parameter is taken as external input. The expected uncertainties for M_W are

$$\begin{aligned} \Delta M_W(\text{LHeC-60}) &= \pm 5_{(\text{exp})} \pm 8_{(\text{PDF})} \text{ MeV} = 10_{(\text{tot})} \text{ MeV} \quad \text{and} \quad (3.39) \\ \Delta M_W(\text{LHeC-50}) &= \pm 8_{(\text{exp})} \pm 9_{(\text{PDF})} \text{ MeV} = 12_{(\text{tot})} \text{ MeV} \end{aligned}$$

for LHeC with $E_e = 60$ GeV or 50 GeV, respectively. The breakdown into experimental and PDF uncertainties is obtained by repeating the fit with PDF parameters fixed. These uncertainties are displayed in Fig. 3.51 and compared to the values obtained by LEP2 [332], Tevatron [331], ATLAS [333] and the PDG value [132]. The LHeC measurement will become the most precise measurement from one single experiment and will greatly improve over the best measurement achieved by H1, which was $M_W(\text{H1}) = 80.520 \pm 0.115$ GeV [316]. If the dominating uncorrelated

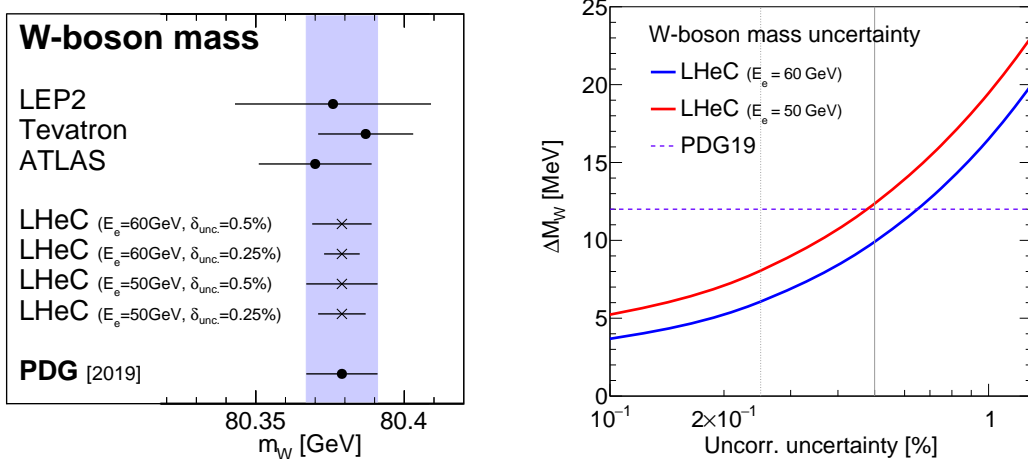


Figure 3.51: Left: Measurements of the W -boson mass assuming fixed values for the top-quark and Z -boson masses at the LHeC for different scenarios in comparison with today’s measurements [331–333] and the world average value (PDG19) [132]. For LHeC, prospects for $E_e = 60$ GeV and 50 GeV are displayed, as well as results for the two scenarios with 0.5 % or 0.25 % uncorrelated uncertainty (see text). Right: Comparison of the precision for M_W for different assumptions of the uncorrelated uncertainty of the pseudodata. The uncertainty of the world average value is displayed as horizontal line. The nominal (and alternative) size of the uncorrelated uncertainty of the inclusive NC/CC DIS pseudodata is indicated by the vertical line (see text).

uncertainties can be reduced from the prospected 0.5 % to 0.25 %¹¹, a precision for M_W of up to

$$\begin{aligned} \Delta M_W(\text{LHeC-60}) &= \pm 3_{(\text{exp})} \pm 5_{(\text{PDF})} \text{ MeV} = 6_{(\text{tot})} \text{ MeV} \quad \text{and} \\ \Delta M_W(\text{LHeC-50}) &= \pm 6_{(\text{exp})} \pm 6_{(\text{PDF})} \text{ MeV} = 8_{(\text{tot})} \text{ MeV} \end{aligned} \quad (3.40)$$

2524 for LHeC-60 and LHeC-50 may be achieved, respectively. A complete dependence of the expected
 2525 total experimental uncertainty ΔM_W on the size of the uncorrelated uncertainty component is
 2526 displayed in Fig. 3.51, and with a more optimistic scenario an uncertainty of up to $\Delta M_W \approx$
 2527 5 MeV can be achieved. In view of such a high accuracy, it will be important to study carefully
 2528 theoretical uncertainties. For instance the parametric uncertainty due to the dependence on
 2529 the top-quark mass of 0.5 GeV will yield an additional error of $\Delta M_W = 2.5$ MeV. Also higher-
 2530 order corrections, at least the dominating 2-loop corrections will have to be studied and kept
 2531 under control. Then, the prospected determination of the W -boson mass from LHeC data will
 2532 be among the most precise determinations and significantly improve the world average value
 2533 of M_W . It will also become competitive with its prediction from global EW fits with present
 2534 uncertainties of about $\Delta M_W = 7$ MeV [132, 334, 335].

2535 While the determination of M_W from LHeC data is competitive with other measurements, the
 2536 experimental uncertainties of a determination of M_Z are estimated to be about 11 MeV and
 2537 13 MeV for LHeC-60 and LHeC-50, respectively. Therefore, the precision of the determination
 2538 of M_Z at LHeC cannot compete with the precise measurements at the Z -pole by LEP+SLD and
 2539 future e^+e^- colliders may even improve on that.

¹¹Due to performance reasons, the pseudodata are generated for a rather coarse grid. With a binning which is closely related to the resolution of the LHeC detector, much finer grids in x and Q^2 are feasible. Already such a change would alter the uncertainties of the fit parameters. However, such an effect can be reflected by a changed uncorrelated uncertainty, and a value of 0.25 % appears like an optimistic, but achievable, alternative scenario.

2540 A simultaneous determination of M_W and M_Z is displayed in Fig. 3.52 (left). Although the
 2541 precision of these two mass parameters is only moderate, a meaningful test of the high-energy
 2542 behaviour of electroweak theory is obtained by using G_F as additional input: The high precision
 2543 of the G_F measurement [336] yields a very shallow error ellipse and a precise test of the SM
 2544 can be performed with only NC and CC DIS cross sections alone. Such a fit determines and
 2545 simultaneously tests the high-energy behaviour of electroweak theory, while using only low-
 2546 energy parameters α and G_F as input (plus values for masses like M_t and M_H needed for loop
 corrections).

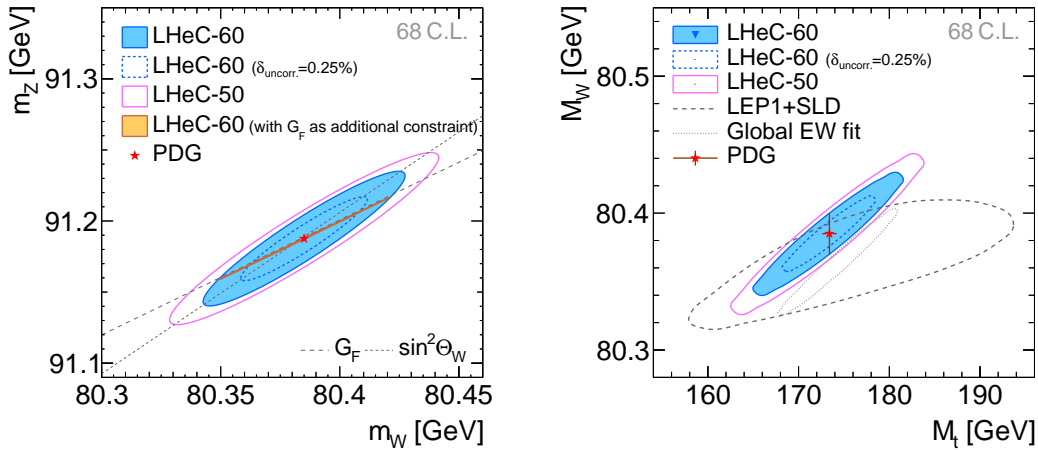


Figure 3.52: Simultaneous determination of the top-quark mass M_t and W -boson mass M_W from LHeC-60 or LHeC-50 data (left). Simultaneous determination of the W -boson and Z -boson masses from LHeC-60 or LHeC-50 data (right).

2547

2548 3.3.4 Further mass determinations

2549 Inclusive DIS data are sensitive to the top-quark mass M_t indirectly through radiative correc-
 2550 tions. M_t -dependent terms are dominantly due to corrections from the gauge boson self-energy
 2551 corrections. They are contained in the ρ and κ parameters and in the correction factor Δr .
 2552 The leading contributions are proportional to M_t^2 . This allows for an indirect determination
 2553 of the top-quark mass using LHeC inclusive DIS data, and a determination of M_t will yield an
 2554 uncertainty of $\Delta M_t = 1.8 \text{ GeV}$ to 2.2 GeV . Assuming an uncorrelated uncertainty of the DIS
 2555 data of 0.25% the uncertainty of M_t becomes as small as

$$\Delta M_t = 1.1 \text{ to } 1.4 \text{ GeV} \quad (3.41)$$

2556 for 60 and 50 GeV electron beams, respectively. This would represent a very precise indirect
 2557 determination of the top-quark mass from purely electroweak corrections and thus being fully
 2558 complementary to measurements based on real t -quark production, which often suffer from
 2559 sizeable QCD corrections. The precision achievable in this way will be competitive with indirect
 2560 determinations from global EW fits after the HL-LHC [337].

2561 More generally, and to some extent depending on the choice of the renormalisation scheme, the
 2562 leading self-energy corrections are proportional to $\frac{M_t^2}{M_W^2}$ and thus a simultaneous determination
 2563 of M_t and M_W is desirable. The prospects for a simultaneous determination of M_t and M_W
 2564 is displayed in Fig. 3.52 (right). It is remarkable that the precision of the LHeC is superior

2565 to that of the LEP+SLD combination [338]. In an optimistic scenario an uncertainty similar
 2566 to the global electroweak fit [335] can be achieved. In a fit without PDF parameters similar
 2567 uncertainties are found (not shown), which illustrates that the determination of EW parameters
 2568 is to a large extent independent of the QCD phenomenology and the PDFs.

2569 The subleading contributions to self-energy corrections have a Higgs-boson mass dependence
 2570 and are proportional to $\log \frac{M_H^2}{M_W^2}$. When fixing all other EW parameters the Higgs boson mass
 2571 could be constrained indirectly through these loop corrections with an experimental uncertainty
 2572 of $\Delta m_H = {}^{+29}_{-23}$ to ${}^{+24}_{-20}$ GeV for different LHeC scenarios, which is again similar to the indirect
 2573 constraints from a global electroweak fit [335], but not competitive with direct measurements.

2574 3.3.5 Weak Neutral Current Couplings

2575 The vector and axial-vector couplings of up-type and down-type quarks to the Z , g_V^q and g_A^q ,
 see Eq. (3.38), are determined in a fit of the four coupling parameters together with the PDFs.

Coupling parameter	PDG value	Expected uncertainties		
		LHeC-60	LHeC-60 ($\delta_{\text{uncor.}}=0.25\%$)	LHeC-50
g_A^u	0.50 ${}^{+0.04}_{-0.05}$	0.0022	0.0015	0.0035
g_A^d	-0.514 ${}^{+0.050}_{-0.029}$	0.0055	0.0034	0.0083
g_V^u	0.18 ± 0.05	0.0015	0.0010	0.0028
g_V^d	-0.35 ${}^{+0.05}_{-0.06}$	0.0046	0.0027	0.0067

Table 3.4: Light-quark weak NC couplings ($g_A^u, g_A^d, g_V^u, g_V^d$) and their currently most precise values from the PDG [132] compared with the prospected uncertainties for different LHeC scenarios. The LHeC prospects are obtained in a simultaneous fit of the PDF parameters and all four coupling parameters determined at a time.

2576

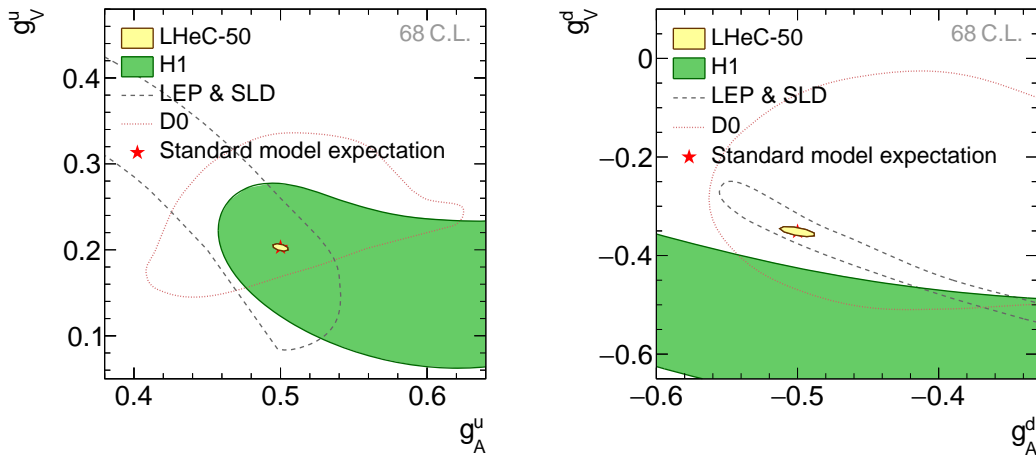


Figure 3.53: Weak NC vector and axial-vector couplings of u -type (left) and d -type quarks (right) at 68% confidence level (C.L.) for simulated LHeC data with $E_e = 50$ GeV. The LHeC expectation is compared with results from the combined LEP+SLD experiments [338], a single measurement from D0 [339] and one from H1 [316]. The standard model expectations are displayed by a red star, partially hidden by the LHeC prospects.

2577 The resulting uncertainties are collected in Tab. 3.4. The two-dimensional uncertainty contours

2578 at 68 % confidence level obtained from LHeC data with $E_e = 50$ GeV are displayed in Fig. 3.53
 2579 for the two quark families and compared with available measurements. While all the current
 2580 determinations from e^+e^- , ep or $p\bar{p}$ data have a similar precision, the future LHeC data will
 2581 greatly improve the precision of the weak neutral-current couplings and expected uncertainties
 2582 are an order of magnitude smaller than the currently most precise ones [132]. An increased
 2583 electron beam energy of $E_e = 60$ GeV or improved experimental uncertainties would further
 2584 improve this measurement.

2585 The determination of the couplings of the electron to the Z boson, g_V^e and g_A^e , can be determined
 2586 at the LHeC with uncertainties of up to $\Delta g_V^e = 0.0013$ and $\Delta g_A^e = \pm 0.0009$, which is similar
 2587 to the results of a single LEP experiment and about a factor three larger than the LEP+SLD
 2588 combination [338].

2589 3.3.6 The neutral-current ρ_{NC} and κ_{NC} parameters

2590 Beyond Born approximation, the weak couplings are subject to higher-order loop corrections.
 2591 These corrections are commonly parameterised by quantities called ρ_{NC} , κ_{NC} and ρ_{CC} . They are
 2592 sensitive to contributions beyond the SM and the structure of the Higgs sector. It is important
 2593 to keep in mind that these effective coupling parameters depend on the momentum transfer
 2594 and are, indeed, form factors rather than constants. It is particularly interesting to investigate
 2595 the so-called effective weak mixing angle defined as $\sin^2 \theta_W^{\text{eff}} = \kappa_{\text{NC}} \sin^2 \theta_W$. At the Z -pole it
 2596 is well accessible through asymmetry measurements in e^+e^- collisions. In DIS at the LHeC,
 2597 the scale dependence of the effective weak mixing angle is not negligible. It can be determined
 2598 only together with the ρ parameter due to the Q^2 dependence and the presence of the photon
 2599 exchange terms. Therefore, we introduce (multiplicative) anomalous contributions to these
 2600 factors, denoted as $\rho'_{\text{NC,CC}}$ and κ'_{NC} , and test their agreement with unity (for more details see
 2601 Ref. [316]), and uncertainties of these parameters are obtained in a fit together with the PDFs.
 The two-dimensional uncertainty contours of the anomalous form factors $\rho'_{\text{NC},f}$ and $\kappa'_{\text{NC},f}$ are

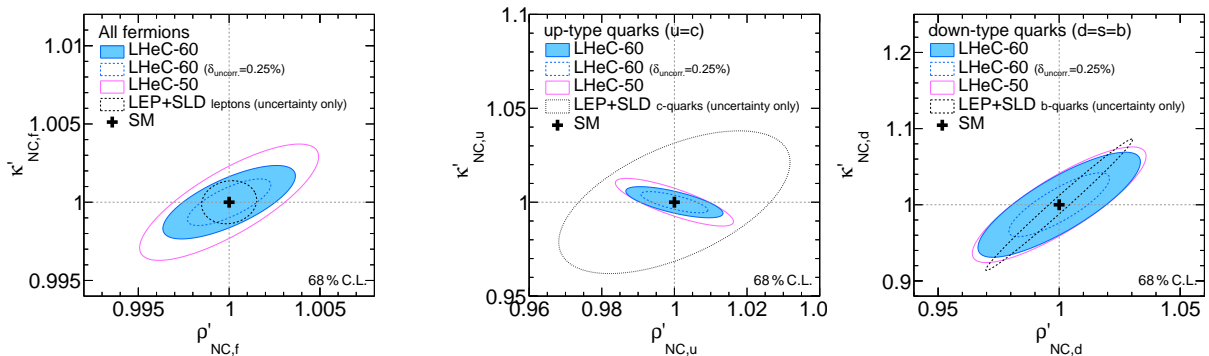


Figure 3.54: Expectations at 68 % confidence level for the determination of the ρ'_{NC} and κ'_{NC} parameters assuming a single anomalous factor equal for all fermions (left). The results for three different LHeC scenarios are compared with the achieved uncertainties from the LEP+SLD combination [338] for the determination the respective leptonic quantities. Right: uncertainties for the simultaneous determination of the anomalous form factors for u and d -type quarks, assuming known values for the electron parameters. The values are compared with uncertainties reported by LEP+SLD for the determination of the values $\rho_{\text{NC},(c,b)}$ and $\sin^2 \theta_W^{\text{eff.}(c,b)}$ for charm or bottom quarks, respectively.

2602
 2603

displayed for three different LHeC scenarios in Fig. 3.54 (left), and compared with uncertainties

2604 from the LEP+SLD combination ¹² [338]. It is found that these parameters can be determined
 2605 with very high experimental precision.

2606 Assuming the couplings of the electron are given by the SM, the anomalous form factors for
 2607 the two quark families can be determined and results are displayed in Fig. 3.54 (right). Since
 2608 these measurements represent unique determinations of parameters sensitive to the light-quark
 2609 couplings, we can compare only with nowadays measurements of the parameters for heavy-quarks
 2610 of the same charge and it is found that the LHeC will provide high-precision determinations of
 2611 the ρ'_{NC} and κ'_{NC} parameters.

2612 A meaningful test of the SM can be performed by determining the effective coupling parameters
 2613 as a function of the momentum transfer. In case of κ'_{NC} , this is equivalent to measuring the
 2614 running of the effective weak mixing angle, $\sin\theta_{\text{W}}^{\text{eff}}(\mu)$ (see also Sec. 3.3.7). However, DIS is quite
 2615 complementary to other measurements since the process is mediated by space-like momentum
 2616 transfer, i.e. $q^2 = -Q^2 < 0$ with q being the boson four-momentum. Prospects for a determi-
 2617 nation of ρ'_{NC} or κ'_{NC} at different Q^2 values are displayed in Fig. 3.55 and compared to results
 obtained by H1. The value of $\kappa'_{\text{NC}}(\mu)$ can be easily translated to a measurement of $\sin\theta_{\text{W}}^{\text{eff}}(\mu)$.

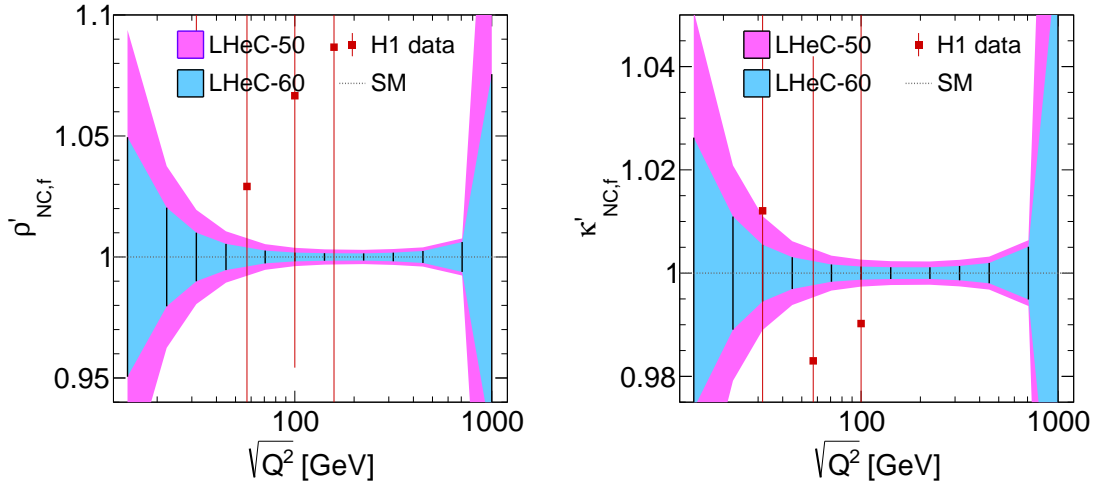


Figure 3.55: Test of the scale dependence of the anomalous ρ and κ parameters for two different LHeC scenarios. For the case of LHeC-60, i.e. $E_e = 60$ GeV, we assume an uncorrelated uncertainty of 0.25%. The uncertainties of the parameter $\kappa'_{\text{NC},f}$ can be interpreted as sensitivity to the scale-dependence of the weak mixing angle, $\sin\theta_{\text{W}}^{\text{eff}}(\mu)$.

2618 From Fig. 3.55 one can conclude that this quantity can be determined with a precision of up to
 2619 0.1% and better than 1% over a wide kinematic range of about $25 < \sqrt{Q^2} < 700$ GeV.
 2620

2621 3.3.7 The effective weak mixing angle $\sin^2\theta_{\text{W}}^{\text{eff},\ell}$

2622 The leptonic effective weak mixing angle is defined as $\sin^2\theta_{\text{W}}^{\text{eff},\ell}(\mu^2) = \kappa_{\text{NC},\ell}(\mu^2)\sin^2\theta_{\text{W}}$. Due to
 2623 its high sensitivity to loop corrections it represents an ideal quantity for precision tests of the
 2624 Standard Model. Its value is scheme dependent and it exhibits a scale dependence. Near the

¹²Since in the LEP+SLD analysis the values of ρ_{NC} and $\kappa_{\text{NC}}\sin^2\theta_{\text{W}}$ are determined, we compare only the size of the uncertainties in these figures. Furthermore it shall be noted, that LEP is mainly sensitive to the parameters of leptons or heavy quarks, while LHeC data is more sensitive to light quarks (u, d, s), and thus the LHeC measurements are highly complementary.

2625 Z pole, $\mu^2 = M_Z^2$, its value was precisely measured at LEP and at SLD. Those analyses were
2626 based on the measurement of asymmetries and their interpretation in terms of the leptonic weak
2627 mixing angle was simplified by the fact that many non-leptonic corrections and contributions
2628 from box graphs cancel or can be taken into account by subtracting their SM predictions. The
2629 highest sensitivity to $\sin^2 \theta_W^{\text{eff},\ell}(M_Z)$ to date arises from a measurement of $A_{\text{fb}}^{0,b}$ [338], where
2630 the non-universal flavour-specific corrections to the quark couplings are taken from the SM
2631 and consequently these measurements are interpreted to be sensitive only to the universal, i.e.
2632 flavour-independent¹³, non-SM contributions to κ_{NC} . Applying this assumption also to the DIS
2633 cross sections, the determination of $\kappa'_{\text{NC},f}$ can directly be interpreted as a sensitivity study of
2634 the leptonic effective weak mixing angle $\sin^2 \theta_W^{\text{eff},\ell}$.

Fit parameters	Parameter of interest	SM value	Expected uncertainties			
			LHeC-50 ($\delta_{\text{uncor.}} = 0.50\%$)	LHeC-60	LHeC-50 ($\delta_{\text{uncor.}} = 0.25\%$)	LHeC-60
$\kappa'_{\text{NC},f}$, PDFs	$\sin^2 \theta_W^{\text{eff},\ell}(M_Z^2)$	0.23154	0.00033	0.00025	0.00022	0.00015
$\kappa'_{\text{NC},f}, \rho'_{\text{NC},f}$, PDFs	$\sin^2 \theta_W^{\text{eff},\ell}(M_Z^2)$	0.23154	0.00071	0.00036	0.00056	0.00023
$\kappa'_{\text{NC},e}$, PDFs	$\sin^2 \theta_W^{\text{eff},e}(M_Z^2)$	0.23154	0.00059	0.00047	0.00038	0.00028
$\kappa'_{\text{NC},e}, \kappa'_{\text{NC},u}, \kappa'_{\text{NC},d}$, PDFs	$\sin^2 \theta_W^{\text{eff},e}(M_Z^2)$	0.23154	0.00111	0.00095	0.00069	0.00056
$\kappa'_{\text{NC},f}$	$\sin^2 \theta_W^{\text{eff},\ell}(M_Z^2)$	0.23154	0.00028	0.00023	0.00017	0.00014

Table 3.5: Determination of $\sin^2 \theta_W^{\text{eff},\ell}(M_Z^2)$ with inclusive DIS data at the LHeC for different scenarios. Since the value of the effective weak mixing angle at the Z pole cannot be determined directly in DIS, a fit of the $\kappa'_{\text{NC},f}$ parameter is performed instead and its uncertainty is translated to $\sin^2 \theta_W^{\text{eff},\ell}(M_Z^2)$. Different assumptions on the fit parameters are studied, and results include uncertainties from the PDFs. Only the last line shows results where the PDF parameters are kept fixed. See text for more details.

2635 The prospects for a determination of $\sin^2 \theta_W^{\text{eff},\ell}$ are listed in Tab. 3.5. Two fits have been studied:
2636 one with a fixed parameter ρ'_{NC} and one where $\sin^2 \theta_W^{\text{eff},\ell}$ is determined together with ρ'_{NC} (see
2637 Fig. 3.54 (left)). At the LHeC, it will be possible to determine the value of $\sin^2 \theta_W^{\text{eff},\ell}(M_Z^2)$ with
2638 an experimental uncertainty of up to

$$\Delta \sin^2 \theta_W^{\text{eff},\ell} = \pm 0.00015, \quad (3.42)$$

2639 where PDF uncertainties are already included. If the PDF parameters are artificially kept
2640 fixed, the uncertainties are of very similar size, which demonstrates that these measurements
2641 are fairly insensitive to the QCD effects and the PDFs. The uncertainties are compared¹⁴ to
2642 recent average values in Fig. 3.56. One can see that the LHeC measurement has the potential to
2643 become the most precise single measurement in the future with a significant impact to the world
2644 average value. It is obvious that a conclusive interpretation of experimental results with such a
2645 high precision will require correspondingly precise theoretical predictions, and the investigation
2646 of two-loop corrections for DIS will become important.

2647 This LHeC measurement will become competitive with measurements at the HL-LHC [136].
2648 Since in pp collisions one of the dominant uncertainty is from the PDFs, future improvements

¹³Flavour-specific tests have been discussed to some extent in the previous Section.

¹⁴It shall be noted, that in order to compare the LHeC measurements with the Z -pole measurements at $\mu^2 = M_Z^2$ in a conclusive way, one has to assume the validity of the SM framework. In particular the scale-dependence of $\kappa_{\text{NC},\ell}$ must be known in addition to the flavour-specific corrections. On the other hand, the scale dependence can be tested itself with the LHeC data which cover a large range of space-like Q^2 . In this aspect, DIS provides a unique opportunity for precision measurements in the space-like regime ($\mu^2 < 0$) as has been discussed in the previous Section, see Fig. 3.55 (right).

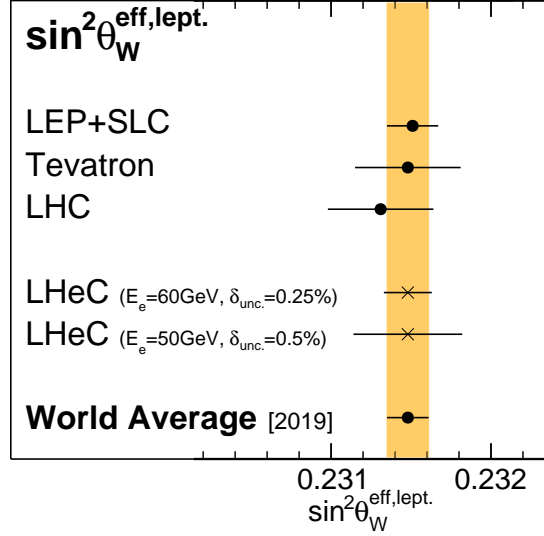


Figure 3.56: Comparison of the determination of $\sin^2 \theta_W^{\text{eff},\ell}(M_Z^2)$ from LHeC inclusive DIS data with recent averaged values. Results from LEP+SLC [338], Tevatron [340], LHC [341–344] and the world average value [344] are all obtained from a combination of various separate measurements (not shown individually) (see also Ref. [345] for additional discussions). For LHeC, the experimental and PDF uncertainties are displayed.

2649 can (only) be achieved with a common analysis of LHeC and HL-LHC data. Such a study will
 2650 yield highest experimental precision and the challenging theoretical and experimental aspects for
 2651 a complete understanding of such an analysis will deepen our understanding of the electroweak
 2652 sector.

2653 It may be further of interest, to determine the value of the effective weak mixing angle of the
 2654 electron separately in order to compare with measurements in pp and test furthermore lepton-
 2655 specific contributions to $\kappa_{\text{NC},\text{lept.}}$. Such fits are summarised in Table 3.5 and a reasonable
 2656 precision is achieved with LHeC.

2657 3.3.8 Electroweak effects in charged-current scattering

2658 The charged-current sector of the SM can be uniquely measured at high scales over many orders
 2659 of magnitude in Q^2 at the LHeC, due to the excellent tracking detectors, calorimetry, and high-
 2660 bandwidth triggers. Similarly as in the NC case, the form factors of the effective couplings of
 2661 the fermions to the W boson can be measured. In the SM formalism, only two of these form
 2662 factors are present, $\rho_{CC,eq}$ and $\rho_{CC,e\bar{q}}$. We thus introduce two anomalous modifications to them,
 2663 $\rho_{CC,(eq/e\bar{q})} \rightarrow \rho'_{CC,(eq/e\bar{q})}\rho_{CC,(eq/e\bar{q})}$ (see Ref. [316]). The prospects for the determination of these
 2664 parameters are displayed in Fig. 3.57, and it is found, that with the LHeC these parameters
 2665 can be determined with a precision up to 0.2–0.3%. Also their Q^2 dependence can be uniquely
 2666 studied with high precision up to $\sqrt{Q^2}$ values of about 400 GeV.

2667 3.3.9 Direct W and Z production and Anomalous Triple Gauge Couplings

2668 The direct production of single W and Z bosons as a crucial signal represents an important
 2669 channel for EW precision measurements. The production of W bosons has been measured at

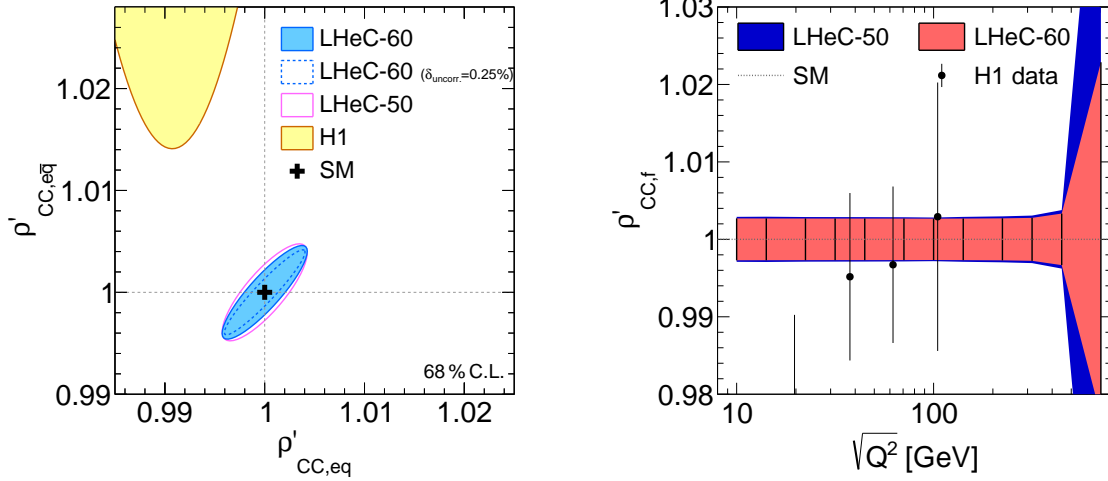


Figure 3.57: Left: anomalous modifications of the charged current form factors $\rho'_{CC,eq}$ and $\rho'_{CC,e\bar{q}}$ for different LHeC scenarios in comparison with the H1 measurement [316]. Right: scale dependent measurement of the anomalous modification of the charged current form factor $\rho'_{CC}(Q^2)$, assuming $\rho'_{CC,eq} = \rho'_{CC,e\bar{q}} = \rho'_{CC}$.

2670 $\sqrt{s} \simeq 320$ GeV at HERA [346–348]. With the full $e^\pm p$ data set collected by the H1 and ZEUS
 2671 experiments together, corresponding to an integrated luminosity of about $\mathcal{L} \sim 1 \text{ fb}^{-1}$, a few
 2672 dozens of W boson event candidates have been identified in the e , μ or τ decay channel.

2673 Detailed studies of direct W/Z production in ep collisions at higher centre-of-mass energies have
 2674 been presented in the past, see Refs. [349–351]. These theoretical studies were performed for
 2675 a proton beam energy of $E_p = 8$ TeV and electron beam energies of $E_e = 55$ GeV or 100 GeV,
 2676 which correspond to a very similar centre-of-mass energy as the LHeC. Measurements at the
 2677 LHeC will benefit considerably from the large integrated luminosity, in comparison to earlier
 2678 projections.

2679 The W or Z direct production in e^-p collisions can be classified into five processes

$$\begin{aligned} e^-p &\rightarrow e^-W^+j, & e^-p &\rightarrow e^-W^-j, \\ e^-p &\rightarrow \nu_e^-W^-j, & e^-p &\rightarrow \nu_e^-Zj \end{aligned} \quad (3.43)$$

2680 and

$$e^-p \rightarrow e^-Zj, \quad (3.44)$$

2681 where j denotes the hadronic the final state (i.e. the *forward jet*). According to the above
 2682 classification, the four processes in Eq.(3.43) can be used to study Tripe Gauge Couplings
 2683 (TGCs), e.g. $WW\gamma$ and WWZ couplings, since some contributing diagrams represent Vector
 2684 Boson Fusion (VBF) processes. The process shown in Eq.(3.44) does not contain any TGC
 2685 vertex. The processes for positron-proton collisions can be easily derived from Eqs. (3.43)
 2686 and (3.44), but are not discussed further here due to the small integrated luminosity of the
 2687 LHeC e^+p data.

2688 The MadGraph5_v2.4.2 program [352] is employed for matrix element calculation and event gener-
 2689 eration and the PDF NNPDF23_nlo_as_0119_qed [353] is used. Technical cuts on the transverse
 2690 momentum of the outgoing scattered lepton, p_T^ℓ , of 10 GeV or alternatively 5 GeV, are imposed

Process	$E_e = 50 \text{ GeV}, E_p = 7 \text{ TeV}$ $p_T^e > 10 \text{ GeV}$	$E_e = 60 \text{ GeV}, E_p = 7 \text{ TeV}$ $p_T^e > 10 \text{ GeV}$	$E_e = 60 \text{ GeV}, E_p = 7 \text{ TeV}$ $p_T^e > 5 \text{ GeV}$
$e^- W^+ j$	1.00 pb	1.18 pb	1.60 pb
$e^- W^- j$	0.930 pb	1.11 pb	1.41 pb
$\nu_e^- W^- j$	0.796 pb	0.956 pb	0.956 pb
$\nu_e^- Z j$	0.412 pb	0.502 pb	0.502 pb
$e^- Z j$	0.177 pb	0.204 pb	0.242 pb

Table 3.6: The SM predictions of direct W and Z production cross sections in $e^- p$ collisions for different collider beam energy options, E_e , and final state forward electron transverse momentum cut, p_T^e . Two different electron beam energy options are considered, $E_e = 50 \text{ GeV}$ and 60 GeV .

2691 and other basic cuts are $p_T^j > 20 \text{ GeV}$, $|\eta_{e,j}| < 5$ and $\Delta R_{ej} < 0.4$. The resulting Standard Model
2692 total cross sections of the above processes are listed in Tab. 3.6.

2693 The process with the largest production cross section in $e^- p$ scattering is the single W^+ boson
2694 production. This will be the optimal channel of both the SM measurement and new physics
2695 probes in the EW sector. Also, this channel is experimentally preferred since the W^+ is produced
2696 in NC scattering, so the beam electron is measured in the detector, and the W -boson has opposite
2697 charge to the beam lepton and thus in a leptonic decay an opposite charge lepton and missing
2698 transverse momentum is observed. Altogether, it is expected that a few million of direct W -
2699 boson events are measured at LHeC.

2700 Several 10^5 direct Z events are measured, which corresponds approximately to the size of the
2701 event sample of the SLD experiment [338], but at the LHeC these Z bosons are predominantly
2702 produced in VBF events.

2703 All these total cross sections increase significantly with smaller transverse momentum of the
2704 outgoing scattered lepton. Therefore it will become important to decrease that threshold with
2705 dedicated electron taggers, see Chapter 10.

2706 The measurement of gauge boson production processes provides a precise measurement of the
2707 triple gauge boson vertex. The measurement is sensitive to new physics contributions in *anoma-*
2708 *lous* Tripe Gauge Couplings (aTGC). The LHeC has advantages of a higher centre-of-mass
2709 energy and easier kinematic analysis in the measurement of aTGCs.

2710 In the effective field theory language, aTGCs in the Lagrangian are generally parameterised as

$$\begin{aligned}
\mathcal{L}_{TGC}/g_{WWV} &= ig_{1,V}(W_{\mu\nu}^+ W_\mu^- V_\nu - W_{\mu\nu}^- W_\mu^+ V_\nu) + i\kappa_V W_\mu^+ W_\nu^- V_{\mu\nu} + \frac{i\lambda_V}{M_W^2} W_{\mu\nu}^+ W_{\nu\rho}^- V_{\rho\mu} \\
&+ g_5^V \epsilon_{\mu\nu\rho\sigma} (W_\mu^+ \overleftrightarrow{\partial}_\rho W_\nu^-) V_\sigma - g_4^V W_\mu^+ W_\nu^- (\partial_\mu V_\nu + \partial_\nu V_\mu) \\
&+ i\tilde{\kappa}_V W_\mu^+ W_\nu^- \tilde{V}_{\mu\nu} + \frac{i\tilde{\lambda}_V}{M_W^2} W_{\lambda\mu}^+ W_{\mu\nu}^- \tilde{V}_{\nu\lambda}, \tag{3.45}
\end{aligned}$$

2711 where $V = \gamma, Z$. The gauge couplings $g_{WW\gamma} = -e$, $g_{WWZ} = -e \cot \theta_W$ and the weak mixing
2712 angle θ_W are from the SM. $\tilde{V}_{\mu\nu}$ and $A \overleftrightarrow{\partial}_\mu B$ are defined as $\tilde{V}_{\mu\nu} = \frac{1}{2} \epsilon_{\mu\nu\rho\sigma} V_{\rho\sigma}$, $A \overleftrightarrow{\partial}_\mu B = A(\partial_\mu B) -$
2713 $(\partial_\mu A)B$, respectively. There are five aTGCs ($g_{1,Z}$, κ_V , and λ_V) conserving the C and CP
2714 condition with electromagnetic gauge symmetry requires $g_{1,\gamma} = 1$. Only three of them are
2715 independent because $\lambda_Z = \lambda_\gamma$ and $\Delta\kappa_Z = \Delta g_{1,Z} - \tan^2 \theta_W \Delta\kappa_\gamma$ [354–356]. The LHeC can set
2716 future constrains on $\Delta\kappa_\gamma$ and λ_γ .

2717 In the direct Z/γ production process, the anomalous WWZ and $WW\gamma$ couplings can be sep-
2718 arately measured without being influenced by their interference [357, 358]. In the direct W

2719 production process, both the deviation in signal cross section and the kinematic distributions
 2720 can effectively constrain the $WW\gamma$ aTGC, while anomalous WWZ contribution in this channel
 2721 is insensitive as a result of the suppression from Z boson mass [359–361].

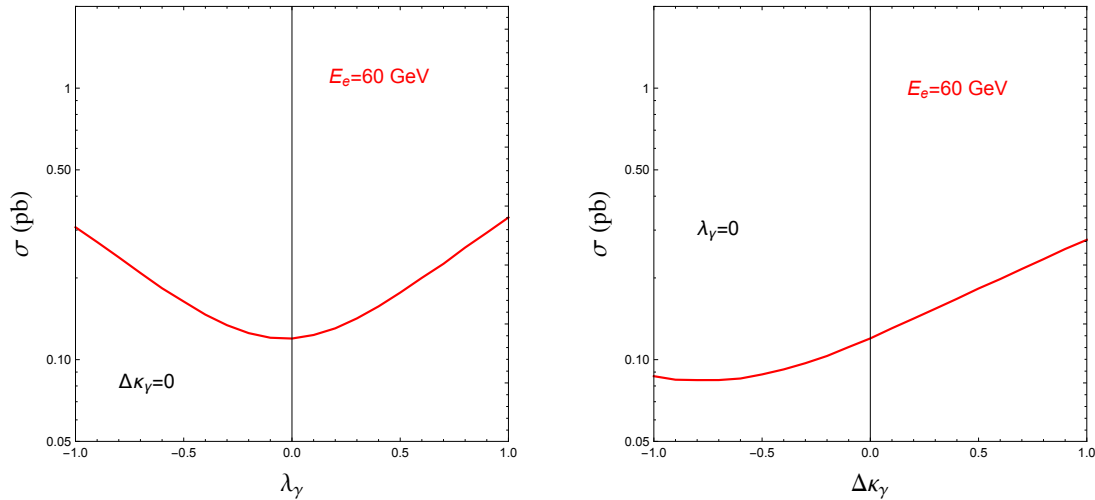


Figure 3.58: Total cross sections of the $e^-p \rightarrow e^-\mu^+\nu_\mu j$ process with varying λ_γ (left plot) and $\Delta\kappa_\gamma$ (right plot).

2722 The W decay into muon channel is the expected optimal measurement for the anomalous $WW\gamma$
 2723 coupling because of the discrimination of final states and mistagging efficiencies [359]. Fig. 3.58
 2724 shows the cross section of single W^+ production process followed by $W^+ \rightarrow \mu^+\nu_\mu$ decay, with
 2725 different λ_γ and $\Delta\kappa_\gamma$ values. Large anomalous coupling leads to measurable deviation to the
 2726 SM prediction. The cross section increases monotonically with $\Delta\kappa_\gamma$ and the absolute value of
 2727 λ_γ within the region of $-1.0 \leq \lambda_\gamma/\Delta\kappa_\gamma \leq 1.0$.

2728 Kinematic analysis is necessary for the precise aTGC measurement. At LHeC, the $e^-p \rightarrow$
 2729 $e^-W^\pm j$ process with leptonic W boson decay can be fully reconstructed because the unde-
 2730 tected neutrino information is reconstructed either with energy-momentum conservation or the
 2731 recoil mass method. This allows to use angular correlation observables, which are sensitive to
 2732 the W boson polarization. Helicity amplitude calculation indicates that a non-SM value of λ_γ
 2733 leads to a significant enhancement in the transverse polarization fraction of the W boson in the
 2734 $e^-p \rightarrow e^-W^+j$ process, while a non-SM value of $\Delta\kappa_\gamma$ leads to enhancement in the longitudinal
 2735 component fraction [349]. The angle $\theta_{\ell W}$ is defined as the angle between the decay product
 2736 lepton ℓ in the W rest frame and W moving direction in the collision rest frame. Making use
 2737 of the energetic final states in the forward direction, a second useful angle $\Delta\phi_{ej}$ is defined as
 2738 the separation of final state jet and electron on the azimuthal plane. In an optimised analysis,
 2739 assuming an integrated luminosity of 1 ab^{-1} , the observable $\Delta\phi_{ej}$ can impose stringent con-
 2740 straints on both λ_γ and $\Delta\kappa_\gamma$, and uncertainties within $[-0.007, 0.0056]$ and $[-0.0043, 0.0054]$
 2741 are achieved, respectively. The $\cos\theta_{\mu W}$ observable is also sensitive to $\Delta\kappa_\gamma$ at the same order,
 2742 but fails to constrain λ_γ . The analysis is described in detail in Ref. [359].

2743 Fig. 3.59 shows the two-parameter aTGC constraint on the λ_γ - $\Delta\kappa_\gamma$ plane based on a χ^2 analysis
 2744 of $\Delta\phi_{ej}$ at parton-level and assuming an electron beam energy of $E_e = 60$ GeV. When comparing
 2745 with the current LHC (blue and green) and LEP (red) bounds, the LHeC has the potential
 2746 to significantly improve the constraints, in particular on the $\Delta\kappa_\gamma$ parameter. The polarised
 2747 electron beam is found to improve the aTGC measurement [358, 361]. In consideration of the
 2748 realistic analysis at detector level, one expects $2\text{-}3 \text{ ab}^{-1}$ integrated luminosity to achieve same
 2749 results [359].

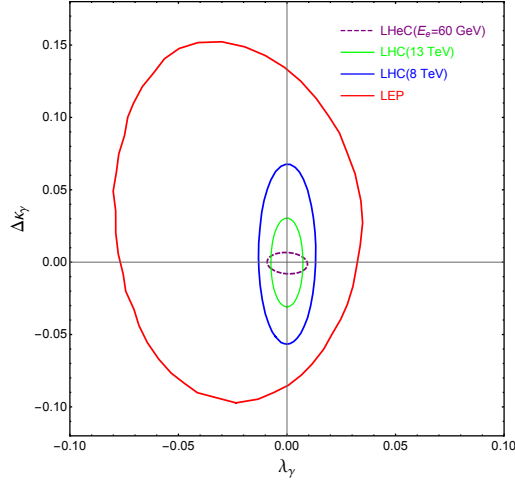


Figure 3.59: The 95% C.L. exclusion limit on the $\Delta\kappa_\gamma$ - λ_γ plane. The purple dashed contour is the projected LHeC exclusion limit with 1 ab^{-1} integrated luminosity [359]. The blue, green and red contours are current bounds from LHC [362, 363] and LEP [364].

2750 One uncertainty in the aTGC measurement at the (HL-)LHC comes from the PDF uncertainty.
 2751 Future LHeC PDF measurement will improve the precision of aTGC measurement in the $x \simeq$
 2752 $\mathcal{O}(10^{-2})$ region.

2753 3.3.10 Radiation Amplitude Zero

2754 The LHeC is ideal for testing a novel feature of the Standard Model: the *radiation amplitude*
 2755 *zero* [365–368] of the amplitude $\gamma W^- \rightarrow c\bar{b}$ and related amplitudes, see Fig. 3.60. The Born
 2756 amplitude is predicted to vanish and change sign at $\cos\theta_{CM} = \frac{e_{\bar{b}}}{e_W} = -1/3$. This LHeC mea-
 2757 surement tests W compositeness and its zero anomalous magnetic moment at leading order:
 2758 $g_W = 2, \kappa_W = 1$, as well as $g_q = 2$ for quarks.. One can also test the radiation amplitude zero
 for the top quark from $\gamma b \rightarrow W^- t$.

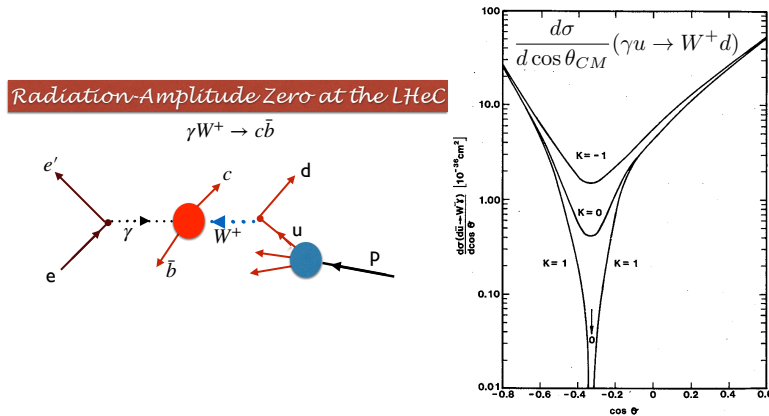


Figure 3.60: The radiation amplitude zero of the Standard Model in $\gamma W^+ \rightarrow c\bar{b}$ and $\gamma u \rightarrow W^+ d$. The prediction for the angular distribution $\frac{d\sigma}{d\cos(\theta_{CM})}(\gamma u \rightarrow W^+ d)$ is from Ref. [368].

2759

2760 **3.3.11 Conclusion**

2761 With LHeC inclusive NC and CC DIS data, unique measurements of electroweak parameters can
 2762 be performed with highest precision. Since inclusive DIS is mediated through space-like momen-
 2763 tum transfer (t -channel exchange) the results are often complementary to other experiments,
 2764 such as pp or e^+e^- collider experiments, where measurements are performed in the time-like
 2765 regime and most often at the Z peak. Among many other quantities, measurements of the weak
 2766 couplings of the light quarks, u and d , or their anomalous form factors $\rho'_{\text{NC},u/d}$ and $\kappa'_{\text{NC},u/d}$,
 2767 can be performed uniquely due to the important contributions of valence quarks in the initial
 2768 state. Also scale dependent measurements of weak interactions can be performed over a large
 2769 range in $\sqrt{Q^2}$, which provides an interesting portal to BSM physics. The W boson mass can be
 2770 determined with very small experimental uncertainties, such that theoretical uncertainties are
 2771 expected to become more important than experimental uncertainties. While the parameters of
 2772 the PDFs are determined together with the EW parameters in the present study, it is found
 2773 that the PDFs do not induce a limitation of the uncertainties. Considering the dominating
 2774 top-quark mass dependence of higher-order electroweak effects, one can realise that the LHeC
 2775 will be competitive with the global electroweak fit after the HL-LHC era [136, 337].

2776 Besides proving its own remarkable prospect on high-precision electroweak physics, the LHeC
 2777 will further significantly improve the electroweak measurements in pp collisions at the LHC by
 2778 reducing the presently sizeable influence of PDF and α_s uncertainties. This is discussed in Sec. 7.

2779 **3.4 Top Quark Physics**

2780 SM top quark production at a future ep collider is dominated by single top quark production,
 2781 mainly via CC DIS production. An example graph is shown in Fig. 3.61 (left). The total cross
 2782 section is 1.89 pb at the LHeC [369] and with an electron beam energy of 60 GeV, and an LHC
 2783 proton beam of 7 TeV, leading to a centre-of-mass energy of 1.3 TeV, respectively. The other
 2784 important top quark production mode is $t\bar{t}$ photoproduction with a total cross section of 0.05 pb
 2785 at the LHeC [370]. An example graph is shown in Fig. 3.61 (right). This makes a future LHeC a
 2786 top quark factory and an ideal tool to study top quarks with a high precision, and to analyse in
 2787 particular their electroweak interaction. Selected highlights in top quark physics are summarised
 2788 here.

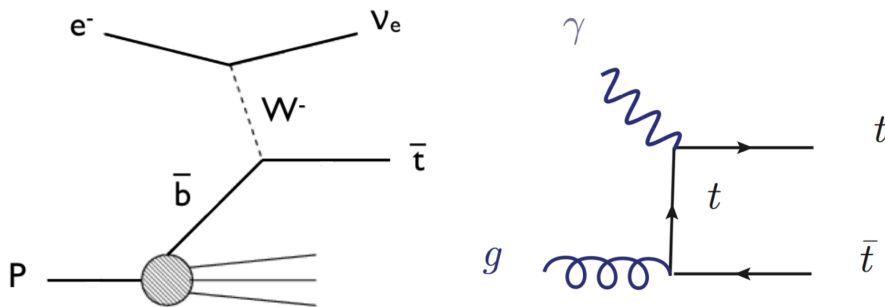


Figure 3.61: Example graphs for CC DIS top quark production (left) and top quark photoproduction (right).

2789 **3.4.1 Wtq Couplings**

2790 One flagship measurement is the direct measurement of the CKM matrix element $|V_{tb}|$, i.e.
 2791 without making any model assumptions such as on the unitarity of the CKM matrix or the
 2792 number of quark generations. An elaborate analysis of the single top quark CC DIS process
 2793 at the LHeC including a detailed detector simulation using the DELPHES package [371] shows
 2794 that already at 100fb^{-1} of integrated luminosity an uncertainty of 1% can be expected. This
 2795 compares to a total uncertainty of 4.1% of the currently most accurate result at the LHC Run-I
 2796 performed by the CMS experiment [372].

2797 The same analysis [369] can also be used to search for anomalous left- and right-handed Wtb
 2798 vector (f_1^L, f_1^R) and tensor (f_2^L, f_2^R) couplings analyzing the following effective Lagrangian:

$$L = -\frac{g}{\sqrt{2}}\bar{b}\gamma^\mu V_{tb}(f_1^L P_L - f_1^R P_R)tW_\mu^- - \frac{g}{\sqrt{2}}\bar{b}\frac{i\sigma^{\mu\nu}q_\nu}{M_W}(f_2^L P_L - f_2^R P_R)tW_\mu^- + h.c. \quad (3.46)$$

2799 In the SM $f_1^L = 1$ and $f_1^R = f_2^L = f_2^R = 0$. The effect of anomalous Wtb couplings is consistently
 2800 evaluated in the production and the decay of the antitop quark, cf. Fig. 3.61 (left). Using
 2801 hadronic top quark decays only, the expected accuracies in a measurement of these couplings
 2802 as a function of the integrated luminosity are presented in Fig. 3.62 (upper left), derived from
 2803 expected 95% C.L. limits on the cross section yields. The couplings can be measured with
 2804 accuracies of 1% for the SM f_1^L coupling determining $|V_{tb}|$ (as discussed above) and of 4% for
 2805 f_2^L , 9% for f_2^R , and 14% for f_1^R at 1ab^{-1} .

2806 Similarly, the CKM matrix elements $|V_{tx}|$ ($x = d, s$) can be extracted using a parameterisation of
 2807 deviations from their SM values with very high precision through W boson and bottom (light)
 2808 quark associated production channels, where the W boson and b -jet (light jet $j = d, s$) final
 2809 states can be produced via s-channel single top quark decay or t-channel top quark exchange as
 2810 outlined in [373]. As an example, analysing the processes

2811 Signal 1: $pe^- \rightarrow \nu_e \bar{t} \rightarrow \nu_e W^- \bar{b} \rightarrow \nu_e \ell^- \nu_\ell \bar{b}$

2812 Signal 2: $pe^- \rightarrow \nu_e W^- b \rightarrow \nu_e \ell^- \nu_\ell b$

2813 Signal 3: $pe^- \rightarrow \nu_e \bar{t} \rightarrow \nu_e W^- j \rightarrow \nu_e \ell^- \nu_\ell j$

2814 in an elaborate analysis including a detailed detector simulation using the DELPHES pack-
 2815 age [371], the expected accuracies on $|V_{td}|$ and $|V_{ts}|$ at the 2σ confidence level (C.L.) are shown
 2816 as a function of the integrated luminosity in Fig. 3.62 (upper right, middle left). At 1ab^{-1} of
 2817 integrated luminosity and an electron polarization of 80%, the 2σ limits improve on existing
 2818 limits from the LHC [374] (interpreted by [375]) by a factor of ≈ 3.5 . Analyzing Signal 3 alone,
 2819 and even more when combining Signals 1, 2 and 3, will allow for the first time to achieve an ac-
 2820 curacy of the order of the actual SM value of $|V_{ts}^{\text{SM}}| = 0.04108_{-0.0057}^{+0.0030}$ as derived from an indirect
 2821 global CKM matrix fit [376], and will therefore represent a direct high precision measurement
 2822 of this important top quark property. In these studies, upper limits at the 2σ level down to
 2823 $|V_{ts}| < 0.06$, and $|V_{td}| < 0.06$ can be achieved.

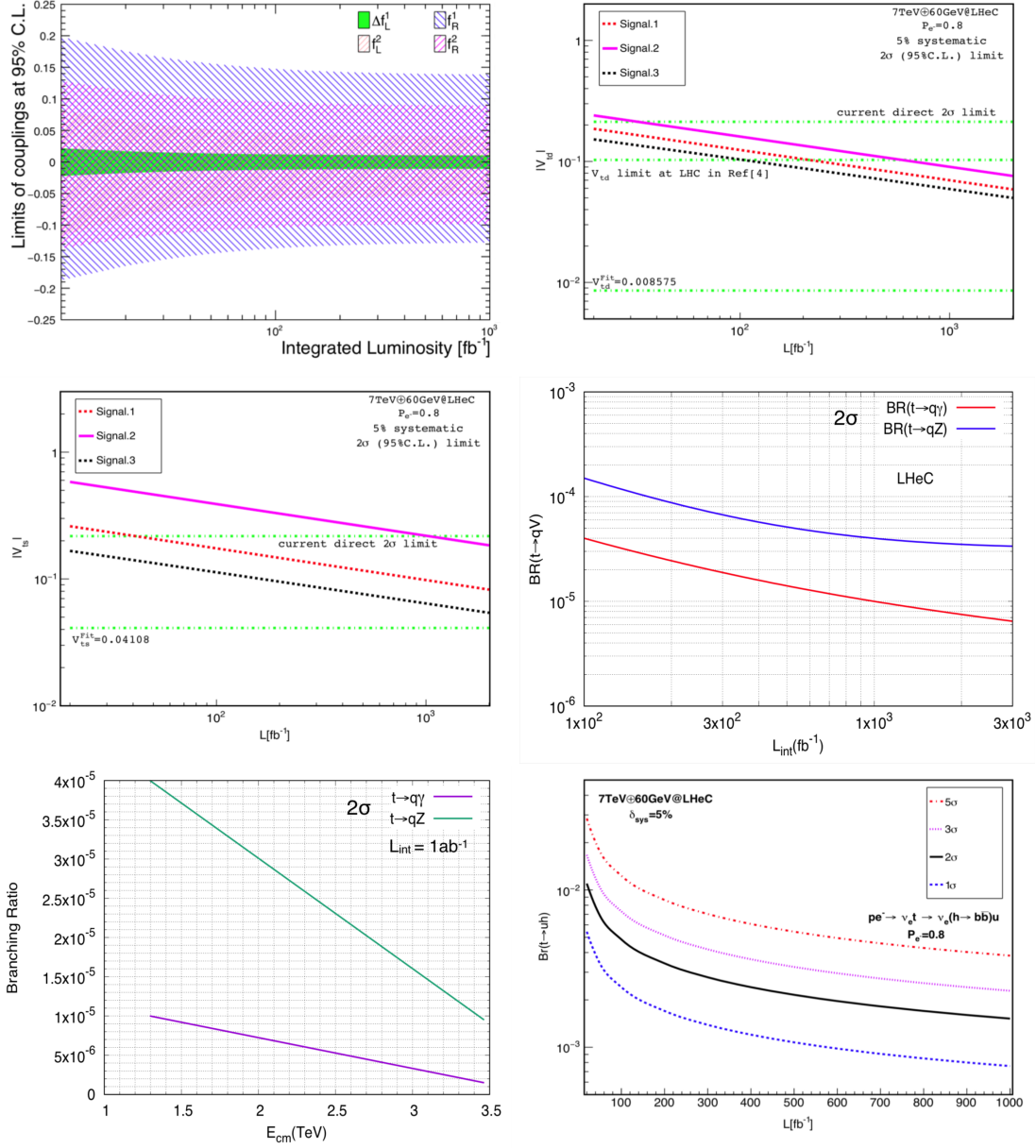


Figure 3.62: Expected sensitivities as a function of the integrated luminosity on the SM and anomalous Wtb couplings [369] (upper left), on $|V_{td}|$ (upper right) and $|V_{ts}|$ (middle left) [373], on FCNC $t \rightarrow qV$ branching ratios (middle right) [377, 378], and on FCNC $t \rightarrow uH$ branching ratios [379] (lower left). The expected upper limits on FCNC $t \rightarrow qV$ branching ratios are also shown as a function of the centre-of-mass-energy (lower right).

2824 **3.4.2 FCNC Top Quark Couplings**

2825 Single top quark NC DIS production can be used to search for flavour Changing Neutral Current
 2826 (FCNC) $tu\gamma$, $tc\gamma$, tuZ , and tcZ couplings [377, 378] as represented by the Lagrangian

$$L = \sum_{q=u,c} \left(\frac{g_e}{2m_t} \bar{t}\sigma^{\mu\nu} (\lambda_q^L P_L + \lambda_q^R P_R) q A_{\mu\nu} + \frac{g_W}{4c_W m_Z} \bar{t}\sigma^{\mu\nu} (\kappa_q^L P_L + \kappa_q^R P_R) q Z_{\mu\nu} \right) + h.c. , \quad (3.47)$$

2827 where g_e (g_W) is the electromagnetic (weak) coupling constant, c_W is the cosine of the weak
 2828 mixing angle, $\lambda_q^{L,R}$ and $\kappa_q^{L,R}$ are the strengths of the anomalous top FCNC couplings (the values
 2829 of these couplings vanish at the lowest order in the SM). In an elaborate analysis events including
 2830 at least one electron and three jets (hadronic top quark decay) with high transverse momentum
 2831 and within the pseudorapidity acceptance range of the detector are selected. The distributions
 2832 of the invariant mass of two jets (reconstructed W boson mass) and an additional jet tagged as
 2833 b -jet (reconstructed top quark mass) are used to further enhance signal over background events,
 2834 mainly given by W + jets production. Signal and background interference effects are included.
 2835 A detector simulation with DELPHES [371] is applied.

2836 The expected limits on the branching ratios $\text{BR}(t \rightarrow q\gamma)$ and $\text{BR}(t \rightarrow qZ)$ as a function of the
 2837 integrated luminosity at the 2σ C.L. are presented in Fig. 3.62 (middle right). Assuming an
 2838 integrated luminosity of 1 ab^{-1} , limits of $\text{BR}(t \rightarrow q\gamma) < 1 \cdot 10^{-5}$ and $\text{BR}(t \rightarrow qZ) < 4 \cdot 10^{-5}$ are
 2839 expected. This level of precision is close to actual predictions of concrete new phenomena models,
 2840 such as SUSY, little Higgs, and technicolour, that have the potential to produce FCNC top quark
 2841 couplings. This will improve on existing limits from the LHC by one order of magnitude [12].
 2842 Fig. 3.62 (lower left) shows how this sensitivity on $\text{BR}(t \rightarrow q\gamma)$ and $\text{BR}(t \rightarrow qZ)$ changes as a
 2843 function of centre-of-mass energy. At a future FCC-ep [12] with, for example, an electron beam
 2844 energy of 60 GeV, and a proton beam energy of 50 TeV, leading to a centre-of-mass energy of
 2845 3.5 TeV, the sensitivity on FCNC $tq\gamma$ couplings even exceed expected sensitivities from the High
 2846 Luminosity-LHC (HL-LHC) with 300 fb^{-1} at $\sqrt{s} = 14 \text{ TeV}$, and from the International Linear
 2847 Collider (ILC) with 500 fb^{-1} at $\sqrt{s} = 250 \text{ GeV}$ [380, 381].

2848 Another example for a sensitive search for anomalous top quark couplings is the one for FCNC
 2849 tHq couplings as defined in

$$L = \kappa_{tuH} \bar{t}uH + \kappa_{tcH} \bar{t}cH + h.c. \quad (3.48)$$

2850 This can be studied in CC DIS production, where singly produced top anti-quarks could decay
 2851 via such couplings into a light anti-quark and a Higgs boson decaying into a bottom quark-
 2852 antiquark pair, $e^-p \rightarrow \nu_e \bar{t} \rightarrow \nu_e H \bar{q} \rightarrow \nu_e b \bar{b} \bar{q}$ [379]. Another signal involves the FCNC tHq
 2853 coupling in the production vertex, i.e. a light quark from the proton interacts via t-channel top
 2854 quark exchange with a W boson radiated from the initial electron producing a b quark and a
 2855 Higgs boson decaying into a bottom quark-antiquark pair, $e^-p \rightarrow \nu_e H b \rightarrow \nu_e b \bar{b}$ [379]. This
 2856 channel is superior in sensitivity to the previous one due to the clean experimental environment
 2857 when requiring three identified b -jets. Largest backgrounds are given by $Z \rightarrow b\bar{b}$, SM $H \rightarrow b\bar{b}$,
 2858 and single top quark production with hadronic top quark decays. A 5% systematic uncertainty
 2859 for the background yields is added. Furthermore, the analysis assumes parameterised resolutions
 2860 for electrons, photons, muons, jets and unclustered energy using typical parameters taken from
 2861 the ATLAS experiment. Furthermore, a b -tag rate of 60%, a c -jet fake rate of 10%, and a light-
 2862 jet fake rate of 1% is assumed. The selection is optimised for the different signal contributions
 2863 separately. Fig. 3.62 (lower right), shows the expected upper limit on the branching ratio
 2864 $\text{Br}(t \rightarrow Hu)$ with 1σ , 2σ , 3σ , and 5σ C.L. as a function of the integrated luminosity for the

2865 $e^-p \rightarrow \nu_e H b \rightarrow \nu_e b\bar{b}b$ signal process. For an integrated luminosity of 1 ab^{-1} , upper limits of
 2866 $\text{Br}(t \rightarrow Hu) < 0.15 \cdot 10^{-3}$ are expected at the 2σ C.L.

2867 In Fig. 3.63 the different expected limits on various flavour-changing neutral current (FCNC)
 2868 top quark couplings from the LHeC are summarised, and compared to results from the LHC
 2869 and the HL-LHC. This clearly shows the competitiveness of the LHeC results, and documents
 2870 the complementarity of the results gained at different colliders.

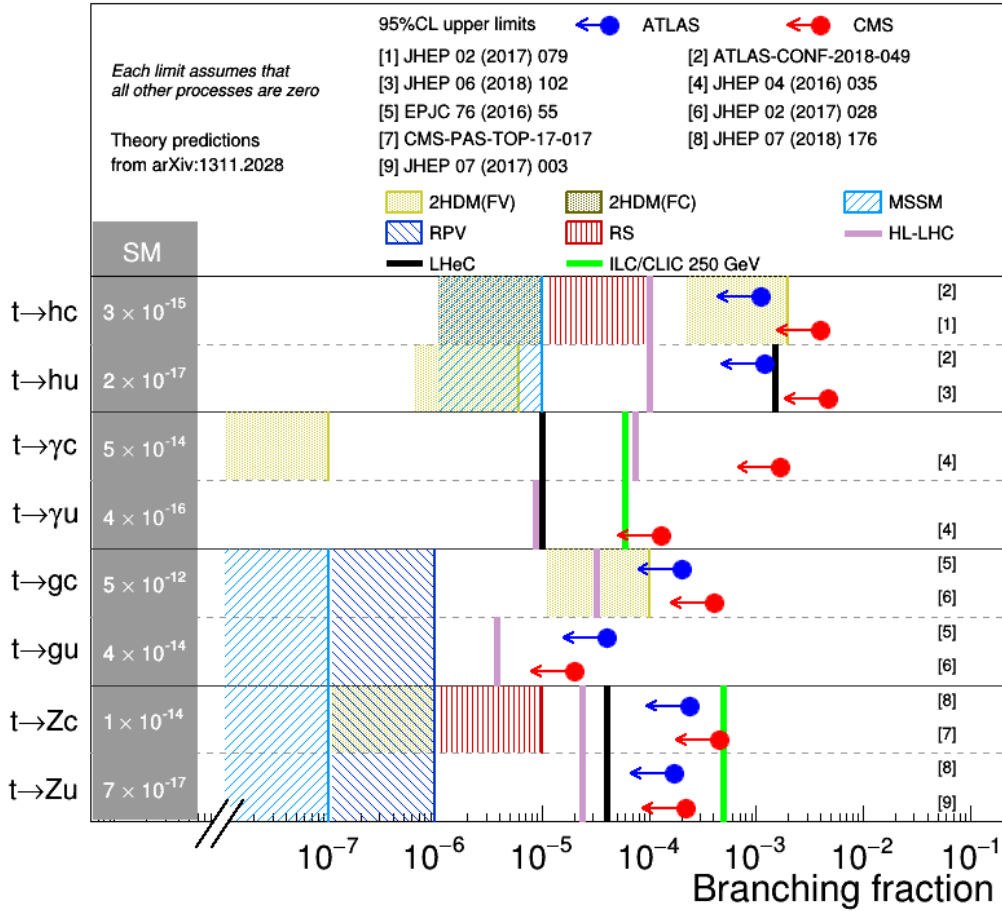


Figure 3.63: Comparison of top quark FCNC branching ratio limits at the LHC, HL-LHC, LHeC, and ILC/CLIC colliders.

2871 3.4.3 Other Top Quark Property Measurements and Searches for New Physics

2872 Other exciting results not presented here involve, for example, the study of the CP-nature
 2873 in $t\bar{t}H$ production [382] (see Section 5.2), searches for anomalous $t\bar{t}\gamma$ and $t\bar{t}Z$ chromoelectric
 2874 and chromomagnetic dipole moments in $t\bar{t}$ production [370], the study of top quark spin and
 2875 polarisation [383], and the investigation of the top quark structure function inside the proton [1,
 2876 384].

2877 3.4.4 Summary Top Quark Physics

2878 Top quark physics at the LHeC represents a very rich and diverse field of research involving high
 2879 precision measurements of top quark properties, and sensitive searches for new physics. Only a

2880 few highlights involving Wtq and FCNC top quark couplings are presented here. One particular
2881 highlight is the expected direct measurement of the CKM matrix element $|V_{tb}|$ with a precision
2882 of less than 1%. Furthermore, FCNC top quark couplings can be studied with a precision high
2883 enough to explore those couplings in a regime that might be affected by actual new phenomena
2884 models, such as SUSY, little Higgs, and technicolour.

2885 It has been shown [12], that results from future e^+e^- -colliders, eh -colliders, and hh -colliders
2886 deliver complimentary information and will therefore give us a more complete understanding of
2887 the properties of the heaviest elementary particle known to date, and of the top quark sector in
2888 general.

Chapter 4

Nuclear Particle Physics with Electron-Ion Scattering at the LHeC

4.1 Introduction

The LHeC accelerator, in addition to being a powerful machine for exploring proton structure, will allow for the first time studies of DIS off nuclei in a collider mode at the energy frontier. The nuclear structure has been previously studied in fixed target experiments with charged lepton and neutrino beams, see [385–397] and references therein. Due to the energy limitations of the machines operating in this mode, the kinematic range covered by these experiments is rather narrow, mostly limited to relatively large values of $x \geq 0.01$ and low to moderate Q^2 , in the range $Q^2 < 100 \text{ GeV}^2$. The precise kinematic range covered by experiments is shown in Fig. 4.1, where the DIS experiments overlap to a large degree with the data from hadronic collisions using the Drell-Yan (DY) process. These fixed target DIS and DY data dominate the data sets used in the fits for the nuclear parton distribution functions. In addition, in some analyses of nuclear PDFs, data on inclusive single hadron production in $d\text{Au}$ collisions at RHIC and on EW bosons and dijets in $p\text{Pb}$ collisions at the LHC are included.

As is clear from Fig. 4.1, the LHeC will be able to cover a very large range in (x, Q^2) in eA , previously unexplored in experiments. It will extend the range in x down to $\sim 10^{-6}$ and have a huge lever arm in Q^2 from very low values up to $\sim 10^6 \text{ GeV}^2$. It will also be complementary to the EIC [224] machine, extending the range in x and Q^2 by about two orders of magnitude with respect to it. The extension of these ranges will be even larger at the FCC-eh.

Due to large statistics and modern, specialised detectors, it will be possible to study nuclear structure at the LHeC with unprecedented precision in a kinematical range far wider than previously possible and with the controlled systematics of one single experiment. There are a large number of important physics topics that can be addressed in eA collisions at the LHeC:

- A precise determination of nuclear parton densities for a single nucleus (lead, and eventually lighter ions) will be possible. In particular, the current huge uncertainties in nuclear gluon and sea quark densities at low x will be dramatically improved using the data from the LHeC. In analogy to the proton PDF extraction described in previous sections, full flavour decomposition in the nuclear case could be achieved using both NC and CC data with heavy flavour identification.
- Precision measurement of semi-inclusive and exclusive processes will enable an exploration

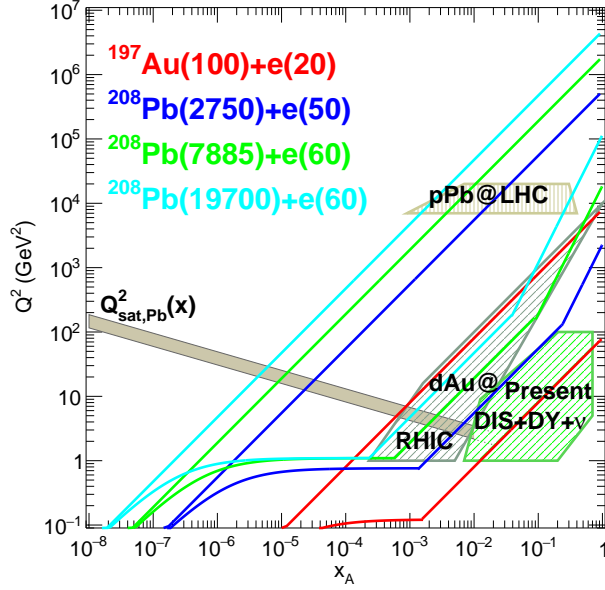


Figure 4.1: Kinematic regions in the $x - Q^2$ plane explored by different data sets (charged lepton and neutrino DIS, DY, dAu at RHIC and pPb at the LHC) used in present nPDF analyses [398], compared to the ones achievable at the EIC (red), the LHeC (ERL against the HL-LHC beams, dark blue) and two FCC-eh versions (with Pb beams corresponding to proton energies $E_p = 20$ TeV - green and $E_p = 50$ TeV - light blue). Acceptance of the detector for the electrons is taken to be $1^\circ < \theta < 179^\circ$, and $0.01(0.001) < y < 1$ for the EIC (all other colliders). The saturation scale Q_{sat} shown here for indicative purposes only, see also [399], has been drawn for a Pb nucleus considering an uncertainty ~ 2 and a behaviour with energy following the model in [400]. Note that it only indicates a region where saturation effects are expected to be important but there is no sharp transition between the linear and non-linear regimes.

2921
2922
2923
2924
2925
2926
2927
2928
2929
2930
2931
2932
2933
2934
2935
2936
2937
2938
2939
2940

of new details of the nuclear structure. Similarly to the proton case, DVCS and exclusive vector-meson production will provide unique insight into 3D nuclear structure.

- The LHeC will offer unprecedented opportunities to extract diffractive parton densities in nuclei for the first time. A first detailed analysis [256] indicates that the achievable precision on diffractive PDFs in nuclei will be comparable to that possible in the proton case. The measurements of diffraction on protons and nuclei as well as the inclusive structure functions in the nuclear case will allow us to explore the very important relation between nuclear shadowing and diffraction [401].
- The LHeC will be able to test and establish or exclude the phenomenon of parton saturation at low x in protons and nuclei. According to the Color Glass Condensate framework [402, 403], parton saturation is a density effect that can be achieved in two ways, either by decreasing the value of x or by increasing the size of the target by increasing A . The LHeC will be a unique machine to address both of their variations, such that the ideas of saturation could be precisely tested. It will be possible to search for parton saturation in a variety of ways which include, among others, the search for tensions in DGLAP fits, the study of the diffraction, in particular the ratios of diffractive to inclusive cross sections, and the study of particle azimuthal de-correlations.
- Finally, the LHeC machine in eA mode will have a huge impact onto physics explored in pA and AA collisions, see Sec. 7.5, where it will provide vital input and constraints on the ‘baseline’ initial state in nuclear collisions, measurements of the impact of a cold nuclear

2941 medium on hard probes and effects of hadronisation. It will also explore the initial state
 2942 correlations on the final state observables relevant for understanding collectivity in small
 2943 systems explored in pp or pA collisions.

2944 As commented below, these aims will require an experimental apparatus with large rapidity
 2945 coverage and associated forward and backward electron, photons, hadron and nuclear detectors.
 2946 In addition the detector design should allow to precisely measure diffractive events in eA and
 2947 allow the clean separation of radiative events, most important for the case of DVCS and exclusive
 2948 diffraction.

2949 In this Chapter we do not address issues on the nuclear modification on jet yields and fragmen-
 2950 tation that are expected to show dramatic effects and to be of great importance for heavy-ion
 2951 collisions. All these aspects were previously discussed in Ref. [1].

2952 4.2 Nuclear Parton Densities

2953 PDFs are essential ingredients in our understanding of the dynamics of the strong interaction.
 2954 First, they encode important information about the structure of hadrons [404,405]. Second, they
 2955 are indispensable for the description of hadronic collisions within standard collinear factorisa-
 2956 tion [42]. Concerning nuclei, it has been known for more than 40 years that structure functions
 2957 are strongly affected by the nuclear environment [396,397] so that they cannot be interpreted as
 2958 a simple superposition of structure functions of free nucleons. In the standard approach, within
 2959 collinear factorization, the nuclear modification is included in the parametrisation of the parton
 2960 densities. This means that the parton densities in a bound nucleon are different from those in
 2961 a free nucleon, and the difference is encoded in the non-perturbative initial conditions of the
 2962 parton densities at some low, initial scale Q_0^2 . The present status of nuclear parton densities
 2963 (nPDFs), see for example [406,407], can be summarised as follows:

- 2964 • Modern analyses [398,408–410] are performed at next-to-leading order (NLO) and next-to-
 2965 next-to-leading order (NNLO) [411,412]. Differences between the different groups mainly
 2966 arise from the different sets of data included in the analyses ¹ and from the different
 2967 functional forms employed for the initial conditions.
- 2968 • Many sets of data are presented as ratios of cross section for a given nucleus over that in
 2969 deuterium, which is loosely bound and isoscalar. Therefore, it has become customary to
 2970 work in terms of ratios of nPDFs:

$$R_i(x, Q^2) = \frac{f_i^A(x, Q^2)}{A f_i^p(x, Q^2)}, \quad i = u, d, s, c, b, g, \dots, \quad (4.1)$$

2971 with $f_i^{p(A)}(x, Q^2)$ the corresponding parton density in a free proton p or in nucleus A .
 2972 These nuclear modification factors are parametrised at initial scale Q_0^2 (assuming isospin
 2973 symmetry to hold). The nPDFs are then obtained multiplying the nuclear modification
 2974 factors by some given set of free proton PDFs.

- 2975 • The available data come from a large variety of nuclei and the number of data points for
 2976 any of them individually is very small compared to the proton analyses. In particular,
 2977 for the Pb nucleus there are less than 50 points coming from the fixed target DIS and

¹The main difference lies in the use or not of neutrino-Pb cross sections (whose usage has been controver-
 sial [413–415], particularly the NuTeV data [386] from the Fe nucleus) from CHORUS and $\pi^{0,\pm}$ transverse mo-
 mentum spectra from dAu collisions at the Relativistic Heavy Ion Collider (RHIC).

2978 DY experiments and from particle production data in p Pb collisions at the LHC. The fit
 2979 for a single nucleus is therefore impossible and the modelling of the A -dependence of the
 2980 parameters in the initial conditions becomes mandatory [398, 410]. The most up to date
 2981 analyses include between 1000 and 2000 data points for 14 nuclei.

- 2982 • The kinematic coverage in Q^2 and x with existing data is very small compared to that
 2983 of present hadronic colliders. The ultimate precision and large coverage of the kinematic
 2984 plane for nPDFs can only be provided by a high energy electron-ion collider. Meanwhile,
 2985 the only experimental collision system where nPDFs can be currently constrained are
 2986 hadronic and ultraperipheral collisions (UPCs). It is important to stress that extracting
 2987 PDFs from these collisions presents many theoretical challenges. These are related to the
 2988 question of applicability of collinear factorization for nuclear collisions, higher twist effects,
 2989 scale choices and other theoretical uncertainties.

2990 All parton species are very weakly constrained at small $x < 10^{-2}$ [416], gluons are poorly
 2991 known at large $x > 0.2$, and the flavour decomposition is largely unknown - a natural fact
 2992 for u and d due to the approximate isospin symmetry in nuclei ². The impact of presently
 2993 available LHC data, studied using reweighting [38, 417] in [418, 419] and included in the fit
 2994 in [398], is quite modest with some constrains on the gluon and the strange quark in the region
 2995 $0.01 < x < 0.3$. On the other hand, theoretical predictions for nuclear shadowing of quark and
 2996 gluon PDFs based on s -channel unitarity and diffractive nucleon PDFs are available down to
 2997 $x \sim 10^{-4} - 10^{-5}$ [401, 420, 421]. Predictions on the flavour dependence of nuclear effects in the
 2998 antishadowing region [422] cannot be confirmed with present data.

2999 Future runs at the LHC will offer some further possibilities for improving our knowledge on
 3000 nPDFs [423]. However, the ideal place to determine parton densities is DIS, either at the Electron
 3001 Ion Collider (EIC) [224] in the USA or, in a much larger kinematic domain (see Fig. 4.1), at the
 3002 LHeC. DIS measurements in such configurations offer unprecedented possibilities to enlarge our
 3003 knowledge of parton densities through a complete unfolding of all flavours.

3004 In the following, we show the possibilities for constraining the PDFs for a Pb nucleus at the
 3005 LHeC. In the next subsection, Subsec. 4.2.1, we discuss the corresponding pseudodata for the
 3006 inclusive cross section in electron-nucleus scattering. Next, in Subsec. 4.2.2 we discuss how the
 3007 pseudodata will be introduced in a global nPDF fit. Finally, in Subsec. 4.2.3 it is demonstrated
 3008 how the PDFs of Pb can be extracted with a very good precision from the LHeC data only,
 3009 without requiring any other set of data.

3010 4.2.1 Pseudodata

3011 The LHeC provides measurements of eA scattering cross sections in the deep inelastic scattering
 3012 region $Q^2 > 1 \text{ GeV}^2$ reaching values of Q^2 up to about $5 \cdot 10^5 \text{ GeV}^2$ and corresponding x values
 3013 between a few times 10^{-6} and near to $x = 1$. This enables the determination of a complete
 3014 set of nPDFs in e Pb scattering at the LHeC from the inclusive neutral and charged current
 3015 cross sections with a clean separation of up and down valence and sea quark distributions. The
 3016 very high Q^2 region which reaches much beyond the W mass squared makes the CC measure-
 3017 ments extremely valuable for the separation of different flavours when taken together with the
 3018 NC, from photon and Z boson exchange. Charm tagging in CC determines the anti-strange
 3019 quark distribution in a wide kinematic range to typically 10 – 20 % precision, while charm and
 3020 beauty tagging in NC provide high precision determinations of xc and xb from nuclei. Using

²The u - d difference is suppressed by a factor $2Z/A - 1$.

3021 coherent data from just this one experiment the uncertainties of these nPDFs will follow from
 3022 a straightforward $\Delta\chi^2 = 1$ criterion.

3023 The QCD analyses of pseudo LHeC cross section data illustrated subsequently employ sets of
 3024 simulated NC and CC measurements under assumptions on precision which are summarised in
 3025 Table 4.1, see Ref. [424]. The cross section simulation was done numerically employing deriva-
 3026 tive formulae from [57] and found to compare well to a detailed Monte Carlo simulation when
 3027 tested for the conditions of the H1 experiment. The assumptions made are all reasonable when
 3028 comparing with the H1 achievements, allowing for further improvements owing to new detector
 3029 techniques and higher statistics. The control of radiative corrections in eA scattering is a spe-
 3030 cial challenge as these grow $\propto Z^2$. The LHeC detector thus needs to be equipped with reliable
 3031 photon detectors and the exploitation of the energy-momentum conservation, via the $E - p_z$
 3032 cut, should further reduce the effect of photon radiation to a few per cent level. It is also to be
 3033 noted that the semi-inclusive measurements of the s , c and b quark distributions carry additional
 uncertainties for tagging, acceptance and background influences.

Source of uncertainty	Error on the source or cross section
Scattered electron energy scale	0.1 %
Scattered electron polar angle	0.1 mrad
Hadronic energy scale	0.5 %
Calorimeter noise ($y < 0.01$)	1–3 %
Radiative corrections	1–2 %
Photoproduction background	1 %
Global efficiency error	0.7 %

Table 4.1: Summary of assumed systematic uncertainties for future inclusive cross section measurements at the LHeC.

3034

3035 Fig. 4.2 illustrates the kinematic reach of the NC+CC pseudodata at the LHeC and the FCC-eh,
 3036 in ep and ePb collisions (for per nucleon integrated luminosities ≤ 1 and 10 fb^{-1} respectively). In
 3037 addition to inclusive data, semi-inclusive measurements with flavour sensitivity are also included.
 3038 They will allow us to determine the strange, charm and beauty (also the top) PDFs. The
 3039 principal technique is charm tagging (in CC for xs , in NC for xc) and beauty tagging (in NC
 3040 for xb). The beam spot of the LHeC has a transverse extension of about $(7 \mu\text{m})^2$. Modern Si
 3041 detectors have a resolution of a few microns to be compared with typical decay lengths of charm
 3042 and beauty particles of hundreds of μm . The experimental challenges then are the beam pipe
 3043 radius, coping at the LHeC with strong synchrotron radiation effects, and the forward tagging
 3044 acceptance, similar to the HL-LHC challenges.

3045 A study was made of the possible measurements of the anti-strange density in nuclei (see Fig. 4.3)
 3046 using impact parameter tagging in eA CC scattering, and of the charm and beauty structure
 3047 functions in NC (see Fig. 4.4). Following experience on heavy flavour tagging at HERA and
 3048 ATLAS, assumptions were made on the charm and beauty tagging efficiencies to be 10 % and
 3049 60 %, respectively. The light quark background in the charm analysis is assumed to be control-
 3050 lable to per cent level, while the charm background in the beauty tagging sample is assumed
 3051 to be 10 %. The tagging efficiencies and background contaminations affect the statistical error.
 3052 Moreover, an additional systematic error is assumed in the simulated NC (CC) measurements
 3053 of 3 (5) %. These result in very promising measurements of the heavier quark distributions: to
 3054 about 10 – 20 % total uncertainty on the strange and 3 – 5 % on the charm and beauty mea-
 3055 surements, for typically x between 10^{-4} and 0.1 and Q^2 extending from below threshold m_Q^2 up
 3056 to a few times 10^4 GeV^2 . The knowledge of the heavy quark densities is of prime relevance for

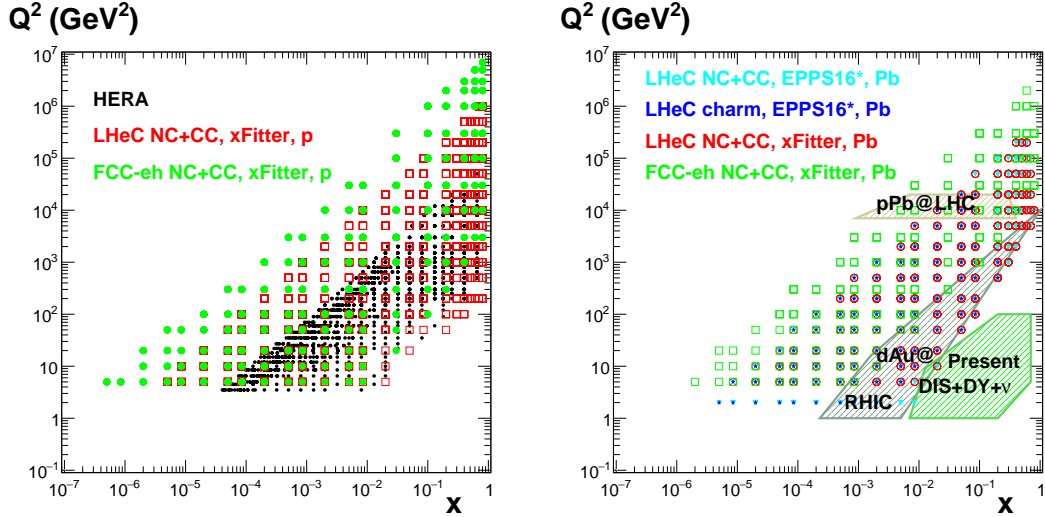


Figure 4.2: Left: kinematic $x - Q^2$ plot of the NC+CC pseudodata on a proton at the LHeC (red symbols) and the FCC-eh (green symbols) used in the xFitter analysis in Section 4.2.3; data used in analysis at HERA (black symbols) are shown for comparison. Right: kinematic $x - Q^2$ plot of the pseudodata on Pb used in the EPPS16 analysis at the LHeC (NC+CC, light blue symbols, and charm, dark blue symbols) in Section 4.2.2, and in the xFitter analysis in Subsec. 4.2.3 (at the LHeC, red symbols, and the FCC-eh, green symbols); the regions explored by currently available data sets (charged lepton and neutrino DIS, DY, dAu at RHIC and pPb at the LHC) used in present nPDF analyses [398] are shown for comparison.

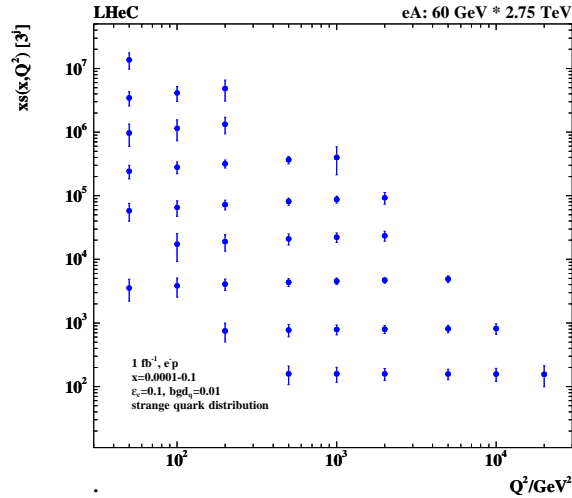


Figure 4.3: Simulation of the measurement of the (anti)-strange quark distribution $x\bar{s}(x, Q^2)$ in charged current eA scattering through the t -channel reaction $W^- \bar{s} \rightarrow c$. The data are plotted with full systematic and statistical errors added in quadrature.

3057 understanding nuclear structure and the development of QCD as has often been emphasised.

3058 4.2.2 Nuclear gluon PDFs in a global-fit context

3059 To illustrate the impact of the LHeC ePb pseudodata in the global context, they have been
 3060 added [425] into the EPPS16 global analysis of nuclear PDFs [398]. The EPPS16 strategy is

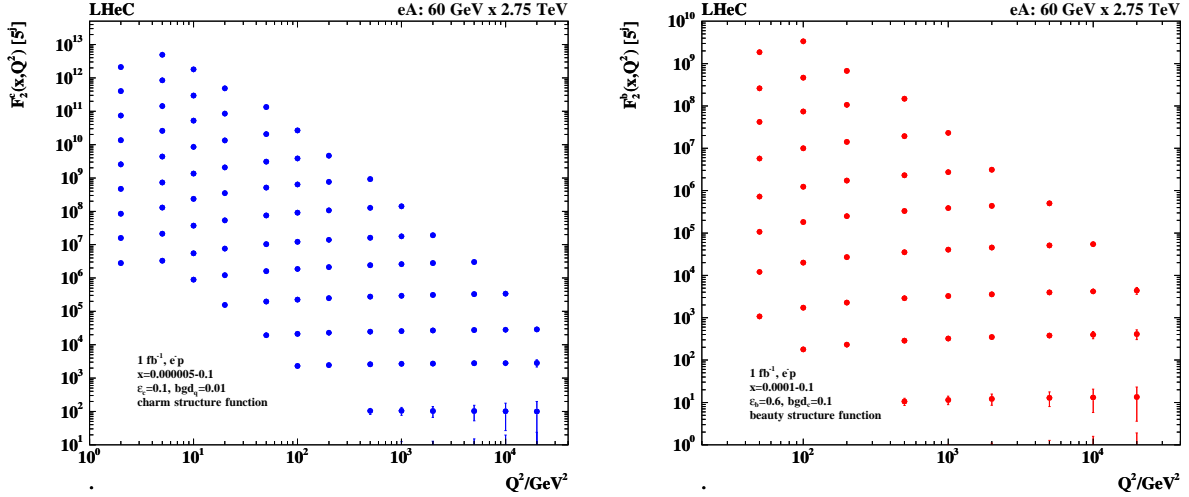


Figure 4.4: Left: Simulation of the measurement of the charm quark distribution expressed as $F_2^c = e_c^2 x(c + \bar{c})$ in neutral current eA scattering; Right: Simulation of the measurement of the bottom quark distribution expressed as $F_2^b = e_b^2 x(b + \bar{b})$ in neutral current eA scattering. The data are plotted with full systematic and statistical errors added in quadrature.

3061 to parametrise the nuclear modification ratios $R_i(x, Q^2)$ between the bound-proton PDFs $f_i^{p/Pb}$
 3062 and proton PDFs f_i^p ,

$$R_i(x, Q^2) \equiv \frac{f_i^{p/Pb}(x, Q^2)}{f_i^p(x, Q^2)}, \quad (4.2)$$

3063 at the charm mass threshold $Q^2 = m_{charm}^2 = (1.3 \text{ GeV})^2$. At higher Q^2 the nuclear PDFs are
 3064 obtained by solving the standard DGLAP evolution equations at next-to-leading order in QCD.
 3065 As the LHeC pseudodata reach to significantly lower x than the data that were used in the
 3066 EPPS16 analysis, an extended small- x parametrisation was used for gluons, see Figure 4.5. The
 3067 framework is almost identical to that in Ref. [426]. The introduced functional form allows for
 3068 rather wild – arguably unphysical – behaviour at small- x where e.g. significant enhancement is
 3069 allowed. This is contrary to the theoretical expectations from the saturation conjecture and looks
 3070 also to be an improbable scenario given the recent LHCb D and B meson measurements [427,428]
 3071 which impressively indicate [429] gluon shadowing down to $x \sim 10^{-5}$ at interaction scales as low
 3072 as $Q^2 \sim m_{charm}^2$. On the other hand, given that there are no prior DIS measurements in this
 3073 kinematic range for nuclei other than the proton, and that the D and B meson production in
 3074 pPb collisions could be affected by strong final-state effects (which could eventually be resolved
 3075 by e.g. measurements of forward prompt photons [430] in pPb), we hypothesise that any kind
 3076 of behaviour is possible at this stage. Anyway, with the extended parametrisation – called
 3077 here EPPS16* – the uncertainties in the small- x regime get significantly larger than in the
 3078 standard EPPS16 set. This is reflected as significantly larger PDF error bands in comparison
 3079 to the projected LHeC pseudodata. It is shown in Figure 4.6 where EPPS16* predictions are
 3080 compared with the LHeC pseudodata for inclusive NC and CC reactions, as well as charm
 3081 production in neutral-current scattering. The uncertainties are estimated using the Hessian
 3082 method [431] and the same overall tolerance $\Delta\chi^2 = 52$ as in the EPPS16 analysis has been used
 3083 when defining the error bands. Because there are no small- x data constraints for gluons, the
 3084 gluon uncertainty is enormous and the Hessian method used for estimating the uncertainties is
 3085 not particularly accurate, i.e. the true $\Delta\chi^2 = 52$ error bands are likely to be even larger. At
 3086 some point the downward uncertainty will be limited by positivity constraints e.g. for F_L , but

3087 will depend strongly on which Q^2 is used to set the positivity constraints (e.g. in the EPPS16
 3088 analysis F_L is required to remain positive at $Q^2 = m_{charm}^2$).

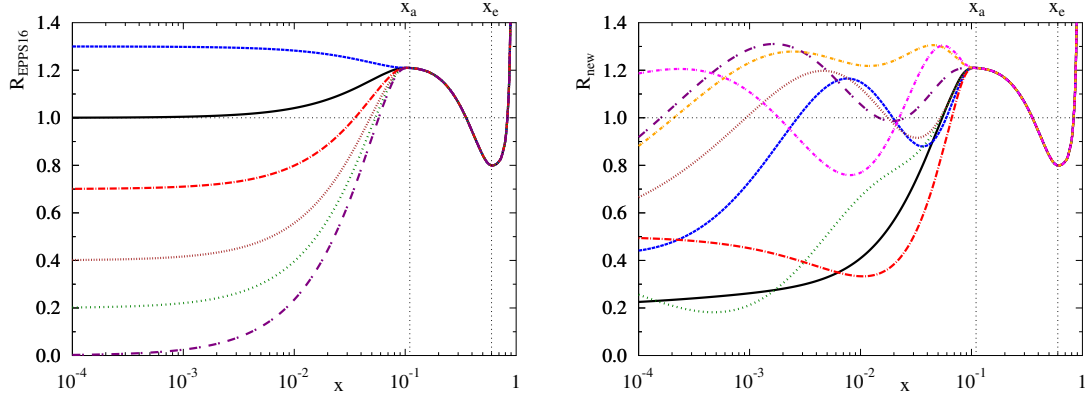


Figure 4.5: Left: Illustration of the functional behaviours allowed at small x in the EPPS16 analysis. Right: Illustration of the possible functional variations at small x in the extended parametrisation that we employ here.

3089 Upon including the LHeC e Pb pseudodata in the fit, the new nPDFs adapt to reproduce the
 3090 pseudodata and their uncertainties are greatly reduced, as shown in Figure 4.7. The overall
 3091 tolerance has been kept fixed to the default value $\Delta\chi^2 = 52$. The impact on the nuclear
 3092 modification of the gluon PDF is illustrated in Figure 4.8 at two values of Q^2 : $Q^2 = 1.69 \text{ GeV}^2$
 3093 (the parametrisation scale) and $Q^2 = 10 \text{ GeV}^2$. Already the inclusive pseudodata are able to
 3094 reduce the small- x gluon uncertainty quite significantly, and the addition of the charm data
 3095 promises an even more dramatic reduction in the errors. The analysis indicates that the LHeC
 3096 will nail the nuclear gluon PDF to a high precision down to x of at least 10^{-5} .

3097 4.2.3 nPDFs from DIS on a single nucleus

3098 Another approach that becomes possible with the large kinematic coverage and volume of data
 3099 for a single nucleus, Pb, at the LHeC and FCC-eh, is to perform a fit to only Pb data in order
 3100 to extract the Pb PDFs, removing the need to interpolate between different nuclei. Then the
 3101 corresponding ratios or nuclear modification factors for each parton species can be obtained
 3102 using either a proton PDF set from a global fit or, as we do here (see [12, 432, 433]), from a
 3103 fit to proton LHeC and FCC-eh pseudodata. In this way, there will be no need to introduce a
 3104 nuclear size dependence in the parameters for the initial condition for DGLAP evolution. Such
 3105 nPDFs can then be used for comparing to those obtained from global fits and for precision tests
 3106 of collinear factorisation in nuclear collisions.

3107 The fits are performed using xFitter [61], where 484 (150) NC+CC Pb data points at the LHeC
 3108 (FCC-eh) have been used in the fitted region $Q^2 > 3.5 \text{ GeV}^2$, see Fig. 4.2. A HERAPDF2.0-
 3109 type parametrisation [45] has been employed to provide both the central values for the reduced
 3110 cross sections (therefore, the extracted nuclear modification factors are centered at 1) and the
 3111 fit functional form; in this way, neither theory uncertainties (treatment of heavy flavours, value
 3112 of α_s , order in the perturbative expansion) nor the uncertainty related to the functional form
 3113 of the initial condition – parametrisation bias – are considered in our study, in agreement
 3114 with our goal of estimating the *ultimate achievable experimental* precision in the extraction of
 3115 nPDFs. We have worked at NNLO using the Roberts-Thorne improved heavy quark scheme,

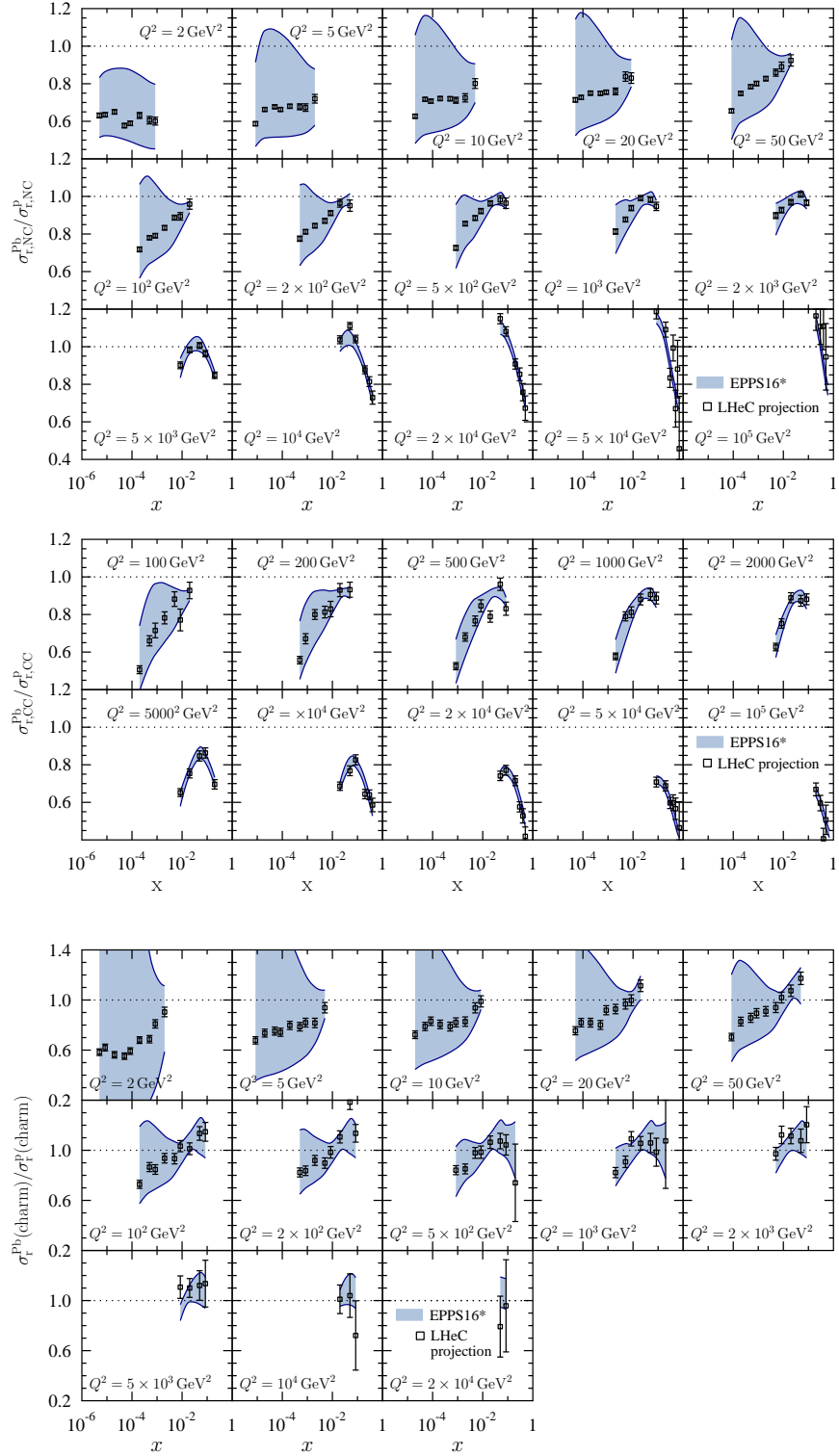


Figure 4.6: Top: Simulated ratios of neutral-current reduced cross sections between $e\text{Pb}$ and ep collisions compared with the predictions from a EPPS16-type global fit of nuclear PDFs using an extended parametrisation for gluons. Middle: Charged-current cross section ratios. Bottom: Neutral-current charm-production cross section ratios.

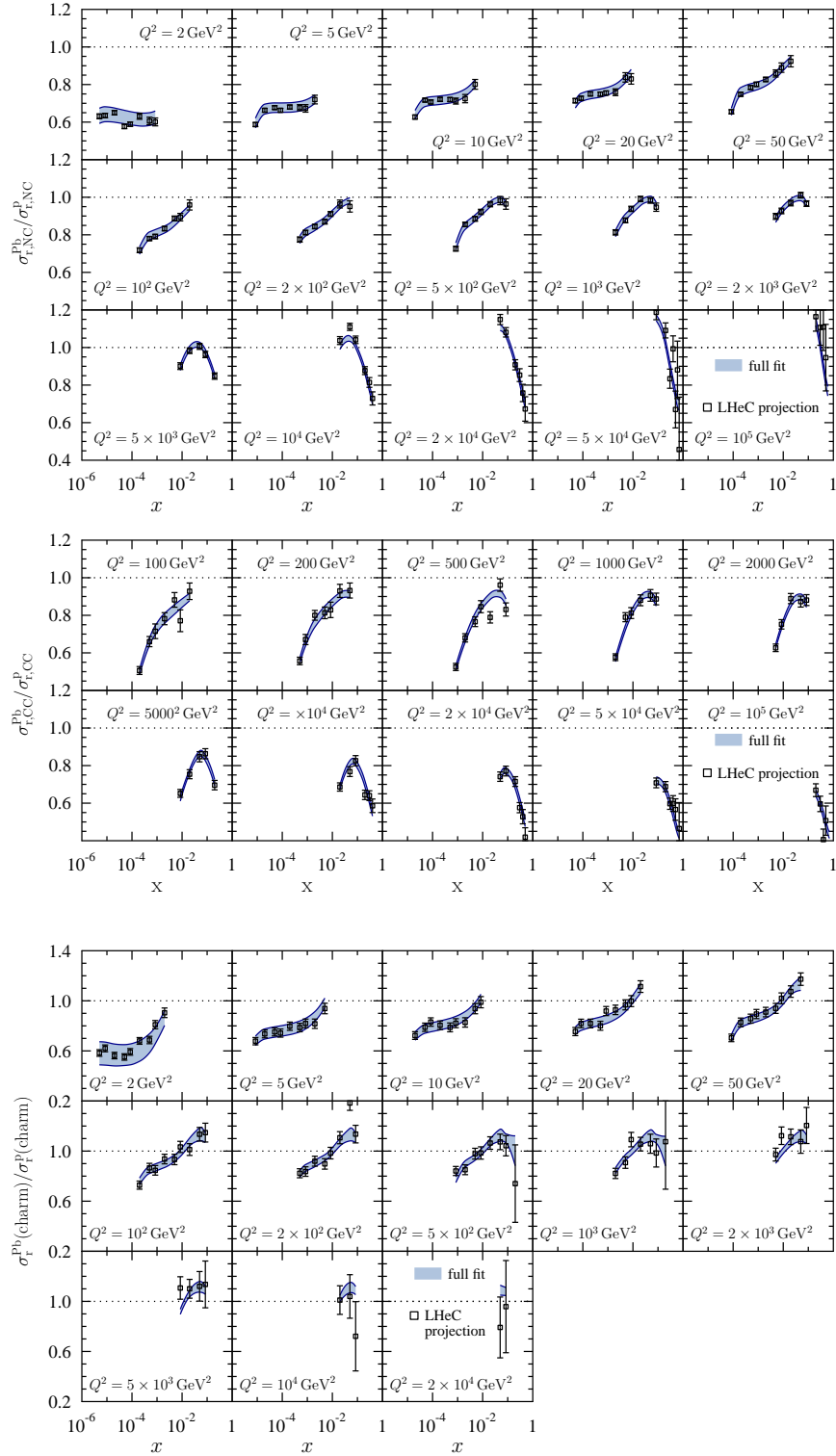


Figure 4.7: As Figure 4.6 but with fit results after including the LHeC pseudodata in the global analysis.

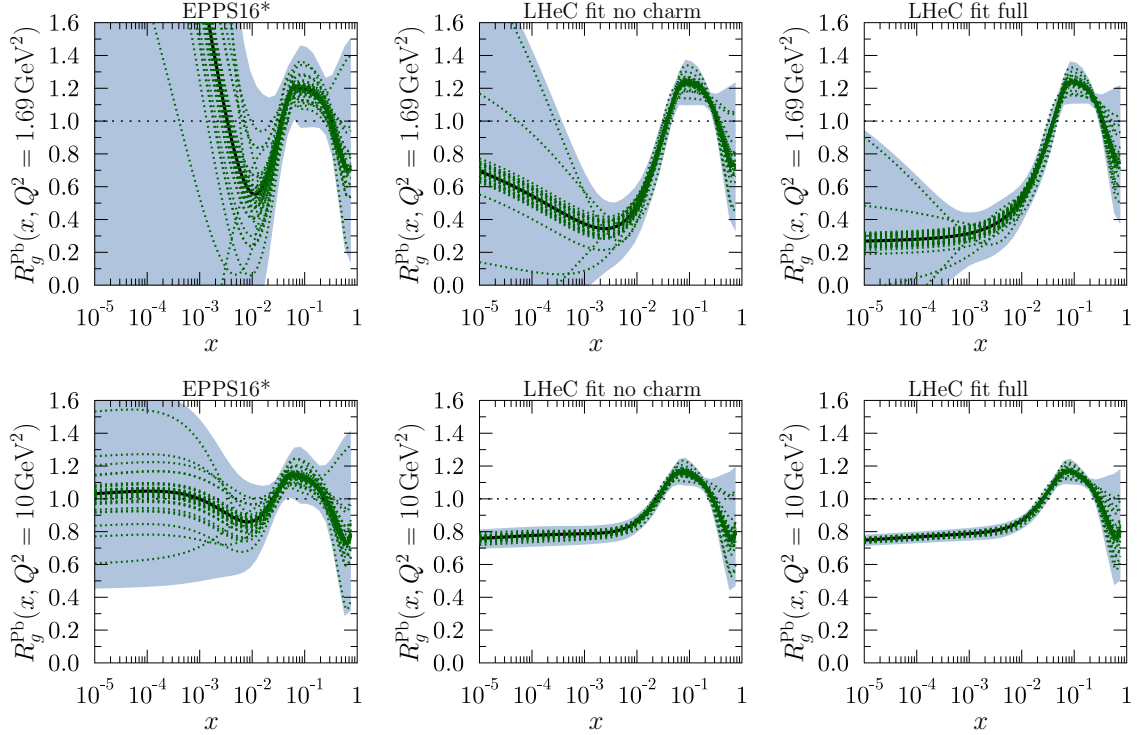


Figure 4.8: Upper panels: The gluon nuclear modification for the Pb nucleus at $Q^2 = 1.69 \text{ GeV}^2$ in EPPS16* (left), LHeC analysis without charm pseudodata (middle), and full LHeC analysis (right). The blue bands mark the total uncertainty and the green dotted curves correspond to individual Hessian error sets. Lower panels: As the upper panels but at $Q^2 = 10 \text{ GeV}^2$.

3116 and $\alpha_s(m_Z^2) = 0.118$. The treatment of systematics and the tolerance $\Delta\chi^2 = 1$ are identical to
 3117 the approach in the HERAPDF2.0 fits, as achievable in a single experiment.

3118 The results for the relative uncertainties in the nuclear modification factors are shown in Figs. 4.9,
 3119 4.10 and 4.11 for valence, sea and gluon, respectively. The uncertainties in these plots reflect the
 3120 assumed uncertainties in the pseudodata, both statistics (mainly at large x) and systematics from
 3121 detector efficiencies, radiative corrections, etc., see Sec. 4.2.1. As expected, the uncertainty in the
 3122 extraction of the valence at small x is sizeably larger than that for the sea and gluon. While a very
 3123 high precision looks achievable at the LHeC and the FCC-eh, for the comparison with EPPS16
 3124 (or any other global fit) shown in the plots and with previous works in that setup [425, 426] some
 3125 caution is required. First, the effective EPPS16 tolerance criterion $\Delta\chi^2 \simeq 52$ implies that naively
 3126 the uncertainty bands should be compared after rescaling by a factor $\sqrt{52}$. Second, the treatment
 3127 of systematics is rather different, considering correlations in the xFitter exercise and taking them
 3128 as fully uncorrelated (and added quadratically to the statistical ones) in the EPPS16 approach.
 3129 Finally, EPPS16 uses parametrisations for the nuclear modification factors for different parton
 3130 species while in xFitter just the (n)PDF combinations that enter the reduced cross sections are
 3131 parametrised and employed for the fit. In this respect let us note that, in analogy to proton
 3132 PDFs, a full flavour decomposition can be achieved using both NC and CC with heavy flavour
 3133 identification that will verify the existing ideas on flavour dependence of nuclear effects on parton
 3134 densities [422].

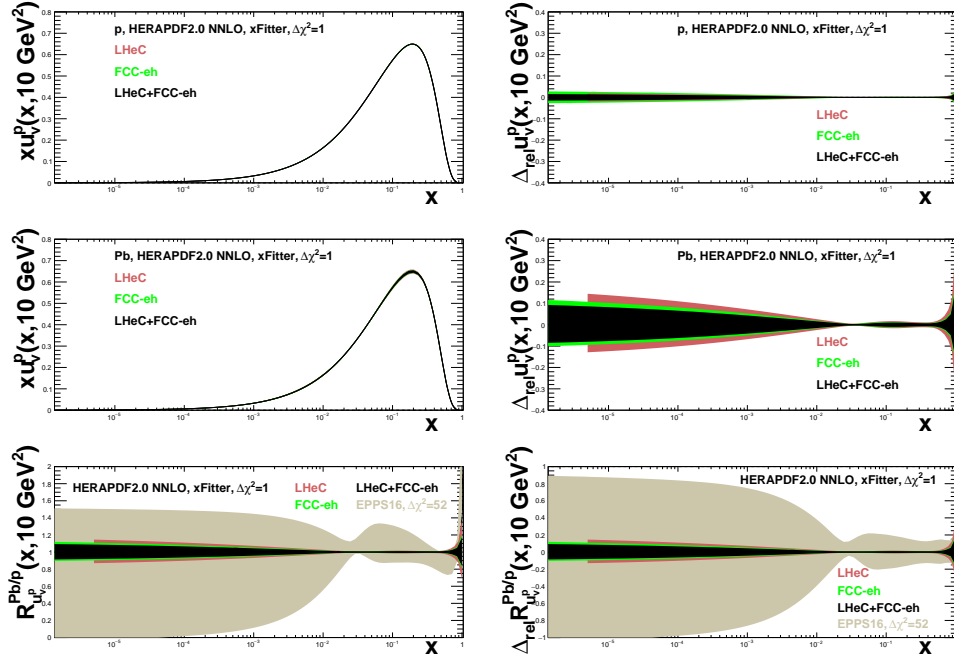


Figure 4.9: Distributions (left) and their relative uncertainties (right) of the valence u -quark density in the proton (top), Pb (middle) and the corresponding nuclear modification factor (bottom) in an analysis of ep and $e\text{Pb}$ LHeC and FCC-eh NC plus CC pseudodata using xFitter (both a single set of data and all combined), compared to the results of EPPS16 [398], see the text for details.

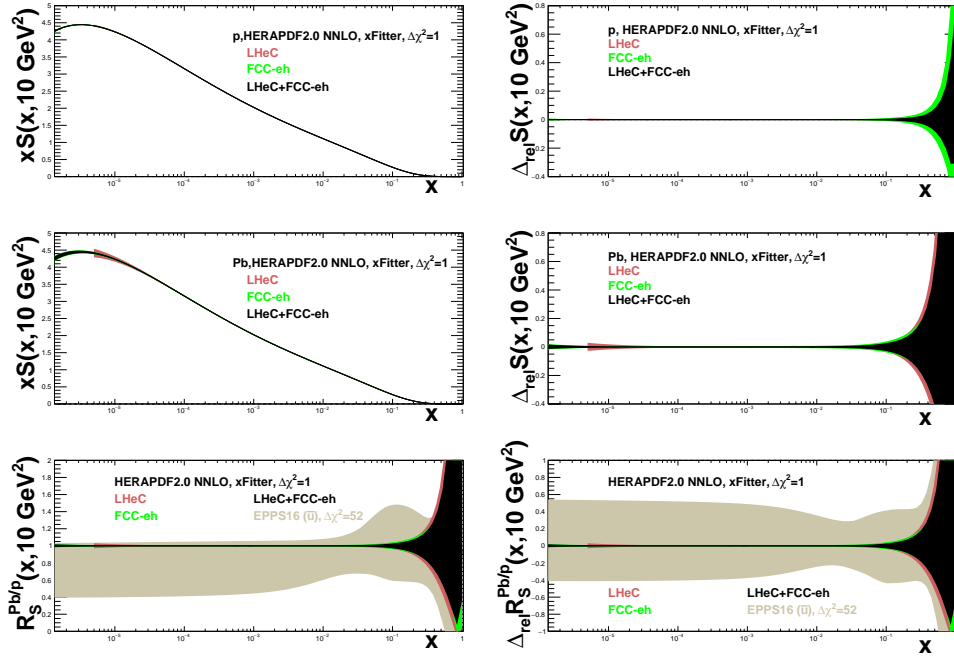


Figure 4.10: Distributions (left) and their relative uncertainties (right) of the sea quark density in the proton (top), Pb (middle) and the corresponding nuclear modifications factor (bottom) in an analysis of ep and $e\text{Pb}$ LHeC and FCC-eh NC plus CC pseudodata using xFitter (both a single set of data and all combined), compared to the results of EPPS16 [398] for \bar{u} , see the text for details.

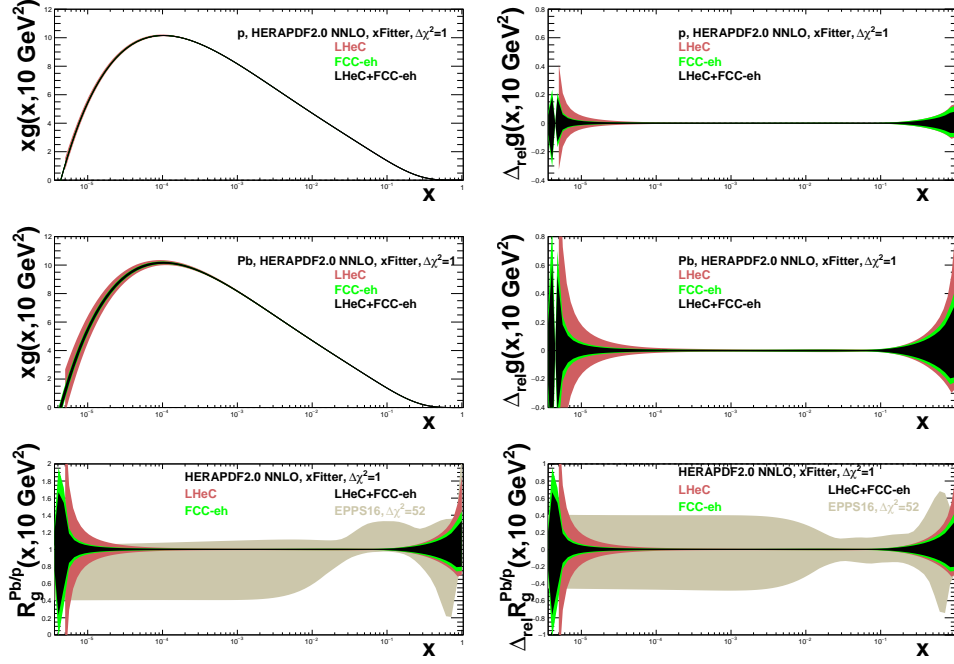


Figure 4.11: Distributions (left) and their relative uncertainties (right) of the gluon density in the proton (top), Pb (middle) and the corresponding nuclear modifications factor (bottom) in an analysis of ep and ePb LHeC and FCC-eh NC plus CC pseudodata using xFitter (both a single set of data and all combined), compared to the results of EPPS16 [398], see the text for details.

3135 4.3 Nuclear diffraction

3136 In Sec. 3.2.5 we have discussed specific processes which will probe the details of the 3D structure
 3137 of the proton. The same processes can be studied in the context of electron-ion scattering
 3138 and used to learn about the partonic structure of nuclei. Inclusive diffraction on nuclei can
 3139 provide important information about the nuclear diffractive parton distribution similarly to the
 3140 diffraction on the proton, see Sec. 3.2.6. Diffractive vector meson production can be studied in
 3141 the nuclear case as well, e.g. within the framework of the dipole model suitable for high energy
 3142 and including non-linear effects in density. In the nuclear case though, one needs to make a
 3143 distinction between coherent and incoherent diffraction. In the coherent process, the nucleus
 3144 scatters elastically and stays intact after the collision. In incoherent diffraction, the nucleus
 3145 breaks up, and individual nucleons can be set free. Still, there will be a large rapidity gap between
 3146 the produced diffractive system and the dissociated nucleus. It is expected that this process will
 3147 dominate the diffractive cross section for medium and large values of momentum transfer. It is
 3148 only in the region of small values of momentum transfer where elastic diffraction is the dominant
 3149 contribution. Dedicated instrumentation in the forward region must be constructed in order to
 3150 clearly distinguish between the two scenarios, see Chapter 10.

3151 4.3.1 Exclusive vector meson diffraction

3152 Calculations for the case of Pb for the coherent diffractive J/ψ production were performed using
 3153 the dipole model [244], see Sec. 3.2.5. In order to apply the dipole model calculation to the
 3154 nuclear case, one takes the independent scattering approximation that is Glauber theory [434].

3155 The dipole amplitude can then be represented in the form

$$N_A(x, \mathbf{r}, \mathbf{b}) = 1 - \prod_{i=1}^A [1 - N(x, \mathbf{r}, \mathbf{b} - \mathbf{b}_i)] . \quad (4.3)$$

3156 Here $N(x, \mathbf{r}, \mathbf{b} - \mathbf{b}_i)$ is the dipole amplitude for the nucleon (see Sec. 3.2.5) and \mathbf{b}_i denotes the
 3157 transverse positions of the nucleons in the nucleus. The interpretation of Eq. (4.3) is that $1 - N$
 3158 is the probability not to scatter off an individual nucleon, and thus $\prod_{i=1}^A [1 - N(\mathbf{r}, \mathbf{b} - \mathbf{b}_i, x)]$ is
 3159 the probability not to scatter off the entire nucleus.

3160 In addition, the following simulation includes the fluctuations of the density profile in the proton,
 3161 following the prescription given in [242–244]. To include these proton structure fluctuations one
 3162 assumes that the gluonic density of the proton in the transverse plane is distributed around
 3163 three constituent quarks (hot spots). These hot spots are assumed to be Gaussian. In practical
 3164 terms one replaces the proton profile $T_p(\mathbf{b})$

$$T_p(\mathbf{b}) = \frac{1}{2\pi B_p} e^{-b^2/(2B_p)} , \quad (4.4)$$

3165 that appears in each individual nucleon scattering probability $N(x, \mathbf{r}, \mathbf{b} - \mathbf{b}_i)$ by the function

$$T_p(\mathbf{b}) = \sum_{i=1}^3 T_q(\mathbf{b} - \mathbf{b}_{q,i}) , \quad (4.5)$$

3166 where the ‘quark’ density profile is given by

$$T_q(\mathbf{b}) = \frac{1}{2\pi B_q} e^{-b^2/(2B_q)} . \quad (4.6)$$

3167 Here $\mathbf{b}_{q,i}$ are the location of the hotspots that are sampled from a two dimensional Gaussian
 3168 distribution whose width is given by parameter B_{qc} . The free parameters B_q and B_{qc} were
 3169 obtained in [243] by comparing with HERA data on coherent and incoherent J/ψ production at
 3170 a photon-proton centre-of-mass energy $W = 75$ GeV, corresponding to fractional hadronic target
 3171 energy loss $x_{IP} = 10^{-3}$. The proton fluctuation parameters obtained are $B_{qc} = 3.3$ GeV $^{-2}$ and
 3172 $B_q = 0.7$ GeV $^{-2}$.

3173 The results for the differential cross section at $t = 0$ for coherent production of J/ψ as a
 3174 function of (virtual) photon-proton energy W for fixed values of Q^2 are shown in Figs. 4.12
 3175 and Figs. 4.13. The calculations for Pb are compared to those on the proton target. We see
 3176 that the cross sections for the nuclear case increase with energy slower than for the proton case
 3177 and are always smaller. Note that, we have already rescaled the diffractive cross section by
 3178 a factor A^2 , as appropriate for comparison of the diffractive cross section on the proton and
 3179 nucleus. In the absence of nuclear corrections their ratio should be equal to 1. The differences
 3180 between the scattering off a nucleus and a proton are also a function of Q^2 . They are larger
 3181 for smaller values of Q^2 and for photoproduction. This is understood from the dipole formulae,
 3182 see Eqs. (3.11), (3.12), (3.13). As explained previously, larger values of scale Q^2 select smaller
 3183 size dipoles, for which the density effects are smaller. Similarly, the differences between the lead
 3184 and proton cases are larger for higher energies. This is because the dipole amplitude grows with
 3185 decreasing values of x which are probed when the energy is increased, and thus the non-linear
 3186 density effects are more prominent at low values of x and Q^2 .

3187 These findings can be summarised by inspecting the ratio of the cross sections, presented as a
 3188 function of x defined as

$$x = \frac{Q^2 + m_{J/\psi}^2}{Q^2 + W^2 + m_{J/\psi}^2 - m_N^2} \quad (4.7)$$

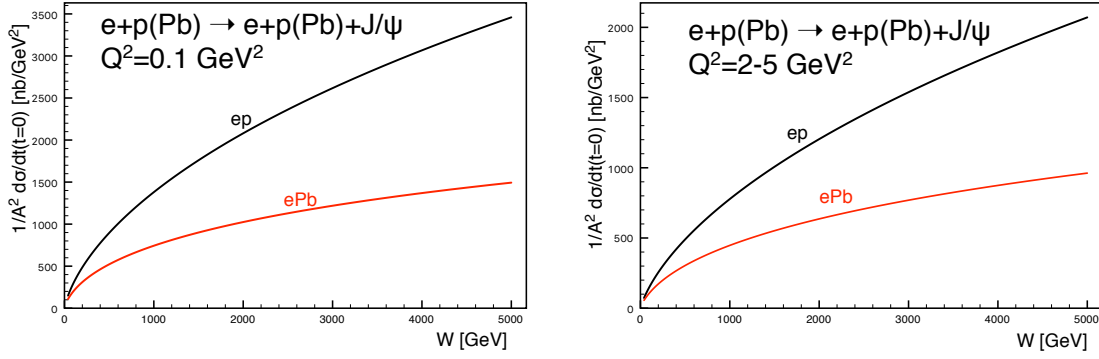


Figure 4.12: Cross section for the coherent diffractive production of the vector meson J/ψ in ePb (red solid curves) and ep (black solid curves) collisions, as a function of the energy W . Left: photoproduction case $Q^2 \simeq 0$, right: $Q^2 = 2 - 5 \text{ GeV}^2$

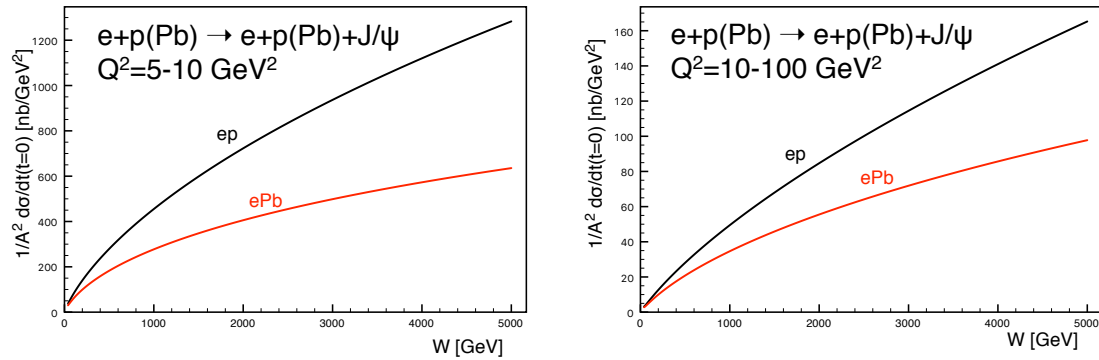


Figure 4.13: Cross section for the coherent diffractive production of the vector meson J/ψ in ePb (red solid curves) and ep (black solid curves) collisions, as a function of the energy W . Left: $Q^2 = 5 - 10 \text{ GeV}^2$, right: $Q^2 = 10 - 100 \text{ GeV}^2$.

3189 which is shown in Fig. 4.14. We observe that the ratio is smaller for smaller values of Q^2 , and it
3190 decreases for decreasing values of x . The results from the dipole model calculations are compared
3191 with the ratio of the gluon density squared obtained from the nuclear PDFs using the EPPS16
3192 set [398]. The reason why one can compare the diffractive cross section ratios with the ratios
3193 for the gluon density squared can be understood from Eqs. (3.11) and (3.12). The diffractive
3194 amplitude is proportional to the gluon density $xg(x, Q^2)$. On the other hand the diffractive cross
3195 section is proportional to the amplitude squared, thus having enhanced sensitivity to the gluon
3196 density. The nuclear PDFs have large uncertainties, which is indicated by the region between
3197 the two sets of dotted lines. The EPPS16 parametrisation is practically unconstrained in the
3198 region below $x = 0.01$. Nevertheless, the estimate based on the dipole model calculation and
3199 the central value of the EPPS16 parametrisation are consistent with each other. This strongly
3200 suggests that it will be hard to disentangle nuclear effects from saturation effects and that only
3201 through a detailed combined analysis of data on the proton and the nucleus firm conclusions
3202 can be established on the existence of a new non-linear regime of QCD.

3203 The differential cross section $d\sigma/dt$ as a function of the negative four momentum transfer squared
3204 $-t$ for the case of coherent and incoherent production is shown in Fig. 4.15. Coherent and inco-
3205 herent diffraction cross sections are computed from the dipole model in the following way. The
3206 coherent diffractive cross section is obtained by averaging the diffractive scattering amplitude

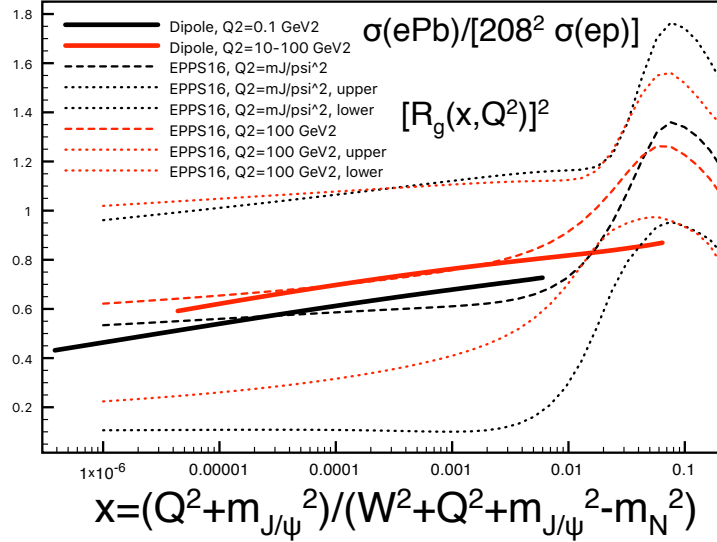


Figure 4.14: Ratio of coherent J/ψ production diffractive cross sections for Pb and proton as a function of the variable x defined in Eq. (4.7). Solid lines: dipole model calculation, for $Q^2 = 0.1 \text{ GeV}^2$ (black) and $Q^2 = 10 - 100 \text{ GeV}^2$ (red). Dotted and dashed lines correspond to the nuclear ratio for the gluon density squared using the EPPS16 parametrisation [398] of the nuclear parton distribution functions. Black and red dashed lines are the central sets for $Q^2 = M_{J/\psi}^2$ and $Q^2 = 100 \text{ GeV}^2$. The dotted lines correspond to the low and high edges of the Hessian uncertainty in the EPPS16 parametrisation. The difference between the two dotted lines is thus indicative of the parametrisation uncertainty for the nuclear ratio. These ratios, that can also be measured in ultraperipheral collisions [435], are larger than the values $0.2 - 0.4$ at $x \simeq 10^{-5}$ predicted by the relation between diffraction and nuclear shadowing [401].

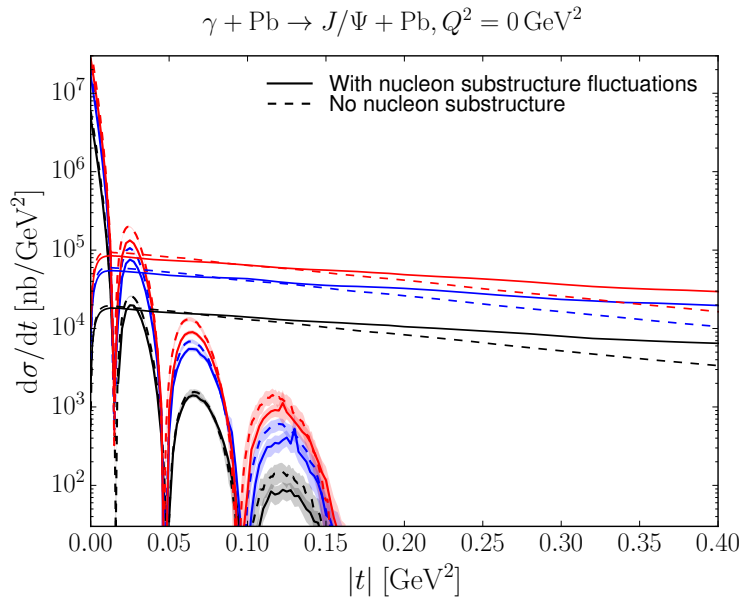


Figure 4.15: The differential cross sections for coherent and incoherent production of J/ψ in $e\text{Pb}$ as a function of the negative four momentum transfer squared $-t$, for photoproduction, $Q^2 = 0$. The lines showing dips are for coherent production, and those extending to large $|t|$ are for incoherent. The solid (dashed) lines are the results with (without) nucleon substructure fluctuations. Black, blue, red are for $W = 0.1, 0.813, 2.5 \text{ TeV}$, respectively.

3207 over the target configurations and taking the square

$$\frac{d\sigma}{dt} = \frac{1}{16\pi} |\langle \mathcal{A}(x, Q, \Delta) \rangle|^2. \quad (4.8)$$

3208 Here the brackets $\langle \dots \rangle$ refer to averages over different configurations of the target. The incoher-
 3209 ent cross section is obtained by subtracting the coherent cross section from the total diffractive
 3210 cross section. It is standardly assumed that it takes the form of a variance of the diffractive
 3211 scattering amplitude

$$\frac{d\sigma}{dt} = \frac{1}{16\pi} \left(\langle |\mathcal{A}(x, Q, \Delta)|^2 \rangle - |\langle \mathcal{A}(x, Q, \Delta) \rangle|^2 \right), \quad (4.9)$$

3212 which should be valid for small $|t|$. The t dependence, and the relation between the impact
 3213 parameter and t through the Fourier transform, makes diffractive scattering a sensitive probe
 3214 of the internal geometric structure of hadrons and nuclei. In particular, because the incoherent
 3215 cross section has the form of a variance of the amplitude, it is sensitive to the amount of
 3216 fluctuations in impact parameter space.

3217 The results in Fig. 4.15 (results for higher Q^2 are very similar) indicate that the incoherent
 3218 production is dominant for most values of $-t$, except for the very small momentum transfers,
 3219 about $|t| < 0.02 \text{ GeV}^2$. Thus, dedicated instrumentation which will allow us to distinguish
 3220 between the two cases is essential if one wants to measure the coherent process in a reasonably
 3221 wide range of $|t|$. As in the proton case, the coherent t distribution exhibits characteristic dips.
 3222 However, in the case of the nuclear targets the dips occur for much smaller values of t . This is
 3223 related to the much larger value of the dipole amplitude for a wide range of impact parameters
 3224 in the case of nuclear targets compared to the proton case.

3225 Another interesting aspect, see Sec. 3.2.5, is the effect of the transverse structure of the target in
 3226 nuclear coherent and incoherent diffraction. For example, in the formulation shown above [244]
 3227 a fixed number of hot spots was considered, while in [248] (see also [245] for a realisation
 3228 using small- x evolution) a growing number with $1/x$ is implemented. In both cases, the ratio
 3229 of incoherent to coherent diffraction decreases with W , being smaller for larger nuclei. This
 3230 decrease is sensitive to the details of the distribution of hot spots - thus, to the fluctuations
 3231 of the gluon distribution in transverse space. It also shows interesting dependencies on the
 3232 mass of the produced vector meson and on Q^2 , resulting in the ratio being smaller for lighter
 3233 vector mesons and for lower Q^2 . Besides, the hot spot treatment also has some effects on the
 3234 distributions in momentum transfer, see Fig. 4.15. In order to check these ideas, both the
 3235 experimental capability to separate coherent from incoherent diffraction, and a large lever arm
 3236 in W and Q^2 as available at the LHeC, are required.

3237 We thus conclude that by investigating coherent and incoherent diffractive scattering on nuclei,
 3238 one gets unique insight into the spatial structure of matter in nuclei. On the one hand, the
 3239 coherent cross section, which is obtained by averaging the amplitude before squaring it, is
 3240 sensitive to the average spatial density distribution of gluons in transverse space. On the other
 3241 hand, the incoherent cross section, which is governed by the variance of the amplitude with
 3242 respect to the initial nucleon configurations of the nucleus, measures fluctuations of the gluon
 3243 density inside the nucleus. In the case of a nucleus, the diffractive production rate is controlled by
 3244 two different scales related to the proton and nucleus size. At momentum scales corresponding
 3245 to the nucleon size $|t| \sim 1/R_p^2$ the diffractive cross section is almost purely incoherent. The
 3246 t -distribution in coherent diffractive production off the nucleus gives rise to a dip-type structure
 3247 for both saturation and non-saturation models, while in the case of incoherent production at
 3248 small $|t|$, both saturation and non-saturation models do not lead to dips [244]. This is in drastic

3249 contrast to the diffractive production off the proton where only saturation models lead to a
 3250 dip-type structure in the t -distribution at values of $|t|$ that can be experimentally accessible.
 3251 Therefore, diffractive production offers a unique opportunity to measure the spatial distribution
 3252 of partons in the protons and nuclei. It is also an excellent tool to investigate the approach to
 3253 unitarity in the high energy limit of QCD.

3254 While we have focused here on J/ψ production, lighter vector mesons like ρ, ω, ϕ could also be
 3255 studied. They should show a different Q^2 dependence and their larger sizes would make them
 3256 lie closer to the black disk regime. Also the dominance of two-jet events in photoproduction
 3257 would provide sensitivity to the approach to the unitarity limit [401].

3258 4.3.2 Inclusive diffraction on nuclei

3259 In Sec. 3.2.6, a study of the prospects for extracting diffractive parton densities in the proton was
 3260 presented following [256]. Similar considerations apply to diffraction in eA as to ep collisions.
 3261 The main difference is the larger contribution from incoherent diffraction ³ $e + A \rightarrow e + X + A^*$
 3262 than from coherent diffraction $e + A \rightarrow e + X + A$, the former dominating for $|t|$ larger than
 3263 a few hundredths of a GeV^2 . In the following we focus on coherent diffraction, which could be
 3264 distinguished from the incoherent case using forward detectors [1].

3265 Assuming the same framework (collinear factorization for hard diffraction, such that Eq. (3.24),
 3266 and Regge factorization, Eq. (3.26) as introduced for ep in Sec. 3.2.6 also hold for eA), nuclear
 3267 diffractive PDFs (nDPDFs) can be extracted from the diffractive reduced cross sections. It
 3268 should be noted that such nDPDFs have never been measured. With the same electron energy
 3269 $E_e = 60 \text{ GeV}$ and nuclear beams with $E_N = 2.76 \text{ TeV/nucleon}$ for the LHeC, the kinematic
 3270 coverage is very similar to that shown in Fig. 3.42. For details, see Ref. [256].

3271 The nuclear modification factors for $F_2^{D(3)}$ and $F_L^{D(3)}$ from the FGS models [401] are shown in
 3272 Fig. 4.16 where, in analogy to Eq. (4.1), the diffractive nuclear modification factor reads

$$R_k^A(\beta, \xi, Q^2) = \frac{f_{k/A}^{D(3)}(\beta, \xi, Q^2)}{A f_{k/p}^{D(3)}(\beta, \xi, Q^2)}. \quad (4.10)$$

3273 The model in [401] employs Gribov inelastic shadowing [252] which relates diffraction in ep
 3274 to nuclear shadowing for total and diffractive eA cross sections. It assumes that the nuclear
 3275 wave function squared can be approximated by the product of one-nucleon densities, neglects
 3276 the t -dependence of the diffractive γ^* -nucleon amplitude compared to the nuclear form factor,
 3277 introduces a real part in the amplitudes [436], and considers the colour fluctuation formalism
 3278 for the inelastic intermediate nucleon states [437]. There are two variants of the model, named
 3279 H and L, corresponding to different strengths of the colour fluctuations, giving rise to larger and
 3280 smaller probabilities for diffraction in nuclei with respect to that in proton, respectively. Results
 3281 from both model versions are shown in Figs. 4.16 and 4.17.

3282 The pseudodata for the reduced cross sections are generated assuming 5% systematic error
 3283 and statistic errors calculated for the integrated luminosity of 2 fb^{-1} . A selected subset of
 3284 the simulated data is shown in Fig. 4.17. The large kinematic coverage and small uncertainty
 3285 (dominated by the assumed systematics) illustrated in this figure compared to Fig. 3.44 make it
 3286 clear that an accurate extraction of nDPDFs in ^{208}Pb in an extended kinematic region, similar
 3287 to that shown in Figs. 3.45 and 3.46, will be possible.

³ A^* denotes a final state in which the nucleus has dissociated to a system of at least two hadrons, but the rapidity gap signature that defines the diffractive event is still present.

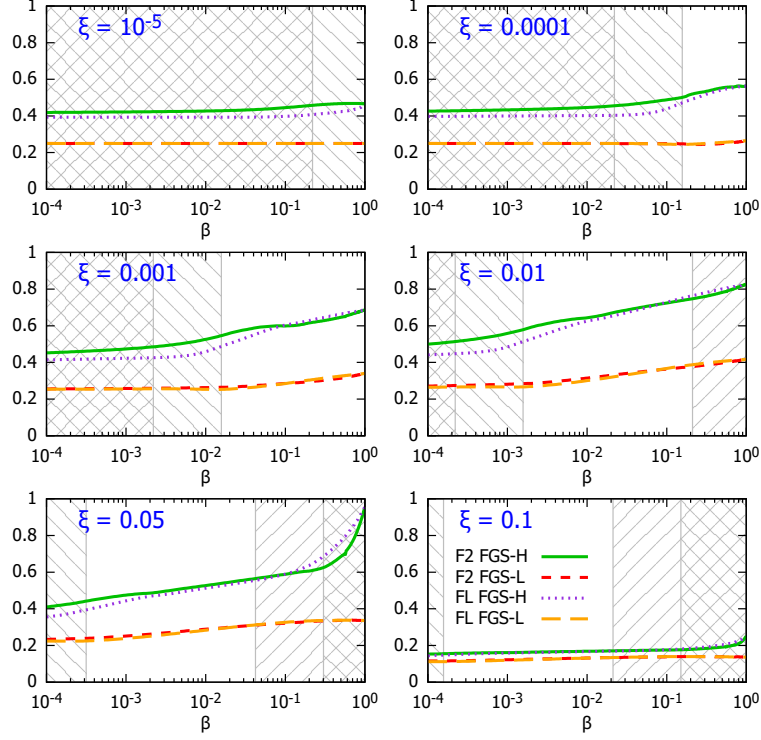


Figure 4.16: Nuclear modification factor, Eq. (4.10), for $F_2^{D(3)}$ and $F_L^{D(3)}$ in ^{208}Pb versus β , at $Q^2 = 10 \text{ GeV}^2$ and for different ξ , for the models H and L in [401]. The ‘\’ and ‘/’ hatched areas show kinematically excluded regions for $E = 2.76$ and 19.7 TeV/nucleon , respectively.

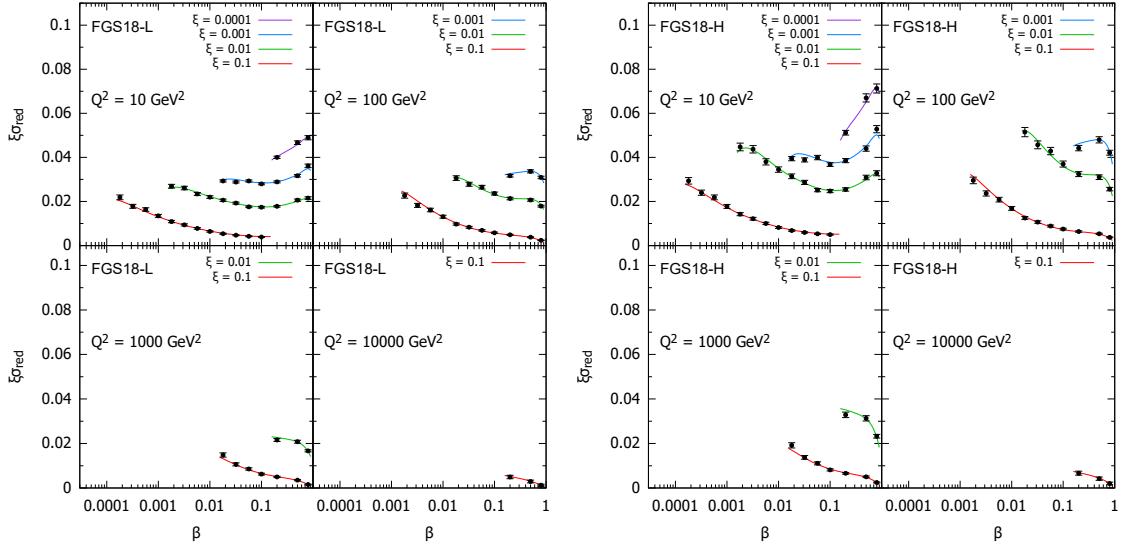


Figure 4.17: An indicative subset of simulated data for the diffractive reduced cross section as a function of β in bins of ξ and Q^2 for $e^{208}\text{Pb}$ collisions at the LHeC, in the models in [401]. The curves for $\xi = 0.01, 0.001, 0.0001$ are shifted up by $0.01, 0.02, 0.03$, respectively.

4.4 New Dynamics at Small x with Nuclear Targets

As discussed in Sec. 3.2.2, theoretical expectations [403] indicate that fixed-order perturbation theory leading to the DGLAP evolution equations should eventually fail. When x decreases, $\alpha_s \ln 1/x$ becomes large and these large logarithms must be resummed, leading to the BFKL equation. Furthermore, when the parton density becomes large, the linear approximation that underlies both DGLAP and BFKL breaks, and non-linear processes must be taken into account to compute parton evolution. The CGC [402] offers a non-perturbative but weak coupling effective theory to treat dense parton systems in a systematic and controlled way. One of the important predictions of the CGC is that in a dense parton system saturation occurs leading to the emergence of a new dynamical scale – the saturation scale Q_{sat} , which increases with the energy.

The parton density in a hadron becomes high both through evolution – when energy or $1/x$ becomes large, and/or when partons are accumulated by overlapping nucleons – when mass number A becomes large in a nucleus. In the nucleus rest frame, the virtual photon fluctuations at small $x < (2m_N R_A)^{-1}$, with m_N the nucleon mass and R_A the nuclear radius, acquire a lifetime larger than the time taken to traverse the nucleus and, thus, all partons within a transverse area $\sim 1/Q^2$ are simultaneously probed. Actually, the parameter determining the transition between linear and non-linear dynamics is the parton density and, therefore, the onset of this new regime of QCD and its explanation must be tested, as commented in [1], exploring both decreasing values of x and increasing values of A in a kinematic $x - Q^2$ region where, in order to be sensitive to differences in evolution, enough lever arm in $Q^2 \gg \Lambda_{\text{QCD}}^2$ at small x is available. The saturation scale Q_{sat} that characterises the typical gluon momentum in a saturated hadron wave function increases with nuclear size, $Q_{sat}^2 \propto A^{1/3}$. Therefore, in eA collisions the perturbatively saturated regime is achieved at parametrically larger x than in a proton – a prediction not only of the CGC but of all multiple scattering models that anticipate an approach to the black disk, unitarity limit.

The opportunities to establish the existence of saturation in lepton-nucleus collisions are numerous. They include inclusive observables, both total and diffractive cross sections, and less inclusive ones like correlations:

- Tension in DGLAP fits for inclusive observables: As discussed in [1, 218] and in Sec. 3.2.4, deviations from fixed-order perturbation theory can be tested by the tension that would appear in the description within a DGLAP fit of observables with different sensitivities to the sea and the glue, for example F_2 and F_L (or reduced cross sections at different energies) or $F_2^{\text{inclusive}}$ and $F_2^{\text{heavy quarks}}$. In [438], such an exercise was performed considering F_2 and F_L pseudodata for eAu collisions at the EIC [224] using reweighting techniques. While the results for EIC energies are shown not to be conclusive due to the reduced lever arm in $Q^2 > Q_{sat}^2 \gg \Lambda_{\text{QCD}}^2$, the much larger centre-of-mass energies at the LHeC (and FCC-eh) should make possible a search for tensions between different observables.
- Saturation effects in diffraction: A longstanding prediction of saturation [229, 439, 440] is a modification of the diffractive cross section in nuclei with respect to protons, with a suppression (enhancement) at small (large) β due to the approach of the nucleus to the black disk limit, where elastic and diffractive scattering become maximal, and the behaviour of the different Fock components of the virtual photon wave function. Such effects can also be discussed in terms of a competition of nuclear shadowing with the probability that the event remains diffractive in the multiple scattering process [401]. This leads to the generic expectation of an enhancement of the ratio of the coherent diffractive

3334 cross section in nucleus over that in protons, in non-linear approaches with respect to
3335 linear ones [224].

3336 • Correlations: Correlations have been considered for a long time as sensitive probes of the
3337 underlying production dynamics. For example, the cross section for the production of
3338 two jets with the same hardness and widely separated in rapidity, called Mueller-Navelet
3339 jets [441], was proposed as a test of BFKL versus DGLAP dynamics, but the effect of
3340 saturation has not been widely studied although it has the large potentiality of differ-
3341 entiating linear resummation from non-linear saturation where non-trivial nuclear effects
3342 could appear. Correlations between jets were analysed in [1] for the LHeC kinematics,
3343 both in inclusive and diffractive events, see the formalism in [442]. On the other hand, the
3344 azimuthal decorrelation of particles and jets when saturation effects are at work – at small
3345 x , studied by the difference between collisions involving proton and nuclei, was proposed
3346 long ago in dAu collisions at the Relativistic Hadron Collider [443, 444]. It was studied
3347 in [1] for the LHeC kinematics, see recent developments in [445] and the extension to
3348 forward dijet production in [446]. It could also be analysed in ultraperipheral collisions at
3349 the LHC, see Sec. 7.5.

3350 4.5 Collective effects in dense environments – the ‘ridge’

3351 One of the most striking discoveries [447] at the LHC is, that in all collision systems, from
3352 small (pp and pA) to large (AA), many of the features that are considered as indicative of the
3353 production of a dense hot partonic medium are observed (see e.g. reviews [448–450] and references
3354 therein). The most celebrated of such features is the long rapidity range particle correlations
3355 collimated in azimuth, named the ‘ridge’, shown in Fig. 4.18. The dynamics underlying this
3356 phenomena, either the formation of QGP and the existence of strong final state interactions, or
3357 some initial state dynamics that leaves imprint on the final observables, is under discussion [451].
3358 While observed in photoproduction on Pb in UPCs at the LHC [452], its existence in smaller
3359 systems like e^+e^- [453] at LEP and ep at HERA [454] has been scrutinised, but the results are
3360 not conclusive.

3361 In this respect, measurements in ep and eA collisions at the LHeC at considerable center-of-
3362 mass energies will offer crucial additional information. For example, the collision of the virtual
3363 photon with the proton at the LHeC can be considered as a high energy collision of two jets or
3364 ‘flux tubes’, as discussed in Refs. [457, 458] and illustrated in Fig. 4.18. This can lead to the
3365 production of ‘ridges’ and other novel configurations of gluons and quarks and will be measured
3366 uniquely at the LHeC.

3367 4.6 Novel QCD Nuclear Phenomena at the LHeC

3368 Beyond the topics discussed above there are many novel phenomena which can be explored in eA
3369 collisions at LHeC or FCC-eh, in a high energy regime and using dedicated instrumentation. We
3370 shall briefly review some of these phenomena, which can be understood utilizing the light-front
3371 framework of QCD, for a review see [459].

3372 One of the most important theoretical tools in high energy physics is Dirac’s light-front (LF)
3373 time: $\tau = x^+ = t + z/c$, the time along the light-front [460], a concept which allows all of the
3374 tools and insights of Schrödinger’s quantum mechanics and the Hamiltonian formalism to be

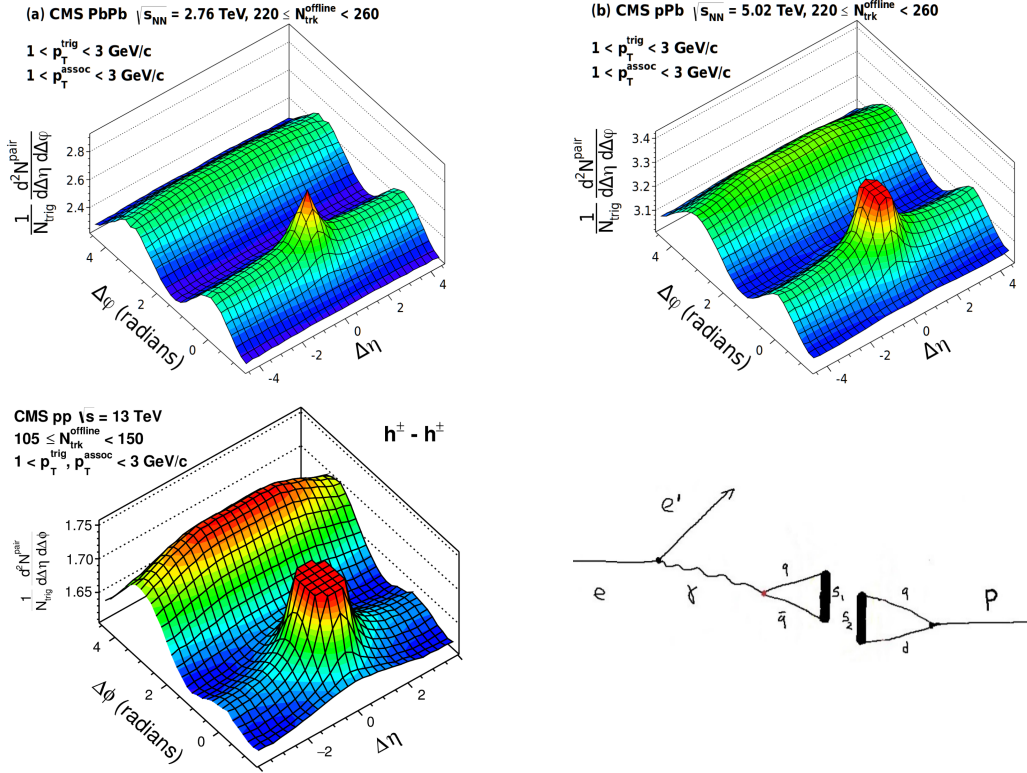


Figure 4.18: Left and top right: Collective effects seen in high-multiplicity two-particle azimuthal correlation, as observed by CMS in PbPb, pPb [455], and pp [456] collisions. Bottom right: Schematic illustration for the production of *ridge*-like effects in ep or eA scattering at the LHeC [457].

3375 applied to relativistic physics [459]. When one takes a photograph, the object is observed at a
 3376 fixed LF time. Similarly, Compton $\gamma p \rightarrow \gamma' p''$ and deep-inelastic lepton-proton scattering are
 3377 measurements of proton structure at fixed LF time. Unlike ordinary *instant time* t , physics at
 3378 fixed τ is Poincaré invariant; i.e. independent of the observer's Lorentz frame. Observations
 3379 at fixed τ are made within the causal horizon. LF time τ reduces to ordinary time t in the
 3380 nonrelativistic limit $c \rightarrow \infty$.

3381 The LF wavefunctions (LFWF) of hadrons are superpositions of $\Psi_n^H(x_i, \vec{k}_{\perp i}, \lambda_i) = \langle \Psi_H | n \rangle$,
 3382 the Fock state projections of the eigensolution of the QCD LF Hamiltonian $H_{QCD} | \Psi_H \rangle =$
 3383 $M_H^2 | \Psi_H \rangle$. They encode the underlying structure of bound states in quantum field theory and
 3384 underlie virtually every observable in hadron physics. Hadronic LFWFs can also be measured
 3385 directly by the Ashery method [461], the coherent diffractive dissociation of high energy hadrons
 3386 into jets [462, 463]. In the diffractive dissociation of a high energy hadron into quark and gluon
 3387 jets by two-gluon exchange, the cross-section measures the square of the second transverse
 3388 derivative of the projectile LFWF. Similarly, the dissociation of a high energy atom such as
 3389 positronium or *true muonium* ($[\mu^+ \mu^-]$) can be used to measure the transverse derivative of its
 3390 LFWFs.

3391 Hadronic LFWFs are defined at fixed $\tau = -x^+ = t + z/c$; they are thus off-shell in the total
 3392 $P^- = P^0 - P^z$, not energy P^0 [459]. Thus LFWFs are also off-shell in $\mathcal{M}^2 = P^+ P^- - P_{\perp}^2 =$
 3393 $[\sum_i k_i^{\mu}]^2 = \sum_i \frac{k_{\perp i}^2 + m^2}{x_i}$, the invariant mass squared of the constituents in the n -particle Fock
 3394 state. LFWFs are thus functions of the invariant mass squared of the constituents in the
 3395 Fock state. For a two-particle Fock state, $\mathcal{M}^2 = \frac{k_{\perp}^2 + m^2}{x(1-x)}$. Thus, the constituent transverse

3396 momenta $k_{\perp i}^2$ do appear alone as a separate factor in the LFWF; the transverse momenta are
 3397 always coupled to the longitudinal LF momentum fractions x_i . This is the light-front version
 3398 of rotational invariance. Only positive $k_i^+ = k_i^0 + k_i^z \geq 0$ and $0 \leq x_i = \frac{k_i^+}{P^+} \leq 1$ appear,
 3399 where $\sum_i x_i = 1$. In addition, $J^z = \sum_i L_i^z + S_i^z$, as well as $P^+ = \sum_i k_i^+$ and $\vec{P}_{\perp} = \sum_i \vec{k}_{\perp i}$ are
 3400 conserved at every vertex – essential covariant kinematical constraints. A remarkable property:
 3401 the anomalous gravitomagnetic moment of every LF Fock state vanishes at $Q^2 = 0$. The
 3402 LFWFs of bound states are off-shell in $P^- = \sum_i k_i^-$, but they tend to be maximal at minimal
 3403 off-shellness; i.e. minimal invariant mass. In fact, in the holographic LFWFs where colour is
 3404 confined, the LFWFs of hadrons have fast Gaussian fall-off in invariant mass. This feature also
 3405 underlie intrinsic heavy quark Fock states: the LFWFs have maximal support when all of the
 3406 constituents have the same rapidity y_i ; i.e. $x_i \propto \sqrt{m_i^2 + k_{\perp i}^2}$. Thus the heavy quarks have the
 3407 highest momentum fractions x_i .

3408 Conversely, light-front wavefunctions provide the boost-invariant transition amplitude which
 3409 convert the free quark and gluons into the hadronic eigenstates of QCD. Thus, knowing the
 3410 LFWFs allows one to compute *hadronization at the amplitude level* – how the coloured quarks
 3411 and gluons produced in a deep inelastic scattering event $ep \rightarrow e'X$ at the LHeC are confined
 3412 and emerge as final-state hadrons.

3413 The LF formalism leads to many novel nuclear phenomena, such as *hidden colour* [464] *colour*
 3414 *transparency* [465], *nuclear-bound quarkonium* [466], *nuclear shadowing and antishadowing* of
 3415 nuclear structure functions, etc. For example, there are five distinct colour-singlet QCD Fock
 3416 state representations of the six colour-triplet quarks of the deuteron. These hidden-colour Fock
 3417 states become manifest when the deuteron fluctuates to a small transverse size, as in mea-
 3418 surements of the deuteron form factor at large momentum transfer. One can also probe the
 3419 hidden-colour Fock states of the deuteron by studying the final state of the dissociation of the
 3420 deuteron in deep inelastic lepton scattering at the LHeC $eD \rightarrow e'X$, where X can be $\Delta^{++} + \Delta^-$,
 3421 six quark jets, or other novel colour-singlet final states.

3422 The LF wave functions provide the input for scattering experiments at the amplitude level,
 3423 encoding the structure of a projectile at a single light-front time τ [459]. For example, consider
 3424 photon-ion collisions. The incoming photon probes the finite size structure of the incoming
 3425 nucleus at fixed LF time, like a photograph – not at a fixed instant time, which is acausal.
 3426 Since the nuclear state is an eigenstate of the LF Hamiltonian, its structure is independent of
 3427 its momentum, as required by Poincaré invariance. One gets the same answer in the ion rest
 3428 frame, the CM frame, or even if the incident particles move in the same direction, but collide
 3429 transversely. There are no colliding *pancakes* using the LF formalism.

3430 The resulting photon-ion cross-section is not point-like; it is shadowed: $\sigma(\gamma A \rightarrow X) = A^{\alpha} \sigma(\gamma N \rightarrow$
 3431 $X)$, where A is the mass number of the ion, N stands for a nucleon, and the power $\alpha \approx 0.8$
 3432 reflects Glauber shadowing [467]. The shadowing stems from the destructive interference of
 3433 two-step and one-step amplitudes, where the two-step processes involve diffractive reactions on
 3434 a front-surface nucleon which shadows the interior nucleons. Thus the photon interacts primar-
 3435 ily on the front surface. Similarly, a high energy ion-ion collision $A_1 + A_2 \rightarrow X$ involves the
 3436 overlap of the incident frame-independent LFWFs. The initial interaction on the front surface
 3437 of the colliding ions can resemble a shock wave.

3438 In the case of a deep inelastic lepton-nucleus collision $\gamma^* A \rightarrow X$, the two-step amplitude involves
 3439 a leading-twist diffractive deep inelastic scattering (DDIS) $\gamma^* N_1 \rightarrow V^* N_1$ on a front surface
 3440 nucleon N_1 and then the on-shell propagation of the vector system V^* to a downstream nucleon
 3441 N_2 where it interacts inelastically: $V^* N_2 \rightarrow X$. If the DDIS involves Pomeron exchange, the two-

3442 step amplitude interferers destructively with the one-step amplitude $\gamma^* N_1 \rightarrow X$ thus producing
3443 shadowing of the nuclear parton distribution function at low $x < 0.1$. On the other hand, if
3444 the DDIS process involves $I = 1$ Reggeon exchange, the interference is constructive, producing
3445 *flavour-dependent* leading-twist antishadowing [467] in the domain $0.1 < x < 0.2$.

3446 One can also show that the Gribov-Glauber processes, which arise from leading-twist diffractive
3447 deep inelastic scattering on nucleons and underly the shadowing and antishadowing of nuclear
3448 structure functions [467], prevent the application of the operator product expansion to the
3449 virtual Compton scattering amplitude $\gamma^* A \rightarrow \gamma^* A$ on nuclei and thus negate the validity of the
3450 momentum sum rule for deep inelastic nuclear structure functions [468].

Chapter 5

Higgs Physics with LHeC

5.1 Signal Strength and Couplings

5.1.1 Introduction

The Higgs boson was discovered in 2012 by ATLAS [469] and CMS [470] at the Large Hadron Collider (LHC). It is the most recently discovered and least explored part of the Standard Model. The Higgs boson (H) is of fundamental importance as it is related to the spontaneous breaking of a locally symmetric gauge theory, to a mechanism predicted by [312, 313, 471] and independently by [472], in which the intermediate vector bosons are explained to be massive¹ while the photon remains massless. Fermions obtain a mass via the Yukawa couplings with the Higgs field. Following the discovery of the Higgs boson, its physics and thorough exploration has become a central theme of the physics programme at the LHC. Any high-energy future collider project, beginning with the high luminosity upgrade of the Large Hadron Collider, the HL-LHC, underway to collect data in a decade hence, has put the potential to precisely study the properties of the Higgs boson into its center of attention, for understanding its characteristics and hoping to open a new window into physics extending beyond the Standard Model, see for example [473, 474]. In this section we present the potential to explore the SM Higgs physics at the LHeC and to certain extent at FCC-eh also.

A first challenge on the physics of the Higgs boson is to establish whether it indeed satisfies the properties inherent to the Standard Model (SM) regarding its production and decay mechanisms. The SM neutral H boson decays into pairs of fermions, $f\bar{f}$. The dominant decay is $H \rightarrow b\bar{b}$ with a branching fraction of about 58%. The branching scales with the square of the fermion mass, m_f^2 . The next prominent fermionic decay therefore is $H \rightarrow \tau^+\tau^-$ with 6.3% followed by the charm decay with a predicted branching fraction of 2.9%. The Higgs boson also decays into pairs of W and Z bosons at a rate of 21.5% and 2.6%, respectively. Loop diagrams enable the decay into gluon and photon pairs with a branching of 8.2 and 0.2%, respectively. The seven most frequent decay channels, ordered according to descending branching fractions, thus are into $b\bar{b}$, W^+W^- , gg , $\tau^+\tau^-$, $c\bar{c}$, ZZ and $\gamma\gamma$. Together these are predicted to represent a total SM branching fraction of 99.9%. At the LHC these and rarer decays can be reconstructed,

¹ The mass of the W boson, M_W , is generated through the vacuum expectation value, η , of the Higgs field (Φ) and given by the simple relation $M_W = g\eta/\sqrt{2}$ where g is the weak interaction coupling. Here $\eta = \sqrt{-\mu^2/2\lambda}$ with the two parameters of the Higgs potential that is predicted to be $V = -\mu^2\Phi^+\Phi - \lambda(\Phi^+\Phi)^2$. The Higgs mass is given as $M_H = 2\eta\sqrt{\lambda}$ while the mass of the Z boson is related to M_W with the electroweak mixing angle, $M_Z = M_W/\cos\Theta_W$.

3480 with the exception of the charm decay for reasons of prohibitive combinatorial background. The
 3481 main purpose of this paper is to evaluate the prospects for precisely measuring these channels
 3482 in electron-proton scattering.

3483 5.1.2 Higgs Production in Deep Inelastic Scattering

3484 In deep inelastic electron-proton scattering, the Higgs boson is predominantly produced through
 3485 WW fusion in charged current DIS (CC) scattering, Fig. 1. The next large Higgs production
 3486 mode in ep is $ZZ \rightarrow H$ fusion in neutral current DIS (NC) scattering, Fig. 1, which has a smaller
 but still sizable cross section. These ep Higgs production processes are very clean for a number

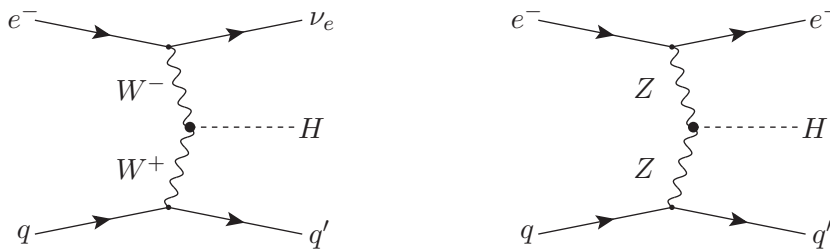


Figure 5.1: Higgs boson production in charged (left) and neutral (right) current deep inelastic electron-proton scattering to leading order.

3487
 3488 of reasons:

- 3489 • even at the high luminosity of $10^{34} \text{ cm}^{-2}\text{s}^{-1}$ the inclusive pileup is only 0.1 (1) for the
 3490 LHeC (FCC-eh) and the final state signature therefore free from event overlap, in contrast
 3491 to the HL-LHC where it will typically be 150;
- 3492 • in ep , contrary to pp , there is no initial nor final state colour (re)connection;
- 3493 • the higher-order corrections are small. For the total CC process they were estimated [475]
 3494 to be of the order of only 1% for the QCD part, subject to cut dependencies yielding
 3495 shape changes up to 20%, and -5% for the QED part (with a weak dependence on
 3496 the PDF choice). The smallness of the QCD corrections was attributed mainly to the
 3497 absorption of gluon and quark radiation effects in the evolution of the parton distributions
 3498 (PDFs) [475]. The PDFs will be measured with very high precision at any of the ep
 3499 colliders here considered, see Chapter 3, thus allowing a unique self-consistency of Higgs
 3500 cross section measurements.

3501 The NC reaction is even cleaner than the CC process as the scattered electron fixes the kinematics
 3502 more accurately than the missing energy. While in pp both WW and ZZ processes are hardly
 3503 distinguishable, in ep they uniquely are, which provides an important, precise constraint on the
 3504 WWH and ZZH couplings.

3505 5.1.3 Kinematics of Higgs Production

3506 At HERA the kinematics was conveniently reconstructed through event-wise measurements of
 3507 Q^2 and y . The reconstruction of the kinematics in charged currents uses the inclusive hadronic
 3508 final state measurements. Based on the energies E'_e and E_h and the polar angles Θ_e and Θ_h

3509 of the scattered electron and the hadronic final state, respectively, one obtains a redundant
 3510 determination of the kinematics in neutral current scattering. This permits a cross calibration
 3511 of calorimetric measurements, of the electromagnetic and hadronic parts and of different regions
 3512 of the detector, which is a major means to achieve superb, sub-percent precision in ep collider
 3513 measurements. Methods have been developed to optimise the kinematics reconstruction and
 3514 maximise the acceptance by exploiting the redundant determination of the scattering kinematics,
 3515 see for example [476]. The basic kinematic distributions of Q^2 , x and y are shown in Fig. 5.2.
 The average (Q^2, x) values for Higgs production at the LHeC [FCC-eh] are $(2000 \text{ GeV}^2, 0.02)$

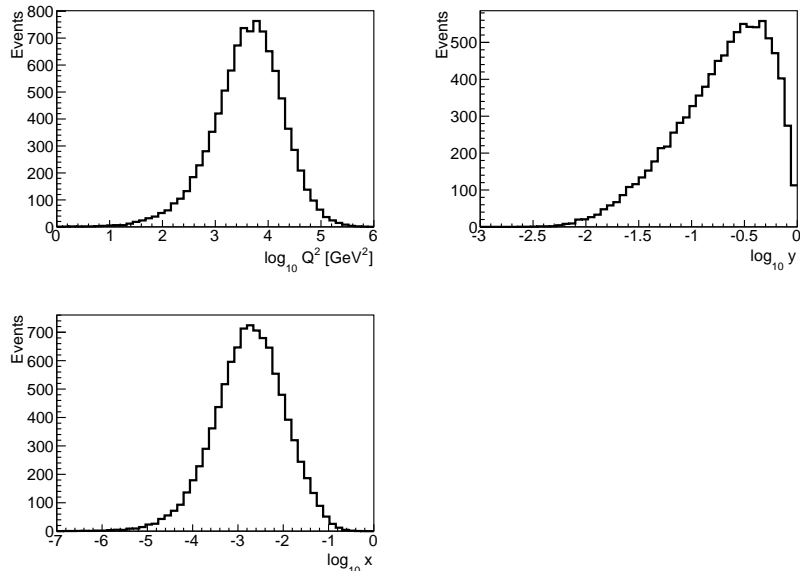


Figure 5.2: Distributions for $ep \rightarrow \nu H X$ events of the parton-level negative 4-momentum transfer squared, Q^2 (top left), Bjorken x (bottom left) and the inelasticity $y = Q^2/sx$ (top right) for the FCC-eh ($\sqrt{s} = 3.5 \text{ TeV}$). Events generated with MadGraph, see Tab. 5.1.

3516 [(6500 $\text{GeV}^2, 0.0016$)]. This is placed very well in the kinematic plane, shown above.
 3517

3518 As is described in this paper elsewhere, constraints for a large pseudorapidity or polar angle,
 3519 $\eta = \ln \tan \theta/2$, acceptance of the apparatus arise i) for the backward region (the polar angle
 3520 is defined w.r.t. the proton beam direction) from the need to reconstruct electrons at low Q^2
 3521 enabling low x physics and ii) for the forward region to cover a maximum region towards large
 3522 x at medium Q^2 with the reconstruction of the hadronic final state. The acceptance therefore
 3523 extends, for the LHeC, to pseudorapidities of $\eta = \pm 5$, which for the FCC-eh case is extended to
 3524 $\eta = \pm 6$. The large acceptance is in particular suitable for the reconstruction of Vector-Boson-
 3525 Fusion Higgs boson event signatures, see Fig. 5.3 for the typical pseudorapidity distributions of
 3526 Higgs boson event signature in DIS at the most asymmetric FCC-eh collider configuration.

3527 Geometric acceptances due to kinematic constraints in the pseudorapidity on the Higgs decay
 3528 products for both LHeC and FCC-eh are further illustrated in Fig. 5.4. The acceptances are
 3529 calculated for a basic selection of all final states with $p_T > 15 \text{ GeV}$ and a coverage of the forward
 3530 jet up to $\eta = 5$ and $\eta = 6$, respectively, for both colliders. As seen from Fig. 5.4, the acceptances
 3531 are higher for the less asymmetric LHeC beam configuration and about the same for hadronic
 3532 calorimetry up to $\eta = 5$ and $\eta = 6$. Hence, the LHeC calorimeter is designed for $\eta = 5$. The
 3533 optimal hadronic calorimetry coverage for FCC-eh is clearly $\eta = 6$ yielding significantly higher
 3534 acceptances in comparison to an $\eta = 5$ calorimetry. From Fig. 5.4, it is apparent that for both
 3535 collider configurations the Higgs decay products would require tagging capabilities up $\eta = 3.5$,

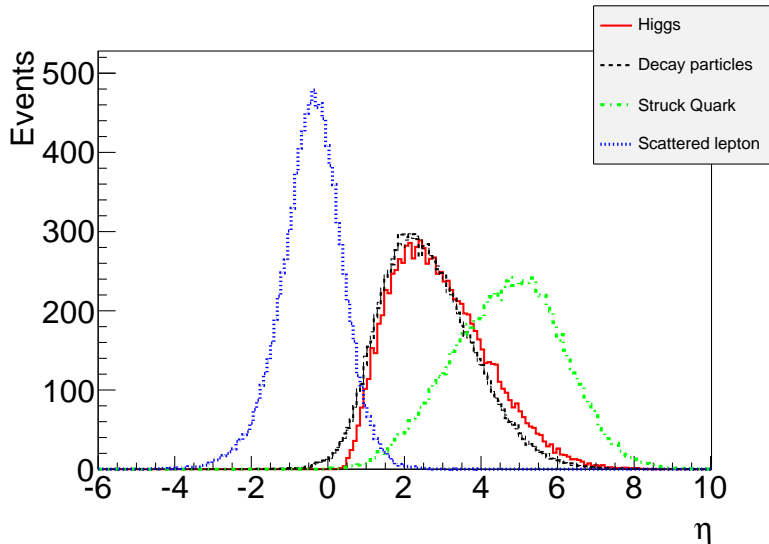


Figure 5.3: Pseudorapidity (η) distributions, at parton-level, characterising the Vector-Boson-Fusion production and decay of the Higgs boson to WW in DIS scattering at FCC-eh. The scattered lepton (blue) in the NC case (or missing energy for CC) has an average η of about -0.5 , i.e. it is scattered somewhat backwards (in electron beam direction). The pseudorapidity distributions of the generated Higgs boson (red) and its decay particles (black) are very similar and peak at $\eta \simeq 2$. The struck quark, especially at the FCC-eh as compared to LHeC, generates a very forward jet requiring forward calorimetry up to $\eta \simeq 6$ as is foreseen in the FCC-eh detector design. Events are generated with MadGraph, see setup in Tab. 5.1.

3536 e.g. for heavy flavour and tau decays. Suitably designed muon detectors covering $\eta = 4$ appear
 3537 feasible for both collider configurations, those would result in high $H \rightarrow \mu\mu$ acceptances of about
 3538 72% (63%) for LHeC (FCC-eh) for selecting all final states with $p_T > 15$ GeV and a coverage
 3539 of the forward jet up to $\eta = 5$ ($\eta = 6$). A further extension to a 1° muon acceptance, would
 3540 change the acceptances marginally to 72.9% (67.5%) for LHeC (FCC-eh).

3541 5.1.4 Cross Sections and Rates

3542 The cross sections for Higgs production in CC and NC DIS e^-p scattering at three different
 3543 proton energies, for LHeC, HE-LHeC and FCC-eh, are summarised in Tab. 5.1. The cross
 3544 sections are calculated to leading order with MadGraph (MG5 v2.5.1) using the CTEQ6L1
 3545 proton PDF and $M_H = 125$ GeV. The CC e^-p cross section is directly proportional to the
 3546 beam polarisation, P , as $\sigma_{CC} \propto (1 - P)$ while the NC cross section only weakly depends on
 3547 the polarisation [317]. It is observed that the CC Higgs production cross section at LHeC is
 3548 comparable to that of a 250 GeV e^+e^- collider. One thus expects, roughly, results of comparable
 3549 sensitivity, the difference being that e^+e^- favours the H to ZZ couplings while ep is dominantly
 3550 sensitive to $WW \rightarrow H$ production. This provides a very basic complementarity. The CC e^-p
 3551 cross section is enlarged with the (negative) electron beam polarisation, P_e , while the NC cross
 3552 section is less sensitive to P_e . The cross section at FCC-eh reaches values of pb. Combined with
 3553 long operation time one reaches sub-permille precision of the Higgs couplings. Similarly, the
 3554 HH cross section approaches one fb values only with the highest energy. It is correspondingly
 3555 a major challenge, investigated in Ref. [479], to access the Higgs self-coupling even at FCC-eh,
 3556 and this is not further discussed here.

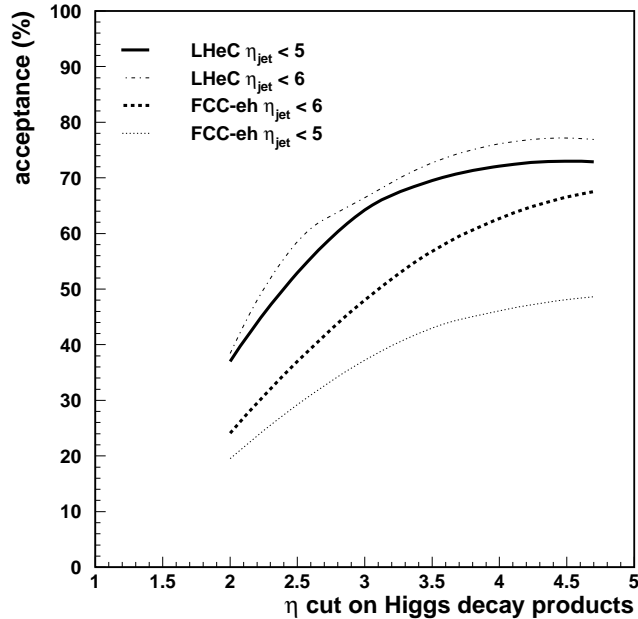


Figure 5.4: Acceptance of DIS Higgs candidates (y axis) in dependence on the pseudorapidity (η) cut requirement on the Higgs decay products (x axis) for two scenarios of the coverage of the hadronic final states. All final states are selected with $p_T > 15$ GeV. The forward jet is accepted up to $\eta = 5$ and $\eta = 6$ for LHeC (full and dashed-dotted lines), and FCC-eh (dotted and dashed lines), respectively. Calculations are at parton-level using MadGraph.

3557 The polarised e^+p cross section is calculated to be significantly smaller than the e^-p value, by a
3558 factor of $197/58 \simeq 6$ at the LHeC, mainly because the $W^-u \rightarrow \bar{d}$ reaction is more frequent than
3559 $W^+d \rightarrow u$. Furthermore, positron sources are currently considered to be much less intense (by
3560 a factor of about ten or even a hundred) than electron sources. It is desirable to take e^+p data
3561 at future ep colliders for electroweak physics but in the linac-ring version their amount will be
3562 limited and unlikely suitable for precision Higgs physics.

3563 Tab. 5.2 provides an illustration, for FCC-eh, of the statistics which is expected to be available
3564 in charged and neutral current scattering for nine decay channels ordered by their branching
3565 ratios. The first seven most frequent channels are used in the subsequent signal strength and
3566 coupling analysis. Accessing rarer SM Higgs decay channels is the particular strength of pp
3567 scattering rather than that of ep or e^+e^- . The statistics at LHeC would be about ten times
3568 lower than that at FCC-eh since the cross section is diminished by $\simeq 1/5$ and due to a shorter
3569 expected running time, the luminosity is assumed to be half of that at FCC-eh. The analyses
3570 subsequently presented deal with the seven most frequent decays representing 99.9% of the SM
3571 decays. In addition, there is a significant potential for a measurement of the $H \rightarrow \mu\mu$ decay at
3572 the FCC-eh, which, as is seen in Tab. 5.2, may provide about 500 (45) events, from CC and NC
3573 DIS at FCC-eh (LHeC). Thus one may be able to measure this process to about 6% precision
3574 at the FCC-eh and 18% at LHeC.

3575 5.1.5 Higgs Signal Strength Measurements

3576 Standard Model Higgs production in deep inelastic ep scattering proceeds via Vector-Boson-
3577 Fusion in either charged or neutral current scattering as is illustrated in Fig. 1. The scattering

Parameter	Unit	LHeC	HE-LHeC	FCC-eh	FCC-eh
E_p	TeV	7	13.5	20	50
\sqrt{s}	TeV	1.30	1.77	2.2	3.46
$\sigma_{CC} (P = -0.8)$	fb	197	372	516	1038
$\sigma_{NC} (P = -0.8)$	fb	24	48	70	149
$\sigma_{CC} (P = 0)$	fb	110	206	289	577
$\sigma_{NC} (P = 0)$	fb	20	41	64	127
HH in CC	fb	0.02	0.07	0.13	0.46

Table 5.1: Total cross sections, in fb, for inclusive Higgs production, $M_H = 125$ GeV, in charged and neutral current deep inelastic e^-p scattering for an $E_e = 60$ GeV electron beam and four different proton beam energies, E_p , for LHeC, HE-LHeC and two values for FCC-eh. The c.m.s. energy squared in ep is $s = 4E_e E_p$. The last row shows the double-Higgs CC production cross sections in fb. The calculations are at LO QCD using the CTEQ6L1 PDF [477] and the default scale of MadGraph [478] with dependencies due to scale choices of 5-10 %.

Channel	Fraction	No. of events at FCC-eh	
		Charged Current	Neutral Current
$b\bar{b}$	0.581	1 208 000	175 000
W^+W^-	0.215	447 000	64 000
gg	0.082	171 000	25 000
$\tau^+\tau^-$	0.063	131 000	20 000
$c\bar{c}$	0.029	60 000	9 000
ZZ	0.026	54 000	7 900
$\gamma\gamma$	0.0023	5 000	700
$Z\gamma$	0.0015	3 000	450
$\mu^+\mu^-$	0.0002	400	70
σ [pb]		1.04	0.15

Table 5.2: Total event rates for SM Higgs decays in the charged ($ep \rightarrow \nu HX$) and neutral ($ep \rightarrow eHX$) current production of the Higgs boson in polarised ($P = -0.8$) electron-proton deep inelastic scattering at the FCC-eh, for an integrated luminosity of 2 ab^{-1} . The branching fractions are taken from [480]. The estimates are at LO QCD using the CTEQ6L1 PDF and the default scale of MadGraph, see setup in Tab. 5.1.

3578 cross sections, including the decay of the Higgs boson into a pair of particles A_i can be written
3579 as

$$\sigma_{CC}^i = \sigma_{CC} \cdot \frac{\Gamma^i}{\Gamma_H} \quad \text{and} \quad \sigma_{NC}^i = \sigma_{NC} \cdot \frac{\Gamma^i}{\Gamma_H}. \quad (5.1)$$

3580 Here the ratio of the partial to the total Higgs decay width defines the branching ratio, br_i ,
3581 for each decay into $A_i \bar{A}_i$. The ep Higgs production cross section and the $\mathcal{O}(1) \text{ ab}^{-1}$ luminosity
3582 prospects enable to consider the seven most frequent SM Higgs decays, i.e. those into fermions
3583 ($b\bar{b}$, $c\bar{c}$, $\tau^+\tau^-$) and into gauge particles (WW , ZZ , gg , $\gamma\gamma$) with high precision at the LHeC
3584 and its higher energy versions.

3585 In ep one obtains constraints on the Higgs production characteristics from CC and NC scattering,
3586 which probe uniquely either the HWW and the HZZ production, respectively. Event by event
3587 via the selection of the final state lepton which is either an electron (NC DIS) or missing energy
3588 (CC DIS) those production vertices can be uniquely distinguished, in contrast to pp . In e^+e^- ,
3589 at the ILC, one has considered operation at 250 GeV and separately at 500 GeV to optimise
3590 the HZZ versus the HWW sensitive production cross section measurements [481]. For CLIC

3591 the c.m.s. energy may be set to 350 GeV as a compromise working point for joint NC and CC
 3592 measurements, including access to top production [482]. The salient advantage of the e^+e^-
 3593 reaction, similarly considered for the more recent circular collider proposals, CEPC [16] and
 3594 FCC-ee [483], stems from the kinematic constraint of the Z -strahlung, $e^+e^- \rightarrow Z^* \rightarrow ZH$,
 3595 which determines the total Higgs production cross section independently of its decay.

3596 The sum of the branching ratios for the seven Higgs decay channels here under study for ep adds
 3597 up to 99.87% of the total SM width [484]. As is discussed in Sect. 5.3, significant constraints
 3598 of the $H \rightarrow invisible$ decay can be set with ep also albeit not being able to exclude exotic,
 3599 unnoticed Higgs decays. The accurate reconstruction of all decays considered here will present
 3600 a severe constraint on the total cross section and with that of the total decay width of the
 3601 Higgs boson in the SM. For the evaluation of the measurement accuracy, the cross section
 3602 measurement prospects for a decay channel i are presented here as relative signal strengths
 3603 $\mu^i(NC, CC)$, obtained from division by the SM cross section.

3604 Initially, detailed simulations and Higgs extraction studies for LHeC were made for the dominant
 3605 $H \rightarrow b\bar{b}$ [485–489] and the challenging $H \rightarrow c\bar{c}$ [489, 490] channels. The focus on the $H \rightarrow b\bar{b}$
 3606 decay has been driven not only by its dominance but as well by the difficulty of its accurate
 3607 reconstruction at the LHC. It has been natural to extend this to the $H \rightarrow c\bar{c}$ which currently is
 3608 considered to not be observable at the HL-LHC, for permutation and large background reasons.
 3609 The results of the updated b and c decay studies, using cuts and boosted decision tree (BDT)
 3610 techniques, are presented below.

3611 A next detailed analysis has been performed for the $H \rightarrow W^+W^-$ decay. The total of the WW
 3612 decays represents 21.5% of the Higgs branching into SM particles. There is a special interest
 3613 in its reconstruction in the DIS charged current reaction as this channel uniquely determines
 3614 the HWW coupling to its fourth power. A complete signal and background simulation and
 3615 eventual BDT analysis of the $H \rightarrow W^+W^-$ decay in charged currents has been performed
 3616 which is subsequently described. Unlike at LHC, this uses the purely hadronic decays which in
 3617 pp are very difficult to exploit.

3618 Finally, as summarised below, an analysis using acceptance, efficiency and signal-to-background
 3619 scale factors has been established for the residual four of the seven dominant decay channels,
 3620 Tab. 5.2. This estimate could be successfully benchmarked with the detailed simulations for
 3621 heavy quark and W decays. The present study therefore covers more than 99% of the SM Higgs
 3622 decays, which in ep are redundantly measured, in both neutral and charged current reactions.
 3623 This opens interesting prospects for precision Higgs physics in ep , but as well in combination
 3624 with pp , i.e. of LHeC with HL-LHC, and later of FCC-eh with FCC-hh.

3625 5.1.6 Higgs Decay into Bottom and Charm Quarks

3626 The Higgs boson decays dominantly into $b\bar{b}$ with a 58% branching ratio in the SM. Its reconstruc-
 3627 tion at the LHC has been complicated by large combinatorial background. Recently this decay
 3628 was established with signal strengths, relatively to the SM, of $\mu_{bb} = 1.01 \pm 0.12(stat) \pm_{0.15}^{0.16}(exp)$
 3629 by ATLAS [491] with a luminosity of 79.8 fb^{-1} and of $\mu_{bb} = 1.01 \pm 0.22$ by CMS [492] with
 3630 a luminosity of 41.3 fb^{-1} . This is a remarkable experimental LHC achievement since for long
 3631 one expected to not be able to measure this decay to better than about 10% at the future
 3632 HL-LHC. Meanwhile this expectation has become more optimistic with the updated HL-LHC
 3633 prospects [493], as is briefly discussed in Sect. 5.1.11, however, the most hopeful assumption for
 3634 the $H \rightarrow c\bar{c}$ decay is a limit to two times the SM expectation.

3635 Because of the special importance of determining the frequent $b\bar{b}$ decay most accurately, and
 3636 with it the full set of SM branchings, the prime attention of the LHeC Higgs prospect studies
 3637 has been given to those two channels. The first PGS detector-level study was published with the
 3638 CDR [1] assuming $M_H = 120$ GeV, shortly before the announcement of the discovery of the Higgs
 3639 boson. This and subsequent analyses use samples generated by MadGraph5 [478], for both signal
 3640 and background events with fragmentation and hadronization via PYTHIA 6.4 [494] in an ep
 3641 customised programme version². Subsequent analyses have been updated to $M_H = 125$ GeV and
 3642 to state-of-the art fast detector simulation with DELPHES 3 [496] as testbed for ep detector
 3643 configurations. Both cut-based and boosted decision tree (BDT) analyses were performed in
 3644 independent evaluations.

3645 As shown in the CDR, the $H \rightarrow b\bar{b}$ decay could be measured via applying classical kinematic
 3646 selection requirements as follows:

- 3647 • CC DIS kinematic cuts of $Q_h^2 > 500$ GeV², $y_h < 0.9$, missing energy $E_T^{\text{miss}} > 30$ GeV, and
 3648 no electrons in the final state to reject NC DIS;
- 3649 • at least three anti-kt $R = 0.7$ jets with $p_T > 20$ GeV which are subject to further b-tagging
 3650 requirements;
- 3651 • a Higgs candidate from two b-tagged jets with b-tagging efficiencies of 60 to 75 %, charm
 3652 (light quark) misidentification efficiencies of 10 to 5 % (1 %) ;
- 3653 • rejection of single-top events via requiring a dijet W candidate mass of greater than
 3654 130 GeV and a three-jet top candidate mass of larger than 250 GeV using a combina-
 3655 tion with one of the b-jets of the Higgs mass candidate;
- 3656 • a forward scattered jet with $\eta > 2$, and a large $\Delta\phi_{b, MET} > 0.2$ between the b-tagged jet
 3657 and the missing energy.

3658 The dominant backgrounds are CC DIS multijet and single top production, while CC Z, W and
 3659 NC Z contributions are small. The background due to multijets from photoproduction, where
 3660 $Q^2 \sim 0$, can be reduced considerably due to the tagging of the small angle scattered electron
 3661 with an electron tagger. The result of a cut-based analysis is shown in Fig. 5.5 where clear Z
 3662 and $H \rightarrow b\bar{b}$ peaks are seen. Assuming that the photoproduction background is vetoed with a
 3663 90 % efficiency, the resulting signal is shown in Fig. 5.5 corresponding to a SM $H \rightarrow b\bar{b}$ signal
 3664 strength $\delta\mu/\mu$ of 2 % for an integrated luminosity of 1000 fb⁻¹ and $P_e = -0.8$. This result
 3665 is consistent with earlier analysis and robust w.r.t. the update of the Higgs mass from 120 to
 3666 125 GeV confirming the high $S/B > 1$ (see also [488] which used a different approach to estimate
 3667 the multijet photoproduction background). The result illustrates that even with harsh kinematic
 3668 requirements and already a small luminosity of 100 fb⁻¹, this important decay channel could be
 3669 measured to an uncertainty of about 6 %.

3670 The stability of the cut-based results has been further shown for different hadronic calorimeter
 3671 resolution setups

$$\frac{\sigma}{E} = \frac{a}{\sqrt{E}} \oplus b \quad \text{for } |\eta| < |\eta_{\text{min}}|, \quad (5.2)$$

$$\frac{\sigma}{E} = \frac{c}{\sqrt{E}} \oplus d \quad \text{for } |\eta_{\text{min}}| < |\eta| < 5, \quad (5.3)$$

²The hadronic showering is not expected to change the kinematics of the DIS scattered lepton. This has been shown, see page 11 of Ref. [495], with the very good level of agreement of NC DIS electron kinematics with and without the ep-customized Pythia showering, i.e. for 99.8 % of events the kinematics in the momentum vector components and for 98 % the energy of the scattered electron are unchanged.

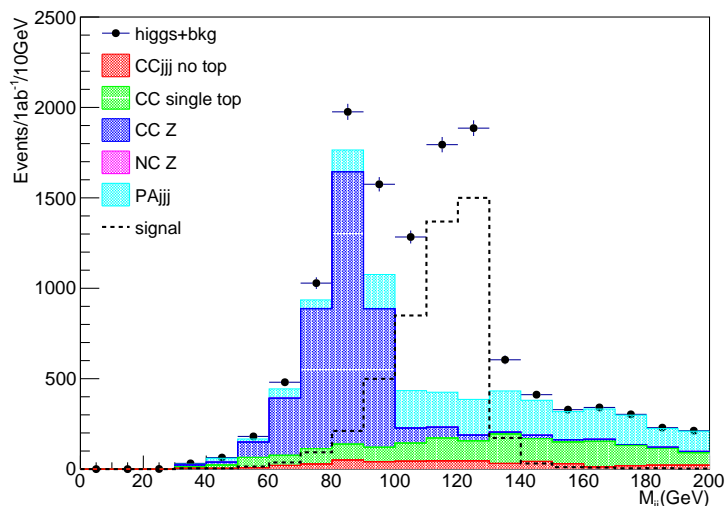


Figure 5.5: Invariant dijet mass distribution at DELPHES detector-level expected for 1 ab^{-1} and -80% electron polarisation at LHeC. The S/B is about 2.9 for the events in the Higgs mass range of 100 to 130 GeV. Events are generated with MadGraph using $M_H = 125 \text{ GeV}$ and showered with PYTHIA 6.4, and subject to cut-based event selection criteria, see text for further details. Note that samples are generated with a minimum dijet mass cut of 60 GeV.

3672 where for $\eta_{\min} = 3$ the parameter b (d) is varied within 1 (3) and 7 (9) % for two resolution
 3673 parameters a (c) of either 30 (60) and 35 (45) %. Alternatively, the central range was restricted
 3674 to $\eta_{\min} = 2$ with parameter b (d) of 3 (5) % for resolution parameters a (c) of 35 (45) %. While
 3675 using the same analysis cuts, the signal yields varied within 34 %, it could be shown that with
 3676 adjusted set of cuts (notably the choices of cuts for Higgs mass range, $\Delta\phi_{b, MET}$, and forward
 3677 η) the SM $H \rightarrow b\bar{b}$ signal strength $\delta\mu/\mu$ varied with a fractional uncertainty of at most 7 %.

3678 The cut-based $H \rightarrow b\bar{b}$ signal strength analyses are suffering from rather low acceptance times
 3679 selection efficiencies in the range of 3 to 4 % only. Similarly a recent cut-based $H \rightarrow c\bar{c}$ study [497]
 3680 showed the potential of those measurements at LHeC and CEPC, however, due to the very harsh
 3681 cuts and too simple analysis strategies with very limited outcome only. Modern state-of-the-
 3682 art analysis techniques, e.g. as performed for finding $H \rightarrow b\bar{b}$ at the LHC regardless of the
 3683 overwhelming QCD jet background, are based on neural networks.

3684 Boosted Decision Tree (BDT) $H \rightarrow b\bar{b}$ and $H \rightarrow c\bar{c}$ analyses using the Toolkit for Multivariate
 3685 Data Analysis with ROOT (TMVA) [498] are performed using independently produced signal
 3686 and background samples based on the same setup as for the cut-based analyses, see Fig. 5.5.
 3687 Those analyses start with loose preselections of at least three anti-kt jets with $p_T > 15 \text{ GeV}$
 3688 without any further heavy flavour tagging in addition to the CC DIS kinematic cuts of $Q_h^2 > 400$
 3689 GeV^2 , $y_h < 0.9$, and missing energy $E_T^{\text{miss}} > 20 \text{ GeV}$. The invariant mass distributions using
 3690 anti-kt $R = 0.5$ jets are illustrated in Fig. 5.6, where the mass distributions in the upper plots
 3691 illustrate in particular the single top contributions and the subsequent significant Higgs signal
 3692 loss if simple anti-top cuts would be applied. In the lower plot of Fig. 5.6 the invariant dijet
 3693 mass distribution of untagged Higgs signal candidates is seen clearly above the background
 3694 contributions in the expected mass range of 100 to 130 GeV. It is observed that the remaining
 3695 background is dominated by CC multi-jets. The quantities represented in the three distributions
 3696 of Fig. 5.6 are important inputs for the BDT neural network in addition to further variables
 3697 describing e.g. the pseudorapidities of the Higgs and forward jet candidates including jet and

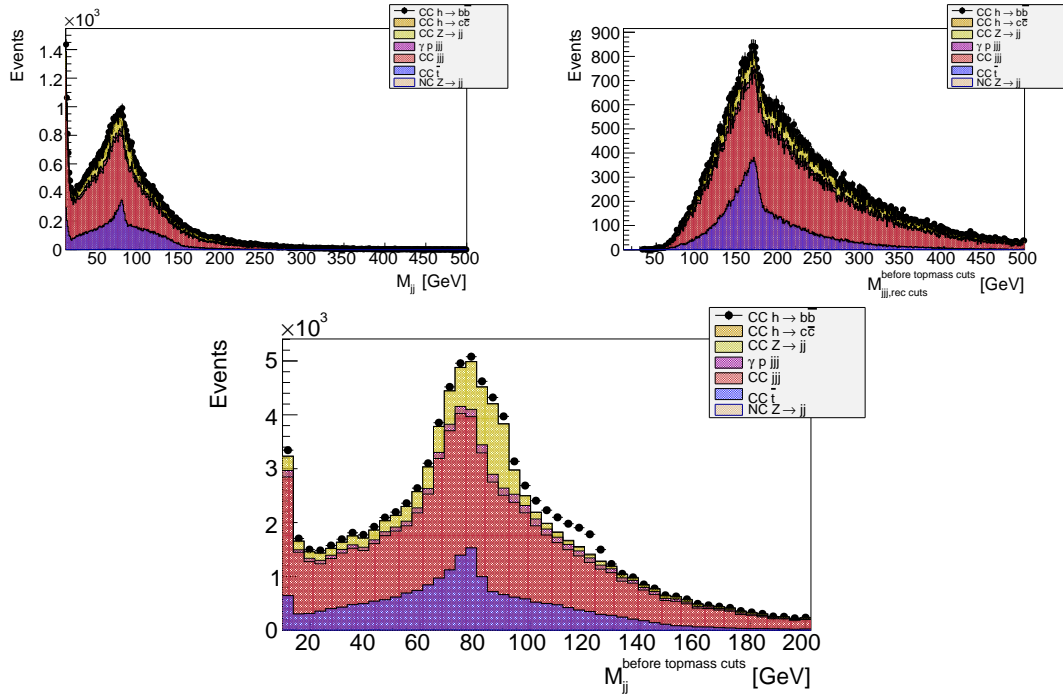


Figure 5.6: Invariant mass distributions at DELPHES detector level for an integrated luminosity of 100 fb^{-1} and -80% electron polarisation. Events passed preselection cuts of $Q_h^2 > 400 \text{ GeV}^2$, $y_h < 0.9$, $E_T^{\text{miss}} > 20 \text{ GeV}$ and at least three, flavour-untagged anti-kt $R = 0.5$ jets with $p_T > 15 \text{ GeV}$. The different colours show the contributions per process, the photoproduction background ($\gamma p \text{ jjj}$) is assumed to be vetoed with 90% . Note that samples are generated with a minimum dijet mass cut of 60 GeV . Upper left: Invariant dijet mass, showing W candidates from single top production (blue), based on combining jets with second and third lowest $|\eta|$ values per event. Upper right: Invariant mass distribution combining the three highest p_T jets per event showing single top mass candidates (blue). Lower middle: Invariant dijet mass, showing Higgs candidates (black dots, including background), combining jets with the two lowest $|\eta|$ values per event.

3698 track heavy flavour probabilities, see details below and further in Ref. [490].

3699 As a novel element in these analyses, heavy flavour tagging based on track and jet probabilities
 3700 has been implemented into the DELPHES detector analysis following the Tevatron D0 experi-
 3701 mental ansatz described e.g. in Ref. [499]. The resulting b and c -jet efficiency versus the light jet
 3702 misidentification efficiencies are illustrated in Fig. 5.7 for assumed nominal impact parameter
 3703 resolution of 10 (5) μm for tracks with $0.5 < p_T < 5$ (> 5) GeV and three choices of distance
 3704 parameter $R = 0.5, 0.7, 0.9$ for the anti-kt jets. In particular for the charm tagging, impact
 3705 parameters are studied with resolutions of 5 (2.5) μm (Half Vertex Resolution), 20 (10) μm
 3706 (Double Vertex Resolution) for tracks with $0.5 < p_T < 5$ (> 5) GeV within $|\eta| < 3.5$. For a
 3707 conservative light jet efficiency of 5% , the b -jet tagging efficiency is rather robust around 60%
 3708 for the considered nominal impact parameter performance and the three considered anti-kt dis-
 3709 tance parameters, in slight favour of the anti-kt $R = 0.5$ choice. For the expected charm tagging,
 3710 however, an excellent impact parameter resolution and $R = 0.5$ jets give the best tagging effi-
 3711 ciency of around 30% . This means a significant improvement e.g. w.r.t. a 23% charm tagging
 3712 efficiency for $R = 0.9$ jets at a nominal impact parameter resolution. These tagging efficiencies
 3713 can be considered as realistic but rather conservative in particular for the remaining light jet
 3714 efficiency which is expected to be about 0.1% at a b -jet efficiency of 60% using LHC-style neural
 3715 network based taggers.

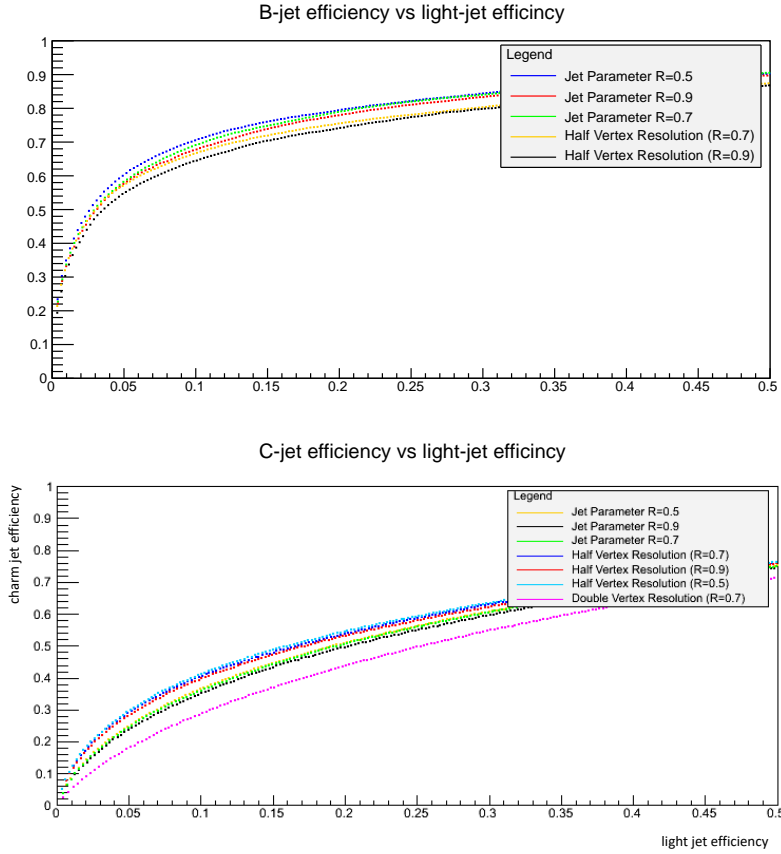


Figure 5.7: Expected average efficiency to tag a b -jet (upper plot) and charm-jet (lower plot) versus the light-jet efficiency (x-axis) based on Tevatron-style jet tagging [499]. Events are selected at DELPHES detector level using a CC multi-jet sample and for an integrated luminosity of 100 fb^{-1} . The coloured lines correspond to the choice of the anti-kt distance parameter R and different assumptions in the impact parameter resolution of 10 (5) μm (nominal, no text added in legend), 5 (2.5) μm (Half Vertex Resolution), 20 (10) μm (Double Vertex Resolution) for tracks with $0.5 < p_T < 5 (> 5)$ GeV within $|\eta| < 3.5$.

3716 A series of BDT score tests has been performed using the preselected signal samples and CC
3717 multi-jet as the main background sample to determine the optimal combination of R and impact
3718 resolution parameters. The resulting number of $H \rightarrow b\bar{b}(c\bar{c})$ signal events versus the BDT score
3719 is illustrated in Fig. 5.8, which shows the evident interplay between detector performance and
3720 choice of jet parameters R , where the $R = 0.9$ anti-kt jets show the worst performance. At
3721 a score of BDT=0, the highest number of signal events are achieved for $R = 0.5$ anti-kt jets
3722 for both charm and beauty decays, where the effect of the impact resolution is much more
3723 stringent for the charm than for the beauty tagging. Following Fig. 5.8, the complete BDT-based
3724 $H \rightarrow b\bar{b}(c\bar{c})$ analyses are performed for anti-kt $R = 0.5$ jets and impact parameter resolution of
3725 5 (2.5) μm (Half Vertex Resolution) for tracks with $0.5 < p_T < 5 (> 5)$ GeV within $|\eta| < 3.5$.
3726 The acceptance times efficiency values are about 28 % for the $H \rightarrow b\bar{b}$ and about 11 % for the
3727 $H \rightarrow c\bar{c}$ channel at BDT=0.

3728 The results of the BDT $H \rightarrow b\bar{b}$ and $H \rightarrow c\bar{c}$ analyses, assuming that each background contri-
3729 bution is understood at the 2 % level via control regions and negligible statistical Monte Carlo
3730 uncertainties for the background predictions for the signal region, are illustrated in Fig. 5.9 .
3731 Using these assumptions, the resulting signal strengths are 0.8 % for the $H \rightarrow b\bar{b}$ and 7.4 % for

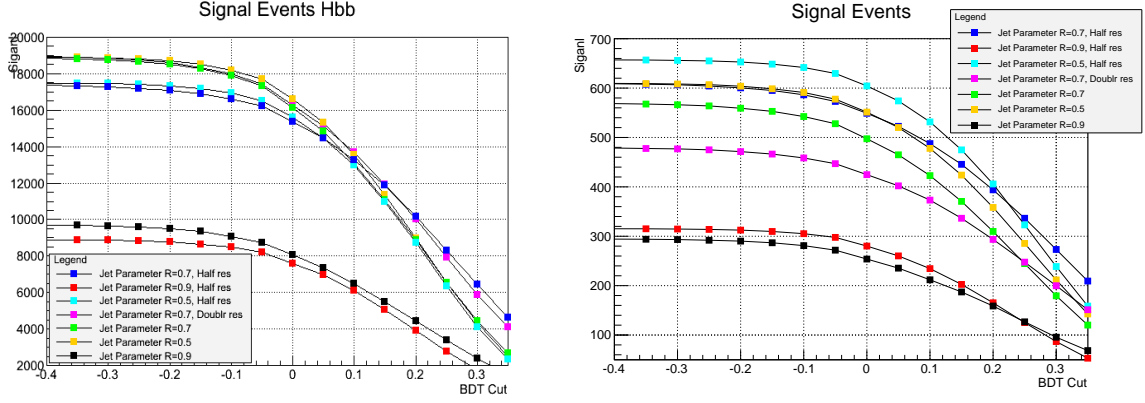


Figure 5.8: Expected $H \rightarrow b\bar{b}$ (left) and $H \rightarrow c\bar{c}$ (right) signal events as a function of the BDT score. Events are selected at DELPHES detector level for an integrated luminosity of 1 ab^{-1} and -80% electron polarisation. The symbols correspond to the choice of the anti-kt distance parameter R and different assumptions in the impact parameter resolution of 10 (5) μm (nominal, no further text in legend added), 20 (10) μm (Doubl res), 5 (2.5) μm (Half res) for tracks with $0.5 < p_T < 5$ (> 5) GeV within $|\eta| < 3.5$.

3732 the $H \rightarrow c\bar{c}$ channel. For the latter, the SM Higgs decays, in particular $H \rightarrow b\bar{b}$, represent
3733 also a part of the cc background contribution but can be controlled by the high precision of
3734 the genuine bb result. Advanced analysis strategies to distinguish bb and cc SM Higgs decays
3735 via several layers of neural networks are discussed e.g. in Ref. [500] for an 250 GeV ILC and
3736 $M_H = 120$ GeV, where the expected $H \rightarrow c\bar{c}$ cross section is 6.9 fb for $M_H = 120$ GeV yields
3737 a signal strength uncertainty of 8.8% in the ZH all hadronic channel ($Z\phi q\bar{q}$) at an integrated
3738 luminosity of 250 fb^{-1} . The ILC charm cross section is quite similar to the 5.7 fb cross section for
3739 $M_H = 125$ GeV at LHeC. The number of preselected charm events and SM Higgs contributions
3740 for the ILC analysis are at a similar level as in this analysis, while the non-Higgs background at
3741 ILC is by a factor 6.8 larger than for the LHeC preselected events. Comparing the two results
3742 gives confidence into the expected $H \rightarrow c\bar{c}$ signal strength results at LHeC using the before
3743 mentioned assumptions.

3744 In conclusion, Higgs to heavy flavour signal strength measurements require an excellent state-of-
3745 the-art calorimetry with high acceptance and excellent resolution as well as an impact parameter
3746 resolution as achieved e.g. with ATLAS inner b-layer. In addition, the details of the analysis
3747 strategy utilising neural network and advanced statistical methods (e.g. via ROOSTat and
3748 ROOFit, see e.g. complex analysis methods using constraints via well measured control regions
3749 in signal fits [501]) will be important to control a high signal at low background yields where
3750 the latter is expected to be constrained via control regions to better than a few %.

3751 5.1.7 Higgs Decay into WW

3752 Inclusive charged current scattering, the CC production of the Higgs boson with a WW decay
3753 and the main backgrounds are illustrated in Fig. 5.10. The $ep \rightarrow \nu H X \rightarrow \nu W^* W X$ process with
3754 hadronic W decays causes a final state which to lowest order comprises the escaping neutrino
3755 (missing energy MET) and $4 + 1$ jets. The pure hadronic WW Higgs decay has a branching
3756 ratio of about 45% . Using MadGraph (MG5) and a version of PYTHIA, customised for ep
3757 DIS, events were produced and analysed with a DELPHES description of the detector. For the
3758 present study jets were reconstructed using the anti- k_T algorithm with a ΔR of 0.7.

3759 The analysis of the fully generated events proceeds in the following steps:

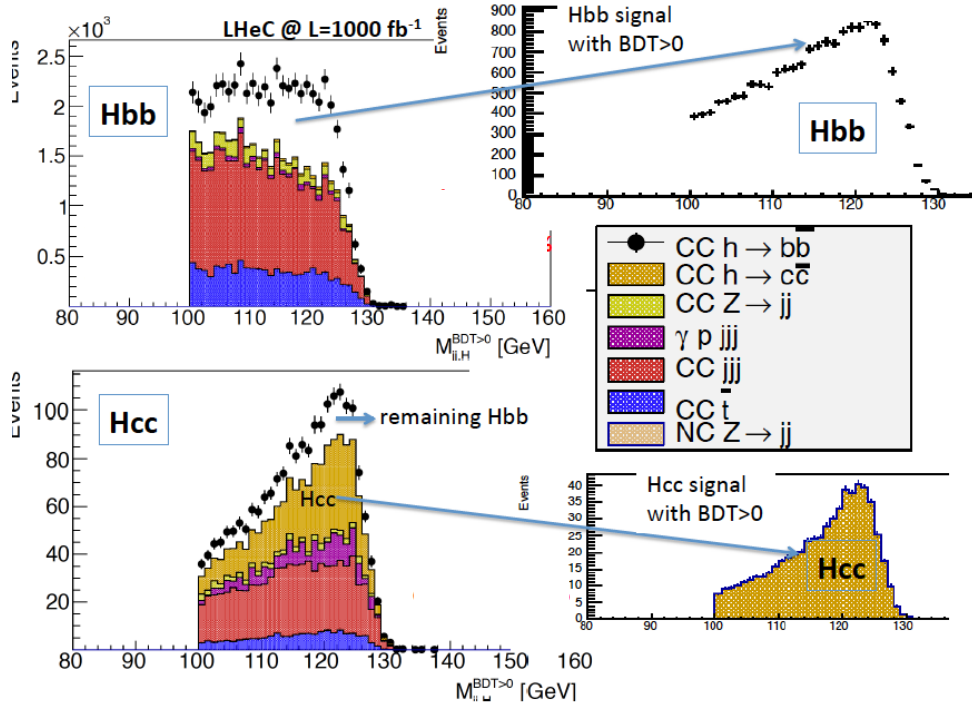


Figure 5.9: Result of the joint $H \rightarrow b\bar{b}$ and $H \rightarrow c\bar{c}$ analysis for an integrated luminosity of 1 ab^{-1} and -80% electron polarisation at the LHeC. Left: Invariant mass distributions for the two channels with signal and background, see text. Right: Expected Higgs signal distributions after background subtraction. The background is assumed to be at the 2% level via control region measurements.

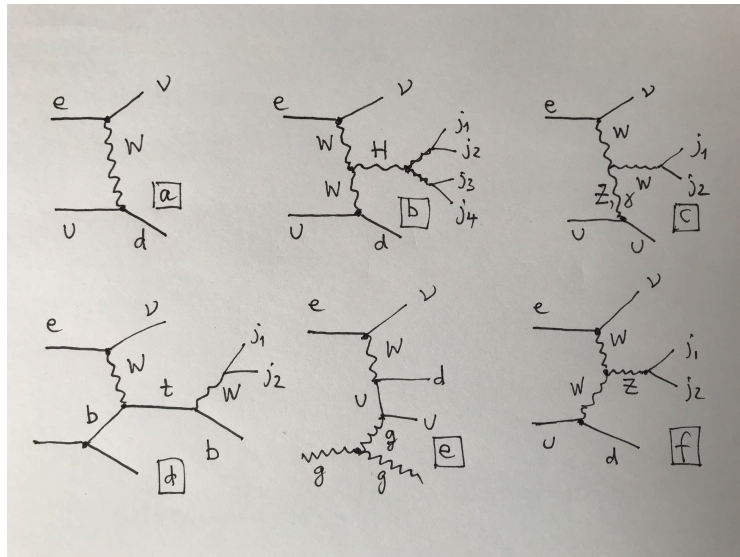


Figure 5.10: Typical lepton-parton diagrams relevant to the $H \rightarrow WW$ analysis: a) inclusive charged current deep inelastic scattering into a neutrino (missing energy) and a scattered jet, here arising from the hadronisation of a d-quark; b) signal: CC DIS with a Higgs produced in the t-channel and its decay into a pair of W bosons which generates a four-jet final state, besides the forward jet. The other diagrams are examples to illustrate background channels which at higher orders, with extra emissions, may mimic the signal configuration: c) single W-boson production; d) single top-quark production; e) QCD multi-jet production and f) single Z-boson production.

- 3760 • Study of the reconstructed event configuration and recognition of its characteristics for
3761 defining a set of loose cuts. These are: the p_T of any jet has to be larger than 6 GeV,
3762 rapidity difference between the forward jet and the reconstructed 4-jet Higgs candidate
3763 to be larger than 1.5, azimuthal difference between that Higgs candidate and either the
3764 forward jet or the scattered lepton (MET) to be larger than 1, two-jet masses of the virtual
3765 and the real W boson candidate to be larger than 12 GeV and below 90 GeV (Z mass).
- 3766 • Verification of truth matching to check that the combinatorial association of jets reproduces
3767 the Higgs and its W decays (this is illustrated in Fig. 5.11).
- 3768 • Application of this algorithm to the simulated background samples. The MadGraph single
3769 W , top and Z production samples are turned to multi-jet background through PYTHIA.
3770 The cross sections are reliably calculated as there is a hard scale available. The initial
3771 cuts reduce this background to about 3% for single vector boson production and to 9%
3772 for top.
- 3773 • Due to the size of the $Hb\bar{b}$ decay and jet radiation, there occurs a residual background
3774 from the Higgs itself which is also reduced to 3% of its MG5 value through the cuts.
- 3775 • The final background is due to multi-jets. The MadGraph cross section for a 4+1 jet
3776 CC configuration is considered much too large in view of the cross section measurement
3777 results as a function of the jet number, both at HERA and the LHC, see for example [502].
3778 The sample was thus scaled using a conservative α_s renormalisation to the inclusive cross
3779 section. The initial cuts reduce the multi-jet background to about 13%.
- 3780 • Following a detailed training study, a BDT analysis was used. This determined a final
3781 event number of about 12k for to a signal-to-background ratio of 0.23.

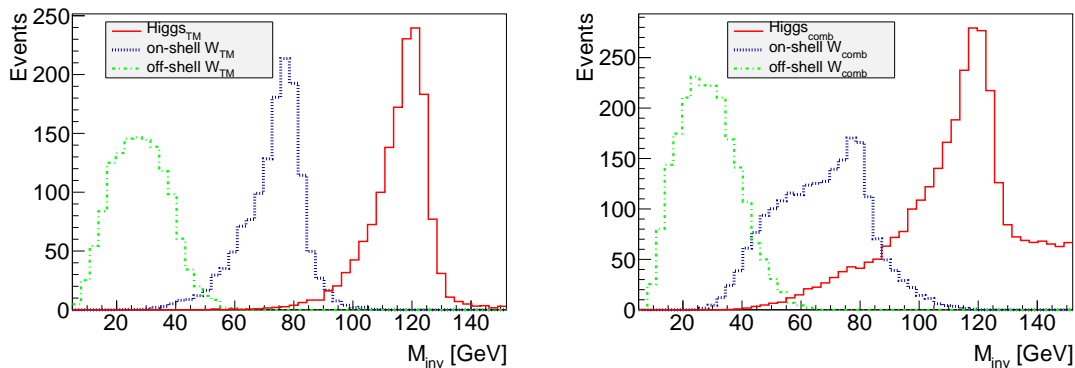


Figure 5.11: Reconstructed signal mass distributions (at DELPHES detector level) of truth matched events (left) and after the just combinatorial association of jets to the two W bosons forming Higgs candidates (right). Green: virtual W^* boson; blue: W boson; red: Higgs signal from W^*W reconstruction. It is observed that the combination causes some background while the respective signal peaks are clearly preserved with a purity of 68% that the correct forward jet is identified.

3782 The result of this analysis translates to an estimated uncertainty on μ_{WW} of 1.9% at FCC-
3783 eh. The 4-jet mass distribution after the BDT requirement exhibits a clear WW Higgs peak
3784 (see Fig. 5.11) which illustrates the suitability to use the electron-proton environment for Higgs
3785 measurements in indeed challenging final state configurations.

3786 **5.1.8 Accessing Further Decay Channels**

3787 Following the detailed studies of the $b\bar{b}$ and $c\bar{c}$ decay channels, presented above, a coarser anal-
 3788 ysis was established for other frequent decay channels both in NC and CC. Here acceptances
 3789 and backgrounds were estimated with MadGraph, and efficiencies, distinguishing leptonic and
 3790 hadronic decay channels for W , Z , and τ , were taken from prospective studies on Higgs cou-
 3791 pling measurements at the LHC [503]. This provided a systematic scale factor, f , on the pure
 3792 statistical error δ_s , which comprised the signal-to-background ratio, S/B , and the product of
 3793 acceptance, A , and extra reconstruction efficiency ϵ , according to

$$f = \sqrt{\frac{1 + \frac{B}{S}}{A \cdot \epsilon}} \quad (5.4)$$

3794 The error on the signal strength μ_i for each of the Higgs decay channels i is determined as
 3795 $\delta\mu_i/\mu_i = f_i \cdot \delta_s$.

Parameter	$b\bar{b}$	WW	gg	$\tau\tau$	cc	ZZ	$\gamma\gamma$
Branching fraction	0.581	0.215	0.082	0.063	0.029	0.026	0.0023
Statistical error (δ_s) [%]	0.09	0.15	0.24	0.28	0.41	0.43	1.41
Acceptance (A)	0.14	0.10	0.40	0.40	0.11	0.10	0.40
Signal/background (S/B)	9	0.2	0.1	0.2	0.43	0.33	0.5
Extra efficiency (ϵ)	1	0.3	0.5	0.43	1	0.5	0.7
Scale factor f	2.8	16	7.4	5.9	5.5	9.0	3.3

Table 5.3: Statistical uncertainty for the seven most abundant Higgs decay channels, for the charged current Higgs measurement prospects with the FCC-eh, together with their systematic scale factor f , Eq. 5.4, resulting from acceptance, background and efficiency effects as given. Note that the results for $b\bar{b}$ and $c\bar{c}$ are taken from the BDT analysis (Sect. 5.1.6) with efficiency 1. The WW result is replaced by the BDT analysis (Sect. 5.1.7) for quoting the expected signal strength uncertainty.

3796 To good approximation these factors apply to LHeC, HE-LHeC and FCC-eh because the de-
 3797 tector dimensions and acceptances scale with the proton energy, conceptually using the same
 3798 technology and very similar resolution assumptions. Therefore there is one main matrix used
 3799 for the subsequent experimental deterioration of the pure statistics precision, both for CC and
 3800 NC. Future detailed analyses will lead to refining this expectation which for the current purpose
 3801 was beyond the scope of the study. The results of the analysis of uncertainties are summarised
 in Tab. 5.3 for the CC channel at the FCC-eh. The resulting signal strength uncertainty values

Setup	$b\bar{b}$	$b\bar{b} \oplus \text{Thy}$	WW	gg	$\tau\tau$	cc	ZZ	$\gamma\gamma$
LHeC NC	2.3	2.4	17	16	15	20	35	42
LHeC CC	0.80	0.94	6.2	5.8	5.2	7.1	12	15
HE-LHeC NC	1.15	1.25	8.9	8.3	7.5	10	17	21
HE-LHeC CC	0.41	0.65	3.2	3.0	2.7	3.6	6.2	7.7
FCC-eh NC	0.65	0.82	5.0	4.7	4.2	5.8	10	12
FCC-eh CC	0.25	0.56	1.9	1.8	1.6	2.2	3.8	4.6

Table 5.4: Summary of estimates on the experimental uncertainty of the signal strength μ , in per cent, for the seven most abundant Higgs decay channels, in charged and neutral currents for the LHeC, the HE-LHeC and the FCC-eh. The $b\bar{b}$ channel is the one which is most sensitive to theoretical uncertainties and for illustration is given two corresponding columns, see Sect. 5.1.9.

3802

3803 are provided in Tab. 5.4. Note that for the beauty, charm and WW channels the table contains
 3804 the BDT analysis ³ results of Sect. 5.1.6 and Sect. 5.1.7, resp. The beauty and charm CC results
 3805 stem from the BDT analysis for LHeC and are applied to FCC-eh with a factor of about 1/3.
 3806 The CC WW results are due to the FCC-eh BDT analysis and are used for LHeC, enlarged by
 3807 a factor of 3.2, determined by the different cross sections and luminosities. For HE-LHC, the
 3808 values are about twice as precise as the LHeC values because the cross section is enlarged by
 3809 about a factor of two, see Tab. 5.1, and the integrated luminosity with 2 ab^{-1} twice that of the
 3810 LHeC. All signal strength uncertainties, in both CC and NC, for the three collider configurations
 are shown in Fig. 5.12.

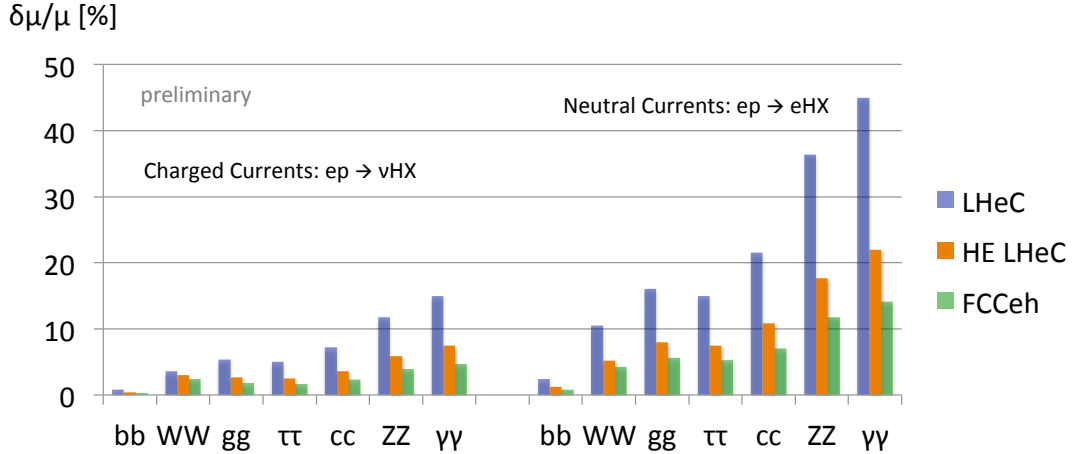


Figure 5.12: Uncertainties of signal strength determinations in the seven most abundant SM Higgs decay channels for the FCC-eh (green, 2 ab^{-1}), the HE LHeC (brown, 2 ab^{-1}) and LHeC (blue, 1 ab^{-1}), in charged and neutral current DIS production.

3811

3812 5.1.9 Systematic and Theoretical Errors

3813 The signal strength is expressed relatively to a theoretical calculation of the charged current
 3814 Higgs cross section, including its decay into a chosen channel, according to

$$\mu = \frac{\sigma_{exp}}{\sigma_{thy}} = \frac{\sigma_{exp}}{\sigma_{Hty} \cdot br}. \quad (5.5)$$

3815 Consequently one can decompose the (relative) error of μ into the genuine measurement error,
 3816 denoted as $\delta\sigma_{exp}$, including a possible systematic error contribution, E , and two further
 3817 components

$$\frac{\delta\mu}{\mu} = \left\{ \left(\frac{\delta\sigma_{exp}}{\sigma_{exp}} \right)^2 \cdot (1 \oplus E) + \left(\frac{\delta\sigma_{Hty}}{\sigma_{Hty}} \right)^2 + \left(\frac{\delta br}{br} \right)^2 \right\}^{1/2}, \quad (5.6)$$

3818 which are due to imperfections to theoretically model the Higgs production cross section, σ_{Hty} ,
 3819 and uncertainties on the branching ratio, br , in the channel under study. Note, that the experi-
 3820 mental uncertainty takes into account possible variations of the backgrounds which are estimated
 3821 conservatively and thus represent more than genuine statistics.

3822 The channel dependent signal strength uncertainties quoted in Tab. 5.4 are estimates of the
 3823 first, experimental term in Eq. 5.6 neglecting extra systematic error effects. They are derived as

³This is in very good agreement with the scale factor method: for example, the WW result in Tab. 5.3 leads to a value of 2.1% slightly worse than the BDT analysis.

3824 stated above from the purely statistical error ($\delta_s = 1/\sqrt{N}$), its increase due to acceptance (A)
 3825 and efficiency (ϵ) effects and, further, the modulation caused by the background-to-signal ratio
 3826 (B/S). These factors are all involved in the BDT analysis but the scale factor equation, Eq. 5.4,
 3827 may be used to estimate further systematic effects for any channel. From the relation

$$\frac{\delta\sigma_{exp}}{\sigma_{exp}} = \delta_s \cdot \sqrt{\frac{1 + B/S}{A \cdot \epsilon}} \quad (5.7)$$

3828 the combined systematic error contribution, E , caused by variations Δ of A , ϵ and the back-
 3829 ground B can be estimated as

$$E = \frac{1}{2} \left\{ \left(\frac{\Delta A}{A} \right)^2 + \left(\frac{\Delta \epsilon}{\epsilon} \right)^2 + \left(\frac{\Delta B}{B} \cdot \frac{B/S}{1 + B/S} \right)^2 \right\}^{1/2}. \quad (5.8)$$

3830 The formula shows that if the background-to-signal ratio is very small, then the background
 3831 effect is suppressed $\propto B/S$. If it is larger than 1, the relative uncertainty of the background
 3832 enters as an additional component of the signal strength error.

3833 Given the fact that the experimental $H \rightarrow b\bar{b}$ result in the CC reaction is especially precise,
 3834 compare Tab. 5.4, an estimate was performed of the systematic error in this channel. The
 3835 following effects were included: a variation of the light-quark misidentification by a factor 3, a
 3836 variation of the reduction of the photo-production via tagging between 2 % and 10 %, a variation
 3837 of the combined acceptance times efficiency effect by 10 % and a variation of the hadronic energy
 3838 resolution, studied in Ref. [486], leading to a 7 % signal variation. The overall effect of these
 3839 contributions determines a systematic error of about 10 % on μ_{bb} , i.e. $\delta\mu/\mu = 0.80 \pm 0.09$ for
 3840 $H \rightarrow b\bar{b}$ at the LHeC in the CC channel. Similar levels of uncertainty are expected to occur for
 3841 other channels but have not been estimated to such detail as those channels are measured less
 3842 precisely.

3843 A separate effect arises from the measurement of the luminosity. While that will be measured
 3844 about as accurate as 0.5 %, based on Bethe-Heitler scattering and its accurate description to
 3845 higher-order QEDC [1], additionally it will be negligible to a good approximation: the LHeC,
 3846 and its successors, will provide a very precise, determination of all parton distributions from
 3847 the ep data alone. Any systematic mistake in the normalisation will therefore affect both the
 3848 measured and the calculated cross section and drop out in their ratio μ .

3849 A next uncertainty on the signal strength arises from the theoretical description of σ_{CCH} to which
 3850 the measured cross section is normalised. From a simulation of the systematic uncertainties
 3851 due to imperfect calibrations and extra efficiencies one may expect the cross section to be
 3852 known to better than 1 %. The prediction will be available to N³LO, α_s be determined to
 3853 0.1 – 0.2 % precision, and it can be gauged with the inclusive cross section measurement. This
 3854 uncertainty, following Eq. 5.8, enters directly as a contribution to the μ measurement result. A
 3855 0.5 % uncertainty, as can be seen in Tab. 5.4, becomes noticeable in most of the $b\bar{b}$ results but
 3856 is negligible for all other channels. In the present analysis values of 0.5 % and 1 % uncertainty
 3857 have been considered and their effect on the κ result been evaluated, see Sect. 5.1.10.

3858 A final uncertainty is caused by the branching fractions and their uncertainty. A recent un-
 3859 certainty estimate [480] quotes on the here most relevant $H \rightarrow b\bar{b}$ branching ratio a theory
 3860 contribution due to missing higher orders of 0.65 %, a parameterisation uncertainty depending
 3861 on the quark masses of 0.73 %, and an α_s induced part of 0.78 %. The LHeC, or similarly the
 3862 higher energy ep colliders, will determine the b mass (in DIS) to about 10 MeV and α_s to per
 3863 mille precision [1] which would render corresponding uncertainty contributions to br_{bb} negligible.

3864 The genuine theoretical uncertainty would also be largely reduced with an extra order pQCD.
 3865 In the subsequent study the contribution from the branching fraction uncertainty has been ne-
 3866 glected. This may also be justified by the programme here sketched, and similarly for other
 3867 future colliders: the ep colliders will measure the couplings, especially of the WW , bb and ZZ
 3868 very precisely, which will enable an iterative treatment of the branching ratio uncertainties.

3869 It may be noticed [480] that the α_s contribution to the $H \rightarrow gg$ branching fraction uncertainty
 3870 is about 3.7%, i.e. twice as large as the estimated signal strength measurement uncertainty of
 3871 this channel at the FCC-eh. There arises another important benefit of the future ep colliders
 3872 and their high precision DIS programme for precision Higgs physics at the combined ep & pp
 3873 facilities.

3874 5.1.10 Higgs Coupling Analyses

3875 In order to quantify possible deviations from the SM expectation one may use the κ parameter-
 3876 isation framework, introduced in Ref. [504], which enables easy comparisons between different
 3877 collider configurations independently of their ability to access the total Higgs decay width. The κ
 3878 formalism avoids extra complications occurring in EFT analyses that deal with extra constraints
 3879 and complicate the genuine comparison of results. The EFT formalism tends to improve the
 3880 perceived accuracy. In the EFT analysis of the ILC 250 GeV potential, for example, values are
 3881 quoted for the Hbb coupling of 3.2% in the κ framework but 1.0% in a full EFT fit [505]⁴. It
 3882 nevertheless would be very interesting to go beyond the κ framework also for the ep colliders
 3883 here presented because out of the 2499 4-fermion parameters altogether $13 \cdot n_g^4 = 1053$ involve
 3884 leptons and quarks [506], for $n_g = 3$ generations. This, however, has been beyond the scope
 3885 of this study. In the following results are presented for the various ep collider configurations
 3886 (Sect. 5.1.10).

3887 The κ parameters are factors to the various Higgs couplings, equal to one in the SM, which scale
 3888 $\sigma_{NC/CC}$ with $\kappa_{Z/W}^2$, the width Γ^i for a channel i with κ_i^2 and lead to replacing Γ_H by the sum
 3889 $\sum_j \kappa_j \Gamma^j$. This defines the following modifications of the cross sections (Eq. 5.1)

$$\sigma_{CC}^i = \sigma_{CC} br_i \cdot \kappa_W^2 \kappa_i^2 \frac{1}{\sum_j \kappa_j^2 br_j} \quad \text{and} \quad \sigma_{NC}^i = \sigma_{NC} br_i \cdot \kappa_Z^2 \kappa_i^2 \frac{1}{\sum_j \kappa_j^2 br_j}. \quad (5.9)$$

3890 Dividing these expressions by the SM cross section predictions one obtains the variations of the
 3891 relative signal strengths, μ^i , for charged and neutral currents and their κ dependence

$$\mu_{CC}^i = \kappa_W^2 \kappa_i^2 \frac{1}{\sum_j \kappa_j^2 br_j} \quad \text{and} \quad \mu_{NC}^i = \kappa_Z^2 \kappa_i^2 \frac{1}{\sum_j \kappa_j^2 br_j}. \quad (5.10)$$

3892 With seven decay channels considered in CC and NC, one finds that for each of the ep collider
 3893 configurations there exist eight constraints on κ_W and κ_Z and two on the other five κ parameters.

⁴ A spectacular difference is observed in [505] between the ratios of the HWW to HZZ couplings within the κ framework and in EFT. This ratio is quoted to be determined to 3.29% and to 0.07% precision, respectively. This likely is due to the custodial symmetry constraint in EFT which binds the WW and ZZ channels. Relying only on the EFT formalism would thus screen genuine differences between various colliders. In the particular case of interest here, an important complementarity between ep and e^+e^- would disappear. For the ILC 250 GeV case, κ_{WW} is quoted with an uncertainty of 3.31% while κ_{ZZ} is expected to be determined within 0.31%, a difference reflecting the dominance of Z Higgsstrahlung in e^+e^- and the small \sqrt{s} of the 250 GeV machine leading to a small WW contribution only. At the LHeC, the result is opposite, albeit to a less drastic extent. The analysis presented below leads to $\delta\kappa_{WW} = 0.7\%$ and $\delta\kappa_{ZZ} = 1.2\%$. The NC e^+e^- reaction provides a better ZZ coupling while the CC ep process determines the WW coupling to higher accuracy, for comparable luminosities.

3894 Using the signal strength uncertainties as listed in Tab. 5.4 fits to all seven channels, in NC and
3895 CC, are performed in a minimisation procedure to determine the resulting uncertainties for
3896 the κ parameters. These are done separately for each of the ep collider configurations with
3897 results listed in Tab. 5.5. A naive expectation would have been that $\delta\kappa \simeq \delta\mu/2$. Comparing
3898 the results, for example for LHeC (top rows), of the signal strengths (Tab. 5.4) with the κ fit
3899 results (Tab. 5.5) one observes that this relation holds approximately for the gg , $\tau\tau$, $c\bar{c}$, $\gamma\gamma$
3900 channels. However, due to the dominance and high precision of μ_{bb} and owing to the presence
3901 of the WWH and ZZH couplings in the initial state, there occurs a reshuffling of the precisions
3902 in the joint fit: κ_{bb} is relatively less precise than μ_{bb} while both κ_{WW} and κ_{ZZ} become more
3903 precise than naively estimated, even when one takes into account that the $H \rightarrow WW$ decay in
CC measures κ_{WW}^4 . The seven channel results are displayed in Fig. 5.13.

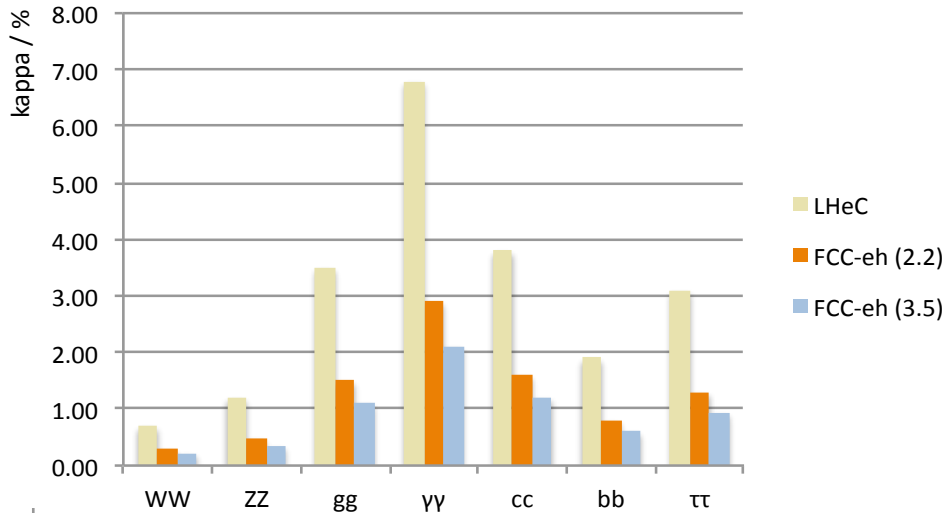


Figure 5.13: Summary of uncertainties of Higgs couplings from ep for the seven most abundant decay channels, for LHeC (gold), FCC-eh at 20 TeV proton energy (brown) and for $E_p = 50$ TeV (blue).

3904

Setup	$b\bar{b}$	WW	gg	$\tau\tau$	cc	ZZ	$\gamma\gamma$
LHeC	1.9	0.70	3.5	3.1	3.8	1.2	6.8
HE-LHeC	1.0	0.38	1.8	1.6	1.9	0.6	3.5
FCC-eh	0.60	0.22	1.1	0.93	1.2	0.35	2.1

Table 5.5: Summary of κ uncertainty values as obtained from separate fits to the signal strength uncertainty estimates for the seven most abundant Higgs decay channels, in charged and neutral currents for the LHeC, the HE-LHeC and the FCC-eh, see text.

3905 In the electroweak theory there is an interesting relation between the ratio of the W and Z
3906 couplings and the mixing angle,

$$\frac{\sigma(WW \rightarrow H \rightarrow AA)}{\sigma(ZZ \rightarrow H \rightarrow AA)} = \frac{\kappa_W^2}{\kappa_Z^2} = (1 - \sin^2 \theta_W)^2 \quad (5.11)$$

3907 This relation can be particularly well tested with the ep colliders as they measure both WWH
3908 and ZZH in one experiment and common theoretical environment. If one assumes the WW
3909 and ZZ measurements to be independent, the resulting error on $\sin^2 \theta_W \simeq 0.23$ is 0.003 for the

3910 LHeC and 0.001 for FCC-eh. However, this probably is smaller because there exist correlations
 3911 in the measurements which a genuine data based analysis would have to evaluate and take into
 3912 account.

3913 The effect of the theory uncertainties has been studied for the FCC-eh where the experimental
 3914 precision is highest. Tab. 5.6 presents the results of a κ analysis using the CC and NC FCC-
 3915 eh signal strength input (Tab. 5.4) neglecting the theoretical uncertainty and adding 0.5% or
 3916 1% in quadrature, to only μ_{bb} where it matters. This results in an about linear increase of
 3917 the uncertainty for bb (by a factor of 1.5), WW (by 1.7) and ZZ (by 1.5), while all other κ
 3918 uncertainties only slightly deteriorate. The effect of such uncertainties for LHeC is much smaller
 3919 as the μ uncertainties are three times those of FCC-eh, see Tab. 5.4. Therefore, in the LHeC
 case, the theory uncertainties are neglected.

Setup	$b\bar{b}$	WW	gg	$\tau\tau$	cc	ZZ	$\gamma\gamma$
FCC-eh (no thy)	0.60	0.22	1.1	0.93	1.2	0.35	2.1
FCC-eh (0.5% thy)	0.72	0.28	1.1	1.0	1.2	0.41	2.2
FCC-eh (1.0% thy)	0.91	0.37	1.1	1.0	1.3	0.53	2.3

Table 5.6: Summary of κ uncertainty values as obtained from separate fits to the signal strength uncertainty estimates for the seven most abundant Higgs decay channels, in charged and neutral currents for the FCC-eh, with no theoretical uncertainty, half a per cent and one per cent uncertainty added.

3920

3921 An interesting question regards the role of the electron beam polarisation. Assuming a maxi-
 3922 mum polarisation of $P = -0.8$, the CC (NC) Higgs cross section is calculated to be 1.8 (1.09)
 3923 times larger than that in unpolarised scattering. Therefore the signal CC and NC strength
 3924 uncertainties scale like 1.34 and 1.09, respectively. This is studied for the LHeC. If the default
 3925 fit is made, then the κ uncertainties quoted in Tab. 5.5 for bb , WW , gg , $\tau\tau$ and cc are enhanced
 3926 by a factor of 1.28. This is due to the combined effect of CC and NC which diminishes the
 3927 deterioration a bit, from 1.34 to 1.28. Thus, for example, the κ_{WW} uncertainty moves from
 3928 0.7 to 0.9% in the unpolarised case. The uncertainty on κ_{ZZ} is enhanced only by a factor of
 3929 1.14, becoming 1.38 instead of 1.21 because the NC channel has a particularly strong effect on
 3930 the ZZH coupling. Since the prospect to detect the $\gamma\gamma$ channel in NC is very poor, the $\kappa_{\gamma\gamma}$
 3931 uncertainty is enlarged by the full CC factor of 1.34. It is for maximum precision very desirable
 3932 to have the beam polarised. This, together with electroweak physics, represents an important
 3933 reason to continue to develop high current polarised electron sources.

3934 5.1.11 Parton Distributions

3935 The momentum distributions of partons inside the proton are best determined in deep inelas-
 3936 tic electron-proton scattering because the pointlike electron (or lepton), being free of strong
 3937 interactions, is able to probe proton substructure in a fundamentally clean way. The parton's
 3938 momentum x can be computed with the scattered electron kinematics, there is no colour recon-
 3939 nection in the final state, DIS theory is free of non-perturbative or hadronisation corrections.
 3940 The experimental reconstruction is clean, even at FCC-eh where the pile-up is one, and the ra-
 3941 diative corrections are suppressed through momentum conservation constraints. The kinematic
 3942 reconstruction is redundant in the NC channel, enabling cross calibrations, and it uniquely dis-
 3943 tinguishes NC and CC events. Furthermore, the four-momentum transfer squared, Q^2 , can be
 3944 freely prescribed, from the DIS minimum, $Q^2 > M_p^2$, up to the kinematic limit $Q^2 \leq s$, which
 3945 at the LHeC (FCC-eh) is as large as $1.68 (12) \cdot 10^6 \text{ GeV}^2$. Due to the large collision energies

3946 of the new ep colliders here considered, neutral electromagnetic and neutral and charged weak
3947 interactions simultaneously probe proton's structure over a huge kinematic range. When com-
3948 plemented with charm and beauty tagging to determine the s , c , b distributions [1], this enables
3949 the six quark contributions, including a separation of valence and sea quarks, to be completely
3950 and precisely reconstructed free of symmetry assumptions or nuclear corrections for the first
3951 time. This also enables determinations of the gluon distribution and the strong coupling con-
3952 stant to unprecedented precision such as $0.1 - 0.2\%$ on α_s . This outstanding potential has been
3953 discussed in Ref. [1, 56]. It is theoretically and practically superior to any attempt to deduce
3954 PDFs from hadron-hadron collisions at the LHC or fixed target DIS scattering data. The LHeC,
3955 when operating concurrently with the LHC, will therefore have a strong impact on LHC Higgs
3956 physics, beyond the ep H measurements, because it will remove the PDF and α_s uncertainties
3957 which compromise the precision obtainable in pp Higgs physics.

3958 The uncertainties derived from PDFs and α_s on Higgs coupling and cross section measurements
3959 at the LHC will be rendered negligible with the LHeC. The recent evaluation of prospects for
3960 Higgs measurements at the LHC by the CMS Collaboration presents theoretical errors, on signal
3961 and background, and their contribution to the full uncertainty [507]. For the signal strength of
3962 the $H \rightarrow b\bar{b}$ decay, for example, CMS estimated a full uncertainty at HL-LHC of μ_{bb} of 7.2%
3963 which is dominated by 5.4% (SigTh). The LHeC would essentially remove that uncertainty
3964 and lead to a 4.8% total error if the BgdTh and Exp error were untouched. It so provided a
3965 safer base for improvements than have been assumed to occur by CMS with their S2 scenario,
3966 in which the theoretical uncertainty is just assumed to be halved.

3967 The role LHeC may play for LHC physics, not least on exploring the Higgs, depends on the
3968 timeline of its installation. The earliest shutdown, when LHeC may come in, is LS4, in the early
3969 thirties. It has been estimated [33] that LHeC would collect 5 fb^{-1} of integrated luminosity in
3970 its first year of operation increasing to 50 fb^{-1} in three years. This means, that in its first year,
3971 the LHeC experiment collected ten times the total luminosity which H1 registered in its lifetime
3972 of 15 years, while after three years the luminosity was hundred times that of H1, taken at much
3973 higher beam energies leading to higher cross sections at fixed x and Q^2 . For pp Higgs physics
3974 at the LHC, the precise determination of the gluon density, xg , at medium $x \sim M_H/\sqrt{s} = 0.01$
3975 is of crucial importance.

3976 Fig. 5.14 shows the precision one can expect to obtain for xg with the LHeC. One notices a very
3977 large improvement with respect to HERA, using the combined H1 and ZEUS data in the LHeC
3978 fit framework, but also the near saturation with respect to increasing the integrated luminosity,
3979 comparing the result for 50 fb^{-1} with the ultimate set of 1 ab^{-1} . In other words, the precise
3980 LHeC QCD information will be available from the first period of data taking and thus be in time
3981 for the HL-LHC, many results of which require the full statistics (as for μ_{bb} for which CMS [507]
3982 quotes a statistical uncertainty of 2.1% within the projected HL-LC lifetime of 3 ab^{-1}).

3983 5.2 Measuring the Top-quark–Higgs Yukawa Coupling

3984 Electron-proton collisions at high energy are known to provide a unique window of opportunity
3985 to perform precision measurements in the top sector [369]. This is due to the large cross-sections
3986 of the production of single top, which amounts to about 2 pb for $E_e = 60 \text{ GeV}$ and $E_p = 7 \text{ TeV}$,
3987 where clean signatures are provided without the challenges posed by pile-up. As a result, the
3988 cross-section of the SM in association with a single top in e^-p collisions is large enough to
3989 perform competitive measurements. This includes the measurement of the absolute value of the
3990 Top Yukawa coupling and, most prominently, its CP-phase [382].

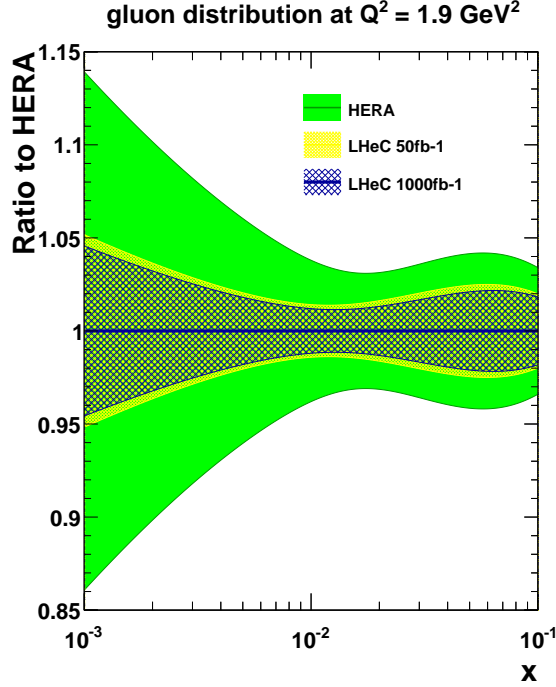


Figure 5.14: Uncertainty on the determination of the gluon distribution in the x range relevant for Higgs measurements at the LHC, based on the combined HERA data (outer band, green) and for the LHeC with the full data set (inner band, blue) and from the first running period (yellow, around the inner band). The LHeC uncertainties comprise full correlated systematic error estimates besides the statistics.

3991 In the SM, the Yukawa coupling of the third generation of quarks can be written down as:

$$\mathcal{L}_Y = -\frac{m_t}{v} \bar{t} t h - \frac{m_b}{v} \bar{b} b h, \quad (5.12)$$

where $v \equiv (\sqrt{2}G_F)^{-1/2} = 2m_W/g \simeq 246$ GeV, and m_t (m_b) is the mass of the top (bottom) quark. Due to the pure scalar nature of the Higgs boson in the SM, the top- and bottom-Higgs couplings are completely CP-even. To investigate any BSM contributions in terms of mixtures of CP-even and CP-odd states, we write a CP-phase dependent generalised Lagrangian as follows [508]:

$$\begin{aligned} \mathcal{L} = & -\frac{m_t}{v} \bar{t} [\kappa \cos \zeta_t + i\gamma_5 \sin \zeta_t] t h \\ & -\frac{m_b}{v} \bar{b} [\cos \zeta_b + i\gamma_5 \sin \zeta_b] b h. \end{aligned} \quad (5.13)$$

3992 Here, ζ_t and ζ_b are the phases of the top-Higgs and bottom-Higgs couplings, respectively. It is
 3993 clear from the Lagrangian in Eq. (5.13) that $\zeta_{t,b} = 0$ or $\zeta_{t,b} = \pi$ correspond to a pure scalar state
 3994 while $\zeta_{t,b} = \frac{\pi}{2}$ to a pure pseudo scalar state. Thus, the ranges $0 < \zeta_{t,b} < \pi/2$ or $\pi/2 < \zeta_{t,b} < \pi$
 3995 represent a mixture of the different CP-states. The case $\kappa = 1$, $\zeta_t = 0$ corresponds to the SM.

3996 In e^-p collisions, the top-Higgs couplings can be probed via associated production of the Higgs
 3997 boson with an anti-top quark $e^-p \rightarrow \bar{t} h \nu_e$. It is necessary to consider a 5-flavour proton including
 3998 the b -quark parton distribution. The Feynman diagrams for the process under investigation are
 3999 shown in Fig. 5.15. It is important to note that three important couplings are involved, namely
 4000 hWW , Wtb and the top-Higgs (tth). A detailed study of hWW and Wtb couplings at the e^-p
 4001 collider have been performed in Refs. [369,509], respectively. For our studies we do not consider

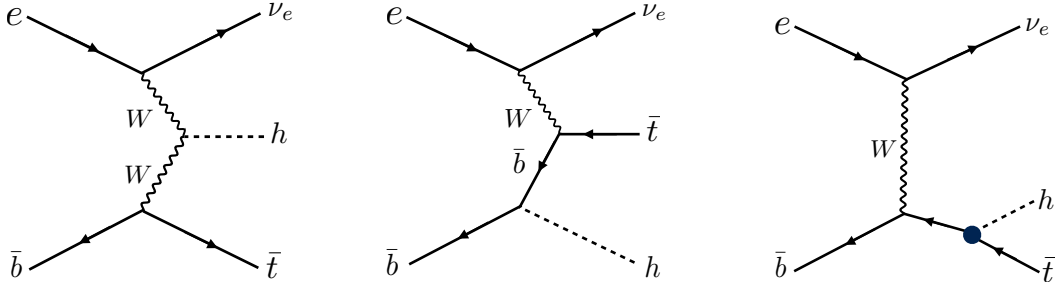


Figure 5.15: Leading order Feynman diagrams contributing to the process $p e^- \rightarrow \bar{t} h \nu_e$ in high energy e^-p collisions. The black dot in the Feynman diagram on the right denotes the top-quark-Higgs coupling of interest in this section.

4002 the BSM bottom-Higgs coupling since the effect of the phase ζ_b on the total production cross
 4003 section or kinematics of top-Higgs production at the LHeC are negligible. Thus in what follows,
 4004 we simply set $\zeta_b = 0$.

4005 In the context of the LHC, quantitatively an interesting feature can be observed: in the pure SM
 4006 case there is constructive interference between the diagrams shown in Fig. 5.15, left and middle,
 4007 for $\zeta_t > \pi/2$ resulting in an enhancement in the total production cross section of associated
 4008 top-Higgs significantly. This is also true for $\zeta_t < \pi/2$ - however the degree of enhancement is
 much smaller owing to the flipped sign of the CP-even part of the coupling.

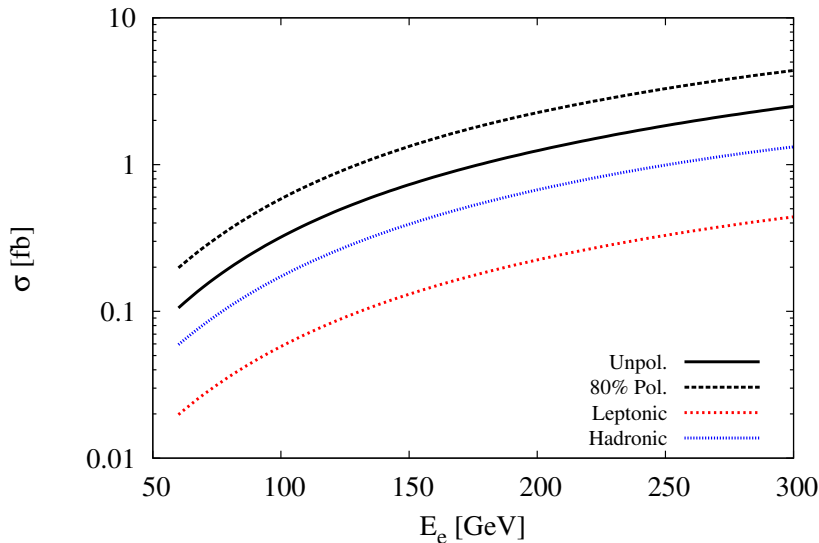


Figure 5.16: Cross-sections of the Higgs boson produced in association with a top quark in e^-p collisions with $E_p = 7$ TeV. for different electron beam energies The dotted and solid *black* lines correspond to $p e^- \rightarrow \bar{t} h \nu_e$ with and without longitudinal polarisation of the electron beam, respectively. The dotted *red* and *blue* lines correspond to $\sigma \times \text{BR}$ for the leptonic and hadronic decay modes of \bar{t} where for this estimation we use basic cuts (see text).

4009

4010 We probe the sensitivity of the top-Higgs couplings in terms of ζ_t by building a model file for
 4011 the Lagrangian in Eq. (5.13) using `FeynRules` [510], and then simulating the charged current
 4012 associated top-Higgs production channel $p e^- \rightarrow \bar{t} h \nu_e$ (see Fig. 5.15), with h further decaying
 4013 into a $b\bar{b}$ pair and the \bar{t} decaying leptonically in the LHeC set-up with centre of mass energy
 4014 of $\sqrt{s} \approx 1.3$ TeV. Here we perform the analysis at parton level only where for signal and back-

4015 ground event generation we use the Monte Carlo event generator package `MadGraph5` [352].
4016 We use `NNPDF23_lo_as_0130_qed` [511, 512] parton distribution functions for all event gener-
4017 ations. The factorisation and renormalisation scales for the signal simulation are fixed at
4018 $\mu_F = \mu_R = (m_t + m_h)/4$ while background simulations are done with the default `MadGraph5` [352]
4019 dynamic scales. The e^- polarisation is assumed to be -80% . We now list and explain various
4020 kinematic observables that can serve as possible discriminants of a CP-odd $t\bar{t}h$ coupling.

4021 In Fig. 5.16 we present the variation of the total cross section against the electron beam energy
4022 for the signal process $pe^- \rightarrow \bar{t}h\nu_e$, by considering un-polarised and polarised e^- beam. Also,
4023 the effect of branchings of $h \rightarrow b\bar{b}$ and the \bar{t} decay for both leptonic and hadronic modes are
4024 shown. Possible background events typically arise from $W+$ multi-jet events, $Wb\bar{b}\bar{b}$ with missing
4025 energy which comes by considering only top-line, only Higgs-line, and without top- nor Higgs-
4026 line, in charged and neutral current deep-inelastic scattering and in photo-production by further
4027 decaying W into leptonic mode. We have estimated the cross sections for signal and all possible
4028 backgrounds imposing only basic cuts on rapidity $|\eta| \leq 10$ for light-jets, leptons and b -jets, the
4029 transverse momentum cut $p_T \geq 10$ GeV and $\Delta R_{\min}=0.4$ for all particles.

4030 We now estimate the sensitivity of the associated top-Higgs production cross-section, $\sigma(\zeta_t)$, as
4031 a function of the CP phase of the $t\bar{t}h$ -coupling as shown in Fig. 5.17 by considering $E_e = 60$
4032 and with fixed $E_p = 7$ TeV. The scale uncertainties are taken as $(m_t + m_h)/8 \leq \mu_F = \mu_R \leq$
4033 $(m_t + m_h)/2$. Here $\sigma(\zeta_t = 0)$ corresponds to the SM cross section. We notice that the cross section
4034 is very sensitive to ζ_t in the region $\zeta_t > \frac{\pi}{2}$ where the interference between the diagrams becomes
4035 constructive. Below $\zeta_t = \frac{\pi}{2}$ the interference is still constructive though its degree decreases
4036 with ζ_t , thus increasing the cross section by around 5 times at $\zeta_t = \frac{\pi}{2}$ which corresponds to
4037 the pure CP-odd case. On the other hand, for pure CP-even case $\zeta_t = \pi$ with opposite-sign of
4038 $t\bar{t}h$ -coupling the cross section can be enhanced by up to 24 times for $E_e = 60$ GeV. The scale
uncertainty on an average is approximately 7% for $E_e = 60$ GeV in the whole range of ζ_t .

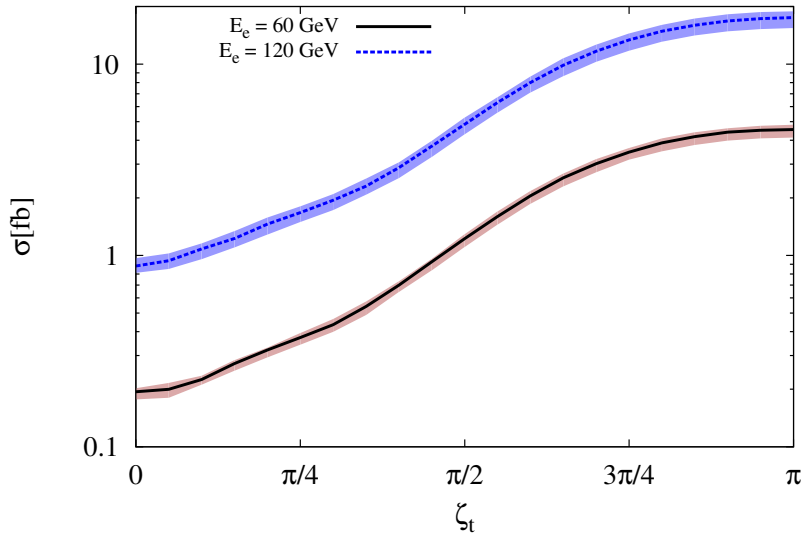


Figure 5.17: Total cross section of the Higgs boson produced in association with a single top as a function of ζ_t , including scale uncertainties. The *black* solid and *blue* dotted lines correspond to $E_e = 60$ and 120 GeV, respectively. These are obtained for fixed $E_p = 7$ TeV and scales $\mu_F = \mu_R = (m_t + m_h)/4$.

4039

4040 In order to evaluate sensitivity to the measurement of the top Yukawa coupling and its P-phase,
4041 we implement the following criteria to select events, referred to as the fiducial selection:

- 4042 • $p_T \geq 20$ GeV for b -tagged jets and light-jets, and $p_T \geq 10$ GeV for leptons.
- 4043 • Since the LHeC collider is asymmetric, event statistics of final state particles are mostly
- 4044 accumulated on the left or right sides of the transverse plane $\eta = 0$ (depending on the
- 4045 initial direction of p and e^-) - we select events within $-2 \leq \eta \leq 5$ for b -tagged jets while
- 4046 $2 \leq \eta \leq 5$ for leptons and light-jets,
- 4047 • The separation distance of all final state particles are taken to be $\Delta R > 0.4$.
- 4048 • Missing transverse energy $\cancel{E}_T > 10$ GeV to select the top events.
- 4049 • Invariant mass windows for the Higgs through b -tagged jets and the top are required to
- 4050 be $115 < m_{bb} < 130$ GeV and $160 < m_t < 177$ GeV, respectively, which are important to
- 4051 reduce the background events substantially.

4052 In these selections the b -tagging efficiency is assumed to be 70%, with fake rates from c -initiated
 4053 jets and light jets to the b -jets to be 10% and 1%, respectively.

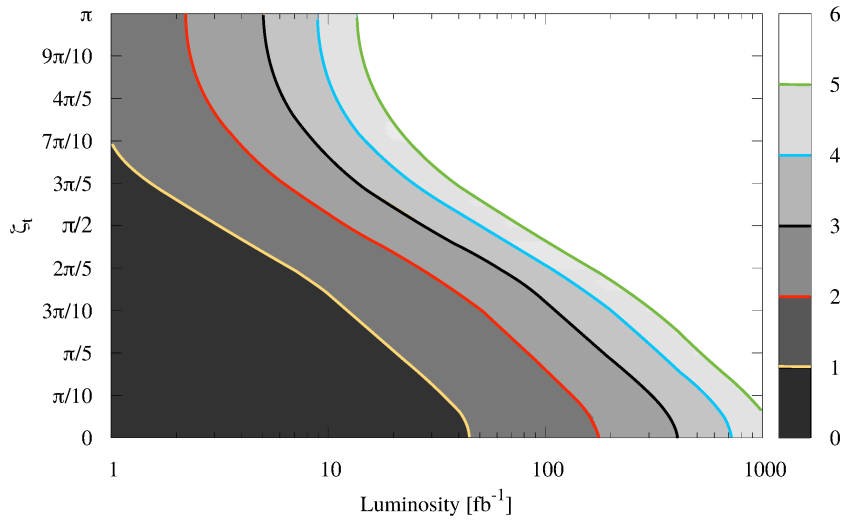


Figure 5.18: Exclusion contours for ζ_t as a function of integrated luminosity for $E_e = 60$ GeV and $E_p = 7$ TeV. The regions beyond each contours are excluded for the particular luminosity, *black* and *red* solid lines correspond to 3σ and 2σ regions. Results are obtained based on fiducial cross-sections (see text).

4054 We estimated the exclusion regions of ζ_t as a function of L in fb^{-1} . The exclusion is based
 4055 on significance using the Poisson formula, where S and B are the number of expected signal
 4056 and background events at a particular luminosity, respectively. Here we used 10% systematic
 4057 uncertainty for background yields only. In Fig. 5.18, we present exclusion contours at various
 4058 confidence levels for $E_e = 60$ GeV – understandably, higher σ -contours demand larger luminosities.
 4059 It is also seen that there is a kink around $\zeta_t = \pi/2$ such that for the region $0 < \zeta_t < \pi/2$, we
 4060 need larger luminosities for exclusion. This is in keeping with the feature exhibited in Fig. 5.17
 4061 where the constructive interference between the signal diagrams enhances the cross-section over
 4062 the SM value much more for $\zeta_t > \pi/2$ thus requiring less luminosity to probe that region. For
 4063 $L = 100 \text{ fb}^{-1}$, regions above $\pi/5 < \zeta_t \leq \pi$ and $3\pi/10 < \zeta_t \leq \pi$ are excluded at 2σ and 3σ C.L.
 4064 While around $L = 400 \text{ fb}^{-1}$, regions above $\pi/6 < \zeta_t \leq \pi$ and $\pi/4 < \zeta_t \leq \pi$ are excluded at 4σ
 4065 and 5σ C.L., respectively.

4066 As a measure of comparison, that asymmetry studies at the HL-LHC [508] help probe up to
 4067 $\zeta_t = \pi/6$ for a total integrated luminosity of 3 ab^{-1} . Thus, it is clear that the LHeC provides a

4068 better environment to test the CP nature of Higgs boson couplings.

4069 For the integrated luminosity $L = 1 \text{ ab}^{-1}$, almost all values of ζ_t can be excluded up to 4σ
4070 C.L. While investigating the overall sensitivity of ζ_t by applying these two observables, it is also
4071 important to measure the accuracy of SM tth coupling κ at the LHeC energies. To measure the
4072 accuracy of κ by using signal and background yields we use the formula $\sqrt{(S+B)}/(2S)$ at a
4073 particular luminosity. And for $E_e = 60 \text{ GeV}$, the measured accuracy at the design luminosity
4074 $L = 1 \text{ ab}^{-1}$ is given to be $\kappa = 1.00 \pm 0.17$ of its expected SM value, where a 10% systematic
4075 uncertainty is been taken in background yields only.

4076 These results are obtained based on the evaluation of the fiducial cross-sections alone. As
4077 pointed out in Ref. [382], a number of other observables carry sensitivity to the structure of the
4078 top-Higgs Yukawa coupling, such as the rapidity difference between the top quark and the Higgs
4079 boson and a number of angular variables. While the fiducial rate studied here is the single most
4080 sensitive observable, it is evident that a multi-variate approach will significantly enhance the
4081 sensitivity reported here.

4082 5.3 Higgs Decay into Invisible Particles

4083 The Higgs decay into invisible particles could be a key to BSM physics. The SM branching
4084 ratio of $H \rightarrow ZZ \rightarrow 4\nu$ is only 0.1%. Any sizable decay rate into invisible particles would
4085 thus indicate an exotic decay, for example to dark matter particles. Its non-observation would
4086 give the SM cross section measurement, reconstructing more than 99% of the ordinary decays
4087 a higher meaning for constraining the total Higgs decay width.

4088 For the LHeC at a luminosity of 1 ab^{-1} , initial parton-level studies of this decay were presented
4089 in Ref. [513], with the estimate of a two σ sensitivity to a branching fraction of 6%. For this
4090 study, NC production via ZZ fusion $eq \rightarrow eqZZ \rightarrow eqH$ was used, which has a cross section
4091 of about 25 fb at the LHeC. The CC production via WW fusion has a larger cross section,
4092 but entails a missing energy signal by itself which requires further study of potentially quite
4093 some gain in precision. This channel, when employed for the invisible decay study, results in a
4094 mono-jet signature which is hard to separate from the SM DIS CC background.

4095 The neutral current study has been repeated using the LHeC Higgs WG analysis tools, intro-
4096 duced above: MadGraph, Pythia and Delphes. Similar to [513], an electron beam of 60 GeV
4097 with a polarization of -80% is assumed. The basic event topology contains the scattered electron,
4098 jet and missing transverse energy. Its main background results from SM W and Z productions
4099 (followed by $W \rightarrow \ell\nu$ and $Z \rightarrow \nu\bar{\nu}$). In the study NC and CC W production and NC Z produc-
4100 tion are considered, while single-top, NC multijets and W photoproduction were all found to be
4101 negligible. Requiring missing transverse energy of 60 GeV, exactly one electron and one jet, and
4102 no other leptons (including τ), as well as imposing several selection criteria on the kinematics of
4103 electron, jet and missing transverse momentum, we get a two σ sensitivity to a branching ratio
4104 of 7.2%, which is similar to the earlier result [513]. Fig. 5.19 shows the electron-jet invariant
4105 mass distribution after the selection for the signal (normalized to a 100% branching ratio) and
4106 the background.

4107 The analysis has been further refined with a usage of multivariate analysis (Boosted Decision
4108 Tree in TVMA package). Basically the set of selection variables used in the cut-based analysis
4109 above was used as inputs to the multivariate analysis, tuned to yield the best output score to
4110 discriminate the signal from backgrounds. Fig. 5.20 shows the distribution of the discriminant

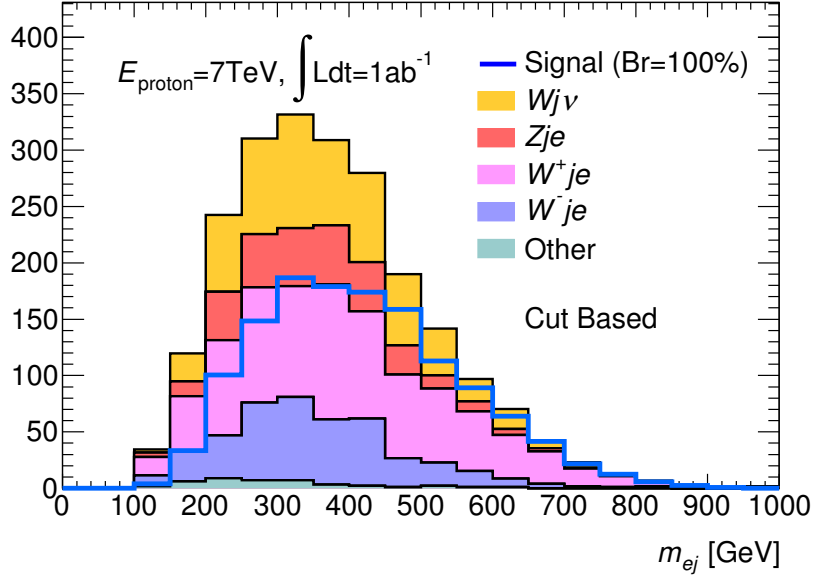


Figure 5.19: Electron-jet invariant mass distribution for the Higgs to invisible decay signal (normalized to 100% branching ratio) and the stacked backgrounds for an integrated luminosity of 1 ab^{-1} at the LHeC after all selection cuts.

4111 variable for the signal and background (both area normalised). An optimization on the statistical
 4112 significance is found at the BDT score > 0.25 , and the resulting mass distribution is shown
 4113 in Fig. 5.21. With 1 ab^{-1} of integrated luminosity, a two σ sensitivity of 5.5% is obtained
 4114 consistent with the previous results. For a comparison, an estimate of 3.5% is given for a HL-
 4115 LHC sensitivity study on this channel [514]. The result on the LHeC may be further improved
 4116 in the future with a refined BDT analysis when one introduces extra parameters, beyond those
 4117 initially introduced with the cut based analysis.

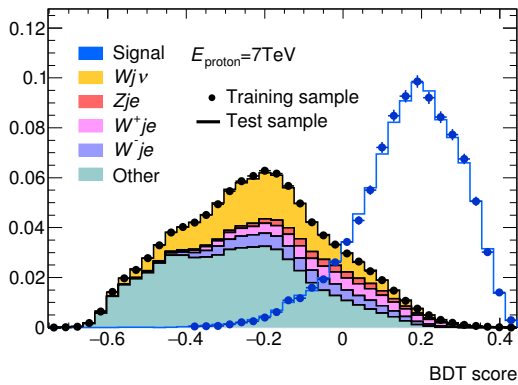


Figure 5.20: BDT output score distribution for the Higgs to invisible decay signal and the stacked backgrounds (both area normalized) at the LHeC.

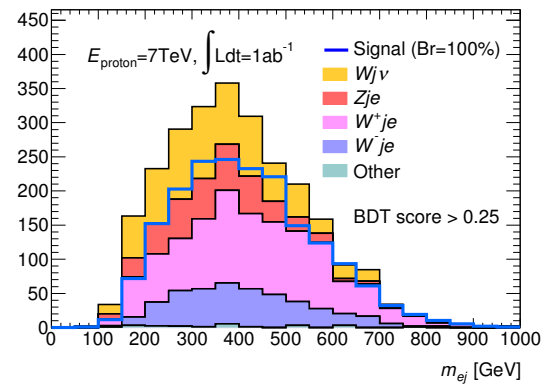


Figure 5.21: Electron-jet invariant mass distribution for the Higgs to invisible decay signal (normalized to 100% branching ratio) and the stacked backgrounds for an integrated luminosity of 1 ab^{-1} at the LHeC after the BDT score cut of 0.25.

4118 In these initial studies no systematic uncertainties were considered. This may be justified with
 4119 the very a clean environment of electron-hadron collider, in which precise measurements of W
 4120 and Z production will be made, for example in their decays to muons, for accurately controlling

4121 the systematics in the background prediction to a negligible level.

4122 The BDT analysis was repeated for higher proton energies. At the HE-LHeC ($E_p=13.5$ TeV)
4123 the NC production cross section increases to 45 fb and the branching ratio sensitivity improves
4124 to 3.4% because the luminosity is doubled in the configurations here assumed. At the FCC-eh,
4125 the cross section rises to 120 fb and the sensitivity of the branching ratio reaches about 1.7%.

Chapter 6

Searches for Physics Beyond the Standard Model

6.1 Introduction

The LHC was originally envisioned as the ultimate machine to search for physics beyond the Standard Model at the TeV scale. The absence of hints from New Physics (NP) in LHC data to date are presently changing this paradigm to two alternative scenarios: NP may actually reside at an even larger energy scale; NP may be at or below the TeV scale but more weakly coupled and thus hidden in the SM backgrounds [515].

The possibility for undiscovered NP below the TeV scale could be addressed by the LHeC, which is projected to operate when the LHC will be in its high luminosity phase. The electron-proton collider will endow the LHC searches with complementary search channels, which will allow to measure the same phenomenon in a different environment, add precision measurements, or lead to the discovery of a weak signal. A similar pp - ep synergy could be envisaged with higher proton beam energies at the FCC 100 km tunnel. With an electron beam of 60 GeV, the expected centre-of-mass energies for ep could be 2.9 TeV for $E_p = 19$ TeV (Low-Energy FCC) and 3.5 TeV for $E_p = 50$ TeV (FCC).

It has been stated that in many cases the LHeC can provide detailed tests of features that are shared by leptons and quarks, see Ref. [1] and references therein. Below we list recent developments which discuss new physics opportunities at the LHeC and its potential future high-energy upgrades.

6.2 Extensions of the SM Higgs Sector

Presently, given the precision of measurements in the Higgs sector, it appears that the discovered 125 GeV scalar is indeed the SM Higgs boson. It is not absolutely clear, however, if the scalar potential is truly that of the SM or if it is extended, possibly with additional degrees of freedom. Several extensions of the Higgs sector have been proposed and can be studied at the ep colliders with results often complementary to those of pp colliders and other future facilities.

4153 6.2.1 Modifications of the Top-Higgs interaction

4154 In electron-proton collisions the heavy top-quarks can be produced in association with a Higgs
4155 boson, which allows us to study the sensitivity of the LHeC or the FCC-he to the top-Higgs
4156 (tH) interaction. In Ref. [382] the sensitivity of the process $pe^- \rightarrow \bar{t}H\nu_e$ to the CP nature of
4157 the tH coupling is investigated, by considering a CP phase ζ_t at the ttH and bbH vertices. The
4158 authors conclude, based on several observables and with appropriate error fitting methodology,
4159 that better limits on ζ_t are obtained at the LHeC than at the HL-LHC. At the design luminosity
4160 of 1 ab^{-1} , almost all values of ζ_t are excluded up to 4σ C.L. and the SM top-Higgs coupling
4161 could be measured relative to its SM value with a precision of $\kappa = 1.00 \pm 0.17$.

4162 Flavour changing neutral currents (FCNC) are completely absent at tree-level in the SM and
4163 strongly constrained especially by low energy experiments. Anomalous flavour changing neutral
4164 current Yukawa interactions between the top quark, the Higgs boson, and either an up or
4165 charm quark are documented in this paper (Chapter 3, Sec. 3.4.2). Among other studies, in
4166 Ref. [516] the authors consider the Higgs decay modes $H \rightarrow \gamma\gamma, bb$ and $\tau\tau$ and considering
4167 $E_e = 150 \text{ GeV}$. The results are updated in Ref. [379] for $E_e = 60 \text{ GeV}$, including estimates for
4168 smaller electron beam energies, and the 2σ sensitivity on the branching ratio $\text{Br}(t \rightarrow uh)$ is
4169 found to be 0.15×10^{-2} . Making use of the polarisation of the electron beam and multivariate
4170 techniques, Ref. [517] shows that limits on the branching ratio $\text{Br}(t \rightarrow uh)$ of $\mathcal{O}(0.1)\%$ can be
4171 obtained, an improvement over present LHC limits of 0.19% [518, 519]. These results vary with
4172 E_e and E_p .

4173 6.2.2 Charged scalars

4174 The prospects to observe a light charged Higgs boson through the decay $H^+ \rightarrow c\bar{b}$ are inves-
4175 tigated within the framework of the Two Higgs Doublet Model (2HDM) Type III, assuming a
4176 four-zero texture in the Yukawa matrices and a general Higgs potential [520]. The charged cur-
4177 rent production processes $e^-p \rightarrow \nu H^+q$ are considered. The analysed signature stems from the
4178 subsequent decay $H^+ \rightarrow c\bar{b}$. The parton level analysis accounts for irreducible SM backgrounds
4179 and considers scenarios up to a mass of 200 GeV which are consistent with present limits from
4180 Higgs and flavour physics. The authors show that for $L = 100 \text{ fb}^{-1}$ a charged Higgs boson
4181 could be observed with about $3 - 4\sigma$ significance. This is to be compared with results from
4182 present LHC searches in which strong limits are set on the branching fraction $B(t \rightarrow H^+b)$,
4183 assuming $B(H^+ \rightarrow c\bar{b}) = 1.0$ or $B(H^+ \rightarrow c\bar{s}) = 1.0$ for the charged Higgs boson mass range
4184 $\sim 90 - 160 \text{ GeV}$ [521, 522].

4185 A similar study for the FCC-he (with $\sqrt{s} \approx 3.5 \text{ TeV}$) is presented in Ref. [523], where a next-to-
4186 minimal supersymmetric model (NMSSM) was considered where $H^\pm \rightarrow sc + su$. Using dedicated
4187 optimisation techniques, the authors show that a light charged boson H^\pm can be observed with
4188 maximal significance of $4.4 (2.2)\sigma$ provided its mass is at most $m_{H^\pm} = 114(121) \text{ GeV}$, for the
4189 total luminosity of 1 ab^{-1} .

4190 The Georgi-Machacek (GM) model extends the Higgs sector by including higher multiplet states
4191 while preserving custodial symmetry. The physical states include, besides the SM Higgs, a
4192 heavier singlet H , a triplet (H_3^+, H_3^0, H_3^-) and a quintuplet $(H_5^{++}, H_5^+, H_5^0, H_5^-, H_5^{--})$. The
4193 H_5 scalars do not couple to fermions and can therefore only be produced by vector boson
4194 fusion. An analysis for the prospects to discover the doubly charged Higgs bosons in the GM
4195 model at the LHeC and the FCC-he is presented in Ref. [524]. Therein the production of a
4196 doubly-charged member of five-plet Higgs-bosons ($H_5^{\pm\pm}$), produced from vector boson fusion is

4197 studied. The authors find that 2 to 3σ limits can be obtained for mixings $\sin(\theta_H)$ as low as 0.2,
4198 for $M(H_5) < 300$ GeV. The prospects can be improved at the FCC-he collider, where doubly
4199 charged Higgs bosons can be tested for masses $M_{H_5} < 400$ GeV, also for small scalar mixing
4200 angles.

4201 The discovery prospects for the singly charged Higgs, H_5^\pm , in the Georgi-Machacek model are
4202 evaluated in Ref. [525]. The authors perform a multivariate analysis, including a fast detector
4203 simulation, and they consider the LHeC and the FCC-he for a mass range from 200–1000 GeV.
4204 They find that the LHeC can improve over current LHC limits on H_5^\pm for masses up to about
4205 400 GeV and scalar mixing angles $\sin\theta_H \sim 0.5$.

4206 6.2.3 Neutral scalars

4207 Neutral scalar bosons generally appear in many extensions of the scalar potential. They can be
4208 added directly, as $SU(1)$ singlets, or be part of higher representation $SU(2)$ multiplets. They
4209 generally mix with the Higgs boson, from which they inherit a Higgs-like phenomenology.

4210 The potential of testing the heavier CP-even scalar that is contained in the 2HDM Type-I is
4211 presented in Ref. [526]. Therein, the lighter scalar particle is considered to be a SM-like Higgs
4212 boson and the properties of a heavy scalar, assumed to have the specific mass 270 GeV, is
4213 discussed. The authors state that the final state $H \rightarrow hh$ is of particular interest, as it connects
4214 to the findings in Ref. [515].

4215 The prospects to search for a generic heavy neutral scalar particle are presented in detail
4216 Ref. [527]. The model is a minimal extension of the SM with one additional complex scalar
4217 singlet that mixes with the SM Higgs doublet, which governs its production and decay mode.
4218 The heavy scalar is produced via vector-boson fusion and decays into two vector bosons. A mul-
4219 tivariate analysis is performed and detector simulation is taken into account. Masses between
4220 200 and 800 GeV and scalar mixings as small as $\sin^2\alpha \sim 10^{-3}$ are considered. The resulting
4221 sensitivity for a total luminosity of 1 ab^{-1} is shown in Fig. 6.1, including existing bounds from
4222 the LHC and future HL-LHC projections. A significant improvement over existing LHC limits
4223 is found, with the LHeC probing scalar boson masses below ~ 500 GeV, a region which remains
4224 difficult at the HL-LHC.

4225 The scalar bosons from the 2HDM Type-III framework may give rise to flavour violating signa-
4226 tures, which is discussed in Ref. [530]. The prospects to observe the light and heavy CP-even
4227 neutral Higgs bosons via their decays into flavour violating $b\bar{s}$ channels were studied with spe-
4228 cific Yukawa textures and a general Higgs potential. The considered signature consists in one jet
4229 originating from b-hadron fragmentation (b-tagged jets) and one light-flavour jet in the central
4230 rapidity region, with a remaining jet in the forward region. Relevant SM backgrounds were
4231 considered and it is found that flavour violating decays of the SM-like Higgs boson would be
4232 accessible with $L = 100 \text{ fb}^{-1}$ at ep colliders, while for the heaviest scalar boson, with a mass of
4233 about 170 GeV, a total luminosity of about 1 ab^{-1} will give rise to $\mathcal{O}(1)$ events.

4234 The prospects of observing the light CP-even neutral Higgs bosons via their decays into b-quarks,
4235 in the neutral and charged current production processes, considering the NMSSM framework, the
4236 MSSM with an additional singlet superfield, are studied in Ref. [531]. In this work the following
4237 constraints are incorporated into the spectrum: neutralino relic density corresponding to the
4238 observed dark matter relic density; direct and indirect mass bounds from searches for specific
4239 sparticles; the SM-like Higgs boson has a mass around 126 GeV and an invisible branching ratio
4240 below 0.25. The signal is given by three jets plus an electron or missing transverse momentum

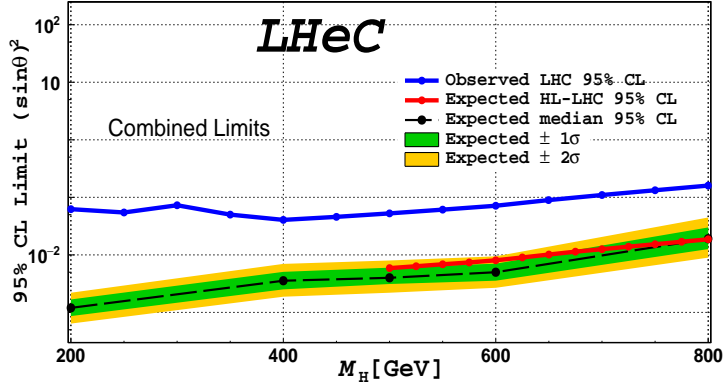


Figure 6.1: Expected exclusion limits (green and yellow bnds) for a heavy scalar search at the LHeC, assuming a systematic uncertainty on the SM background of 2% (from Ref. [527]). The blue line represents the current LHC limit at 95% CL as extracted from [528], the red line the forecast of the HL-LHC sensitivity via $h_2 \rightarrow ZZ$ searches from Ref. [529]. The LHeC results correspond to an integrated luminosity of 1 ab^{-1} .

4241 (E_T^{miss}) arising from the neutral (charged) current interaction, where two jets are required to be
 4242 originating from a b-quark and the remaining jet is required to be in the forward region. For the
 4243 cut-based analysis a number of reducible and irreducible SM backgrounds are considered and it
 4244 includes a fast detector simulation with an adaption of the LHeC detector. It is found that the
 4245 boson h_1 could be observable for some of the NMSSM benchmark points, at up to 2.5σ level in
 4246 the $e + 3j$ channel up to masses of 75 GeV; in the $3j + E_T^{miss}$ channel h_1 could be discovered
 4247 at 2.4σ level up to masses of 88 GeV with $L = 100 \text{ fb}^{-1}$, and a 5σ observation is possible with
 4248 $\mathcal{L} = 1 \text{ ab}^{-1}$ for masses up to 90 GeV.

4249 6.2.4 Modifications of Higgs self-couplings

4250 As in the chapter on Higgs physics above, the e^-p collisions are a very convenient environment
 4251 to study the property of the SM Higgs boson itself. The latter is produced through vector-boson
 4252 fusion processes and the precise measurement of its properties provides a unique opportunity
 4253 to probe the interaction HVV , ($V = W^\pm, Z$). These interactions are in general sensitive to
 4254 certain classes of beyond the SM physics, which can be parametrised, for instance, via higher
 4255 dimensional operators and their coefficients, cf. Refs. [479, 509, 532, 533].

4256 The prospects to infer the strengths of the two couplings HWW and HZZ were studied in
 4257 Refs. [509, 532] in the context of electron-proton collisions. The authors find that the higher-
 4258 dimensional operator coefficients can be tested for values around $\mathcal{O}(10^{-1})$ at the LHeC. This
 4259 sensitivity is improved at the FCC-he due to larger centre-of-mass energies, which in general
 4260 enhances the vector-boson fusion cross sections.

4261 The Higgs self-coupling itself HHH can be tested through the measurement of the di-Higgs
 4262 production cross section as was shown in Ref. [479]. With appropriate error fitting methodology
 4263 this study illustrates that the Higgs boson self-coupling could be measured with an accuracy of
 4264 $g_{HHH}^{(1)} = 1.00_{-0.17(0.12)}^{+0.24(0.14)}$ of its expected SM value at $\sqrt{s} = 3.5(5.0) \text{ TeV}$, considering an ultimate
 4265 10 ab^{-1} of integrated luminosity.

4266 An analysis presented in Ref. [533] studies the LHeC sensitivity to dimension-six operators. The
 4267 authors employ jet substructure techniques to reconstruct the boosted Higgs boson in the final

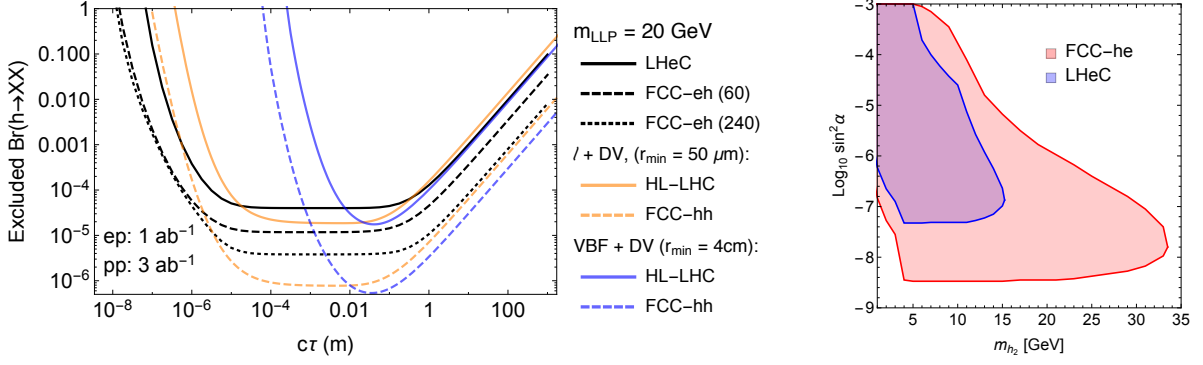


Figure 6.2: Sensitivity contours for displaced vertex searches for Higgs decays into long-lived scalar particles (LLP), which are pair produced from decays of the Higgs boson and decay themselves via scalar mixing into fully visible final states. Left: As a function of the LLP lifetime for a fixed mass from Ref. [535]. Right: For a specific model, where lifetime and production rate of the LLP are governed by the scalar mixing angle. The contours are for 3 events and consider displacements larger than $50 \mu\text{m}$ to be free of background.

4268 state. A shape analysis on the differential cross sections shows in some cases improvements with
 4269 respect to the high-luminosity LHC forecasts.

4270 6.2.5 Exotic Higgs boson decays

4271 The LHeC sensitivity to an invisibly decaying Higgs boson was investigated in Ref. [513]. Therein
 4272 the focus is on the neutral current production channel due to the enhanced number of observ-
 4273 ables compared to the charged current counterpart. The signal contains one electron, one jet
 4274 and large missing energy. A cut-based parton level analysis yields the estimated sensitivity of
 4275 $\text{Br}(h \rightarrow \text{invisible}) = 6\%$ at 2σ level. Exotic decays of the Higgs boson into a pair of light spin-0
 4276 particles referred to as Φ was discussed in Ref. [534]. The studied signature is a final state with
 4277 4 b-quarks, which is well motivated in models where the scalars can mix with the Higgs doublet,
 4278 and suffers from multiple backgrounds at the LHC. The analysis is carried out at the parton
 4279 level, where simple selection requirements render the signature nearly free of SM background
 4280 and makes Φ with masses in the range $[20, 60]$ GeV testable for a hVV ($V = W, Z$) coupling
 4281 strength relative to the SM at a few per-mille level and at 95% confidence level.

4282 The prospects of testing exotic Higgs decays into pairs of light long-lived particles at the LHeC
 4283 were studied in Ref. [535] where it was shown that proper lifetimes as small as μm could be
 4284 tested, which is significantly better compared to the LHC. This is shown in Fig. 6.2 (left). This
 4285 information can be interpreted in a model where the long-lived particles are light scalars that mix
 4286 with the Higgs doublet, where both, production and decay, are governed by this scalar mixing
 4287 angle. The area in the mass-mixing parameter space that give rise to at least 3 observable
 4288 events with a displaced vertex are shown in Fig. 6.1. It is apparent that mixings as small as
 4289 $\sin^2 \alpha \sim 10^{-7}$ can be tested at the LHeC for scalar masses between 5 and 15 GeV (Ref. [Fischer
 4290 et al., input for ESPP]).

6.3 Searches for supersymmetry

Several SUSY scenarios might remain still elusive in searches performed at pp colliders. While the null results from current searches by the LHC experiments have produced impressive constraints on the SUSY coloured sector (squarks and gluinos) because of their large production cross sections in strong interactions, less stringent constraints have been placed on weakly-produced SUSY particles, namely neutralinos $\tilde{\chi}^0$, charginos $\tilde{\chi}^\pm$, and sleptons $\tilde{\ell}^\pm$. Some of these scenarios where ep colliders might have discovery potential complementary to that of the HL-LHC are discussed below. These include R-parity conserving SUSY models, e.g. motivated by dark matter, or R-parity violating SUSY models, e.g. including single production of bottom and top squarks and low mass gluinos.

6.3.1 Search for the SUSY Electroweak Sector: prompt signatures

Electroweakino scenarios where charginos, neutralinos, and sleptons are close in mass can be characterised with the neutralino mass m and the mass splitting between charginos and neutralinos Δm . Scenarios with $\Delta m < 50$ GeV are referred to as *compressed*. A subtlety arises for $\Delta m \leq 1$ GeV, when the $\tilde{\chi}_1^\pm/\tilde{\chi}_2^0$ becomes long lived and its decays are displaced. For $\Delta m > 1$ GeV the decays are prompt, the visible decay products from $\tilde{\ell}$ and $\tilde{\chi}_1^\pm/\tilde{\chi}_2^0$ have very soft transverse momenta (p_T) and the SM backgrounds are kinematically similar to the signal. The analyses therefore become challenging and sensitivities decrease substantially. Two SUSY scenarios are considered in Ref. [536] where the LSP $\tilde{\chi}_1^0$ is Bino-like, $\tilde{\chi}_1^\pm$ and $\tilde{\chi}_2^0$ are Wino-like with almost degenerate masses, and the mass difference between $\tilde{\chi}_1^0$ and $\tilde{\chi}_1^\pm$ is small. The signal is produced via the process “ $pe^- \rightarrow je^- \tilde{\chi}\tilde{\chi}$ ”, where $\tilde{\chi} = \tilde{\chi}_1^0, \tilde{\chi}_1^\pm$ or $\tilde{\chi}_2^0$. Conservative leading order cross sections are considered for the SUSY signal models. The kinematic observables are input to the TMVA package to perform a multivariate analysis at the detector level.

In the compressed-slepton scenario, the case where the left-handed slepton $\tilde{\ell}_L$ and sneutrino $\tilde{\nu}$ are slightly heavier than $\tilde{\chi}_1^\pm$ or $\tilde{\chi}_2^0$ is considered. When fixing the mass difference $\Delta m = m_{\tilde{\ell}} - m_{\tilde{\chi}_1^\pm, \tilde{\chi}_2^0} = 35$ GeV and ignoring the systematic uncertainty on the background, the analysis indicates that the 2 (5) σ limits on the $\tilde{\chi}_1^\pm, \tilde{\chi}_2^0$ mass are 616 (517) GeV for 2.5 ab^{-1} luminosity at the FCC-eh, and 266 (227) GeV for 1 ab^{-1} luminosity at the LHeC, respectively. An illustration of the model assumptions in terms of sleptons and neutralino masses and the current constraints at the LHC is presented in Fig. 6.3 (left). Results are illustrated in Fig. 6.3 (right). The effects of varying Δm are investigated: fixing $m_{\tilde{\chi}_1^\pm, \tilde{\chi}_2^0}$ to be 400 GeV, it is found that at the FCC-eh the significance is maximal when Δm is around 20 GeV.

In the decoupled-slepton scenarios where only $\tilde{\chi}_1^0, \tilde{\chi}_1^\pm$ and $\tilde{\chi}_2^0$ are light and other SUSY particles are heavy and decoupled, the 2σ limits obtained on the $\tilde{\chi}_1^\pm, \tilde{\chi}_2^0$ mass are 230 GeV for 2.5 ab^{-1} luminosity at the FCC-eh when neglecting the systematic uncertainty on the background. Large systematic uncertainties on the SM background processes can substantially affect the sensitivity, hence good control of experimental and theoretical sources of uncertainties is very important.

Finally, it is also found that the possibility of having a negatively polarised electron beam ($Pe^- = 80\%$) could potentially extend the sensitivity to electroweakinos by up to 40%.

Overall, since the sensitivity to the electroweak SUSY sector depends on the mass hierarchy of $\tilde{\chi}_1^\pm, \tilde{\chi}_1^0, \tilde{\chi}_2^0$ and sleptons, and given the difficulty to probe efficiently small Δm regions at the current LHC and possibly at the HL-LHC, measurements at ep colliders may prove to offer complementary or additional reaches, in particular for the compressed scenarios.

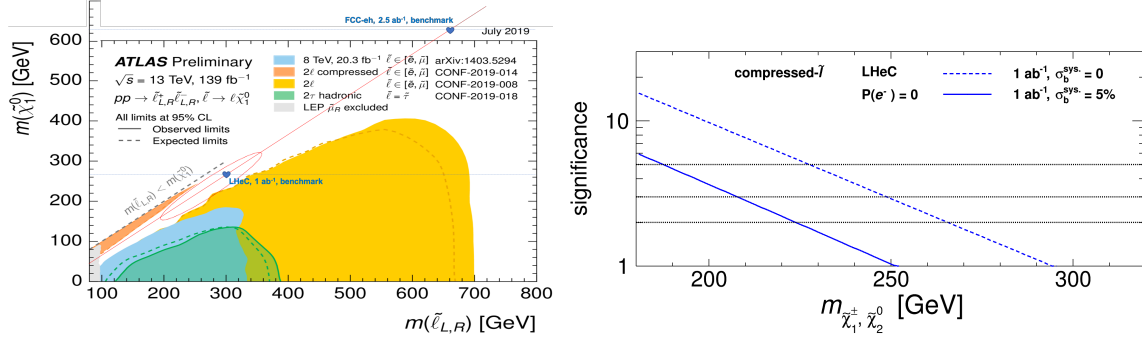


Figure 6.3: *Left:* Benchmark assumption on slepton masses and 2019 reach of current ATLAS searches for sleptons (Ref. ATLAS public twiki). *Right:* Significances as varying the masses of $\tilde{\chi}_1^\pm$ and $\tilde{\chi}_2^0$ for the compressed-slepton scenario at the LHeC with unpolarised beams and 1 ab⁻¹ luminosity. For dashed (solid) curve, a systematic uncertainty of 0% (5%) on the background is considered. The figure is from Ref. [536].

6.3.2 Search for the SUSY Electroweak Sector: long-lived particles

Studies on Higgsinos (χ) with masses $\mathcal{O}(100)$ GeV are motivated by natural SUSY theories and help to avoid large fine-tuning on the Higgs boson mass. In these scenarios the low energy charginos (χ^+)/neutralinos (χ^0) are all Higgsino-like and their masses are nearly degenerate, only slightly above the neutralino.

As mentioned above, a compressed spectrum with nearly degenerate masses results in a kinematic suppression of the heavier χ^+ decays into $W^\pm\chi^0$, which has twofold consequences: it yields final states without hard leptons; it enhances the χ^+ lifetime up to $\mathcal{O}(1)$ mm. At the LHC the absence of hard leptons with sizable transverse momentum makes this signature difficult to investigate. One possibility is to search for the tracks from χ^+ , which effectively disappear once it decays and are thus called *disappearing tracks*.

The discovery prospects for prompt signatures of electroweakino decays in electron-proton collisions are presented in Ref. [537]. The light χ^+ (and χ^0) can be produced in pairs via in vector boson fusion of the charged or neutral currents. A cut-based analysis of these processes at the LHeC, assuming prompt χ^+ decays, yields 2 σ discovery prospects for masses up to 120 GeV.

Taking into account the finite lifetime of the charginos, two comments are in order: first, the lifetimes and boosts of the χ^+ are in general too small to resolve a disappearing track; second, the soft final state is not a problem per se and can in principle be observed.

Instead of searching for a disappearing track, the long lifetimes of the χ^+ can be exploited via the measurement of the impact parameter of the soft hadronic final, as is discussed in Ref. [535]. The crucial machine performance parameters are the tracking resolution, which is as good as $\mathcal{O}(10)$ μm , and the absence of pile up, which allows to identify and measure a single soft pion's impact parameter. In this way the LHeC can test χ with masses up to 200 GeV, the corresponding sensitivity is shown in Fig. 6.4, and the bounds on disappearing track searches at the HL-LHC are shown as black lines in the figure. Considering non-prompt decays of Higgsinos thus significantly improves the discovery prospects compared to the prompt analysis. Further means of improving the prospects is an increased centre-of-mass energy, which enhances the production rate of the Higgsinos.

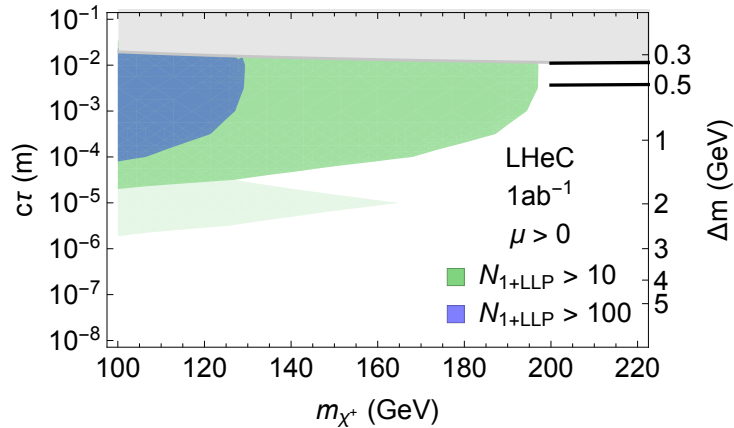


Figure 6.4: Exclusion limits on Higgsino masses as a function of their lifetime from Ref. [535]. Coloured regions denote where 10 or 100 events with at least one LLP decay are observed. Light shading indicates the uncertainty in the predicted number of events due to different hadronisation and LLP reconstruction assumptions. The black curves are the optimistic and pessimistic projected bounds from HL-LHC disappearing track searches.

4362 6.3.3 R-parity violating signatures

4363 Supersymmetry typically evokes the so-called R-parity, which implies that each fundamental
 4364 vertex contains an even number of sparticles and helps preventing rapid proton decays. In
 4365 general, R-parity need not be an exact symmetry of the theory, such that interactions can be
 4366 present that allow for sparticles to decay into SM particles and include the possibility to violate
 4367 lepton and/or baryon number.

4368 R-parity violating interactions are particularly interesting in electron-proton collisions, where
 4369 single superpartners might be produced resonantly, and detected via the corresponding $2 \rightarrow 2$
 4370 process. This is discussed in Refs. [538, 539] for the case of the *sbottom*, showing that a good
 4371 level of precision could be achieved at LHeC compared with all the knowledge derived from
 4372 indirect measurements.

4373 Single (anti-)top quark production associated with a lightest neutralino in the MSSM with
 4374 R-parity breaking coupling is investigated in Ref. [540] for the LHeC. The study includes calcu-
 4375 lations of the NLO QCD contributions and concluded that the available constraints would allow
 4376 a notable production rate.

4377 Certain SUSY scenarios might produce prompt signals of multiple soft jets, which generally
 4378 resemble QCD backgrounds at the LHC and are thus notoriously difficult to test. The largely
 4379 QCD-free environment of electron-proton collisions allows to test this class of signatures. One
 4380 example of this signal can come from gluinos, which are tested at the LHC via signatures that
 4381 involve large amounts of missing energy. If the gluino has an all-hadronic decay – as in R-parity
 4382 violating scenarios or Stealth SUSY models – the current experimental searches have a gap in
 4383 sensitivity for masses between about 50 to 70 GeV [541]. Gluinos within this gap can be tested at
 4384 the LHeC [542], where a three sigma exclusion sensitivity was demonstrated with simple signal
 4385 selection cuts.

4386 6.4 Feebly Interacting Particles

4387 New physics may interact with the SM via the so-called portal operators, including the vector,
4388 scalar, pseudoscalar, or neutrino portal. In these scenarios, the SM is often extended by an
4389 entire sector of new physics, comprising new forces and several particle species, which may be
4390 connected to the big open questions of Dark Matter or the origin of neutrino mass.

4391 These hypothetical new sectors derive their typically very feeble interaction strength with the
4392 known particles from mass mixing with a SM particle that shares their quantum numbers. Some
4393 examples are being discussed below.

4394 6.4.1 Searches for heavy neutrinos

4395 The observation of neutrino oscillations requires physics beyond the SM that gives rise to the light
4396 neutrino masses. One well-motivated class of models for this purpose is the so-called symmetry
4397 protected type I seesaw scenario, which features heavy neutrinos with signatures that are in
4398 principle observable at colliders, cf. Ref. [543] and references therein. A comprehensive overview
4399 over collider searches for the heavy and mostly sterile neutrinos can be found in Ref. [544], where
4400 the promising signatures for such searches at electron-proton colliders have been identified.

4401 In electron-proton collisions heavy neutrinos can be produced via the charged current. The heavy
4402 neutrino production cross section is dependent on the active-sterile neutrino mixing with the
4403 electron flavour called $|\theta_e|^2$. The most promising searches at the LHeC are given by processes
4404 with lepton flavour violating final states and displaced vertices, the prospects of which are
4405 evaluated in Ref. [545] and are shown in Fig. 6.5. It is remarkable, that the prospects to detect
4406 heavy neutrinos with masses above about 100 GeV are much better in electron-proton collisions
4407 compared to proton-proton or electron-positron, due to the much smaller reducible backgrounds.

4408 The prospects of heavy neutrino detection can be further enhanced with jet substructure tech-
4409 niques when the W boson in the decay $N \rightarrow eW$, $W \rightarrow jj$ is highly boosted. Ref. [546] shows
4410 that these techniques can help to distinguish the heavy neutrino signal from the few SM back-
4411 grounds. A considerable improvement in the bounds of $|V_{eN}|^2$ over present limits from LHC,
4412 $0\nu 2\beta$ experiments and from electroweak precision data is obtained with 1 ab^{-1} of integrated
4413 luminosity at the LHeC.

4414 An alternative approach is employed in Ref. [552] where the dominant sterile neutrino inter-
4415 actions with the SM are taken to be higher dimension effective operators (parameterizing a
4416 wide variety of UV-complete new physics models) while contributions from neutrino mixing is
4417 neglected. The study shows prospects of Majorana neutrino detection for masses lower than
4418 700 and 1300 GeV can be discovered at the LHeC with $E_e = 50$ and 150 GeV, respectively, for
4419 $E_p = 7 \text{ TeV}$. Recently the influence of vector and scalar operators on the angular distribution of
4420 the final anti-lepton was investigated. The forward-backward asymmetry is studied in Ref. [553],
4421 wherein, in particular, the feasibility of initial electron polarisation as a discriminator between
4422 different effective operators is studied.

4423 Prospects of testing left-right symmetric models, featuring additional charged and neutral gauge
4424 bosons and heavy neutrinos, were studied in the context of electron-proton collisions in Refs. [554,
4425 555]. The authors show that the production of heavy right-handed neutrinos of mass $\mathcal{O}(10^2$ -
4426 $10^3)$ GeV at the LHeC, with a lepton number violating final state, can yield information on
4427 the parity breaking scale in left-right symmetric theories. Heavy neutrinos of sub-TeV mass in
4428 inverse see-saw model with Yukawa coupling of $\mathcal{O}(0.1)$ are investigated for the LHeC in Ref. [556].

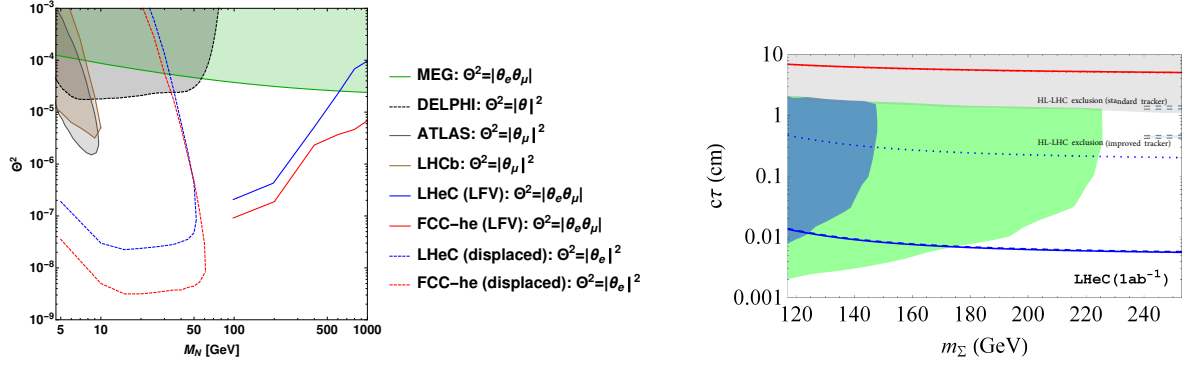


Figure 6.5: Left: Sensitivity of the LFV lepton-trijet searches (at 95 % C.L.) and the displaced vertex searches (at 95 % C.L.) from Ref. [545] compared to the current exclusion limits from ATLAS [547], LHCb [548], LEP [549], and MEG [550]. Right: Prospects of displaced vertex searches from charged fermion triplet Σ^\pm . The blue and green shaded regions denote the expected observability of 10 (100) events, dashed lines denote HL-LHC exclusion sensitivity, and the red line is connected to the light neutrino properties. For details, see text and Ref. [551].

4429 6.4.2 Fermion triplets in type III seesaw

4430 Another technically natural way of generating the light neutrino masses is the so-called Type
 4431 III seesaw mechanism, which extends the SM with a fermion $SU(2)$ triplet. In minimal versions
 4432 of these models the neutral and charged triplet fermions have almost degenerate masses around
 4433 the TeV scale.

4434 The prospects of studying this mechanism via searches for the new fermions are evaluated in
 4435 Ref. [551], wherein signatures from long-lived particles at various experiments were considered.
 4436 The triplet fermions, primarily produced through their gauge interactions, can be observed via
 4437 displaced vertices and disappearing track searches for masses of a few hundred GeV.

4438 The authors find that the LHeC can observe displaced vertices from the decays of the charged
 4439 fermion triplet components via the soft pion impact parameters for triplet masses up to about
 4440 220 GeV and has a complementary sensitivity to the light neutrino mass scale, which governs
 4441 the lifetime of the neutral fermion, compared the LHC and MATHUSLA. The final results from
 4442 Ref. [551] for the LHeC are shown in the right panel of Fig. 6.5.

4443 6.4.3 Dark photons

4444 Minimal extensions of the SM often involve additional gauge factors. In particular the $U(1)_X$ ex-
 4445 tensions are interesting, because they are often connected to a dark charge that can be associated
 4446 with the dark matter.

4447 An SM-extending $U(1)_X$ predicts an additional gauge boson that naturally mixes with the $U(1)_Y$
 4448 factor of the SM kinetically [557]. This kinetic mixing lets the SM photon couple to fermions that
 4449 carry the dark charge X , and the other gauge boson to the electric charge. Both interactions
 4450 are suppressed by the mixing parameter ϵ . In most models the additional gauge boson also
 4451 receives a mass, possibly from spontaneous breaking of the $U(1)_X$, and the corresponding mass
 4452 eigenstate is called a dark photon. Dark photons typically have masses around the GeV scale
 4453 and their interactions are QED-like, scaled with the small mixing parameter ϵ . It can decay to
 4454 pairs of leptons, hadrons, or quarks, which can give rise to a displaced vertex signal due to its
 4455 long lifetime.

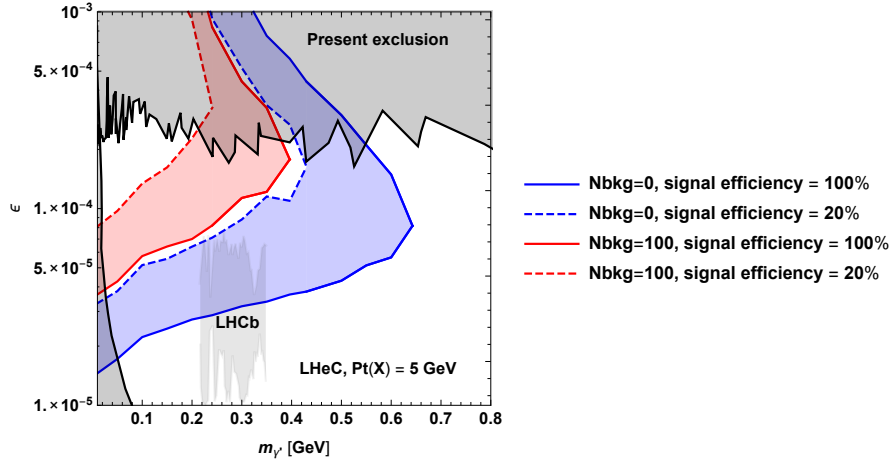


Figure 6.6: Projected sensitivity of dark photon searches at the LHeC via displaced dark photon decays from Ref. [558]. The sensitivity contour lines are at the 90 % confidence level and consider a transverse momentum cut on the final state hadrons of 5 GeV. The blue and red areas denote the assumption of zero and 100 background events, respectively, the solid and dashed lines correspond to a reconstruction efficiency of 100 % and 20 %, respectively. See Ref. [558] for details.

4456 The prospects for the dark photon searches via their displaced decays in ep collisions are pre-
 4457 sented in Ref. [558]. The most relevant performance characteristics of the LHeC are the very
 4458 good tracking resolution and the very low level of background, which allow the detection of a
 4459 secondary vertex with a displacement of $\mathcal{O}(0.1)$ mm.

4460 The resulting sensitivity contours in the mass-mixing parameter space are shown in Fig. 6.6,
 4461 where the different colours correspond to different assumptions on the irreducible background
 4462 and the solid and dashed lines consider different signal reconstruction efficiencies. Also shown
 4463 for comparison are existing exclusion limits from different experiments, and the region that is
 4464 currently investigated by the LHCb collaboration [559].

4465 The domain in parameter space tested in electron-proton collisions is complementary to other
 4466 present and planned experiments. In particular for masses below the di-muon threshold, searches
 4467 at the LHC are practically impossible. It is remarkable that dark photons in this mass range can
 4468 be part of a dark sector that explains the observed Dark Matter in the Universe via a freeze-in
 4469 mechanism, cf. e.g. Ref. [560].

4470 6.4.4 Axion-like particles

4471 The axion is the Goldstone boson related to a global $U(1)$ symmetry, which is spontaneously
 4472 broken at the so-called Peccei-Quinn scale, assumed to be around the GUT scale. Its mass,
 4473 being inversely proportional to the Peccei-Quinn scale, is therefore usually in the sub-eV regime
 4474 and the axion provides a dynamical solution to the strong CP problem of the standard model.
 4475 Axions are a very attractive candidate for *cold* dark matter, despite their tiny mass.

4476 Axion-like particles (ALP) are motivated by the original idea of the QCD axion and similarly,
 4477 they are good dark matter candidates. ALPs are pseudoscalar particles that are usually assumed
 4478 to be relatively light (i.e. with masses around and below one GeV) and couple to the QCD field
 4479 strength. In addition, they may have a number of further interactions, for instance they can
 4480 interact with the other fields of the SM and also mix with the pion. Particularly interesting is
 4481 the possibility to produce ALPs via vector boson fusion processes.

4482 A recent study [561] has evaluated the prospects of detecting ALPs at the LHeC via the process
 4483 $e^- \gamma \rightarrow e^- a$ in a model independent fashion. The investigated signature is the decay $a \rightarrow \gamma \gamma$,
 4484 which allows to test the effective ALP-photon coupling for ALPs with masses in the range
 4485 of $10 \text{ GeV} < m_a < 3 \text{ TeV}$. It was found that sensitivities can improve current LHC bounds
 4486 considerably, especially for ALP masses below 100 GeV, and the authors state that ALP searches
 4487 at ep colliders might become an important handle on this class of new physics scenarios [561].

4488 6.5 Anomalous Gauge Couplings

4489 New physics beyond the SM can modify SM interactions, for instance at the loop level. Such
 4490 contributions could either modify the interaction strength of SM particles or introduce additional
 4491 interactions that are not present in the SM, like flavour changing neutral couplings.

4492 Searches for anomalous couplings of top quarks are summarised in Section 3.4. They are
 4493 parametrised via an effective Lagrangian and are studied by analysing specific processes. For
 4494 example, anomalous Wtb couplings are studied in $e^- p \rightarrow \nu_e \bar{t}$, and anomalous $t\bar{t}\gamma$ and $t\bar{t}Z$ cou-
 4495 plings are studied in top quark pair production. In addition FCNC $tu\gamma$ and tuZ couplings are
 4496 analysed in NC DIS single top quark production, and FCNC tHu couplings are investigated in
 4497 CC DIS single top quark production. Limits on the corresponding FCNC branching ratios are
 4498 discussed in Section 3.4.2 and summarised and compared to different colliders in Fig. 3.63.

4499 Triple gauge boson couplings (TGC) W^+W^-V , $V = \gamma, Z$ are precisely defined in the SM and any
 4500 significant deviation from the predicted values could indicate new physics. Present constraints
 4501 on anomalous triple vector boson couplings are dominated by LEP (but they are not free of
 4502 assumptions) and the WWZ and $WW\gamma$ vertices can be tested at LHeC in great detail.

4503 The search for anomalous $WW\gamma$ and WWZ couplings with polarised electron beam were studied
 4504 in Ref. [358] via the processes $ep \rightarrow \nu q \gamma X$ and $ep \rightarrow \nu q ZX$. It was found that the LHeC
 4505 sensitivity with $E_e = 60 \text{ GeV}$ and $L = 100/\text{fb}$ is comparable with existing experimental limits
 4506 from lepton and hadron colliders, and that anomalous Z couplings might be better, reaching
 4507 $(\Delta\kappa_{\gamma,Z}, \lambda_{\gamma,Z})$ as small as $\mathcal{O}(10^{-1}, 10^{-2})$. In general, beam polarisation and larger electron beam
 4508 energies improve the sensitivity, and the LHeC was found to give complementary information
 4509 on the anomalous couplings compared to the LHC.

4510 The prospects of testing anomalous triple gauge couplings are also investigated in Ref. [357].
 4511 Therein the authors study the kinematics of an isolated hard photon and a single jet with a
 4512 substantial amount of missing transverse momentum. They show that the LHeC is sensitive
 4513 to anomalous triple gauge couplings via the azimuthal angle differences in the considered final
 4514 state. It is pointed out that in such an analysis it is possible to probe the $WW\gamma$ vertex sep-
 4515 arately, with no contamination from possible BSM contributions to the WWZ coupling. The
 4516 estimations consider $E_e = 100, 140, 200 \text{ GeV}$ and it is claimed that while higher energies yield
 4517 better sensitivities, the differences are not very large. For $L = 200/\text{fb}$ and $E_e = 140 \text{ GeV}$ the
 4518 exclusion power of the LHeC is superior to all existing bounds, including those from LEP.

4519 The process $e^- p \rightarrow e^- \mu^+ \nu j$ is investigated in Ref. [359]. The analysis is carried out at the parton
 4520 level and includes the cross section measurement and a shape analysis of angular variables, in
 4521 particular of the distribution of the azimuthal angle between the final state forward electron and
 4522 jet. It is shown that the full reconstruction of leptonic W decay can be used for W polarization
 4523 which is another probe of anomalous triple gauge couplings. The results show that the LHeC
 4524 could reach a sensitivity to λ_γ and Δk_γ as small as $\mathcal{O}(10^{-3})$ for $L = 2 - 3/\text{ab}$.

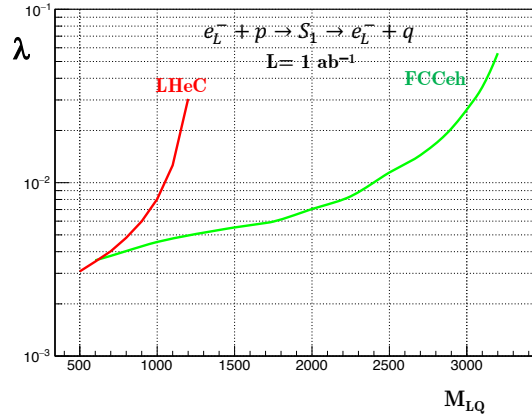


Figure 6.7: Estimated 2σ significance for the coupling λ at LHeC and FCC-eh for the scalar lepto-quark S_1 as a function of its mass, assuming 1 ab^{-1} luminosity.

6.6 Theories with heavy resonances

Many other BSM scenarios exist which could manifest via the presence of new resonances. The high centre-of-mass energy of pp colliders allow a better reach in most of these scenarios. Nonetheless, the LHeC and FCC-eh can contribute to searches for new physics in this area, relevant studies on various areas including scalar and vector-lepton quarks and excited leptons, are collected in this section.

6.6.1 Leptoquarks

In recent years the experiments that study heavy flavoured mesons revealed intriguing hints for new physics: in semi-leptonic decays of B mesons. A violation of lepton flavour universality at the level of 3 to 5σ is apparent in both the charged current and neutral current mediated processes [562]. In this context BSM theories involving leptoquarks (LQs) have gained renewed interest as they can give rise to the lepton universality violating decays of heavy mesons at tree level. Leptoquarks first appeared in Ref. [563] in Pati and Salam's $SU(4)$ model, where lepton number was considered to be the fourth colour. They also appear in Grand Unified theories, extended technicolor models and compositeness models. The nomenclature and classification are based on their transformation properties under the SM gauge groups [564, 565].

In ep collisions LQs can be produced in an s-channel resonance, the signature being a peak in the invariant mass of the outgoing ℓq system. Contrary to what is achievable in the LHC environment, at the LHeC many properties of the LQs can be measured with high precision [1].

The search for LQs at the LHC is essentially insensitive to the coupling λ , as the dominant pair production process is via the strong interaction. Recent searches have therefore been able to exclude LQs of the first generation up to 1.4 TeV, assuming a branching ratio to charged leptons = 1.0. For other generations, the bounds are ~ 1 TeV. (for the latest results, see, for example Ref. [566, 567]). Nevertheless, there remains some parameter space where the LHeC can make a significant contribution in the search for LQs: cross-generational mixing: $eq \rightarrow \mu q$, or $eq \rightarrow eb$, for example, or if the branching ratio in the decay of the LQ to a charged lepton is very low.

For LQs with masses below the centre-of-mass energy of the collider, suitable searches promise a sensitivity to λ as small as $\mathcal{O}(10^{-3})$. As shown in [568], production of the first generation

4553 scalar leptoquarks at LHeC can have much larger cross section than at the LHC. The authors
 4554 also show that a sensitivity to the Yukawa coupling for the LQs called $R_2^{5/3} \sim (\mathbf{3}, \mathbf{2}, 7/6)$ and
 4555 $\tilde{R}_2^{2/3} \sim (\mathbf{3}, \mathbf{2}, 1/6)$ better than the electromagnetic strength (~ 0.3) of 5σ can be reached up to a
 4556 mass of 1.2 TeV.

4557 For the S_1 scalar leptoquark $(\bar{\mathbf{3}}, \mathbf{1}, 1/3)$, an estimate of the sensitivity of the LHeC and the FCC-
 4558 eh as a function of the LQ mass and LL Yukawa coupling is shown in Fig. 6.7, assuming 1 ab^{-1}
 4559 of integrated luminosity. Here, the signal was generated at leading order using MadGraph with
 4560 the model files from Ref. [569], with hadronisation performed by Herwig7 [570,571] and detector
 4561 simulation with Delphes [371]. The SM background $e^-p \rightarrow e^-j$ was also generated at leading
 4562 order. A simple set of cuts on the p_T of the leading electron and jet and a window on the
 4563 invariant mass of the e-jet system was applied.

4564 The $\tilde{R}_2^{2/3}$ scalar LQ allows for coupling to right-handed neutrinos, providing interesting search
 4565 channels. Its signatures at ep colliders have been investigated recently [572,573]. In the lepton +
 4566 jet final state, it is found that LHeC can probe up to 1.2 TeV at 3σ significance with an e^- beam,
 4567 and at 5σ discovery with an e^+ beam and 1 ab^{-1} of integrated luminosity. At FCC-eh, a 5σ
 4568 discovery can be reached with an e^- beam up to $\sim 2.3 \text{ TeV}$ and 1 ab^{-1} of integrated luminosity.

4569 6.6.2 Vector-like quarks

4570 In composite Higgs models, new vector-like quarks are introduced, in particular the top-partner
 4571 (T) with charge $2/3$. The prospects of detecting T at the LHeC are discussed in Ref. [574]. For
 4572 this search a simplified model is considered where T is produced from positron proton scattering
 4573 via intergenerational mixing and decays as $T \rightarrow tZ$, with the final state $\nu_e \ell^+ \ell^- b j j'$, considering
 4574 $E_e = 140 \text{ GeV}$. The authors find that for $L = 1/\text{ab}$ masses for the top partner T around 800 GeV
 4575 can be tested when the model-related coupling constants are $\mathcal{O}(0.1)$ and that mixing between
 4576 T and the first generation quarks can significantly enhance the LHeC sensitivity.

4577 Another search strategy for singly produced top partners is given by their decays $T \rightarrow Wb$ and
 4578 $T \rightarrow th$, which is presented in Ref. [575]. The analysis is based on a simplified model where
 4579 the top partner is an $SU_L(2)$ singlet and interacts only with the third generation of quarks. It
 4580 considers collisions of positrons and protons with $E_e = 140 \text{ GeV}$, the analysis is carried out at
 4581 the parton level and investigates the kinematic distributions of the final states. Useful kinematic
 4582 variables for the bW final state were found to be the transverse momentum of the lepton, b -jet
 4583 missing energy, while for the th final state the most useful observable is the transverse hadronic
 4584 energy. For masses of $\mathcal{O}(1) \text{ TeV}$ the LHeC is found to be sensitive to the new interactions when
 4585 they are $\mathcal{O}(0.1)$ for $L = 1/\text{ab}$, in agreement with [574]. A very similar analysis was performed
 4586 for the $T \rightarrow Wb$ signal channel with comparable results [576].

4587 6.6.3 Excited fermions (ν^* , e^* , u^*)

4588 The potential of searches for excited spin-1/2 and spin-3/2 neutrinos are discussed in Ref. [577].
 4589 For the analysis the authors consider effective currents that describe the interactions between
 4590 excited fermions, gauge bosons, and SM leptons. For the signature, the production of the
 4591 excited electron neutrino ν^* and its subsequent decay $\nu^* \rightarrow We$ with $W \rightarrow jj$ was chosen. The
 4592 analysis is carried out at the parton level, considers $E_e = 60 \text{ GeV}$, and consists in a study of
 4593 the kinematic distributions of the final states. It is concluded that the signature can be well

4594 distinguished from backgrounds, and that other lepton-hadron colliders would be required to
4595 test the excited neutrinos of different flavours.

4596 Analyses in similar models, considering electron-proton collisions at energies of the FCC-he and
4597 beyond, were carried out for excited electron neutrinos and are presented in Ref. [578]. An
4598 analysis for the prospects of testing excited electrons is discussed in Ref. [579], and testing
4599 excited quarks in a composite model framework is investigated in Ref. [580].

4600 6.6.4 Colour octet leptons

4601 Unresolved issues of the SM, like family replication and quark-lepton symmetry, can be addressed
4602 by composite models, where quarks, leptons, and gauge bosons are composite particles made up
4603 of more basic constituents. One general class of particles, predicted in most composite models,
4604 are colour octet leptons, which are bound states of a heavy fermion and a heavy scalar particle
4605 that is assumed to be colour-charged. In this scenario each SM lepton is accompanied by a colour
4606 octet lepton, which may have spin 1/2 or 3/2. Since they are unobserved, the compositeness
4607 scale is expected to be at least $\mathcal{O}(1)$ TeV.

4608 At the LHeC, the colour octet partner of the electron e_8 can be produced through the process
4609 $e^- p \rightarrow e_8 g + X$ and studied via its decays products. An analysis including the study of kinematic
4610 distributions that were obtained at the parton level is presented in Ref. [581]. It was shown that
4611 discovery prospects exist for masses of $\mathcal{O}(\text{TeV})$. A similar analysis is performed for the FCC-he
4612 at much higher energies in Ref. [582].

4613 6.6.5 Electric precursor to QCD

4614 An electric precursor to QCD was formulated in 1969 that assumed hadron constituents are
4615 highly electrically charged, where the magnitudes of the high electric charges were determined
4616 by the Gell-Mann-Low-Johnson-Willey-Baker eigenvalue equation for finite vacuum polarization,
4617 and where the strong attraction between positive and negative constituents was assumed to bind
4618 them together [583].

4619 Both the electric model, and Schwinger's comparable model of monopoles [584], remained seri-
4620 ously incomplete since their original formulations. Neither was shown to reproduce the observed
4621 particle spectrum of hadrons, or the observed pattern of weak interactions. In addition, the
4622 expectation of a large but unobserved electric dipole moment of the neutron was not accounted
4623 for in the monopole model. Balanced against these questions are several long-standing questions
4624 raised by the SM, such as those enumerated in Section 1.1.1 above. Perhaps most seriously, the
4625 SM does not appear to provide a clear, dynamical *raison d'être* for the existence of quarks.

4626 In 2019 the ATLAS Collaboration reported searches for free magnetic monopoles and free highly
4627 electrically charged particles produced in p-p collisions at 13 TeV [585]. No candidates were
4628 detected with one or two Dirac magnetic charges or with electric charges $20e < |z| < 100e$.
4629 This extended the results of previous searches made at lower energies and in cosmic rays or
4630 bulk matter. Model dependent lower limits on the masses of monopoles and highly electrically
4631 charged particles were reported in the range 1,000 to 2,000 GeV. An alternative to seeking
4632 free monopoles or free highly electrically charged particles would be to seek evidence in e-p
4633 collisions of substructure associated with massive constituents. Assuming substructure scales as
4634 the inverse of constituent mass, we may expect a substructure scale $\leq 10^{-19}$ m. This may co-
4635 exist with structure at a larger scale $\sim 10^{-15}$ m caused by the meson cloud [586]. Substructure

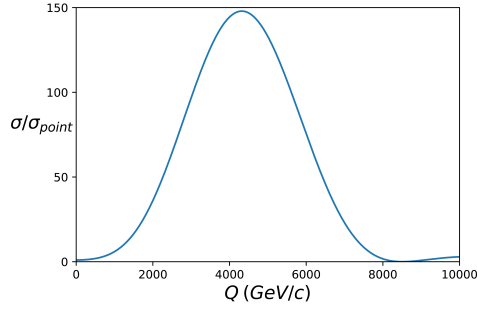


Figure 6.8: Form factor effect in the e-p interaction produced by substructure according to Model II of Hofstadter [590] with the model parameters given in the text.

4636 at a scale $\sim 10^{-19}$ m could be detectable in e-p interactions at energies below those required to
 4637 produce free monopoles or free highly electrically charged particles. Momentum transfers to the
 4638 electron bigger than 1,000 GeV would be required. Momentum transfers of a few 100 GeV were
 4639 already observed at HERA. Initial results [587, 588] by ZEUS and H1 with a modest integrated
 4640 luminosity below 0.1 fb^{-1} suggested threshold behaviour consistent with highly charged particles
 4641 beginning to be resolved, but the results were subject to the statistical uncertainties of small
 4642 event numbers. Final results [589] obtained at 10 times higher luminosity with a modified
 4643 analysis technique were ambiguous. It would be of interest to conduct further measurements
 4644 at higher momentum transfers. The LHeC is currently planned to collide 50-60 GeV electrons
 4645 with 6-7 TeV protons to yield peak momentum transfers ~ 1000 GeV at very high luminosity.
 4646 This could probe substructure scales down to 10^{-19} m using techniques similar to those already
 4647 developed at HERA. A simple picture of what might emerge with highly electrically charged
 4648 constituents is obtained by modeling the proton's substructure by a charge of (say) $21|e|$ smeared
 4649 uniformly over a region of radius 10^{-19} m, and two charges of $-10|e|$ smeared over a larger
 4650 region of radius 2×10^{-19} m. The model II by Hofstadter [590] predicts the results shown in
 4651 the figure below. These are consistent with the upper limit for substructure of 4.7×10^{-19} m
 4652 set by Abramowicz et al [589]. If substructure is present at the level proposed here, it would be
 4653 detectable with the proposed LHeC collider.

4654 6.7 Summary and conclusion

4655 The lack of new physics at the LHC to date forces the community to develop new theoretical
 4656 ideas as well as to explore the complementarities of pp machines with other possible future
 4657 facilities. In the context of ep colliders, several studies are being carried out to understand the
 4658 potential to search for new physics, i.e. considering that many interactions can be tested at high
 4659 precision that are otherwise not easily accessible.

4660 At ep colliders, most BSM physics is accessed via vector-boson fusion, which suppresses the
 4661 production cross section quickly with increasing mass. Nonetheless, scalar extensions of the SM
 4662 as well as neutrino-mass related BSM physics can be well tested at ep due to the smallness and
 4663 reducibility of the SM backgrounds. The absence of pile up and complicated triggering makes
 4664 searches for soft-momenta final state particles feasible, so that results for BSM theories for
 4665 example characterised by the presence of non-prompt, long-lived particles are complementary to
 4666 those at the LHC. Additionally, the excellent angular acceptance and resolution of the detector
 4667 also renders the LHeC a very suitable environment for displaced vertex searches. An increase
 4668 in the centre-of-mass energy as high as the one foreseen at the FCC would naturally boost the

4669 reach in most scenarios considerably.

4670 Finally, it is worth noting that the LHeC can offer different or indirect ways to search for
4671 new physics. It was shown recently that Lorentz invariance violation in the weak vector-boson
4672 sector can be studied in electron-proton scattering [591] via a Fourier-analysis of the parity
4673 violating asymmetry in deep inelastic scattering. Moreover, New Physics could be related to
4674 nucleon, nuclear, and top structure functions as discussed in Refs. [384, 592, 593]. Investigating
4675 of the $B_c^{(*)}$ meson and doubly heavy baryon also was shown to have discovery potential for New
4676 Physics [594–596].

Chapter 7

Influence of the LHeC on Physics at the HL-LHC

After almost 10 years of scientific exploitation of the LHC and about 175 fb^{-1} of proton-proton collision data delivered to each of the ATLAS and CMS experiments, the sensitivity of a significant fraction of leading measurements and searches becomes limited by systematic uncertainties. Uncertainties induced by the strong interaction, in particular related to the proton structure, play a prominent role, and tend to saturate the physics reach of the experiments. This context will only become more evident when the LHC enters its high-luminosity era.

With high precision PDFs measured independently from the other LHC experiments, the LHeC project can resolve this situation. It allows a clean study of the pure QCD effects it aims at measuring, resolving the ambiguity between new physics effects at high mass and PDF uncertainties that intrinsically affects the interpretation of proton-proton data alone. At the weak scale, improved PDFs provide a significant boost to the achievable precision of measurements of the Higgs boson properties and of fundamental electroweak parameters. The LHeC is thus a perfect companion machine for the HL-LHC, allowing a full exploitation of the data and significantly extending its reach.

The present chapter illustrates this with a few selected examples in the domain of precision measurements of the W -, Z - and Higgs boson properties. The impact of precise PDFs on searches for TeV-scale new physics is also illustrated, as well as the impact of electron-nucleus scattering data on heavy-ion physics at the LHC.

7.1 Precision Electroweak Measurements at the HL-LHC

7.1.1 The effective weak mixing angle

Prospective studies for the measurement of the effective weak mixing angle using the forward-backward asymmetry, A_{FB} , in Drell-Yan di-lepton events at the HL-LHC were performed at ATLAS [597], CMS [598] and LHCb [599] and reported in the CERN report on Standard Model physics at the HL-LHC [136]. A brief summary is given here, focusing on the impact of the LHeC on this measurement.

At leading order, lepton pairs are produced through the annihilation of a quark and antiquark via the exchange of a Z boson or a virtual photon. The definition of A_{FB} is based on the angle

4707 θ^* between the initial- and final-state fermions:

$$A_{\text{FB}} = \frac{\sigma_{\text{F}} - \sigma_{\text{B}}}{\sigma_{\text{F}} + \sigma_{\text{B}}} \quad (7.1)$$

4708 where σ_{F} and σ_{B} are the cross sections in the forward ($\cos \theta^* > 0$) and backward ($\cos \theta^* < 0$)
4709 hemispheres, respectively.

4710 A non-zero A_{FB} in dilepton events arises from the vector and axial-vector couplings of elec-
4711 troweak bosons to fermions. At tree level, the vector and axial-vector couplings of the Z boson
4712 to a fermion f are

$$g_V^f = T_3^f - 2Q_f \sin^2 \theta_W, \quad g_A^f = T_3^f. \quad (7.2)$$

4713 The coupling ratio, $g_V^f/g_A^f = 1 - 4|Q_f| \sin^2 \theta_W$, generates the asymmetry: defining

$$\mathcal{A}_f = 2 \frac{g_V^f/g_A^f}{1 + (g_V^f/g_A^f)^2} \quad (7.3)$$

4714 one finds, for a given sub-process $q\bar{q} \rightarrow \ell^+\ell^-$,

$$A_{\text{FB}} = \frac{3}{4} \mathcal{A}_q \mathcal{A}_\ell. \quad (7.4)$$

4715 As discussed in Chapt. 3 and Sect. 7.1.3 below, Eq. (7.2) is subject to radiative corrections
4716 introducing the effective weak mixing angle $\sin^2 \theta_{\text{eff}}^\ell$ in replacement of the leading order observable
4717 $\sin^2 \theta_W$. The asymmetry definitions downstream are however unchanged.

4718 The angle θ^* is uniquely defined in e^+e^- collisions, where the directions of the e^+ and e^-
4719 beams is known. In proton-antiproton collisions, at the Tevatron, the incoming quarks and
4720 anti-quarks also have preferred directions, and a non-zero asymmetry exists for all lepton-pair
4721 rapidities. At the LHC the beams are symmetric, and a non-zero asymmetry only appears for
4722 high-rapidity events, as the direction of the longitudinal boost reflects, on average, the direction
4723 of the incoming valence quark. While the expected Z -boson statistics are very large, with
4724 $\mathcal{O}(3 \times 10^9)$ events expected in ATLAS and CMS, the measurement is thus highly affected by
4725 PDF uncertainties, and in particular by the u and d valence and sea distributions.

4726 Prospective studies were performed by ATLAS, CMS and LHCb, including a discussion of
4727 expected PDF uncertainties. The impact of LHeC PDFs was evaluated by ATLAS and is
4728 discussed further. Tab. 7.1 compares the published ATLAS result [342] with the prospects for
4729 3 ab^{-1} , for a variety of PDF sets. The statistical uncertainty is at the level of 3×10^{-5} with this
4730 sample, and the experimental systematic uncertainties are improved by 10 – 25% depending on
4731 the PDF scenario considered. While MMHT2014 [600] and CT14 [601] claim comparable PDF
4732 uncertainties, the size of the PDF uncertainty is reduced at the HL-LHC thanks to the increased
4733 sample size, which helps constraining this component *in situ*. The HL-LHC PDF set [35], which
4734 incorporates the expected constraints from present and future LHC data, further decreases the
4735 associated uncertainty by about 20%. The LHeC projection [602] results from a QCD fit to
4736 1 ab^{-1} of ep scattering pseudodata, with $E_e = 60 \text{ GeV}$ and $E_p = 7 \text{ TeV}$; in this case, the PDF
4737 uncertainty is subleading compared to the experimental systematics.

4738 Fig. 7.1 compares the ATLAS sensitivity studies of $\sin^2 \theta_{\text{eff}}^\ell$ to previous measurements from the
4739 LHC experiments [341–343, 603], and to the legacy measurements by the experiments at LEP
4740 and SLC [338] and the Tevatron [340]. The precision of the measurement of the weak mixing
4741 angle in Z -boson events, using 3000 fb^{-1} of pp collision data at $\sqrt{s} = 14 \text{ TeV}$, exceeds the
4742 precision achieved in all previous single-experiments to date. The LHeC is thus essential in
4743 exploiting the full potential of the HL-LHC data for this measurement.

Parameter	Unit	ATLAS (Ref. [342])	HL-LHC projection		
		MMHT2014	CT14	HL-LHC PDF	LHeC PDF
Centre-of-mass energy, \sqrt{s}	TeV	8	14	14	14
Int. luminosity, \mathcal{L}	fb^{-1}	20	3000	3000	3000
Experimental uncert.	10^{-5}	± 23	± 9	± 7	± 7
PDF uncert.	10^{-5}	± 24	± 16	± 13	± 3
Other syst. uncert.	10^{-5}	± 13	–	–	–
Total uncert., $\Delta \sin^2\theta_W$	10^{-5}	± 36	± 18	± 15	± 8

Table 7.1: The breakdown of uncertainties of $\sin^2\theta_W$ from the ATLAS preliminary results at $\sqrt{s} = 8$ TeV with 20 fb^{-1} [342] is compared to the projected measurements with 3000 fb^{-1} of data at $\sqrt{s} = 14$ TeV for two PDF sets considered in this note. All uncertainties are given in units of 10^{-5} . Other sources of systematic uncertainties, such as the impact of the MC statistical uncertainty, evaluated in Ref. [342] are not considered in the HL-LHC prospect analysis.

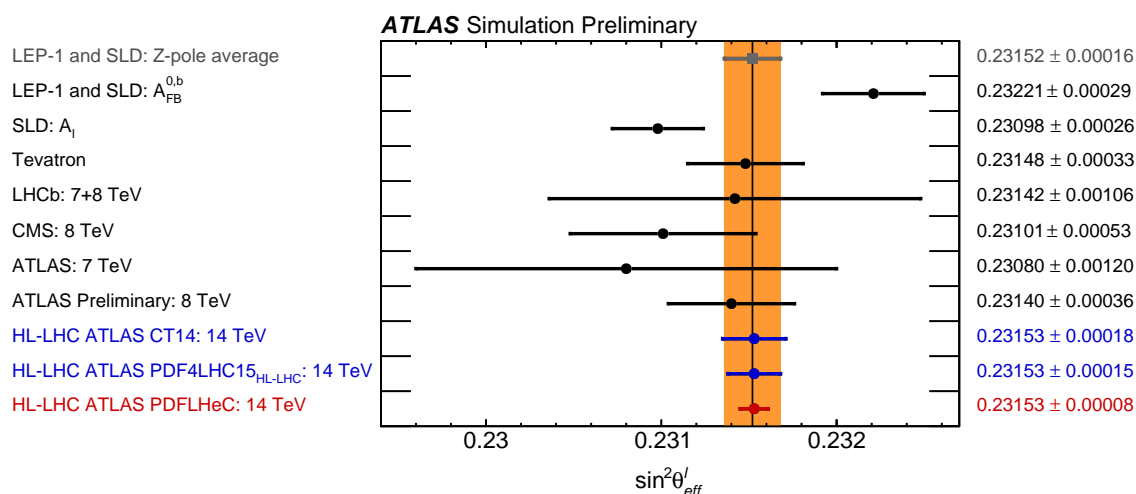


Figure 7.1: Comparison of measurements or combinations of $\sin^2\theta_{\text{eff}}^{\ell}$ with the world average value (orange band) and the projected uncertainties of measurements at the HL-LHC. For the HL-LHC the central values are set to the world average value and uncertainties are displayed for different assumptions of the available PDF sets, similar to Tab. 7.1.

4744 7.1.2 The W -boson mass

4745 This section summarises a prospective study describing prospects for the measurement of m_W
4746 with the upgraded ATLAS detector, using low pile-up data collected during the HL-LHC pe-
4747 riod [604]. Similar features and performance are expected for CMS.

4748 Proton-proton collision data at low pile-up are of large interest for W boson physics, as the low
4749 detector occupancy allows an optimal reconstruction of missing transverse momentum, and the
4750 W production cross section is large enough to achieve small statistical uncertainties in a moderate
4751 running time. At $\sqrt{s} = 14$ TeV and for an instantaneous luminosity of $\mathcal{L} \sim 5 \times 10^{32} \text{ cm}^{-2}\text{s}^{-1}$,
4752 corresponding to two collisions per bunch crossing on average at the LHC, about $\times 10^7$ W boson
4753 events can be collected in one month. Such a sample provides a statistical sensitivity at the
4754 permille level for cross section measurements, at the percent level for measurements of the W
4755 boson transverse momentum distribution, and below 4 MeV for a measurement of m_W .

4756 Additional potential is provided by the upgraded tracking detector, the ITk, which extends the

4757 coverage in pseudorapidity beyond $|\eta| < 2.5$ to $|\eta| < 4$. The increased acceptance allows W -
4758 boson measurements to probe a new region in Bjorken x at $Q^2 \sim m_W^2$. This will in turn allow
4759 further constraints on the parton density functions (PDFs) from cross section measurements,
4760 and reduce PDF uncertainties in the measurement of m_W . A possible increase of the LHC
4761 centre-of-mass energy, such as the HE-LHC program with $\sqrt{s} = 27$ TeV [605], could play a
4762 similar role on a longer timescale.

4763 Leptonic W boson decays are characterised by an energetic, isolated electron or muon, and sig-
4764 nificant missing transverse momentum reflecting the decay neutrino. The hadronic recoil, u_T , is
4765 defined from the vector sum of the transverse momenta of all reconstructed particles in the event
4766 excluding the charged lepton, and provides a measure of the W boson transverse momentum.
4767 Lepton transverse momentum, p_T^ℓ , missing transverse momentum, E_T^{miss} , and the hadronic recoil
4768 are related through $\vec{E}_T^{\text{miss}} = -(\vec{p}_T^\ell + \vec{u}_T)$. The p_T^ℓ and E_T^{miss} distributions have sharp peaks at
4769 $p_T^\ell \sim E_T^{\text{miss}} \sim m_W/2$. The transverse mass m_T , defined as $m_T = \sqrt{2p_T^\ell E_T^{\text{miss}} \cos(\phi_\ell - \phi_{\text{miss}})}$,
4770 peaks at $m_T \sim m_W$.

4771 Events are selected applying the following cuts to the object kinematics, after resolution correc-
4772 tions:

- 4773 • $p_T^\ell > 25$ GeV, $E_T^{\text{miss}} > 25$ GeV, $m_T > 50$ GeV and $u_T < 15$ GeV;
- 4774 • $|\eta_\ell| < 2.4$ or $2.4 < |\eta_\ell| < 4$.

4775 The first set of cuts select the range of the kinematic peaks of the W boson decay products,
4776 restricting to the region of small p_T^W to maximise the sensitivity of the distributions to m_W .
4777 Two pseudorapidity ranges are considered, corresponding to the central region accessible with
4778 the current ATLAS detector, and to the forward region accessible in the electron channel with
4779 the ITk.

4780 The W -boson mass is determined comparing the final state kinematic peaks in the simulation
4781 to those observed in the data, and adjusting the value of m_W assumed in the former to optimise
4782 the agreement. The shift in the measured value of m_W resulting from a change in the assumed
4783 PDF set is estimated using a set of template distributions obtained for different values of m_W
4784 and a given reference PDF set, and “pseudo-data” distributions obtained for an alternate set
4785 representing, for example, uncertainty variations with respect to the reference set. The PDF
4786 uncertainty for a given set is calculated by summing the shifts obtained for all uncertainty
4787 variations in quadrature.

4788 The PDF uncertainty is calculated for the CT14 [601], MMHT2014 [600], HL-LHC [35] and
4789 LHeC [602] PDF sets and their associated uncertainties. Compared to current sets such as
4790 CT14 and MMHT2014, the HL-LHC set incorporates the expected constraints from present and
4791 future LHC data; it starts from the PDF4LHC convention [37] and comes in three scenarios
4792 corresponding to more or less optimistic projections of the experimental uncertainties.

4793 The expected statistical and PDF uncertainties are illustrated in Tab. 7.2 and Fig. 7.2. The
4794 CT10 and CT14 sets yield comparable uncertainties. The MMHT2014 uncertainties are about
4795 30 % lower. The three projected HL-LHC PDF sets give very similar uncertainties; scenario 2
4796 is the most conservative and shown here. Compared to CT10 and CT14, a reduction in PDF
4797 uncertainty of about a factor of two is obtained in this case.

4798 The LHeC sample can be collected in about five years, synchronously with the HL-LHC op-
4799 eration. In this configuration, the neutral- and charged-current DIS samples are sufficient to
4800 disentangle the first and second generation parton densities without ambiguity, and reduce the

4801 PDF uncertainty below 2 MeV, a factor 5–6 compared to present knowledge. Also in this case
4802 the m_W measurement will benefit from the large W boson samples collected at the LHC, and
4803 from the combination of the central and forward categories. In this context, PDF uncertainties
4804 would be sub-leading even with 1 fb^{-1} of low pile-up LHC data.

Parameter	Unit	ATLAS (Ref. [333])		HL-LHC projection		
		CT10	CT14	HL-LHC	LHeC	LHeC
Centre-of-mass energy, \sqrt{s}	TeV	7	14	14	14	14
Int. luminosity, \mathcal{L}	fb^{-1}	5	1	1	1	1
Acceptance		$ \eta < 2.4$	$ \eta < 2.4$	$ \eta < 2.4$	$ \eta < 2.4$	$ \eta < 4$
Statistical uncert.	MeV	± 7	± 5	± 4.5	± 4.5	± 3.7
PDF uncert.	MeV	± 9	± 12	± 5.8	± 2.2	± 1.6
Other syst. uncert.	MeV	± 13	-	-	-	-
Total uncert. Δm_W	MeV	± 19	13	7.3	5.0	4.1

Table 7.2: Measurement uncertainty of the W -boson mass at the HL-LHC for different PDF sets (CT14, HL-LHC PDF and LHeC PDF) and lepton acceptance regions in comparison with a measurement by ATLAS [333]. The HL-LHC projections are obtained from a combined fit to the simulated p_T^ℓ and m_T distributions.

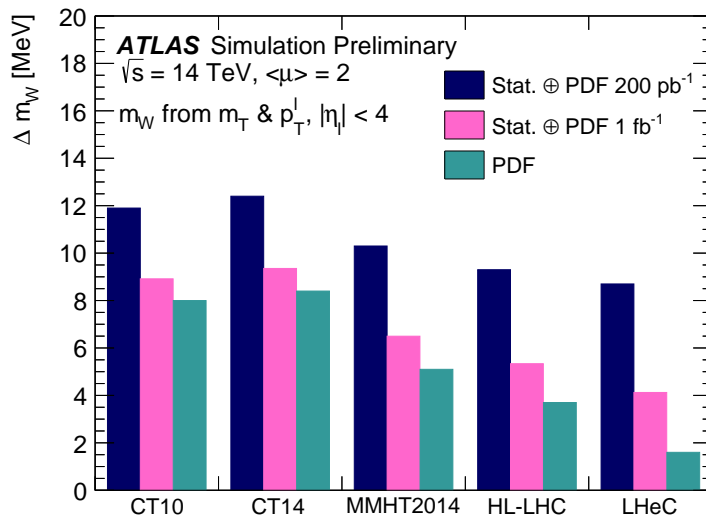


Figure 7.2: Measurement uncertainty of m_W at the HL-LHC with 200 pb^{-1} (dark blue) and 1 fb^{-1} (pink) of collected low pile-up data for different present and future PDF sets. The green area indicates the PDF uncertainty from those sets alone. The projections are obtained from a combined fit to the simulated p_T^ℓ and m_T distributions in the acceptance $|\eta| < 4$.

4805 7.1.3 Impact on electroweak precision tests

4806 The theoretical expressions for the electroweak parameters discussed above are functions of the
4807 other fundamental constants of the theory. In the Standard Model, an approximate expression
4808 for m_W , valid at one loop for $m_H > m_W$, is [338]

$$m_W^2 = \frac{m_Z^2}{2} \cdot \left(1 + \sqrt{1 - \frac{\sqrt{8} \cdot \pi \cdot \alpha_{em}}{G_F \cdot m_Z^2} \frac{1}{1 - \Delta r}} \right), \text{ where} \quad (7.5)$$

$$\Delta r = \Delta\alpha_{em} - \frac{\cos^2\theta_W}{\sin^2\theta_W} \Delta\rho, \text{ and} \quad (7.6)$$

$$\Delta\rho = \frac{3G_F m_W^2}{8\sqrt{2}\pi^2} \left[\frac{m_{\text{top}}^2}{m_W^2} - \frac{\sin^2\theta_W}{\cos^2\theta_W} \left(\ln \frac{m_H^2}{m_W^2} - \frac{5}{6} \right) + \dots \right]. \quad (7.7)$$

4809 where Δr includes all radiative corrections to m_W , $\Delta\alpha_{em}$ is the difference between the electro-
 4810 magnetic coupling constant evaluated at $q^2 = 0$ and $q^2 = m_Z^2$, and $\Delta\rho$ is the quantum correction
 4811 to the tree-level relation $\rho \equiv m_W/(m_Z \cos^2\theta_W) = 1$, and defined as $\rho = 1 + \Delta\rho$.

4812 Similarly, approximate one-loop expressions for the vector and axial-vector couplings between
 4813 the Z boson and the fermions, g_V and g_A , are

$$g_V = \sqrt{1 + \Delta\rho} (T_3 - 2 \cdot Q \cdot (1 + \Delta\kappa) \sin^2\theta_W), \quad (7.8)$$

$$g_A = \sqrt{1 + \Delta\rho} T_3 \quad (7.9)$$

4814 where

$$\Delta\kappa = \frac{3G_F m_W^2}{8\sqrt{2}\pi^2} \left[\frac{\cos^2\theta_W}{\sin^2\theta_W} \frac{m_{\text{top}}^2}{m_W^2} - \frac{10}{9} \left(\ln \frac{m_H^2}{m_W^2} - \frac{5}{6} \right) + \dots \right]. \quad (7.10)$$

4815 At two loops, also the strong coupling constant enters.

4816 A large class of theories beyond the SM predict particles that contribute to the W - and Z -
 4817 boson self-energies, modifying the above expressions. These modifications can generically be
 4818 parameterised using so-called *oblique* parameters, called S , T and U [606]. Their values are by
 4819 definition 0 in the SM and, for example, a significant violation of the relation between m_W , m_H
 4820 and m_{top} would translate into non-zero values for S and T .

4821 A typical application of this formalism consists in using the measured properties of the W
 4822 and Z bosons, the top quark mass, and the values of coupling constants, to derive an indirect
 4823 determination of the Higgs boson mass in the SM and compare the latter to the measured value.
 4824 Beyond the SM, the measured values can be used to derive allowed contours in the (S, T) plane.

4825 Present and future measurement uncertainties for the most relevant electroweak parameters are
 4826 summarised in Tab.7.3, and are used to evaluate the impact of the improved measurements
 4827 on electroweak precision tests. Specifically, we consider the effect of improved measurements
 4828 of m_W and $\sin^2\theta_{\text{eff}}^\ell$ discussed in this chapter, and of the improved precision of α_s discussed in
 4829 Chapter 3. In addition, we consider an ultimate precision of 300 MeV for the top quark mass,
 4830 measured at the LHC.

4831 The results are illustrated in Figs.7.3 and 7.4. The former results from a fit performed using
 4832 the GFitter framework [335], and compares the indirect determinations of the Higgs boson mass
 4833 for the present and expected measurement precisions. The indirect uncertainty in m_H reduces
 4834 from about 20 % to 10 %.

4835 Fig.7.4 was performed using HEPFIT [607], and compares allowed contours for the S and T
 4836 parameters. Here also, the allowed region is reduced by a factor of about two from the improved
 4837 measurements of m_W , $\sin^2\theta_{\text{eff}}^\ell$, m_{top} and α_s . Improved theoretical calculations in the SM will
 4838 provide an additional reduction of 10-15 %.

Parameter	Unit	Value	Uncertainty	
			Present	Expected
m_Z	MeV	91187.6	2.1	2.1
m_W	MeV	80385	15	5
$\sin^2\theta_{\text{eff}}^\ell$		0.23152	0.00016	0.00008
m_{top}	GeV	173.1	0.7	0.3
$\alpha_s(M_Z)$		0.1179	0.0010	0.0001

Table 7.3: Present uncertainties for the relevant EW precision observables [89, 132, 338], and their expected precision in the LHeC and HL-LHC era.

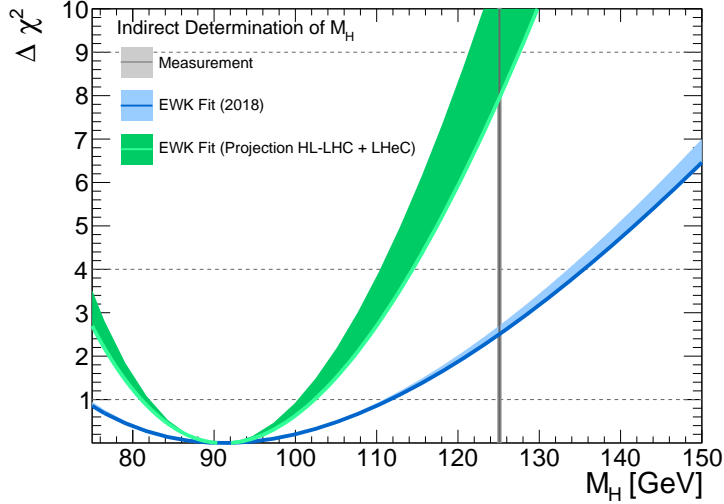


Figure 7.3: Comparisons of χ^2 distributions for different Higgs boson mass values, using present and future experimental uncertainties. The theoretical uncertainties are indicated by the filled areas. The Gfitter program [335] was used for this analysis.

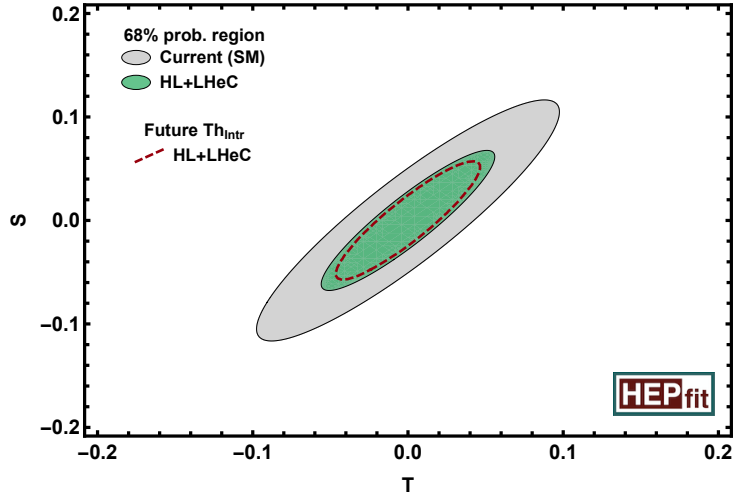


Figure 7.4: Allowed regions in the (S, T) plane. The grey and green areas indicate the currently allowed region and the LHeC projection, respectively. The dashed line indicates the effect of expected theoretical improvements. The HEPFIT program [607] was used for this analysis.

4839 In summary, the LHeC data promises significant improvements in the measurement precision
 4840 of fundamental electroweak parameters such as m_W and $\sin^2\theta_{\text{eff}}^\ell$. The improved measurements
 4841 enhance the sensitivity of electroweak tests by a factor of two or more.

4842 7.2 Higgs Physics

4843 7.2.1 Impact of LHeC data on Higgs cross section predictions at the LHC

4844 A detailed analysis of Higgs boson production cross sections was given in the report on Higgs
 4845 Physics at the HL-LHC and HE-LHC [608]. Central values at $\sqrt{s} = 14$ TeV and the corre-
 4846 sponding uncertainties are reported in Tab. 7.4. Perturbative uncertainties (labelled $\Delta\sigma_{\text{scales}}$ in
 4847 Tab. 7.4) generally dominate compared to the contributions of α_s and the PDFs. This is espe-
 4848 cially true for gluon fusion, where the residual theoretical uncertainties correspond to missing
 4849 corrections beyond N³LO in QCD, and for $t\bar{t}H$ production which is known to NLO QCD+EW
 4850 accuracy. The weak boson fusion, WH and ZH cross sections are known to NNLO QCD + NLO
 4851 EW accuracy; residual theoretical uncertainties are smaller for these weak interaction processes.

4852 In Ref. [608], α_s -related uncertainties are propagated assuming $\alpha_s = 0.118 \pm 0.0015$, and the
 4853 assumed PDF uncertainties reflect the HL-LHC prospects [35]. They are in excess of 3% for
 4854 gluon fusion and $t\bar{t}H$, below 2% for WH and ZH , and 0.4% for weak boson fusion. The LHeC
 4855 uncertainties in Tab. 7.4 are calculated using MCFM [609], interfaced to PDFs determined from
 4856 LHeC pseudodata as described in Chapter 3. Assuming the prospects for α_s and PDFs described
 4857 in Chapter 3, and with the exception of weak-boson fusion production, the corresponding un-
 4858 certainties decrease by a factor 5 to 10.

Process	σ_H [pb]	$\Delta\sigma_{\text{scales}}$	$\Delta\sigma_{\text{PDF}+\alpha_s}$	
			HL-LHC PDF	LHeC PDF
Gluon-fusion	54.7	5.4 %	3.1 %	0.4 %
Vector-boson-fusion	4.3	2.1 %	0.4 %	0.3 %
$pp \rightarrow WH$	1.5	0.5 %	1.4 %	0.2 %
$pp \rightarrow ZH$	1.0	3.5 %	1.9 %	0.3 %
$pp \rightarrow t\bar{t}H$	0.6	7.5 %	3.5 %	0.4 %

Table 7.4: Predictions for Higgs boson production cross sections at the HL-LHC at $\sqrt{s} = 14$ TeV and its associated relative uncertainties from scale variations and two PDF projections, HL-LHC and LHeC PDFs, $\Delta\sigma$. The PDF uncertainties include uncertainties of α_s .

4859 The important, beneficial role of ep PDF information for LHC Higgs physics can also be illus-
 4860 trated using the predictions for the total cross section, $pp \rightarrow HX$ at the LHC. This has recently
 4861 been calculated [610] to N³LO pQCD. In Fig. 7.5 calculations of this cross section are shown
 4862 for several recent sets of parton distributions, calculated with the iHix code [611], including the
 4863 LHeC set.

4864 The effect of these improvements on Higgs boson coupling determination at the HL-LHC is at
 4865 present modest, due to the combined effect of still significant perturbative uncertainties and
 4866 of the expected experimental systematic uncertainties. The influence of the LHeC on these
 4867 measurements is further discussed in the next section.

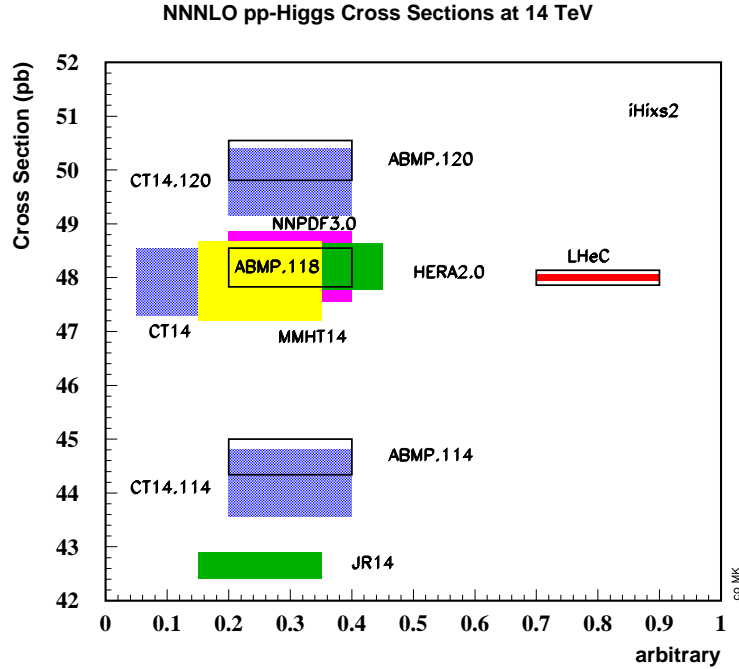


Figure 7.5: Cross sections of Higgs production calculated to N^3 LO using the iHix program [611] for existing PDF parameterisation sets (left side) and for the LHeC PDFs (right side). The widths of the areas correspond to the uncertainties as quoted by the various sets, having rescaled the CT14 uncertainties from 90 to 68 % C.L. Results (left) are included also for different values of the strong coupling constant $\alpha_s(M_Z^2)$, from 0.114 to 0.120. The inner LHeC uncertainty band (red) includes the expected systematic uncertainty due to the PDFs while the outer box illustrates the expected uncertainty resulting from the determination of α_s with the LHeC.

4868 7.2.2 Higgs Couplings from a simultaneous analysis of pp and ep collision 4869 data

4870 The LHC data collected during the Runs I and II have provided a first exploration of the prop-
4871 erties of the Higgs boson. The so-called κ framework [612] – which allows modifications of the
4872 SM-like couplings of the Higgs boson to each SM particle i , parameterised by coupling modifiers
4873 κ_i – has been widely used for the interpretation of these measurements. With current data, the
4874 κ parameters associated to the main couplings of the Higgs can be determined to a precision of
4875 roughly 10-20 %, see e.g. [613].¹ This knowledge will be further improved at the high-luminosity
4876 phase of the LHC, reaching a precision in many cases well below the 10 % level [608]. Even at the
4877 HL-LHC it will be, however, difficult to obtain sensible measurements of certain Higgs interac-
4878 tions, e.g. the coupling to charm quarks. Such gap could be covered by the precise measurements
4879 of that channel at the LHeC, as described in Section 5.1, which brings a nice complementar-
4880 ity between the measurements that would be possible at both machines. Furthermore, as also
4881 explained in that section, the LHeC environment allows very precise determinations of certain
4882 interactions, well beyond of what will be possible at the high-luminosity pp collider. In this
4883 subsection we briefly describe the complementarity between the Higgs measurements at the pp

¹Note that at the LHC one can only determine coupling ratios.

4884 and ep colliders, illustrated via a combined fit to the HL-LHC and LHeC projections in the κ
 4885 framework.

4886 For a detail descriptions of the Higgs physics program at the LHeC we refer to Chapter 5. The
 4887 only information not included in the fit presented in this section is that of the determination of
 4888 the Top Yukawa coupling, since projections from that study are performed assuming any coupling
 4889 other than κ_t to be SM like. Comments in this regard will be made, when necessary, below.
 4890 For the HL-LHC inputs of the combined fit we rely on the projections presented in Ref. [608],
 4891 as used in the comparison study in Ref. [614]. These HL-LHC inputs include projections for
 4892 the total rates in the main production (ggF, VBF, VH and ttH) and decay channels ($H \rightarrow$
 4893 bb , $\tau\tau$, $\mu\mu$, ZZ^* , WW^* , $\gamma\gamma$, $Z\gamma$). They are available both for ATLAS and CMS. Regarding
 4894 the theory systematics in these projections, we assume the scenario S2 described in [608], where
 4895 the SM theory uncertainties are reduced by roughly a factor of two with respect to their current
 4896 values. Theory systematics are assumed to be fully correlated between ATLAS and CMS. These
 4897 projections are combined with LHeC ones, where, as in Ref. [614], we use the future projections
 4898 for the SM theory uncertainties in the different production cross sections and decay widths. In
 4899 the κ fit performed here we assume: (1) no Higgs decays into particles other than the SM ones;
 4900 (2) heavy particles are allowed to modify the SM loops, so we use effective κ parameters to
 4901 describe the SM loop-induced processes, i.e. we use κ_g , κ_γ , $\kappa_{Z\gamma}$ as free parameters. The total
 4902 list of free parameters considered for this combined HLLHC+LHeC κ fit is, therefore,

$$\{\kappa_b, \kappa_t, \kappa_\tau, \kappa_c, \kappa_\mu, \kappa_Z, \kappa_W, \kappa_g, \kappa_\gamma, \kappa_{Z\gamma}\}, \quad (7.11)$$

4903 for a total of 10 degrees of freedom. Coupling modifiers associated to any other SM particles
 4904 are assumed to be SM-like, $\kappa_i = 1$.

Parameter	Uncertainty		
	HL-LHC	LHeC	HL-LHC+LHeC
κ_W	1.7	0.75	0.50
κ_Z	1.5	1.2	0.82
κ_g	2.3	3.6	1.6
κ_γ	1.9	7.6	1.4
$\kappa_{Z\gamma}$	10	–	10
κ_c	–	4.1	3.6
κ_t	3.3	–	3.1
κ_b	3.6	2.1	1.1
κ_μ	4.6	–	4.4
κ_τ	1.9	3.3	1.3

Table 7.5: Results of the combined HL-LHC + LHeC κ fit. The output of the fit is compared with the results of the HL-LHC and LHeC stand-alone fits. The uncertainties of the κ values are given in per cent.

4905 The results of the HL-LHC+LHeC fit, which has been performed using the `HEPfit` code [607],
 4906 are shown in Tab. 7.5 and Fig. 7.6 ². The increment in constraining power after adding the LHeC
 4907 measurements is apparent for the couplings to W bosons and b quarks, bringing an improvement
 4908 with respect to the HL-LHC result of a factor ~ 3 . As explained at the beginning of this section,
 4909 the LHeC measurements also bring the possibility of setting sensible constraints on the Higgs
 4910 interactions with charm quarks, with a precision of roughly 4%. The HL-LHC measurements,
 4911 in turn, fill some of the *gaps* in the fit at the LHeC, where there is little sensitivity to the

² The plot leaves out the results on κ_γ , $\kappa_{Z\gamma}$, κ_t and κ_μ which are rarer channels all measured much better in pp than ep . It yet is interesting to observe that the global analysis also improves the κ_γ result from 1.9 to 1.4%.

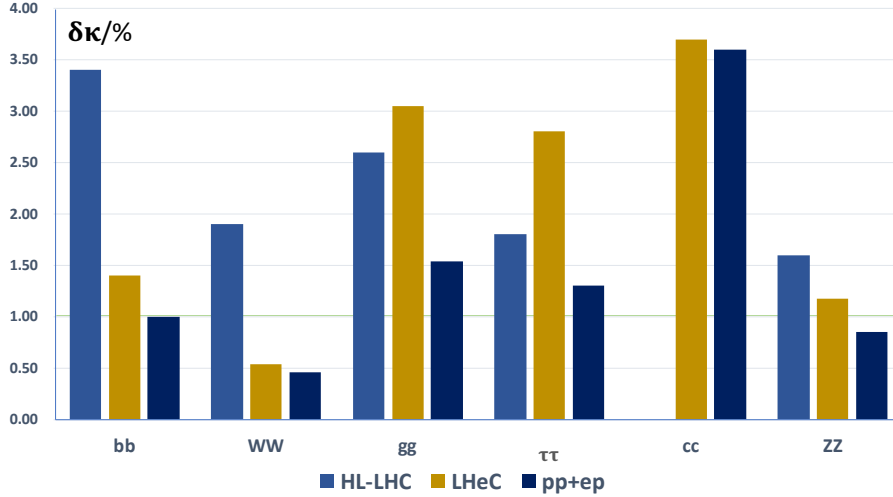


Figure 7.6: Results of the combined HL-LHC + LHeC κ fit. The output of the fit is compared with the results of the HL-LHC and LHeC stand-alone fits.

4912 couplings involved in rare Higgs decays, e.g. $H \rightarrow \mu\mu$ and $H \rightarrow Z\gamma$. This makes apparent the
4913 complementarity between the measurements at ep and pp machines, with the former leading
4914 in terms of precision in the largest Higgs couplings, while the high-luminosity of the latter
4915 brings sensitivity to the smaller interactions. Finally, as mentioned at the beginning, we did not
4916 include in this combined $ep+pp$ fit the projections for Top Yukawa interactions at the LHeC from
4917 Section 5.2, as these were not derived in a global setup, but rather setting all other interactions
4918 involved in $\bar{t}H\nu_e$ product to their SM values. However, the main uncertainty from the other κ
4919 parameters is expected to come from the W and b couplings, κ_W and κ_b , which are determined
4920 with an overall precision of $\sim 0.8\%$ and 2% . Therefore one expects the LHeC result, $\delta\kappa_t \sim 17\%$
4921 for $L = 1 \text{ ab}^{-1}$, to be minimally affected. This number is, however, significantly less precise
4922 than the HL-LHC projection of $\sim 4\%$, which is expected to dominate in a combined result.

7.3 Further precision Standard Model measurements at the HL-LHC

DB. New Section. Stil in progress.

The LHeC measurements and the results from their phenomenological interpretations will have an important impact on many areas of the HL-LHC physics programme. This goes far beyond the precision electroweak and the Higgs physics, as discussed at hand of dedicated analyses in the previous sections, and BSM or eA physics as discussed in the subsequent sections. In this section a few further selected topics of the Standard Model (SM) physics programme at the LHC and HL-LHC are discussed, where substantial improvements due to the LHeC can be expected.

In general, two distinct aspects can be considered for any SM measurement in that respect³:

- improvements of the analysis of the recorded event data, and
- improvements of the phenomenological interpretation of the measurements.

In order to assess the impact of the LHeC for the first bullet, one must recollect that an essential key ingredient of the analysis of any hadron collider data is the utilisation of phenomenological models, and commonly QCD inspired Monte Carlo (MC) event generators are employed. These are used for calibration, corrections of limited acceptance and resolution effects (*unfolding*), training of machine learning algorithms for event or object classification, extrapolations from the *fiducial* to the *full* phase space, estimates of different background sources and also signal extraction. Although the implemented models are derived from more fundamental equations like the QCD Lagrangian, a number of model parameters remain poorly known and have to be *tuned* with data. Also, since most models involve approximations and may be numerically limited, any model needs to be validated, or invalidated, with independent measurements prior to its usage, of course. With more and more data being recorded at the (HL-)LHC, statistical uncertainties become very small and systematic uncertainties are reduced due to improved calibration and analysis algorithms, so that uncertainties associated to the MC event models become important and are limiting the accuracy of the HL-LHC measurements. It must be noted, that the MC parameters should be tuned with data from another experiment in order to avoid a potential bias of the actual measurement due to experimental correlations.

For the second bullet, the phenomenological interpretation of hadron collider measurements, like for instance tests of pQCD or the determination of SM parameters (e.g. $\alpha_s(M_Z)$, $\sin^2\theta_{\text{eff}}^\ell$, m_W , the κ parameters, ...), the proton PDFs and SM parameter which are input to the prediction must be known with high accuracy, most noteworthy the value of $\alpha_s(M_Z)$.

The most important inputs of the LHeC to the HL-LHC measurements are of course the precise determination of the PDFs and $\alpha_s(M_Z)$, see Chapter 3. These will improve both, the data analysis and its interpretation. Beyond that, the measurements of charged particle spectra, jet shape and jet substructure observables, jet cross sections and event shape observables or heavy flavor cross sections will help to improve MC models further, for instance with the determination of charm and bottom-quark masses, heavy quark (c , b) fragmentation functions and fragmentation fractions, finding optimal choices for all scales involved in a MC model, or determining the optimal parameters for the parton shower, Λ_{QCD} . Such measurements can be performed with high precision at the LHeC, since DIS represents a superior QCD laboratory. This is because in the

³In some cases, a model- or physics parameter is directly extracted from the experiment data and the two applications are merged into a single analysis workflow, for instance in many LHC top-quark mass analyses. Additionally to these two aspects, of course, the complementarity of the physics case of ep collisions enhances our understanding of the fundamental laws of physics.

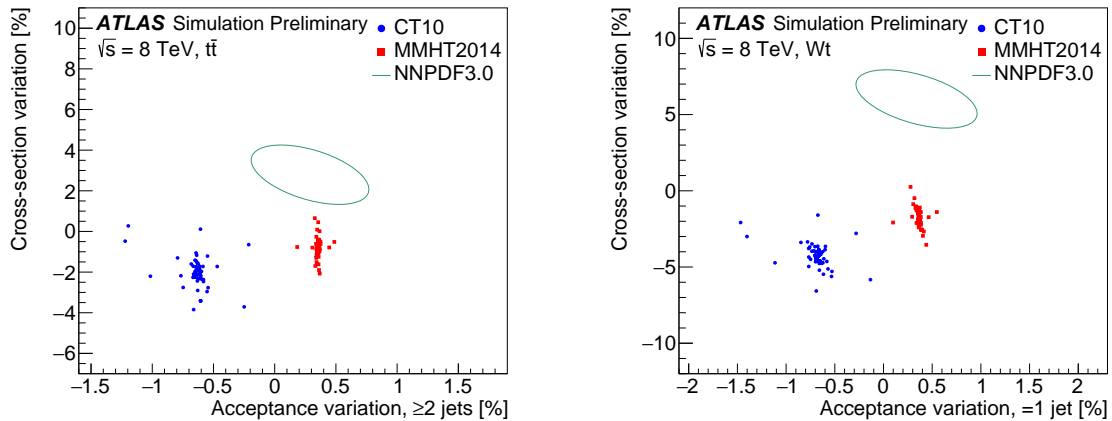


Figure 7.7: Left: Impact of PDF uncertainty from CT10 and MMHT2014 eigenvectors or NNPDF3.0 replicas, on the cross section and the acceptance correction for top pair production $t\bar{t}$ (left) and single top production Wt (right) (taken from Ref. [615]). Events are selected with at least two jets or with exactly one jet, respectively. Depending on the PDF set and eigenvector employed, the cross sections varies by up to 5–7% for top-pair and more than 10% for single-top production. Also the acceptance correction varies by about 0.5–1% for different PDF sets, and can become as large as 2.5% for different PDF sets and eigenvectors. Since the acceptance correction has to be imposed for the measurement, the limited knowledge of the PDFs introduces a sizeable modelling uncertainty on the measurement.

4964 final state there is always a lepton, which is used for trigger and vertexing, and simultaneously
 4965 a hadronic system which is then subject of interest. In addition the overconstraint kinematic
 4966 system allows for the precise calibration of hadronic final state objects, and furthermore limiting
 4967 effects like minimum bias or pile-up are absent.

4968 In the following, a few selected subjects are discussed at hand of LHC analyses performed with
 4969 Run-I data at $\sqrt{s} = 8$ or 13 TeV, and thus giving a tangible indication about challenges at future
 4970 HL-LHC measurements:

- 4971 • The measurement of the integrated top-quark pair cross section represents an outstanding
 4972 benchmark quantity for the entire field of top-quark physics. Its measurement for
 4973 top-transverse momenta $p_T^t > 400$ GeV in the *lepton+jets* decay channel yields a high
 4974 experimental precision with both, small statistical and systematic uncertainties. However,
 4975 its measurement precision is limited by theoretical uncertainties (also called *modelling*
 4976 uncertainties), and the largest individual source stems from the PDFs [132, 616]. A related
 4977 study of PDF effects on the acceptance correction for the integrated top-pair production
 4978 cross section and single-top production Wt is displayed in Fig. 7.7. The acceptance correc-
 4979 tion changes by up to 0.5–1% for different PDF sets, and can become as large as 2.5% for
 4980 different PDF sets and eigenvectors. Another very important uncertainty for top-quark
 4981 measurements is from the modelling of the parton shower. Both, uncertainties from the
 4982 PDFs and from parton shower modelling, are expected to be significantly reduced with
 4983 LHeC data.
- 4984 • The determination of the top-quark mass m_t from LHC data requires the precise modelling
 4985 of the physics and all background processes with suitable MC models. Today, the value
 4986 of m_t is determined most precisely from a combination of such individual analyses, and
 4987 uncertainties of 0.4–0.8 GeV are reported [132, 617–621]. Any of these individual precision
 4988 determinations are limited by model uncertainties, and therefore improvements at the
 4989 HL-LHC cannot be obtained with more data, but only with improved models. Some of

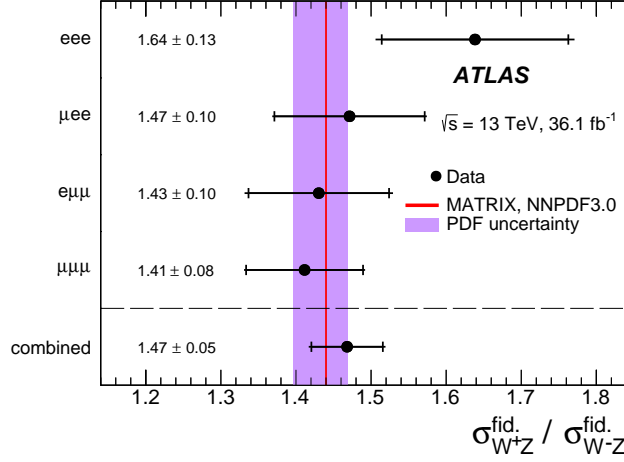


Figure 7.8: Measurement of the ratio of di-boson $\sigma(W^+Z)/\sigma(W^-Z)$ integrated cross sections in a fiducial phase space for four different decay channels and their combination at $\sqrt{s} = 13$ TeV in comparison with NNLO predictions [632, 633] (taken from Ref. [634]). The total uncertainties of the data points are dominated by statistical uncertainties and will be reduced in the future. The shaded violet band indicates the size of the PDF uncertainties and limit the overall interpretation of the measurement.

4990

the model uncertainties, e.g. PDF, parton shower, hadronisation or fragmentation related uncertainties can be expected to be reduced with LHeC data.

4991

4992

- At the HL-LHC also rare decay channels can be exploited for precision measurements. For example, the top-quark mass can be determined from top-quark pair production with a subsequent decay, where one b -quark hadronises into B -hadron which then decays through a J/ψ -meson into a pair of muons, $t\bar{t} \rightarrow W^+bW^-b \rightarrow \ell\nu_\ell J/\psi (\rightarrow \mu^+\mu^-) Xqq'b$ [622]. Such a measurement requires the precise knowledge of b -quark fragmentation, which can be well measured at the LHeC, and such improving the HL-LHC measurement. (to be discussed.)

4993

4994

4995

4996

4997

4998

- The value of the strong coupling constant $\alpha_s(M_Z)$ is one of the least known fundamental parameters in physics and an improved determination with new measurement constitutes a real challenge for LHC and HL-LHC experiments. A large number of observables at the LHC are *per-se* sensitive to $\alpha_s(M_Z)$, and its value was determined in the past from various definitions of jet cross section observables (see e.g. [111, 112, 623, 624]) or transverse energy-energy correlations [625], Z +jet cross sections [626], integrated [627] or differential top-quark cross sections [628], inclusive W or Z production [629, 630], prompt photon data [631], and many other observables (see Ref. [132] for a review). Although the harsh environment in high-luminosity hadron-hadron collisions requires sophisticated analysis techniques and dedicated measurements, small experimental uncertainties for $\alpha_s(M_Z)$ could be achieved. Hence, α_s determinations are nowadays limited due to theoretical uncertainties and the dominant uncertainties are most commonly PDF related [626, 627, 629, 630] (only for observables, where NNLO predictions are not yet applicable, the scale uncertainties may overshoot the PDF uncertainties). Therefore, already today the knowledge of the PDFs represent the limiting factor, and a significant reduction of the total uncertainty for $\alpha_s(M_Z)$ can (only) be achieved with PDFs determined at the LHeC.

4999

5000

5001

5002

5003

5004

5005

5006

5007

5008

5009

5010

5011

5012

5013

5014

- The production of $W^\pm Z$ pairs in pp collisions provides a crucial test of the electroweak sector of the SM, since di-boson production is sensitive to the gauge-boson self-interactions. Already small deviations in the observed distributions could provide indications for new physics. The process can be well measured in a high-pile up environment and can be

5015

5016

5017

5018 well separated from huge QCD background. However, due to the relatively small $W^\pm Z$
5019 cross sections high statistical precision can only be achieved with high luminosity. Recent
5020 measurement of $W^\pm Z$ pairs at $\sqrt{s} = 13 \text{ TeV}$ based on 36 fb^{-1} of integrated luminosity
5021 have been performed by ATLAS and CMS [634, 635]. In Fig. 7.8 the ratio of fiducial cross
5022 sections $\sigma_{W^+Z}/\sigma_{W^-Z}$ is displayed. The largest individual uncertainty is the statistical
5023 uncertainty and therefore future measurements at the LHC and HL-LHC are of great
5024 importance in order to reach higher precision. Nonetheless, already today, the overall
5025 phenomenological interpretation is limited by PDF uncertainties, as visible from Fig. 7.8,
5026 and these can be improved best with PDFs from LHeC.

5027 In the situation of the absence of indications for new physics, an important goal of the future
5028 LHC and HL-LHC physics programme has to be devoted to precision measurements. From
5029 the examples discussed above (W -boson mass and Higgs measurements are discussed in above's
5030 sections), it becomes obvious that limiting factors of such measurements arise from the signal
5031 and MC modelling, where PDF uncertainties constitute a limiting factor and also improved
5032 understandings of parton shower, hadronisation and fragmentation processes are of importance.
5033 These aspects can all be improved with independent precision measurements at the LHeC.

5034 Similarly, the phenomenological interpretation of many processes is already today limited by
5035 PDF uncertainties, and as outlined, α_s determinations, di-boson processes, top-mass or top-
5036 cross section measurements, and many other topics, require a higher precision for PDFs already
5037 today. In the HL-LHC era, where data and predictions are more precise, the detailed knowledge
5038 of the PDFs will become of even greater importance.

7.4 High Mass Searches at the LHC

7.4.1 Strongly-produced supersymmetric particles

The potential of the HL- and HE-LHC to discover supersymmetry was extensively discussed in Ref. [636]. Here we focus on searches for gluinos within MSSM scenarios. Gluino pairs are produced through the strong interaction, and their production cross section is relatively large; naturalness considerations indicate that gluino masses should not exceed a few TeV and lie not too far above the EW scale. Hence they are certainly among the first particles that could be discovered at HL-LHC.

In the following we assume that a simplified topology dominates the gluino decay chain, culminating in jets plus missing energy originating from a massless LSP, $\tilde{\chi}_0$. Ref. [636] evaluated the sensitivity of the HL- and HE-LHC to gluino pair production with gluinos decaying exclusively to $q\bar{q}\tilde{\chi}_0$, through off-shell first and second generation squarks, using a standard search for events with jets and missing transverse energy. Currently, the reach for this simplified model with 36 fb^{-1} of 13 TeV data is roughly 2 TeV gluinos, for a massless LSP [637, 638]. Extrapolating to 3 ab^{-1} at 14 TeV, the limit grows to 3.2 TeV. For 15 ab^{-1} at 27 TeV, a limit of 5.7 TeV was found.

When deriving limits, an overall systematic uncertainty of 20% was assumed on the SM background contributions, and a generic 10% uncertainty was assumed on the signal normalisation, not taking into account PDF-related uncertainties which are as large as 50% for gluinos around 3 TeV. The effect of this additional source of uncertainty was found to induce a variation in the mass limit by $\pm 200\text{ GeV}$ at the HL-LHC, and as much as $\pm 500\text{ GeV}$ at the HE-LHC.

We can revert this argument, and claim that with present PDF knowledge, mass limits could be as low as 3.0 TeV and 5.3 TeV at the HL- and HE-LHC, respectively. Data from the LHeC would make this contribution negligible compared to other sources of uncertainty. Compared to the most conservative scenario, the increase in sensitivity would correspond to an increase in centre-of-mass energy by approximately 5 to 10%.

7.4.2 Contact interactions

New, high-mass gauge bosons are most often searched for in resonant final states. Peaks in the invariant-mass distributions of electron, muon or jet pairs directly reflect the presence of such new particles; the accessible mass range is limited by the available centre-of-mass energy.

Particles with a mass beyond the kinematic limit generally interfere with the Z boson and the photon, generating non-resonant deviations in the invariant mass distributions. Such models can be parameterised as contact interactions (CI) between two initial-state quarks and two final-state leptons of given chirality:

$$\mathcal{L}_{\text{CI}} = \frac{g^2}{\Lambda^2} \eta_{ij} (\bar{q}_i \gamma_\mu q_i) (\bar{\ell}_i \gamma^\mu \ell_i), \quad (7.12)$$

where $i, j = \text{L or R}$ (for left- or right-handed chirality), g is a coupling constant set to be 4π by convention, and Λ is the CI scale. The sign of η_{ij} determines whether the interference between the SM Drell–Yan (DY) process, $q\bar{q} \rightarrow Z/\gamma^* \rightarrow \ell^+\ell^-$, is constructive or destructive.

The size and sign of the observed deviation with respect to the SM probes the scale and interference pattern of the interaction. The sensitivity of the search is limited by experimental

5078 uncertainties (finite statistics and experimental systematic uncertainties) and by uncertainties
5079 in the theoretical modelling of the DY background.

5080 The most recent results of the ATLAS and CMS Collaborations [639, 640] are based on e^+e^-
5081 and $\mu^+\mu^-$ final states in 36 fb^{-1} of data, and probe CI's up to a typical scale of 25 TeV, de-
5082 pending on the chirality and sign of the interaction coupling parameter. The limits derived by
5083 ATLAS, summarised in Tab. 7.6, accounted for theoretical uncertainties induced by the PDFs
5084 and by α_s . The dominant PDF uncertainty was estimated from the 90% CL uncertainty in
5085 the CT14nnlo PDF set, adding an envelope from the comparison of the CT14nnlo, MMHT2014
5086 and NNPDF3.0 [641] central sets. The strong coupling constant uncertainty was propagated
5087 assuming $\alpha_s = 0.118 \pm 0.003$, with a subleading effect.

5088 The present study evaluates the sensitivity of this search at the HL-LHC. The increase in
5089 sensitivity is estimated using samples of Standard-Model like pseudo data, corresponding to the
5090 integrated luminosity of 3 ab^{-1} . In a first step, both the experimental and theoretical systematic
5091 uncertainties are kept in the publication. In this regime, the extrapolated statistical uncertainty
5092 is typically a factor 5 to 10 smaller than the theoretical uncertainty. Improvements from the
5093 LHeC in α_s and in the proton PDFs are incorporated in a second step. Assuming the prospects
5094 described in Chapter 3, α_s and PDF uncertainties are smaller than the statistical fluctuations
5095 and can be neglected in first approximation.

5096 The results are summarised in Tab. 7.6. Everything else equal, increasing the sample size from
5097 36 fb^{-1} to 3 ab^{-1} enhances the CI reach by a typical factor of two. Accounting for the improve-
5098 ment in the theoretical modelling of the DY process brought by the LHeC brings another factor
5099 of 1.5–1.8 in the limits. In the last case, the limits reach well into range directly accessible with
5100 proton-proton collisions at $\sqrt{s} = 100\text{ TeV}$, as envisioned at the FCC-hh.

Model	ATLAS (Ref. [639])		HL-LHC	
	$\mathcal{L} = 36\text{ fb}^{-1}$ (CT14nnlo)	$\mathcal{L} = 3\text{ ab}^{-1}$ (CT14nnlo)	$\mathcal{L} = 3\text{ ab}^{-1}$ (LHeC)	
LL (constr.)	28 TeV	58 TeV	96 TeV	
LL (destr.)	21 TeV	49 TeV	77 TeV	
RR (constr.)	26 TeV	58 TeV	84 TeV	
RR (destr.)	22 TeV	61 TeV	75 TeV	
LR (constr.)	26 TeV	49 TeV	81 TeV	
LR (destr.)	22 TeV	45 TeV	62 TeV	

Table 7.6: Contact interaction limits from ATLAS based on 36 fb^{-1} of data [639], and extrapolated to the full HL-LHC dataset (3 ab^{-1}). The extrapolation is performed assuming the same PDF and α_s uncertainties as in Ref. [639], and assuming the improved uncertainties as obtained from the LHeC.

5101 7.5 Heavy Ion Physics with eA Input

5102 The study of hadronic collisions at RHIC and the LHC, proton-proton, proton-nucleus and
5103 nucleus-nucleus, has produced several observations of crucial importance for our understanding
5104 of QCD in complex systems where a large number of partons is involved [642, 643]. The different
5105 stages of a heavy ion collision, as we presently picture it, are schematically drawn in Fig 7.9.

5106 First, the hot and dense partonic medium created in heavy ion collisions, the quark-gluon plasma
5107 (QGP), experiences a collective behaviour of which azimuthal asymmetries and transverse spec-
5108 tra with a specific ordering in particle masses are the most prominent observables. This collec-

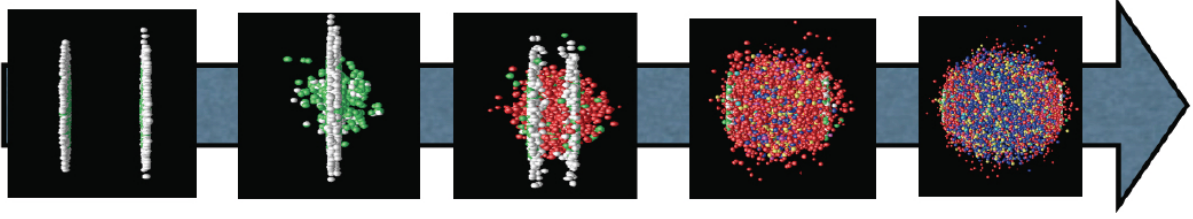


Figure 7.9: Sketch of a heavy ion collision with time running left to right, going from the approach of two ultrarelativistic Lorentz-contracted nuclei, the collision and parton creation in the central rapidity region, the beginning of expansion and formation of the QGP, the expansion of the QGP until hadronisation, and finally the expansion of the hadronic gas.

5109 tivity can be very well described by relativistic hydrodynamics [644]. For this description, the
 5110 system has to undergo some dynamics leading to rough isotropisation in a short time, $\lesssim 1$ fm/c,
 5111 for which both strong and weak coupling explanations have been proposed [451].

5112 Second, collisions between smaller systems, pp and pA , show many of the features [448–450] that
 5113 in heavy ion collisions are taken as indicative of the production of a dense hot partonic medium.
 5114 The most celebrated of such features, the long rapidity range particle correlations collimated in
 5115 azimuth, named the ridge (see Sec. 4.5), has been found in all collisions systems. The dynamics
 5116 underlying this phenomena, either the formation of QGP and the existence of strong final state
 5117 interactions, or some initial state dynamics that leaves imprint on the final observables, is under
 5118 discussion [451].

5119 Finally, the QGP is extremely opaque to both highly energetic partons [645] and quarkonia [646]
 5120 traversing it. These observables, whose production in pp can be addressed through perturba-
 5121 tive methods, are called hard probes [647]. The quantification of the properties of the QGP
 5122 extracted through hard probes is done by a comparison with predictions based on assuming a
 5123 nuclear collision to be a superposition of collisions among free nucleons. Such predictions contain
 5124 uncertainties coming both from nuclear effects other than those in QGP (named cold nuclear
 5125 matter effects), and from uncertainties in the dynamics determining the interaction between the
 5126 energetic parton or bound state and the medium. In the case of partons, this has motivated the
 5127 development of sophisticated jet studies in heavy ion collisions [648].

5128 eA collisions studied in the energy range relevant for the corresponding hadronic accelerator – the
 5129 LHeC for the LHC – would substantially improve our knowledge on all these aspects and, indeed,
 5130 on all stages of a heavy ion collisions depicted in Fig. 7.9. Besides, they can reduce sizeably the
 5131 uncertainties in the extracted QGP parameters, the central goal of the heavy program for the
 5132 understanding of the different phases of QCD. Here we provide three examples of such synergies:

- 5133 • Nuclear parton densities: The large lack of precision presently existing in the determina-
 5134 tion of parton densities induce large uncertainties in the understanding of several signatures
 5135 of the QGP. For example, for J/ψ suppression, its magnitude at midrapidity at the LHC is
 5136 compatible with the sole effect of nuclear shadowing on nPDFs [646], see Fig. 7.10. While
 5137 from data at lower energies and at forward and backward rapidities it is clear that this is
 5138 not the only effect at work, only a reduction on the nPDF uncertainty as feasible at the
 5139 LHeC, see Sec. 4.2, will make possible a precise quantification of the different mechanisms
 5140 producing either suppression (screening, gluon dissociation, energy loss) or enhancement
 5141 (recombination or coalescence), that play a role in this observable.
- 5142 • Initial conditions for the collective expansion and the small system problem: At present,
 5143 the largest uncertainty in the determination of the transport coefficients of the partonic

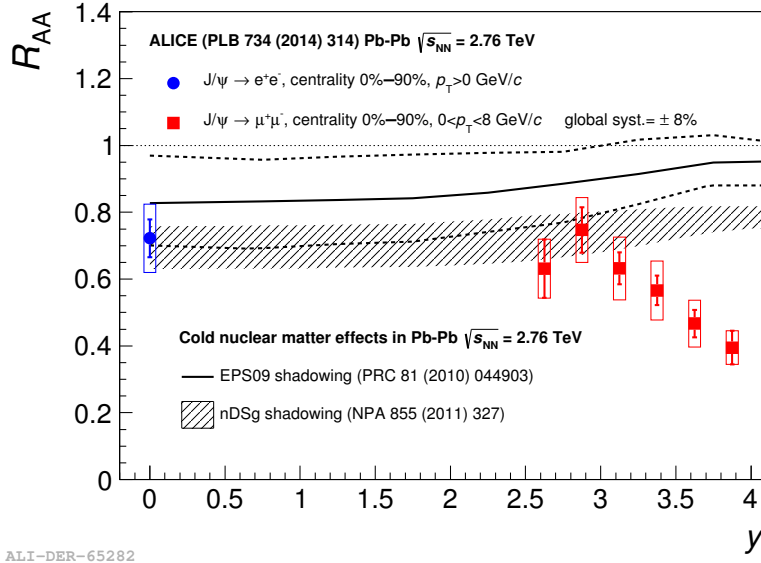


Figure 7.10: ALICE inclusive J/ψ nuclear modification factor versus rapidity [649], compared to nPDF calculations. Taken from [646].

5144 matter created in heavy ion collisions [650, 651] (see Fig. 7.11), required in hydrodynamic
5145 calculations, and in our understanding of the speed of the approach to isotropisation and
5146 of the dynamics prior to it [652], comes from our lack of knowledge of the nuclear wave
5147 function and of the mechanism of particle production at small to moderate scales – i.e. the
5148 soft and semihard regimes. Both aspects determine the initial conditions for the application
5149 of relativistic hydrodynamics. This is even more crucial in the discussion of small systems,
5150 where details of the transverse structure of protons are key [653] not only to provide
5151 such initial conditions but also to establish the relative role of initial versus final state
5152 dynamics. For example, the description of azimuthal asymmetries in pp and pPb collisions
5153 at the LHC demands that the proton is modelled as a collection of constituent quarks or
5154 hot spots [644, 653]. ep and eA collisions at the LHeC can constrain both aspects in the
5155 pertinent kinematic region, Secs. 3.2.5 and 4.3. Besides, they can clarify the mechanisms
5156 of particle production and the possible relevance of initial state correlations on the final
5157 state observables as suggested e.g. by CGC calculations, see Secs. 3.2.2 and 4.4, whose
5158 importance for LHC energies can be established at the LHeC.

- 5159 • Impact on hard probes: Besides the improvement in the determination of nPDFs that
5160 affects the quantification of hard probes, commented above, eA collisions can help to un-
5161 derstand the dynamics of the probes by analysing the effects of the nuclear medium on
5162 them. As two examples, the abundant yields of jets and large transverse momentum parti-
5163 cles at the LHeC [1] will allow precise studies of the nuclear effects on jet observables and of
5164 hadronisation inside the nuclear medium. These two aspects are of capital importance not
5165 only in heavy ion collisions but also in small systems where the lack of jet modification is
5166 the only QGP-like characteristics not observed in pPb . On the other hand, measurements
5167 of exclusive quarkonium production at the LHeC [1] will provide a better understanding
5168 of the cold nuclear matter effects on this probe, on top of which the effects of the QGP
5169 will provide a quantitative characterisation of this new form of QCD matter.

5170 As discussed in Sec. 4.2, pPb and $PbPb$ collisions at the LHC offer possibilities for constraining
5171 nPDFs, through the measurement of EW vector boson production [657], dijets [417], D mesons at
5172 forward rapidities [429] and exclusive charmonium and dijet photoproduction in ultraperipheral

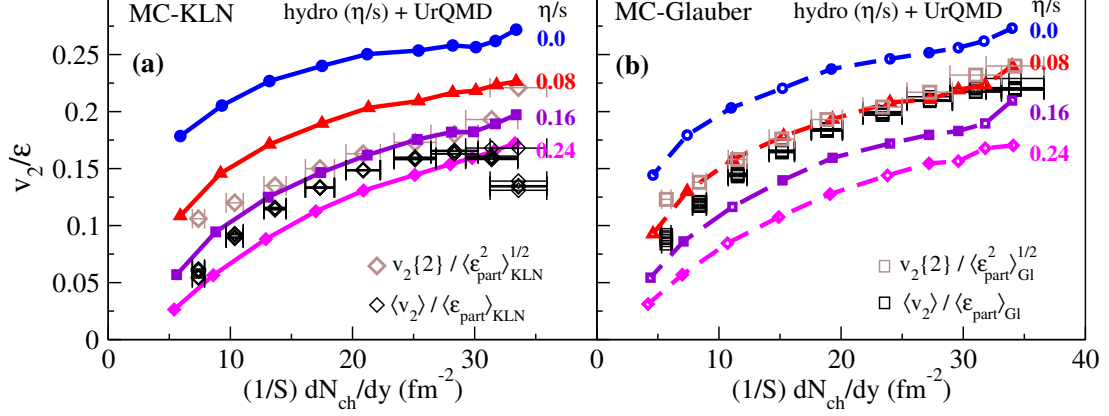


Figure 7.11: Comparison of the universal $v_2(\eta/s)/\epsilon$ vs. $(1/S)(dN_{\text{ch}}/dy)$ curves with experimental data for $\langle v_2 \rangle$ [654], $v_2\{2\}$ [655], and dN_{ch}/dy [656] from the STAR Collaboration. The experimental data used in (a) and (b) are identical, but the normalisation factors $\langle \epsilon_{\text{part}} \rangle$ and S used on the vertical and horizontal axes, as well as the factor $\langle \epsilon_{\text{part}}^2 \rangle^{1/2}$ used to normalize the $v_2\{2\}$ data, are taken from the MC-KLN model in (a) and from the MC-Glauber model in (b). Theoretical curves are from simulations with MC-KLN initial conditions in (a) and with MC-Glauber initial conditions in (b). Taken from [650].

5173 collisions [658–660]. Specifically, dijets in UPCs could constrain nPDFs in the region $10^{-3} \lesssim$
5174 $x \lesssim 0.7$ and $200 \lesssim Q^2 \lesssim 10^4 \text{ GeV}^2$. eA collisions would provide more precise nPDFs, whose
5175 compatibility with these mentioned observables would clearly establish the validity of collinear
5176 factorisation and the mechanisms of particle production in collisions involving nuclei.

5177 Furthermore, eA offers another system where photon-photon collisions, recently measured in
5178 UPCs at the LHC [661], can be studied. For example, the observed acoplanarity of the produced
5179 muon pairs can be analysed in eA in order to clarify its possible origin and constrain the parton
5180 densities in the photon.

5181 Finally, the possible existence of a new non-linear regime of QCD - saturation - at small x is
5182 also under study at the LHC, for example using dijets in the forward rapidity region in $p\text{Pb}$
5183 collisions [662]. As discussed in Sec. 4.5, the ridge phenomenon (two particle correlations peaked
5184 at zero and π azimuthal angles and stretched along the full rapidity of the detector) observed in
5185 all collision systems, pp , $p\text{Pb}$ and PbPb at the LHC, has been measured in photoproduction on
5186 Pb in UPCs at the LHC [452]. For the time being, its existence in smaller systems like e^+e^- [453]
5187 at LEP and ep at HERA [454] has been scrutinised but the results are not conclusive. These
5188 studies are fully complementary to those in ep and eA , where its search at the smallest possible
5189 values of x at the LHeC would be most interesting. For example, the collision of the virtual
5190 photon with the proton at the LHeC can be considered as a high energy collision of two jets or
5191 “flux tubes”.

5192 In conclusion, ep and eA collisions as studied at the LHeC will have a large impact on the
5193 heavy ion programme, as the comparison of the kinematic reach of DIS and hadronic machines
5194 shown in Fig. 7.12 makes evident. It should be noted that there exist proposals for extending
5195 such programme into Run 5 and 6 of the LHC [423], by running lighter ions and with detector
5196 upgrades in ATLAS and CMS (starting in Run 4) and LHCb (Upgrade II [663]).

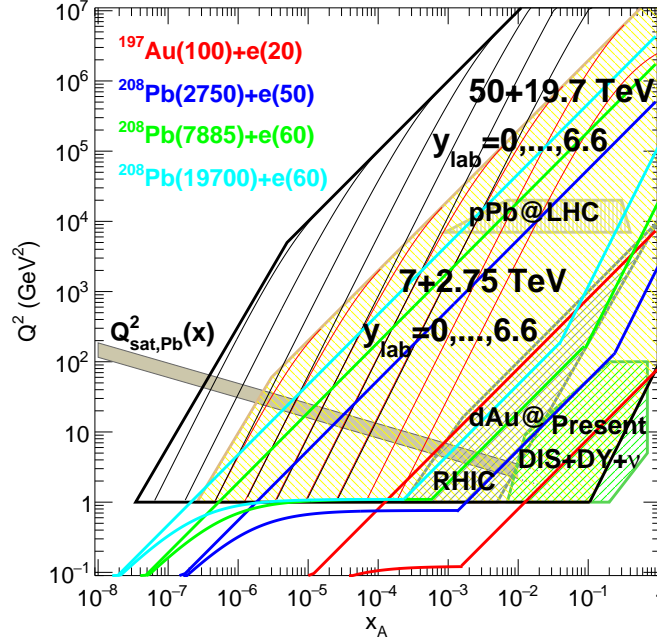


Figure 7.12: Kinematic regions in the $x - Q^2$ plane explored by data sets (charged lepton and neutrino DIS, DY, dAu at RHIC and pPb at the LHC) used in present nPDF analyses [398], compared to the ones achievable at the EIC (red), the LHeC (ERL against the HL-LHC beams, dark blue) and two FCC-eh versions (with Pb beams corresponding to proton energies of 20 TeV - green and 50 TeV - light blue). Acceptance is taken to be $1^\circ < \theta < 179^\circ$, and $0.01(0.001) < y < 1$ for the EIC (all other colliders). The areas delimited by thick brown and black lines show the regions accessible in pPb collisions at the LHC and the FCC-hh (50 TeV) respectively, while the thin lines represent constant rapidities from 0 (right) to 6.6 (left) for each case. The saturation scale Q_{sat} shown here for indicative purposes only, see also [399], has been drawn for a Pb nucleus considering an uncertainty ~ 2 and a behaviour with energy following the model in [400]. Note that it only indicates a region where saturation effects are expected to be important but there is no sharp transition between the linear and non-linear regimes.

Chapter 8

The Electron Energy Recovery Linac

We studied different options for the electron accelerator for LHeC in Ref. [1], of which the Energy Recovery Linac (ERL) option is retained in this update of the CDR. This is due to the higher achievable luminosity of the Linac-Ring option, as compared to the Ring-Ring option, as well as the interference of the installation of an electron ring in the LHC tunnel with its operation [664]. The clear advantage of the ERL compared to its contenders in 2012 is the possibility to keep the overall energy consumption at bay, albeit in its baseline configuration and size of the return arcs operation is still limited to lepton energies below 70 GeV to avoid excessive synchrotron radiation losses and is thus practically excluded. Since there is no fundamental beam loading in an ERL by its principle, higher average currents and thus higher luminosities would not lead to larger power consumption.

8.1 Introduction – Design Goals

The main guidelines for the design of the Electron ERL and the Interaction Region (IR) with the LHC are:

- electron-hadron operation in parallel with high luminosity hadron-hadron collisions in LHC/HL-LHC;
- centre-of-mass collision energy in the TeV scale;
- power consumption of the electron accelerator smaller than 100 MW;
- peak luminosity approaching $10^{34} \text{ cm}^{-2}\text{s}^{-1}$;
- integrated luminosity exceeding by at least two orders of magnitude that achieved by HERA at DESY.

The electron energy E_e chosen in the previous version of the CDR [1] was 60 GeV. This could be achieved with an ERL circumference of 1/3 of that of the LHC. Cost considerations and machine–detector performance aspects, in particular the amount of synchrotron radiation losses in the IR, have led to define a new reference configuration with $E_e = 49.2 \text{ GeV}$ and a circumference of $\approx 5.4 \text{ km}$, 1/5 of that of the LHC.

The ERL consists of two superconducting (SC) linacs operated in CW connected by at least three pairs of arcs to allow three accelerating and three decelerating passes (see Fig. 8.1). The length of the high energy return arc following the interaction point should be such as to provide

5227 a half RF period wavelength shift to allow the deceleration of the beam in the linac structures
 5228 in three passes down to the injection energy and its safe disposal. SC Cavities with an unloaded
 5229 quality factor Q_0 exceeding 10^{10} are required to minimise the requirements on the cryogenic
 5230 cooling power and to allow an efficient ERL operation. The choice of having three accelerating
 5231 and three decelerating passes implies that the circulating current in the linacs is six times the
 5232 current colliding at the Interaction Point (IP) with the hadron beam.

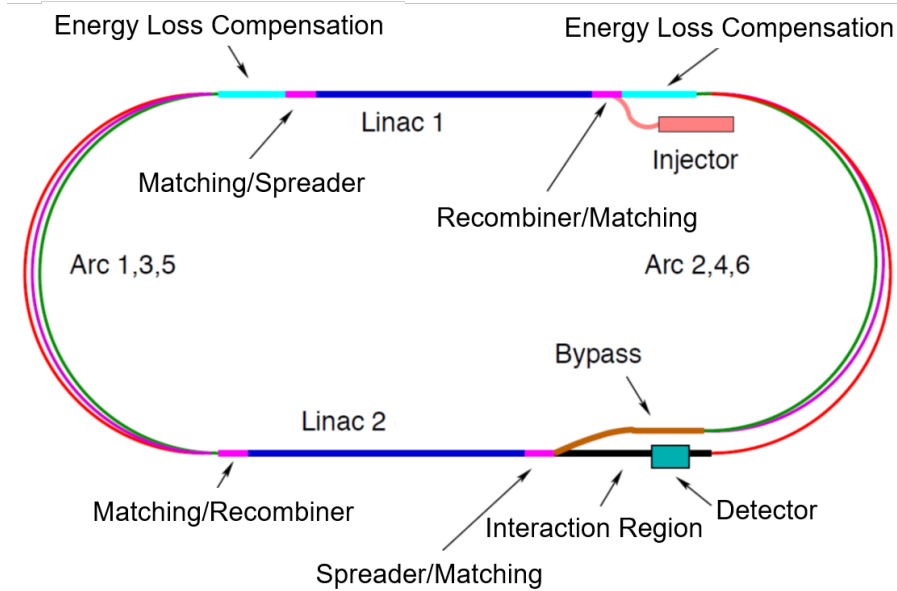


Figure 8.1: Schematic layout of the LHeC design based on an Energy Recovery Linac.

5233 The choice of an Energy Recovery Linac offers the advantage of a high brightness beam and it
 5234 avoids performance limitations due to the beam-beam effect seen by the electron beam [665],
 5235 which was a major performance limitation in many circular lepton colliders (e.g. LEP) and for
 5236 the LHeC Ring-Ring option. The current of the ERL is limited by its source and an operational
 5237 goal of $I_e = 20$ mA has been set, corresponding to a bunch charge of 500 pC at a bunch frequency
 5238 of 40 MHz. This implies operating the SRF cavities with the very high current of 120 mA for a
 5239 virtual beam power (product of the beam current at the IP times the maximum beam energy) of
 5240 1 GW. The validation of such performance in terms of source brightness and ERL 3-turn stable
 5241 and efficient operation in the PERLE facility [8] is a key milestone for the LHeC design.

5242 A small beam size at the IP is required to maximize luminosity and approach peak luminosities
 5243 of 10^{34} cm⁻²s⁻¹ and integrated luminosities of 1 ab⁻¹ in the LHeC lifetime. In particular $\beta^* <$
 5244 10 cm needs to be achieved for the colliding proton beam compatibly with the optics constraints
 5245 imposed by the operation in parallel to proton-proton physics in the other Interaction Points
 5246 (IPs) during the HL-LHC era [2]. The peak luminosity values quoted above exceed those at
 5247 HERA by 2-3 orders of magnitude. The operation of HERA in its first, extended running
 5248 period 1992–2000, provided and integrated luminosity of about 0.1 fb⁻¹ for the H1 and ZEUS
 5249 experiments, corresponding to the expected integrated luminosity collected over 1 day of LHeC
 5250 operation.

5251 8.2 The ERL Configuration of the LHeC

5252 The main parameters of the LHeC ERL are listed in Tab. 8.1; their choices and optimisation criteria will be discussed in the following sections.

Parameter	Unit	Value
Injector energy	GeV	0.5
Total number of linacs		2
Number of acceleration passes		3
Maximum electron energy	GeV	49.19
Bunch charge	pC	499
Bunch spacing	ns	24.95
Electron current	mA	20
Transverse normalized emittance	μm	30
Total energy gain per linac	GeV	8.114
Frequency	MHz	801.58
Acceleration gradient	MV/m	19.73
Cavity iris diameter	mm	130
Number of cells per cavity		5
Cavity length (active/real estate)	m	0.918/1.5
Cavities per cryomodule		4
Cryomodule length	m	7
Length of 4-CM unit	m	29.6
Acceleration per cryomodule (4-CM unit)	MeV	289.8
Total number of cryomodules (4-CM units) per linac		112 (28)
Total linac length (with with spr/rec matching)	m	828.8 (980.8)
Return arc radius (length)	m	536.4 (1685.1)
Total ERL length	km	5.332

Table 8.1: Parameters of LHeC Energy Recovery Linac (ERL).

5253

5254 8.2.1 Baseline Design – Lattice Architecture

5255 The ERL, as sketched in Fig. 8.1, is arranged in a racetrack configuration; hosting two supercon-
5256 ducting linacs in the parallel straights and three recirculating arcs on each side. The linacs are
5257 828.8 m long and the arcs have 536.4 m radius, additional space of 76 m is taken up by utilities
5258 like Spreader/Recombiner, matching and energy loss compensating sections adjacent to both
5259 ends of each linac (total of 4 sections) [666]. The total length of the racetrack is 5.332 km: 1/5
5260 of the LHC circumference $2 \cdot (828.8 + 2 \cdot 76 + 536.4\pi)$ m. Each of the two linacs provides 8.114
5261 GV accelerating voltage, therefore a 49.19 GeV energy is achieved in three turns. After the
5262 collision with the protons in the LHC, the beam is decelerated in the three subsequent turns.
5263 The injection and dump energy has been chosen at 0.5 GeV.

5264 Injection into the first linac is done through a fixed field injection chicane, with its last magnet
5265 (closing the chicane) being placed at the beginning of the linac. It closes the orbit *bump* at the
5266 lowest energy, injection pass, but the magnet (physically located in the linac) will deflect the
5267 beam on all subsequent linac passes. In order to close the resulting higher pass *bumps*, the so-
5268 called re-injection chicane is instrumented, by placing two additional opposing bends in front of
5269 the last chicane magnet. The chosen arrangement is such that, the re-injection chicane magnets
5270 are only *visible* by the higher pass beams. The second linac in the racetrack is configured exactly

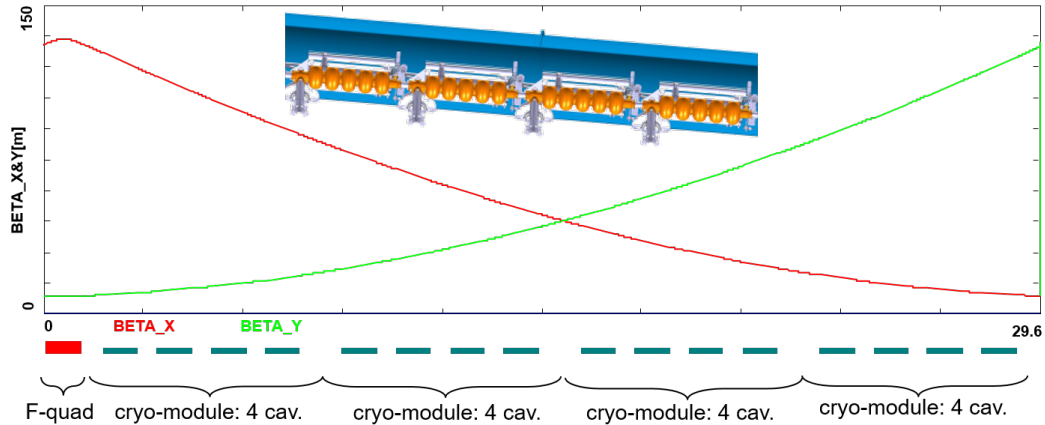


Figure 8.2: Layout of a half-cell composed out of four cryo-modules (each hosting four, 5-cell cavities: top insert) and a focusing quad. Beta functions reflect 130° FODO optics.

5271 as a mirror image of the first one, with a replica of the re-injection chicane at its end, which
 5272 facilitates a fixed-field extraction of energy recovered beam to the dump.

5273 Linac Configuration and Multi-pass Optics

5274 Appropriate choice of the linac optics is of paramount importance for the transverse beam
 5275 dynamics in a multi-pass ERL. The focusing profile along the linac (quadrupole gradients) need
 5276 to be set (and they stay constant), so that multiple pass beams within a vast energy range may
 5277 be transported efficiently. The chosen arrangement is such that adequate transverse focusing
 5278 is provided for a given linac aperture. The linac optics is configured as a strongly focusing,
 5279 130° FODO. In a basic FODO cell a quadrupole is placed every four cryomodules, so that the
 5280 full cell contains two groups of 16 RF cavities and a pair of quads (F, D) as illustrated in
 5281 Fig. 8.2. The entire linac is built out of 14 such cells. Energy recovery in a racetrack topology
 5282 explicitly requires that both the accelerating and decelerating beams share the individual return
 5283 arcs [667]. This in turn, imposes specific requirements for TWISS function at the linacs ends:
 5284 TWISS functions have to be identical for both the accelerating and decelerating linac passes
 5285 converging to the same energy and therefore entering the same arc. There is an alternative
 5286 scheme, proposed by Peter Williams, who has argued that it would be beneficial to separate
 5287 the accelerating and decelerating arcs. This would simplify energy compensation systems and
 5288 linac-to-arc matching. However, doubling number of arcs is a very costly proposition. On the
 5289 other hand, C-BETA experiment is pioneering a multi-pass arcs to transport a vast energy range
 5290 through the same beam-line and it still intends to use them for energy recovery. Our approach,
 5291 based on proven, CEBAF-like, RLA technology [668] is somewhere in the 'middle'.

5292 To visualize beta functions for multiple accelerating and decelerating passes through a given
 5293 linac, it is convenient to reverse the linac direction for all decelerating passes and string them
 5294 together with the interleaved accelerating passes, as illustrated in Fig. 8.3. This way, the cor-
 5295 responding accelerating and decelerating passes are joined together at the arc's entrance/exit.
 5296 Therefore, the matching conditions are automatically built into the resulting multi-pass linac
 5297 beamline. One can see that both linacs uniquely define the TWISS functions for the arcs: Linac
 5298 1 fixes input to all odd arcs and output to all even arcs, while Linac 2 fixes input to all even
 5299 arcs and output to all odd arcs. The optics of the two linacs are mirror-symmetric; They were

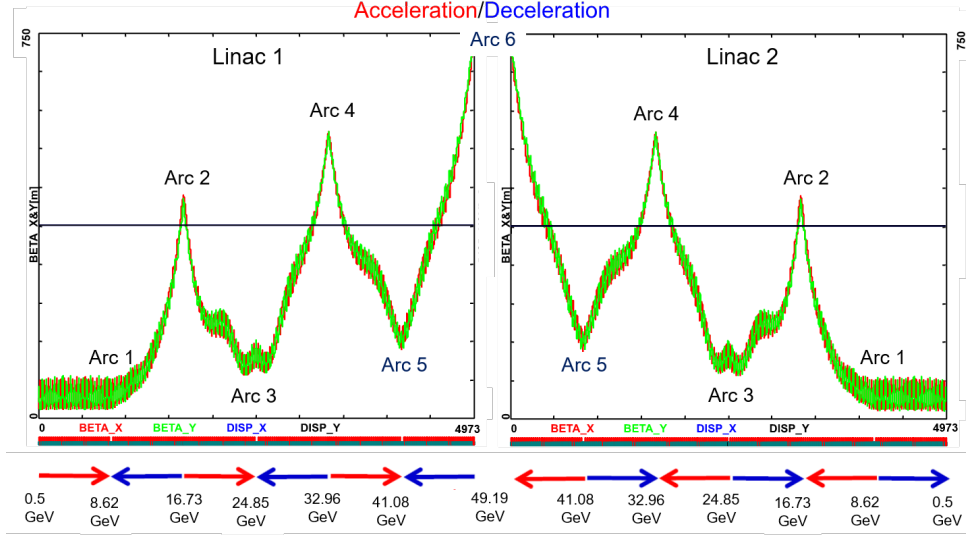


Figure 8.3: Beta function in the optimised multi-pass linacs (3 accelerating passes and 3 decelerating passes in each of two linacs). The matching conditions are automatically built into the resulting multi-pass linac beamline.

5300 optimised so that, Linac 1 is periodic for the first accelerating pass and Linac 2 has this feature
 5301 for last decelerating one. In order to maximize the BBU threshold current [669], the optics is
 5302 tuned so that the integral of β/E along the linac is minimised. The resulting phase advance per
 5303 cell is close to 130° . Non-linear strength profiles and more refined merit functions were tested,
 5304 but they only brought negligible improvements.

5305 Recirculating Arcs – Emittance Preserving Optics

5306 Synchrotron radiation effects on beam dynamics, such as the transverse emittance dilution
 5307 induced by quantum excitations have a paramount impact on the collider luminosity. All six
 5308 horizontal arcs are accommodated in a tunnel of 536.4m radius. The transverse emittance
 5309 dilution accrued through a given arc is proportional to the emittance dispersion function, H ,
 5310 averaged over all arc's bends [670]:

$$\Delta\epsilon = \frac{2\pi}{3} C_q r_0 \langle H \rangle \frac{\gamma^5}{\rho^2}, \quad (8.1)$$

5311 where

$$C_q = \frac{55}{32\sqrt{3}} \frac{\hbar}{mc} \quad (8.2)$$

5312 and r_0 is the classical electron radius and γ is the Lorentz boost. Here, $H = (1 + \alpha^2)/\beta \cdot$
 5313 $D^2 + 2\alpha DD' + \beta \cdot D'^2$ where D, D' are the bending plane dispersion and its derivative, with
 5314 $\langle \dots \rangle = \frac{1}{\pi} \int_{\text{bends}} \dots d\theta$.

5315 Therefore, emittance dilution can be mitigated through appropriate choice of arc optics (values
 5316 of α, β, D, D' at the bends). In the presented design, the arcs are configured with a FMC
 5317 (Flexible Momentum Compaction) optics to ease individual adjustment of, $\langle H \rangle$, in various
 5318 energy arcs.

5319 Optics design of each arc takes into account the impact of synchrotron radiation at different
 5320 energies. At the highest energy, it is crucial to minimise the emittance dilution due to quantum

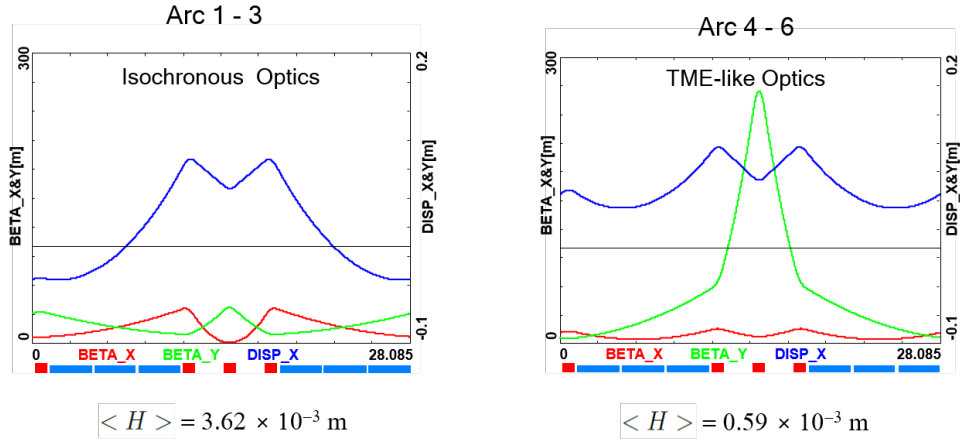


Figure 8.4: Two styles of FMC cells appropriate for different energy ranges. Left: lower energy arcs (Arc 1–3) configured with *Isochronous* cells, Right: higher energy arcs configured with *TME-like* cells. Corresponding values of the emittance dispersion averages, $\langle H \rangle$, are listed for both style cells.

5321 excitations; therefore, the cells are tuned to minimise the emittance dispersion, H , in the bending
 5322 sections, as in the TME (Theoretical Minimum Emittance) lattice. On the other hand, at the
 5323 lowest energy, it is beneficial to compensate for the bunch elongation with isochronous optics.
 5324 The higher energy arcs (4,5 and 6) configured with the TME cells are still quasi-isochronous. To
 5325 fully compensate remnant bunch elongation one could set higher pass linacs slightly off-crest to
 5326 compress the bunches, since one has full control of gang-phases for individual linac passes. All
 5327 styles of FMC lattice cells, as illustrated in Fig. 8.4, share the same footprint for each arc. This
 5328 allows us to stack magnets on top of each other or to combine them in a single design. Here,
 5329 we use substantially shorter than in the 60 GeV design, 28.1 m, FMC cell configured with six
 5330 3 m bends, in groups of flanked by a quadrupole singlet and a triplet, as illustrated in Fig. 8.4.
 5331 The dipole filling factor of each cell is 63%; therefore, the effective bending radius ρ is 336.1 m.
 5332 Each arc is followed by a matching section and a recombiner (mirror symmetric to spreader and
 5333 matching section). Since the linacs are mirror-symmetric, the matching conditions described
 5334 in the previous section, impose mirror-symmetric arc optics (identical betas and sign reversed
 5335 alphas at the arc ends).

5336 Path-length adjusting chicanes were also foreseen to tune the beam time of flight in order to hit
 5337 the proper phase at each linac injection. Later investigations proved them to be effective only
 5338 with lower energy beams, as these chicanes trigger unbearable energy losses, if applied to the
 5339 highest energy beams. A possible solution may consist in distributing the perturbation along
 5340 the whole arc with small orbit excitations. This issue will be fully addressed in a subsequent
 5341 section on 'Synchrotron Radiation Effects - Emittance Dilution'.

5342 Spreaders and Recombiners

5343 The spreaders are placed directly after each linac to separate beams of different energies and
 5344 to route them to the corresponding arcs. The recombiners facilitate just the opposite: merging
 5345 the beams of different energies into the same trajectory before entering the next linac. As
 5346 illustrated in Fig. 8.5, each spreader starts with a vertical bending magnet, common for all
 5347 three beams, that initiates the separation. The highest energy, at the bottom, is brought back
 5348 to the horizontal plane with a chicane. The lower energies are captured with a two-step vertical
 5349 bending adapted from the CEBAF design [668].

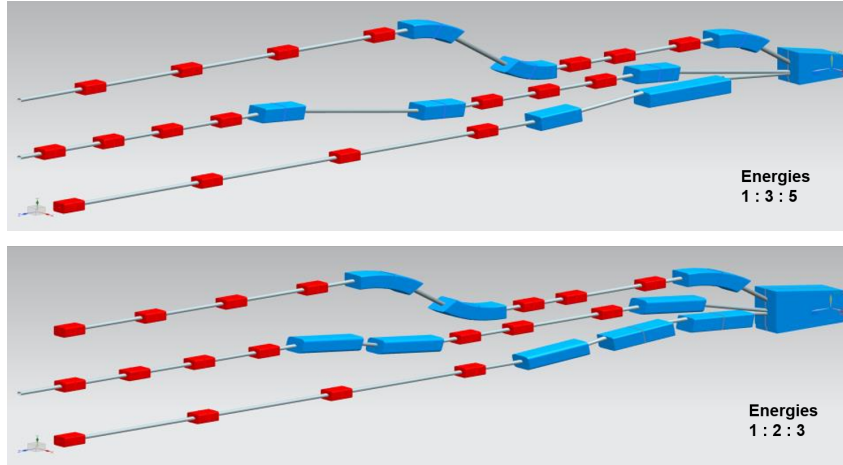


Figure 8.5: Layout of a three-beam switch-yard for different energy ratios: 1:3:5 and 1:2:3 corresponding to specific switch-yard geometries implemented on both sides of the racetrack

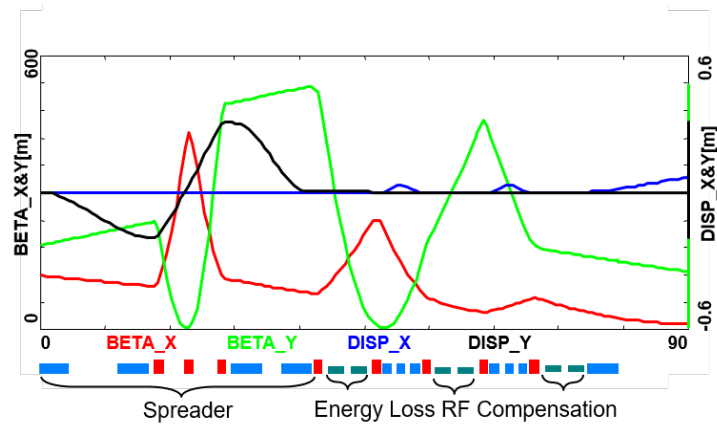


Figure 8.6: Spreader 3 (24.8 GeV) optics; featuring a vertical achromat with three dispersion suppressing quads in-between the two steps, a pair of path-length adjusting dogleg chicanes and four betatron matching quads, interleaved with three energy loss compensating sections (2-nd harmonic rf cavities marked in green).

5350 Functional modularity of the lattice requires spreaders and recombiners to be achromats (both
 5351 in the horizontal and vertical plane). To facilitate that, the vertical dispersion is suppressed by
 5352 a pair of quadrupoles located in-between vertical steps; they naturally introduce strong vertical
 5353 focusing, which needs to be compensated by the middle horizontally focusing quad. The overall
 5354 spreader optics is illustrated in Fig. 8.6. Complete layout of two styles of switch-yard with
 5355 different energy ratios is depicted in Fig. 8.5. Following the spreader, there are four matching
 5356 quads to *bridge* the Twiss function between the spreader and the following 180° arc (two betas
 5357 and two alphas). Combined spreader-arc-recombiner optics, features a high degree of modular
 5358 functionality to facilitate momentum compaction management, as well as orthogonal tunability
 5359 for both the beta functions and dispersion, as illustrated in Fig. 8.7.

5360 IR Bypasses

5361 After the last spreader the 49.19 GeV beam goes straight to the interaction region. However the
 5362 lower energy beams; at 16.7 and 33.0 GeV, need to be further separated horizontally in order

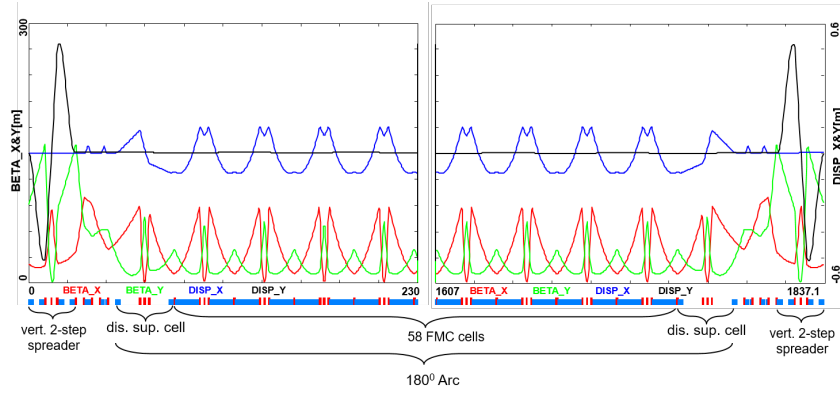


Figure 8.7: Complete Optics for Arc 3 (including switch-yard); featuring: low emittance 180° arc based on isochronous cells (30 cells flanked by dispersion suppression cell with missing dipoles on each side), spreaders and recombiners with matching sections and doglegs symmetrically placed on each side of the arc proper.

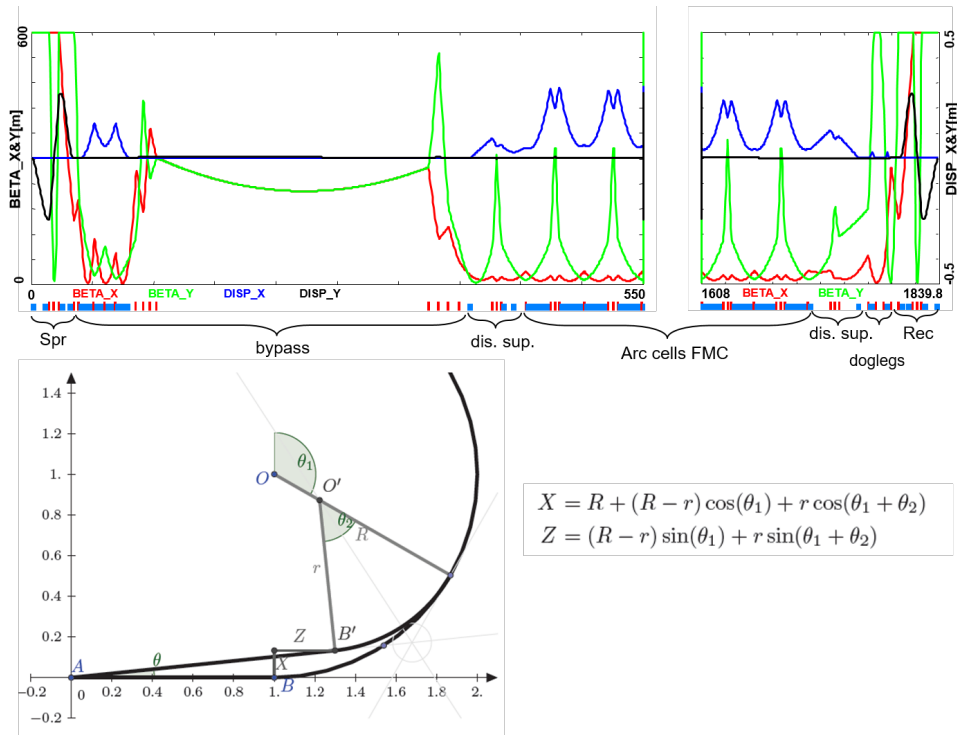


Figure 8.8: Optics and layout of Arc 4 including the detector bypass. The lattice (top insert) features a vertical spreader, an initial horizontal bending, a straight section, a modified dispersion suppressor, seven junction cells, and four regular cells. The bypass geometry (bottom insert), features a long IP line, AB, which for visual reasons has been purposely stretched, being actually about 1/5 of the arc radius. All geometric dependencies of the bypass parameters are summarized in the inserted formulae.

5363 to avoid interference with the detector. Different design options for the bypass section were
 5364 explored [671] and the one that minimises the extra bending has been chosen and implemented
 5365 in the lattice.

5366 Ten arc-like dipoles are placed very close to the spreader, to provide an initial bending, θ , which
 5367 results in $X = 10$ m separation from the detector located 120 m downstream. The straight
 5368 section of the bypass is approximately 240 m long. After the bypass, in order to reconnect to
 5369 the footprint of Arc 6, 7 of 30 standard cells in Arc 2 and Arc 4 are replaced with 7 higher field,
 5370 junction cells. The number of junction cells is a compromise between the field strength increase
 5371 and the length of additional bypass tunnel, as can be inferred from the scheme summarised in
 5372 Fig. 8.8. The stronger bending in the junction cells creates a small mismatch, which is corrected
 5373 by adjusting the strengths of the quadrupoles in the last junction cell and in the first regular
 5374 cell.

5375 Synchrotron Radiation Effects – Emittance Dilution

5376 ERL efficiency as a source of multi-GeV electrons for a high luminosity collider is limited by the
 5377 incoherent synchrotron radiation effects on beam dynamics; namely the transverse emittance
 5378 dilution and the longitudinal momentum spread (induced by quantum excitations). The first
 5379 effect, the transverse emittance increase, will have a paramount impact on the collider luminosity,
 5380 due to stringent limits on the allowed emittance increase. The second one, accrued momentum
 5381 spread, governs asymmetries of accelerated and decelerated beam profiles. These asymmetries
 5382 substantially complicate multi-pass energy recovery and matching, and ultimately they limit the
 5383 energy reach of the ERLs due to recirculating arc momentum acceptance.

5384 Arc optics was designed to ease individual adjustment of momentum compaction (needed for the
 5385 longitudinal phase-space control, essential for operation with energy recovery) and the horizontal
 5386 emittance dispersion, H , in each arc. Tab. 8.2 lists arc-by-arc dilution of the transverse, $\Delta\epsilon$,
 5387 and longitudinal, $\Delta\sigma_{\frac{\Delta E}{E}}$, emittance dilution due to quantum excitations calculated using analytic
 5388 formulas, Eqs. (8.3), (8.4) and (8.5), introduced by M. Sands [670]:

$$\Delta E = \frac{2\pi}{3} r_0 m c^2 \frac{\gamma^4}{\rho} \quad (8.3)$$

5389

$$\Delta\epsilon_N = \frac{2\pi}{3} C_q r_0 \langle H \rangle \frac{\gamma^6}{\rho^2}, \quad (8.4)$$

5390

$$\frac{\Delta\epsilon_E^2}{E^2} = \frac{2\pi}{3} C_q r_0 \frac{\gamma^5}{\rho^2}, \quad (8.5)$$

5391 where C_q is given by Eq. (8.2). Here, $\Delta\epsilon_E^2$ is an increment of energy square variance, r_0 is
 5392 the classical electron radius, γ is the Lorentz boost and $C_q \approx 3.832 \cdot 10^{-13}$ m for electrons (or
 5393 positrons).

5394 Apart from the horizontal 180° arcs, there are other sources of emittance dilution due to syn-
 5395 chrotron radiation, namely vertical Spreaders and Recombiners, as well as horizontal 'Doglegs'
 5396 used to compensate seasonal variation of path-length. To minimise their contribution to the ver-
 5397 tical emittance dilution, special optics with small vertical $\langle H \rangle$ has been introduced in Spr/Rec
 5398 sections. The effects on vertical emittance dilution coming from these beamlines (Spr/Rec) are
 5399 summarized in Tab. 8.3.

5400 Similarly, the horizontal emittance dilution induced by the Doglegs (four dogleg chicanes per
 5401 arc) in various arcs is summarized in Tab. 8.4. Each dogleg chicane is configured with four 1

Beamline	Beam energy [GeV]	ΔE [MeV]	$\Delta\epsilon_N^x$ [mm mrad]	$\Delta\sigma_{\frac{\Delta E}{E}}$ [%]
arc 1	8.62	0.7	0.0016	0.0005
arc 2	16.73	10	0.085	0.0027
arc 3	24.85	49	0.91	0.0072
arc 4	32.96	152	0.81	0.015
arc 5	41.08	368	3.03	0.026
arc 6	49.19	758	8.93	0.040

Table 8.2: Energy loss and emittance dilution (horizontal and longitudinal) due to synchrotron radiation generated by all six 180° arcs (not including Spreaders, Recombiners and Doglegs). Here, $\Delta\sigma_{\frac{\Delta E}{E}} = \sqrt{\frac{\Delta\epsilon_E^2}{E^2}}$

Beamline	Beam energy [GeV]	ΔE [MeV]	$\Delta\epsilon_N^y$ [mm mrad]	$\Delta\sigma_{\frac{\Delta E}{E}}$ [%]
Spr/Rec 1	8.62	0.2	0.035	0.0008
Spr/Rec 2	16.73	3.0	0.540	0.0044
Spr/Rec 3	24.85	6.0	0.871	0.0066
Spr/Rec 4	32.96	21.6	5.549	0.0143
Spr/Rec 5	41.08	7.1	0.402	0.0062
Spr/Rec 6	49.19	39.2	3.92	0.0205

Table 8.3: Energy loss and emittance dilution (vertical and longitudinal) due to synchrotron radiation generated by a Spreader, or Recombiner of a given arc. Here, $\Delta\sigma_{\frac{\Delta E}{E}} = \sqrt{\frac{\Delta\epsilon_E^2}{E^2}}$

5402 meter bends (1 Tesla each), so that they bend the lowest energy beam at 8.6 GeV by 2 degrees.
5403 The corresponding path-lengths gained in the Doglegs of different arcs are also indicated.

Beamline	Beam energy [GeV]	ΔE [MeV]	$\Delta\epsilon_N^x$ [mm mrad]	$\Delta\sigma_{\frac{\Delta E}{E}}$ [%]	path-length [mm]
Doglegs 1	8.62	2	0.201	0.007	7.32
Doglegs 2	16.73	9	0.667	0.009	1.96
Doglegs 3	24.85	19	5.476	0.014	0.84
Doglegs 4	32.96	33	5.067	0.014	0.52
Doglegs 5	41.08	52	12.067	0.028	0.36
Doglegs 6	49.19	74	2.836	0.011	0.28

Table 8.4: Energy loss and emittance dilution (horizontal and longitudinal) due to synchrotron radiation generated by the Doglegs (four dogleg chicanes) of a given arc. Here, $\Delta\sigma_{\frac{\Delta E}{E}} = \sqrt{\frac{\Delta\epsilon_E^2}{E^2}}$

5404 As indicated in Tab. 8.4, the Doglegs in the highest energy arcs, Arc 5 and Arc 6, provide only
5405 sub mm path-length gain with large synchrotron radiation effects. They are not very effective
5406 and generate strong, undesired emittance dilution. Therefore, it is reasonable to eliminate them
5407 from both Arc 5 and 6. Instead, one could resort to an alternative path-length control via
5408 appropriate orbit steering with both horizontal and vertical correctors present at every girder
5409 and distributed evenly throughout the arc.

5410 Combining all three contributions: (180° arc, Spreader, Recombiner and Doglegs (no Doglegs in
5411 Arcs 5 and 6), the net cumulative emittance dilution is summarized in Tab. 8.5.

Beamline	Beam energy [GeV]	ΔE [MeV]	$\Delta^{\text{cum}}\epsilon_N^x$ [mm mrad]	$\Delta^{\text{cum}}\epsilon_N^y$ [mm mrad]	$\Delta^{\text{cum}}\sigma_{\frac{\Delta E}{E}}$ [%]
Arc 1	8.62	3	0.2	0.1	0.01
Arc 2	16.73	25	1.0	1.2	0.03
Arc 3	24.85	80	7.3	2.9	0.06
Arc 4	32.96	229	13.2	14.0	0.12
Arc 5	41.08	383	16.2	14.8	0.16
IR	49.19	39	16.2	18.7	0.18
Arc 6	49.19	797	25.2	22.6	0.24
Arc 5	41.08	383	28.2	23.4	0.28
Arc 4	32.96	229	34.1	34.5	0.33
Arc 3	24.85	80	40.5	36.3	0.37
Arc 2	16.73	25	41.2	37.4	0.39
Arc 1	8.62	3	41.4	37.4	0.40
Dump	0.5		41.4	37.4	0.40

Table 8.5: Energy loss and cumulative emittance dilution (transverse and longitudinal) due to synchrotron radiation at the end of a given beam-line (complete Arc including: 180° arc, Spreader, Recombiner and Doglegs in arcs 1-4). The table covers the entire ER cycle: 3 passes 'up' + 3 passes 'down'. Cumulative emittance dilution values just before the IP (past Arc 5 and Spr 6), which are critical for the luminosity consideration are highlighted in 'bold'. That row accounts for contributions from Spr 6 (the last bending section before the IR) to energy loss, as well as the vertical and longitudinal emittance dilutions. Here, $\Delta\sigma_{\frac{\Delta E}{E}} = \sqrt{\frac{\Delta\epsilon_E^2}{E^2}}$

5412 Tab. 8.5 shows, the LHeC luminosity requirement of total transverse emittance dilution in either
5413 plane (normalized) at the IP (at the end of Arc 5), not to exceed 20 mm mrad (hor: 16.2 mm mrad
5414 and ver: 18.7 mm mrad) is met by-design, employing presented low emittance lattices in both
5415 the arcs and switch-yards.

5416 Finally, one can see from Eqs. (8.4) and (8.5) an underlying universal scaling of the transverse
5417 (unnormalized) and longitudinal emittance dilution with energy and arc radius; they are both
5418 proportional to γ^5/ρ^2 . This in turn, has a profound impact on arc size scalability with energy;
5419 namely the arc radius should scale as $\gamma^{5/2}$ in order to preserve both the transverse and longi-
5420 tudinal emittance dilutions, which is a figure of merit for a synchrotron radiation dominated
5421 ERL.

5422 8.2.2 30 GeV ERL Options

5423 One may think of an upgrade path from 30 to 50 GeV ERL, using the same 1/5 of the LHC
5424 circumference (5.4 km), footprint. In this scenario, each linac straight (front end) would initially
5425 be *loaded* with 18 cryo-modules, forming two 5.21 GV linacs. One would also need to decrease
5426 the injector energy by factor of 5.21/8.11. The top ERL energy, after three passes, would reach
5427 31.3 GeV. Then for the upgrade to 50 GeV, one would fill the remaining space in the linacs
5428 with additional 10 cryo-moduls each; 2.9 GV worth of RF in each linac. This way the energy
5429 ratios would be preserved for both 30 and 50 GeV ERL options, so that the same switch-yard
5430 geometry could be used. Finally, one would scale up the entire lattice; all magnets (dipoles and
5431 quads) by 8.11/5.21 ratio. If one wanted to stop at the 30 GeV option with no upgrade path,
5432 then the 1/12 of the LHC circumference (2.2 km) would be a viable footprint for the racetrack,
5433 featuring: two linacs, 533 m each, (18 cryo-modules) and arcs of 136 m radius. Again, assuming
5434 0.32 GeV injection energy, the top ERL energy would reach 31.3 GeV.

5435 **8.2.3 Component Summary**

5436 This closing section will summarise active accelerator components: magnets (bends and quads)
 5437 and RF cavities for the 50 GeV baseline ERL. The bends (both horizontal and vertical) are
 5438 captured in Tab. 8.6, while the quadrupole magnets and RF cavities are collected in Tab. 8.7.

5439 One would like to use a combined aperture (3-in-one) arc magnet design with 50 cm vertical
 5440 separation between the three apertures, proposed by Attilio Milanese. That would reduce net
 5441 arc bend count from 2112 to 704. As far as the Spr/Rec vertical bends are concerned, the design
 5442 was optimised to include an additional common bend separating the two highest passes. So,
 5443 there are a total of 8 trapezoid B-com magnets, with second face tilted by 3° and large 10 cm
 5444 vertical aperture, the rest are simple rectangular bends with specs from the summary Tab. 8.6.

Section	Arc dipoles (horiz.)				Spr/Rec dipoles (vert.)				<i>Dogleg</i> dipoles (horiz.)			
	<i>N</i>	<i>B</i> [T]	<i>g</i> /2[cm]	<i>L</i> [m]	<i>N</i>	<i>B</i> [T]	<i>g</i> /2[cm]	<i>L</i> [m]	<i>N</i>	<i>B</i> [T]	<i>g</i> /2[cm]	<i>L</i> [m]
Arc 1	352	0.087	1.5	3	8	0.678	2	3	16	1	1.5	1
Arc 2	352	0.174	1.5	3	8	0.989	2	3	16	1	1.5	1
Arc 3	352	0.261	1.5	3	6	1.222	2	3	16	1	1.5	1
Arc 4	352	0.348	1.5	3	6	1.633	2	3	16	1	1.5	1
Arc 5	352	0.435	1.5	3	4	1.022	2	3				
Arc 6	352	0.522	1.5	3	4	1.389	2	3				
Total	2112				36				64			

Table 8.6: 50 GeV ERL – Dipole magnet count along with basic magnet parameters: Magnetic field (*B*), Half-Gap (*g*/2), and Magnetic length (*L*).

Section	Quadrupoles				RF cavities			
	<i>N</i>	<i>G</i> [T/m]	<i>a</i> [cm]	<i>L</i> [m]	<i>N</i>	<i>f</i> [MHz]	cell	<i>G</i> _{RF} [T/m]
Linac 1	29	1.93	3	1	448	802	5	20
Linac 2	29	1.93	3	1	448	802	5	20
Arc 1	255	9.25	2.5	1				
Arc 2	255	17.67	2.5	1				
Arc 3	255	24.25	2.5	1	6	1604	9	30
Arc 4	255	27.17	2.5	1	12	1604	9	30
Arc 5	249	33.92	2.5	1	18	1604	9	30
Arc 6	249	40.75	2.5	1	36	1604	9	30
Total	1576				968			

Table 8.7: 50 GeV ERL – Quadrupole magnet and RF cavities count along with basic magnet/RF parameters: Magnetic field gradient (*G*), Aperture radius (*a*), Magnetic length (*L*), Frequency (*f*), Number of cells in RF cavity (cell), and RF Gradient (*G*_{RF}).

5445 **8.3 Electron-Ion Collisions**

5446 Besides colliding proton beams, the LHC also provides collisions of nuclear (fully-stripped ion)
 5447 beams with each other (AA collisions) or with protons (*pA*). Either of these operating modes
 5448 offers the possibility of electron-ion (*eA*) collisions in the LHeC configuration¹

¹ In *pA* operation of the LHC the beams may be reversed (*Ap*) for some part of the operating time. Only one direction (ions in Beam 2) would provide *eA* collisions while the other would provide *ep* collisions at significantly

5449 Here we summarise the considerations leading to the luminosity estimates given in Tab. 2.4 for
5450 collisions of electrons with $^{208}\text{Pb}^{82+}$ nuclei, the nominal heavy ion species collided in the LHC.
5451 Other, lighter, nuclei are under consideration for future LHC operation [423] and could also be
5452 considered for electron-ion collisions.

5453 The heavy ion beams that the CERN injector complex can provide to the LHC, the HE-LHC
5454 and the FCC provide a unique basis for high energy, high luminosity deep inelastic electron-ion
5455 scattering physics. Since HERA was restricted to protons only, the LHeC or FCC-eh would
5456 extend the kinematic range in Q^2 and $1/x$ by 4 or 5 orders of magnitude. This is a huge increase
5457 in coverage and would be set to radically change the understanding of parton dynamics in nuclei
5458 and of the formation of the quark gluon plasma.

5459 An initial set of parameters in the maximum energy configurations was given in [32]. The
5460 Pb beam parameters are essentially those foreseen for operation of the LHC (or HL-LHC)
5461 in Run 3 and Run 4 (planned for the 2020s). These parameters have already been largely
5462 demonstrated [672] except for the major remaining step of implementing slip-stacking injection
5463 in the SPS which would reduce the basic bunch spacing from 100 to 50 ns [673]. With respect
5464 to the proton spacing of 25 ns, this allows the electron bunch intensity to be doubled while still
5465 respecting the limit on total electron current. In fact, without the slip-stacking in the SPS,
5466 the initial luminosity would be the same with a 100 ns Pb spacing (and quadrupled electron
5467 bunch intensity). However one must remember that the evolution of the Pb beam intensity will
5468 be dominated by luminosity burn-off by the concurrent PbPb collisions at the other interaction
5469 points and integrated luminosity for both PbPb and ePb collisions will be higher with the higher
5470 total Pb intensity. The details of this will depend on the operating scenarios, number of active
5471 experiments, etc, and are not considered further here. The time-evolution of eA luminosity will
5472 be determined by that of PbPb and pPb collisions, as discussed, for example, in Ref. [14,423,674].

5473 Combining these assumptions with the default 50 GeV electron ERL for LHeC and 60 GeV for
5474 FCC-eh, yields the updated parameter sets and initial luminosities given in Tab. 2.4, earlier in
5475 the present report.

5476 Radiation damping of Pb beams in the hadron rings is about twice as fast as for protons and can
5477 be fully exploited since it takes longer to approach the beam-beam limit at the PbPb collisions
5478 points. For the case of the FCC-hh [14], one can expect the emittance values in Tab. 2.4 to be
5479 reduced during fills [14, 423, 674].

5480 The Pb beam will be affected by ultraperipheral collision effects, mainly bound-free pair pro-
5481 duction and Coulomb dissociation of the nuclei, induced by the electromagnetic fields of the
5482 electrons, seen as pulses of virtual photons. The relevant cross-sections will be similar to those
5483 in pPb collisions which are down by a factor of Z^2 compared to those in PbPb collisions and
5484 can be neglected in practice.

5485 8.4 Beam-Beam Interactions

5486 In the framework of the Large Hadron electron Collider, the concept of an Energy Recirculating
5487 Linac (ERL) allows to overcome the beam-beam limit that one would face in a storage ring. The
5488 electron beam can be heavily disturbed by the beam collision process, while the large acceptance
5489 of the ERL will still allow for a successful energy recovery during the deceleration of the beam
5490 so that the power consumption is minimised. In order to compare the relevant beam-beam

reduced luminosity compared to the pp mode, since there would be fewer proton bunches of lower intensity.

5491 parameters and put them into the context of other colliders, two tables are shown highlighting,
 5492 on the one hand, the parameters from LEP and LHC runs in Tab. 8.8, and on the other hand,
 5493 the parameters planned for LHeC at HL-LHC in Tab. 8.9.

Parameter	Unit	LEP	LHC
Beam sizes σ_x / σ_y	μm	180 / 7	16.6 / 16.6
Intensity	10^{11} particles/bunch	4.00	1.15
Energy	GeV	100	7000
β_x^*/β_y^*	cm	125/5	55/55
Crossing angle	μrad	0	0/285
Beam-beam tune shift $\Delta Q_x/\Delta Q_y$		0.0400/0.0400	0.0037/0.0034
Beam-beam parameter ξ		0.0700	0.0037

Table 8.8: Comparison of parameters for the LEP collider and LHC. Taken from CDR 2012, p.286.

Beam parameter	Unit	LHeC at HL-LHC	
		Proton beam	Electron beam
Energy	GeV	7000	49.19
Normalized emittance	mm·mrad	2.5	50
Beam sizes $\sigma_{x,y}$	μm	5.8	5.8
Intensity	10^9 particles/bunch	220.00	3.12
Bunch length σ_s	mm	75.5	0.6
$\beta_{x,y}^*$	cm	10.00	6.45
Disruption factor		1.2×10^{-5}	14.5
Beam-beam parameter ξ		1.52×10^{-4}	0.99

Table 8.9: Comparison of parameters for the LHeC at HL-LHC. The parameters presented correspond to the default design.

5494 In the case of LHeC, the β -functions at the interaction point are chosen such that the transverse
 5495 beam sizes of e^- and p^- beam are equal in both transverse planes. Although the proton and
 5496 electron emittances are different, the beta functions at the interaction point are set accordingly
 5497 so that the two beams conserve $\sigma_x^e = \sigma_x^p$ and $\sigma_y^e = \sigma_y^p$.

5498 8.4.1 Effect on the electron

5499 The disruption parameter for the electron beam is of the order of 14.5 which corresponds, in
 5500 linear approximation, to almost 2 oscillations of the beam envelope within the proton bunch.
 5501 The non linearity of the interaction creates a distortion of the phase space and a mismatch from
 5502 the design optics see Fig. 8.9. The mismatch and distortion can be minimized by tuning the
 5503 Twiss parameters (α^*, β^*) at the interaction point.

5504 In a series of studies the optics parameters of the electron beam were tracked back to the
 5505 interaction point in presence of the beam-beam forces in order to show the impact of the beam-
 5506 beam effect for different values of the electron Twiss parameters at the IP. In addition, the
 5507 influence of a waist shift from the IP (proportional to α^*), similar to changing the foci of the
 5508 interacting beams, has been studied and allows to keep the electron beam for a longer time
 5509 within the proton bunch, thus optimizing the luminosity. The modification of the electron
 5510 beta function (β^*) leads to more freedom and gives access, among all the possibilities, to two
 5511 different optima regarding the luminosity and the mismatch from the design optics. The results
 5512 are summarized in the contour plots Fig.8.10.

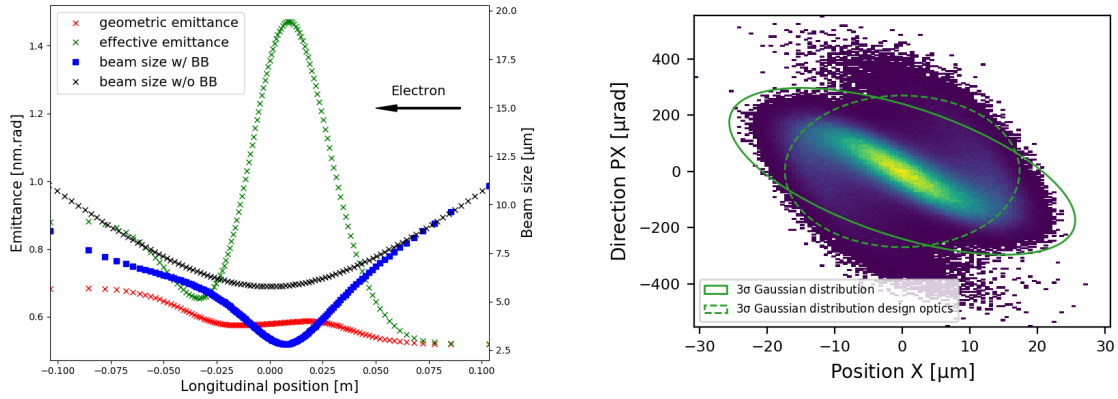


Figure 8.9: Left: Electron beam sizes with (blue) and without (black) the beam-beam forces exerted on the electron beam. The geometric emittance is represented in red and the effective emittance that takes into account the mismatch from the original optics is illustrated in green. Right: The horizontal phase space of the spent electron distribution backtracked to the interaction point. 3σ Gaussian distributions are highlighted for the post-collided distribution (solid line) and the design optics (dashed line).

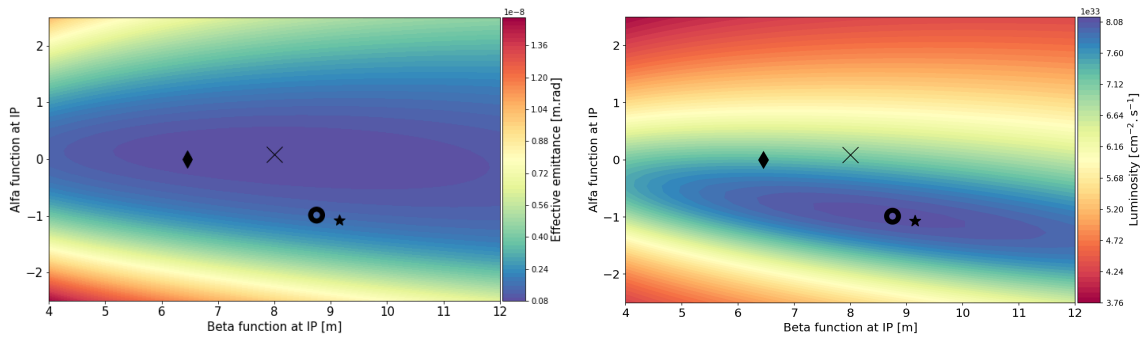


Figure 8.10: Left : Contour plot describing the effective emittance post collision as a function of the alfa and beta functions at IP. Right : Contour plot describing the luminosity as a function of the alfa and beta functions at IP. The diamond marker represents the initial Twiss parameters, the circle shows the luminosity optimum, the cross symbolizes the smallest mismatch from the original optics and the star illustrates the minimal geometric emittance growth.

5513 As a consequence, the Twiss parameters at the interaction point can be set in a way, to minimize
 5514 the mismatch of the optics (i.e. the effective emittance) or to maximize the luminosity. In case
 5515 the optimization of the luminosity is chosen (see the circle marker Fig. 8.10), a modified capture
 5516 optics in the beam transfer to the arc structure will be needed to re-match the modified Twiss
 5517 functions perturbed by the non-linear beam beam effects.

5518 The effect of possible offsets between the two colliding beams has been characterized in previous
 5519 beam-beam studies [675], and – if uncorrected – might lead to an electron beam emittance
 5520 growth. The parameters for these studies have been updated and the results are presented in
 5521 Fig. 8.11. As any offset between the two beams is amplified, it results in a larger increase of the
 5522 beam envelope. As a solution, a fast feed-forward system is proposed, across the Arc 6 which
 5523 would aim at damping the transverse motion so that the beam emittance can be recovered.
 5524 Using two sets of kickers placed at the center and at the end of the arc, an offset of 0.16σ can be
 5525 damped. A single set cutting across the whole arc can correct a 1σ offset with approximately
 5526 4.4 kV.

5527 Additionally, the coupling of the beam-beam effect with long range wakefields has been ad-

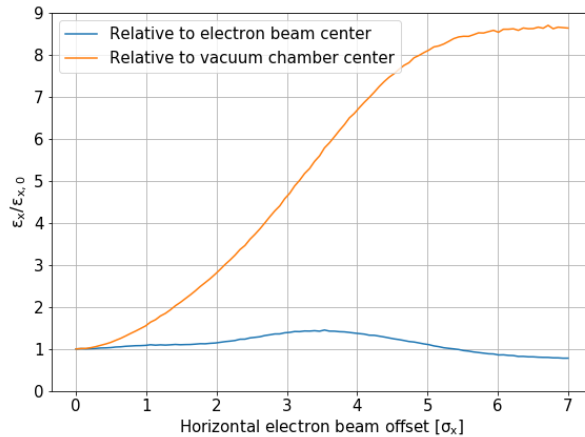


Figure 8.11: Electron beam emittance relative change with respect to its centroid (blue) and with respect to the vacuum chamber center (orange).

5528 dressed [675]. Assuming a misaligned bunch injected among a train of nominal bunches, the
 5529 coupling of the beam-beam effect with the wakefields leads to a reduction of the damping of
 5530 the excitation created by the misaligned bunch. Nevertheless it can be shown that the beam
 5531 stability is conserved and the total amplification remains acceptable with respect to the study
 5532 that was not considering the coupling.

5533 8.4.2 Effect on the proton

5534 The beam-beam interaction between the electron and proton beams is asymmetric in terms of
 5535 beam rigidities. Although the lower energetic 49.19 GeV electron beam is heavily distorted by
 5536 the strong 7 TeV proton beam, the proton beam will suffer from an emittance growth adding up
 5537 over turn by turn [675] due to the build up of the tiny disruption created by the offset between
 5538 the beams. In fact, the previous studies gave a growth rate of around 0.01 %/s for a jitter of
 5539 20 % σ_x . As long as an adequate control of the bunches is preserved, this effect should lie
 5540 in the shadow of other effects leading to emittance blow-up in the LHC (e.g. IBS). Since the
 5541 electron beam energy decreased from 60 GeV to 49.19 GeV this study needs to be updated and
 5542 the results should remain in agreement with the previous statement.

5543 8.5 Arc Magnets

5544 In this section, a conceptual design of the main magnets needed for the Linac-Ring (LR) accel-
 5545 erator at 50 GeV is described. The number and types of magnets is listed in Tabs. 8.6 and 8.7.

5546 8.5.1 Dipole magnets

5547 The bending magnets are used in the arcs of the recirculator. Each of the six arcs needs 352
 5548 horizontal bending dipoles. Additional dipoles are needed in the straight sections: 36 vertical
 5549 bending dipoles in the spreader/recombiner and 72 horizontal bending dipoles for the “dogleg”.
 5550 These magnets are not considered at the moment.

5551 In the CDR issued in 2012 for a LR at 60 GeV, a design based on three independent dipoles
 5552 stacked on top of each other was proposed. A post CDR design with three apertures dipoles was
 5553 introduced in 2014 [676]. This solution allows reducing the Ampere-turns and the production
 5554 cost of the dipoles. For a LR at 50 GeV, the three apertures dipole design is adapted to fulfil
 5555 new magnetic field requirements.

5556 The 352 horizontal bending dipoles needed for each arc, combined in three apertures dipoles re-
 5557 sult in a total of 704 units. These magnets are 3 m long and provide a field in the 30 mm aperture
 5558 ranging from 0.087 T to 0.522 T depending on the arc energy, from 8.62 GeV to 49.19 GeV.

Parameter	Unit	Value
Beam energy	GeV	8.62 to 49.19
Magnetic field	T	0.087 to 0.522
Magnetic length	m	3
Vertical aperture	mm	30
Pole width	mm	90
Number of apertures		3
Distance between apertures	mm	500
Mass	8000	kg
Number of magnets		704
Current	A	4250
Number of turns per magnet		4
Current density	A/mm ²	1
Conductor material		aluminum
Magnet resistance	mΩ	0.17
Power	kW	3
Total power consumption six arcs	MW	2.1
Cooling		air

Table 8.10: 50 GeV ERL – Main parameters of the three apertures bending magnets.

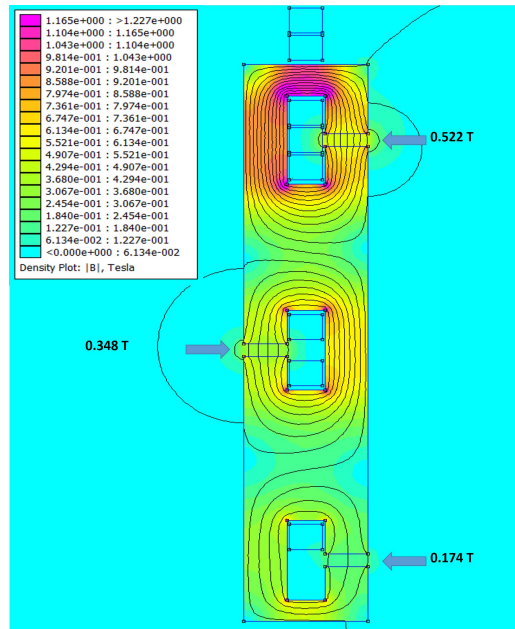


Figure 8.12: 50 GeV ERL - Cross section of the three apertures bending magnet, arc 2, 4 and 6 with 500 mm between each arcs - FEM.

5559 In the proposed design, the three apertures are stacked vertically but offset transversely. This
 5560 allows recycling the Ampere-turns from one aperture to the other. The coils are centrally located
 5561 on the yoke and are made of simple aluminium bus-bars all powered in series. A current density
 5562 of 1 A/mm^2 in the coils is sufficiently low to not have water-cooling but in order to limit the
 5563 temperature in the tunnel it may be required. Trim coils can be added on two of the apertures
 5564 to provide some tuning. Alternatively, each stage could be powered separately. The dipole yokes
 5565 are made of low carbon steel plates. The relevant parameters are summarised in Tab. 8.10 and
 5566 the cross section is illustrated in Fig. 8.12 for 500 mm between each arcs.

5567 8.5.2 Quadrupole magnets

5568 Quadrupoles for recirculator arcs

5569 In total 1518 quadrupoles are needed for the recirculator arcs: 255 for each of the arcs one to four
 5570 and 249 for each of the arcs five and six. The required integrated gradients, comprised between
 5571 9.25 T and 40.75 T, can be achieved using one type of quadrupole of one meter long. However,
 5572 instead of operating the magnets at low current for lower arcs energy, it can be considered to
 5573 have a shorter model of 0.6 meter long for arcs one to three. These quadrupoles require water-
 5574 cooling for the coils. The relevant parameters are summarised in Tab. 8.11 and the cross section
 5575 is illustrated in Fig. 8.13 (left).

5576 Also for quadrupoles, in order to reduce the power consumption, it could be envisaged to use
 5577 a hybrid configuration, with most of the excitation given by permanent magnets. The gradient
 5578 strength could be varied by trim coils or by mechanical methods.

Parameter	Unit	Value
Beam energy	GeV	8.62 to 49.19
Field gradient	T/m	9.25 to 40.75
Magnetic length	m	1
Aperture radius	mm	25
Mass	kg	550
Number of magnets		1518
Current at 40.75 T/m	A	560
Number of turns per pole		17
Current density at 40.75 T/m	A/mm ²	6.7
Conductor material		copper
Magnet resistance	mΩ	33
Power at 8.62 GeV	kW	0.5
Power at 16.73 GeV	kW	1.9
Power at 24.85 GeV	kW	3.7
Power at 32.96 GeV	kW	4.6
Power at 41.08 GeV	kW	7.2
Power at 49.19 GeV	kW	10.3
Total power consumption six arcs	MW	7.1
Cooling		water

Table 8.11: 50 GeV ERL – Main parameters of the arc quadrupoles.

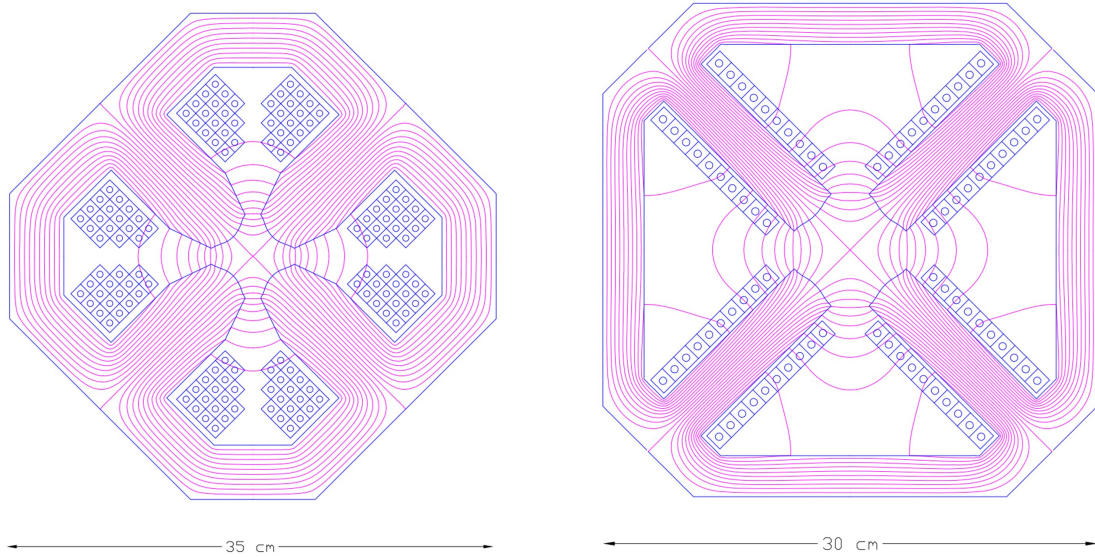


Figure 8.13: 50 GeV ERL. Left: Cross section of the arc quadrupole magnets. Right: Cross section of the linac quadrupole magnets.

5579 **Quadrupoles for the two 8.1 GeV linacs**

5580 In the two 8.1 GeV linacs, 29 + 29 quadrupoles each providing 1.93 T integrated strength are
 5581 required. The present design solution considers 30 mm aperture radius magnets. The relevant
 5582 parameters are summarised in Tab. 8.12 and the cross section is illustrated in Fig. 8.13 (right).

Parameter	Unit	Value
Beam energy	GeV	8.62 to 49.19
Field gradient	T/m	7.7
Magnetic length	m	0.25
Aperture radius	mm	30
Mass	kg	110
Number of magnets		56
Current at 7.7 T/m	A	285
Number of turns per pole		10
Current density at 7.7 T/m	A/mm ²	3
Conductor material		copper
Magnet resistance	mΩ	6
Power at 8.1 GeV	kW	0.5
Total power consumption 2 linacs	MW	0.03
Cooling		water

Table 8.12: 50 GeV ERL – Main parameters of the linac quadrupoles.

5583 **8.6 LINAC and SRF**

5584 Each of the two main linacs has an overall length of 828.8 m and provides an acceleration of
 5585 8.114 GV. Each linac consists of 112 cryomodules, arranged in 28 units of 4 cryomodules with
 5586 their focussing elements – each cryomodule contains four 5-cell cavities, optimised to operate

5587 with large beam current (up to 120 mA at the HOM frequencies). The operating temperature
 5588 is 2 K; the cavities are based on modern SRF technology and are fabricated from bulk Nb
 5589 sheets; they are described in detail in section 8.6.2 below. The nominal acceleration gradient is
 5590 19.73 MV/m.

5591 In addition to the main linacs, the synchrotron losses in the arcs will make additional linacs
 5592 necessary, referred to here as the *loss compensation linacs*. These will have to provide different
 5593 accelerations in the different arcs, depending on the energy of the beams as shown in Tab. 8.13.
 5594 The quoted beam energies are at entry into the arc. Their natural placement would be at the
 5595 end of the arcs just before the combiner, where the different energy beams are still separate. The
 5596 largest of these linacs would have to compensate the SR losses at the highest energy, requiring a
 5597 total acceleration of about 700 MV. The loss compensation linacs will be detailed in section 8.6.5
 below.

Section	Beam energy [GeV]	ΔE [MeV]
Arc 1	8.62	3
Arc 2	16.73	25
Arc 3	24.85	80
Arc 4	32.96	229
Arc 5	41.08	383
Arc 6	49.19	836

Table 8.13: Synchrotron radiation losses for the different arc energies

5598

5599 Through all arcs but Arc 6, the beam passes twice, once while accelerated and once while decel-
 5600 erated. It is planned to operate these additional *loss compensation linacs* at 1603.2 MHz, which
 5601 allows energy compensation of both the accelerated and the decelerated beam simultaneously.
 5602 This subject will be discussed in detail in a subsequent section 8.6.5.

5603 8.6.1 Choice of Frequency

5604 The RF frequency choice primarily takes into account the constraints of the LHC bunch repeti-
 5605 tion frequency, f_0 , of 40.079 MHz, while allowing for a sufficiently high harmonic, h , for a flexible
 5606 system. For an ERL with $n_{pass} = 3$ recirculating passes and in order to enable equal bunch
 5607 spacing for the 3 bunches – though not mandatory – it was originally considered to suppress all
 5608 harmonics that are not a multiple of $n_{pass} \cdot f_0 = 120.237$ MHz. Initial choices for instance were
 5609 721.42 MHz ($h = 18$) and 1322.61 MHz ($h = 33$) in consideration of the proximity to the frequen-
 5610 cies used for state-of-the-art SRF system developments worldwide [677]. In synergy with other
 5611 RF system developments at CERN though, the final choice was 801.58 MHz ($h = 20$), where
 5612 the bunching between the 3 recirculating bunches can be made similar but not exactly equal.
 5613 Note that this frequency is also very close to the 805 MHz SRF proton cavities operating at the
 5614 Spallation Neutron Source (SNS) at ORNL, so that one could leverage from the experience in
 5615 regard to cryomodule and component design at this frequency.

5616 Furthermore, in the frame of an independent study for a 1 GeV CW proton linac, a capital
 5617 plus operational cost optimisation was conducted [678]. This optimisation took into account
 5618 the expenditures for cavities, cryomodules, the linac tunnel as well as the helium refrigerator
 5619 expenses as a function of frequency and thus component sizes. Labor costs were included based
 5620 on the existing SNS linac facility work breakdown structure. It was shown that capital plus
 5621 operating costs could be minimised with a cavity frequency between 800 MHz and 850 MHz,

5622 depending also on the choice of the operating He bath temperature (1.8 K to 2.1 K). Clear benefit
5623 of operating in this frequency regime are the comparably small dynamic RF losses per installation
5624 length due to a relatively small BCS surface resistance as well as low residual resistance of
5625 the niobium at the operating temperature. This could be principally verified as part of the
5626 prototyping effort detailed in the next sub-section. Note that the cost optimum also favors
5627 cavities operating at rather moderate field levels (< 20 MV/m). This comes as a benefit in
5628 concern of field emission and associated potential performance degradations.

5629 8.6.2 Cavity Prototype

5630 Given the RF frequency of 801.58 MHz, JLab has collaborated with CERN, and consequently
5631 proposed a five-cell cavity design that was accepted for prototyping, see Fig. 8.14. The cavity
shape has also been adopted for PERLE. Tab. 8.14 summarises the relevant cavity parameters.

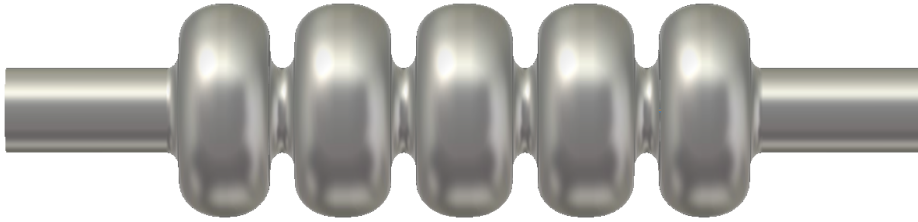


Figure 8.14: Bare 802 MHz five-cell cavity design (RF vacuum) with a 130 mm iris and beam tube aperture.

5632

Parameter	Unit	Value
Frequency	MHz	801.58
Number of cells		5
active length l_{act}	mm	917.9
loss factor	V pC ⁻¹	2.742
R/Q (linac convention)	Ω	523.9
$R/Q \cdot G$ per cell	Ω^2	28788
Cavity equator diameter	mm	327.95
Cavity iris diameter	mm	130
Beam tube inner diameter	mm	130
diameter ratio equator/iris		2.52
E_{peak}/E_{acc}		2.26
B_{peak}/E_{acc}	mT/(MV/m)	4.2
cell-to-cell coupling factor k_{cc}	%	3.21
TE ₁₁ cutoff frequency	GHz	1.35
TM ₀₁ cutoff frequency	GHz	1.77

Table 8.14: Parameter table of the 802 MHz prototype five-cell cavity.

5633 The cavity exhibits a rather large iris and beam tube aperture (130 mm) to consider beam-
5634 dynamical aspects such as HOM-driven multi-bunch instabilities. Despite the comparably large
5635 aperture, the ratio of the peak surface electric field, E_{pk} , respectively the peak surface magnetic
5636 field, B_{pk} , and the accelerating field, E_{acc} , are reasonably low, while the factor $R/Q \cdot G$ is
5637 kept reasonably high, concurrently to limit cryogenic losses. This is considered as a generically
5638 well *balanced* cavity design [679]. The cavity cell shape also avoids that crucial HOMs will

5639 coincide with the main spectral lines (multiples of 801.58 MHz), while the specific HOM coupler
 5640 development is pending.

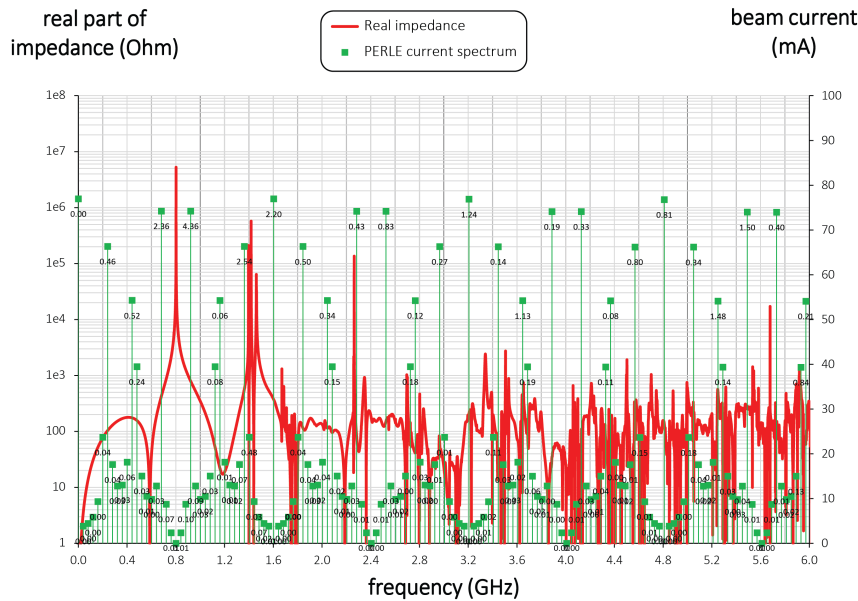


Figure 8.15: Real monopole impedance spectrum of the five-cell 802 MHz cavity prototype (red) together with the considered beam current lines (green) for the 3-pass PERLE machine (25 mA injected current). The numbers associated with the spectral lines denote the power dissipation (in Watt).

5641 Furthermore, as shown in Fig. 8.15 for the case of the bunch recombination pattern considered for
 5642 PERLE originally, the much denser intermediate beam current lines (green) are not coinciding
 5643 with cavity HOMs. Here the figure plots the real part of the beam-excited cavity monopole
 5644 impedance spectrum up to 6 GHz, and denotes the power deposited at each spectral line (in
 5645 Watt) for an injected beam current of 25 mA. For instance, the summation of the power in
 5646 this spectral range results in a moderate 30 Watts. This covers the monopole modes with the
 5647 highest impedances residing below the beam tube cutoff frequency. The HOM-induced heat has
 5648 to be extracted from the cavity and shared among the HOM couplers attached to the cavity
 5649 beam tubes. The fraction of the power escaping through the beam tubes above cutoff can be
 5650 intercepted by beam line absorbers.

5651 Note that for Fig. 8.15 a single HOM-coupler end-group consisting of three scaled TESLA-
 5652 type coaxial couplers was assumed to provide damping. Instead of coaxial couplers, waveguide
 5653 couplers could be utilized, which for instance have been developed at JLab in the past for high
 5654 current machines. These are naturally broadband and designed for high power capability, though
 5655 some penalty is introduced as this will increase the complexity of the cryomodule. Ultimately,
 5656 the aim is to efficiently damp the most parasitic longitudinal and transverse modes (each polar-
 5657 ization). The evaluation of the total power deposition is important for LHeC to decide which
 5658 HOM coupler technology is most appropriate to cope with the dissipated heat and whether
 5659 active cooling of the couplers is a requirement.

5660 Though the prototype efforts focused on the five-cell cavity development, JLab also produced
 5661 single-cell cavities, i.e. one further Nb cavity and two OFE copper cavities. The former has been
 5662 shipped to FNAL for N-doping/infusion studies, whereas the latter were delivered to CERN for
 5663 Nb thin-film coating as a possible alternative to bulk Nb cavities. In addition, a copper cavity
 5664 was built for low power bench measurements, for which multiple half-cells can be mechanically
 5665 clamped together. Presently, a mock-up can be created with up to two full cells. This cavity

5666 has been produced in support of the pending HOM coupler development. The ensemble of
 5667 manufactured cavities resonating at 802 MHz is shown in Fig. 8.16.

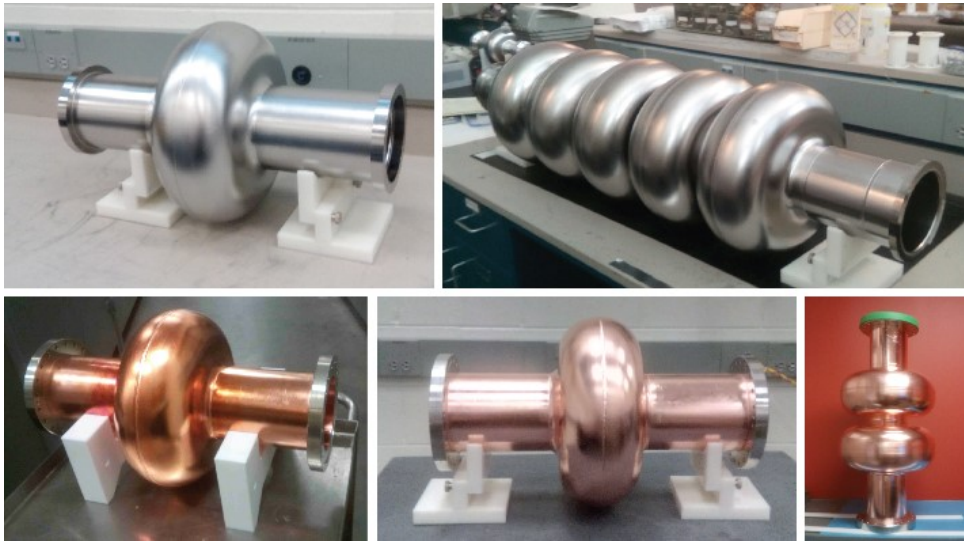


Figure 8.16: Ensemble of 802 MHz cavities designed and built at JLab for CERN. The Nb cavities have been tested vertically at 2 Kelvin in JLab’s vertical test area.

5668 Results for the Nb cavities - made from fine grain high-RRR Nb - were encouraging since both
 5669 cavities reached accelerating fields, E_{acc} , slightly above 30 MV/m ultimately limited by thermal
 5670 breakdown (quench). Moreover, the RF losses were rather small as a benefit of the relatively
 5671 low RF frequency as anticipated. The residual resistance extracted from the measurement data
 5672 upon cooldown of the cavity was $3.2 \Omega \pm 0.8 \Omega$. This resulted in unloaded quality factors,
 5673 Q_0 , well above 4×10^{10} at 2 K at low field levels, while Q_0 -values beyond 3×10^{10} could be
 5674 maintained for the five-cell cavity up to ~ 27 MV/m (see Fig. 8.17). Only standard interior
 5675 surface post-processing methods were applied including bulk buffered chemical polishing, high
 5676 temperature vacuum annealing, light electropolishing, ultrapure high-pressure water rinsing,
 5677 and a low temperature bake-out. While the vertical test results indicate generous headroom for
 5678 a potential performance reduction once a cavity is equipped with all the ancillary components
 5679 and installed in a cryomodule, clean cavity assembly procedure protocols must be established
 5680 for the cryomodules to minimise the chance of introducing field-emitting particulates.

5681 8.6.3 Cavity-Cryomodule

5682 The ERL cryomodules hosting the superconducting RF cavities are a key component of the
 5683 accelerator. They should provide the proper mechanical, vacuum and cryogenic environment
 5684 to the SRF cavities equipped with their ancillaries systems: helium tank, power coupler and
 5685 high order mode couplers. Each cryomodule is containing 4 superconducting 801.58 MHz 5-cells
 5686 elliptical cavities described in the previous chapters.

5687 Recently, several projects worldwide have designed cryomodules for elliptical cavities with a
 5688 cavity configuration (number, length and diameter) quite close to the one required by LHeC
 5689 ERL:

- 5690 • SNS [680]: two different sized cryomodules host either 4 elliptical 6-cells 805 MHz cavities
 5691 of $\beta = 0.81$ or 4 elliptical 6-cells 805 MHz of $\beta = 0.61$

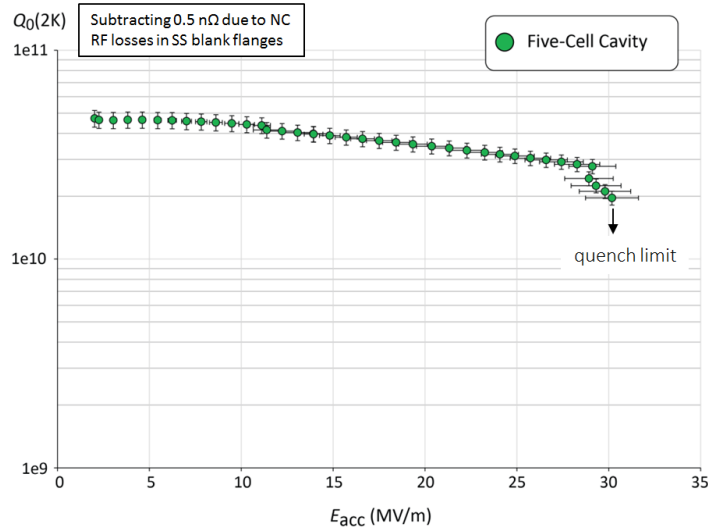


Figure 8.17: Vertical test result of the five-cell 802 MHz niobium cavity prototype.

- 5692 • SPL [681]: the cryomodule is designed to integrate 4 elliptical 5-cells 704 MHz cavities of
5693 $\beta = 1$
- 5694 • ESS [682]: two cryomodules of the same length can host either 4 elliptical 6-cells 704 MHz
5695 cavities of $\beta = 0.67$ or 4 elliptical 5-cells 704 MHz cavities of $\beta = 0.85$.

5696 These three cryomodule designs are based on two completely different concepts for the cavity
5697 string support structure. SNS and ESS cryomodules are based on an intermediate support
5698 system, called the spaceframe, which is horizontally translated inside the cryomodule vacuum
5699 vessel. The low pressure cryogenic line is located above the cavities string and connected to the
5700 cryogenic transfer line by a double angled connection, the jumper. RF waveguides are connected
5701 underneath the cryomodule, using door-knob transition to the couplers. All the hanging and
5702 alignment operations of the cavities string and shielding are implemented outside the vacuum
5703 tank, using the spaceframe. In the ESS case, each cavity is hung by 2 sets of 4 cross rods. The
5704 thermal shield is also hung to these rods by the mean of an aluminium “elastic boxes” that
5705 allow the thermal shrinkage while maintaining the transverse stability. The thermal shield is
5706 made of 2.5mm thick aluminium and wrapped with multi-layer insulation. It is fastened directly
5707 to the support rods of the cavities string.

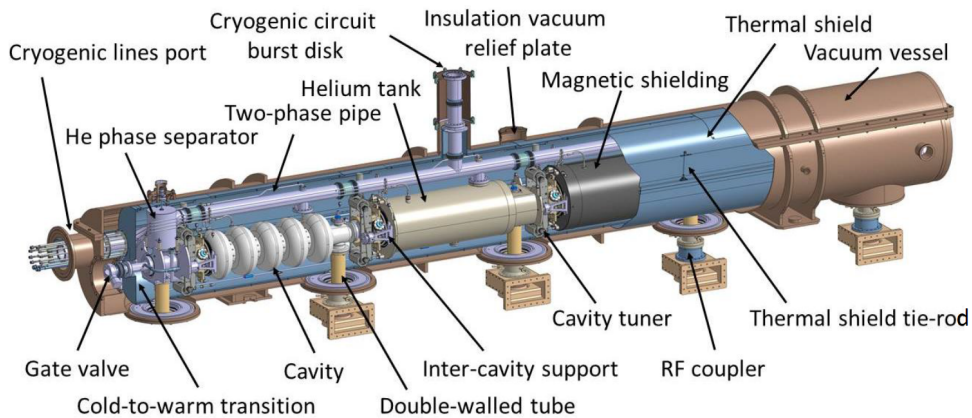


Figure 8.18: SPL cryomodule general assembly view

5708 In the SPL cryomodule, the cavity string is directly supported by the power coupler and with
 5709 dedicated inter-cavity support features. Moreover, the SPL cryomodule integrates a full length
 5710 demountable top lid, enabling the cavity string assembly from the cryomodule top (Fig. 8.18).
 5711 The thermal shield is made of rolled aluminium sheets, and is composed of four main parts
 5712 assembled before the vertical insertion of the string of cavities. The shield, wrapped with multi-
 5713 layer insulation, is suspended to the vacuum vessel via adjustable tie rods in titanium alloy which
 5714 also cope, by angular movements, with its thermal contractions. The cavity stainless steel helium
 5715 tanks are connected by a 100-mm-diameter two-phase pipe placed above the cavities. This pipe
 5716 ensures liquid feeding to the cavities by gravity, and is also used as a pumping line for gaseous
 5717 helium.

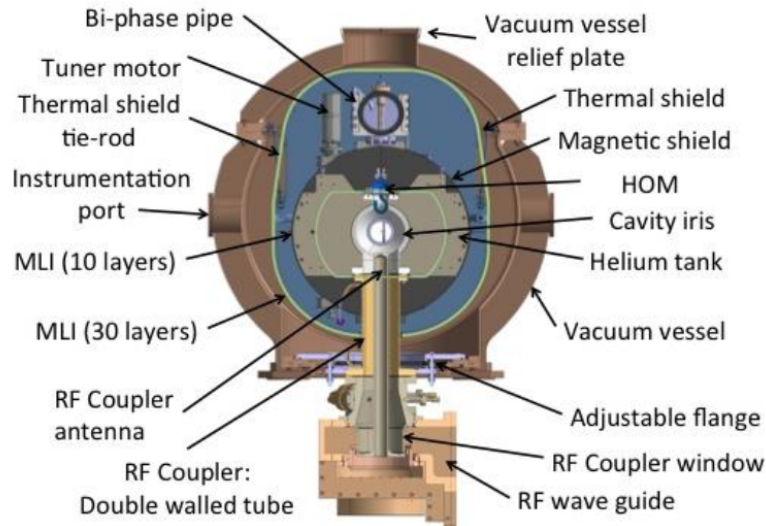


Figure 8.19: Cross-view of the SPL cryomodule

5718 With the aim of minimizing static heat loads from room temperature to 2 K by solid thermal
 5719 conduction, the number of mechanical elements between the two extreme temperatures is re-
 5720 duced to the strict minimum: the cavities are supported directly via the external conductor of
 5721 the RF coupler (Fig. 8.19), the double-walled tube (DWT). The latter is made out of a stainless
 5722 steel tube with an internal diameter of 100 mm, which is actively cooled by gaseous helium
 5723 circulating inside a double-walled envelope in order to improve its thermal efficiency.

5724 An additional supporting point to keep cavity straightness and alignment stability within re-
 5725 quirements is obtained by supporting each cavity on the adjacent one via the inter-cavity support,
 5726 which is composed of a stem sliding inside a spherical bearing. As a result, a pure vertical sup-
 5727 porting force is exchanged by adjacent cavities whereas all other degrees of freedom remain unre-
 5728 strained allowing thermal contraction movements to occur unhindered. The thermo-mechanical
 5729 behaviour of this supporting system has been extensively studied on a dedicated test bench at
 5730 CERN, proving its efficiency and reliability.

5731 There are some specific additional constraints or requirements for a cryomodule to be use in an
 5732 ERL, and some of them are quite challenging, The first set of constraints is linked to the CW op-
 5733 eration of the cryomodules (contrary to SNS, SPL and ESS which are pulsed accelerators), where
 5734 dynamic heat loads are much larger than the static ones. Thus, reaching high Q_0 (low cryogenic
 5735 losses) is a main objective in these machines and beside specific optimization on cavity design
 5736 and preparation (such as N-doping), magnetic shielding should be carefully studied: material,
 5737 operating temperature, numbers of layers, active and/or passive shielding. Another important

5738 constraint is linked to relative high power to be extracted by the High Order Mode (HOM)
5739 couplers: thermal analysis should be carefully performed to have an optimized evacuation of the
5740 HOM thermal load not to degrade the cryogenic performances of the cryomodule.

5741 We recently decided to push further away the analysis to use the SPL cryomodule for the LHeC
5742 ERL, thanks to its geometrical compatibility with the LHeC ERL superconducting cavities,
5743 but also because it fits quite well the overall ERL requirements. One of the clear advantages
5744 of the SPL configuration is a much simplified assembly procedure (Fig. 8.20), with its top-lid
configuration which also allows an easier maintenance.

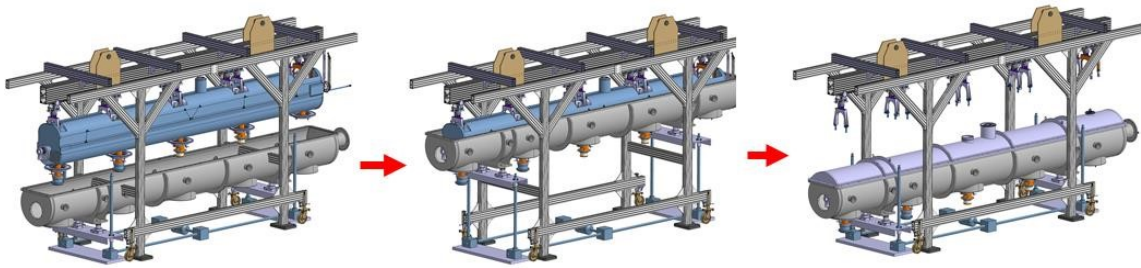


Figure 8.20: Cryomodule assembly procedure main steps

5745

5746 The first study performed was to analyse the possibility to integrate the ERL cavities instead
5747 of the SPL ones. The 802 MHz cavities are a little bit shorter than the SPL ones and the cells
5748 are also smaller in diameter. The beam port internal diameter is about the same, as well as
5749 the power coupler port. As a result, the SPL cryomodule is well fitted to the ERL 802 MHz
5750 superconducting cavities from the geometrical point of view, and they could be easily integrated
5751 providing minor mechanical features adaptations.

5752 The second analysed point is the beam vacuum. As the SPL cryomodule existing design was
5753 done for a prototype, intended for RF and cryogenic test only, without beam, the vacuum valve
5754 is a VAT CF63 “vatterfly” valve with viton seal and manual actuator, which is not adapted for
5755 a real operating cryomodule. Integration of an all-metal gate valve instead is not an issue and
5756 we also designed a specific solution based on a two stages valves (Fig. 8.21) to adapt the already
5757 fabricated SPL prototype cryomodule in order to be able to integrate the 802 MHz cavities.

5758 The third study performed is the compatibility of the SPL cryogenic features with the ERL
5759 requirements. SPL was designed to operate 702 MHz cavities at 25 MV/m with a Q_0 of 5.109
5760 with a 8.2 % duty cycle. The LHeC ERL will operate SRF cavities in CW regime, but at a
5761 lower field (20 MV/m) and with a higher expected Q_0 at the nominal gradient (about 1.5 109).
5762 As a result, and despite the different duty cycle, the dynamic cryogenic losses are estimated
5763 to be only about 30% more in the ERL case. The overall cryogenic dimensioning is then fully
5764 compatible, providing some unavoidable adaptation of a few internal cryogenic piping. The
5765 main issue still to address is the need and consequences of the HOM coupler cooling. Even if
5766 the present engineering analysis showed that this point will not be a showstopper, it might have
5767 an impact on some cryogenic piping and cooling circuit.

5768 Detailed engineering studies are being pursued to transform the SPL cryomodule prototype into
5769 an ERL LHeC cryomodule prototype. We are taking benefit of all the design and fabrication
5770 work previously performed on the SPL, and also on the fact some parts, such as the thermal and
5771 magnetic shielding are not yet fabricated and could be exactly adapted to the ERL requirements.
5772 This will give the possibility to have an earlier full prototype cryomodule RF and cryogenic test as
5773 compared to a standard experimental plan where the complete study and fabrication is starting

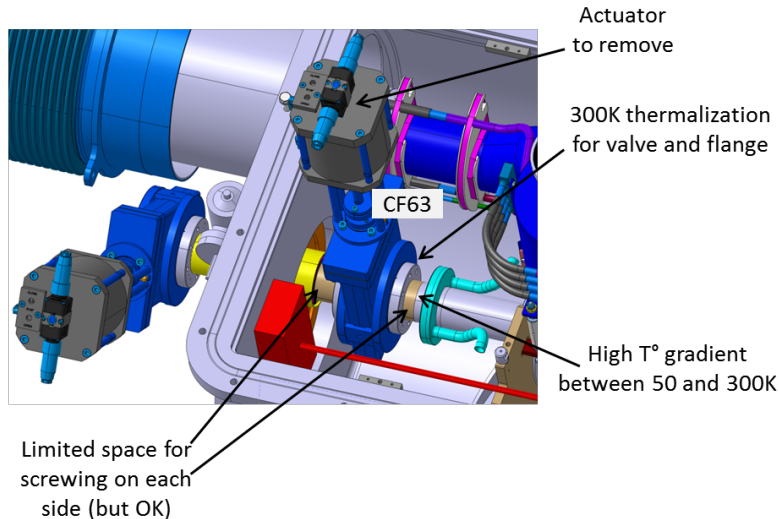


Figure 8.21: The two stages vacuum valve solution for adapting the SPL cryomodule prototype to the 802 MHz cavities of the LHeC ERL.

5774 from scratch.

5775 8.6.4 Electron sources and injectors

5776 Specification of electron sources

5777 Operation of the LHeC with an electron beam, delivered by a full energy ERL imposes specific
 5778 requirements on the electron source. It should deliver a beam with the charge and temporal
 5779 structure required at the Interaction Point. Additionally as during acceleration in a high energy
 5780 ERL both longitudinal and transverse emittances of the beam are increased due to Synchrotron
 5781 Radiation (SR), the 6D emittance of the beam delivered by electron source should be small
 5782 enough to mitigate this effect. The general specification of the electron source are shown in
 5783 Tab. 8.15. Some parameters in this table such as RMS bunch length, uncorrelated energy
 5784 spread and normalised transverse emittance are given on the basis of the requirements for the
 5785 acceleration in ERL and to pre-compensate the effects of SR. The most difficult of the parameters
 5786 to specify is injector energy. It should be as low as possible to reduce the unrecoverable power
 5787 used to accelerate the beam before injection into the ERL while still being high enough to deliver
 5788 short electron bunches with high peak current. Another constraint on the injection energy is
 5789 the average energy and energy spread of the returned beam. The average energy cannot be
 5790 less than the energy of electron source, but the maximum energy in the spectrum should not
 5791 exceed 10 MeV the neutron activation threshold. An injection energy of 7 MeV is a reasonable
 5792 compromise to meet this constraint.

5793 The required temporal structure of the beam and the stringent requirements for beam emittance
 5794 do not allow the use of conventional thermionic electron sources for the LHeC ERL without using
 5795 a bunching process involving beam losses. While this option cannot completely be excluded as a
 5796 source of unpolarised electrons. The additional requirement to deliver polarised beam can only
 5797 be met with photoemission based electron sources.

5798 There are now four possible designs of electron sources for delivering unpolarised beams and
 5799 (potentially) three for delivering polarised beams:

Parameter	Unit	Value
Booster energy	MeV	7*
Bunch repetition rate	MHz	40.1
Average beam current	mA	20
Bunch charge	pC	500
RMS bunch length	mm	3
Normalised transverse emittance	$\pi \cdot \text{mm} \cdot \text{mrad}$	<6
Uncorrelated energy spread	keV	10
Beam polarisation		Unpolarised/Polarised

Table 8.15: General specification of the LHeC ERL electron source.

- 5800 1. A thermionic electron source with RF modulated grid or gate electrode with following
5801 (multi)stage compression and acceleration. The electron source could be either a DC
5802 electron gun or an RF electron source in this case. Although these sources are widely
5803 used in the injectors of IR FELs [683] their emittance is not good enough to meet the
5804 specification of the LHeC injector. Moreover, thermionic sources cannot deliver polarised
5805 electrons.
- 5806 2. A VHF photoemission source. This is a type of normal conducting RF source which
5807 operates in the frequency range 160 MHz – 200 MHz. The relatively low frequency of these
5808 sources means that they are large enough that sufficient cooling should be provided to
5809 permit CW operation. This type of source has been developed for the new generation
5810 of CW FELs such as LCLS-II [684], SHINE [685] and a back-up option of the European
5811 XFEL upgrade [686], but they have not yet demonstrated the average current required
5812 for the LHeC injector. The possibility of generating polarised electrons with this type of
5813 source has not investigated yet.
- 5814 3. A superconducting RF photoemission source. This type of sources are under development
5815 for different applications such as CW FEL's (ELBE FEL [687], SRF option of LCLS-II
5816 injector [688], European XFEL upgrade [689]), as a basis of injectors for ERL's (bERLin-
5817 Pro [690]) and for electron cooling (BNL [691]). Though this type of sources has already
5818 demonstrated the possibility of delivering the average current, required for the LHeC with
5819 unpolarised beams (BNL), and has the potential for operation with GaAs type photocath-
5820 odes (HZDR) which are required for delivery of polarised beams, the current technology
5821 of SRF photoelectron source cannot be considered as mature enough for use in the LHeC.
- 5822 4. A DC photoemission source. In this type of source the electrons are accelerated imme-
5823 diately after emission by a potential difference between the source cathode and anode.
5824 This type of source is the most common for use in ERL injectors. It has been used in the
5825 projects which are already completed (JLAB [692], DL [693]), is being used for ongoing
5826 projects (KEK [694], Cornell/CBeta [695]) and is planned to be used in new projects such
5827 as the LHeC prototype PERLE [696]. The technology of DC photoelectron sources is
5828 well-developed and has demonstrated the average current and beam emittance required
5829 for the LHeC ERL (Cornell). Another advantage of the photoelectron source with DC
5830 acceleration is the possibility of operation with GaAs based photocathodes for delivering
5831 of polarised beam. Currently it's the only source, which can delivery of highly polarised
5832 electron beams with the current of several mA's which is already in the range of LHeC
5833 specifications (JLab [697]).

5834 Based on this analysis at CDR stage we consider the use of DC photoelectron source as a basic

5835 option, keeping in mind that in the course of the injector development other types of electron
5836 sources may be considered, especially for providing of unpolarised beam.

5837 The LHeC unpolarised injector

The injector layout follows the scheme depicted in Fig. 8.22. Its design will be similar to the

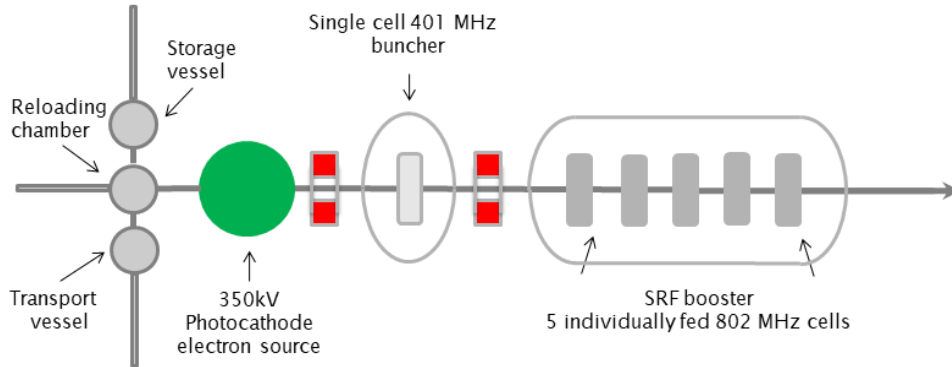


Figure 8.22: The layout of the unpolarised injector.

5838

5839 unpolarised variant of the PERLE injector [696]. The electron source with DC acceleration
5840 delivers a CW beam with the required bunch charge and temporal structure. Immediately
5841 after the source is a focusing and bunching section consisting of two solenoids with a normal
5842 conducting buncher placed between them. The solenoids have two purposes. Firstly to control
5843 the transverse size of the space charge dominated beam which will otherwise rapidly expand
5844 transversely. This ensures that the beam will fit through all of the apertures in the injector
5845 beamline. Secondly the solenoids are used for emittance compensation to counter the space
5846 charge induced growth in the projected emittance. This is then followed by a superconducting
5847 booster linac. This accelerates the beam up to its injection energy, provides further longitudinal
5848 bunch compression and continues the emittance compensation process.

5849 The DC electron source will have an accelerating voltage of 350 kV using a high quantum ef-
5850 ficiency antimonide based photocathode such as Cs₂K₂Sb. The photoinjector laser required for
5851 this cathode type will be a 532 nm green laser. There will be a load lock system to allow pho-
5852 tocathodes to be replaced without breaking the source vacuum. This significantly reduces the
5853 down time required for each replacement which is a major advantage in a user facility such as the
5854 LHeC where maximising uptime is very important. The cathode electrode will be mounted from
5855 above similar to the Cornell [698] and KEK [699] sources. This electrode geometry makes the
5856 addition of a photocathode exchange mechanism much easier as photocathode can be exchanged
5857 through the back of the cathode electrode. In addition the cathode electrode will be shaped to
5858 provide beam focusing. The operational voltage of 350 kV for the source was chosen as practical
5859 estimate of what is achievable. A higher voltage would produce better performance but would
5860 be challenging to achieve in practice. The highest operational voltage successfully achieved is
5861 500 kV by the DC electron source that is used for the cERL injector [700]. However 350 kV is
5862 sufficient to achieve the required beam quality [696].

5863 **Polarised electron source for ERL**

5864 Providing polarised electrons has always been challenging process, especially at relatively high
 5865 average current as required for the LHeC. The only practically usable production mechanism
 5866 of polarised electrons is the illumination of activated to Negative Electron Affinity (NEA) state
 5867 GaAs based photocathodes with circularly polarised laser light. The vacuum requirements for
 5868 these cathodes mean that this must be done in a DC electron source only. In the course of the
 5869 last 30 years significant progress has been achieved in improving the performance of polarised
 5870 electron sources. The maximum achievable polarisation has reached 90% and the maximum
 5871 Quantum Efficiency (QE) of the photocathode at the laser wavelength of maximum polarisation
 5872 has reached 6%. Meanwhile the implementation of a polarised electron source into the LHeC
 5873 remains a challenge as the practical operational charge lifetime of the GaAs based photocathode
 5874 does not exceed hundreds Coulombs (JLAB [701]) at an operational current in mA range.

In Fig. 8.23 a preliminary design of the LHeC polarised injector is shown. In general, the design

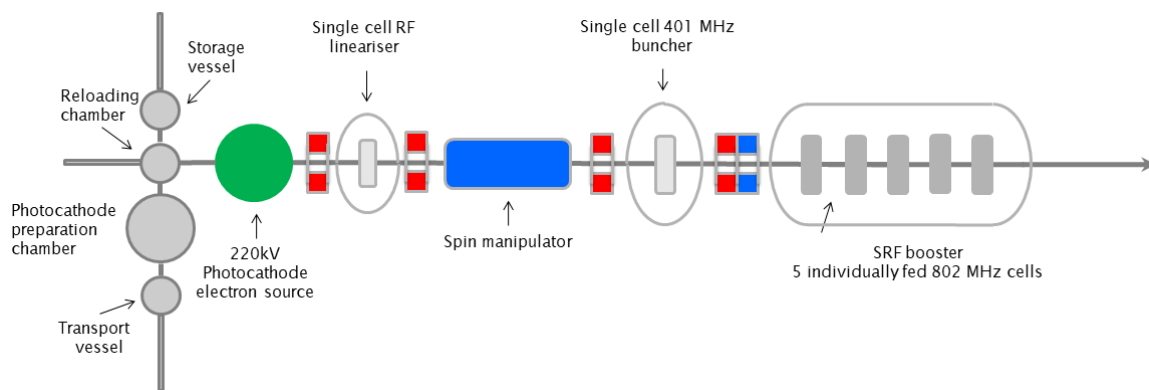


Figure 8.23: The layout of the polarised injector.

5875 of the polarised electrons injector is close to that of the unpolarised injector and is based on a
 5876 DC electron source where a photocathode is illuminated by a pulsed laser beam. The choice of a
 5877 DC source is dictated by the necessity of achieving extra high vacuum, with a pressure at a level
 5878 of 10^{-12} mbar, in the photocathode area. This level of vacuum is necessary for providing long
 5879 lifetime of the photocathode. In order to reduce photocathode degradation caused by electron
 5880 stimulated gas desorption accelerating voltage in the source is reduced to 220 kV. The main
 5881 differences with unpolarised injector are the presence of a photocathode preparation system,
 5882 permanently attached to the source, and a Wien filter based spin manipulator between the source
 5883 and the buncher. In order to reduce depolarisation of the beam in the spin manipulator, caused
 5884 by the space charge induced energy spread of the beam, an RF dechirper is installed between
 5885 the source and the spin manipulator. The injector is also equipped with a Mott polarimeter to
 5886 characterise the polarisation of the beam delivered by the source.
 5887

5888 An important consideration of the operation with interchangeable photocathodes is minimisation
 5889 of the down time required for the photocathode exchange. It typically takes few hours to replace
 5890 the photocathode and to characterise polarisation of the beam. For large facility like LHeC this
 5891 is unacceptable. A practical solution could be operation with 2 or more electron sources which
 5892 operate in rotation similar to the way which was proposed at BNL [702]. Another motivation
 5893 for using multi-source injector is the nonlinear dependence of photocathode charge lifetime on
 5894 average beam current (JLAB [697]), which reduces with increasing of the average current. For
 5895 example in case of 3 electron sources 2 of them can be operated with half operation frequency

5896 20.05 MHz in opposite phase delivering average current of 10 mA each, while the third is in stand
5897 by regime with freshly activated photocathode. The only time which is necessary to switch it
5898 on is the time required for rising the high voltage. Another advantage of using a multi-source
5899 scheme is the reduction of the average laser power deposited on the photocathode and as result
5900 relaxing requirements for the photocathode cooling. In order to implement the multi-source
5901 polarised electron injector, development of a deflection system which is able to merge the beams
5902 from different sources before the spin rotator is required.

5903 Lasers for electron sources

5904 In the proposed design of the LHeC injection system at least 2 lasers must be used. In the
5905 unpolarised electron injector, which is going to operate with antimionide-based photocathode,
5906 a laser with a wavelength of 532 nm is required. Typical initial QE of these photocathodes is
5907 10% and for practical application reduction of QE up to 1 % may be expected. For polarised
5908 electron source typical QE varies from 1 % down to 0.1 % and laser with a wavelength of 780 nm
5909 is required. The optimised parameters of the required lasers are summarised in Tab. 8.16. Laser
5910 temporal profile and spot size on the photocathode are given on the basis of source optimisation
for operation at 350 kV for unpolarised regime and 220 kV for polarised.

Laser beam parameter	Unit	Unpolarised mode	Polarised mode
Laser wavelength	nm	532	780
Laser pulse repetition rate	MHz	40.1	40.1
Energy in the single pulse at photocathode QE=1 %	μJ	0.12	
Average laser power at photocathode QE=1 %	W	4.7*	
Energy in the single pulse at photocathode QE=0.1 %	μJ		0.79
Average laser power at photocathode Qe=0.1 %	W		32*
Laser pulse duration	ps FWHM	118	80
Laser pulse rise time	ps	3.2	3.2
Laser pulse fall time	ps	3.2	3.2
Spot diameter on the photocathode surface	mm	6.4	8
Laser spot shape on the photocathode surface		Flat top	

Table 8.16: Parameters of the electron source drive laser.

5911

5912 8.6.5 Compensation of Synchrotron Radiation Losses

5913 Depending on energy, each arc exhibits fractional energy loss due to the synchrotron radiation,
5914 which scales as γ^4/ρ^2 (see Eq. (8.3)). Arc-by-arc energy loss was previously summarised in
5915 Tab. 8.13. That energy loss has to be replenished back to the beam, so that at the entrance
5916 of each arc the accelerating and decelerating beams have the same energy. Before or after each
5917 arc, a matching section adjusts the optics from and to the linac. Adjacent to these, additional
5918 cells are placed, hosting the RF compensating sections. The compensation makes use of a
5919 second harmonic RF at 1603.2 MHz to replenish the energy loss for both the accelerating and
5920 the decelerating beams, therefore allowing them to have the same energy at the entrance of each
5921 arc, as shown in Fig. 8.24.

5922 Parameters of the RF compensation cryomodules, shown in Tab. 8.17, have been extrapolated
5923 from the ILC cavity design, expecting that the higher frequency and lower gradient would

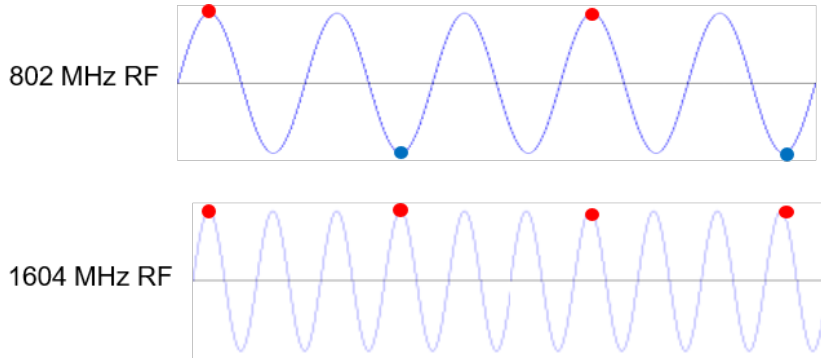


Figure 8.24: The second-harmonic RF restores the energy loss in both the accelerating and decelerating passes.

support continuous operation.

Parameter	Unit	Value
Frequency	MHz	1603.2
Gradient	MV/m	30
Design		Nine cells
Cells length	mm	841
Structure length	m	1
Cavity per cryomodule		6
Cryomodule length	m	6
Cryomodule voltage	MV	150

Table 8.17: A tentative list of parameter for the compensating rf cryomodules extrapolated from the ILC design.

5924

5925 The compensating cryo-modules are placed into Linac 1 side of the racetrack, before the bending
 5926 section of Arc 1, Arc 3, and Arc 5 and after the bending section of Arc 2, Arc 4, and Arc 6. This
 5927 saves space on Linac 2 side to better fit the interaction point (IP) line and the bypasses. Note
 5928 that with the current vertical separation of 0.5 m it will not be possible to stack the cryomodules
 5929 on top of each other; therefore, they will occupy 36 m on the Arc 4 and Arc 6 side and 18 m
 5930 on the Arc 3 and Arc 5 side of the racetrack. Each of the compensating cavities in Arc 5
 5931 needs to transfer up to 1 MW to the beam. Although a 1 MW continuous wave klystron are
 5932 available [703], the cryomodule integration and protection system will require a careful design.
 5933 Tab. 8.18 shows the energy loss for each arc and the corresponding synchrotron radiated power,
 5934 along with number of cryomodules at 1603.2 MHz RF frequency required to replenish the energy
 5935 loss.

5936 8.6.6 LINAC Configuration and Infrastructure

5937 Since the power supplied to the beam in the main linacs will be recovered, the average RF power
 5938 requirements at 802 MHz are relatively small and determined by the needs to handle transients
 5939 and microphonics.

5940 The RF power required for the second-harmonic RF system however is substantial – it can be
 5941 estimated from Tab. 8.13 with the nominal current of 20 mA.

5942 some text is missing here.

Section	ΔE [MeV]	P [MW]	Cryomodules
Arc 1	3	0.2	0
Arc 2	25	1.2	0
Arc 3	80	4.0	1
Arc 4	229	11.5	2
Arc 5	383	19.1	3
Arc 6	836	41.8	6

Table 8.18: Arc-by-arc synchrotron radiated power and number of 2-nd harmonic RF cryomodules required to compensate energy loss.

5943 8.7 Interaction Region

5944 ???

5945 8.7.1 Layout

5946 The basic principle of the Linac-Ring Interaction Region (IR) design remains unchanged and
5947 it is shown in Fig. 8.25: the two proton beams are brought onto intersecting orbits by strong
5948 separation and recombination dipoles. A collision of the proton beams at the Interaction Point
5949 (IP) is avoided via timing. The large crossing angle keeps the long range beam-beam effect
5950 small and separates the beams enough to allow septum quadrupoles to focus only the colliding
5951 beam (the anti-clockwise rotating LHC beam – Beam 2). The non-colliding beam (the clockwise
5952 rotating LHC beam – Beam 1) is unfocused and passes the septum quadrupoles in a field free
5953 aperture. The electron beam is brought in with an even larger angle, partly sharing the field free
5954 aperture of the septum quadrupoles with the non-colliding beam. A weak dipole in the detector
5955 region bends the electron beam into head-on collisions with the colliding proton beam. The two
5956 proton beams are also exposed to the dipole field but, due to the large beam rigidity, they are
5957 barely affected. After the interaction point a dipole with opposite polarity separates the orbits
5958 of the electron and proton beam.

5959 The high electron current (cf. Tab. 8.1) required to approach the goal peak luminosity of
5960 $10^{34} \text{cm}^{-2} \text{s}^{-1}$ poses a potential problem for the interaction region (IR) as it increases the al-
5961 ready high synchrotron radiation.

5962 The ERL parameters are not the only major change the new IR design has to account for.
5963 The first design of the quadrupole septa featured a separation of 68 mm for the two proton
5964 beams. However, this design focused strongly on providing a field free region for the non-
5965 colliding beam. Unfortunately, this led to a poor field quality for the strongly focused colliding
5966 beam. The first quadrupole Q1 was a half quadrupole design effectively acting as a combined
5967 function magnet with a dipole component of 4.45 T [704]. The sextupole field component was
5968 also prohibitively high. Consequently, a new design approach focusing on the field quality in the
5969 quadrupole aperture was necessary. The parameters relevant for the interaction region design
5970 are summarised in Tab. 8.19.

5971 It is noteworthy that the minimum separation of the two beams at the entrance of the first
5972 quadrupole Q1A increased from 68 mm to 106 mm requiring a stronger bending of the electron
5973 beam. This would increase the already high synchrotron radiation in the detector region even
5974 more. In order to compensate this increase, it was decided to increase L^* to 15 m, an approach
5975 that was shown to have a strong leverage on the emitted power [706].

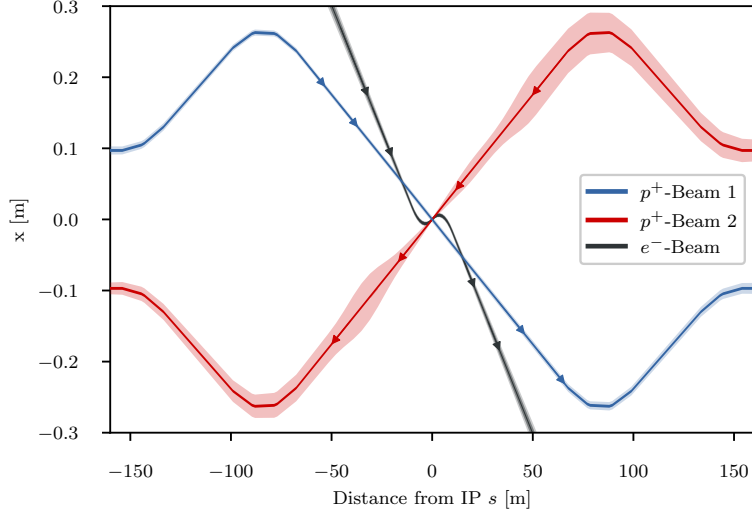


Figure 8.25: Geometry of the interaction region with 10σ envelopes. The electron beam is colliding with the focussed anti-clockwise rotating LHC beam (Beam 2) while the clockwise rotating LHC beam is unfocussed and passes the Interaction Region without interacting with the other two beams

Magnet	Gradient [T/m]	Length [m]	Free aperture radius [mm]
Q1A	252	3.5	20
Q1B	164	3.0	32
Q2 type	186	3.7	40
Q3 type	175	3.5	45

Table 8.19: Parameters of the final focus quadrupole septa. The parameters of Q1A/B and Q2 are compatible with the Nb₃Sn based designs from [705] assuming the inner protective layer of Q2 can be reduced to 5 mm thickness.

5976 The increased separation of the two proton beams, the longer L^* and the overall longer final
5977 focus triplet make longer and stronger separation and recombination dipoles necessary. The
5978 dipoles differ from the arc dipoles in that the magnetic field in both apertures has the same
5979 direction. Consequently the cross talk between both apertures is significant and the maximum
5980 reachable field is lower. The new geometry keeps the required field below 5.6 T. The required
5981 lengths and strength of these dipoles are listed in Tab. 8.20. It should be noted that the inter-
5982 beam distance is different for each of the five magnets per side, so each magnet will likely require
5983 an individual design. The design of the D1 dipoles is further complicated by the fact that an
5984 escape line for neutral collision debris traveling down the beam pipe will be necessary [1], as well
5985 as a small angle electron tagger. These issues have not been addressed so far, further studies
5986 will require detailed dipole designs.

Magnet	Field strength [T]	Interbeam distance [mm]	Length [m]	Number
D1	5.6	≥ 496 mm	9.45	6
D2	4.0	≥ 194 mm	9.45	4
IP Dipole	0.21	-	10	-

Table 8.20: Parameters of the separation and recombination dipoles. The respective interbeam distances are given for the magnet with the lowest value.

5987 The first design of the LHeC interaction region featured detector dipoles occupying almost the
 5988 entire drift space between the interaction point and first quadrupole. The approach was to have
 5989 the softest synchrotron radiation possible to minimise the power. However, since the purpose
 5990 of the dipoles is to create a spacial separation at the entrance of the first quadrupole, it is
 5991 possible to make use of a short drift between dipole and quadrupole to increase the separation
 5992 without increasing the synchrotron radiation power. A dipole length of $\frac{2}{3}L^*$ is the optimum in
 5993 terms of synchrotron radiation power [707]. Compared to the full length dipole it reduces the
 5994 power by 15.6 % at the cost of a 12.5 % higher critical energy. With an L^* of 15 m the optimum
 5995 length of the detector dipoles is 10 m. A magnetic field of 0.21 T is sufficient to separate the
 5996 electron and proton beams by 106 mm at the entrance of the first quadrupole. With these
 5997 dipoles and an electron beam current of 20 mA at 49.19 GeV the total synchrotron radiation
 5998 power is 38 kW with a critical energy of 283 keV to be compared with a power of 83 kW and a
 5999 critical energy of 513 keV for the electron beam energy of 60 GeV. More detailed studies on the
 6000 synchrotron radiation for different options and including a beam envelope for the electron beam
 6001 are summarised in Tab. 8.23 below.

6002 A schematic layout of the LHeC interaction region with the dipoles discussed above is shown in
 Fig. 8.26. The corresponding beam optics will be discussed in the following sections.

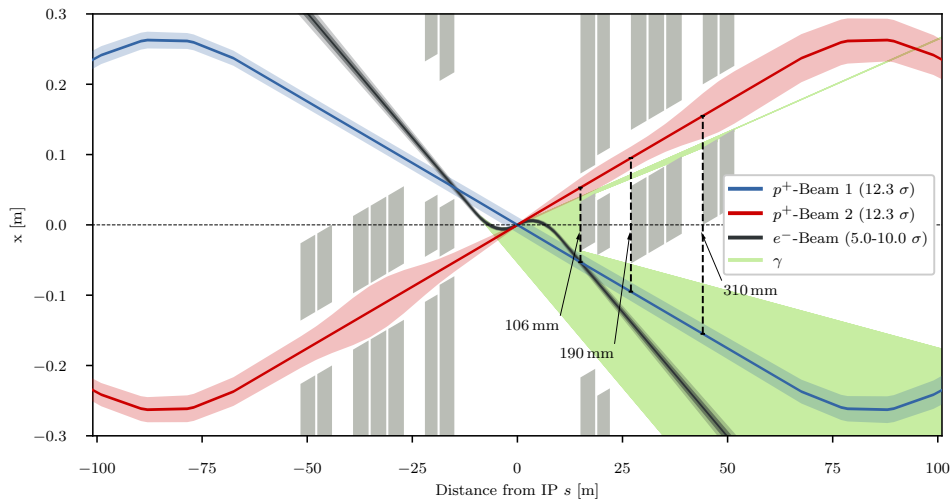


Figure 8.26: Schematic layout of the LHeC interaction region. The colliding proton beam and the electron beam are shown at collision energy while the non-colliding beam is shown at injection energy when its emittance is the largest.

6003

6004 8.7.2 Proton Optics

6005 As discussed above, the L^* was increased to 15 m in order to compensate the increased syn-
 6006 chrotron radiation due to the larger separation. The final focus system is a triplet consisting
 6007 of the quadrupoles Q1A and Q1B (see Tab. 8.19), three elements of the Q2 type and two of
 6008 the Q3 type. Between the elements a drift space of 0.5 m was left to account for the magnet
 6009 interconnects in a single cryostat. Between Q1 and Q2 as well as Q2 and Q3 a longer drift of
 6010 5 m is left for cold-warm transitions, Beam Position Monitors (BPMs) and vacuum equipment.
 6011 Behind Q3, but before the first element of the recombination dipole D1, another 16 m of drift
 6012 space are left to allow for the installation of non-linear correctors in case the need arises, as well

6013 as a local protection of the triplet magnets from asynchronous beam dumps caused by failures
 6014 of the beam dump kickers (MKD) as discussed below.

6015 As the recombination dipoles D1 and D2 for the LHeC interaction region require more space
 6016 than the current ALICE interaction region, the quadrupoles Q4 and Q5 had to be moved further
 6017 away from the IP. The position of Q6 is mostly unchanged but due to a need for more focusing
 6018 the length was increased by replacing it with two elements of the MQM magnet class of LHC.

6019 With the triplet quadrupole parameters provided in Tab. 8.19 we were able to match optics with
 6020 a minimum β^* of 10 cm. The corresponding optics are shown in Fig. 8.27 and feature maximum
 β functions in the triplet in the order of 20 km. With these large β functions, the free apertures

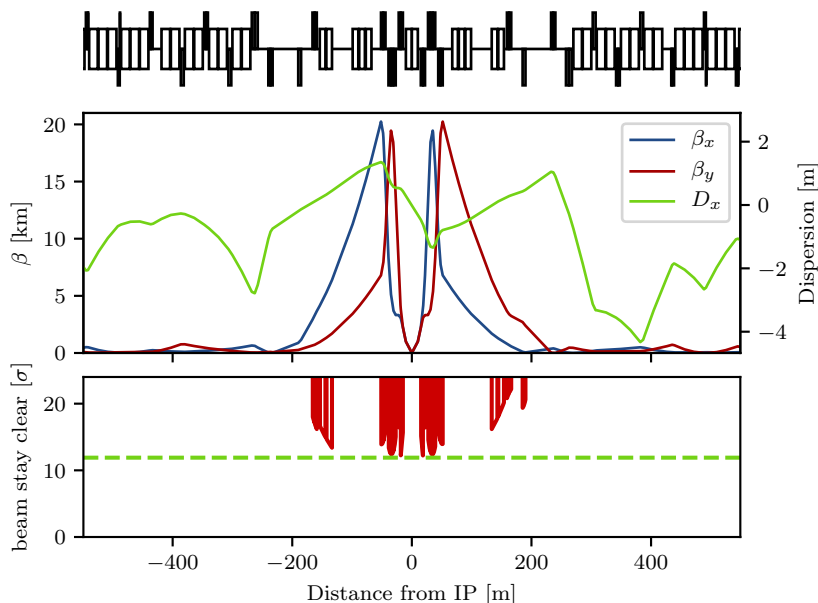


Figure 8.27: Optics (top) and beam stay clear (bottom) of the colliding beam with $\beta^* = 10$ cm.

6021 of the quadrupoles leave just enough space for a beam stay clear of 12.3σ , the specification of the
 6022 LHC. This is illustrated in Fig 8.27. However, since the LHeC is supposed to be incorporated
 6023 in the HL-LHC lattice, this minimum beam stay clear requires specific phase advances from
 6024 the MKD kicker to the protected aperture as detailed later. The large β functions not only
 6025 drive the aperture need in the final focus system, but also the required chromaticity correction
 6026 in the adjacent arcs. To increase the leverage of the arc sextupoles, the Achromatic Telescopic
 6027 Squeezing scheme (ATS) developed for HL-LHC [708] was extended to the arc upstream of IP2 for
 6028 the colliding beam (Beam 2) (see Fig. 8.28). This limited the optical flexibility in the matching
 6029 sections of IR2, specifically of the phase advances between arc and IP2. As a consequence, the
 6030 optical solution that has been found (Fig. 8.27) still has a residual dispersion of 15 cm at the IP
 6031 and the polarities of the quadrupoles Q4 and Q5 on the left side of the IP break up the usual
 6032 sequence of focusing and defocusing magnets. It needs to be studied whether this is compatible
 6033 with the injection optics. The latest optics designs can be found at the webpage [709].
 6034

6035 The free apertures given in Tab. 8.19 include a 10 mm thick shielding layer in Q1 and 5 mm in
 6036 Q2 and Q3. This is necessary to protect the superconducting coils from synchrotron radiation
 6037 entering the magnets as can be seen in Fig. 8.26. The absorber must also protect the magnets
 6038 from collision debris. Simulations of both synchrotron radiation and collision debris are yet to
 6039 be conducted in order to confirm the feasibility of this design.

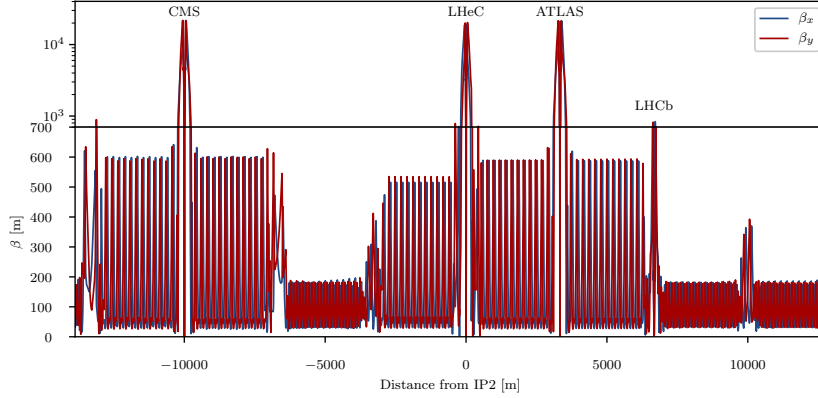


Figure 8.28: Optics of full ring of the colliding LHC proton beam (Beam 2).

6040 A separation between the two proton beams in time is currently foreseen, i.e. while the orbits
 6041 of the two proton beams do cross, the bunches do not pass through the IP at the same time.
 6042 This approach is complicated by the fact that the timing of the bunches in the other three
 6043 interaction points should not be affected. The easiest way to accomplish this is by shifting the
 6044 interaction point of LHeC by a quarter of a bunch separation, i.e. $6.25 \text{ ns} \times c \approx 1.87 \text{ m}$ upstream
 6045 or downstream of the current ALICE IP. This will of course have an impact in the integration
 6046 of the detector in the underground cavern [710], however it seems feasible [711].

6047 The LHC protected aperture in the event of an asynchronous beam dump significantly depends
 6048 on the phase advance between the MKD kicker and the local aperture protection [712]. This
 6049 is due to the oscillation trajectory of bunches deflected during the kicker rise time. With a
 6050 phase advance of 0° or 180° from the kicker to the protected aperture, a direct hit should be
 6051 unlikely, so aperture bottlenecks should be close to that. For a beam stay clear of 12.3σ a phase
 6052 advance of less than 30° from either 0° or 180° was calculated to be acceptable [712]. The major
 6053 complication comes from the fact that not only the final focus system of LHeC, but also of the
 6054 two main experiments ATLAS and CMS need to have to correct phase advances and since the
 6055 phase advances between IP2 (LHeC) and IP1 (ATLAS) are locked in the achromatic telescopic
 6056 squeezing scheme there are few degrees of freedom to make adaptations.

6057 The Achromatic Telescopic Squeezing (ATS) scheme [708] is a novel optical solution proposed
 6058 for the HL-LHC to strongly reduce the β^* while controlling the chromatic aberrations induced,
 6059 among other benefits.

6060 The principles of the ATS as implemented for the HL-LHC are as follows: first, in the presqueeze
 6061 stage, a standard matching procedure is performed in the interaction regions to obtain a value of
 6062 β^* which is achievable in terms of quadrupole strengths and chromaticity correction efficiency,
 6063 in the case of HL-LHC this corresponds to IR1 and IR5. A further constraint at this point is
 6064 to match the arc cell phase advance on the regions adjacent to the low β^* interaction regions to
 6065 exactly $\pi/2$. Later, at the collision stage, the low β^* insertions remain unchanged and instead
 6066 the adjacent interaction regions contribute to the reduction of β^* , that is IR8 and IR2 for IR1,
 6067 and IR4 and IR6 for IR5. The $\pi/2$ phase advance allows the propagation of β -waves in the
 6068 arc. If phased correctly with the IP, these β -waves will reach their maximum at every other
 6069 sextupoles, increasing the β function at their location at the same rate that the decrease in β^* .
 6070 The increase of the β function at the location of the sextupoles will result in an increase of their
 6071 efficiency, allowing the system to correct the high chromaticity produced by the high- β function
 6072 in the inner triplet. This way, the ATS allows a further reduction of the β^* at the same time

6073 that correcting the chromaticity aberrations produced in the low β insertions.

6074 Following the experience for HL-LHC, the ATS scheme was proposed for the LHeC project to
6075 overcome some of the challenges of this design in terms of limits in the quadrupole strengths of
6076 the interaction region and in the chromaticity correction.

6077 A first integration of the LHeC IR into the HL-LHC lattice using the ATS scheme for the
6078 previous nominal case with $\beta^* = 10$ cm and $L^* = 10$ m was presented by extending the β wave
6079 into the arc 23 [706]. The flexibility of this design was later explored to study the feasibility
6080 of minimising β^* , to increase the luminosity, and increasing L^* , to minimise the synchrotron
6081 radiation. It was found that increasing L^* to 15 m provided a good compromise but keeping the
6082 β^* to 10 cm.

6083 The changes made to the HLLHCv1.3 lattice [713] to obtain the LHeC lattice and the detailed
6084 matching procedure are described in Ref. [714]. At the end of this process a lattice for the
6085 required collision optics in all IRs ($\beta^*=15$ cm for IR1 and IR5 and $\beta^*=10$ cm for IR2) has
6086 been obtained, with the appropriate corrections (crossing, dispersion, tune and chromaticity).
6087 The phases between the MKD kicker in IR6 and the different low β^* triplets were also checked,
6088 resulting in 15° from the horizontal for IR1, 22° for IR2 and 26° for IR5, therefore fulfilling the
6089 $< 30^\circ$ requirement for all three IRs.

6090 Similarly the chromaticity correction for the LHeC lattice further develops from the HL-LHC
6091 chromaticity correction scheme [714] allowing to correct the chromaticity for the case with
6092 $\beta^* = 10$ cm in IP2 within the available main sextupole strength. Lattices with $\beta^* = 7, 8$ and
6093 9 cm and $L^* = 15$ m were also successfully matched in terms of both the β^* and the chromaticity
6094 correction. It must be noted however that these cases require a larger aperture in the inner
6095 triplet.

6096 Dynamic aperture (DA) studies were performed to analyze the stability of the lattice designs
6097 using SixTrack [715] on a thin-lens version of the LHeC lattice at collision ($\beta^* = 0.15$ m in
6098 IP1 and IP5, $\beta^* = 10$ cm in IP2) over 10^5 turns with crossing angles on, 30 particles pairs per
6099 amplitude step of 2σ , 5 angles in the transverse plane and a momentum offset of 2.7×10^{-4} .
6100 The energy was set to 7 TeV and the normalised emittance of the proton beam to $\epsilon = 2.5 \mu\text{m}$.
6101 No beam-beam effects were included in this study.

6102 Previous DA studies had been performed for an earlier version of the LHeC lattice [706]. These
6103 studies did not include triplet errors of either of the low- β interaction regions, as these errors
6104 were not available at that stage. These studies were updated for the newer version of the LHeC
6105 lattice described in the previous sections and included errors on the triplets of IR1 and IR5. For
6106 the case of IR2 errors tables for the new triplet are not yet available but it was estimated that
6107 the same field quality than the triplets for the HL-LHC IR can be achieved for these magnets,
6108 and therefore the same field errors were applied but adjusted to the LHeC triplet apertures.

6109 The initial DA resulted in 7σ but following the example of HL-LHC and FCC studies [716] two
6110 further corrections were implemented: the use of non-linear correctors to compensate for the non
6111 linear errors in the LHeC IR, and the optimisation of the phase advance between IP1 and IP5.
6112 With these corrections the DA was increased to 10.2σ , above the target of 10σ . The case for
6113 lower β^* , particularly for the case of interest with $\beta^* = 7$ cm proved to be more challenging, as
6114 expected, when adding errors on the LHeC IR; however with the use of the latest corrections a
6115 DA of 9.6σ was achieved, that is not far off from the target. The DA versus angle for both these
6116 cases are shown in Fig. 8.29. It is important to point out that the challenge for the $\beta^*=7$ cm
6117 case comes instead from the quadrupole aperture and gradient requirements, particularly in the
6118 first magnet.

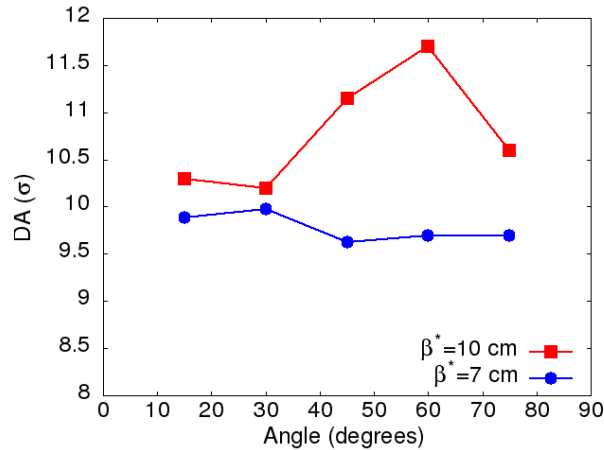


Figure 8.29: Dynamic aperture vs angle for 60 seeds for the LHeC lattice at collision for the cases $\beta^* = 10$ cm (red) and $\beta^* = 5$ cm in IP2.

6119 β^* values lower than 10 cm require a completely different final focus system as the lower β^* means
 6120 the beam size in the triplet will become larger. Larger apertures are required and consequently
 6121 the gradients in the quadrupoles will decrease. However similar integrated focusing strengths
 6122 will be required so the overall length of the triplet will increase. As this will in turn increase the
 6123 β functions in the triplet further it is imperative to optimise the use of the available space. An
 6124 example of available space is the drift between the detector region dipoles and the triplet magnets
 as shown in Fig. 8.30. The optimum dipole lengths in terms of synchrotron radiation power was

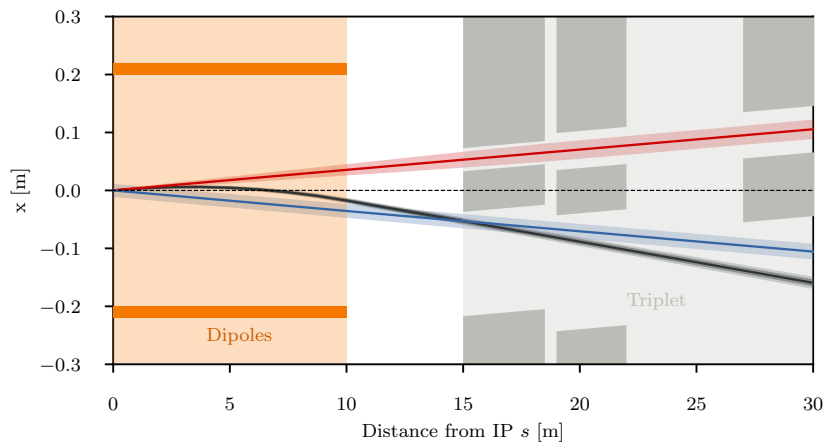


Figure 8.30: Empty space between the detector dipole and the superconducting quadrupoles of the final focus triplet.

6125 determined to be $2/3 \cdot L^*$ so a drift of 5 m is left. Now it is immediately clear that this region
 6126 cannot be occupied by a superconducting quadrupole septum as that would effectively decrease
 6127 L^* and thus increase the synchrotron radiation power as a stronger separation is necessary.
 6128 Instead it is thinkable that a normal conducting quadrupole septum can be built that either
 6129 does not require a yoke or similar structure between the beams or has a very thin yoke, or a
 6130 septum that has a very limited and controlled field in the region of the electron beam trajectory.
 6131 In the later case it might even be used as part of the final focus system of the electron beam.
 6132 Either way, it is clear that such a normal conducting septum must have a pole tip field way below
 6133 the saturation limit of iron. The section on electron optics shows that a normal quadrupole of
 6134

6135 this kind can also have benefits in terms of synchrotron radiation, but studies remained to be
 6136 done to make sure the parameters work for both cases. For our calculation a pole tip field of
 6137 1 T was assumed. For $\beta^* = 5$ cm an aperture radius of 20 mm is required at a distance of 14 m
 6138 from the IP, resulting in a pole tip field of 50 T/m for the normal conducting septum called Q0.
 6139 Possible ratios of apertures and gradients for the remaining triplet magnets were approximately
 6140 based on the quadrupole parameters shown in Tab. 8.19, however these parameters would require
 6141 a magnet design for confirmation. With the quadrupole parameters shown in Tab. 8.21 we were
 able to obtain triplet optics that can accommodate a beam with a minimum β^* of 5 cm.

Magnet	Gradient [T/m]	Length [m]	Aperture radius [mm]
Q0 (nc)	50	3.0	20
Q1A	110	3.5	27
Q1B	162	5.0	37
Q2	123	5.0	62
Q3	123	4.5	62

Table 8.21: Parameters of the final focus quadrupole septa required to accommodate a β^* of 5 cm. The normal conducting quadrupole is called Q0 although it has the same polarity as Q1A/B.

6142

The corresponding optics are shown in Fig. 8.31. So from the triplet point of view it appears

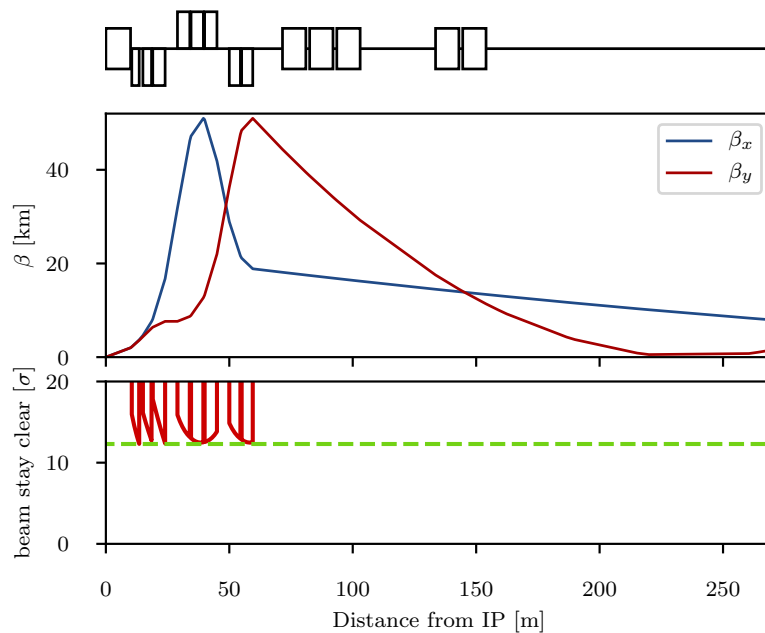


Figure 8.31: Optics (top) and beam stay clear (bottom) in the triplet region of colliding beam with $B^* = 5$ cm.

6143

6144 possible to reach lower β^* , however many assumptions need verification: First the magnetic
 6145 design for the normal conducting quadrupole septum must be shown to be possible. If there
 6146 is a residual field in the space of the electron beam trajectory, the impact on the electron
 6147 beam and the synchrotron radiation power must be evaluated. The parameters of the modified
 6148 superconducting triplet quadrupole septa, although scaled conservatively, must be confirmed.
 6149 Furthermore the larger aperture radius of Q1 might require a larger separation at the entrance of
 6150 Q1, increasing the synchrotron power that is already critical. Thus a full design of such magnets

6151 is required. Lastly, the interaction region must be integrated into the full ring to verify that
6152 chromaticity correction is possible. Studies in Ref. [714] that were conducted on the normal
6153 triplet without regard for aperture constraints suggest that a chromaticity correction is only
6154 possible for a β^* down to around 7 cm.

6155 So far the optics of the final focus system featured asymmetrically powered triplets on the two
6156 sides of the IP. This is inherited from the ALICE final focus system where the aperture is shared
6157 and the antisymmetry guarantees the same optics for both beams and similar chromaticities
6158 in both horizontal and vertical planes. In the LHeC final focus system however, the apertures
6159 of the quadrupoles are not shared between both beams, so the antisymmetry is not strictly
6160 necessary, although it eases the integration in the full ring. An alternative approach that is
6161 worth studying is a symmetric doublet. Doublets feature a large β function in one plane and a
6162 relatively low one in the other plane. Since the non-colliding proton beam is of no concern for
6163 LHeC it makes sense to create doublets on each side of the IP that have the peak β function in the
6164 horizontal plane as the chromaticity correction was limited in the vertical plane. Furthermore,
6165 in a doublet the integrated focusing strength needed is lower as fewer quadrupoles act against
6166 each other. This further reduces the chromaticity and should also reduce the overall length of
6167 the final focus system. With the space saved by the doublet it is possible to either shift the
6168 recombination dipoles D1 and D2 closer to the IP, reducing the needed integrated strengths,
6169 or even to increase L^* to further reduce the synchrotron radiation power and critical energy.
6170 In order to make best use of the available doublet quadrupole aperture, it is also thinkable to
6171 collide with flat beams. The main disadvantage of symmetric doublets is the breaking of the
6172 sequence of focusing and defocusing quadrupoles. As no changes should be made to the arcs,
6173 the left-right symmetry needs to be broken up again in one of the matching sections, either by
6174 introducing another quadrupole on one side of the IP, or by overfocusing the beam.

6175 At collision energy the non-colliding beam has no optics specification within the straight section.
6176 Consequently the optics should transfer the beam from the left arc to the right arc without hitting
6177 the aperture and at a specific phase advance. The same is true at injection energy, but with a
6178 larger emittance, making the satisfaction of the aperture constraint more difficult. Thus it is
6179 sufficient to find working injection optics, as no squeeze will be required for this beam. This
6180 approach of course will require some tuning as at least one arc will apply the ATS scheme at
6181 collision, but as the aperture constraint is less tight at higher energy there should be enough
6182 degrees of freedom available.

6183 Finding injection optics appears trivial at first but is complicated by the fact that the distance
6184 between the IP and the first quadrupole magnet Q4 is larger than 159 m. A total distance
6185 of 318 m needs to be bridged without any focusing available. A solution has been found with
6186 $\beta^* = 92$ m and $\alpha^* = \pm 0.57$ with the required beam size in the quadrupole septa and Q4 [714].
6187 The corresponding optics are shown in Fig. 8.32. For the magnets Q4 and Q5 LHC quadrupoles
6188 of the large aperture MQY type with 70 mm aperture diameter and a 160 T/m gradient were
6189 assumed. As can be seen in the aperture plot, the triplet quadrupole septa and Q4 are just below
6190 the minimum beam stay clear at injection of 12.6σ but it is expected that nominal aperture can
6191 be achieved With some minor optimisation. However the Q5 magnets only have a beam stay
6192 clear of about 9.2σ with little chance of decreasing the beam size without increasing it both
6193 in Q4 and in the quadrupole septa. Consequently it will be necessary to use quadrupoles with
6194 apertures larger than 106 mm and make up for the lower gradient by increasing the length or by
6195 using Nb₃Sn technology. At injection energy the remaining magnets in the IR have strengths
6196 according to the HL-LHC specification and thus do not pose any problems. However the injection
6197 optics shown in Fig. 8.32 will require some changes during the ramp as Q4, Q5 and Q6 would
6198 become too strong at collision energy. This is not considered a problem though, as the emittance

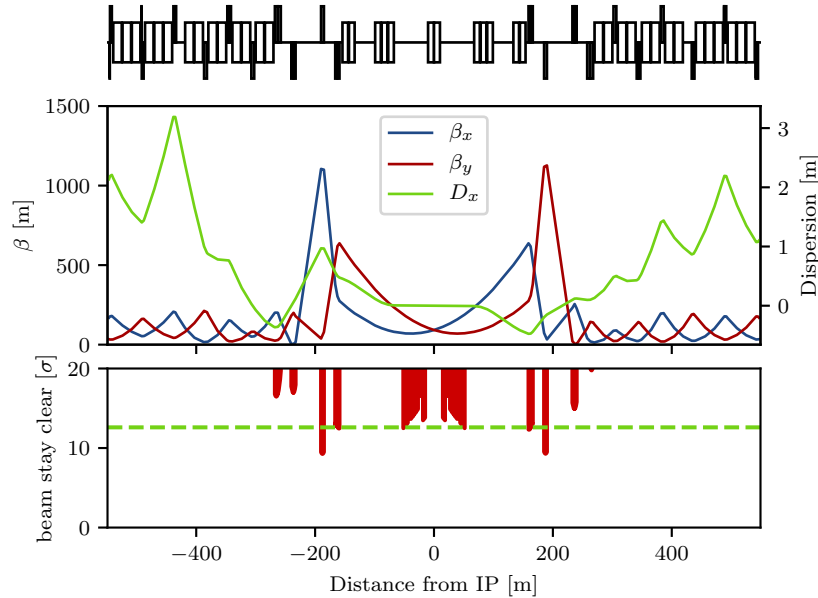


Figure 8.32: Optics (top) and beam stay clear of the non-colliding beam at injection energy. The Q5 quadrupole magnets on either side of the IP currently are aperture bottlenecks. It should be possible to mitigate this problem by replacing the magnets with longer, larger aperture magnets.

6199 shrinking will ease the aperture requirements.

6200 The non-colliding proton beam does not need to be focused and consequently passes the quadrupole
 6201 septa of the colliding beam in the field free region.

6202 The large angle of $7200 \mu\text{rad}$ between the two beams (compared to $590 \mu\text{rad}$ in the high lumi-
 6203 nosity IPs) should suffice to mitigate long range beam-beam effects, considering that the shared
 6204 aperture is only 30 m long as opposed to the main experiments where the shared aperture exceeds
 6205 a length of 70 m.

6206 8.7.3 Electron Optics

6207 First ideas of a possible layout and design of the Interaction Region IR between the LHeC lepton
 6208 and proton beam have already been presented in Ref. [1]. Based on the principles explained there,
 6209 a further optimisation of the beam separation scheme has been established, with the ultimate
 6210 goal of lowest synchrotron radiation power and critical energy in the direct environment of the
 6211 particle detector. Depending on the requests from the actual detector geometry and shielding,
 6212 the flexibility of the new IR layout allows to optimise for either side.

6213 The basic principle is – as before – based on the large ratio (approximately 140) of the proton
 6214 to electron beam momentum (or beam rigidity, $B\rho = p/e$) that makes a magnetic field based
 6215 separation scheme the straightforward solution to the problem, using effective dipole fields.

6216 Boundary conditions are set however due to the limited longitudinal space, resulting from the
 6217 distance of the first focusing elements of the proton lattice, located at $L^* = 15$ m, and the need for
 6218 sufficient transverse separation, defined by the technical design of this first proton quadrupole.
 6219 The size of the two beams and – clear enough – the power of the emitted synchrotron radiation
 6220 P_{syn} and the critical energy E_{crit} have to be taken into account in addition. The well known

dependencies of these two parameters on the beam energy $E_e = m_e c^2 \gamma$ and bending radius ρ are given by

$$P_{\text{syn}} = \frac{e^2 c}{6\pi\epsilon_0} \frac{\gamma^4}{\rho^2} \quad \text{and} \quad E_{\text{crit}} = \frac{3 \hbar c \gamma^3}{2 \rho}. \quad (8.6)$$

The schematic layout of the original design of the electron interaction region shown in Fig. 8.26 is reproduced in Fig. 8.33 (a). The long dipole magnet B, used to deflect the electron beam, is

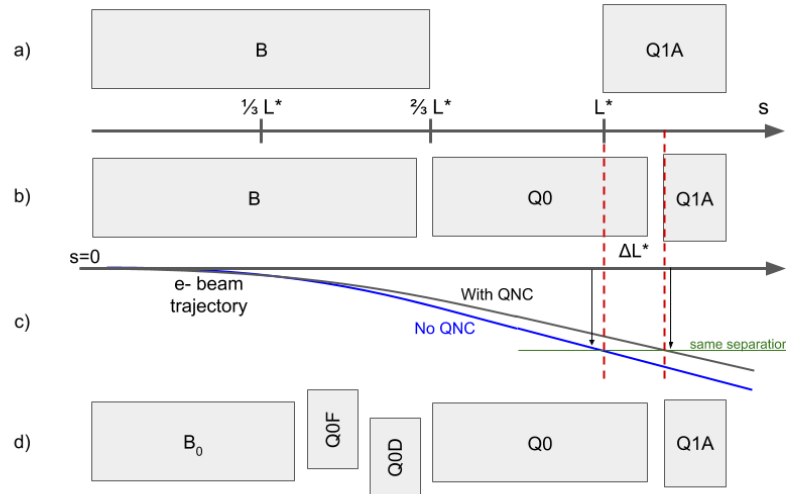


Figure 8.33: Separation scheme based on a long dipole magnet B (a) and improved layout using Q0, a normal conducting half-quadrupole as first focusing element of the proton beam (b). The last design features a doublet of off-centered quadrupoles to minimise the electron beam size at the entrance of Q1A (d).

embedded inside the detector structure which is ranging from -6 m to 4 m around the interaction point, extended by ± 1.65 m of muon chamber. Basic interaction region designs with and without chromaticity correction were presented [717, 718] but were not fully integrated in the ERL. The electron final quadrupoles were placed at 30 m from the IP [719], compatible with the proton layout described above. While this approach is straightforward, the only parameter that can be used to minimise the power of the emitted synchrotron radiation is the length of the separator-dipole field [707]. In addition, the installation of the first focusing elements of the electron beam downstream of the triplet focussing the colliding proton beam leads to a considerable increase of the electron beam size in the separation plane.

Lattices including chromaticity correction had a significant length of 150 m. However, the whole straight section between Linac and arc is only 290 m long [1] and the IR design did not include a matching and splitting section or a focus system for the spent, outgoing electron beam. Without chromaticity correction in the electron final focus, aberrations at the IP decrease luminosity by about 20% [720].

Investigations have been launched to minimise critical energy and emitted synchrotron radiation power by reducing the separation in two main steps:

- introduce a compact mirror-plate half quadrupole (QNC) in front of Q1A (on the IP side) to focus the colliding proton beam and provide a field free region for the electron and non-interacting proton beam. This reduces the required bending field of the separation dipole B for the same separation at Q1A. In addition, the normal conducting magnet QNC will

6245 act as shielding of the superconducting triplet magnets that would otherwise be subject to
 6246 direct synchrotron radiation. Additional shielding is foreseen, to protect the SC magnets
 6247 and avoid as much as possible backshining to the detector. In addition, sufficient space
 6248 will be provided to correct the vertical orbit and coupling of the electrons coming from
 6249 the solenoid.

- 6250 • reduce the beam size of the electron beam by a very early focusing of the beam. As positive
 6251 side effect this leads to a considerable reduction of the chromaticity of the electron lattice.

6252 The first step is sketched in Fig. 8.33 (b) and the corresponding electron beam trajectory is
 6253 shown in Fig. 8.33 (c).

6254 The introduction of the mirror plate half quadrupole QNC allows to reduce the length of the
 6255 Q1A quadrupole while conserving the total integrated gradient, therefore leaving the overall
 6256 focusing properties of the proton lattice quasi untouched. The entry of Q1A is therefore moved
 6257 away from the IP to relax the separation fields.

6258 Scanning the Q1A entry position leads to either an optimum of the critical energy or to a
 6259 minimum of the emitted synchrotron power. Both cases are shown in Fig. 8.34 and for each of
 6260 them the new Q1A entry position has been determined. The power of the emitted radiation
 6261 is reduced by up to 28 %. The colliding proton beam, passing through this half quadrupole
 6262 with a certain offset to guarantee sufficient beam stay clear, will receive a deflecting kick in the
 6263 horizontal plane of about 90 μ rad. It supports the dipole based beam separation, provided by
 the so-called D1 / D2 magnets in LHC, and will be integral part of the LHC design orbit.

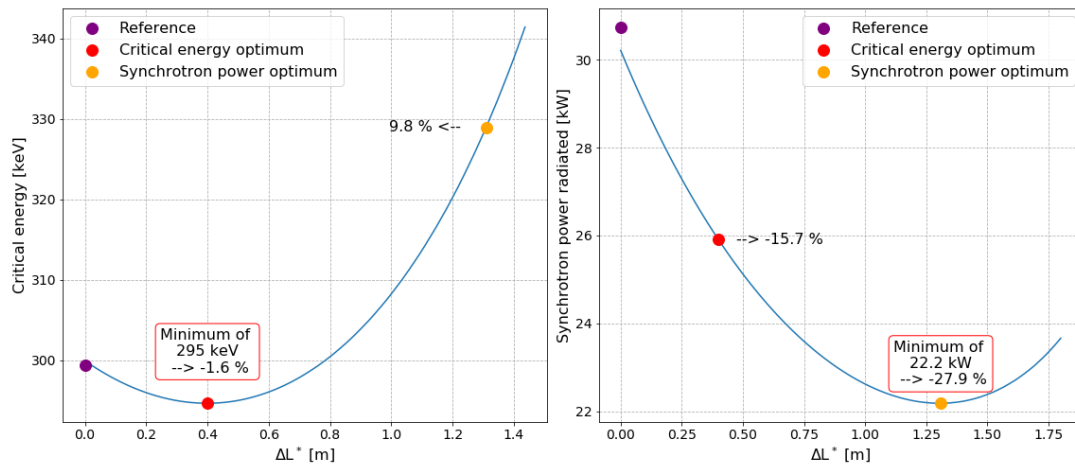


Figure 8.34: Improved critical energy and power of the synchrotron radiation for the half quadrupole based proton lattice. Left side: critical energy, right side: synchrotron radiation power. The horizontal axis refers to the shift ΔL^* of the position of the first proton superconducting magnet Q1A.

6264

6265 The resulting beam optics of the protons differs only marginally from the original version and
 6266 only a slight re-match is needed. However by carefully choosing the gradient of the new magnet
 6267 the parameters of the superconducting proton quadrupoles are untouched and the phase advance
 6268 at the end of the interaction region lattice is conserved in both planes.

6269 **Improved Electron lattice**

6270 A further improvement of the emitted synchrotron power and critical energy is obtained by
 6271 introducing an early focusing scheme of the electrons, which leads to a reduced electron beam
 6272 size and thus to softer separation requirements.

6273 The reduction of the electron beam size is obtained by installing a quadrupole doublet in the
 6274 electron lattice between the separation dipole and the QNC (half-) quadrupole. A carefully
 6275 matched focusing strength of this doublet will minimise the β function of the electrons at the
 6276 location of Q1A. At the same time an effective dipole field, that is needed to maintain the
 6277 separation of proton and electron beams, is provided by shifting the magnet centres of the
 6278 doublet lenses off axis. The horizontal offset of these quadrupoles has been chosen to provide
 6279 the same bending radius as the separation dipole, thus leading in first order to the same critical
 6280 energy of the emitted light in all separation fields. A detailed calculation of the divergence of the
 6281 photons, the geometry of the radiation fan and the position of the absorbers and collimators will
 6282 be one of the essential next steps within the so-called machine-detector-interface considerations.

6283 Fig. 8.33 (d) shows the new layout – compared to the previous version. The doublet providing
 6284 the early focusing of the electron beam is embedded in the separator dipole, i.e. it is positioned
 6285 at $s = 6.3$ m and acts in combination with the separation dipole. The quadrupole gradients have
 6286 been chosen for optimum matching conditions of the electron beam and the transverse shift of the
 6287 field centres provide the same separation dipole effect as used in the long dipole.

6288 The early focusing of the electron beam allows for a softer separation of the beams, and leads
 6289 therefore directly to a reduced critical energy E_{crit} and power P_{syn} of the emitted radiation.
 6290 Fig. 8.35 shows the dependence of E_{crit} and P_{syn} on the β -function at $s = L^*$ for the electron
 6291 optics for different values of the required electron beam stay-clear expressed in units of the
 6292 electron beam size σ . The beam separation has been re-calculated and the critical energy
 6293 and radiation power are plotted. The graphs include different assumptions for the beam size
 6294 considered. Including orbit tolerances, a beam stay-clear of 20σ is considered as the most
 relevant case, which refers to the red curve in the graph.

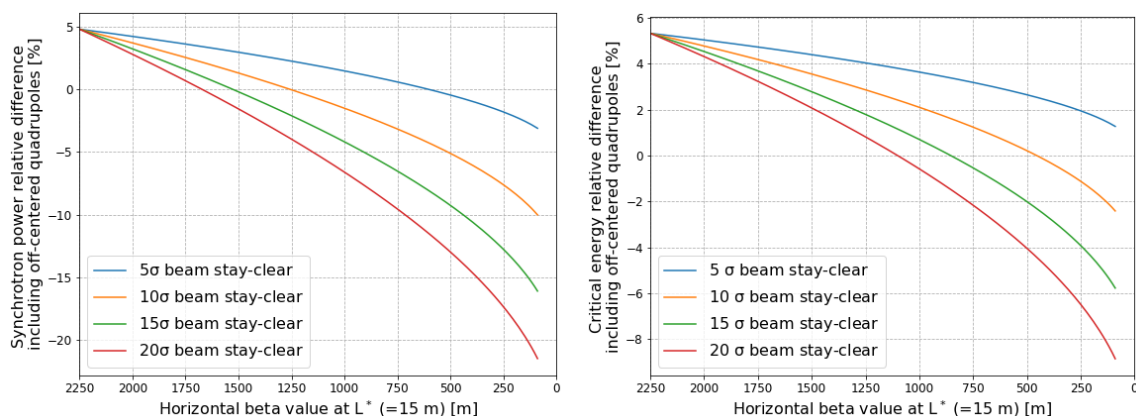


Figure 8.35: Relative difference with respect to the single dipole separation scheme for different values of the required beam stay-clear expressed in σ . Left : for the power of the emitted radiation, as function of the β -function of the electron beam at position $s=15$ m. Left: for the critical energy of the emitted radiation, as function of the β -function of the electron beam at position $s=15$ m. The early focusing of the electron beam allows for a much reduced separation field and thus to a reduced critical energy and power of the emitted radiation. The initial beta value is 2250 m.

6295

6296 In order to provide a complete study with the lattice featuring the off-centered quadrupoles, the
 6297 new interaction region has been embedded in between the high energy end of the acceleration
 6298 part of the linac and the *Arc 6* of the ERL, which marks the start of the energy recovery lattice.
 6299 An optimum has been found for a beam optics with a beta function in the plane of the beam
 6300 separation (i.e. horizontal) of $\beta_x = 90$ m at $L^* \approx 15$ m

6301 An improvement of about 9 % for the critical energy and close to 25 % of the radiated power is
 6302 obtained, if an electron beam optics with $\beta_x = 90$ m at the entrance of Q1A is used. For this
 most promising case the matched beam optics is shown in Fig. 8.36.

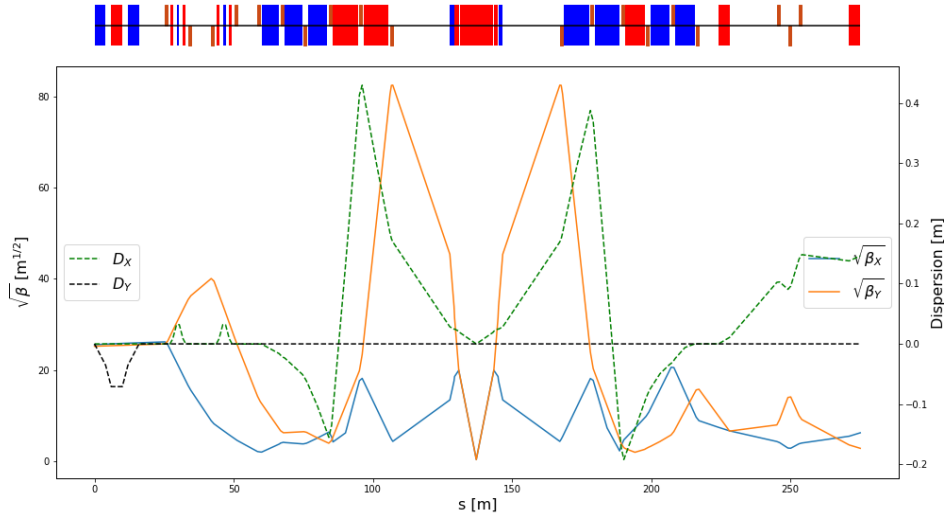


Figure 8.36: Electron beam optics for the new lattice including the early focusing scheme. The offset of the new doublet quadrupoles are chosen to provide the same separation field as in the dipole. The new optics is matched on the left side of the plot to the end of the acceleration linac. The right hand side is connected to Arc 6, the beginning of the decelerating ERL part. At the position of the first superconducting proton magnet the β -function in the (horizontal) separation plane of the electron beam is reduced to 90 m for lowest possible synchrotron radiation load.

6303

6304 The lower β -function of the electron beam at the focusing elements has the additional positive
 6305 feature of reducing considerably the chromaticity of the new lattice, which is a crucial parameter
 6306 for the performance of the energy recovery process (details are described below in the chapter
 6307 on tracking calculations). Compared to the dipole based separation and a late focusing, Q' is
 6308 reduced to a level of 13 % horizontally and to a level of 11 % in the vertical plane. The details
 6309 are listed in Tab. 8.22. Further studies will investigate the orbit correction scheme of the new
 IR, and an eventual interplay of the solenoid fringe field and the quadrupoles.

	Dipole based separation	Early focusing scheme
ξ_x	-116	-15
ξ_y	-294	-32

Table 8.22: Chromaticity of the dipole based separation scheme and the new lattice based on early focusing, off-axis quadrupole lenses.

6310

6311 The influence of the electron doublet magnets on the proton optics is marginal – as can be
 6312 expected due to the large difference in beam rigidity: If uncorrected, the electron doublet creates
 6313 a distortion (a so-called *beta-beat*) of the proton optics of roughly 1 %. Still it has been calculated

6314 and taken into account in the context of a re-match of the proton beam optics.

6315 Combining the two improvement factors, namely the effective lengthening of L^* due to the
 6316 use of a half quadrupole in front of the superconducting triplet, and the early focusing scheme
 6317 in the lattice of the electrons, leads to an overall improvement of the interaction region with
 6318 respect to synchrotron radiation power and critical energy that is shown in Fig. 8.37. The
 6319 overall improvement factor is plotted with reference to the baseline dipole separation design
 6320 with originally $\beta = 2250$ m at the separation point $s = L^*$. Using a normal conducting half
 6321 quadrupole in combination with the early focusing scheme, the power of the emitted synchrotron
 radiation is reduced by 48 % for an electron beam stay-clear of 20σ .

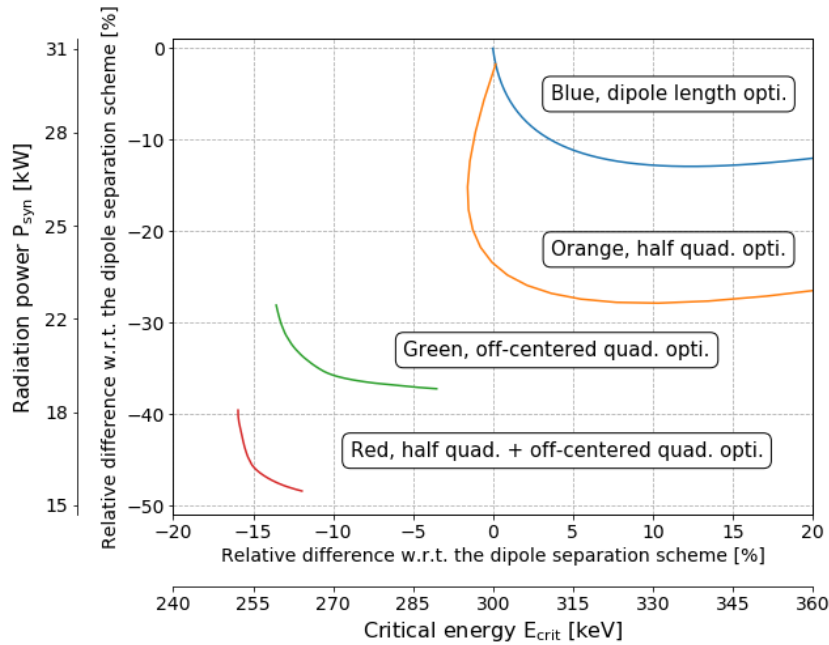


Figure 8.37: Relative differences with respect to the original single dipole separation scheme. The synchrotron radiated power is plotted as a function of the critical energy for different optimisation results: only optimising the dipole length (blue), only using a mirror quadrupole (orange), only using off-centered quadrupoles (green) and combining the mirror quadrupole with an earlier focusing (red).

6322

6323 The estimated synchrotron radiation power and critical energy for the different optimisations
 6324 are plotted in Fig. 8.37 and the results are summarised in Tab. 8.23. Referring to a beam energy
 6325 of 49.19 GeV and the design current of 20 mA an overall power of 16.2 kW is emitted within one
 6326 half of the interaction region.

6327 Depending on the boundary conditions imposed by the integration of the particle detector, one
 6328 of the two optimum layouts can be chosen – or a combination of both, i.e. an overall minimum
 6329 defined by critical energy and radiated power.

6330 The basic main parameters of the proton mirror plate half quadrupole are summarised in
 6331 Tab. 8.24 for the two optimum scenarios explained above: the optimum found for smallest
 6332 synchrotron radiation power and the optimum for smallest critical energy of the emitted radia-
 6333 tion. The values result from the optics studies of the previous sections. The presented gradients
 6334 lead to a pole tip field of $B_p \approx 1.3$ T.

6335 In both cases, the proton aperture radius has been chosen to include an orbit tolerance of 2 mm,
 6336 a 10 % tolerance on the beam size due to optics imperfections (beta-beating) and a beam size

Optimised scheme	Synchrotron radiation		Critical energy	
	Radiation power [kW]	Critical energy [keV]	Radiation power [kW]	Critical energy [keV]
Reference design	30.8	300	30.8	300
Dipole length optimum	26.8	336	30.8	300
Half quadrupole optimum	22.2	331	26.1	295
Off-centered quadrupoles opti.	19.3	290	22.1	259
Half quad. + Off-centered quad. opti.	16.2	265	17.4	255

Table 8.23: Synchrotron radiation power and critical energy for the different optimised separation schemes.

Half quadrupole parameter	Unit	Minimum synchrotron radiation power	Minimum critical energy
$\gamma\varepsilon_p$	mm-mrad	2.50	2.50
Gradient	T/m	48.2	50.7
Aperture radius	mm	27.0	25.6
Length	m	6.84	2.08

Table 8.24: Magnet gradient of the proposed half quadrupole for lowest synchrotron radiation power and lowest critical energy. An aperture of $15\sigma + 20\%$ beta-beating + 2 mm orbit tolerances has been assumed.

6337 that corresponds to $n = 15\sigma$ for a proton beam normalised emittance $\varepsilon_p = 2.50\mu m$. A value
6338 that is comfortably larger than the requirements of the HL-LHC standard lattice. The injection
6339 proton optics has been taken into account and although it features a larger emittance it clearly
6340 fit in the aperture, see the red dashed line in Fig. 8.38. The electron beam and the non-colliding
6341 proton beam will pass through the field free region delimited by the mirror plate.

6342 The aperture requirements inside the half quadrupole are determined on one side by the colliding
6343 proton beam optics in the main aperture of the magnet. The beam separation scheme and optics
6344 of electron and non-colliding proton beam on the other side have to fit into the field free region
6345 beyond the mid plane of the mirror plate. As described below, a crossing angle of 7 mrad is
6346 assumed for the non-colliding protons. These requirements are illustrated in Fig. 8.38. For
6347 the case of smallest synchrotron radiation power, the three beams are plotted at the entrance
6348 and exit of the quadrupole lens. For both proton beams the beam size shown in the graph
6349 corresponds to 15 sigma plus 2 mm orbit tolerance and 10% beam size beating. Due to the
6350 mini-beta optics the colliding proton beam fills nearly the given aperture of the magnet. The
6351 non-colliding proton beam follows a relaxed optics with very limited aperture need. The envelope
6352 of the electron beam is shown for 20 σ beam size in both transverse planes.

6353 In contrast to the proton half quadrupole, the doublet magnets of the early focusing scheme
6354 will house the three beams in one single aperture. In addition to the beam envelopes, the offset
6355 that has been chosen to provide the beam separation effect has to be taken into account and
6356 included in the aperture considerations.

6357 In Fig. 8.39 the situation is visualised. On the left side the first off-center quadrupole (powered
6358 as focusing lens) is presented. Following the field direction, the electron beam is offset towards
6359 the outer side of the ring (right side of the plot) as defined by the proton beam closed orbit.
6360 The right part of the figure shows the second quadrupole (powered as defocusing lens) with
6361 the electron beam offset shifted to the other direction. In order to provide sufficient aperture

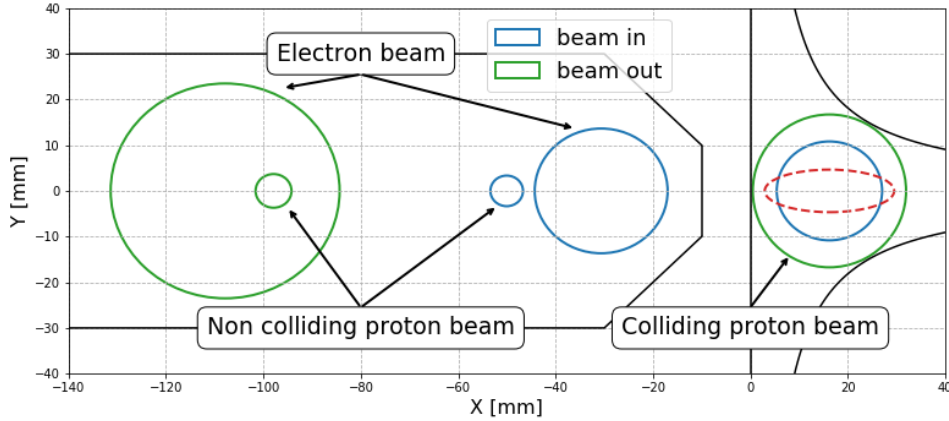


Figure 8.38: The position of the three beams at the entrance (blue) and exit (green) of the half quadrupole. The colliding proton beam is centered inside the main magnet aperture, while the second proton beam and the electrons are located in the field free region. The dashed red line represents the injection proton beam at the output of the half quadrupole.

6362 for the three beams, an elliptical shape has been chosen for the vacuum chamber. It defines
 6363 enough space for the beam envelopes and the off-centre design trajectories. The black ellipses
 6364 correspond to the beams at the entrance of the magnet while the red shapes represent the beams
 6365 at the exit. From left to right the three beams are respectively the non colliding proton beam
 6366 (tiny circles), electron beam (squeezed ellipses) and the colliding proton beam. As defined before
 6367 we refer to a beam size of 20σ in case of the electrons and 15 sigma plus beta-beating plus 2
 6368 mm orbit tolerance for the colliding and non-colliding proton beam.

6369 In this context it should be pointed out that the non-colliding proton beam, travelling in the
 6370 same direction as the electrons, is shifted in time by half the bunch spacing. While the projected
 6371 beam envelopes in Figs. 8.39 and 8.38 seem to overlap in the transverse plane, they are well
 6372 separated by 12.5 ns, corresponding to 3.75 m, in the longitudinal direction.

6373 The minimum required gradients and pole tip radius of the quadrupoles of the doublet are listed
 in Tab. 8.25. Following the increasing beam size after the IP, the two quadrupoles are optimised

Parameter	Unit	Q0F	Q0D
$\gamma\varepsilon_e$	mm-mrad	50	50
$\gamma\varepsilon_p$	mm-mrad	2.50	2.50
Gradient	T/m	36.2	26.1
Min. pole-tip radius	mm	28.9	38.1
Length	m	1.86	1.86

Table 8.25: Magnet gradient and pole tip aperture of the quadrupoles of the doublet for the synchrotron power optimum.

6374 for sufficient free aperture for the collidng beams and their design orbits. Accordingly a different
 6375 layout has been chosen for the magnets, to provide the best conditions for the radiation power
 6376 and critical energy. An alternative approach has been studied, based on a single quadrupole
 6377 design for both lenses of the doublet. While an optics solution still is possible, it does however
 6378 not allow for minimum radiation power and sets more stringent requirements on the shielding
 6379 and absorption of the synchrotron light fan.
 6380

6381 The chromatic effect of the two lattice versions as a function of the momentum spread is shown

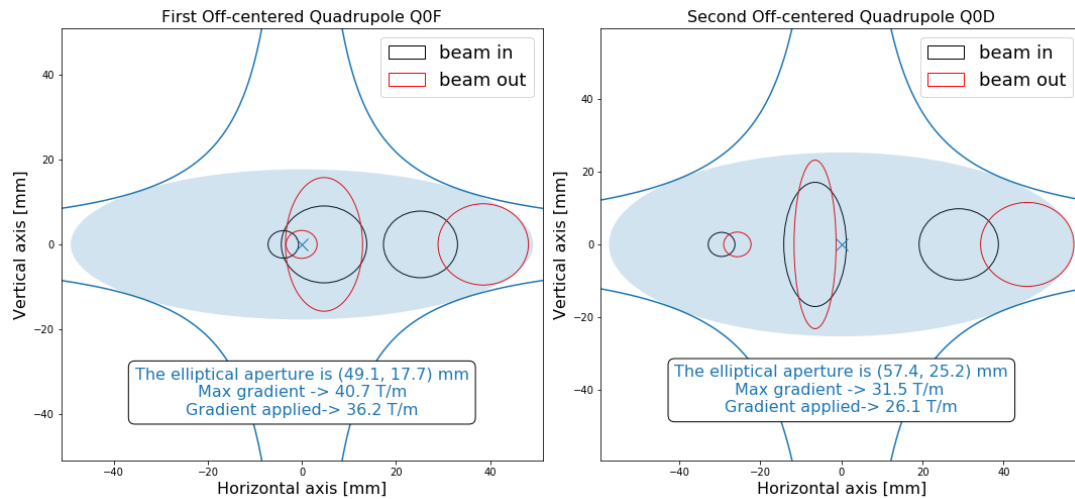


Figure 8.39: The position of the three beams at the entrance (black) and exit (red) of the electron doublet magnets. Following the internal convention, 15σ plus 20% beta beating plus 2 mm orbit tolerances beam envelopes are chosen for the proton beams. The beam size of the electrons refer to 20σ . From left to right the three beams are respectively the non colliding proton beam (tiny circles), electron beam (squeezed ellipses) and the colliding proton beam.

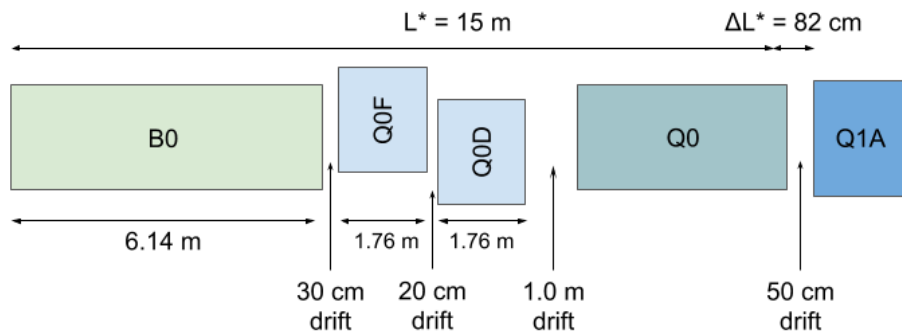


Figure 8.40: Possible optimised design featuring a 1.0 m drift between the off-centered quadrupoles and the half quadrupole in order to leave space for shielding material.

6382 in Fig. 8.41. The lattice based on a single dipole magnet and late focusing of the electron
 6383 beam, shows an increase of the beta function of up 40% in the vertical plane for particles with
 6384 a momentum deviation up to the design value of $\frac{\Delta p}{p} = 2.6 \cdot 10^{-4}$ (vertical cursor line in the
 6385 graph) and a corresponding luminosity loss of 20% for those particles. The optimised design,
 6386 based on the early focusing scheme, shows a much reduced chromatic effect and the resulting
 6387 off-momentum beta-beating at the IP is limited to a few percent. As direct consequence the
 6388 luminosity loss is well below the 1.5% level. A special local chromaticity correction scheme,
 6389 therefore, dealing with the aberrations at IP, is thus not considered as necessary. Further studies
 6390 will include the recirculation of the beam post-collision and the energy recovery performance and
 6391 might nevertheless highlight the need of explicit sextupoles to mitigate the growing momentum
 6392 spread through the deceleration process and to avoid beam losses.

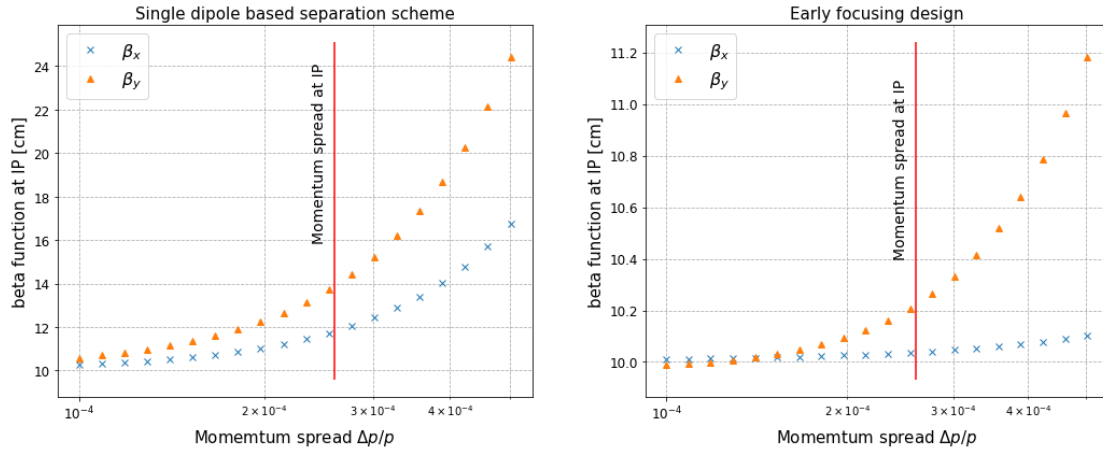


Figure 8.41: Beta function at the IP as a function of the momentum spread. Left : Situation for the single dipole based separation scheme. Right : With the design featuring an earlier focusing. The graphs show the increase of β^* due to the chromaticity of the lattice.

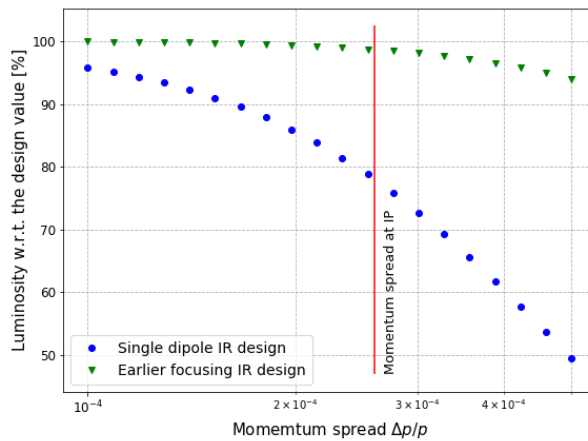


Figure 8.42: The resulting luminosity as a function of the momentum spread for the single dipole based separation scheme (blue circles) and the design featuring an earlier focusing (green triangles).

This figure is not referenced!

6393 8.7.4 Interaction Region Magnet Design

6394 Triplet Magnet Design

6395 While the Q1 magnets remain in the range achievable with the well proven Nb-Ti superconductors,
 6396 operated at 1.8 K, the Q2 magnets require Nb₃Sn technology at an operation temperature
 6397 of 4.2 K. The working points on the load-line are given for both superconducting technologies in
 6398 Fig. 8.43.

6399 The thickness of a coil layer is limited by the flexural rigidity of the cable, which will make the
 6400 coil-end design difficult. Therefore multi-layer coils must be considered. However, a thicker,
 6401 multi-layer coil will increase the beam separation between the proton and the electron beams.
 6402 The results of the field computation are given in Tab. 8.26. Unlike with the design proposed
 6403 in the CDR of 2012 [1], the increased beam separation distance between the colliding proton
 6404 beam and the electron beam makes it possible to neglect the fringe fields in the electron beam

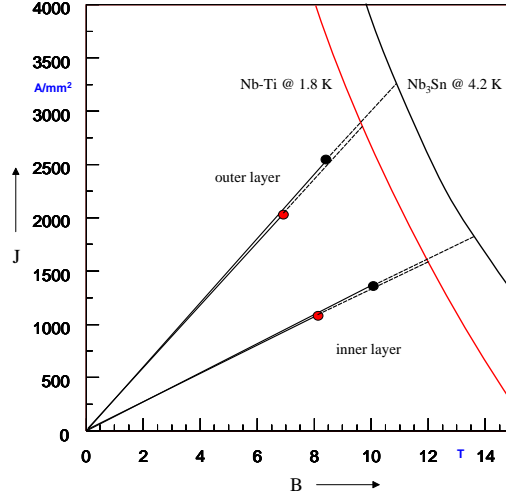


Figure 8.43: Working points on the load-line for both Nb-Ti and Nb₃Sn variants of Q1A.

Magnet parameter	Unit	Magnet type			
		Q1A	Q1B	Q2 type	Q3 type
SC		Nb-Ti	Nb-Ti	Nb ₃ Sn	Nb ₃ Sn
R	mm	20	32	40	45
I_{nom}	A	7080	6260	7890	9260
g	T/m	252	164	186	175
LL	%	78	64	71	75
S_{beam}	mm	106-143	148-180	233-272	414-452

Table 8.26: type of superconductor (SC), field gradient (g), radius of the aperture (R , without coldbore and beam-screen), percentage on the load line of the superconductor material (LL), operational current (I_{nom}), beam separation distance (S_{beam}), **these are missing: fringe field in the aperture for the electron beam (B_{fringe}), gradient field in the aperture for the electron beam (g_{fringe}).** **Todo. Improve caption.**

6405 pipe. For the Q2 and Q3 magnets, the electron beam is outside of the quadrupole cold-mass
 6406 and consequently, an HL-LHC inner-triplet magnet design can be adapted.

6407 For the Nb₃Sn material we assume composite wire produced with the internal Sn process (Nb
 6408 rod extrusions) [721]. The non-Cu critical current density is 2900 A/mm² at 12 T and 4.2 K.
 6409 The filament size of 46 μm in Nb₃Sn strands give rise to higher persistent current effects in
 6410 the magnet. The choice of Nb₃Sn would impose a considerable R&D and engineering design
 6411 effort, which is however, not more challenging than other accelerator magnet projects, such as
 6412 the HL-LHC.

6413 The conceptual design of the mechanical structure of the Q1 magnets is shown in Fig. 8.44
 6414 (right). The necessary prestress in the coil-collar structure, which must be high enough to
 6415 avoid unloading at full excitation, cannot be exerted with the stainless-steel collars alone. Two
 6416 interleaved sets of yoke laminations (a large one comprising the area of the yoke keys and
 6417 a smaller, floating lamination with no structural function) provide the necessary mechanical
 6418 stability of the magnet during cooldown and excitation. Preassembled yoke packs are mounted
 6419 around the collars and put under a hydraulic press, so that the keys can be inserted. The sizing
 6420 of these keys and the amount of prestress before the cooldown will have to be calculated using
 6421 mechanical FEM programs. This also depends on the elastic modulus of the coil, which has to

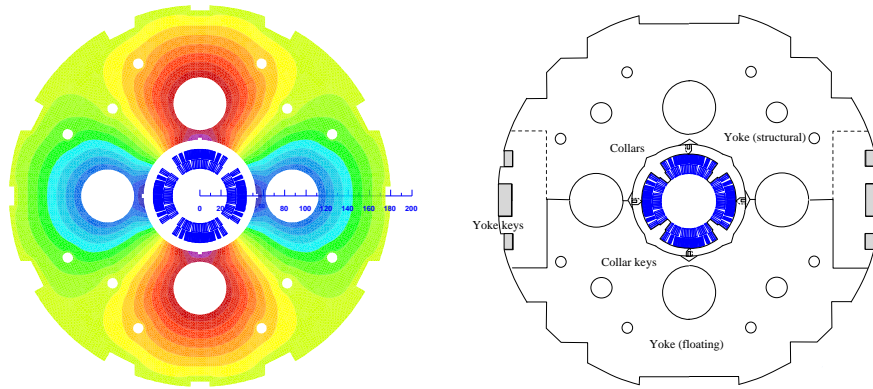


Figure 8.44: Conceptual design of the final focus septa Q1. Left: Magnetic vector potential (field lines). Right: Sketch of the mechanical structure.

6422 be measured with a short-model equipped with pressure gauges. Special care must be taken to
 6423 avoid nonallowed multipole harmonics because the four-fold symmetry of the quadrupole will
 6424 not entirely be maintained.

6425 For the Q2 and Q3 magnets, a HL-LHC inner triplet desing using a bladder and key mechanical
 6426 structure can be adapted.

6427 Normal-Conducting Magnet Design

6428 The proposed mini-beta doublet of the electron lattice, providing an early focusing of the beam,
 6429 and the normal conducting proton-half quadrupole are new magnet concepts. These have been
 6430 studied conceptually to determine their technical feasibility. The geometry of the QNC magnet
 6431 is shwon in Fig. 8.45 (left). Left of the mirror plate, the field free region will provide space for
 6432 the electron beam and the non-colliding proton beam. The thickness of the mirror plate at the
 6433 magnet mid-plane is 20 mm, allowing for sufficient mechanical stability at the minimal beam
 6434 separation between the electron and proton beams.

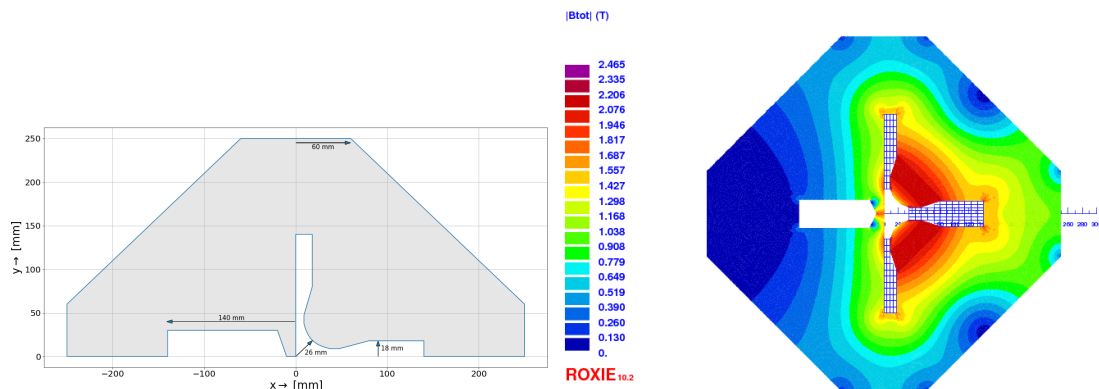


Figure 8.45: Left: Mechanical layout of the new half quadrupole for the proton beam. Right : Field distribution in the half quadrupole for the proton beam.

6435 Field calculations, using the magnet design code ROXIE [722] are presented in Fig. 8.45 (right).
 6436 The achieved field gradient is 50 T/m for a current of 400 A, assuming a current density of
 6437 21.14 A/mm². This is in line with conductor geometries used for normal conducting magnets

6438 installed in the CERN injector complex, for example, ID: PXMQNDD8WC, which is rated at
6439 860 A corresponding to 45.45 A/mm^2 . A more comprehensive design study must also include a
6440 further reduction of the multipole field components.

6441 The geometry of the Q0F and Q0D quadrupoles are given in Fig. 8.39 and the main specifications
6442 are provided in Tab. 8.25. A maximum magnetic field of 1.2 T at the pole tip is well within
6443 reach for a normal conducting quadrupole.

6444 8.8 Civil Engineering

6445 Since the beginning of the LHeC study which proposes a electron-hadron collider, various shapes
6446 and sizes of the eh collider were studied around CERN region. Two main options were initially
6447 considered, namely the Ring-Ring and the Linac-Ring. For civil engineering, these options
6448 were studied taking into account geology, construction risks, land features as well as technical
6449 constraints and operations of the LHC. The Linac-Ring configuration was selected, favouring
6450 a higher achievable luminosity. This chapter describes the civil engineering infrastructure re-
6451 quired for an Energy Recovery Linac (ERL) injecting into the ALICE cavern at Point 2 LHC.
6452 Fig. 8.46 shows three options for the ERL of different sizes, represented as fractions of the LHC
circumference, respectively $1/3$, $1/4$ and $1/5$ of the LHC circumference.



Figure 8.46: Racetrack options proposed for LHeC at Point 2 LHC. The color coding illustrated different options with $1/3$, $1/4$ and $1/5$ of the LHC circumference, resulting in different electron beam energies.

6453

6454 8.8.1 Placement and Geology

6455 The proposed siting for the LHeC is in the North-Western part of the Geneva region at the
6456 existing CERN laboratory. The proposed Interaction Region is fully located within existing
6457 CERN land at LHC Point 2, close to the village of St. Genis, in France. The CERN area is

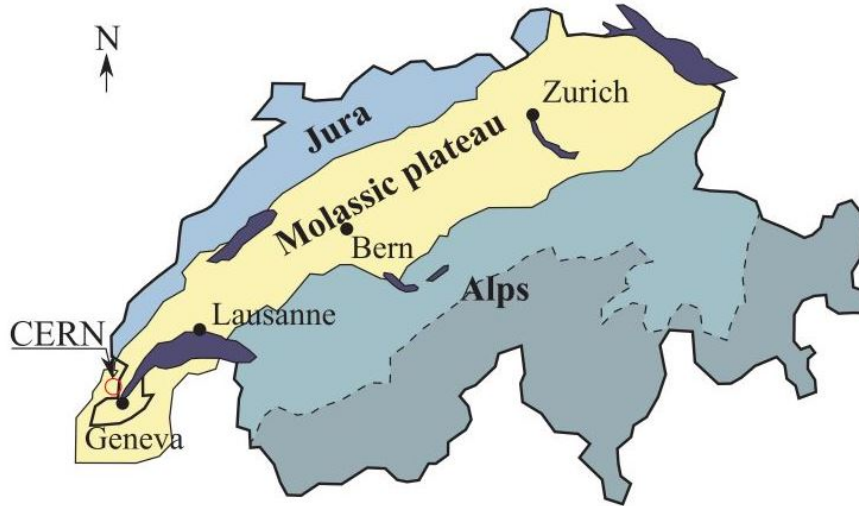


Figure 8.47: Simplified map of Swiss geology.

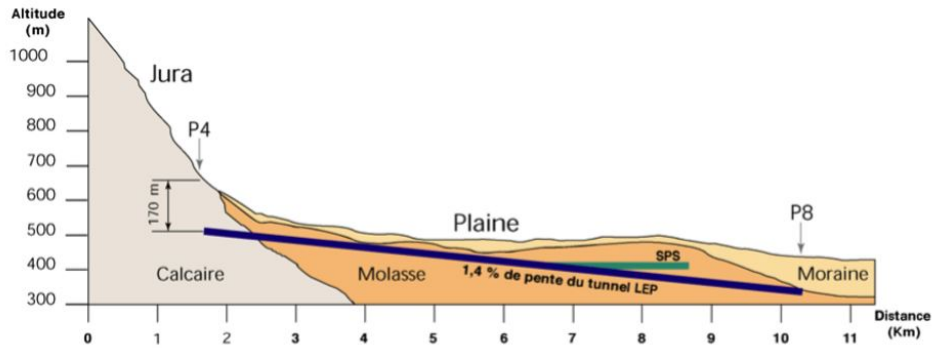


Figure 8.48: Geological profile of the LHC tunnel.

6458 extremely well suited to housing such a large project, with well understood ground conditions
 6459 having several particle accelerators in the region for over 50 years. Extensive geological records
 6460 exist from previous projects such as LEP and LHC and more recently, further ground inves-
 6461 tigations have been undertaken for the High-Luminosity LHC project. Any new underground
 6462 structures will be constructed in the stable molasse rock at a depth of 100–150 m in an area with
 6463 low seismic activity.

6464 The LHeC is situated within the Geneva basin, a sub-basin of the large molassic plateau
 6465 (Fig. 8.47). The molasse is a weak sedimentary rock which formed from the erosion of the
 6466 Alps. It comprises of alternating layers of marls and sandstones (and formations of intermediate
 6467 compositions), which show a high variety of strength parameters [723]. The molasse is overlaid
 6468 by the Quaternary glacial moraines. A simplified geological profile of the LHC is shown in
 6469 Fig. 8.48. Although placed mainly within the molasse plateau, one sector of the LHC is situated
 6470 in the Jura limestone.

6471 The physical positioning of the LHeC has been developed based on the assumption that the
 6472 maximum underground volume should be placed within the molasse rock and should avoid as
 6473 much as possible any known geological faults or environmentally sensitive areas. Stable and
 6474 dry, the molasse is considered a suitable rock type for TBM excavation. In comparison, CERN

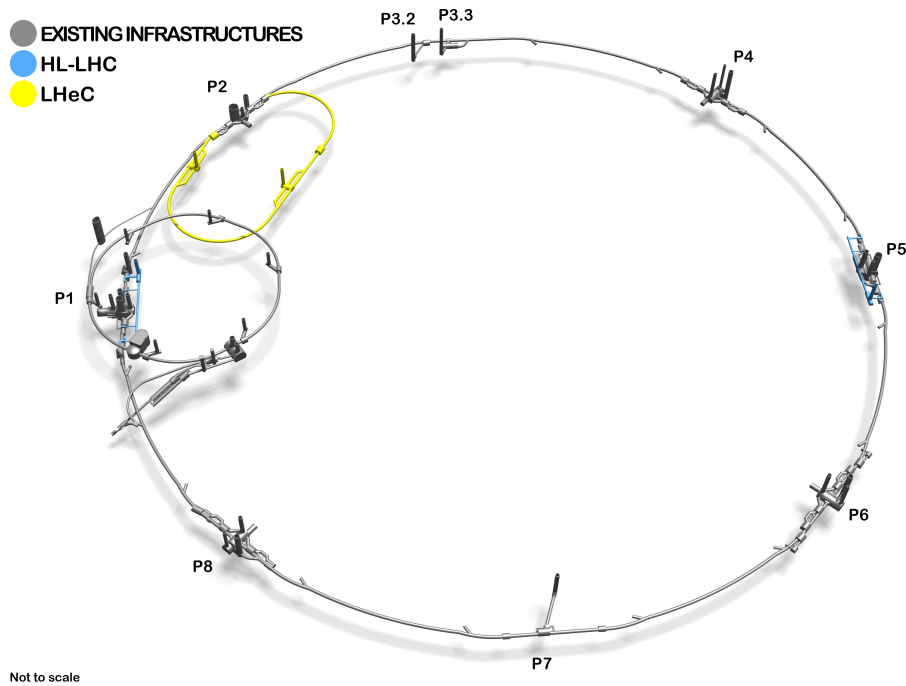


Figure 8.49: 3D Schematic showing proposed underground structures of LHeC (shown in yellow). The HL-LHC structures are highlighted in blue.

6475 has experienced significant issues with the underground construction of sector 3-4 in the Jura
 6476 limestone. There were major issues with water ingress at and behind the tunnel face [724].
 6477 Another challenging factor for limestone is the presence of karsts. These are formed by chemical
 6478 weathering of the rock and often they are filled with water and sediment, which can lead to
 6479 water infiltration and instability of the excavation.

6480 The ERL will be positioned inside the LHC layout, in order to ensure that new surface facilities
 6481 are located on existing CERN land. The proposed underground structures for a Large Hadron
 6482 electron Collider (LHeC) at high luminosity aiming for an electron beam energy of 60 GeV are
 6483 shown in Fig. 8.49. The LHeC tunnel will be tilted similarly to the LHC at a slope of 1.4% to
 6484 follow a suitable layer of molasse rock.

6485 8.8.2 Underground infrastructure

6486 The underground structures proposed for LHeC option 1/3 LHC require a 9 km long tunnel
 6487 including two LINACs. The internal diameter of the tunnel is 5.5 m. Parallel to the LINACs, at
 6488 10m distance apart, there are the RF galleries, each 1070 m long. Waveguides of 1 m diameter
 6489 and four connection tunnels are connecting the RF galleries and LINACs. These structures are
 6490 listed in Tab. 8.27. Two additional caverns, 25 m wide and 50 m long are required for cryogenics
 6491 and technical services. These are connected to the surface via two 9m diameter shafts, provided
 6492 with lifts to allow access for equipment and personnel. Additional caverns are needed to house
 6493 injection facilities and a beam dump. As shown in Tab. 8.27, the underground structures
 6494 proposed for LHeC options 1/5 LHC and 1/3 LHC are similar with the exception of the main
 6495 tunnel and the RF galleries which have different lengths.

6496 Shaft locations were chosen such that the surface facilities are located on CERN land. The scope
 6497 of work for surface sites is still to be defined. New facilities are envisaged for housing technical

Structure	Quantities	Span [m]	1/3 LHC	1/5 LHC
			Length [m]	Length [m]
Machine tunnels	-	5.5	9000	5400
Service caverns	2	25	50	50
Service shafts	2	9	80	80
Injection caverns	1	25	50	50
Dump cavern	1	16.8	90	90
Junction caverns	3	16.8	20	20
RF galleries	2	5.5	1070	830
Waveguide connections	50	1	10	10
Connection tunnels	4	3	10	10

Table 8.27: List of underground structures for LHeC for two different options with 1/3 or 1/5 of the LHC circumference.

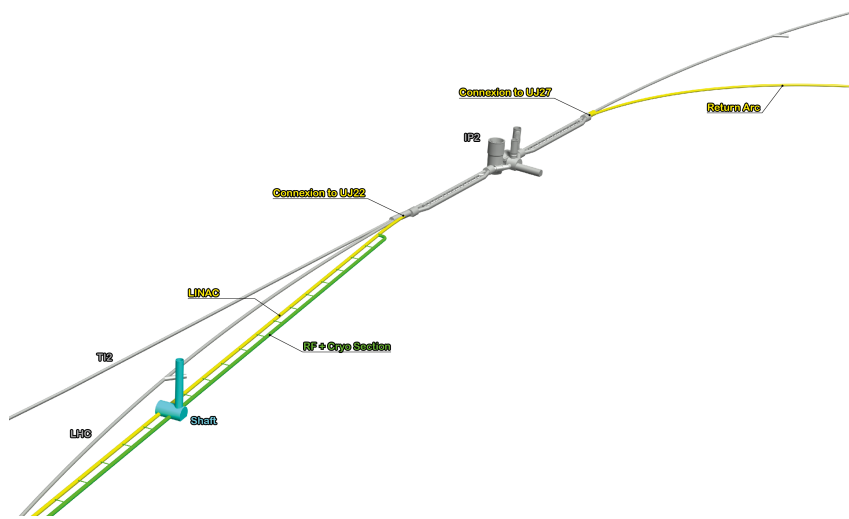


Figure 8.50: ERL injection area into IP2 and junction cavern

6498 services such as cooling and ventilation, cryogenics and electrical distribution.

6499 In addition to the new structures, the existing LHC infrastructure requires some modifications.
 6500 To ensure connection between LHC and LHeC tunnels, the junction caverns UJ22 and UJ27
 6501 need to be enlarged. Fig. 8.50 shows the location of these caverns. Localised parts of the cavern
 6502 and tunnel lining will be broken out to facilitate the excavation of the new spaces and the new
 6503 connections, requiring temporary support.

6504 Infrastructure works for LEP were completed in 1989, for which a design lifespan of 50 years
 6505 was specified. If the LHC infrastructure is to be re-used, refurbishment and maintenance works
 6506 are needed.

6507 8.8.3 Construction Methods

6508 A Tunnel Boring Machines (TBM) would be utilised for the excavation of the main tunnel to
 6509 achieve the fastest construction. When ground conditions are good and the geology is consistent,
 6510 TBMs can be two to four times faster than conventional methods. A double shield TBM could



Figure 8.51: Left: Roadheader being used for shaft excavation at HL-LHC Point 1. Right: Rockbreaker used for new service tunnels excavation at HL-LHC Point 5 (Credit: Z. Arenas).

6511 be employed, installing pre-cast segments as primary lining, and injecting grouting behind the
 6512 lining.

6513 For the excavation of the shafts, caverns and connection tunnels, typical conventional techniques
 6514 could be used. Similar construction methods used during HL-LHC construction can be adopted
 6515 for LHeC, for example using roadheaders and rockbreakers. This machinery is illustrated in
 6516 Fig. 8.51, showing the excavation works at Point 1. One main constraint that dictated what
 6517 equipment to be used for the HL-LHC excavation, was the vibration limit. Considering the
 6518 sensitivity of the beamline, diesel excavators have been modified and equipped with an electric
 6519 motor in order to reduce vibrations that could disrupt LHC operation. Similar equipment could
 6520 be required for LHeC, if construction works are carried out during operation of the LHC.

6521 Existing boreholes data around IP2 shows that the moraines layer is approximately 25–35 m deep
 6522 before reaching the molasse. Temporary support of the excavation, for example using diaphragm
 6523 walls is recommended. Once reaching a stable ground in dry conditions, common excavation
 6524 methods can be adopted. The shaft lining will consist of a primary layer of shotcrete with
 6525 rockbolts and an in-situ reinforced concrete secondary lining, with a waterproofing membrane
 6526 in between the two linings.

6527 8.8.4 Civil Engineering for FCC-eh

6528 A facility allowing collisions between protons and electrons was considered in the study for the
 6529 Future Circular Collider (FCC). Figure 8.52 shows the baseline position for FCC and the eh
 6530 machine located at Point L.

6531 During FCC feasibility stage, a bespoke GIS based tool (the Tunnel Optimisation Tool) was
 6532 used to optimise the placement and layout of the FCC ring. The current baseline location
 6533 was chosen such that the FCC tunnel avoids difficult geology (90% of the tunnel is placed in
 6534 molasse), the depth of the shafts and the overburden is minimised and tunnel under Geneva
 6535 Lake goes through the lake bed, passing through reasonably stable ground. More investigations
 6536 are needed to determine the feasibility of tunnelling under Geneva Lake. The baseline position
 6537 also allows connections to the LHC. Figure 8.53 shows the geological profile of the tunnel in
 6538 baseline position. The Tunnel Optimisation Tool (TOT) was used to evaluate different layouts
 6539 and positions for the FCC ring and assess the impact on the location of the eh machine. The
 6540 candidate locations for the eh tunnels were the experimental points A, B, G and L. Point L
 6541 was selected because it provides good geological conditions, being fully buried in the molasse

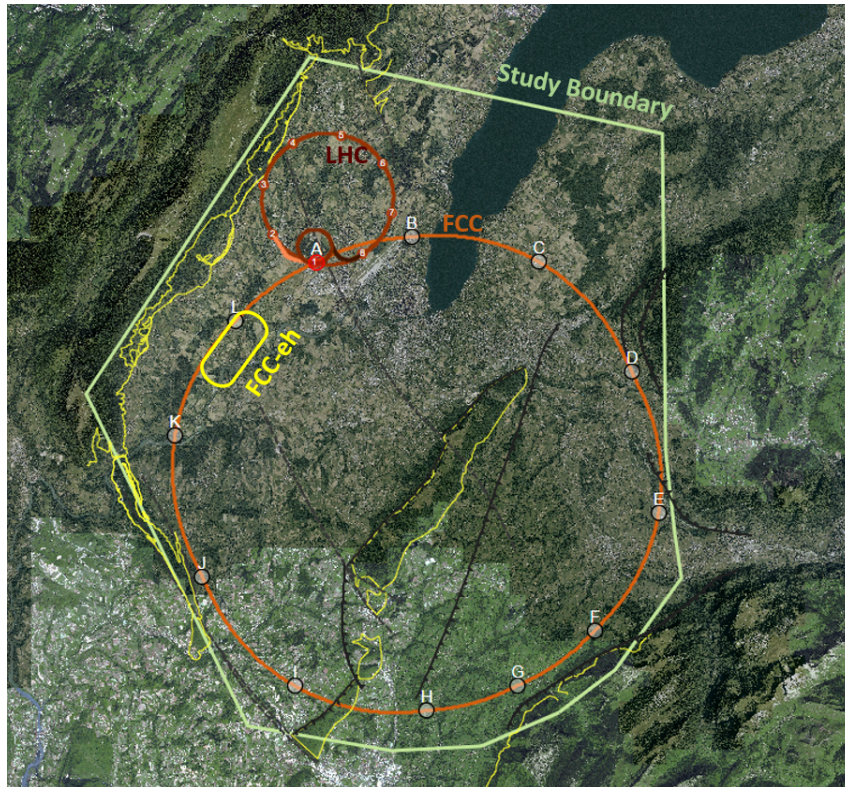


Figure 8.52: Baseline position and layout for FCC. FCCeh location is shown at Point L.

6542 layer at a depth of 180m. In comparison, Point G is much deeper, Point A is challenging due
 6543 to proximity of the LHC and Point B is located in a congested urban area. Similarly to LHeC,
 6544 the eh machine will be located inside the FCC ring, in this instance to avoid the Jura limestone.
 6545 The entire FCC-eh infrastructure is located in the molasse.

6546 The geological data captured within the tool was collected from various sources including previ-
 6547 ous underground projects at CERN, the French Bureau de Recherches Géologiques et Minières
 6548 (BRGM), and existing geological maps and boreholes for geothermal and petroleum exploration.
 6549 The data was processed to produce rock-head maps and to create the geological layers. No
 6550 ground investigations have been conducted specifically for the FCC project [725]. In order to
 6551 validate its baseline alignment and determine the geotechnical parameters required for the de-
 6552 tailed design, site investigation campaigns will be carried out. The Site investigations will start
 6553 with the high risk areas (shown in red in Fig. 8.54) which can have a high impact on the tunnel
 6554 alignment. Figure 8.54 puts in perspective the current availability of data and understanding of
 6555 the geology along FCC ring. Some boreholes exist in the region of Point L, reducing the uncer-
 6556 tainty of the ground conditions. However, further ground investigations are needed in order to
 6557 verify the boundary between geological layers. The geological features of interest around Point
 6558 L are the Allondon Fault and possible zones of poor rock and level of limestone, which should
 6559 be avoided.

6560 The collision point will be in the experimental cavern at point L, defined as an experimental
 6561 point for FCC-hh. The layout of the ERL and the underground infrastructure for the FCC-eh
 6562 is similar to LHeC (see Table 8.27), with the exception of the shafts which are 180m deep.
 6563 The schematic layout and proposed civil engineering structures are shown in Fig. 8.55. The
 6564 initial excavation for each shaft will be through the moraines. Based on available geological

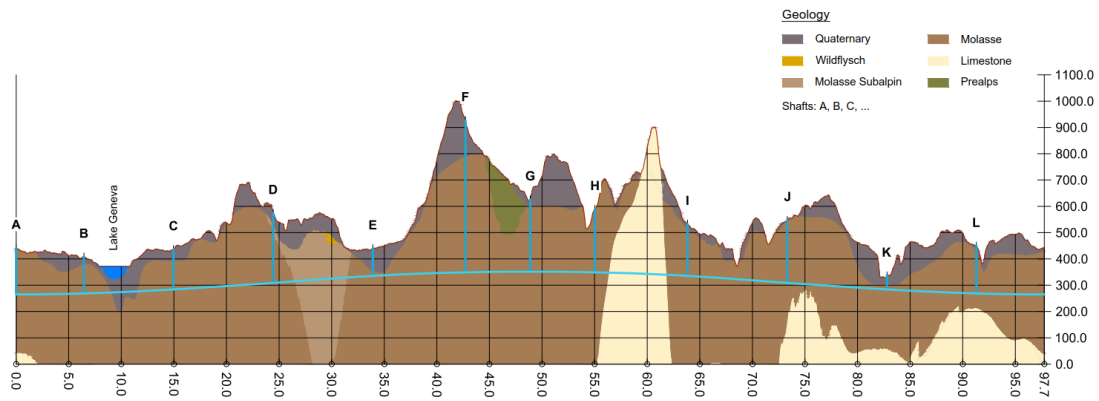


Figure 8.53: Geological profile along FCC tunnel circumference

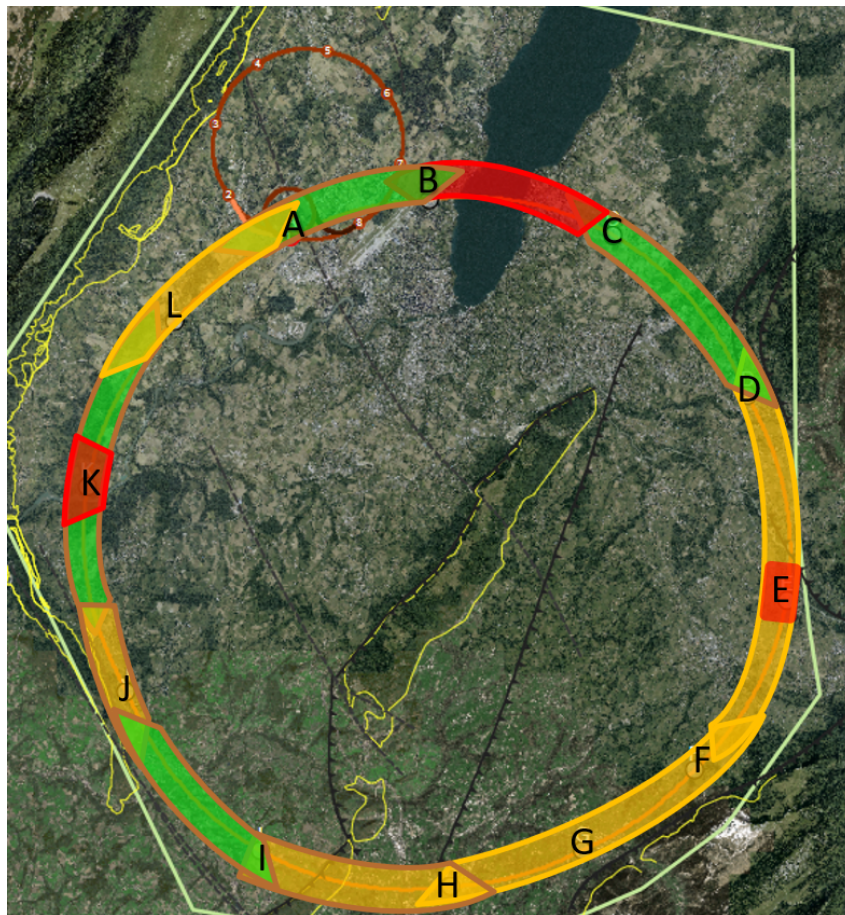


Figure 8.54: Geological risks along FCC ring. Green indicates the available information is reliable and the alignment is not in close proximity to a boundary between geology types. Amber indicates that either the data is lacking in the area or the alignment is close to a geographical boundary. Red indicates the high risk areas where there is a significant lack of data and proximity to a geological boundary

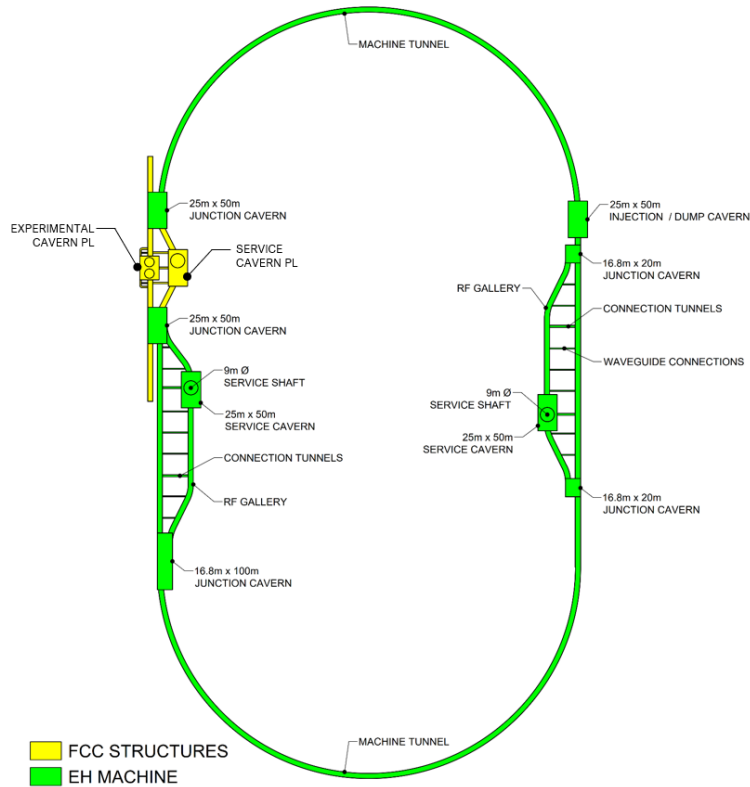


Figure 8.55: Schematic showing proposed underground structures for FCC-eh

6565 data, the moraines layer should be approximately 30m deep. Similar construction methods as
 6566 described in Section 8.8.3 could be used. For FCC, the alternative technology that has been
 6567 considered for deep shafts is using a Vertical Shaft Sinking Machine. In addition, the new
 6568 junction caverns connecting the eh tunnel with the FCC tunnel must be designed such that they
 6569 fit the requirements for the new collider and allow integration with to eh machine. The junction
 6570 caverns near Point L will connect three tunnels, the FCC main tunnel, the eh machine tunnel
 6571 and the RF galleries. These caverns are 25 m span and 50 m long.

6572 For the FCC TBM excavations, different lining designs have been developed corresponding to
 6573 conditions of the rock [725]. Good ground conditions have been assumed based on available
 6574 geological information in the area where the eh machine tunnels are positioned, therefore a
 6575 single-pass pre-cast lining is proposed.

6576 8.8.5 Cost estimates

6577 The cost for underground civil engineering for FCC-eh facility was estimated to 430 MCHF.
 6578 The construction programme for eh tunnels, caverns and shafts is currently integrated into the
 6579 overall FCC construction schedule.

6580 A detailed cost estimate was prepared for a 9 km ERL located at Point 2 of LHC, using the
 6581 same unit prices as for FCC. More recently for LHeC, the cost figures were adapted to fit the
 6582 smaller version, the 5.4 km racetrack at Point 2 (option 1/5 LHC). The civil engineering costs
 6583 amount to about 25 % of the total project costs. The 9 km ERL (1/3 LHC option) the civil
 6584 engineering was estimated to 386 MCHF and for a 5.4 km configuration (1/5 LHC) the costs

6585 would be 289MCHF. These costs do not include surface structures. Where possible, existing
6586 surface infrastructure will be re-used.

6587 The cost estimates include the fees for preliminary design, approvals and tender documents
6588 (12%), site investigations (2%) and contractor's profit (3%).

6589 **8.8.6 Spoil management**

As with all construction projects, environmental aspects play an important role. A detailed study is being conducted at CERN to find a potential re-use for of the spoil that will be generated from the FCC underground excavations. The amount of spoil calculated is approximately 10 million cubic meters, of which 778,000 cubic metres of spoil would be generated from the eh tunnel construction.

Chapter 9

Technology of ERL and PERLE

9.1 Energy Recovery Linac Technology - Status and Prospects

In instances where high beam power is required, the concept of energy recovery presents an attractive solution. Energy recovering linacs (ERLs) are a class of novel accelerators which are uniquely qualified to meet the demands for a wide variety of applications by borrowing features from traditional architectures to generate linac quality beams with near storage ring efficiency [726]. After acceleration through a linac section, the electrons in an ERL are returned 180° out of phase with respect to the radio frequency (RF) accelerating field for energy recovery. The beam deposits energy into cavity fields, which can then accelerate newly injected bunches, thereby effectively canceling the beam loading effects of the accelerated beam. Therefore ERLs can accelerate very high average currents with only modest amounts of RF power. Because the beam is constantly being renewed, it never reaches an equilibrium state. Consequently this provides flexibility to manipulate the phase space and tailor the beam properties for a specific application. Further, since the energy of the decelerated beam is approximately equal to the injection energy, the dump design becomes considerably easier.

9.1.1 ERL Applications

Historically, nearly all ERLs built and operated were used to drive a free-electron laser (FEL). The requirement for high peak current bunches necessitated bunch compression and handling the attendant beam dynamical challenges. In recent years, ERLs have turned from being drivers of light sources toward applications for nuclear physics experiments, Compton backscattering sources and strong electron cooling. Unlike an FEL, these latter use cases require long, high charge bunches with small energy spread. Where once a short bunch length was the key performance metric, now there is a premium on maintaining a small correlated energy spread (with a commensurately long bunch).

9.1.2 Challenges

Energy recovery linacs are not without their own set of challenges. In the following sections a brief survey of some of the most relevant are given. These include collective effects, such as space charge, the multipass beam breakup (BBU) instability, coherent synchrotron radiation (CSR) and the microbunching instability (μ BI), beam dynamic issues such as halo, the interaction of

6620 the beam with the RF system and other environmental impedances as well as issues related to
6621 common transport lines.

6622 **Space Charge**

6623 The role of space charge forces (both transverse and longitudinal) often dictate many operational
6624 aspects of the machine. Maintaining beam brightness during the low energy injection stage is
6625 vitally important. In addition to the low energy, ERL injectors must also preserve beam quality
6626 through the merger system that directs the beam to the linac axis. Once injected into the
6627 linac, the beam energy at the front end is often still low enough that space charge forces cannot
6628 be neglected. Just as important is the longitudinal space charge (LSC) force which manifests
6629 itself by an energy spread asymmetry about the linac on-crest phase [727]. The LSC wake acts
6630 to accelerate the head of the bunch while decelerating the tail. Operating on the rising part
6631 of the waveform leads to a decrease in the correlated energy spread, while accelerating on the
6632 falling side leads to an increase. These observations inform where acceleration, and how the
6633 longitudinal match, is performed.

6634 **Beam Breakup Instability**

6635 The beam breakup instability is initiated when a beam bunch passes through an RF cavity
6636 off-axis, thereby exciting dipole higher-order modes (HOMs). The magnetic field of an excited
6637 mode deflects following bunches traveling through the cavity. Depending on the details of the
6638 machine optics, the deflection produced by the mode can translate into a transverse displacement
6639 at the cavity after recirculation. The recirculated beam induces, in turn, an HOM voltage which
6640 depends on the magnitude and direction of the beam displacement. Thus, the recirculated beam
6641 completes a feedback loop which can become unstable if the average beam current exceeds the
6642 threshold for stability [728]. Beam breakup is of particular concern in the design of high average
6643 current ERLs utilizing superconducting RF (SRF) technology. If not sufficiently damped by the
6644 HOM couplers, dipole modes with quality factors several orders of magnitude higher than in
6645 normal conducting cavities can exist, providing a threat for BBU to develop. For single pass
6646 ERLs, beam optical suppression techniques – namely, interchanging the horizontal and vertical
6647 phase spaces to break the feedback loop between the beam and the offending HOM – are effective
6648 at mitigating BBU [729].

6649 **Coherent Synchrotron Radiation**

6650 Coherent synchrotron radiation poses a significant challenge for accelerators utilizing high bright-
6651 ness beams. When a bunch travels along a curved orbit, fields radiated from the tail of the bunch
6652 can overtake and interact with the head. Rather than the more conventional class of head-tail
6653 instabilities where the tail is affected by the actions of the head, CSR is a tail-head instability.
6654 The net result is that the tail loses energy while the head gains energy leading to an undesirable
6655 redistribution of particles in the bunch. Because the interaction takes place in a region of dis-
6656 persion, the energy redistribution is correlated with the transverse positions in the bend plane
6657 and can lead to projected emittance growth. While there has been much progress in recent years
6658 to undo the effects of CSR in the bend plane with an appropriate choice of beam optics [730],
6659 it is more difficult to undo the gross longitudinal distortion caused by the CSR wake. This is
6660 particularly true in applications where the intrinsic energy spread is small and/or where the

6661 effect can accumulate over multiple recirculations. One possible mitigation is shielding the CSR
6662 wake using an appropriately sized beam pipe [731].

6663 **Microbunching Instability**

6664 Microbunching develops when an initial density modulation, either from shot noise or from the
6665 drive laser, is converted to energy modulations through short-range wakefields such as space
6666 charge and CSR. The energy modulations are then transformed back to density modulations
6667 through the momentum compaction of the lattice. Danger arises when a positive feedback is
6668 formed and the initial modulations are enhanced. This phenomenon has been studied exten-
6669 sively, both theoretically and experimentally, in bunch compressor chicanes [732, 733]. Only
6670 recently has there been a concerted effort to study the microbunching instability in recirculating
6671 arcs [734–736]. Because the beam is subject to space charge and/or CSR throughout an ERL,
6672 density modulations can be converted to energy modulations. And because of the native mo-
6673 mentum compaction of the lattice (in arcs, spreaders/recombiners, chicanes, etc.) those energy
6674 modulations may be converted back to density modulations. Therefore, ERLs offer potentially
6675 favorable conditions for seeding the microbunching instability, which requires careful attention
6676 in the early design stages.

6677 **Halo**

6678 Halo is defined as the relatively diffuse and potentially irregularly distributed components of
6679 beam phase space that can reach large amplitudes. It is of concern because ERL beams are
6680 manifestly non-Gaussian and can have beam components of significant intensity beyond the
6681 beam core [737]. Though sampling large amplitudes, halo responds to the external focusing of
6682 the accelerator transport system in a predictable manner. It is therefore not always at large
6683 spatial amplitude, but will at some locations instead be small in size but strongly divergent.
6684 Halo can therefore present itself as *hot spots* in a beam distribution, and thus may be thought
6685 of as a lower-intensity, co-propagating beam that is mismatched to the core beam focusing,
6686 timing, and energy. Beam loss due to halo scraping is perhaps the major operational challenge
6687 for higher-power ERLs. Megawatt-class systems must control losses at unshielded locations to
6688 better than 100 parts-per-million to stay within facility radiation envelopes. Scaling to 100 MW
6689 suggests that control must be at the part-per-million level. This has been demonstrated – but
6690 only at specific locations within an ERL [738].

6691 **RF Transients**

6692 Dynamic loading due to incomplete energy recovery is an issue for all ERLs [739]. In some
6693 machines it is due to unintentional errors imposed on the energy recovered beam; for instance,
6694 path length errors in large-scale systems. In other machines, such as high power ERL-based FEL
6695 drivers, it is done intentionally. In cases where there is the potential for rapid changes in the
6696 relative phase of the energy recovered beam, dynamic loading would be difficult to completely
6697 control using fast tuners. In such cases adequate headroom in the RF power will have to be
6698 designed into the system. These transient beam-loading phenomena are widely unrecognized
6699 and/or neglected. RF drive requirements for an ERL are often viewed as *minimal*, because in
6700 steady-state operation the recovered beam notionally provides RF power for acceleration. It
6701 has however been operationally established that RF drive requirements for ERLs are defined

6702 not by the steady-state, but rather by beam transients and environmental/design factors such
6703 as microphonics [740]. As a result, the RF power required for stable ERL operation can differ
6704 dramatically from naïve expectations.

6705 **Wakefields and Interaction of Beam with Environment**

6706 As with other system architectures intended to handle high-brightness beams, ERLs can be
6707 performance-limited by wakefield effects. Not only can beam quality be compromised by in-
6708 teraction of the beam with environmental impedances, there is also significant potential for
6709 localized power deposition in beamline components. Resistive wall and RF heating have proven
6710 problematic during ERL operation in the past [741]. Extrapolation of this experience to higher
6711 bunch charges and beam powers leads to serious concern regarding heating effects. Careful
6712 analysis and management of system component impedances is required.

6713 **Multi-turn, Common Transport**

6714 Future systems must evolve to utilize multiple turns; it is a natural cost optimization method [742]
6715 and multi-turn systems can in principle provide performance equal to that of 1-pass up/down
6716 ERLs at significantly lower cost. In addition to the use of multiple turns, cost control motivates
6717 use of extended lengths of common transport, in which both accelerated and recovered passes
6718 are handled simultaneously using the same beam lines. This presents unique challenges for high
6719 energy ERLs, like LHeC in particular, where energy loss due to synchrotron radiation cannot
6720 be ignored and causes an energy mismatch for common transport lines. But addressing these
6721 challenges will open up exciting new opportunities for ERLs. In addition to PERLE and LHeC,
6722 a multi-turn ERL design from Daresbury illustrates the manner in which the cost/complexity
6723 optimum lies toward shorter linacs, more turns, and multiple beams in fewer beam lines [743].
6724 This also drives the use of multiple turns in stacking rings for hadron cooling; the more turns
6725 the cooling beam can be utilized, the lower the current required from the driver ERL, which
6726 mitigates challenges associated with source lifetime [744].

6727 **9.1.3 ERL Landscape**

6728 One way to view the current state of ERLs globally is the so-called *ERL landscape* shown in
6729 Fig. 9.1 [745]. Every data point represents a machine that demonstrated energy recovery and is
6730 positioned in (maximum) energy and (average) current parameter space. For clarity, the plot is
6731 restricted to continuous-wave (CW), SRF-based ERLs only and includes legacy machines, those
6732 under construction and currently in operation as well as the LHeC and PERLE (proposed).
6733 The size of the marker is indicative of the charge per bunch while a black line around the
6734 marker indicates it was/is a *true ERL*. That is, where the beam power exceeds the installed
6735 RF power (they are represented in the plot by the three FEL drivers that were designed, built,
6736 commissioned and operated at Jefferson Laboratory).

6737 A cursory look at Fig. 9.1 illustrates several of the challenges facing the next generation of
6738 ERLs. While getting from the current state-of-the-art to the LHeC requires only a modest
6739 increase in average current, it requires a significant increase in bunch charge and addressing
6740 the consequent collective effects [746]. Most significantly, however, is the leap in energy from
6741 systems that have operated in the 100 MeV range to several tens of GeV. Note that PERLE is
6742 strategically positioned to address incremental changes in both average current, bunch charge

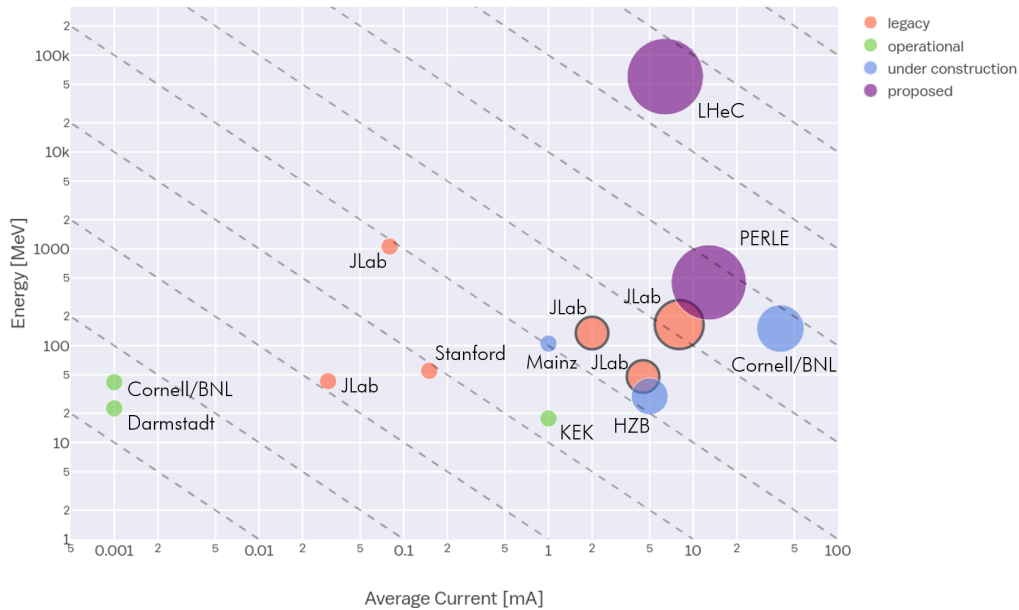


Figure 9.1: The *ERL landscape*, where data points are restricted to CW, SRF-based ERLs. The dashed lines represent lines of constant beam power – starting from 10 W in the lower left and going to 10 GW in the upper right. Note that both axes use a log scale.

6743 and energy. As such, it provides a convenient test bed facility to address the issues described
 6744 previously [747]. Several ERLs are still in the nascent stages and as they ramp up beam power,
 6745 will also be valuable in advancing the state-of-the-art. For instance, though it uses a Fixed Field
 6746 Alternating Gradient (FFAG) arc, the Cornell/Brookhaven ERL Test Accelerator (CBETA) will
 6747 address multi-turn energy recovery for the first time in an SRF system [748]. Note that with
 6748 only minor modifications Jefferson Laboratory’s Continuous Electron Beam Accelerator Facility
 6749 (CEBAF) could be operated with multi-pass energy recovery at several GeV using common
 6750 transport with the same topology as LHeC (i.e. bisected linacs of equal energy gain with arcs
 6751 vertically separated by energy using spreaders and recombiners) [749].

6752 9.2 The ERL Facility PERLE

6753 PERLE is a compact three-pass ERL based on SRF technology, a new generation machine
 6754 uniquely covering the 10 MW power regime of beam current and energy. Its Conceptual Design
 6755 Report appeared recently [4]. Apart from low energy experiments it could host, thanks to its
 6756 beam characteristics, PERLE will serve as a hub for the validation of a broad range of accelerator
 6757 phenomena and the development of ERL technology for future energy frontiers colliders which
 6758 was introduced above. Particularly, the basic 3-turn configuration, design challenges and beam
 6759 parameters (see Tab. 9.1) are chosen to enable PERLE as a testbed for the injection line and
 6760 SRF technology development, as well as multi-turn and high current ERL operation techniques
 6761 for the Large Hadron electron Collider. While the concept and promise of ERL’s has been
 6762 kick-started by demonstration machines based on existing accelerator technology, PERLE will
 6763 be the first machine designed from the ground up to use fully optimised ERL-specific designs
 6764 and hardware.

6765 The PERLE collaboration involves today CERN, Jefferson Laboratory, STFC-Daresbury, Uni-
 6766 versity of Liverpool, BINP-Novosibirsk and the newly formed Irene Curie Lab at Orsay. Four

6767 of these international partners have been pioneering the development of ERL technology, the
6768 other are leading laboratories on SRF technology and accelerator physics. The Orsay Lab is
6769 leading the effort to develop and later host PERLE at Orsay campus in close collaboration with
6770 the LHeC coordination.

6771 The following PERLE summary focuses on the power challenge, the lattice, site and time sched-
6772 ule. PERLE uses a cryo-module with four 5-cell cavities like the LHeC. The prototype cavity
6773 production and test as well as the design status of the cryo-module are described in the LHeC
6774 linac chapter. There one also finds a section on the source and injector and as well arc magnets,
6775 dipoles of a 3-in-1 design and quadrupoles, which will similarly be used for PERLE.

6776 9.2.1 Configuration

6777 In its final configuration, a high average current electron beam (20 mA) is accelerated through
6778 three passes to the maximum energy (500 MeV) in the superconducting RF CW linear acceler-
6779 ators. The beam is then used for its intended purpose such as photon generation by Compton
6780 back-scattering, a cooling source for ion beams or a beam for colliding against fixed targets. The
6781 3-passes up in energy may significantly increase the energy spread or emittance of the electron
6782 beam but the major part of the beam power remains. The beam is then sent back through the
6783 accelerators again only this time roughly 180 degrees off the accelerating RF phase so the beam
6784 is decelerated through the same number of passes and then sent to a beam dump at around the
6785 injection energy. Several benefits arise from this configuration: the required RF power (and its
6786 capital cost and required electricity) is significantly reduced to that required to establish the
6787 cavity field; the beam power that must be dissipated in the dump is reduced by a large factor,
6788 and often the electron beam dump energy can be reduced below the photo-neutron threshold so
6789 that activation of the dump region can be reduced or eliminated.

6790 9.2.2 Importance of PERLE towards the LHeC

6791 PERLE is an important and necessary step accompanying the LHeC realisation. Together
6792 with other ERL facilities, CBETA, bELRin-Pro and possibly others, it will bridge the gap of
6793 power level between the currently reached maximum (CEBAF-ER at 1 MW) and the targeted
6794 performances of LHeC (1 GW) by exploring a next higher operational power regime of around
6795 10 MW. Moreover, sharing the same conceptual design with the LHeC, a racetrack configuration
6796 with 3 acceleration and 3 deceleration passes, identical injection line and the same SRF system,
6797 as well as the same beam current in the SRF cavities will allow to acquire with PERLE an
6798 enormous insight on multiple pass operation and common transport from full energy, before and
6799 possibly during LHeC operation too.

6800 Up to date, existing SRF systems have demonstrated stability at only a modest fraction ($\leq 20\%$)
6801 of the current envisaged for the LHeC. Though threshold currents have been indirectly measured
6802 at higher values, there is no direct evidence that multi-pass systems will be sufficiently resistant
6803 to BBU at the higher current, nor has the sensitivity of the instability threshold to linac length,
6804 dynamic range, and number of passes been directly or systematically measured as yet. PERLE
6805 will provide a single datum on linac length, and can directly measure the dependence on the
6806 number of passes and the turn-to-turn transfer matrix.

6807 The dynamic range (which is the ratio of injected/extracted energy to full energy) is a critical
6808 design parameter, in as much as it defines the sensitivity of the overall system to magnetic

6809 field errors. Errors at full energy drive phase/energy errors that are magnified by adiabatic
6810 anti-damping during recovery, and can exceed the dump acceptance should the errors be too
6811 large. Thus, the field quality needed is inversely proportional to the ratio of full energy to dump
6812 energy: that is, a very high energy machine (or one with very low dump energy) needs very
6813 high-quality magnets. For PERLE, the dynamic range is 70 : 1 (7 MeV injected and 490 MeV
6814 full energy). This implies a need of $\Delta B/B_{dipole} \simeq 0.001\%$ field flatness (extrapolated from JLAB
6815 ERL needs) to recover cleanly enough. This implies a tight constraint on magnet performances
6816 and impact their cost, even when it is the SRF which drives the overall cost of the facility,
6817 for LHeC. PERLE has a very large dynamic range and a transport system with considerable
6818 symmetry and flexibility. It is therefore a suitable tool to explore this issue and evaluate the
6819 cost implications for larger scale systems.

6820 Existing systems have operated at maximum 1 MW full beam power. This is too low for a precise
6821 understanding and control of beam halo. Extrapolation to 10 MW will demand suppression of
6822 localised losses to, or below, parts per million. Higher power requires a lower fractional loss.
6823 It is not yet well understood how to do this - in particular, collimation systems require a more
6824 optimised control of CW losses at rates observed in linacs. PERLE will provide a platform
6825 on which the next step in understanding can be taken. Other halo effects may become visible
6826 at only the higher CW powers under consideration in PERLE (including Touschek and intra-
6827 beam scattering, beam-gas scattering, and ion trapping). These lead to scattering events that
6828 adiabatically anti-damp and result in intolerable loss in the back end of the machine, limiting
6829 dynamic range. There is no experience with these phenomena, although theoretical studies
6830 suggest they are problematic. PERLE will be the first system capable of directly exploring
6831 these issues.

6832 There are many collective effects that have proven challenging at lower beam powers - including
6833 RF heating, resistive wall heating, THz emission heating... - that will have greater impact at
6834 both higher power and higher energy. There are at present no operating ERL systems that can
6835 study these. PERLE is the only system proposed or under construction that combines sufficient
6836 beam power with sufficient operational flexibility to study and test mitigation algorithms and
6837 methods. Without PERLE, higher energy/power machines will have very little insight regarding
6838 these problems and lack the ability to test solutions.

6839 Beam quality preservation in the presence of collective effects is a significant challenge for modern
6840 machines. In particular, Longitudinal Space Charge (LCS), Coherent Synchrotron Radiation
6841 (CSR), and the micro-bunching instability have serious deleterious impact on performance, and
6842 can prevent a machine from producing beam consistent with user requirements - or, worse, from
6843 being able to operate at significant powers. PERLE probes the regions of parameter space
6844 where these effects are observable, and offers an opportunity to benchmark models and explore
6845 mitigation methods.

6846 9.2.3 PERLE Layout and Beam Parameters

6847 The PERLE accelerator complex is arranged in a racetrack configuration hosting two cryo-
6848 modules (containing four, five-cell cavities operating at 801.6 MHz frequency), each located in
6849 one of two parallel straights completed with a vertical stack of three recirculating arcs on each
6850 side. The straights are 10 m long and the 180° arcs are 5.5 m across. Additional space is taken
6851 by 4 m long spreaders/recombiners, including matching sections. As illustrated in Fig. 9.2, the
6852 total footprint of PERLE is: $24 \times 5.5 \times 0.8 \text{ m}^3$, accounting for 40 cm vertical separation between
6853 arcs. Each of the two cryo-modules provides up to 82 MeV energy boost per path. Therefore, in

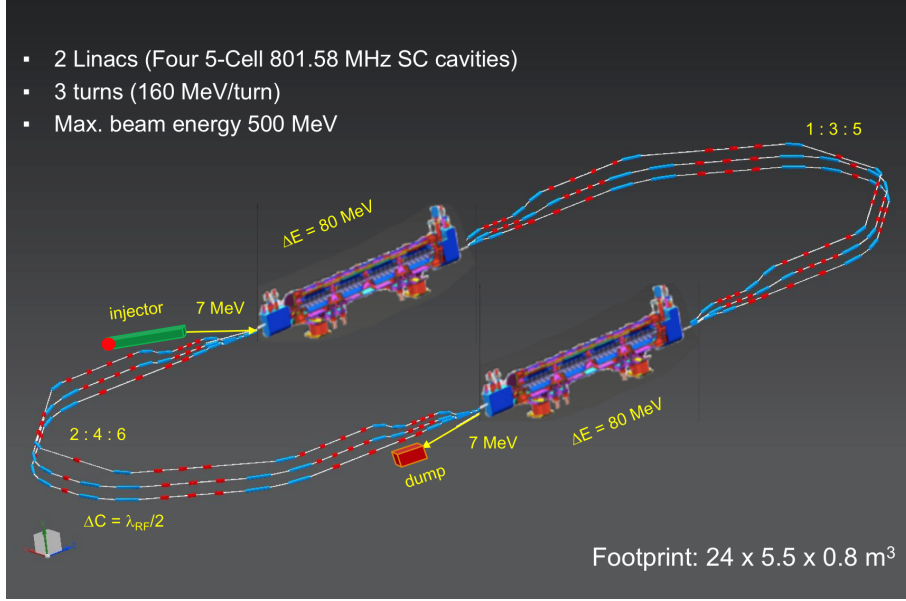


Figure 9.2: PERLE facility layout featuring two parallel linacs each hosting a cryomodule housing four 5-cell SC cavities, achieving 500 MeV in three passes, see text.

6854 three turns, a 492 MeV energy beam is generated. Adding the initial injection energy of 7 MeV
 6855 yields the total energy of approximately 500 MeV. The main beam parameters of PERLE facility
 are summarised in Tab. 9.1

Target parameter	Unit	Value
Injection energy	MeV	7
Electron beam energy	MeV	500
Norm. emittance $\gamma\epsilon_{x,y}$	mm-mrad	6
Average beam current	mA	20
Bunch charge	pC	500
Bunch length	mm	3
Bunch spacing	ns	25
RF frequency	MHz	801.6
Duty factor		CW

Table 9.1: Summary of main PERLE beam parameters.

6856

6857 As mentioned in the introduction, the essential PERLE parameters are the same as the LHeC.
 6858 The frequency choice, emittance, beam current and the time structure are chosen regarding the
 6859 requirements of the electron-proton collisions in the LHeC. Hereafter, we explain the choice of
 6860 the frequency for the LHeC and thus for PERLE.

6861 9.2.4 PERLE Lattice

6862 Multi-pass energy recovery in a racetrack topology explicitly requires that both the accelerat-
 6863 ing and decelerating beams share the individual return arcs (Fig. 9.2). Therefore, the TWISS
 6864 functions at the linac ends have to be identical, for both the accelerating and decelerating linac
 6865 passes converging to the same energy and therefore entering the same arc.

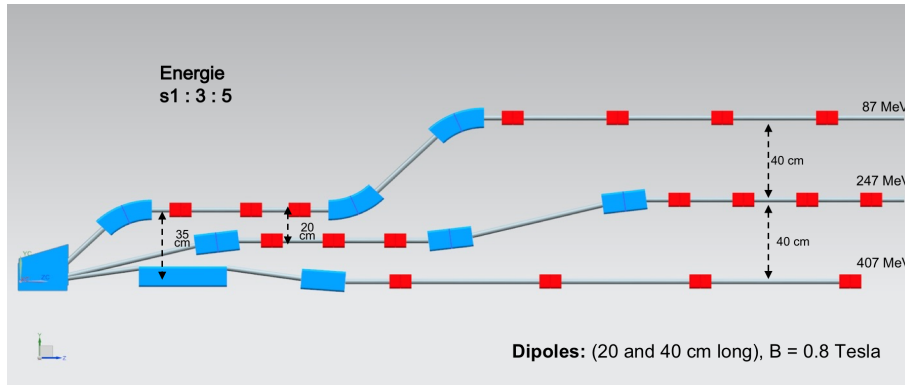


Figure 9.3: PERLE spreader design and matching to three circulating arcs.

6866 Injection at 7 MeV into the first linac is done through a fixed field injection chicane, with its
6867 last magnet (closing the chicane) being placed at the beginning of the linac. It closes the orbit
6868 bump at the lowest energy, injection pass, but the magnet (physically located in the linac) will
6869 deflect the beam on all subsequent linac passes. In order to close the resulting higher pass
6870 bumps, the so-called re-injection chicane is instrumented, by placing two additional bends in
6871 front of the last chicane magnet. This way, the re-injection chicane magnets are only visible by
6872 the higher pass beams. The spreaders are placed directly after each linac to separate beams of
6873 different energies and to route them to the corresponding arcs. The recombiners facilitate just
6874 the opposite: merging the beams of different energies into the same trajectory before entering
6875 the next linac. The spreader design (Fig. 9.3) consists of a vertical bending magnet, common
6876 for all three beams, that initiates the separation. The highest energy, at the bottom, is brought
6877 back to the horizontal plane with a chicane. The lower energies are captured with a two-step
6878 vertical bending. The vertical dispersion introduced by the first step bends is suppressed by the
6879 three quadrupoles located appropriately between the two steps. The lowest energy spreader is
6880 configured with three curved bends following the common magnet, because of a large bending
6881 angle (45°) the spreader is configured with. This minimises adverse effects of strong edge focusing
6882 on dispersion suppression in the spreader. Following the spreader there are four matching quads
6883 to bridge the TWISS function between the spreader and the following 180° arc (two betas and
6884 two alphas). All six, 180° horizontal arcs are configured with Flexible Momentum Compaction
6885 (FMC) optics to ease individual adjustment of M56 in each arc (needed for the longitudinal
6886 phase-space reshaping, essential for operation with energy recovery). The lower energy arcs (1,
6887 2, 3) are composed of four 45.6 cm long curved 45° bends and of a series of quadrupoles (two
6888 triplets and one singlet), while the higher arcs (4, 5, 6) use double length, 91.2 cm long, curved
6889 bends. The usage of curved bends is dictated by a large bending angle (45°). If rectangular
6890 bends were used, their edge focusing would have caused significant imbalance of focusing, which
6891 in turn, would have had adverse effect on the overall arc optics. Another reason for using curved
6892 bends is to eliminate the problem of magnet sagitta, which would be especially significant for
6893 longer, 91.2 cm, bends. Each arc is followed by a matching section and a recombiner (both
6894 mirror symmetric to previously described spreader and matching segments). As required in case
6895 of identical linacs, the resulting arc features a mirror symmetric optics (identical betas and sign
6896 reversed alphas at the arc ends).

6897 The presented arc optics with modular functionality facilitates momentum compaction manage-
6898 ment (isochronicity), as well as orthogonal tunability for both beta functions and dispersion.
6899 The path-length of each arc is chosen to be an integer number of RF wavelengths except for the
6900 highest energy pass, arc 6, whose length is longer by half of the RF wavelength to shift the RF

6901 phase from accelerating to decelerating, switching to the energy recovery mode.

6902 **9.2.5 The Site**

6903 The Irene Curie Lab Orsay intends to host PERLE. The footprint of this facility occupies a
6904 rectangle of $24 \times 5.5 \text{ m}^2$. This area should be enclosed by shielding at a sufficient distance to
6905 allow passage and maintenance operations. We estimate the required passage and half thickness
6906 of the accelerator component to 2 m. A concrete shielding is assumed here to stop photons and
6907 neutrons produced by halo electrons. A more detailed study of the radiation generated by the
6908 impinging electron will be necessary at a following stage. An increase of the shielding required
6909 could be alleviated by the use of denser materials.

6910 The PERLE operation at the design beam parameters (Tab. 9.1) required an in-depth study of
6911 the machine failure scenario to estimate the power left in the machine during operation after
6912 beam losses and how to handle and control it. The study aimed at looking if the PERLE facility
6913 will be classified as INB (Infrastructure Nucleaire de Base) or not, with respect to the French
6914 radioprotection and nuclear safety rules. This conclusion is crucial for the decision of hosting
6915 PERLE at Orsay as such INB facilities require heavy regulation procedures and a very high
6916 investment to fulfil the requirements and ensure the safety provisions to be implemented. The
6917 outcome of the study had concluded that PERLE shall not be considered as INB, even if the
6918 beam parameters are quite demanding, because for several failure scenarios the energy of the
6919 beam is brought back to the injection energy and safely dumped, thanks to the recovery mode.
6920 For other scenarios, hard interlocks and the machine safety system are fast enough to manage
6921 the situation. The complete report of this study has been delivered by the IRSD team at Orsay.

6922 Besides the central area required for machine implementation, space needs to be allocated for the
6923 auxiliary systems (power converters for magnets, septa and kickers, RF power, Water cooling,
6924 Cryogenics, Electron source, Dump). One has also to consider sufficient space for experiments
6925 that may use the PERLE beam. These have been sketched in the PERLE CDR [4]. As a rough
6926 estimate one would need to triple the area of the accelerator itself to accommodate all services,
6927 with shielding included. The building that is foreseen to host this version of PERLE is a former
6928 experimental hall (Super ACO). It is equipped with cranes and electricity. The ground of the
6929 building is made of concrete slabs with variable ground resistance. More than half of the hall
6930 area has a sufficient resistance to allow the installation PERLE. Being next to the tunnel of the
6931 old Orsay Linac and close to the *Igloo*, where new accelerators are being installed currently, the
6932 building is partially shielded and some equipment (water-cooling circuits, electrical transformer)
6933 can be shared with the other machines. The building gives the possibility to install the RF source
6934 and the power supplies at a different level than the accelerator. An existing control room that
6935 overlooks the experimental hall may be used for PERLE. Since all the accelerators installed
6936 nearby are based on warm technology, a cryogenic plant will be built. All the needed support
6937 for infrastructure could be assured by the CPER program. Altogether, this appears to be a well
6938 suitable place which has the great advantage to be available.

6939 **9.2.6 Staging Strategy and Time Schedule**

6940 The PERLE configuration (Cf. Fig. 9.2) entails the possibility to construct PERLE in stages,
6941 starting by installing a single linac in the first straight and initially replacing the second one
6942 by beam lines. Such a consideration is determined by the existence of the SPL cryomodule
6943 at CERN (see the discussion in Chapter 9), which will permit a rather rapid realisation of a

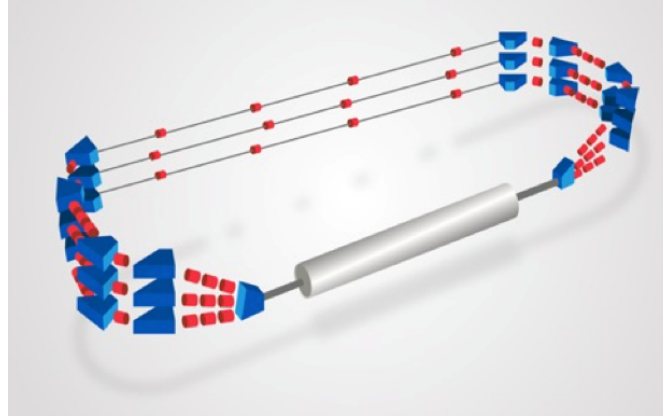


Figure 9.4: PERLE-Phase 1 layout featuring a single Linac in the first straight and beam line in the second straight, achieving 250 MeV in three passes.

6944 250 MeV machine, in what currently and tentatively is considered Phase 1 of PERLE. This will
 6945 allow in relatively short time to test with beam the various SRF components, to prove the
 6946 multi-turn ERL operation and to gain essential operation experience. Nevertheless, important
 6947 achievements and steps are needed to realise these purposes. A tentative time schedule for the
 realisation of Phase 1 of PERLE is presented in Tab.9.2.

Phase 1 milestone	Targeted date	Collaborator(s) involvement
<u>Studies & prototyping</u>		
Dressed cavity design completion	Oct 2019	CERN-JLAB
SPL cryomodule design completion	May 2020	CERN
Injection line design completion	Mid 2020	STFC-Univ. Liverpool
Final design cavity fabrication and V. test	Mid 2020	JLAB-CERN
Arc and switchyard dipole prototypes	End 2020	BINP Novosibirsk
Booster cryomodule design completion	End 2021	–
Technical Design Report	End 2021	All
<u>Assembling, test & installation</u>		
DC gun installation (1)	Early 2021	STFC
Booster assembly & RF test (2)	Mid 2023	STFC
Injector installation & commissioning (3)	End 2023	STFC
SPL cryomodule assembly and RF test (2)	Early 2024	CERN
Sequential installation at Orsay (4)	End 2024	–
Phase 1 operation	2025	Open to all

Table 9.2: Tentative time schedule to realise PERLE at Orsay in its first phase. (1) Most likely the Gun upgrade will be deferred to Phase 2 and Phase 1 will use the 5 mA ALICE DC gun which was received at Orsay on May 2019; (2) Booster test requires installation of cryogenics, RF power source, shielding, CC; (3) Injection line commissioning requires installation of cryogenics, RF power source, shielding, beam dump, diagnostics, CC, photocathode laser, vacuum, cabling, safety control systems, fluids, etc.; (4) only one spreader and one recombiner are needed for Phase 1. Final arc configuration will be installed.

6948

6949 It is foreseen from the beginning to size the infrastructure and equipment as for their final use
 6950 (beam dump, cryogenics, cooling circuit, shielding, electrical power, etc.)

6951 The second phase is for the realisation of PERLE at its design parameters, as a 10 MW machine
 6952 which requires the nominal electron current, i.e. the upgraded e^- gun and the completion of

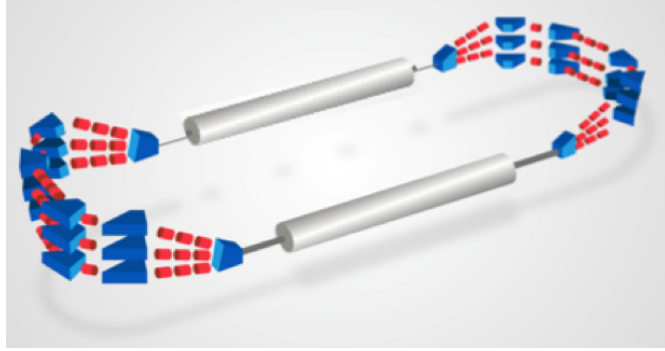


Figure 9.5: PERLE-Phase 2 layout featuring two Linac in each straight, achieving 500 MeV in three passes.

6953 the production of a further cryo-module, possibly newly designed. Also, a second spreader and
 6954 recombiner need to be installed on both sides of the second cryo-module. The timeline of this
 6955 second phase is given in Tab. 9.3. It is expected that the PERLE Collaboration will evolve which
 will affect these plans.

Phase 2 milestone	Targeted date	Collaborator(s) involvement
DC gun upgrade	2026	STFC
Second cryomodule completion	2027	CERN
PERLE phase 2 operation	2028	Open to all

Table 9.3: Tentative plans for Phase 2 of PERLE.

6956

6957 9.2.7 Concluding Remark

6958 Currently the focus of the planning for PERLE is on the development of ERL as a means for high
 6959 power, large energy accelerator design, technology and realisation. PERLE has a considerable
 6960 potential for low energy particle and nuclear physics too. Its intensity is orders of magnitude
 6961 higher than that of ELI. This opens a huge field of physics and industrial applications for a
 6962 user facility once the machine has been understood and operates close to its design in a reliable
 6963 manner. With recent increased interest in energy recovery technology applications at LHeC,
 6964 but also FCC and EIC, PERLE may become an important cornerstone for future high energy
 6965 and nuclear physics. The re-use of power is a *per se* green technology which is an example as
 6966 to how science may react to the low power requirements of our time.

Chapter 10

Experimentation at the LHeC

10.1 Introduction

The LHeC Conceptual Design Report [1] contained a very detailed description of a core detector concept for the LHeC. At the time of writing, the target luminosity was of order $10^{33} \text{ cm}^{-2} \text{ s}^{-1}$ and, whilst evidence was building, the Higgs boson had yet to be discovered. A detector design based on established technologies either in use by the LHC General Purpose Detectors or being developed for their upgrades was found to be adequate to realise the physics priorities of the project at the time and could comply with the *ep* machine constraints at an affordable cost, provided the angular acceptance was sufficient (nominally to within 1° of the beamline).

This chapter provides a short overview of a revised detector design, with more detail on those aspects which have been substantially updated since the 2012 version (notably the central tracking). To a large extent, the considerations in the CDR are still valid and are taken forward here. However, this update also profits from the evolution of the design in the subsequent years in light of changes in the experiment's interaction region and running conditions, the updated and longer term physics priorities with the higher achievable luminosities, and also introduces new technologies where they are becoming available. In more detail, the major considerations which motivate an update of the detector with respect to the 2012 baseline are:

- The design instantaneous luminosity has been extended considerably. The increased luminosity to the level of $10^{34} \text{ cm}^{-2} \text{ s}^{-1}$ translates into a higher pile-up, reaching a maximum of around 1, compared with 0.1 previously. Whilst this is still far from the values of order 200 planned for the HL-LHC, it still has implications in terms of unfolding the hardest scattering processes from multiple overlaid minimum bias events, in particular pushing the design towards higher granularity. It also requires a reassessment of radiation hardness requirements, including the use of more radiation hard detectors in specific regions.
- The increased luminosity and the confirmation of a Higgs boson discovery at a mass of around 125 GeV open new opportunities for the LHeC to provide a set of precision measurements of Higgs properties, in particular, percent-level measurements of many of its couplings. The possibility of obtaining world-leading measurements of couplings to beauty and charm place a heavy emphasis on the inner tracking and vertexing. The tracking region has therefore been extended radially. The requirement to maximise the acceptance for Higgs decays places an even heavier requirement on angular coverage than was the case in 2012, with forward tracking and vertexing being of particular importance.

- 7000 • The fast development of detector technologies and related infrastructure in some areas ne-
7001 cessitates a fresh look at the optimum choices. Most notably, silicon detector technologies
7002 have advanced rapidly in response to both commercial and particle physics requirements.
7003 The low material budget and potential high granularity and radiation hardness offered by
7004 monolithic active pixel sensor (MAPS) solutions such as HV-CMOS are particularly at-
7005 tractive and can reasonably be assumed to be in wide use in future particle physics collider
7006 detector contexts.
- 7007 • There have been changes in the interaction region and the shape and nature of the magnetic
7008 fields in which the LHeC detector is required to operate. In particular, the dipole field,
7009 required to steer the electron beam and allow for head-on collisions, permeates the inner
7010 parts of the detector throughout its longitudinal extent, bringing corresponding challenges.
- 7011 • The long term, high energy, high luminosity world collider physics program, including FCC
7012 and possibilities in the Far East as well as the ultimate use of the LHC in pp mode for two
7013 more decades, will require precise, independent, measurements to determine PDFs over an
7014 even wider range of x and Q^2 than has previously been possible. The implication for the
7015 LHeC is a need to further improve and extend the detector acceptance and performance,
7016 especially in the forward region.
- 7017 • Options in which the LHeC centre-of-mass energy is increased require a further rein-
7018 forcement of the detector design in the forward (outgoing proton) direction, increasing the
7019 overall size of the detector. In particular the calorimetry depth scales so as to fully contain
7020 particles from very high energy forward-going hadronic showers and to allow for precise
7021 measurements of actual and missing energy.

7022 The design described in the following addresses the points above, leading to a somewhat revised
7023 and more ambitious baseline tracking detector design than was the case in 2012. Whilst they
7024 are both realisable in terms of technology readiness, in some sense the 2012 and 2020 versions
7025 can be considered as two example solutions to the LHeC detector needs, towards the lower and
7026 higher ends of the spectrum of performance and cost, respectively. The design is performed
7027 using the DD4hep [750] framework.

7028 The updated detector requirements point towards the need for higher spatial resolution, im-
7029 proved precision in energy and momentum measurements and enhanced primary and secondary
7030 vertexing capabilities. The design must be optimised for accurate measurements of hadronic jets
7031 and missing transverse energy, as well as isolated charged and neutral particle production. Both
7032 the overall event kinematics (much larger proton than electron beam energy) and the specific
7033 acceptance requirements for the key Higgs production process imply an asymmetric design with
7034 enhanced hadronic final state detection capabilities in the forward direction (i.e. at low azimuthal
7035 angles θ). A dipole magnet bends the electron beam into head-on collision with the colliding
7036 proton beam and after the interaction point a further dipole with opposite polarity separates
7037 the orbits of the electron and proton beam. These weak bending dipoles are placed outside of
7038 the tracker and electromagnetic calorimeter regions. The resulting synchrotron radiation fan
7039 has to be given free space and the beam pipe geometry is designed specifically to accommodate
7040 it. The residual synchrotron radiation background requires an advanced detector layout such
7041 that all components can tolerate the load.

7042 **10.2 Overview of Main Detector Elements**

7043 A side projection overview of the revised detector design is shown in Fig. 10.1, illustrating the
 7044 main detector components. The overall size remains compact by recent standards, with overall
 7045 dimensions of approximately 13 m in length and 9 m in diameter, small compared with ATLAS
 7046 (45×25 m) and even CMS (21×15 m). The inner silicon tracker contains a central barrel
 7047 component ('Tracker'), with additional disks in the forward and backward directions ('Tracker
 7048 Fwd' and 'Tracker Bwd', respectively). It is surrounded at larger radii by the Electromag-
 7049 netic Barrel ('EMC-Barrel') and in the forward and backward directions by the electromagnetic
 7050 forward and backward plug calorimeters ('FEC-Plug-Fwd' and 'BEC-Plug-Bwd', respectively).
 7051 The solenoid magnet is placed at radii immediately outside the EMC-Barrel, and is housed in
 7052 a cryostat, which it shares with the weak dipole, which is required by the machine to achieve
 7053 head-on collisions of the electron beam with the colliding proton beam. The Hadronic-Barrel
 7054 calorimeter (HCAL-Barrel) is located at radii beyond the solenoid and dipole, whilst the for-
 7055 ward and backward hadronic plug detectors (FHC-Plug-Fwd and BHC-Plug-Bwd, respectively)
 7056 lie beyond their electromagnetic counterparts in the longitudinal coordinate. The Muon Detec-
 7057 tor forms a near-hermetic envelope around all other parts of the main detector. It has a mixture
 7058 of triggering and measurement-focused layers using similar technologies to those employed by
 7059 ATLAS, as described in the 2012 CDR.

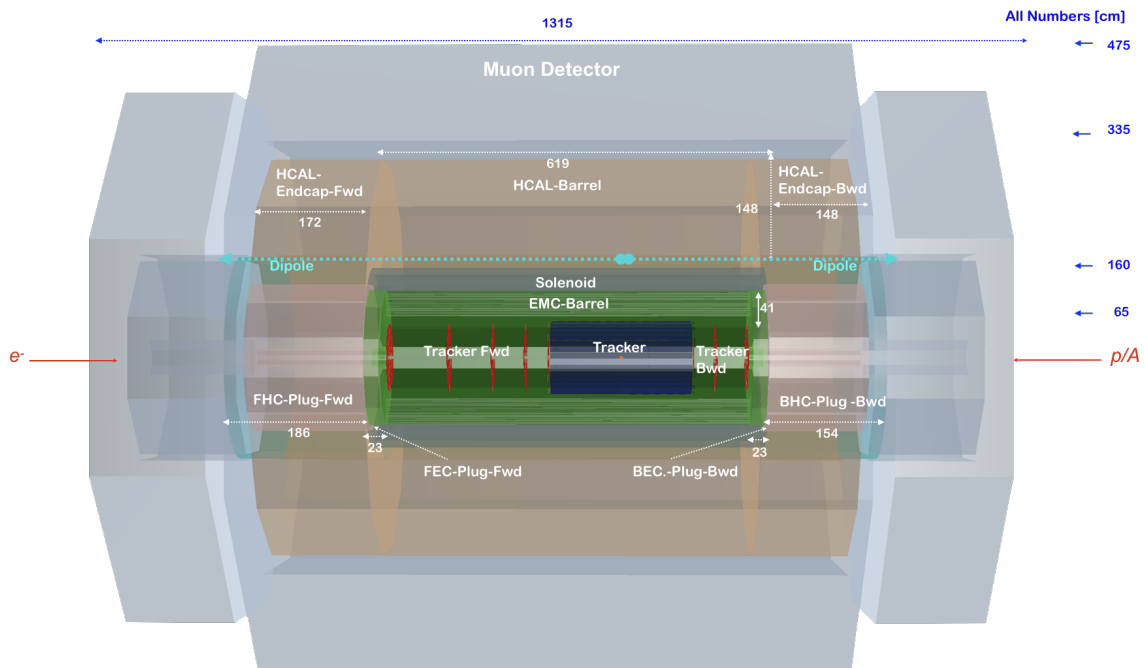


Figure 10.1: Side view of the new baseline LHeC detector concept, providing an overview of the main detector components and their locations. See text for details.

7060 A magnified view of the inner part of the detector, including the magnet elements, is shown in
 7061 Fig. 10.2. The solenoid and steering dipoles enclose the electromagnetic calorimeters and the
 7062 tracker setup completely, the steering dipoles extending over the full 10 m length of the inner
 7063 detector and forward and backward plugs. If liquid argon is chosen for the sensitive material
 7064 in the EMC as in the 2012 design, the EMC will be mounted inside the cryostat, alongside the
 7065 solenoid and dipoles. The hadronic calorimeter components remain outside the cryostat and
 7066 magnet elements under all circumstances.

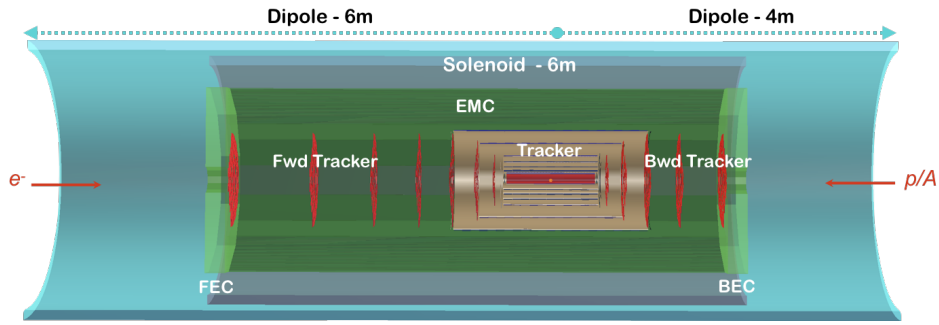


Figure 10.2: Zoomed side projection of the central part of the updated detector design, illustrating the solenoid and electron-beam-steering dipoles. See text for further details

7067 Exploiting the current state of the art, the beam pipe is constructed of beryllium of 2.5 – 3 mm
 7068 thickness. As in the 2012 CDR, the beam pipe has an asymmetric shape in order to accommodate
 7069 the synchrotron radiation fan from the dipole magnets. It is thus 2.2 cm distant from the
 7070 interaction region, except in the outer rear direction of the synchrotron fan, where it is increased
 7071 to 10.0 cm with a semi-elliptical profile. The beam pipe shape has implications for the design
 7072 of the inner detector components, as illustrated in Fig. 10.3. The first layer of the barrel
 7073 tracker follows the circular-elliptical beam pipe shape as closely as possible, with the profiles of
 7074 subsequent layers reverting to a circular geometry.

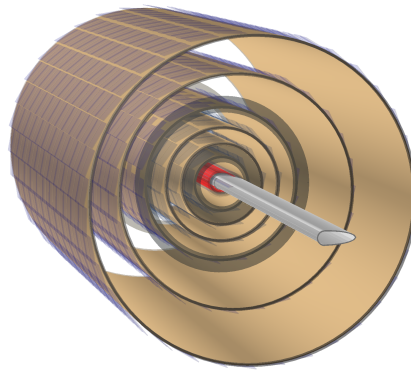


Figure 10.3: End-on view of the arrangement of the inner barrel tracker layers around the beam pipe.

7075 10.3 Inner Tracking

7076 A schematic view of the updated tracking region is shown in Fig. 10.4. The layouts in the
 7077 central, forward and backward directions have been separately optimised using the tkLayout
 7078 performance estimation tool for silicon trackers [751]. The result is seven concentric barrel
 7079 layers with the innermost layer approximately 3 cm from the beam line and approximately equal
 7080 radial spacing thereafter, supplemented by seven forward wheels and five backward wheels of
 7081 which, respectively, four and two are mounted beyond the central tracker enclosure.

7082 HV-CMOS MAPS sensors are employed, restricting dead material associated with the sensors
 7083 to 0.1 mm. The strip detector sensors have a larger thickness of 0.2 mm. The exact silicon

7084 solutions chosen change with radial distance from the interaction point, so as to provide the
 7085 highest spatial resolution in the layers closest to the the interaction point. The barrel is formed
 7086 from one layer of pixel-wafers, with three layers of macro-pixels between 10 cm and 30 cm and a
 7087 further three layers of strip-sensors beyond 30 cm.

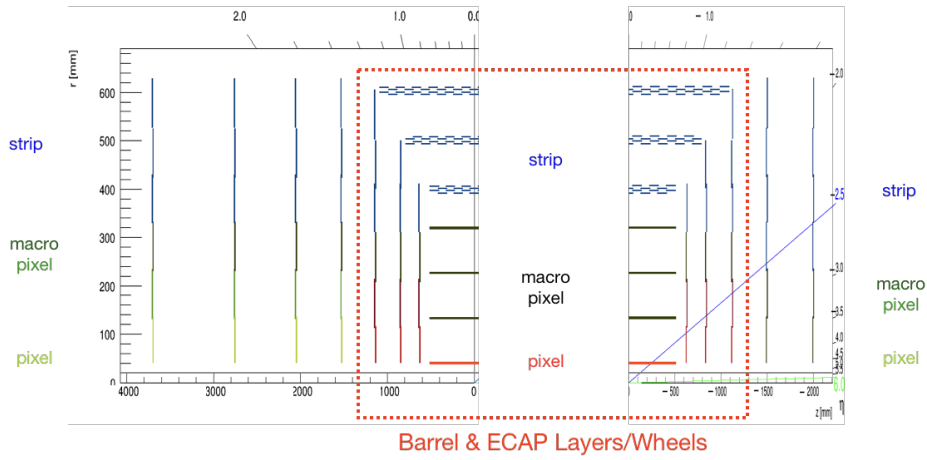


Figure 10.4: Schematic side-view of the tracker, subdivided into forward and backward parts and including disks as well as barrel components. The layers/wheels forming the barrel part are enclosed by the red-dotted box. The innermost pixel layers are coloured red, the macro-pixel layers are shown in black and the strip detectors in blue. For the forward and backward wheels (outside the dashed red box), the pixels, macro-pixels and strip detectors are shown in light green, dark green and blue, respectively.

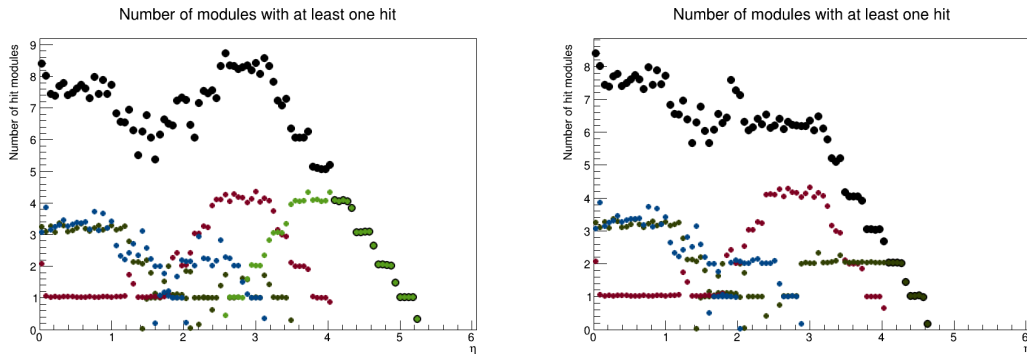


Figure 10.5: Numbers of silicon layers that provide acceptance for charged particles as a function of absolute value of pseudorapidity in the forward (left) and backward (right) directions, summed across the central, forward and backward trackers. The distributions are broken down according to sensor type, with colour coding of red for pixels, light or dark green for macro-pixels, blue for strips and black for the sum.

7088 Tabs. 10.1 and 10.2 summarise the overall basic properties of the tracker modules, including
 7089 total numbers of channels and total area of silicon coverage, as well as spatial resolutions and
 7090 material budgets. The inner barrel has a pseudorapidity coverage $|\eta| < 3.3$ for hits in at least
 7091 one layer, increasing to $|\eta| < 4.1$ when the endcaps are also taken into account. The additional
 7092 disks beyond the central tracker enclosure extend the coverage to $\eta = 5.3$ and $\eta = -4.0$ in the
 7093 forward and backward directions, respectively. Fig. 10.5 shows these features in more detail,
 7094 displaying the numbers of layers that provide acceptance as a function of pseudorapidity in both
 7095 the forward and backward directions, also broken down into different sensor types. Charged
 7096 particles are sampled in between 6 and 8 layers throughout the entire range $-3 < \eta < 4$, with

Tracker (LHeC) ¹⁾	Inner Barrel			ECAP		
	pix	pix _{macro}	strip	pix	pix _{macro}	strip
η_{\max}, η_{\min}	3.3, -3.3	2.1, -2.1	1.4, -1.4	$\pm[4.1, 1.8]$	$\pm[2.4, 1.5]$	$\pm[2.0, 1.0]$
Layers (Barrel)	1	3	3			
Rings (ECAP)				2	1	1-3
Modules/Sensors	320	4420	3352	192	192	552
Total Si area [m ²]	0.3	4.6	17.6	0.8	1.0	3.3
Read-out-Channels [10 ⁶]	224.5	1738	20.6	322.4	36.6	17.0
$\sigma^{r-\phi}$ [μm]	7.5	9.5	9.5	7.5-9.5	9.5	9.5
σ^z [μm]	15	115	2.9k	15-30	115-2.9k	2.9k
Average X_0/Λ_I [%]		7.2 / 2.2			3.0 / 1.0	

¹⁾ Based on tklayout calculations [751]

Table 10.1: Summary of the main properties of the Barrel and Endcap tracker modules in the revised LHeC detector configuration based on calculations performed using tkLayout. For each module, the rows correspond to the pseudorapidity coverage, numbers of barrel and disk layers, numbers of sensors, total area covered by silicon sensors, numbers of readout channels, resolutions in the $(r - \phi)$ plane and in z and the average material budget in terms of radiation lengths and interaction lengths. Where appropriate, the numbers are broken down into separate contributions from pixels, macro-pixels and strips. See Tab. 10.2 for a sum of all tracker components.

7097 sampling in at least two layers provided for $-4 < \eta < 5$.

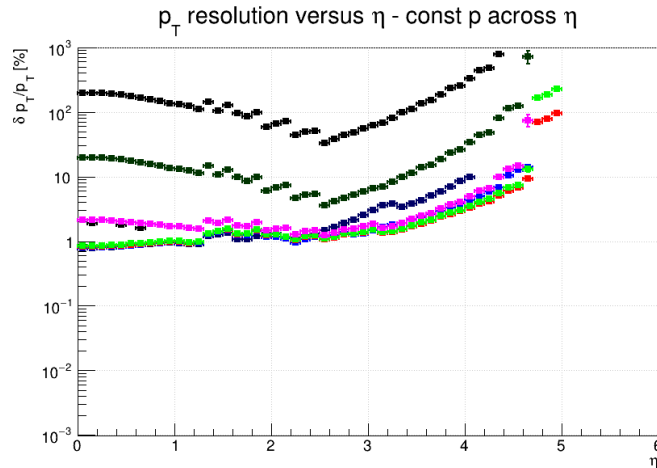


Figure 10.6: Simulated transverse momentum track resolution using all modules in the revised LHeC tracking system. Results are shown in terms of fractional p_T resolution as a function of pseudorapidity for several constant momenta, $p = 100$ MeV (Black), 1 GeV (Dark Blue), 2 GeV (Light Blue), 5 GeV (Red), 10 GeV (Light Green), 100 GeV (Magenta), 1 TeV (Dark Green) and 10 TeV (Black, top).

7098 As can be seen in Tabs. 10.1 and 10.2, spatial resolutions in the $r - \phi$ plane are at the level of
7099 $7.5 - 9.5 \mu\text{m}$ for all of the tracking modules. These resolutions are propagated using tkLayout
7100 to produce simulated charged particle transverse momentum resolutions, as shown in Fig. 10.6.
7101 Both active and passive material contributions are included, with a 2.5 mm beam pipe thickness.
7102 An excellent resolution ($\delta p_T/p_T$) at the level of 1 – 2% is achieved over a wide range of pseu-
7103 dorapidity and transverse momentum. The precision degrades slowly in the forward direction,
7104 remaining at the sub 10 % level up to very forward pseudorapidities $\eta \sim 4.5$. Central tracks with
7105 transverse momenta up to 1 TeV are measured with 10 – 20 % precision.

Tracker (LHeC) ¹⁾	Fwd Tracker			Bwd Tracker			Total (incl. Tab. 10.1)
	pix	pix _{macro}	strip	pix	pix _{macro}	strip	
η_{\max}, η_{\min}	5.3, 2.6	3.5, 2.2	3.1, 1.6	-4.0, -2.6	-2.9, -2.2	-2.5, -1.6	5.3, -4.6
Rings	2	1	3	2	1	3	
Modules/Sensors	144	144	560	36	36	140	10088
Total Si area [m ²]	0.6	0.7	3.9	0.2	0.2	1.0	34.2
Read-out-Channels [10 ⁶]	323.9	55.1	17.2	81.0	13.8	4.3	2854.4
$\sigma^{r-\phi}$ [μm]	7.5–9.5	9.5	9.5	7.5–9.5	9.5	9.5	
σ^z [μm]	15–30	115–2.9k	2.9k	15–30	115–2.9k	2.9k	
Average X_0/Λ_I [%]	2.5 / 0.8			0.9 / 0.3			
incl. beam pipe [%]							35 / 23

¹⁾ Based on tklayout calculations [751]

Table 10.2: Summary of the main properties of the forward and backward tracker modules in the revised LHeC detector configuration based on calculations performed using tkLayout. For each module, the rows correspond to the pseudorapidity coverage, numbers of barrel and disk layers, numbers of sensors, total area covered by silicon sensors, numbers of readout channels, resolutions in the $(r - \phi)$ plane and in z and the average material budget in terms of radiation lengths and interaction lengths. Where appropriate, the numbers are broken down into separate contributions from pixels, macro-pixels and strips. The column *Total* contains the sum of corresponding values of table 10.1.

7106 A major requirement of the tracking detectors will be the precise determination of vertex coordinates and of track impact parameters relative to the primary vertex in order to give the best
7107 possible sensitivity to secondary vertices from heavy flavour decays, for example for the study of
7108 the Higgs in its dominant $b\bar{b}$ decay mode. The simulated results for longitudinal and transverse
7109 track impact parameter resolutions using the full new tracking layout are shown in Fig. 10.7.
7110 The resolutions are at the highly competitive level of $10 - 50 \mu\text{m}$ over a wide range of transverse
7111 momentum and pseudorapidity, extending well into the forward direction.
7112

7113 The total material budget contribution from the sensors summed across all layers is given in
7114 Tab. 10.2. This is largest for the inner barrel, where it amounts to 7.2% of a radiation length.
7115 The sensors in the central tracker endcap and the forward and backward tracking rings contribute
7116 3.0%, 2.5% and 0.9% of a radiation length, respectively. These material contributions are all
7117 small on the scale of the average $0.35X_0$ contributed by the beam pipe. The material budget
7118 simulations, propagated for the full system and including passive contributions, are shown in
7119 Fig. 10.8. The use of thin sensors keeps the total material to the level of $0.2 - 0.4X_0$ throughout
7120 the entire tracking region up to $\eta \sim 5$.

7121 10.4 Calorimetry

7122 The 2012 CDR detector design leaned heavily on current technologies employed by ATLAS
7123 for calorimetry in the barrel region, adopting a lead / liquid argon sampling electromagnetic
7124 calorimeter with an accordion geometry and a steel / scintillating tile sampling hadronic com-
7125 ponent. For the updated detector described here, an alternative solution of a lead / scintillator
7126 electromagnetic calorimeter has been investigated. This has the advantage of removing the need
7127 for cryogenics, whilst maintaining an acceptable performance level. The liquid argon option is
7128 not excluded yet and will be evaluated further-on. The hadronic calorimeter retains the steel
7129 and scintillating tile design, similar to ATLAS. As in the 2012 CDR, plug sampling calorimeters
7130 are also incorporated at large $|\eta|$, the forward and backward components using tungsten and

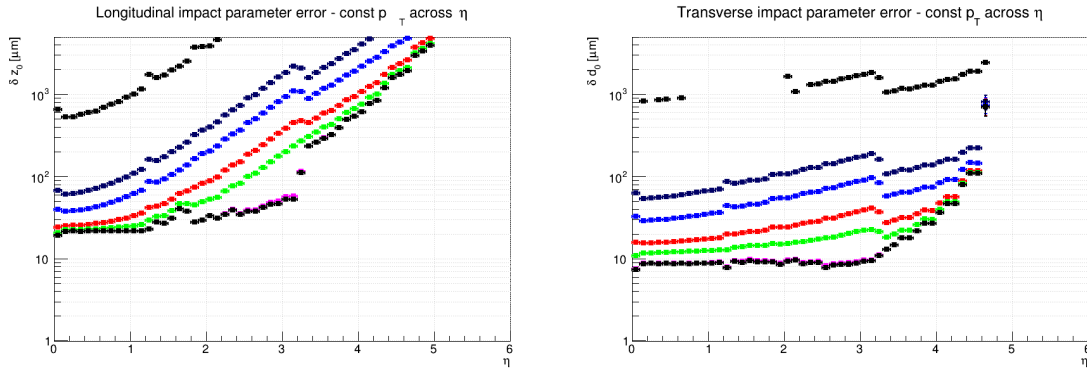


Figure 10.7: Simulated longitudinal (left) and transverse (right) impact parameter resolutions using all modules in the revised LHeC tracking system. Results are shown as a function of pseudorapidity for several constant momenta, $p = 100$ MeV (Black), 1 GeV (Dark Blue), 2 GeV (Light Blue), 5 GeV (Red), 10 GeV (Light Green), 100 GeV (Magenta), 1 TeV (Dark Green) and 10 TeV (Black, top).

7131 lead absorber material, respectively, with both using silicon based sensitive readout layers. The
 7132 steel structures in the central and plug calorimetry close the outer field of the central solenoid.
 7133 The main features of the new calorimeter layout are summarised in Tab. 10.3 and 10.4. The
 7134 pseudorapidity coverage of the electromagnetic barrel is $-1.4 < \eta < 2.4$, whilst the hadronic
 7135 barrel and its end cap cover $-1.5 < \eta < 1.9$. Also including the forward and backward plug
 7136 modules, the total coverage is very close to hermetic, spanning $-5.0 < \eta < 5.5$. The total
 7137 depth of the electromagnetic section is 30 radiation lengths in the barrel and backward regions,
 7138 increasing to almost $50X_0$ in the forward direction where particle and energy densities are high-
 7139 est. The hadronic calorimeter has a depth of between 7.1 and 9.6 interaction lengths, with the
 7140 largest values in the forward plug region.

7141 The performance of the new calorimeter layout has been simulated by evaluating the mean sim-
 7142 ulated response to electromagnetic (electron) and hadronic (pion) objects with various specific
 7143 energies using GEANT4 [752] and interpreting the results as a function of energy in terms of
 7144 sampling (a) and material / leakage (b) terms in the usual form $\sigma_E/E = a/\sqrt{E} \oplus b$. Example
 7145 results from fits are shown for the barrel electromagnetic and hadronic calorimeters in Fig. 10.9
 7146 and for the forward plug electromagnetic and hadronic calorimeters in Fig. 10.10. The results
 7147 for the a and b parameters are summarised in Tabs. 10.3 and 10.4. The response of the barrel
 7148 electromagnetic calorimeter to electrons in terms of both sampling ($a = 12.4\%$) and material
 7149 ($b = 1.9\%$) terms is only slightly worse than that achieved with liquid argon sampling in the
 7150 2012 CDR. The resolutions of the forward and backward electromagnetic plug calorimeters are
 7151 comparable to those achieved in the 2012 design. A similar pattern holds for the hadronic re-
 7152 sponse, with sampling terms at the sub-50% level and material terms of typically 5% throughout
 7153 the barrel end-caps and forward and backward plugs.

7154 10.5 Muon Detector

7155 Muon identification is an important aspect for any general purpose HEP experiment like the
 7156 LHeC. At the LHeC the muon detector can widen the scope and the spectrum of many mea-
 7157 surements, of which only a few are listed here:

- 7158 • Higgs decay,

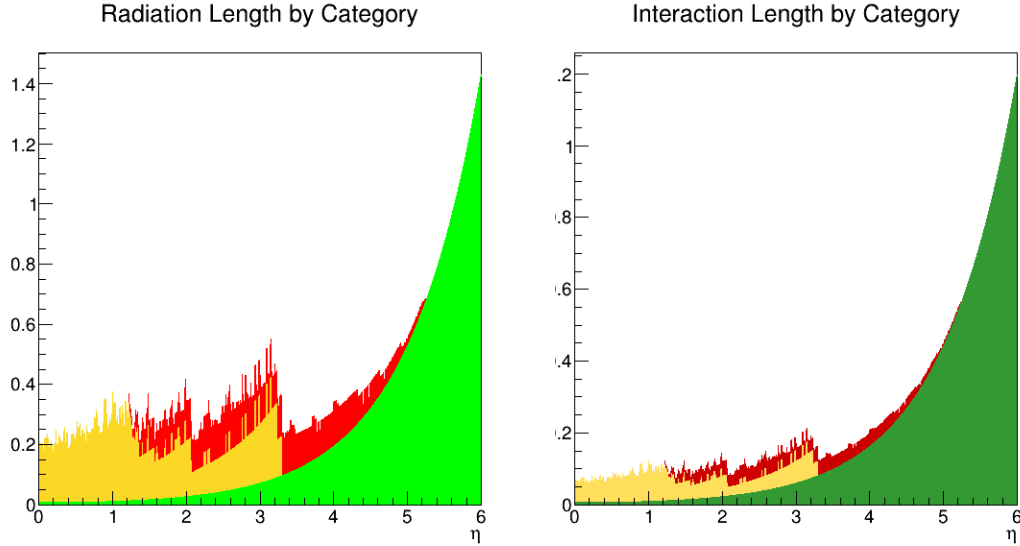


Figure 10.8: Material contributions from the tracking modules as a function of pseudorapidity. Results are given in terms of radiation lengths (left) and hadronic interaction lengths (right). The results are broken down into contributions from barrel modules (yellow) and endcap / additional disk modules (red) and are compared with the contribution from the 2.5 mm beam pipe (green).

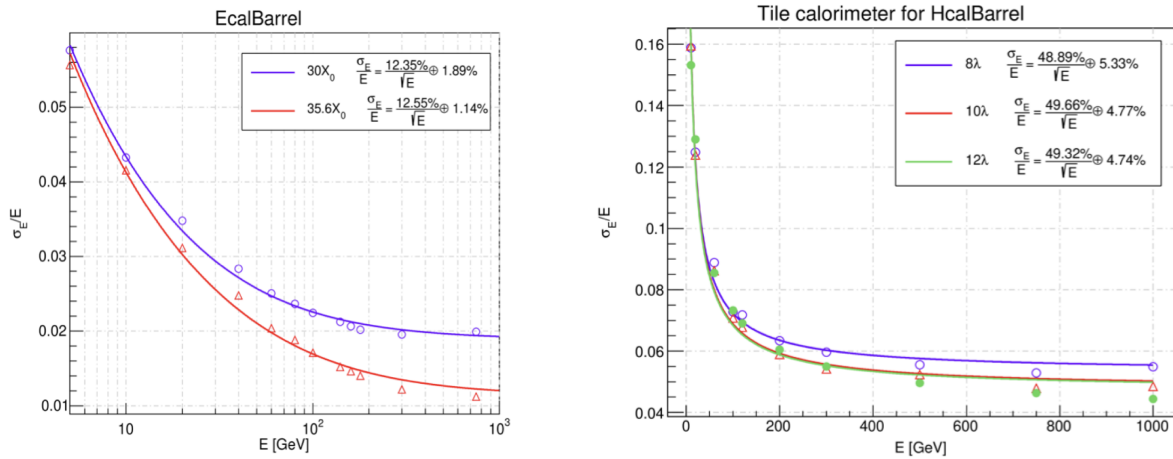


Figure 10.9: Crystal Ball fitted energy dependent resolution for the barrel electromagnetic (left) and barrel hadronic (right) calorimeters EMC and HCAL, respectively. The first (*a*) term includes shower fluctuations and transverse leakages and the second (*b*) term includes leakages from the calorimeter volume longitudinally.

- 7159 • Semi-leptonic decays of heavy flavoured hadrons,
- 7160 • Vector meson production,
- 7161 • Direct W and Z production,
- 7162 • Di-muon production,
- 7163 • Leptoquarks, lepton flavour violation, and other BSM phenomena.

7164 The primary target of the muon detector at the LHeC is to provide a reliable muon tag signature
 7165 which can be uniquely used in conjunction with the central detector for muon identification,
 7166 triggering and precision measurements. This option also well fits the constraints of limited

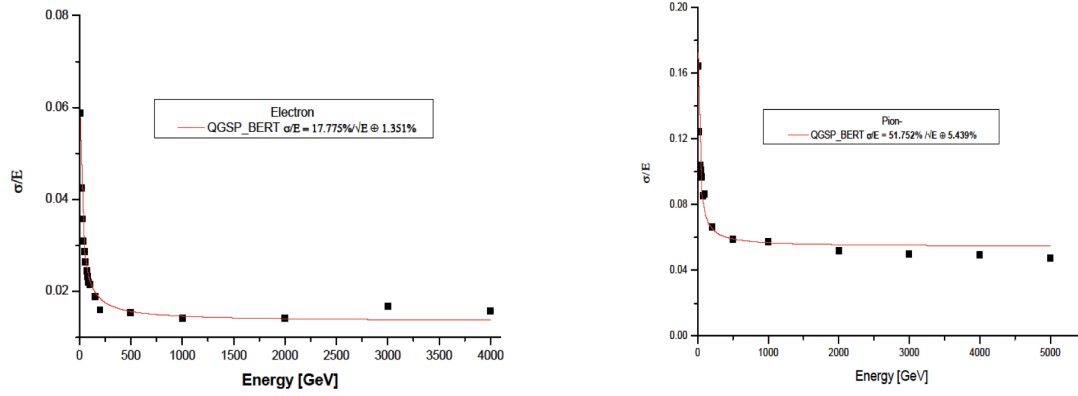


Figure 10.10: Crystal Ball fitted energy dependent resolution for the forward electromagnetic (left) and forward hadronic (right) plug calorimeters FEC and FHC, respectively. The first (*a*) term includes shower fluctuations and transverse leakages and the second (*b*) term includes leakages from the calorimeter volume longitudinally.

Calo (LHeC)	EMC		HCAL	
	Barrel	Ecap Fwd	Barrel	Ecap Bwd
Readout, Absorber	Sci,Pb	Sci,Fe	Sci,Fe	Sci,Fe
Layers	38	58	45	50
Integral Absorber Thickness [cm]	16.7	134.0	119.0	115.5
η_{\max}, η_{\min}	2.4, -1.4	1.9, 1.0	1.6, -0.7	-1.5, -1.0
$\sigma_E/E = a\sqrt{E} \oplus b$	[%] 12.4/1.9	46.5/3.8	48.23/5.6	51.7/4.3
Λ_I / X_0	$X_0 = 30.2$	$\Lambda_I = 8.2$	$\Lambda_I = 8.3$	$\Lambda_I = 7.1$
Total area Sci	[m ²] 1174	1403	3853	1209

Table 10.3: Basic properties and simulated resolutions of barrel calorimeter modules in the new LHeC detector configuration. For each of the modules, the rows indicate the absorber and sensitive materials, the pseudorapidity coverage, the contributions to the simulated resolution from the sampling (*a*) and material (*b*) terms in the form *a/b*, the depth in terms of radiation or interaction lengths and the total area covered by the sensitive material.

GEANT4 [752] simulation based fits using crystal ball function [753] [754] [755].

7167 space ¹ and the lack of a dedicated magnetic field as in the baseline design. The muon chambers
7168 surround Muon chambers surround the central detector and covering as far as possible the solid
7169 angle and provide, by means of a compact multilayer structure, a pointing trigger and a precise
7170 timing measurement which is used to separate muons coming from the interaction point from
7171 cosmics, beam halo or non prompt particles. This tagging feature does not include the muon
7172 momentum measurement which is performed only in conjunction with the central detector. A
7173 trigger candidate in the muon detector is characterised by the coincidence over a majority of
7174 the layers in a range of η , ϕ , and t compatible with an *ep* interaction of interest in the main
7175 detector. The muon candidates are combined with the trigger information coming from the
7176 central detector (mainly the calorimetry at Level 1 trigger) to reduce the fake rate or more
7177 complex event topologies.

7178 Concerning the choice of the technologies for the muon detector, at the the time of the 2012

¹As in the 2012 CDR, the baseline LHeC detector including the muon system and all of the services and supports is expected to fit into the octagonal shape envelop of the L3 magnet (11.6 m minimum diameter).

Calo (LHeC)	FHC Plug Fwd	FEC Plug Fwd	BEC Plug Bwd	BHC Plug Bwd
Readout, Absorber Layers	Si,W 300	Si,W 49	Si,Pb 49	Si,Cu 165
Integral Absorber Thickness [cm]	156.0	17.0	17.1	137.5
η_{\max}, η_{\min}	5.5, 1.9	5.1, 2.0	-4.4, -4.5	-4.5, -5.0
$\sigma_E/E = a/\sqrt{E} \oplus b$ [%]	51.8/5.4	17.8/1.4	14.4/2.8	49.5/7.9
Λ_I / X_0	$\Lambda_I = 9.6$	$X_0 = 48.8$	$X_0 = 30.9$	$\Lambda_I = 9.2$
Total area Si [m ²]	1354	187	187	745

Table 10.4: Basic properties and simulated resolutions of forward and backward plug calorimeter modules in the new LHeC detector configuration. For each of the modules, the rows indicate the absorber and sensitive materials, the pseudorapidity coverage, the contributions to the simulated resolution from the sampling (a) and material (b) terms in the form a/b , the depth in terms of radiation or interaction lengths and the total area covered by the sensitive material.

GEANT4 [752] simulation based fits using crystal ball function [753] [754] [755].

7179 CDR the LHC experiments and the ongoing R&D programs in HEP detector indicated the
7180 options in use in ATLAS and CMS and their planned upgrades as adequate for LHeC. With the
7181 exception of the very forward region, muon and background rates in LHeC are expected to be
7182 lower than in pp and with less busy event topologies. The option of an LHeC muon detector
7183 composed by layers of Resistive Plate Chambers (RPC), providing the Level 1 trigger and a 2 two
7184 coordinate (η, ϕ) measurement possibly aided by Monitored Drift Tubes (MDT) for additional
7185 precision measurement appears to be still valid. Recent developments as presented in LHC
7186 Phase 2 Upgrade Technical Design Reports ([756, 757]) do further strengthen this choice. New
7187 thin-RPC (1 mm gas gap) operated with lower HV, provide a sharper time response (few ns),
7188 a higher rate capability (tens of kHz/cm²), and extend the already good aging perspective. A
7189 crucial role is coming from the advances on low-noise high-bandwidth front-end electronics which
7190 can also improve the performance of older detectors. Similar arguments also hold for smaller
7191 tube MDTs (15 mm diameter) which provide lower occupancy and eight-fold rate capability.

7192 Fig. 10.11 shows an adaptation for LHeC of an RPC-MDT assembly as will be implemented for
7193 the inner muon layer of ATLAS already during the Phase-1 upgrade as pilot for the Phase-2. A
7194 triplet of thin gap RPCs each with 2 coordinate measurement, is combined with two superlayers
7195 of small MDTs. It is also important to note the reduced volume of this structure, in particular
7196 of the RPC part which would provide the muon tag. For the LHeC a baseline would be having
7197 one or two of such stations forming a near-hermetic envelope around the central detector.

7198 Finally, as already presented in the 2012 CDR, detector extensions, with a dedicated magnetic
7199 field in the muon detector, be this a second solenoid around the whole detector or extra dipole
7200 or toroid in the forward region are, at this stage, left open as possible developments only for
7201 upgrade scenarios for a late installation in the FCC.

7202 10.6 Forward and Backward Detectors

7203 In the 2012 CDR, initial plans for beamline instrumentation were provided for the LHeC. In the
7204 backward direction, low angle electron and photon calorimeters were placed with the primary
7205 intention of measuring luminosity via the Bethe-Heitler process $ep \rightarrow eXp$ and the side-effect of
7206 providing an electron tagger to identify photoproduction ($\gamma p \rightarrow X$) processes at intermediate y
7207 values. The current design carries forward the 2012 version of this backward instrumentation,

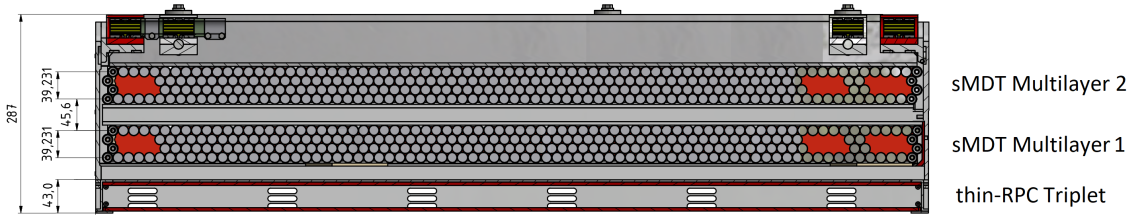


Figure 10.11: A transverse view of a RPC-MDT assembly as adapted from a drawing of the ATLAS Phase-1 muon upgrade [756]. In this case a station is composed of an RPC triplet for trigger and 2-coordinate readout and two MDT superlayers for precise track measurements.

7208 though it will need to be revisited in the future in light of the synchrotron load in the updated
7209 magnet design.

7210 In the forward direction, Roman pot detectors were included in the region of $z \sim 420$ m, capable
7211 of detecting scattered protons over a range of fractional energy loss $10^{-3} < \xi < 3 \times 10^{-2}$ and wide
7212 transverse momentum acceptance, based on extensive previous work in the LHC context by the
7213 FP420 collaboration. This also forms the basis of forward proton tagging in the revised design.
7214 However, as is the case at ATLAS and CMS / TOTEM, further Roman pot detectors in the
7215 region of 200 m and (with HL-LHC optics) perhaps around 320 m would extend the acceptance
7216 towards higher ξ values up to around 0.2 allowing the study of diffractive processes $ep \rightarrow eXp$
7217 where the dissociation system X has a mass extending into the TeV regime. It is worth noting
7218 that Roman pot technologies have come of age at the LHC, with the TOTEM collaboration
7219 operating 14 separate detectors at its high point. Silicon sensor designs borrowed from the
7220 innermost regions of the ATLAS and CMS vertexing detectors have been used, providing high
7221 spatial resolution and radiation hardness well beyond the needs of LHeC. Very precise timing
7222 detectors based on fast silicon or Cherenkov radiation signals from traversing protons in quartz
7223 or diamond have also been deployed. It is natural that these advances and the lessons from their
7224 deployment at the LHC will be used to inform the next iteration of the LHeC design.

7225 The forward beamline design also incorporates a zero angle calorimeter, designed primarily
7226 to detect high energy leading neutrons from semi-inclusive processes in ep scattering and to
7227 determine whether nuclei break up in eA events. This component of the detector was not
7228 considered in detail in 2012 and is therefore discussed here.

7229 10.6.1 Zero-Degree (Neutron) Calorimeter

7230 The Zero-Degree Calorimeter (ZDC) measures final state neutral particles produced at angles
7231 near the incoming hadron beam direction. They typically have large longitudinal momentum
7232 ($x_F \gg 10^{-2}$), but with transverse momentum of order of Λ_{QCD} . Such a calorimeter has been
7233 instrumented in experiments for ep collisions (H1 and ZEUS) and for pp , pA and AA collisions at
7234 RHIC (STAR and PHENIX) and at the LHC (ATLAS, CMS, ALICE and LHCf at the ATLAS
7235 IP). The detector's main focus is to study the soft-hard interplay in the QCD description of ep
7236 and eA collisions by studying the dependence of forward-going particles with small transverse
7237 momentum on the hard variables e.g. Q^2 and x . The detector also allows the tagging of spectator
7238 neutrons to detect nuclear breakup in eA collisions. It also enables the precise study of the EMC
7239 effect by using neutron-tagged DIS on small systems, such as $e^3\text{He} \rightarrow ed + n \rightarrow eX + n$. For
7240 heavier ions, several tens of neutrons may enter within the aperture of the ZDC. Inclusive π^0
7241 production has been measured by the LHCf experiments for pp collisions. It is of great
7242 interest to compare with DIS measurements at the same proton energies. Precise understanding

7243 of the inclusive spectrum of the forward-going particles is a key ingredient in simulating air
7244 showers from ultra-high energy cosmic rays.

7245 **Physics requirement for forward neutron and π^0 production measurement**

7246 It is known from various HERA measurements that the slope parameter b is about 8 GeV^{-2} in the
7247 exponential parameterisation e^{bt} of the t distribution of leading neutrons. In order to precisely
7248 determine the slope parameter it is necessary to measure the transverse momentum of the
7249 neutrons up to or beyond 1 GeV . The aperture for forward neutral particles does not have to be
7250 very large, thanks to the large boost on the proton and heavy ion beam. For example, collisions
7251 with $E_p = 7 \text{ TeV}$ need 0.14 mrad for $p_T = 1 \text{ GeV}$ neutrons at $E_{\text{particle}}/E_{\text{beam}} \equiv x_F = 1.0$, or
7252 0.56 mrad for $x_F = 0.25$.

7253 The energy or x_F resolution for neutrons would not be a dominant factor thanks to the high
7254 energy of the produced particles. The energy resolution of a neutron with $x_F = 0.1$ is about
7255 2% for cutting-edge hadron calorimeters with $\sigma_E/E = 50\%/\sqrt{E}$, where E is in GeV . Such a
7256 resolution can be achieved if non-unity e/h can be compensated either by construction of the
7257 calorimeter or by software weighting, and if the size of the calorimeter is large enough so that
7258 shower leakage is small.

7259 On the other hand, the resolution requirement on the transverse momentum is rather stringent.
7260 For example, 1 mm resolution on hadronic showers from the neutron measured at 100 m down-
7261 stream from the interaction point corresponds to 0.01 mrad or 70 MeV , which is rather moderate
7262 ($\leq 10\%$ resolution for large p_T hadrons with $p_T > 700 \text{ MeV}$). For smaller p_T it is more appro-
7263 priate to evaluate the resolution in terms of $t \simeq -(1 - x_F)p_T^2$ i.e. $\Delta t \simeq 2(\Delta p_T)p_T$ at $x_F = 1$.
7264 At $t = 0.1 \text{ GeV}^2$ or $p_T \simeq 300 \text{ MeV}$, Δt is about 50% . A shower measurement with significantly
7265 better than 1 mm position resolution, therefore, would improve the t -distribution measurement
7266 significantly.

7267 According to the current LHC operation conditions with $\beta^* = 5 \text{ cm}$, the beam spread is $8 \times$
7268 10^{-5} rad or 0.56 GeV . This is much larger than the required resolution in p_T . It is, therefore,
7269 neither possible to measure the particle flow nor control the acceptance of the forward aperture.
7270 For precision measurement of forward particles, it is necessary to have runs with $\beta^* \geq 1 \text{ m}$,
7271 corresponding to $\sigma(p_T) < 70 \text{ MeV}$.

7272 The calorimeter should be able to measure more than 30 neutrons of 5 TeV for tagging spectator
7273 neutrons from heavy-ion collisions. The dynamic range of the calorimeter should exceed 100 TeV
7274 with good linearity.

7275 As for π^0 measurements, the LHCf experiment has demonstrated that a position resolution of
7276 $200 \mu\text{m}$ on electromagnetic showers provides good performance for the inclusive photon spectrum
7277 measurements [758]. This also calls for fine segmentation sampling layers.

7278 **ZDC location for the Linac-Ring IP design**

7279 According to the IP design, a possible location for the ZDC is after the first bending of the
7280 outgoing colliding proton beam at around $Z = 110 \text{ m}$, where no beam magnet is placed (see
7281 Fig. 10.12). It is anyhow planned to place a neutral particle dump around this location in order
7282 to protect accelerator components. A ZDC could serve as the first absorbing layer at zero
7283 degrees.

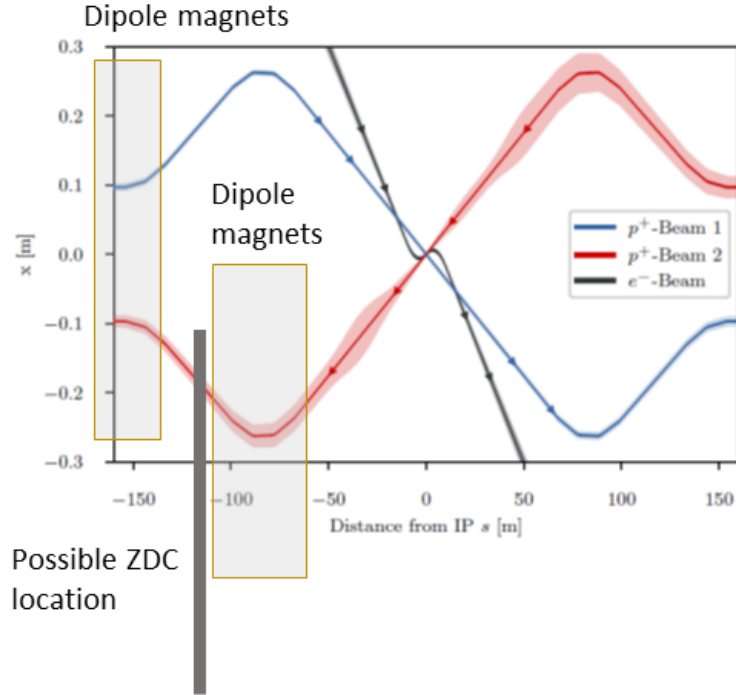


Figure 10.12: Possible location for a ZDC for the linac–ring design of LHeC. The solid rectangle represents the ZDC. The two boxes in front of and behind the ZDC indicate the locations for bending magnets.

7284 The aperture to the ZDC would be determined by the last quadrupole magnet at around $z = 50$ m.
 7285 Assuming a typical aperture for the LHC magnets of 35 mm, the aperture could be as large as
 7286 0.7 mrad. The horizontal aperture of the dipole magnets between 75 and 100 m would be larger
 7287 since otherwise the magnets receive significant radiation from neutral particles produced from
 7288 the collisions at the IP. Even if the aperture is limited by the vertical aperture of the last dipole
 7289 at $z = 100$ m, the aperture is 0.35 mrad, corresponding to 2.4 GeV in p_T for 7 GeV particles.
 7290 This fulfills the physics requirement.

7291 The space for the ZDC location in the transverse direction should be at least $\pm 2\lambda_I$ to avoid
 7292 large leakage of hadronic showers. This can be achieved if the proton beam traverses inside the
 7293 calorimeter, about 20 cm from the centre of the calorimeter. The total size of the calorimeter
 7294 could then be $60 \times 60 \times 200$ cm or larger according to the current layout of the beam and
 7295 accelerator components. This would provide about $\pm 3\lambda_I$ in the transverse direction and about
 7296 $10\lambda_I$ in depth.

7297 Radiation requirement for the ZDC

7298 It can safely be assumed that the energy spectrum of the neutral particles produced in ep
 7299 and pp events are very similar. According to the LHCf simulation, their tungsten–scintillator
 7300 sandwich calorimeter receives about 30 Gy/nb^{-1} or $10^8 \text{ events/nb}^{-1}$ assuming $\sigma_{pp}^{\text{tot}} = 100 \text{ mb}$,
 7301 i.e. $3 \times 10^{-7} \text{ Joule/event}$. This means that about 1/4 of the total proton beam energy ($7 \text{ TeV} \simeq$
 7302 $1.12 \times 10^{-6} \text{ Joule/event}$) is deposited in 1 kg material in pp collisions. The ep total cross section
 7303 is $68 \mu\text{b}$ or 680 kHz at $10^{34} \text{ cm}^2\text{s}^{-1}$. A 7 TeV beam or $1.12 \times 10^{-6} \text{ Joule/event}$ corresponds
 7304 to 0.76 Joule/s at this instantaneous luminosity. A quarter of the total dose is then about

7305 0.2 Gy/sec or 0.02 Gy/nb, which is in accordance with the expectation from $\sigma_{pp}^{\text{tot}} \simeq 10^3 \sigma_{ep}^{\text{tot}}$. The
7306 contribution from beam-gas interactions is estimated to be much smaller ($\mathcal{O}(100 \text{ kHz})$).

7307 Assuming that the ZDC is always operational during LHeC running, one year of ep operation
7308 amounts to 2.5 MGy/year assuming 10^7 sec operation, or $\mathcal{O}(10 \text{ MGy})$ throughout the lifetime of
7309 the LHeC operation. This approximately corresponds to $10^{14} - 10^{15}$ 1 MeV neutron equivalent.

7310 Possible calorimeter design

7311 The high dose of $\mathcal{O}(10 \text{ MGy})$ requires calorimeters based on modern crystals (e.g. LYSO) or
7312 silicon as sampling layers, at least for the central part of the calorimeter where the dose is
7313 concentrated. Since we also need very fine segmentation for photons, it is desirable to use finely
7314 segmented silicon pads of order of 1 mm. As for the absorbers, tungsten should be used for good
7315 position resolution of photons and the initial part of hadronic showers.

7316 In the area outside the core of the shower i.e. well outside the aperture, the dose may be much
7317 smaller and small scintillator tiles could be used for absorbers, which allows measurements with
7318 good e/h ratio. If we choose a uniform design using silicon across the detector, the segmentation
7319 of the outer towers could be order of a few cm, which still makes it possible to use software
7320 compensation technology developed for ILC calorimeters. It may also be possible to use lead
7321 instead of tungsten for outer towers to reduce the cost.

7322 10.7 Detector Installation and Infrastructure

7323 The usual constraints that apply to HEP detector integration and assembly studies, are made
7324 here also. They hold even tighter since the detector has to be installed in the shortest allowable
7325 time, given by the duration of an LHC machine shutdown, which is typically two years. Since the
7326 new LHeC detector would be installed at the place of IP2, see Fig. 10.13, time needed to remove
7327 the old detector and its services has to be added to the overall schedule. Thus the only realistic
7328 possibility to accomplish the timely dismantling of the old detector and the installation of the
7329 new one is to complete as much as possible the assembling and testing of the LHeC detector
7330 on surface, where the construction can proceed without impacting on the LHC physics runs.
7331 Condition for doing this, is the availability of equipped free space at LHC-P2 surface, namely a
7332 large assembly hall with one or two cranes. To save time, most of the detector components have
7333 been designed to match the handling means available on site, i.e. bridge crane in surface hall
7334 and experiment cavern. Nevertheless, a heavy lifting facility (about 300 tons capacity) will be
7335 rented for the time needed to lower the heaviest detector components, such as HCal barrel and
7336 plug modules. Large experience with this will be acquired during LHC Long Shutdown 3, when
7337 a significant part of ATLAS and CMS detectors will be replaced by new elements. At CMS, for
7338 instance, a new Endcap Calorimeter weighing about 220 tons will be lowered into the experiment
7339 cavern, a scenario very close to what is here envisaged for the LHeC detector assembly.

7340 The detector has been split in the following main parts for assembly purposes:

- 7341 • Coil cryostat, including the superconducting coil, the two integrated dipoles and eventually
7342 the EMCal.
- 7343 • Five HCal tile calorimeter barrel modules, fully instrumented and cabled (5).
- 7344 • Two HCal plugs modules, forward and backward (2).



Figure 10.13: View on the hall surface infrastructure at Point 2, near St.Genis.

- 7345 • Two EMCal plugs, forward and backward (2).
- 7346 • Inner Tracking detector (1).
- 7347 • Beam-pipe (1).
- 7348 • Central Muon detector (1 or 2).
- 7349 • Endcaps Muon detector (2).

7350 The full detector, including the Muon chambers, fits inside the former L3 detector Magnet Yoke,
 7351 once the four large doors are taken away. The goal is to prevent losing time in dismantling the
 7352 L3 Magnet barrel yoke and to make use of its sturdy structure to hold the detector central part
 7353 on a platform supported by the magnet crown, whilst the Muon chambers will be inserted into
 7354 lightweight structures (space-frames) attached to the inner surface of the octagonal L3 magnet.

7355 The assembly on surface of the main detector elements, as previously defined, can start at any
 7356 time, providing that the surface facilities are available, without sensible impact on the LHC
 7357 run. The Coil system commissioning on site ($t = 0$) could require 3 months and preparation for
 7358 lowering three months, including some contingency. In the same time window, the L3 Magnet
 7359 will be freed up and prepared for the new detector ². Lowering of the main detector components
 7360 into the cavern, illustrated in Fig. 10.14, is supposed to take one week per piece (15 pieces in
 7361 total). Underground integration of the central detector elements inside the L3 Magnet would
 7362 require about 6 months, cabling and connection to services some 8 to 10 months, in parallel
 7363 with the installation of the Muon chambers, the Tracker and the Calorimeter Plugs. Fig. 10.15
 7364 shows the installed complete detector housed in the L3 magnet support.

² The actual delay depends on the level of activation and the procedure adopted for dismantling the existing detector. Here again the experience acquired during the long shutdown (LS) 2 with the upgrades of ALICE and LHCb and later with ATLAS and CMS upgrades during LS3 will provide important insight for defining procedures and optimising the schedule.

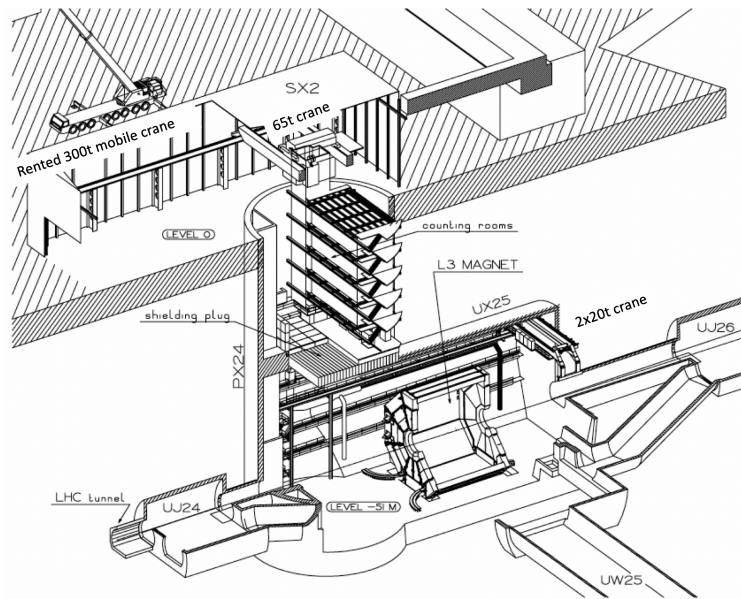


Figure 10.14: View on the cavern infrastructure at Point 2. In the centre one recognises the support structure of the magnet of the L3 experiment which is thought to house and support also the LHeC detector, not least for its removal would cost significant extra time.

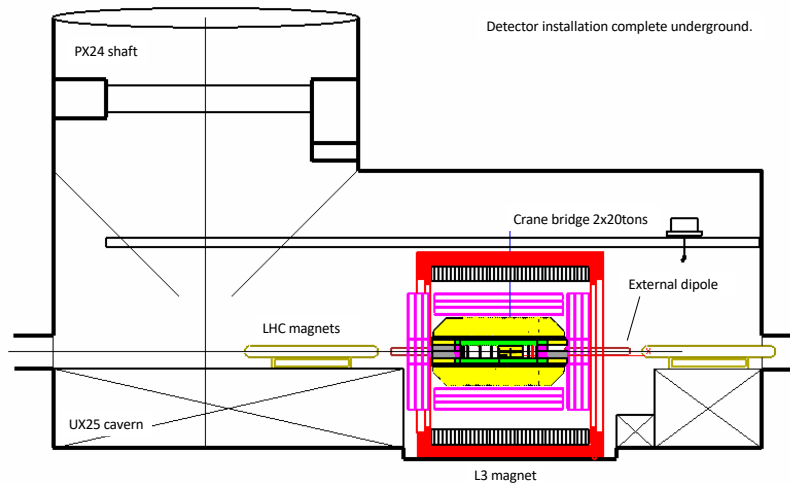


Figure 10.15: View on the LHeC detector, housed in the L3 magnet support structure, after installation at the interaction point.

7365 The total estimated time, from the starting of the testing of the Coil system on surface to the
 7366 commissioning of the detector underground is thus 20 months. The beam-pipe bake out and
 7367 vacuum pumping could take another 3 months and the final detector check-out one additional
 7368 month. Some contingency (2–3 months in total) is foreseen at the beginning and the end of the
 7369 installation period. A sketch of the installation schedule is provided in Fig. 10.16

7370 Concerning the detector infrastructures, not much can be said at this stage. The LHeC detector
 7371 superconducting coil will need cryogenics services and a choice has to be made between pur-

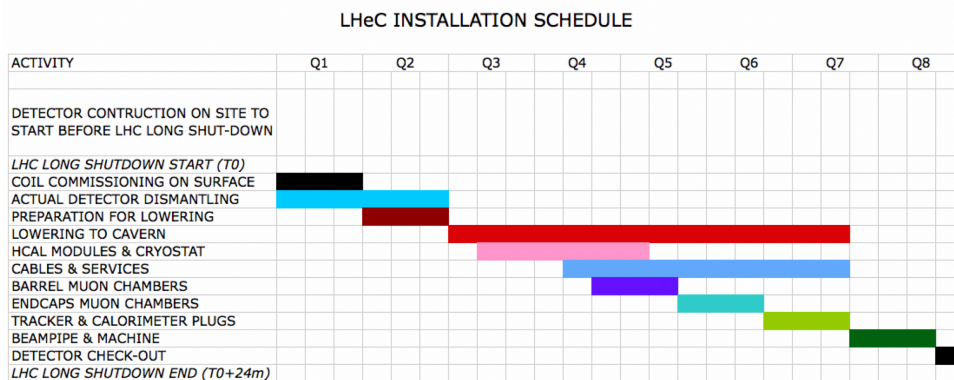


Figure 10.16: Time schedule of the sequential installation of the LHeC detector in point 2 as described in the text.

7372 chasing a dedicated liquid helium refrigeration plant or profit of the existing LHC cryogenics
 7373 infrastructures to feed the detector magnet. Electrical and water cooling network present at
 7374 LHC-P2 are already well sized for the new detector and only minor interventions are expected
 7375 there.

7376 10.8 Detector Design for a Low Energy FCC-eh

7377 Although not the primary focus of this document, it is worth noting that a full detector design
 7378 has also been carried out for an *ep* facility based on an FCC tunnel with proton-ring magnet
 7379 strengths limited such that the proton energy is 20 TeV. The basic layout is similar to the LHeC
 7380 detector. Similar or better performance is obtained compared with the LHeC detector, provided
 7381 that additional disks are included in the forward and backward trackers and the calorimeter
 7382 depths are scaled logarithmically with the beam energies. The basic layout is shown in Fig. 10.17.

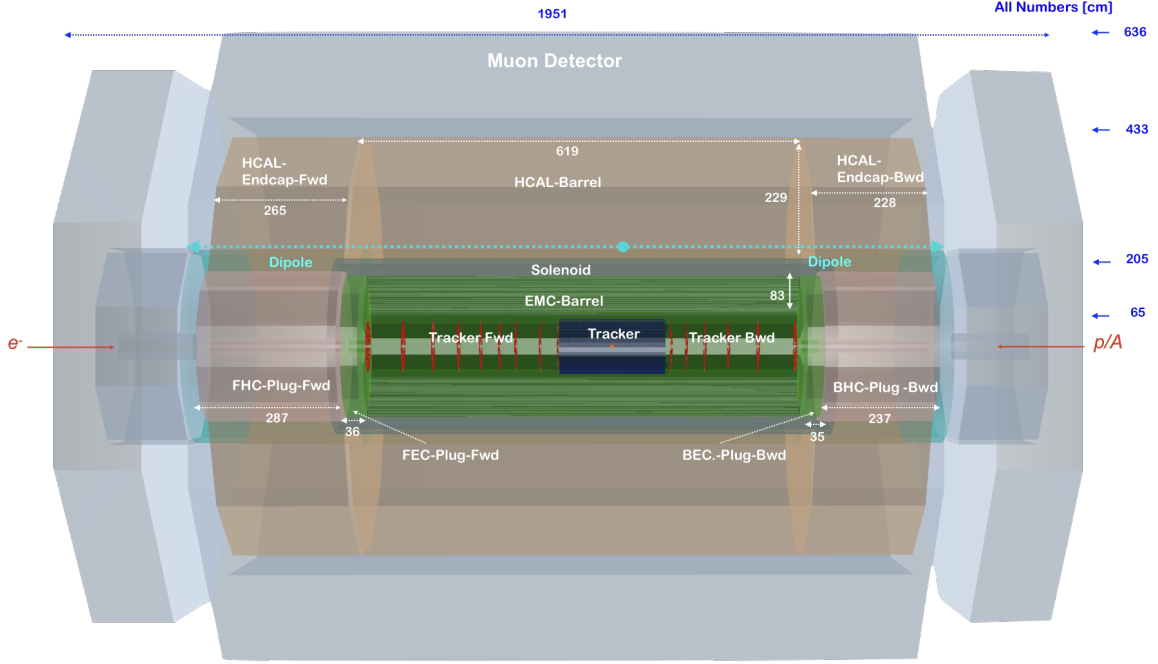


Figure 10.17: Side view of a low energy FCCeh ($E_p = 20$ TeV) concept detector, designed using the DD4hep framework [750], showing the essential features. The solenoid is again placed between the ECAL-Barrel and Hadronic-Barrel calorimeters and is housed in a cryostat in common with the beam steering dipoles extending over the full length of the barrel and plug hadronic calorimeters. The sizes have been chosen such that the solenoid/dipoles and ECAL-Barrel systems as well as the whole tracker are also suitable to operate after an upgrade of the beam energy to $E_p = 50$ TeV.

Calo (lowE-FCCeh)	EMC		HCAL	
	Barrel	Ecap Fwd	Barrel	Ecap Bwd
Readout, Absorber	Sci,Pb	Sci,Fe	Sci,Fe	Sci,Fe
Layers	49	91	68	78
Integral Absorber Thickness [cm]	36.6	206.0	184.0	178.0
η_{\max}, η_{\min}	2.8, -1.7	2.0, 0.8	1.6, -0.8	-1.4, -1.8
$\sigma_E/E = a\sqrt{E} \oplus b$	[%] 12.6/1.1	38.9/3.3	42.4/4.2	40.6/3.5
Λ_I / X_0	$X_0 = 66.2$	$\Lambda_I = 12.7$	$\Lambda_I = 11.3$	$\Lambda_I = 11.0$
Total area Sci	[m ²] 2915	4554	12298	3903

Table 10.5: Basic properties and simulated resolutions of barrel calorimeter modules in a scaled LHeC detector configuration, illustrating a low energy FCC detector setup. For each of the modules, the rows indicate the absorber and sensitive materials, the pseudorapidity coverage, the contributions to the simulated resolution from the sampling (a) and material (b) terms in the form a/b , the depth in terms of radiation or interaction lengths and the total area covered by the sensitive material.

GEANT4 [752] simulation based fits using crystal ball function [753] [754] [755].

Calo (lowE-FCCeh)	FHC Plug Fwd	FEC Plug Fwd	BEC Plug Bwd	BHC Plug Bwd
Readout, Absorber	Si,W	Si,W	Si,Pb	Si,Cu
Layers	296	49	59	238
Integral Absorber Thickness [cm]	256.9	29.6	27.9	220.8
η_{\max}, η_{\min}	5.8, 1.8	5.4, 1.8	-5.1, -5.2	-5.2, -5.6
$\sigma_E/E = a/\sqrt{E} \oplus b$ [%]	61.9/0.5	26.5/0.4	24.7/0.4	46.7/4.4
Λ_I / X_0	$\Lambda_I = 15.5$	$X_0 = 84.7$	$X_0 = 50.2$	$\Lambda_I = 14.7$
Total area Si [m ²]	2479	364	438	1994

Table 10.6: Basic properties and simulated resolutions of forward and backward plug calorimeter modules in a scaled LHeC detector configuration, illustrating a low energy FCC detector setup. For each of the modules, the rows indicate the absorber and sensitive materials, the pseudorapidity coverage, the contributions to the simulated resolution from the sampling (a) and material (b) terms in the form a/b , the depth in terms of radiation or interaction lengths and the total area covered by the sensitive material. **GEANT4** [752] simulation based fits using crystal ball function [753] [754] [755].

Chapter 11

Conclusion

The Large Hadron Collider determines the energy frontier of experimental collider physics for the next two decades. Following the current luminosity upgrade, the LHC can be further upgraded with a high energy, intense electron beam such that it becomes a twin-collider facility, in which ep collisions are registered concurrently with pp . A joint ECFA, CERN and NuPECC initiative led to a detailed conceptual design report (CDR) [1] for the Large Hadron Electron Collider published in 2012. The present paper represents an update of the original CDR in view of new physics and technology developments.

The LHeC uses a novel, energy recovery linear electron accelerator which enables TeV energy electron-proton collisions at high luminosity, of $O(10^{34}) \text{ cm}^{-2}\text{s}^{-1}$, exceeding that of HERA by nearly three orders of magnitude. The discovery of the Higgs boson and the surprising absence of BSM physics at LHC demand to extend the experimental base of particle physics suitable to explore the energy frontier, beyond pp collisions at the LHC. The LHC infrastructure is the largest single investment the European and global particle physics community ever achieved, and the addition of an electron accelerator a most appropriate way to build on it, and to sustain the HL-LHC programme by adding necessary elements which are provided by high energy deep inelastic scattering. As has been shown in this paper, the external DIS input transforms the LHC to a much more powerful facility, with a resolution of matter substructure, a more precise Higgs programme challenging and complementing that of a next e^+e^- collider and with a hugely extended potential to find new physics beyond the Standard Model.

The very high luminosity and the substantial extension of the kinematic range in deep inelastic scattering compared to HERA, make the LHeC on its own a uniquely powerful TeV energy collider. Realising the *Electrons for LHC* programme developed with the previous and the present white papers, will create the cleanest, high resolution microscope accessible to the world, one may term a “CERN Hubble Telescope for the Micro-Universe”. It is directed to unravel the substructure of matter encoded in the complex dynamics of the strong interaction, a necessary input for the HL-LHC and for future hadron colliders. This regards the complete resolution of the partonic densities in a unprecedented range of small dimensions, the foundations for new, generalised views on proton structure and the long awaited clarification of the QCD dynamics at high densities, as are observed at small Bjorken x . New high precision measurements on diffraction and vector mesons will shed new light on the puzzle of confinement. As a complement to the LHC and a possible future e^+e^- machine, the LHeC would scrutinise the Standard Model (SM) deeper than ever before, and possibly discover new physics in the electroweak and chromodynamic sectors. Through the extension of the kinematic range by about three orders of magnitude in lepton-nucleus (eA) scattering, the LHeC is the most powerful electron-ion

7419 research facility one can build in the next decades, for elucidating the chromodynamic origin of
7420 the Quark-Gluon-Plasma and clarifying the partonic substructure and dynamics inside nuclei
7421 for the first time. The Higgs programme is very rich as it relies on CC and NC precision
7422 measurements for which an inverse ab is desirable to achieve. The BSM prospects as on right-
7423 handed neutrinos, long lived particles and electroweak SUSY are indeed exciting due to the high
7424 energy and absence of pile-up in ep .

7425 The LHeC physics programme reaches far beyond any specialised goal which underlines the
7426 unique opportunity for particle physics to build a novel laboratory for accelerator based energy
7427 frontier research at CERN. The project is fundable within the CERN budget, and not preventing
7428 much more massive investments into the further future. It offers the possibility for the current
7429 generation of accelerator physicists to build a new collider using and developing novel technology
7430 while preparations proceed for the next grand step in particle physics for generations ahead.

7431 The main innovation through the LHeC is the first ever high energy application of energy recov-
7432 ery technology, based on high quality superconducting RF developments, a major contribution
7433 to the development of *green* collider technology which is an appropriate response to demands
7434 of our time. The ERL technique is more and more seen to have major further applications, be-
7435 yond ep at HE-LHC and FCC-eh, such as for FCC-ee, as a $\gamma\gamma$ Higgs facility or, beyond particle
7436 physics, as the highest energy XFEL of hugely increased brightness.

7437 The paper describes the plans and configuration of PERLE, the first 10 MW power ERL facility
7438 which is being prepared in international collaboration for built at Irene Curie Laboratory at
7439 Orsay. PERLE has adopted the 3-pass configuration, cavity and cryomodule technology, source
7440 and injector layout, frequency and electron current parameters from the LHeC. This qualifies
7441 it to be the ideal machine to accompany the development of the LHeC. With its challenging
7442 parameters, such as an intensity exceeding that of ELI by orders of magnitude, PERLE has
7443 an independent, far reaching low energy nuclear and particle physics programme with new and
7444 particularly precise measurements. It also has a possible program on industrial applications,
7445 which have not been discussed in the present paper.

7446 The LHeC provides an opportunity for building a novel collider detector which is sought for as
7447 the design of the HL-LHC detector upgrades is approaching completion. A novel ep experiment
7448 enables modern detection technology, such as HV CMOS Silicon tracking, to be further developed
7449 and exploited in a new generation, 4π acceptance, no pile-up, high precision collider detector in
7450 the decade(s) hence. This paper presented an update of the 2012 detector design, in response
7451 to demands from the development of physics, especially Higgs and BSM, and technology in
7452 detectors and analysis.

7453 The next steps in this development are rather clear: it needs PERLE to proceed, limited funds for
7454 prototypes, especially of the IR magnets, be made available and a proto-detector Collaboration
7455 to emerge such that in a few years time a decision on building the LHeC at CERN may be taken,
7456 in the context also of what these years may bring for physics, with higher LHC luminosity, for
7457 Asia, with decisions about ILC and CEPC, and for the further future and support of CERN as
7458 the world's leading laboratory for particle physics, including its way of cooperation globally and
7459 with its surrounding major laboratories.

7460 The recent history teaches a lesson about the complementarity required for energy frontier
7461 particle physics. In the seventies and eighties, CERN hosted the $p\bar{p}$ energy frontier, with UA1
7462 and UA2, and the most powerful DIS experiments with muons (EMC, BCDMS, NMC) and
7463 neutrinos (CDHSW, CHARM), while $e + e^-$ physics was pursued at PEP, PETRA and also
7464 TRISTAN. Following this, the Fermi scale could be explored with the Tevatron, HERA and

7465 LEP. The here advertised next logical step is to complement the HL-LHC by a most powerful
7466 DIS facility, the LHeC, while preparations will take shape for a new e^+e^- collider, currently at
7467 CERN and in Asia. This scenario would give a realistic and yet exciting base for completing
7468 the exploration of TeV scale physics which may not be achieved with solely the LHC.

7469 The ERL concept and technology here presented has the potential to accompany the FCC for
7470 realising the FCC-eh machine when the time comes for the next, higher energy hadron collider,
7471 and the search for new physics at the O(10) TeV scale.

7472 **Acknowledgement**

7473

7474 The analyses and developments here presented would not have been possible without the CERN
7475 Directorate and other labs and Universities supporting this study. We thank the technicians
7476 contributing to this work, such as with their competence in building the first 802 MHz SC
7477 cavity. We thank many colleagues for their interest in this work and a supportive attitude when
7478 time constraints could have caused lesser understanding. Special thanks are also due to the
7479 members and chair of the International Advisory Committee for their attention and guidance
7480 to the project. From the beginning of the LHeC study, it has been supported by ECFA and its
7481 chairs which was a great help and stimulus for undertaking this work which has been performed
7482 outside our usual duties. During the time, a number of students, in master and PhD courses,
7483 have made very essential contributions to this project for which we are especially grateful. This
7484 also extends to colleagues with whom we have been working closely but who meanwhile left this
7485 development, perhaps temporarily, or work at non-particle physics institutions while wishing
7486 LHeC success. The current situation of particle physics reminds us on the potential we have
7487 when resources and prospects are unified, for which this study is considered to be a contribution.

7488 **Appendix A**

7489 **Statement of the International** 7490 **Advisory Committee**

7491 End of 2014, the CERN Directorate appointed an International Advisory Committee (IAC) for
7492 advice on the direction of energy frontier electron-hadron scattering at CERN, for their mandate
7493 see below. The committee and its chair, em. DG of CERN Herwig Schopper, was reconfirmed
7494 when a new DG had been appointed. The IAC held regular sessions at the annual LHeC
7495 workshops in which reports were heard by the co-coordinators of the project, Oliver Brüning
7496 and Max Klein. Its work and opinion shaped the project development considerably and it was
7497 pivotal for the foundation of the PERLE project. The committee was in close contact and
7498 advised especially on the documents, on the LHeC [5,7] and PERLE [8], submitted end of 2018
7499 to the update of the European strategy on particle physics. In line with the present updated
7500 LHeC design report and the strategy process, which began in 2018 and is due to conclude in
7501 spring 2020, the IAC formulated a brief report to the CERN DG, in which its observations
7502 and recommendations have been summarised. This report was also sent to the members of the
7503 European particle physics strategy group. It is reproduced here.

7504 **Report by the IAC on the LHeC to the DG of CERN**

7505 The development of the LHeC project was initiated by CERN and ECFA, in cooperation
7506 with NuPECC. It culminated in the publication of the Conceptual Design Report (CDR),
7507 arXiv:1206.2913 in 2012, which received by now about 500 citations. In 2014, the CERN Di-
7508 rectorate invited our committee to advise the CERN Directorate, and the Coordination Group,
7509 on the directions of future energy frontier electron-hadron scattering as are enabled with the
7510 LHC and the future FCC (for the mandate see below). In 2016, Council endorsed the HL-LHC,
7511 which offers a higher LHC performance and strengthened the interest in exploring the Higgs
7512 phenomenon. In view of the imminent final discussions for the European Road Map for particle
7513 physics, a short summary report is here presented.

7514 Main Developments 2014–2019

7515 A series of annual workshops on the LHeC and FCC-eh was held, and this report is given
7516 following the latest workshop <https://indico.cern.ch/event/835947> , October 24/25, 2019.

7517 Based on recent developments concerning the development of the LHC accelerator and physics,
7518 and the progress in technology, a new default configuration of the LHeC and FCC-eh has been
7519 worked out with a tenfold increased peak luminosity goal, of $10^{34} \text{ cm}^{-2} \text{ s}^{-1}$, as compared to the
7520 CDR. A comprehensive paper, “The LHeC at the HL-LHC”, is being finalised for publication
7521 this year.

7522 Within this work, it has been shown that the LHeC represents the cleanest, high resolution
7523 microscope the world can currently build, a seminal opportunity to develop and explore QCD,
7524 to study high precision Higgs and electroweak physics and to substantially extend the range
7525 and prospects for accessing BSM physics, on its own and in combination of pp with ep. The
7526 LHeC, in eA scattering mode, has a unique discovery potential on nuclear structure, dynamics
7527 and QGP physics.

7528 Intense eh collisions with LHeC and FCC-eh are enabled through a special electron-beam race-
7529 track arrangement with energy recovery linac (ERL) technology. If LHeC were to be considered
7530 either on its own merits, or as a bridge project to FCC-eh, it seemed important to find a config-
7531 uration, which could be realised within the existing CERN budget. Several options were studied
7532 and found.

7533 Before a decision on such a project can be taken, the ERL technology has to be further developed.
7534 Considerable progress has been made in the USA, and a major effort is now necessary to develop
7535 it further in Europe. An international collaboration (ASTeC, BINP, CERN, Jefferson Lab,
7536 Liverpool, Orsay) has been formed to realise the first multi-turn 10 MW ERL facility, PERLE
7537 at Orsay, with its main parameters set by the LHeC and producing the first encouraging results
7538 on 802 MHz cavity technology, for the CDR see arXiv:1705.08783.

7539 This radically new accelerator technology, ERL, has an outstanding technical (SRF), physics
7540 (nuclear physics) and industrial (lithography, transmutations, ..) impact, and offers possible
7541 applications beyond ep (such as a racetrack injector or ERL layout for FCC-ee, a high energy
7542 FEL or $\gamma\gamma$ collider).

7543 In conclusion it may be stated

- 7544 • The installation and operation of the LHeC has been demonstrated to be commensurate
7545 with the currently projected HL-LHC program, while the FCC-eh has been integrated into
7546 the FCC vision;
- 7547 • The feasibility of the project as far as accelerator issues and detectors are concerned has
7548 been shown. It can only be realised at CERN and would fully exploit the massive LHC
7549 and HL-LHC investments;
- 7550 • The sensitivity for discoveries of new physics is comparable, and in some cases superior,
7551 to the other projects envisaged;
- 7552 • The addition of an ep/A experiment to the LHC substantially reinforces the physics pro-
7553 gram of the facility, especially in the areas of QCD, precision Higgs and electroweak as
7554 well as heavy ion physics;
- 7555 • The operation of LHeC and FCC-eh is compatible with simultaneous pp operation; for
7556 LHeC the interaction point 2 would be the appropriate choice, which is currently used by
7557 ALICE;

- 7558 • The development of the ERL technology needs to be intensified in Europe, in national
7559 laboratories but with the collaboration of CERN;
7560 • A preparatory phase is still necessary to work out some time-sensitive key elements, es-
7561 pecially the high power ERL technology (PERLE) and the prototyping of Intersection
7562 Region magnets.

7563 **Recommendations**

7564 i) It is recommended to further develop the ERL based ep/A scattering plans, both at LHC
7565 and FCC, as attractive options for the mid and long term programme of CERN, resp. Before
7566 a decision on such a project can be taken, further development work is necessary, and should
7567 be supported, possibly within existing CERN frameworks (e.g. development of SC cavities and
7568 high field IR magnets).

7569

7570 ii) The development of the promising high-power beam-recovery technology ERL should be in-
7571 tensified in Europe. This could be done mainly in national laboratories, in particular with the
7572 PERLE project at Orsay. To facilitate such a collaboration, CERN should express its interest
7573 and continue to take part.

7574

7575 iii) It is recommended to keep the LHeC option open until further decisions have been taken.
7576 An investigation should be started on the compatibility between the LHeC and a new heavy ion
7577 experiment in Interaction Point 2, which is currently under discussion.

7578

7579 After the final results of the European Strategy Process will be made known, the IAC considers
7580 its task to be completed. A new decision will then have to be taken for how to continue these
7581 activities.

7582

7583 Herwig Schopper, Chair of the Committee,

Geneva, November 4, 2019

7584 **Mandate of the International Advisory Committee**

7585 Advice to the LHeC Coordination Group and the CERN directorate by following the develop-
7586 ment of options of an ep/eA collider at the LHC and at FCC, especially with: Provision of
7587 scientific and technical direction for the physics potential of the ep/eA collider, both at LHC
7588 and at FCC, as a function of the machine parameters and of a realistic detector design, as well
7589 as for the design and possible approval of an ERL test facility at CERN. Assistance in building
7590 the international case for the accelerator and detector developments as well as guidance to the
7591 resource, infrastructure and science policy aspects of the ep/eA collider. (December 2014)

7592 **Members of the Committee**

Sergio Bertolucci (Bologna)
Nichola Bianchi (INFN, now Singapore)
Frederick Bordy (CERN)
Stan Brodsky (SLAC)
7593 Oliver Brüning (CERN, coordinator)
Hesheng Chen (Beijing)
Eckhard Elsen (CERN)
Stefano Forte (Milano)
Andrew Hutton (Jefferson Lab)
Young-Kee Kim (Chicago)

Max Klein (Liverpool, coordinator)
Shin-Ichi Kurokawa (KEK)
Victor Matveev (JINR Dubna)
Aleandro Nisati (Rome I)
Leonid Rivkin (PSI Villigen)
Herwig Schopper (CERN, em.DG, Chair)
Jürgen Schukraft (CERN)
Achille Stocchi (Orsay)
John Womersley (ESS Lund)

Bibliography

- [1] LHeC Study Group, J. L. Abelleira *et al.*, *J. Phys.* G39 (2012) 075001, [arXiv:1206.2913](#).
- [2] G. Apollinari, I. Béjar Alonso, O. Brüning, P. Fessia, M. Lamont, L. Rossi and L. Tavian (eds.), *High-Luminosity Large Hadron Collider (HL-LHC)*, vol. 4. CERN Yellow Rep. Monogr., CERN-2017-007-M, 2017.
- [3] L. Rossi and O. Brüning, “Progress with the High Luminosity LHC project at CERN,” in *Proceedings, 10th International Particle Accelerator Conference (IPAC2019): Melbourne, Australia, May 19-24, 2019*, Jun 2019.
- [4] D. Angal-Kalinin *et al.*, *J. Phys.* G45 (2018) 065003, [arXiv:1705.08783](#).
- [5] LHeC Study Group, O. Brüning, M. Klein *et al.*, “Exploring the Energy Frontier with Deep Inelastic Scattering at the LHC,” A Contribution to the Update of the European Strategy on Particle Physics, CERN-ACC-NOTE-2018-0084, Dec 2018.
- [6] LHeC and PERLE Collaborations, O. Brüning, M. Klein *et al.*, *J. Phys.* G46 (2019) 123001.
- [7] LHeC Study Group, O. Brüning, M. Klein *et al.*, “Addendum. Exploring the Energy Frontier with Deep Inelastic Scattering at the LHC,” A Contribution to the Update of the European Strategy on Particle Physics, CERN-ACC-NOTE-2018-0085, Dec 2018.
- [8] PERLE Collaboration, M. Klein, A. Stocchi *et al.*, “PERLE: A High Power Energy Recovery Facility for Europe,” A Contribution to the Update of the European Strategy on Particle Physics, CERN-ACC-NOTE-2018-0086, Dec 2018.
- [9] S. Hossenfelder, *Lost in math*. Basic Books, New York, 2018.
- [10] G. Altarelli, *Frascati Phys. Ser.* 58 (2014) 102, [arXiv:1407.2122](#).
- [11] J. De Hondt, “Talk on the Future of Particle Physics and on ECFA Matters,” Plenary Session, ECFA, CERN, November, 2019.
- [12] FCC Collaboration, A. Abada *et al.*, *Eur. Phys. J.* C79 (2019) 474.
- [13] FCC Collaboration, A. Abada *et al.*, *Eur. Phys. J.* ST 228 (2019) 261.
- [14] FCC Collaboration, A. Abada *et al.*, *Eur. Phys. J.* ST 228 (2019) 755.
- [15] CEPC-SPPC Study Group, M. Ahmad *et al.*, “CEPC-SPPC Preliminary Conceptual Design Report. 2. Accelerator,” IHEP-CEPC-DR-2015-01, IHEP-AC-2015-01, 2015.
- [16] CEPC Study Group, M. Dong *et al.*, “CEPC Conceptual Design Report: Volume 2 - Physics & Detector,” 2018. [arXiv:1811.10545](#).
- [17] R. P. Feynman, *Photon-hadron interactions*. Westview Press, Reading, MA, 1972.
- [18] E. D. Bloom *et al.*, *Phys. Rev. Lett.* 23 (1969) 930.
- [19] M. Breidenbach, J. I. Friedman, H. W. Kendall, E. D. Bloom, D. H. Coward, H. C. DeStaebler, J. Drees, L. W. Mo and R. E. Taylor, *Phys. Rev. Lett.* 23 (1969) 935.
- [20] R. P. Feynman, *Phys. Rev. Lett.* 23 (1969) 1415.
- [21] J. D. Bjorken and E. A. Paschos, *Phys. Rev.* 185 (1969) 1975.
- [22] C. Y. Prescott *et al.*, *Phys. Lett.* 77B (1978) 347.
- [23] S. Weinberg, *Phys. Rev. Lett.* 19 (1967) 1264.
- [24] B. H. Wiik, *Acta Phys. Polon.* B16 (1985) 127.
- [25] M. Klein and R. Yoshida, *Prog. Part. Nucl. Phys.* 61 (2008) 343, [arXiv:0805.3334](#).

- [26] A. De Rujula, S. L. Glashow, H. D. Politzer, S. B. Treiman, F. Wilczek and A. Zee, *Phys. Rev. D* **10** (1974) 1649.
- [27] FCC Collaboration, A. Abada *et al.*, *Eur. Phys. J. ST* **228** (2019) 1109.
- [28] F. Marhauser *et al.*, “802 MHz ERL Cavity Design and Development,” in *Proceedings, 9th International Particle Accelerator Conference (IPAC 2018): Vancouver, BC Canada, April 29-May 4, 2018*, 2018.
- [29] V. N. Litvinenko, T. Roser and M. Chamizo Llatas, [arXiv:1909.04437](https://arxiv.org/abs/1909.04437).
- [30] O. Brüning, “FCC-eh Cost Estimate,” CERN-Acc-Note-2018-0061, 2018.
- [31] A. Bogacz, “The LHeC ERL - Optics and Performance Optimisation,” Talk given at ERL Workshop, Berlin, 2019.
- [32] O. Brüning, J. Jowett, M. Klein, D. Pellegrini, D. Schulte and F. Zimmermann, “Future Circular Collider Study FCC-eh Baseline Parameters,” 2017. CERN FCC-ACC-RPT-012.
- [33] F. Bordry *et al.*, “Machine Parameters and Projected Luminosity Performance of Proposed Future Colliders at CERN,” 2018. [arXiv:1810.13022](https://arxiv.org/abs/1810.13022).
- [34] T. J. Hobbs, J. T. Londergan, D. P. Murdock and A. W. Thomas, *Phys. Lett. B* **698** (2011) 123, [arXiv:1101.3923](https://arxiv.org/abs/1101.3923).
- [35] R. Abdul Khalek, S. Bailey, J. Gao, L. Harland-Lang and J. Rojo, *Eur. Phys. J. C* **78** (2018) 962, [arXiv:1810.03639](https://arxiv.org/abs/1810.03639).
- [36] R. Abdul Khalek, S. Bailey, J. Gao, L. Harland-Lang and J. Rojo, [arXiv:1906.10127](https://arxiv.org/abs/1906.10127).
- [37] J. Butterworth *et al.*, *J. Phys. G* **43** (2016) 023001, [arXiv:1510.03865](https://arxiv.org/abs/1510.03865).
- [38] H. Paukkunen and P. Zurita, *JHEP* **12** (2014) 100, [arXiv:1402.6623](https://arxiv.org/abs/1402.6623).
- [39] C. Schmidt, J. Pumplin, C. P. Yuan and P. Yuan, *Phys. Rev. D* **98** (2018) 094005, [arXiv:1806.07950](https://arxiv.org/abs/1806.07950).
- [40] B.-T. Wang, T. J. Hobbs, S. Doyle, J. Gao, T.-J. Hou, P. M. Nadolsky and F. I. Olness, *Phys. Rev. D* **98** (2018) 094030, [arXiv:1803.02777](https://arxiv.org/abs/1803.02777).
- [41] T. J. Hobbs, B.-T. Wang, P. M. Nadolsky and F. I. Olness, *PoS DIS2019* (2019) 247, [arXiv:1907.00988](https://arxiv.org/abs/1907.00988).
- [42] J. C. Collins, D. E. Soper and G. F. Sterman, *Adv. Ser. Direct. High Energy Phys.* **5** (1989) 1, [arXiv:hep-ph/0409313](https://arxiv.org/abs/hep-ph/0409313).
- [43] LHeC Study Group, J. L. Abelleira *et al.*, “On the Relation of the LHeC and the LHC,” 2012. [arXiv:1211.5102](https://arxiv.org/abs/1211.5102).
- [44] S. Moch, B. Ruijl, T. Ueda, J. A. M. Vermaseren and A. Vogt, *JHEP* **10** (2017) 041, [arXiv:1707.08315](https://arxiv.org/abs/1707.08315).
- [45] H1 and ZEUS Collaborations, H. Abramowicz *et al.*, *Eur. Phys. J. C* **75** (2015) 580, [arXiv:1506.06042](https://arxiv.org/abs/1506.06042).
- [46] HERAFitter Group, S. Alekhin *et al.*, *Eur. Phys. J. C* **75** (2015) 304, [arXiv:1410.4412](https://arxiv.org/abs/1410.4412).
- [47] H1 and ZEUS Collaborations, F. Aaron *et al.*, *JHEP* **1001** (2010) 109, [arXiv:0911.0884](https://arxiv.org/abs/0911.0884).
- [48] H1 Collaboration, F. Aaron *et al.*, *Eur. Phys. J. C* **64** (2009) 561, [arXiv:0904.3513](https://arxiv.org/abs/0904.3513).
- [49] M. Botje, *Comput. Phys. Commun.* **182** (2011) 490, [arXiv:1005.1481](https://arxiv.org/abs/1005.1481).
- [50] R. Thorne, *Phys.Rev. D* **73** (2006) 054019, [arXiv:0601245](https://arxiv.org/abs/0601245).
- [51] R. Thorne, *Phys.Rev. D* **86** (2012) 074017, [arXiv:1201.6180](https://arxiv.org/abs/1201.6180).
- [52] F. James and M. Roos, *Comp. Phys. Comm.* **10** (1975) 343.
- [53] H1, ZEUS and NNLOJET Collaborations, “HERAPDF2.0NNLOJets, preliminary,” 2019. [H1prelim-19-041](https://arxiv.org/abs/1904.041), [ZEUS-prel-19-001](https://arxiv.org/abs/1904.001).
- [54] H1 Collaboration, C. Adloff *et al.*, *Eur. Phys. J. C* **21** (2001) 33, [arXiv:hep-ex/0012053](https://arxiv.org/abs/hep-ex/0012053).
- [55] S. Alekhin, J. Blümlein and S. O. Moch, *Mod. Phys. Lett. A* **31** (2016) 1630023.
- [56] M. Klein, “Future Deep Inelastic Scattering with the LHeC,” in *From My Vast Repertoire: Guido Altarelli's Legacy*, A. Levy, S. Forte and G. Ridolfi (eds.), p. 303. 2019. [arXiv:1802.04317](https://arxiv.org/abs/1802.04317).
- [57] J. Blümlein and M. Klein, “Kinematics and resolution at future e p colliders,” in *1990 DPF Summer Study on High-energy Physics: Research Directions for the Decade (Snowmass 90) Snowmass, Colorado, June 25-July 13, 1990*, 1990.
- [58] S. J. Brodsky and G. R. Farrar, *Phys. Rev. Lett.* **31** (1973) 1153.
- [59] S. J. Brodsky and G. R. Farrar, *Phys. Rev. D* **11** (1975) 1309.
- [60] V. A. Matveev, R. M. Muradian and A. N. Tavkhelidze, *Lett. Nuovo Cim.* **7** (1973) 719.

- [61] HERAFitter Group, S. Alekhin *et al.*, *Eur. Phys. J. C*75 (2015) 304, [arXiv:1410.4412](#).
- [62] A. M. Cooper-Sarkar and K. Wichmann, *Phys. Rev. D*98 (2018) 014027, [arXiv:1803.00968](#).
- [63] H. Abdolmaleki *et al.*, [arXiv:1907.01014](#).
- [64] ATLAS Collaboration, G. Aad *et al.*, *Phys. Rev. Lett.* 109 (2012) 012001, [arXiv:1203.4051](#).
- [65] ATLAS Collaboration, M. Aaboud *et al.*, *Eur. Phys. J. C*77 (2017) 367, [arXiv:1612.03016](#).
- [66] ATLAS Collaboration, G. Aad *et al.*, *JHEP* 05 (2014) 068, [arXiv:1402.6263](#).
- [67] CMS Collaboration, S. Chatrchyan *et al.*, *JHEP* 02 (2014) 013, [arXiv:1310.1138](#).
- [68] M. A. G. Aivazis, F. I. Olness and W.-K. Tung, *Phys. Rev. Lett.* 65 (1990) 2339.
- [69] M. A. G. Aivazis, F. I. Olness and W.-K. Tung, *Phys. Rev. D*50 (1994) 3085, [arXiv:hep-ph/9312318](#).
- [70] M. A. G. Aivazis, J. C. Collins, F. I. Olness and W.-K. Tung, *Phys. Rev. D*50 (1994) 3102, [arXiv:hep-ph/9312319](#).
- [71] R. S. Thorne and R. G. Roberts, *Eur. Phys. J. C*19 (2001) 339, [arXiv:hep-ph/0010344](#).
- [72] S. Alekhin, J. Blümlein and S. Moch, *Phys. Rev. D*86 (2012) 054009, [arXiv:1202.2281](#).
- [73] S. Alekhin, J. Blümlein and S. Moch, *Phys. Rev. D*89 (2014) 054028, [arXiv:1310.3059](#).
- [74] S. Alekhin, J. Blümlein, S. Klein and S. Moch, *Phys. Rev. D*81 (2010) 014032, [arXiv:0908.2766](#).
- [75] S. Forte, E. Laenen, P. Nason and J. Rojo, *Nucl. Phys. B*834 (2010) 116, [arXiv:1001.2312](#).
- [76] A. D. Martin, W. J. Stirling, R. S. Thorne and G. Watt, *Eur. Phys. J. C*70 (2010) 51, [arXiv:1007.2624](#).
- [77] R. D. Ball, V. Bertone, F. Cerutti, L. Del Debbio, S. Forte, A. Guffanti, J. I. Latorre, J. Rojo and M. Ubiali, *Nucl. Phys. B*849 (2011) 296, [arXiv:1101.1300](#).
- [78] S. J. Brodsky, P. Hoyer, C. Peterson and N. Sakai, *Phys. Lett.* 93B (1980) 451.
- [79] S. J. Brodsky, A. Kusina, F. Lyonnet, I. Schienbein, H. Spiesberger and R. Vogt, *Adv. High Energy Phys.* 2015 (2015) 231547, [arXiv:1504.06287](#).
- [80] S. J. Brodsky and S. Gardner, *Phys. Rev. Lett.* 116 (2016) 019101, [arXiv:1504.00969](#).
- [81] G. F. de Teramond and S. J. Brodsky, *Phys. Rev. Lett.* 102 (2009) 081601, [arXiv:0809.4899](#).
- [82] SELEX Collaboration, A. Ocherashvili *et al.*, *Phys. Lett. B*628 (2005) 18, [arXiv:hep-ex/0406033](#).
- [83] ANDY Collaboration, L. C. Bland *et al.*, [arXiv:1909.03124](#).
- [84] G. Zweig, “An SU(3) model for strong interaction symmetry and its breaking. Version 1,” 1964.
- [85] H. Fritzsch, M. Gell-Mann and H. Leutwyler, *Phys. Lett.* 47B (1973) 365–368.
- [86] D. J. Gross and F. Wilczek, *Phys. Rev. Lett.* 30 (1973) 1343–1346.
- [87] H. D. Politzer, *Phys. Rev. Lett.* 30 (1973) 1346–1349.
- [88] G. Dissertori, *Adv. Ser. Direct. High Energy Phys.* 26 (2016) 113–128, [arXiv:1506.05407](#).
- [89] Particle Data Group, M. Tanabashi *et al.*, *Phys. Rev. D*98 (2018) 030001.
- [90] D. d’Enterria *et al.*, *PoS ALPHAS2019* (2019) 001, [arXiv:1907.01435](#).
- [91] K. H. Streng, T. F. Walsh and P. M. Zerwas, *Z. Phys. C*2 (1979) 237.
- [92] H1 Collaboration, F. D. Aaron *et al.*, *Eur. Phys. J. C*67 (2010) 1, [arXiv:0911.5678](#).
- [93] S. D. Ellis and D. E. Soper, *Phys. Rev. D*48 (1993) 3160–3166, [arXiv:hep-ph/9305266](#).
- [94] H1 Collaboration, C. Adloff *et al.*, *Eur. Phys. J. C*13 (2000) 397, [arXiv:hep-ex/9812024](#).
- [95] H1 Collaboration, C. Adloff *et al.*, *Eur. Phys. J. C*19 (2001) 289, [arXiv:hep-ex/0010054](#).
- [96] H1 Collaboration, C. Adloff *et al.*, *Phys. Lett. B*542 (2002) 193, [arXiv:hep-ex/0206029](#).
- [97] H1 Collaboration, A. Aktas *et al.*, *Eur. Phys. J. C*33 (2004) 477, [arXiv:hep-ex/0310019](#).
- [98] H1 Collaboration, A. Aktas *et al.*, *Eur. Phys. J. C*37 (2004) 141, [arXiv:hep-ex/0401010](#).
- [99] H1 Collaboration, A. Aktas *et al.*, *Phys. Lett. B*653 (2007) 134, [arXiv:0706.3722](#).
- [100] H1 Collaboration, F. D. Aaron *et al.*, *Eur. Phys. J. C*65 (2010) 363, [arXiv:0904.3870](#).
- [101] H1 Collaboration, V. Andreev *et al.*, *Eur. Phys. J. C*75 (2015) 65, [arXiv:1406.4709](#).
- [102] H1 Collaboration, V. Andreev *et al.*, *Eur. Phys. J. C*77 (2017) 215, [arXiv:1611.03421](#).
- [103] ZEUS Collaboration, J. Breitweg *et al.*, *Phys. Lett. B*479 (2000) 37, [arXiv:hep-ex/0002010](#).
- [104] ZEUS Collaboration, S. Chekanov *et al.*, *Eur. Phys. J. C*23 (2002) 13, [arXiv:hep-ex/0109029](#).

- [105] ZEUS Collaboration, S. Chekanov *et al.*, *Phys. Lett.* B547 (2002) 164, [arXiv:hep-ex/0208037](#).
- [106] ZEUS Collaboration, S. Chekanov *et al.*, *Eur. Phys. J.* C35 (2004) 487, [arXiv:hep-ex/0404033](#).
- [107] ZEUS Collaboration, S. Chekanov *et al.*, *Nucl. Phys.* B765 (2007) 1, [arXiv:hep-ex/0608048](#).
- [108] ZEUS Collaboration, S. Chekanov *et al.*, *Phys. Lett.* B649 (2007) 12, [arXiv:hep-ex/0701039](#).
- [109] ZEUS Collaboration, H. Abramowicz *et al.*, *Eur. Phys. J.* C70 (2010) 965, [arXiv:1010.6167](#).
- [110] ZEUS Collaboration, H. Abramowicz *et al.*, *Phys. Lett.* B691 (2010) 127, [arXiv:1003.2923](#).
- [111] CMS Collaboration, V. Khachatryan *et al.*, *JHEP* 03 (2017) 156, [arXiv:1609.05331](#).
- [112] K. Rabbertz, *Springer Tracts Mod. Phys.* 268 (2017) 1.
- [113] ATLAS Collaboration, M. Aaboud *et al.*, *JHEP* 09 (2017) 020, [arXiv:1706.03192](#).
- [114] ATLAS Collaboration, M. Aaboud *et al.*, *JHEP* 05 (2018) 195, [arXiv:1711.02692](#).
- [115] J. Currie, T. Gehrmann and J. Niehues, *Phys. Rev. Lett.* 117 (2016) 042001, [arXiv:1606.03991](#).
- [116] J. Currie, T. Gehrmann, A. Huss and J. Niehues, *JHEP* 07 (2017) 018, [arXiv:1703.05977](#).
- [117] T. Gehrmann *et al.*, *PoS RADCOR2017* (2018) 074, [arXiv:1801.06415](#).
- [118] T. Kluge, K. Rabbertz and M. Wobisch, “FastNLO: Fast pQCD calculations for PDF fits,” in *Proceedings, 14th International Workshop of deep inelastic scattering (DIS 2006), Tsukuba, Japan, April 20-24, 2006*, 2006. [arXiv:hep-ph/0609285](#).
- [119] D. Britzger, K. Rabbertz, F. Stober and M. Wobisch, “New features in version 2 of the fastNLO project,” in *Proceedings, 20th International Workshop on Deep-Inelastic Scattering and Related Subjects (DIS 2012): Bonn, Germany, March 26-30, 2012*, 2012. [arXiv:1208.3641](#).
- [120] D. Britzger *et al.*, *Eur. Phys. J.* C79 (2019) 845, [arXiv:1906.05303](#).
- [121] H1 Collaboration, V. Andreev *et al.*, *Eur. Phys. J.* C77 (2017) 791, [arXiv:1709.07251](#).
- [122] R. Kogler, *Measurement of jet production in deep-inelastic e p scattering at HERA*. PhD thesis, Hamburg U., 2011.
- [123] CMS Collaboration, V. Khachatryan *et al.*, *JINST* 12 (2017) P02014, [arXiv:1607.03663](#).
- [124] ATLAS Collaboration, M. Aaboud *et al.*, “Determination of jet calibration and energy resolution in proton-proton collisions at $\sqrt{s} = 8$ TeV using the ATLAS detector,” 2019. [arXiv:1910.04482](#).
- [125] J. R. Ellis, E. Gardi, M. Karliner and M. A. Samuel, *Phys. Lett.* B366 (1996) 268, [arXiv:hep-ph/9509312](#).
- [126] S. J. Brodsky and X.-G. Wu, *Phys. Rev.* D85 (2012) 034038, [arXiv:1111.6175](#). [Erratum: *Phys. Rev.* D86,079903(2012)].
- [127] S. J. Brodsky and X.-G. Wu, *Phys. Rev. Lett.* 109 (2012) 042002, [arXiv:1203.5312](#).
- [128] S. J. Brodsky and L. Di Giustino, *Phys. Rev.* D86 (2012) 085026, [arXiv:1107.0338](#).
- [129] M. Mojaza, S. J. Brodsky and X.-G. Wu, *Phys. Rev. Lett.* 110 (2013) 192001, [arXiv:1212.0049](#).
- [130] S. J. Brodsky, M. Mojaza and X.-G. Wu, *Phys. Rev.* D89 (2014) 014027, [arXiv:1304.4631](#).
- [131] S.-Q. Wang, S. J. Brodsky, X.-G. Wu, J.-M. Shen and L. Di Giustino, *Phys. Rev.* D100 (2019) 094010, [arXiv:1908.00060](#).
- [132] Particle Data Group, M. Tanabashi *et al.*, “2019 Update of the Review of Particle Physics,”. <http://pdg.lbl.gov/2019/>. unpublished.
- [133] Flavour Lattice Averaging Group, S. Aoki *et al.*, [arXiv:1902.08191](#).
- [134] D. Boito, M. Golterman, K. Maltman, J. Osborne and S. Peris, *Phys. Rev.* D91 (2015) 034003, [arXiv:1410.3528](#).
- [135] Gfitter Group, M. Baak, J. Cúth, J. Haller, A. Hoecker, R. Kogler, K. Mönig, M. Schott and J. Stelzer, *Eur. Phys. J.* C74 (2014) 3046, [arXiv:1407.3792](#).
- [136] P. Azzi *et al.*, *CERN Yellow Rep. Monogr.* 7 (2019) 1–220, [arXiv:1902.04070](#).
- [137] I. Abt, A. M. Cooper-Sarkar, B. Foster, V. Myronenko, K. Wichmann and M. Wing, *Phys. Rev.* D96 (2017) 014001, [arXiv:1704.03187](#). [*Phys. Rev.* D96,014001(2017)].
- [138] M. Dasgupta and G. P. Salam, *J. Phys.* G30 (2004) R143, [arXiv:hep-ph/0312283](#).
- [139] H1 Collaboration, A. Aktas *et al.*, *Eur. Phys. J.* C46 (2006) 343–356, [arXiv:hep-ex/0512014](#).
- [140] ZEUS Collaboration, S. Chekanov *et al.*, *Nucl. Phys.* B767 (2007) 1–28, [arXiv:hep-ex/0604032](#).
- [141] D. Kang, C. Lee and I. W. Stewart, *Phys. Rev.* D88 (2013) 054004, [arXiv:1303.6952](#).

- [142] Z.-B. Kang, X. Liu and S. Mantry, *Phys. Rev. D*90 (2014) 014041, [arXiv:1312.0301](#).
- [143] D. Kang, C. Lee and I. W. Stewart, *PoS DIS2015* (2015) 142.
- [144] G. Abelof, R. Boughezal, X. Liu and F. Petriello, *Phys. Lett. B*763 (2016) 52–59, [arXiv:1607.04921](#).
- [145] S. Höche, S. Kuttimalai and Y. Li, *Phys. Rev. D*98 (2018) 114013, [arXiv:1809.04192](#).
- [146] J. Currie, T. Gehrmann, E. W. N. Glover, A. Huss, J. Niehues and A. Vogt, *JHEP* 05 (2018) 209, [arXiv:1803.09973](#).
- [147] T. Gehrmann, A. Huss, J. Mo and J. Niehues, [arXiv:1909.02760](#).
- [148] H1 Collaboration, C. Adloff *et al.*, *Eur. Phys. J. C*29 (2003) 497–513, [arXiv:hep-ex/0302034](#).
- [149] H1 Collaboration, A. Aktas *et al.*, *Phys. Lett. B*639 (2006) 21–31, [arXiv:hep-ex/0603014](#).
- [150] ZEUS Collaboration, S. Chekanov *et al.*, *Phys. Rev. D*76 (2007) 072011, [arXiv:0706.3809](#).
- [151] ZEUS Collaboration, H. Abramowicz *et al.*, *Nucl. Phys. B*864 (2012) 1–37, [arXiv:1205.6153](#).
- [152] M. Klasen, *Rev. Mod. Phys.* 74 (2002) 1221–1282, [arXiv:hep-ph/0206169](#).
- [153] M. Glück, E. Reya and A. Vogt, *Phys. Rev. D*46 (1992) 1973–1979.
- [154] K. Sasaki, T. Ueda and T. Uematsu, *CERN Proc.* 1 (2018) 7.
- [155] O. Behnke, A. Geiser and M. Lisovsky, *Prog. Part. Nucl. Phys.* 84 (2015) 1–72, [arXiv:1506.07519](#).
- [156] O. Zenaiev, *Eur. Phys. J. C*77 (2017) 151, [arXiv:1612.02371](#).
- [157] H1 and ZEUS Collaborations, H. Abramowicz *et al.*, *JHEP* 09 (2015) 149, [arXiv:1503.06042](#).
- [158] H1 and ZEUS Collaborations, H. Abramowicz *et al.*, *Eur. Phys. J. C*78 (2018) 473, [arXiv:1804.01019](#).
- [159] A. J. Larkoski, I. Moult and B. Nachman, [arXiv:1709.04464](#).
- [160] J. R. Andersen *et al.*, “Les Houches 2017: Physics at TeV Colliders Standard Model Working Group Report,” 2018. [arXiv:1803.07977](#).
- [161] F. Ringer, *PoS ALPHAS2019* (2019) 010.
- [162] I. I. Balitsky and L. N. Lipatov, *Sov. J. Nucl. Phys.* 28 (1978) 822. [*Yad. Fiz.*28,1597(1978)].
- [163] E. A. Kuraev, L. N. Lipatov and V. S. Fadin, *Sov. Phys. JETP* 45 (1977) 199. [*Zh. Eksp. Teor. Fiz.*72,377(1977)].
- [164] L. N. Lipatov, *Sov. Phys. JETP* 63 (1986) 904. [*Zh. Eksp. Teor. Fiz.*90,1536(1986)].
- [165] V. S. Fadin and L. N. Lipatov, *Phys. Lett. B*429 (1998) 127, [arXiv:hep-ph/9802290](#).
- [166] M. Ciafaloni and G. Camici, *Phys. Lett. B*430 (1998) 349, [arXiv:hep-ph/9803389](#).
- [167] J. Blümlein and A. Vogt, *Phys. Rev. D*58 (1998) 014020, [arXiv:hep-ph/9712546](#).
- [168] D. A. Ross, *Phys. Lett. B*431 (1998) 161, [arXiv:hep-ph/9804332](#).
- [169] Y. V. Kovchegov and A. H. Müller, *Phys. Lett. B*439 (1998) 428, [arXiv:hep-ph/9805208](#).
- [170] E. Levin, *Nucl. Phys. B*545 (1999) 481, [arXiv:hep-ph/9806228](#).
- [171] N. Armesto, J. Bartels and M. A. Braun, *Phys. Lett. B*442 (1998) 459, [arXiv:hep-ph/9808340](#).
- [172] M. Ciafaloni, *Nucl. Phys. B*296 (1988) 49.
- [173] B. Andersson, G. Gustafson and J. Samuelsson, *Nucl. Phys. B*467 (1996) 443.
- [174] J. Kwiecinski, A. D. Martin and P. J. Sutton, *Z. Phys. C*71 (1996) 585, [arXiv:hep-ph/9602320](#).
- [175] J. Kwiecinski, A. D. Martin and A. M. Stasto, *Phys. Rev. D*56 (1997) 3991, [arXiv:hep-ph/9703445](#).
- [176] G. P. Salam, *JHEP* 07 (1998) 019, [arXiv:hep-ph/9806482](#).
- [177] M. Ciafaloni, D. Colferai and G. P. Salam, *JHEP* 10 (1999) 017, [arXiv:hep-ph/9907409](#).
- [178] M. Ciafaloni, D. Colferai and G. P. Salam, *Phys. Rev. D*60 (1999) 114036, [arXiv:hep-ph/9905566](#).
- [179] M. Ciafaloni, D. Colferai, D. Colferai, G. P. Salam and A. M. Stasto, *Phys. Lett. B*576 (2003) 143, [arXiv:hep-ph/0305254](#).
- [180] M. Ciafaloni, D. Colferai, G. P. Salam and A. M. Stasto, *Phys. Lett. B*587 (2004) 87, [arXiv:hep-ph/0311325](#).
- [181] M. Ciafaloni, D. Colferai, G. P. Salam and A. M. Stasto, *Phys. Rev. D*68 (2003) 114003, [arXiv:hep-ph/0307188](#).
- [182] M. Ciafaloni, D. Colferai, G. P. Salam and A. M. Stasto, *JHEP* 08 (2007) 046, [arXiv:0707.1453](#).

- [183] G. Altarelli, R. D. Ball and S. Forte, *Nucl. Phys.* B575 (2000) 313, [arXiv:hep-ph/9911273](#).
- [184] G. Altarelli, R. D. Ball and S. Forte, *Nucl. Phys.* B599 (2001) 383, [arXiv:hep-ph/0011270](#).
- [185] G. Altarelli, R. D. Ball and S. Forte, *Nucl. Phys.* B621 (2002) 359, [arXiv:hep-ph/0109178](#).
- [186] G. Altarelli, R. D. Ball and S. Forte, *Nucl. Phys.* B674 (2003) 459, [arXiv:hep-ph/0306156](#).
- [187] G. Altarelli, R. D. Ball and S. Forte, *Nucl. Phys.* B799 (2008) 199, [arXiv:0802.0032](#).
- [188] R. S. Thorne, *Phys. Rev.* D64 (2001) 074005, [arXiv:hep-ph/0103210](#).
- [189] A. Sabio Vera, *Nucl. Phys.* B722 (2005) 65, [arXiv:hep-ph/0505128](#).
- [190] M. Bonvini, S. Marzani and T. Peraro, *Eur. Phys. J.* C76 (2016) 597, [arXiv:1607.02153](#).
- [191] V. Bertone, S. Carrazza and J. Rojo, *Comput. Phys. Commun.* 185 (2014) 1647, [arXiv:1310.1394](#).
- [192] M. Bonvini, S. Marzani and C. Muselli, *JHEP* 12 (2017) 117, [arXiv:1708.07510](#).
- [193] R. Gandhi, C. Quigg, M. H. Reno and I. Sarcevic, *Phys. Rev.* D58 (1998) 093009, [arXiv:hep-ph/9807264](#).
- [194] IceCube Collaboration, M. G. Aartsen *et al.*, *JINST* 12 (2017) P03012, [arXiv:1612.05093](#).
- [195] J. Kwiecinski, A. D. Martin and A. M. Stasto, *Phys. Rev.* D59 (1999) 093002, [arXiv:astro-ph/9812262](#).
- [196] IceCube Collaboration, M. G. Aartsen *et al.*, *Nature* 551 (2017) 596, [arXiv:1711.08119](#).
- [197] T. K. Gaisser, *Cosmic rays and particle physics*. 1990.
<http://www.cambridge.org/uk/catalogue/catalogue.asp?isbn=0521326672>.
- [198] IceCube Collaboration, M. G. Aartsen *et al.*, *Phys. Rev. Lett.* 113 (2014) 101101, [arXiv:1405.5303](#).
- [199] G. Gelmini, P. Gondolo and G. Varieschi, *Phys. Rev.* D61 (2000) 056011, [arXiv:hep-ph/9905377](#).
- [200] A. Bhattacharya, R. Enberg, Y. S. Jeong, C. S. Kim, M. H. Reno, I. Sarcevic and A. Stasto, *JHEP* 11 (2016) 167, [arXiv:1607.00193](#).
- [201] L. N. Hand, D. G. Miller and R. Wilson, *Rev. Mod. Phys.* 35 (1963) 335.
- [202] G. Miller *et al.*, *Phys. Rev.* D5 (1972) 528.
- [203] E. M. Riordan, A. Bodek, M. Breidenbach, D. L. Dubin, J. E. Elias, J. I. Friedman, H. W. Kendall, J. S. Poucher, M. R. Sogard and D. H. Coward, *Phys. Rev. Lett.* 33 (1974) 561.
- [204] H1 Collaboration, F. D. Aaron *et al.*, *Eur. Phys. J.* C71 (2011) 1579, [arXiv:1012.4355](#).
- [205] G. Altarelli and G. Martinelli, *Phys. Lett.* 76B (1978) 89.
- [206] M. Glück, E. Hoffmann and E. Reya, *Z. Phys.* C13 (1982) 119.
- [207] C. Ewerz and O. Nachtmann, *Annals Phys.* 322 (2007) 1670, [arXiv:hep-ph/0604087](#).
- [208] H. Abdolmaleki *et al.*, *Eur. Phys. J.* C78 (2018) 621, [arXiv:1802.00064](#).
- [209] H1 Collaboration, V. Andreev *et al.*, *Eur. Phys. J.* C74 (2014) 2814, [arXiv:1312.4821](#).
- [210] ATLAS Collaboration, G. Aad *et al.*, *Phys. Rev.* D85 (2012) 072004, [arXiv:1109.5141](#).
- [211] G. Altarelli, *Nuovo Cim.* C035N1 (2012) 1, [arXiv:1106.3189](#).
- [212] J. Blümlein and M. Klein, *Nucl. Instrum. Meth.* A329 (1993) 112.
- [213] S. Bentvelsen, J. Engelen and P. Kooijman, “Reconstruction of (x, Q^{*2}) and extraction of structure functions in neutral current scattering at HERA,” in *Workshop on Physics at HERA Hamburg, Germany, October 29-30, 1991*, 1992.
- [214] U. Bassler and G. Bernardi, *Nucl. Instrum. Meth.* A426 (1999) 583, [arXiv:hep-ex/9801017](#).
- [215] A. H. Müller, *Nucl. Phys.* B335 (1990) 115.
- [216] R. D. Ball, V. Bertone, M. Bonvini, S. Marzani, J. Rojo and L. Rottoli, *Eur. Phys. J.* C78 (2018) 321, [arXiv:1710.05935](#).
- [217] S. Carrazza, S. Forte, Z. Kassabov, J. I. Latorre and J. Rojo, *Eur. Phys. J.* C75 (2015) 369, [arXiv:1505.06736](#).
- [218] J. Rojo and F. Caola, “Parton distributions and small-x QCD at the Large Hadron Electron Collider,” in *17th International Workshop on Deep-Inelastic Scattering and Related Subjects (DIS 2009): Madrid, Spain, April 26-30, 2009*, Berlin, Germany, 2009. [arXiv:0906.2079](#).
- [219] J. Bartels, K. J. Golec-Biernat and H. Kowalski, *Phys. Rev.* D66 (2002) 014001, [arXiv:hep-ph/0203258](#).
- [220] K. J. Golec-Biernat and S. Sapeta, *Phys. Rev.* D74 (2006) 054032, [arXiv:hep-ph/0607276](#).
- [221] K. Golec-Biernat and S. Sapeta, *JHEP* 03 (2018) 102, [arXiv:1711.11360](#).

- [222] J. Gao, L. Harland-Lang and J. Rojo, *Phys. Rept.* 742 (2018) 1, [arXiv:1709.04922](#).
- [223] V. Bertone, R. Gauld and J. Rojo, *JHEP* 01 (2019) 217, [arXiv:1808.02034](#).
- [224] A. Accardi *et al.*, *Eur. Phys. J. A52* (2016) 268, [arXiv:1212.1701](#).
- [225] A. V. Belitsky, X.-d. Ji and F. Yuan, *Phys. Rev. D*69 (2004) 074014, [arXiv:hep-ph/0307383](#).
- [226] N. N. Nikolaev and B. G. Zakharov, *Z. Phys.* C49 (1991) 607.
- [227] N. Nikolaev and B. G. Zakharov, *Z. Phys.* C53 (1992) 331.
- [228] N. N. Nikolaev and B. G. Zakharov, *J. Exp. Theor. Phys.* 78 (1994) 598. [Zh. Eksp. Teor. Fiz.105,1117(1994)].
- [229] N. N. Nikolaev, B. G. Zakharov and V. R. Zoller, *Z. Phys.* A351 (1995) 435.
- [230] A. H. Müller, *Nucl. Phys.* B415 (1994) 373.
- [231] A. H. Müller and B. Patel, *Nucl. Phys.* B425 (1994) 471, [arXiv:hep-ph/9403256](#).
- [232] U. Amaldi and K. R. Schubert, *Nucl. Phys.* B166 (1980) 301.
- [233] S. Munier, A. M. Stasto and A. H. Müller, *Nucl. Phys.* B603 (2001) 427, [arXiv:hep-ph/0102291](#).
- [234] N. Armesto and A. H. Rezaeian, *Phys. Rev. D*90 (2014) 054003, [arXiv:1402.4831](#).
- [235] H. Kowalski and D. Teaney, *Phys. Rev. D*68 (2003) 114005, [arXiv:hep-ph/0304189](#).
- [236] H. Kowalski, L. Motyka and G. Watt, *Phys. Rev. D*74 (2006) 074016, [arXiv:hep-ph/0606272](#).
- [237] G. Watt and H. Kowalski, *Phys. Rev. D*78 (2008) 014016, [arXiv:0712.2670](#).
- [238] Y. Hatta, B.-W. Xiao and F. Yuan, *Phys. Rev. Lett.* 116 (2016) 202301, [arXiv:1601.01585](#).
- [239] T. Altinoluk, N. Armesto, G. Beuf and A. H. Rezaeian, *Phys. Lett.* B758 (2016) 373, [arXiv:1511.07452](#).
- [240] H. Mäntysaari, N. Müller and B. Schenke, *Phys. Rev. D*99 (2019) 074004, [arXiv:1902.05087](#).
- [241] F. Salazar and B. Schenke, *Phys. Rev. D*100 (2019) 034007, [arXiv:1905.03763](#).
- [242] H. Mäntysaari and B. Schenke, *Phys. Rev. Lett.* 117 (2016) 052301, [arXiv:1603.04349](#).
- [243] H. Mäntysaari and B. Schenke, *Phys. Rev. D*94 (2016) 034042, [arXiv:1607.01711](#).
- [244] H. Mäntysaari and B. Schenke, *Phys. Lett.* B772 (2017) 832, [arXiv:1703.09256](#).
- [245] H. Mäntysaari and B. Schenke, *Phys. Rev. D*98 (2018) 034013, [arXiv:1806.06783](#).
- [246] J. Cepila, J. G. Contreras and J. D. Tapia Takaki, *Phys. Lett.* B766 (2017) 186, [arXiv:1608.07559](#).
- [247] D. Bendova, J. Cepila and J. G. Contreras, *Phys. Rev. D*99 (2019) 034025, [arXiv:1811.06479](#).
- [248] M. Krelina, V. P. Goncalves and J. Cepila, *Nucl. Phys.* A989 (2019) 187, [arXiv:1905.06759](#).
- [249] H1 Collaboration, C. Adloff *et al.*, *Z. Phys.* C76 (1997) 613, [arXiv:hep-ex/9708016](#).
- [250] ZEUS Collaboration, J. Breitweg *et al.*, *Eur. Phys. J. C*1 (1998) 81, [arXiv:hep-ex/9709021](#).
- [251] P. Newman and M. Wing, *Rev. Mod. Phys.* 86 (2014) 1037, [arXiv:1308.3368](#).
- [252] V. N. Gribov, *Sov. Phys. JETP* 29 (1969) 483. [Zh. Eksp. Teor. Fiz.56,892(1969)].
- [253] J. C. Collins, *Phys. Rev. D*57 (1998) 3051, [arXiv:hep-ph/9709499](#). [Erratum: Phys. Rev.D61,019902(2000)].
- [254] A. Berera and D. E. Soper, *Phys. Rev. D*53 (1996) 6162, [arXiv:hep-ph/9509239](#).
- [255] L. Trentadue and G. Veneziano, *Phys. Lett.* B323 (1994) 201.
- [256] N. Armesto, P. R. Newman, W. Slominski and A. M. Stasto, *Phys. Rev. D*100 (2019) 074022, [arXiv:1901.09076](#).
- [257] H. Khanpour, *Phys. Rev. D*99 (2019) 054007, [arXiv:1902.10734](#).
- [258] H1 Collaboration Collaboration, A. Aktas *et al.*, *Eur.Phys.J.* C48 (2006) 715, [arXiv:hep-ex/0606004](#).
- [259] ZEUS Collaboration Collaboration, S. Chekanov *et al.*, *Nucl.Phys.* B816 (2009) 1, [arXiv:0812.2003](#).
- [260] H1 Collaboration Collaboration, F. Aaron *et al.*, *Eur.Phys.J.* C72 (2012) 2074, [arXiv:1203.4495](#).
- [261] H1 and ZEUS Collaborations, F. D. Aaron *et al.*, *Eur. Phys. J. C*72 (2012) 2175, [arXiv:1207.4864](#).
- [262] ZEUS Collaboration, S. Chekanov *et al.*, *Nucl. Phys.* B713 (2005) 3, [arXiv:hep-ex/0501060](#).
- [263] H1 Collaboration, A. Aktas *et al.*, *Eur. Phys. J. C*48 (2006) 749, [arXiv:hep-ex/0606003](#).
- [264] ZEUS Collaboration Collaboration, S. Chekanov *et al.*, *Nucl.Phys.* B831 (2010) 1, [arXiv:0911.4119](#).
- [265] H1 Collaboration, F. Aaron *et al.*, *Eur.Phys.J.* C71 (2011) 1578, [arXiv:1010.1476](#).

- [266] V. N. Gribov and L. N. Lipatov, *Sov. J. Nucl. Phys.* 15 (1972) 675. [*Yad. Fiz.*15,1218(1972)].
- [267] V. N. Gribov and L. N. Lipatov, *Sov. J. Nucl. Phys.* 15 (1972) 438. [*Yad. Fiz.*15,781(1972)].
- [268] G. Altarelli and G. Parisi, *Nucl. Phys.* B126 (1977) 298.
- [269] Y. L. Dokshitzer, *Sov. Phys. JETP* 46 (1977) 641. [*Zh. Eksp. Teor. Fiz.*73,1216(1977)].
- [270] J. C. Collins and W.-K. Tung, *Nucl. Phys.* B278 (1986) 934.
- [271] R. S. Thorne and W. K. Tung, [arXiv:0809.0714](#).
- [272] J. F. Owens, *Phys. Rev.* D30 (1984) 943.
- [273] M. Glück, E. Reya and A. Vogt, *Z. Phys.* C53 (1992) 651.
- [274] R. S. Thorne and R. G. Roberts, *Phys. Rev.* D57 (1998) 6871, [arXiv:hep-ph/9709442](#).
- [275] ATLAS Collaboration, G. Aad *et al.*, *Phys. Lett.* B754 (2016) 214–234, [arXiv:1511.00502](#).
- [276] D. Britzger, J. Currie, T. Gehrmann, A. Huss, J. Niehues and R. Žlebčík, *Eur. Phys. J.* C78 (2018) 538, [arXiv:1804.05663](#).
- [277] Z. Nagy, *Phys. Rev.* D68 (2003) 094002, [arXiv:hep-ph/0307268](#).
- [278] S. J. Brodsky, G. F. de Teramond, H. G. Dosch and J. Erlich, *Phys. Rept.* 584 (2015) 1, [arXiv:1407.8131](#).
- [279] G. F. de Teramond, H. G. Dosch and S. J. Brodsky, *Phys. Rev.* D87 (2013) 075005, [arXiv:1301.1651](#).
- [280] V. de Alfaro, S. Fubini and G. Furlan, *Nuovo Cim.* A34 (1976) 569.
- [281] G. Veneziano, *Nuovo Cim.* A57 (1968) 190.
- [282] A. Deur, S. J. Brodsky and G. F. de Teramond, *Prog. Part. Nucl. Phys.* 90 (2016) 1, [arXiv:1604.08082](#).
- [283] G. Grunberg, *Phys. Lett.* 95B (1980) 70. [Erratum: *Phys. Lett.*110B,501(1982)].
- [284] J. D. Bjorken, *Phys. Rev.* 148 (1966) 1467.
- [285] A. Deur *et al.*, *Phys. Rev. Lett.* 93 (2004) 212001, [arXiv:hep-ex/0407007](#).
- [286] A. Deur, Y. Prok, V. Burkert, D. Crabb, F. X. Girod, K. A. Griffioen, N. Guler, S. E. Kuhn and N. Kvaltine, *Phys. Rev.* D90 (2014) 012009, [arXiv:1405.7854](#).
- [287] A. Deur *et al.*, *Phys. Rev.* D78 (2008) 032001, [arXiv:0802.3198](#).
- [288] S. J. Brodsky and H. J. Lu, *Phys. Rev.* D51 (1995) 3652, [arXiv:hep-ph/9405218](#).
- [289] S. J. Brodsky, G. F. de Teramond and A. Deur, *Phys. Rev.* D81 (2010) 096010, [arXiv:1002.3948](#).
- [290] A. Deur, S. J. Brodsky and G. F. de Teramond, *Phys. Lett.* B750 (2015) 528, [arXiv:1409.5488](#).
- [291] S. J. Brodsky, G. F. de Teramond, A. Deur and H. G. Dosch, *Few Body Syst.* 56 (2015) 621, [arXiv:1410.0425](#).
- [292] A. Deur, V. Burkert, J.-P. Chen and W. Korsch, *Phys. Lett.* B650 (2007) 244, [arXiv:hep-ph/0509113](#).
- [293] A. Deur, V. Burkert, J. P. Chen and W. Korsch, *Phys. Lett.* B665 (2008) 349, [arXiv:0803.4119](#).
- [294] S. J. Brodsky, *J. Phys. Conf. Ser.* 1137 (2019) 012027.
- [295] G. P. Lepage and S. J. Brodsky, *Phys. Lett.* 87B (1979) 359.
- [296] A. V. Efremov and A. V. Radyushkin, *Phys. Lett.* 94B (1980) 245.
- [297] S. J. Brodsky, G. F. De Teramond and H. G. Dosch, *Phys. Lett.* B729 (2014) 3, [arXiv:1302.4105](#).
- [298] S. J. Brodsky, *Few Body Syst.* 57 (2016) 703, [arXiv:1601.06328](#).
- [299] R. S. Sufian, G. F. de Teramond, S. J. Brodsky, A. Deur and H. G. Dosch, *Phys. Rev.* D95 (2017) 014011, [arXiv:1609.06688](#).
- [300] HLFHS Collaboration, G. F. de Teramond, T. Liu, R. S. Sufian, H. G. Dosch, S. J. Brodsky and A. Deur, *Phys. Rev. Lett.* 120 (2018) 182001, [arXiv:1801.09154](#).
- [301] T. Gutsche, V. E. Lyubovitskij, I. Schmidt and A. Vega, *Phys. Rev.* D91 (2015) 114001, [arXiv:1501.02738](#).
- [302] T. Gutsche, V. E. Lyubovitskij and I. Schmidt, *Phys. Rev.* D94 (2016) 116006, [arXiv:1607.04124](#).
- [303] H. G. Dosch, G. F. de Teramond and S. J. Brodsky, *Phys. Rev.* D91 (2015) 085016, [arXiv:1501.00959](#).
- [304] S. J. Brodsky, G. F. de Teramond, H. G. Dosch and C. Lorcé, *Int. J. Mod. Phys.* A31 (2016) 1630029, [arXiv:1606.04638](#).
- [305] M. Nielsen, S. J. Brodsky, G. F. de Teramond, H. G. Dosch, F. S. Navarra and L. Zou, *Phys. Rev.* D98 (2018) 034002, [arXiv:1805.11567](#).

- [306] G. F. de Teramond, H. G. Dosch and S. J. Brodsky, *Phys. Rev. D*91 (2015) 045040, [arXiv:1411.5243](#).
- [307] S. L. Glashow, *Nucl. Phys.* 22 (1961) 579.
- [308] S. Weinberg, *Phys. Rev. Lett.* 27 (1971) 1688.
- [309] S. Weinberg, *Phys. Rev. D*5 (1972) 1412.
- [310] A. Salam and J. C. Ward, *Phys. Lett.* 13 (1964) 168.
- [311] P. W. Higgs, *Phys. Lett.* 12 (1964) 132.
- [312] P. W. Higgs, *Phys. Rev. Lett.* 13 (1964) 508.
- [313] F. Englert and R. Brout, *Phys. Rev. Lett.* 13 (1964) 321.
- [314] H1 Collaboration, A. Aktas *et al.*, *Phys. Lett.* B632 (2006) 35, [arXiv:hep-ex/0507080](#).
- [315] ZEUS Collaboration, H. Abramowicz *et al.*, *Phys. Rev. D*93 (2016) 092002, [arXiv:1603.09628](#).
- [316] H1 Collaboration, V. Andreev *et al.*, *Eur. Phys. J. C*78 (2018) 777, [arXiv:1806.01176](#).
- [317] M. Klein and T. Riemann, *Z. Phys.* C24 (1984) 151.
- [318] M. Böhm and H. Spiesberger, *Nucl. Phys.* B294 (1987) 1081.
- [319] D. Yu. Bardin, C. Burdik, P. C. Khristova and T. Riemann, *Z. Phys.* C42 (1989) 679.
- [320] W. Hollik, D. Yu. Bardin, J. Blümlein, B. A. Kniehl, T. Riemann and H. Spiesberger, “Electroweak parameters at HERA: Theoretical aspects,” in *Workshop on physics at HERA Hamburg, Germany, October 29-30, 1991*, 1992.
- [321] M. Böhm and H. Spiesberger, *Nucl. Phys.* B304 (1988) 749.
- [322] D. Yu. Bardin, K. C. Burdik, P. K. Khristova and T. Riemann, *Z. Phys.* C44 (1989) 149.
- [323] A. Sirlin, *Phys. Rev. D*22 (1980) 971.
- [324] M. Bohm, H. Spiesberger and W. Hollik, *Fortsch. Phys.* 34 (1986) 687.
- [325] W. F. L. Hollik, *Fortsch. Phys.* 38 (1990) 165.
- [326] H1 Collaboration, F. D. Aaron *et al.*, *JHEP* 09 (2012) 061, [arXiv:1206.7007](#).
- [327] D. Britzger and M. Klein, *PoS DIS2017* (2018) 105.
- [328] M. Botje, “Erratum for the time-like evolution in QCDNUM,” 2016. [arXiv:1602.08383](#).
- [329] H. Spiesberger, “EPRC: A program package for electroweak physics at HERA,” in *Future physics at HERA. Proceedings, Workshop, Hamburg, Germany, September 25, 1995-May 31, 1996. Vol. 1, 2*, 1995.
- [330] G. Cowan, K. Cranmer, E. Gross and O. Vitells, *Eur. Phys. J. C*71 (2011) 1554, [arXiv:1007.1727](#). [Erratum: *Eur. Phys. J. C*73 (2013) 2501].
- [331] CDF and D0 Collaborations, [arXiv:1204.0042](#).
- [332] ALEPH, DELPHI, L3, OPAL, LEP Electroweak Collaboration, S. Schael *et al.*, *Phys. Rept.* 532 (2013) 119, [arXiv:1302.3415](#).
- [333] ATLAS Collaboration, M. Aaboud *et al.*, *Eur. Phys. J. C*78 (2018) 110, [arXiv:1701.07240](#). [Erratum: *Eur. Phys. J. C*78,no.11,898(2018)].
- [334] J. de Blas, M. Ciuchini, E. Franco, S. Mishima, M. Pierini, L. Reina and L. Silvestrini, *JHEP* 12 (2016) 135, [arXiv:1608.01509](#).
- [335] J. Haller, A. Hoecker, R. Kogler, K. Mönig, T. Peiffer and J. Stelzer, *Eur. Phys. J. C*78 (2018) 675, [arXiv:1803.01853](#).
- [336] MuLan Collaboration, V. Tishchenko *et al.*, *Phys. Rev. D*87 (2013) 052003, [arXiv:1211.0960](#).
- [337] M. Schott, “Global EW fits: experimental and theoretical issues,” Talk presented at the Ultimate Precision at Hadron Colliders, Sarclay, France, 2019.
- [338] ALEPH, DELPHI, L3, OPAL, SLD Collaborations, LEP Electroweak Working Group, SLD Electroweak Heavy Flavour Groups, S. Schael *et al.*, *Phys. Rept.* 427 (2006) 257, [arXiv:hep-ex/0509008](#).
- [339] D0 Collaboration, V. M. Abazov *et al.*, *Phys. Rev. D*84 (2011) 012007, [arXiv:1104.4590](#).
- [340] CDF and D0 Collaborations, T. A. Aaltonen *et al.*, *Phys. Rev. D*97 (2018) 112007, [arXiv:1801.06283](#).
- [341] LHCb Collaboration, R. Aaij *et al.*, *JHEP* 11 (2015) 190, [arXiv:1509.07645](#).
- [342] ATLAS Collaboration, T. A. collaboration, .
- [343] CMS Collaboration, A. M. Sirunyan *et al.*, *Eur. Phys. J. C*78 (2018) 701, [arXiv:1806.00863](#).

- [344] J. Erler, “Global fits of the SM parameters,” in *7th Large Hadron Collider Physics Conference (LHCP 2019) Puebla, Puebla, Mexico, May 20-25, 2019*, 2019. [arXiv:1908.07327](#).
- [345] J. Erler and M. Schott, *Prog. Part. Nucl. Phys.* 106 (2019) 68, [arXiv:1902.05142](#).
- [346] ZEUS Collaboration, S. Chekanov *et al.*, *Phys. Lett. B* 672 (2009) 106, [arXiv:0807.0589](#).
- [347] H1 Collaboration, F. D. Aaron *et al.*, *Eur. Phys. J. C* 64 (2009) 251, [arXiv:0901.0488](#).
- [348] H1 and ZEUS Collaborations, F. D. Aaron *et al.*, *JHEP* 03 (2010) 035, [arXiv:0911.0858](#).
- [349] U. Baur and D. Zeppenfeld, *Nucl. Phys.* B325 (1989) 253.
- [350] U. Baur, B. A. Kniehl, J. A. M. Vermaseren and D. Zeppenfeld, “Single W and Z production at LEP / LHC,” in *ECFA Large Hadron Collider Workshop, Aachen, Germany, 4-9 Oct 1990: Proceedings.2.*, 1990.
- [351] U. Baur, J. A. M. Vermaseren and D. Zeppenfeld, *Nucl. Phys.* B375 (1992) 3.
- [352] J. Alwall, R. Frederix, S. Frixione, V. Hirschi, F. Maltoni, O. Mattelaer, H. S. Shao, T. Stelzer, P. Torrielli and M. Zaro, *JHEP* 07 (2014) 079, [arXiv:1405.0301](#).
- [353] NNPDF Collaboration, R. D. Ball, V. Bertone, S. Carrazza, L. Del Debbio, S. Forte, A. Guffanti, N. P. Hartland and J. Rojo, *Nucl. Phys.* B877 (2013) 290, [arXiv:1308.0598](#).
- [354] K. Hagiwara, S. Ishihara, R. Szalapski and D. Zeppenfeld, *Phys. Rev.* D48 (1993) 2182.
- [355] K. Hagiwara, S. Ishihara, R. Szalapski and D. Zeppenfeld, *Phys. Lett.* B283 (1992) 353.
- [356] A. De Rujula, M. B. Gavela, P. Hernandez and E. Masso, *Nucl. Phys.* B384 (1992) 3.
- [357] S. S. Biswal, M. Patra and S. Raychaudhuri, [arXiv:1405.6056](#).
- [358] I. T. Cakir, O. Cakir, A. Senol and A. T. Tasci, *Acta Phys. Polon.* B45 (2014) 1947, [arXiv:1406.7696](#).
- [359] R. Li, X.-M. Shen, K. Wang, T. Xu, L. Zhang and G. Zhu, *Phys. Rev.* D97 (2018) 075043, [arXiv:1711.05607](#).
- [360] M. Köksal, A. A. Billur, A. Gutiérrez-Rodríguez and M. A. Hernández-Ruíz, [arXiv:1910.06747](#).
- [361] A. Gutiérrez-Rodríguez, M. Köksal, A. A. Billur and M. A. Hernández-Ruíz, [arXiv:1910.02307](#).
- [362] CMS Collaboration, A. M. Sirunyan *et al.*, *Phys. Lett. B* 772 (2017) 21, [arXiv:1703.06095](#).
- [363] CMS Collaboration, A. M. Sirunyan *et al.*, [arXiv:1907.08354](#).
- [364] S. Villa, *Nucl. Phys. Proc. Suppl.* 142 (2005) 391, [arXiv:hep-ph/0410208](#).
- [365] K. O. Mikaelian, M. A. Samuel and D. Sahdev, *Phys. Rev. Lett.* 43 (1979) 746.
- [366] S. J. Brodsky and R. W. Brown, *Phys. Rev. Lett.* 49 (1982) 966.
- [367] R. W. Brown, K. L. Kowalski and S. J. Brodsky, *Phys. Rev.* D28 (1983) 624. [Addendum: *Phys. Rev.* D29,2100(1984)].
- [368] M. A. Samuel and J. H. Reid, *Prog. Theor. Phys.* 76 (1986) 184.
- [369] S. Dutta, A. Goyal, M. Kumar and B. Mellado, *Eur. Phys. J. C* 75 (2015) 577, [arXiv:1307.1688](#).
- [370] A. O. Bouzas and F. Larios, *Phys. Rev.* D88 (2013) 094007, [arXiv:1308.5634](#).
- [371] S. Oryn, X. Rouby and V. Lemaitre, “DELPHES, a framework for fast simulation of a generic collider experiment,” 2009. [arXiv:0903.2225](#).
- [372] CMS Collaboration, V. Khachatryan *et al.*, *JHEP* 06 (2014) 090, [arXiv:1403.7366](#).
- [373] H. Sun, *PoS DIS2018* (2018) 167.
- [374] CMS Collaboration, V. Khachatryan *et al.*, *Phys. Lett. B* 736 (2014) 33–57, [arXiv:1404.2292](#).
- [375] J. A. Aguilar-Saavedra, *Acta Phys. Polon.* B35 (2004) 2695–2710, [arXiv:hep-ph/0409342](#).
- [376] J. Charles *et al.*, *Phys. Rev.* D91 (2015) 073007, [arXiv:1501.05013](#).
- [377] I. Turk Cakir, A. Yilmaz, H. Denizli, A. Senol, H. Karadeniz and O. Cakir, *Adv. High Energy Phys.* 2017 (2017) 1572053, [arXiv:1705.05419](#).
- [378] O. Cakir, A. Yilmaz, I. Turk Cakir, A. Senol and H. Denizli, *Nucl. Phys.* B944 (2019) 114640, [arXiv:1809.01923](#).
- [379] H. Sun and X. Wang, *Eur. Phys. J. C* 78 (2018) 281, [arXiv:1602.04670](#).
- [380] J. A. Aguilar-Saavedra and T. Riemann, “Probing top flavor changing neutral couplings at TESLA,” in *5th Workshop of the 2nd ECFA, Obernai, France, October 16-19, 1999*, 2001. [arXiv:hep-ph/0102197](#).

- [381] Top Quark Working Group, K. Agashe *et al.*, “Working Group Report: Top Quark,” in *Community Summer Study on the Future of U.S. Particle Physics: Minneapolis, MN, USA, July 29-August 6, 2013*, 2013. [arXiv:1311.2028](#).
- [382] B. Coleppa, M. Kumar, S. Kumar and B. Mellado, *Phys. Lett.* B770 (2017) 335–341, [arXiv:1702.03426](#).
- [383] S. Atag and B. Sahin, *Phys. Rev.* D73 (2006) 074001.
- [384] G. R. Boroun, *Phys. Lett.* B744 (2015) 142–145, [arXiv:1503.01590](#).
- [385] European Muon Collaboration, J. J. Aubert *et al.*, *Phys. Lett.* 123B (1983) 275.
- [386] CHORUS Collaboration, G. Onengut *et al.*, *Phys. Lett.* B632 (2006) 65.
- [387] J. Gomez *et al.*, *Phys. Rev.* D49 (1994) 4348.
- [388] New Muon Collaboration, P. Amaudruz *et al.*, *Nucl. Phys.* B441 (1995) 3, [arXiv:hep-ph/9503291](#).
- [389] NuTeV Collaboration, M. Tzanov *et al.*, *Phys. Rev.* D74 (2006) 012008, [arXiv:hep-ex/0509010](#).
- [390] New Muon Collaboration, M. Arneodo *et al.*, *Nucl. Phys.* B441 (1995) 12, [arXiv:hep-ex/9504002](#).
- [391] New Muon Collaboration, M. Arneodo *et al.*, *Nucl. Phys.* B481 (1996) 3.
- [392] European Muon Collaboration, J. Ashman *et al.*, *Z. Phys.* C57 (1993) 211.
- [393] New Muon Collaboration, M. Arneodo *et al.*, *Nucl. Phys.* B481 (1996) 23.
- [394] New Muon Collaboration, P. Amaudruz *et al.*, *Nucl. Phys.* B371 (1992) 3.
- [395] J. P. Berge *et al.*, *Z. Phys.* C49 (1991) 187.
- [396] M. Arneodo, *Phys. Rept.* 240 (1994) 301.
- [397] D. F. Geesaman, K. Saito and A. W. Thomas, *Ann. Rev. Nucl. Part. Sci.* 45 (1995) 337.
- [398] K. J. Eskola, P. Paakkinen, H. Paukkunen and C. A. Salgado, *Eur. Phys. J.* C77 (2017) 163, [arXiv:1612.05741](#).
- [399] C. A. Salgado *et al.*, *J. Phys.* G39 (2012) 015010, [arXiv:1105.3919](#).
- [400] K. J. Golec-Biernat and M. Wusthoff, *Phys. Rev.* D59 (1998) 014017, [arXiv:hep-ph/9807513](#).
- [401] L. Frankfurt, V. Guzey and M. Strikman, *Phys. Rept.* 512 (2012) 255, [arXiv:1106.2091](#).
- [402] F. Gelis, E. Iancu, J. Jalilian-Marian and R. Venugopalan, *Ann. Rev. Nucl. Part. Sci.* 60 (2010) 463, [arXiv:1002.0333](#).
- [403] Y. V. Kovchegov and E. Levin, *Camb. Monogr. Part. Phys. Nucl. Phys. Cosmol.* 33 (2012) 1.
- [404] B. L. Ioffe, V. S. Fadin and L. N. Lipatov, *Quantum chromodynamics: Perturbative and nonperturbative aspects*, vol. 30. Cambridge Univ. Press, 2010.
- [405] J. Collins, *Camb. Monogr. Part. Phys. Nucl. Phys. Cosmol.* 32 (2011) 1.
- [406] H. Paukkunen, *Nucl. Phys.* A967 (2017) 241, [arXiv:1704.04036](#).
- [407] H. Paukkunen, *PoS HardProbes2018* (2018) 014, [arXiv:1811.01976](#).
- [408] K. J. Eskola, H. Paukkunen and C. A. Salgado, *JHEP* 04 (2009) 065, [arXiv:0902.4154](#).
- [409] D. de Florian, R. Sassot, P. Zurita and M. Stratmann, *Phys. Rev.* D85 (2012) 074028, [arXiv:1112.6324](#).
- [410] K. Kovarik *et al.*, *Phys. Rev.* D93 (2016) 085037, [arXiv:1509.00792](#).
- [411] H. Khanpour and S. Atashbar Tehrani, *Phys. Rev.* D93 (2016) 014026, [arXiv:1601.00939](#).
- [412] NNPDF Collaboration, R. Abdul Khalek, J. J. Ethier and J. Rojo, *Eur. Phys. J.* C79 (2019) 471, [arXiv:1904.00018](#).
- [413] H. Paukkunen and C. A. Salgado, *JHEP* 07 (2010) 032, [arXiv:1004.3140](#).
- [414] K. Kovarik, I. Schienbein, F. I. Olness, Y. Yu, C. Keppel, J. G. Morfin, J. F. Owens and T. Stavreva, *Phys. Rev. Lett.* 106 (2011) 122301, [arXiv:1012.0286](#).
- [415] H. Paukkunen and C. A. Salgado, *Phys. Rev. Lett.* 110 (2013) 212301, [arXiv:1302.2001](#).
- [416] N. Armesto, *J. Phys.* G32 (2006) R367, [arXiv:hep-ph/0604108](#).
- [417] K. J. Eskola, P. Paakkinen and H. Paukkunen, *Eur. Phys. J.* C79 (2019) 511, [arXiv:1903.09832](#).
- [418] N. Armesto, H. Paukkunen, J. M. Penín, C. A. Salgado and P. Zurita, *Eur. Phys. J.* C76 (2016) 218, [arXiv:1512.01528](#).
- [419] A. Kusina, F. Lyonnet, D. B. Clark, E. Godat, T. Jezo, K. Kovarik, F. I. Olness, I. Schienbein and J. Y. Yu, *Eur. Phys. J.* C77 (2017) 488, [arXiv:1610.02925](#).

- [420] N. Armesto, A. Capella, A. B. Kaidalov, J. Lopez-Albacete and C. A. Salgado, *Eur. Phys. J. C* **29** (2003) 531, [arXiv:hep-ph/0304119](#).
- [421] N. Armesto, A. B. Kaidalov, C. A. Salgado and K. Tywoniuk, *Eur. Phys. J. C* **68** (2010) 447, [arXiv:1003.2947](#).
- [422] S. J. Brodsky, I. Schmidt and J.-J. Yang, *Phys. Rev. D* **70** (2004) 116003, [arXiv:hep-ph/0409279](#).
- [423] Z. Citron *et al.*, “Future physics opportunities for high-density QCD at the LHC with heavy-ion and proton beams,” in *HL/HE-LHC Workshop: Workshop on the Physics of HL-LHC, and Perspectives at HE-LHC Geneva, Switzerland, June 18-20, 2018*, 2018. [arXiv:1812.06772](#).
- [424] M. Klein, *EPJ Web Conf.* **112** (2016) 03002.
- [425] LHeC Study Group, H. Paukkunen, *PoS DIS2017* (2018) 109, [arXiv:1709.08342](#).
- [426] E. C. Aschenauer, S. Fazio, M. A. C. Lamont, H. Paukkunen and P. Zurita, *Phys. Rev. D* **96** (2017) 114005, [arXiv:1708.05654](#).
- [427] LHCb Collaboration, R. Aaij *et al.*, *JHEP* **10** (2017) 090, [arXiv:1707.02750](#).
- [428] LHCb Collaboration, R. Aaij *et al.*, *Phys. Rev. D* **99** (2019) 052011, [arXiv:1902.05599](#).
- [429] K. J. Eskola, I. Helenius, P. Paakkinen and H. Paukkunen, [arXiv:1906.02512](#).
- [430] I. Helenius, K. J. Eskola and H. Paukkunen, *JHEP* **09** (2014) 138, [arXiv:1406.1689](#).
- [431] J. Pumplin, D. Stump, R. Brock, D. Casey, J. Huston, J. Kalk, H. L. Lai and W. K. Tung, *Phys. Rev. D* **65** (2001) 014013, [arXiv:hep-ph/0101032](#).
- [432] N. Armesto, “Nuclear pdfs.” 2nd FCC Physics Workshop (CERN, January 15th-19th 2018), 2018.
- [433] N. Armesto, *PoS HardProbes2018* (2019) 123.
- [434] T. Lappi and H. Mäntysaari, *Phys. Rev. C* **87** (2013) 032201, [arXiv:1301.4095](#).
- [435] A. J. Baltz, *Phys. Rept.* **458** (2008) 1, [arXiv:0706.3356](#).
- [436] V. N. Gribov and A. A. Migdal, *Sov. J. Nucl. Phys.* **8** (1969) 583. [*Yad. Fiz.* **8**,1002(1968)].
- [437] L. L. Frankfurt, G. A. Miller and M. Strikman, *Ann. Rev. Nucl. Part. Sci.* **44** (1994) 501, [arXiv:hep-ph/9407274](#).
- [438] C. Marquet, M. R. Moldes and P. Zurita, *Phys. Lett. B* **772** (2017) 607, [arXiv:1702.00839](#).
- [439] L. L. Frankfurt and M. I. Strikman, *Phys. Lett. B* **382** (1996) 6.
- [440] H. Kowalski, T. Lappi, C. Marquet and R. Venugopalan, *Phys. Rev. C* **78** (2008) 045201, [arXiv:0805.4071](#).
- [441] A. H. Mueller and H. Navelet, *Nucl. Phys. B* **282** (1987) 727.
- [442] M. Deak, F. Hautmann, H. Jung and K. Kutak, *Eur. Phys. J. C* **72** (2012) 1982, [arXiv:1112.6354](#).
- [443] J. L. Albacete and C. Marquet, *Phys. Rev. Lett.* **105** (2010) 162301, [arXiv:1005.4065](#).
- [444] T. Lappi and H. Mäntysaari, *Nucl. Phys. A* **908** (2013) 51, [arXiv:1209.2853](#).
- [445] A. Stasto, S.-Y. Wei, B.-W. Xiao and F. Yuan, *Phys. Lett. B* **784** (2018) 301, [arXiv:1805.05712](#).
- [446] A. van Hameren, P. Kotko, K. Kutak, C. Marquet, E. Petreska and S. Sapeta, *JHEP* **12** (2016) 034, [arXiv:1607.03121](#). [Erratum: *JHEP* **02**,158(2019)].
- [447] CMS Collaboration, V. Khachatryan *et al.*, *JHEP* **09** (2010) 091, [arXiv:1009.4122](#).
- [448] S. Schlichting and P. Tribedy, *Adv. High Energy Phys.* **2016** (2016) 8460349, [arXiv:1611.00329](#).
- [449] C. Loizides, *Nucl. Phys. A* **956** (2016) 200, [arXiv:1602.09138](#).
- [450] B. Schenke, *Nucl. Phys. A* **967** (2017) 105, [arXiv:1704.03914](#).
- [451] P. Romatschke, *Eur. Phys. J. C* **77** (2017) 21, [arXiv:1609.02820](#).
- [452] ATLAS Collaboration, “Two-particle azimuthal correlations in photo-nuclear ultra-peripheral Pb+Pb collisions at 5.02 TeV with ATLAS,” ATLAS-CONF-2019-022, 2019.
- [453] A. Badea, A. Baty, P. Chang, G. M. Innocenti, M. Maggi, C. McGinn, M. Peters, T.-A. Sheng, J. Thaler and Y.-J. Lee, *Phys. Rev. Lett.* **123** (2019) 212002, [arXiv:1906.00489](#).
- [454] ZEUS Collaboration, “Two-particle azimuthal correlations as a probe of collective behaviour in deep inelastic *ep* scattering at HERA,” 2019. [arXiv:1912.07431](#).
- [455] CMS Collaboration, S. Chatrchyan *et al.*, *Phys. Lett. B* **724** (2013) 213–240, [arXiv:1305.0609](#).
- [456] CMS Collaboration, V. Khachatryan *et al.*, *Phys. Lett. B* **765** (2017) 193–220, [arXiv:1606.06198](#).

- [457] S. D. Glazek, S. J. Brodsky, A. S. Goldhaber and R. W. Brown, *Phys. Rev. D* **97** (2018) 114021, [arXiv:1805.08847](#).
- [458] J. D. Bjorken, S. J. Brodsky and A. Scharff Goldhaber, *Phys. Lett.* **B726** (2013) 344, [arXiv:1308.1435](#).
- [459] S. J. Brodsky, H.-C. Pauli and S. S. Pinsky, *Phys. Rept.* **301** (1998) 299, [arXiv:hep-ph/9705477](#).
- [460] P. A. M. Dirac, *Rev. Mod. Phys.* **21** (1949) 392.
- [461] D. Ashery, *Nucl. Phys. Proc. Suppl.* **161** (2006) 8, [arXiv:hep-ex/0511052](#).
- [462] G. Bertsch, S. J. Brodsky, A. S. Goldhaber and J. F. Gunion, *Phys. Rev. Lett.* **47** (1981) 297.
- [463] L. Frankfurt, G. A. Miller and M. Strikman, *Phys. Rev. D* **65** (2002) 094015, [arXiv:hep-ph/0010297](#).
- [464] S. J. Brodsky, C.-R. Ji and G. P. Lepage, *Phys. Rev. Lett.* **51** (1983) 83.
- [465] S. J. Brodsky and A. H. Müller, *Phys. Lett.* **B206** (1988) 685.
- [466] S. J. Brodsky, I. A. Schmidt and G. F. de Teramond, *Phys. Rev. Lett.* **64** (1990) 1011.
- [467] S. J. Brodsky and H. J. Lu, *Phys. Rev. Lett.* **64** (1990) 1342.
- [468] S. J. Brodsky, I. Schmidt and S. Liuti, [arXiv:1908.06317](#).
- [469] ATLAS Collaboration, G. Aad *et al.*, *Phys. Lett.* **B716** (2012) 1, [arXiv:1207.7214](#).
- [470] CMS Collaboration, S. Chatrchyan *et al.*, *Phys. Lett.* **B716** (2012) 30, [arXiv:1207.7235](#).
- [471] G. S. Guralnik, C. R. Hagen and T. W. B. Kibble, *Phys. Rev. Lett.* **13** (1964) 585–587. [,162(1964)].
- [472] A. A. Migdal and A. M. Polyakov, *Sov. Phys. JETP* **24** (1967) 91–98. [Zh. Eksp. Teor. Fiz.51,135(1966)].
- [473] S. Gori, C. Grojean, A. Juste and A. Paul, *JHEP* **01** (2018) 108, [arXiv:1710.03752](#).
- [474] T. Cohen, N. Craig, G. F. Giudice and M. McCullough, *JHEP* **05** (2018) 091, [arXiv:1803.03647](#).
- [475] J. Blümlein, G.J.van Oldenborgh and R. Rückl, *Nucl. Phys.* **B395** (1993) 35–59, [arXiv:hep-ph/9209219](#).
- [476] U. Bassler and G. Bernardi, *Nucl. Instrum. Meth.* **A361** (1995) 197–208, [arXiv:hep-ex/9412004](#).
- [477] J. Pumplin, D. R. Stump, J. Huston, H. L. Lai, P. M. Nadolsky and W. K. Tung, *JHEP* **07** (2002) 012, [arXiv:hep-ph/0201195](#).
- [478] J. Alwall, R. Frederix, S. Frixione, V. Hirschi, F. Maltoni, O. Mattelaer, H.-S. Shao, T. Stelzer, P. Torrielli and M. Zaro, *Journal of High Energy Physics* **2014** (2014) .
- [479] M. Kumar, X. Ruan, R. Islam, A. S. Cornell, M. Klein, U. Klein and B. Mellado, *Phys. Lett.* **B764** (2017) 247–253, [arXiv:1509.04016](#).
- [480] LHC Higgs Cross Section Working Group Collaboration, D. de Florian *et al.*, [arXiv:1610.07922](#).
- [481] D. M. Asner *et al.*, “ILC Higgs White Paper,” in *Proceedings, 2013 Community Summer Study on the Future of U.S. Particle Physics: Snowmass on the Mississippi (CSS2013): Minneapolis, MN, USA, July 29-August 6, 2013*, 2013. [arXiv:1310.0763](#).
<http://www.slac.stanford.edu/econf/C1307292/docs/submittedArxivFiles/1310.0763.pdf>.
- [482] H. Abramowicz *et al.*, *Eur. Phys. J.* **C77** (2017) 475, [arXiv:1608.07538](#).
- [483] FCC Collaboration, A. Abada *et al.*, .
- [484] Higgs Cross Section Working Group, <https://twiki.cern.ch/twiki/bin/view/LHCPhysics/CERNYellowReportPageBR> .
- [485] T. Han and B. Mellado, *Phys. Rev. D* **82** (2010) 016009, [arXiv:0909.2460](#).
- [486] M. Tanaka, *Bachelor Thesis, Tokyo Institute of Technology (in Japanese)* (2014) .
- [487] E. Kay, *Master Thesis, Liverpool University* (2014) .
- [488] U. Klein, *Poster at 37th International Conference on High Energy Physics (ICHEP), Valencia* (2014) .
- [489] U. Klein, *Talk at Chavannes* (2015) .
- [490] D. Hampson and I. Harris, *Theses, Liverpool University* (2016 and 2017) .
- [491] ATLAS Collaboration, M. Aaboud *et al.*, *Phys. Lett.* **B786** (2018) 59–86, [arXiv:1808.08238](#).
- [492] CMS Collaboration, A. M. Sirunyan *et al.*, *Phys. Rev. Lett.* **121** (2018) 121801, [arXiv:1808.08242](#).
- [493] ATLAS and CMS Collaborations, *CERN Yellow Rep. Monogr.* **7** (2019) Addendum, [arXiv:1902.10229](#).
- [494] T. Sjstrand, S. Mrenna and P. Skands, *Journal of High Energy Physics* **2006** (2006) 026?026.
- [495] , *Talk at Chavannes* (2014) . https://indico.cern.ch/event/278903/contributions/631181/attachments/510303/704309/Chavannes_UKLein_20.01.2014.pdf.

- [496] J. de Favereau, C. Delaere, P. Demin, A. Giammanco, V. Lemaître, A. Mertens and M. Selvaggi, *Journal of High Energy Physics* 2014 (2014) .
- [497] R. Li, B.-W. Wang, K. Wang, X. Zhang and Z. Zhou, *Phys. Rev. D*100 (2019) 053008, [arXiv:1905.09457](#).
- [498] A. Höcker *et al.*, “TMVA - Toolkit for Multivariate Data Analysis,” CERN-OPEN-2007-007, 2007. [arXiv:physics/0703039](#).
- [499] S. Greder, *b quark tagging and cross-section measurement in quark pair production at D0*. PhD thesis, Louis Pasteur U., Strasbourg I, 2004.
- [500] Y. Banda, T. Lastovicka and A. Nomerotski, “Measurement of the higgs boson decay branching ratio to charm quarks at the ilc,” 2009.
- [501] ATLAS Collaboration, G. Aad *et al.*, *Phys. Rev. D*100 (2019) 032007, [arXiv:1905.07714](#).
- [502] ATLAS Collaboration, M. Aaboud *et al.*, *Eur. Phys. J. C*77 (2017) 361, [arXiv:1702.05725](#).
- [503] C. Englert, R. Kogler, H. Schulz and M. Spannowsky, *Eur. Phys. J. C*76 (2016) 393, [arXiv:1511.05170](#).
- [504] LHC Higgs Cross Section Working Group Collaboration, S. Dittmaier *et al.*, [arXiv:1101.0593](#).
- [505] T. Barklow, K. Fujii, S. Jung, R. Karl, J. List, T. Ogawa, M. E. Peskin and J. Tian, *Phys. Rev. D*97 (2018) 053003, [arXiv:1708.08912](#).
- [506] M. Trott, *Invited Talk at the LHeC Workshop, Chavannes* (2014) .
- [507] C. Collaboration, *CMS PAS FTR-18-011* (2018) .
- [508] S. D. Rindani, P. Sharma and A. Shivaji, *Phys. Lett. B*761 (2016) 25, [arXiv:1605.03806](#).
- [509] S. S. Biswal, R. M. Godbole, B. Mellado and S. Raychaudhuri, *Phys. Rev. Lett.* 109 (2012) 261801, [arXiv:1203.6285](#).
- [510] A. Alloul, N. D. Christensen, C. Degrande, C. Duhr and B. Fuks, *Comput. Phys. Commun.* 185 (2014) 2250, [arXiv:1310.1921](#).
- [511] R. D. Ball *et al.*, *Nucl. Phys. B*867 (2013) 244, [arXiv:1207.1303](#).
- [512] NNPDF Collaboration, C. S. Deans, “Progress in the NNPDF global analysis,” in *Proceedings, 48th Rencontres de Moriond on QCD and High Energy Interactions: La Thuile, Italy, March 9-16, 2013*, 2013. [arXiv:1304.2781](#). <https://inspirehep.net/record/1227810/files/arXiv:1304.2781.pdf>.
- [513] Y.-L. Tang, C. Zhang and S.-h. Zhu, *Phys. Rev. D*94 (2016) 011702, [arXiv:1508.01095](#).
- [514] C. Bernaciak, T. Plehn, P. Schichtel and J. Tattersall, *Phys. Rev. D*91 (2015) 035024, [arXiv:1411.7699](#).
- [515] S. Buddenbrock, A. S. Cornell, Y. Fang, A. Fadol Mohammed, M. Kumar, B. Mellado and K. G. Tomiwa, *JHEP* 10 (2019) 157, [arXiv:1901.05300](#).
- [516] W. Liu, H. Sun, X. Wang and X. Luo, *Phys. Rev. D*92 (2015) 074015, [arXiv:1507.03264](#).
- [517] X. Wang, H. Sun and X. Luo, *Adv. High Energy Phys.* 2017 (2017) 4693213, [arXiv:1703.02691](#).
- [518] ATLAS Collaboration, M. Aaboud *et al.*, *Phys. Rev. D*98 (2018) 032002, [arXiv:1805.03483](#).
- [519] CMS Collaboration, V. Khachatryan *et al.*, *JHEP* 02 (2017) 079, [arXiv:1610.04857](#).
- [520] J. Hernandez-Sanchez, O. Flores-Sanchez, C. G. Honorato, S. Moretti and S. Rosado, *PoS CHARGED2016* (2017) 032, [arXiv:1612.06316](#).
- [521] CMS Collaboration, A. M. Sirunyan *et al.*, *JHEP* 11 (2018) 115, [arXiv:1808.06575](#).
- [522] CMS Collaboration, V. Khachatryan *et al.*, *JHEP* 12 (2015) 178, [arXiv:1510.04252](#).
- [523] S. P. Das, J. Hernandez-Sanchez, S. Moretti and A. Rosado, [arXiv:1806.08361](#).
- [524] H. Sun, X. Luo, W. Wei and T. Liu, *Phys. Rev. D*96 (2017) 095003, [arXiv:1710.06284](#).
- [525] G. Azuelos, H. Sun and K. Wang, *Phys. Rev. D*97 (2018) 116005, [arXiv:1712.07505](#).
- [526] C. Mosomane, M. Kumar, A. S. Cornell and B. Mellado, *J. Phys. Conf. Ser.* 889 (2017) 012004, [arXiv:1707.05997](#).
- [527] L. Delle Rose, O. Fischer and A. Hammad, *Int. J. Mod. Phys. A*34 (2019) 1950127, [arXiv:1809.04321](#).
- [528] CMS Collaboration, A. M. Sirunyan *et al.*, *JHEP* 06 (2018) 127, [arXiv:1804.01939](#). [Erratum: *JHEP*03,128(2019)].
- [529] CMS Collaboration, “Search for a new scalar resonance decaying to a pair of Z bosons at the High-Luminosity LHC,” CMS-PAS-FTR-18-040, 2019.
- [530] S. P. Das, J. Hernández-Sánchez, S. Moretti, A. Rosado and R. Xoxocotzi, *Phys. Rev. D*94 (2016) 055003, [arXiv:1503.01464](#).

- [531] S. P. Das and M. Nowakowski, *Phys. Rev. D*96 (2017) 055014, [arXiv:1612.07241](#).
- [532] I. T. Cakir, O. Cakir, A. Senol and A. T. Tasci, *Mod. Phys. Lett. A*28 (2013) 1350142, [arXiv:1304.3616](#).
- [533] H. Hesari, H. Khanpour and M. Mohammadi Najafabadi, *Phys. Rev. D*97 (2018) 095041, [arXiv:1805.04697](#).
- [534] S. Liu, Y.-L. Tang, C. Zhang and S.-h. Zhu, *Eur. Phys. J. C*77 (2017) 457, [arXiv:1608.08458](#).
- [535] D. Curtin, K. Deshpande, O. Fischer and J. Zurita, *JHEP* 07 (2018) 024, [arXiv:1712.07135](#).
- [536] G. Azuelos, M. D’Onofrio, S. Iwamoto and K. Wang, [arXiv:1912.03823](#).
- [537] C. Han, R. Li, R.-Q. Pan and K. Wang, *Phys. Rev. D*98 (2018) 115003, [arXiv:1802.03679](#).
- [538] S. Kuday, *J. Korean Phys. Soc.* 64 (2014) 1783–1787, [arXiv:1304.2124](#).
- [539] R.-Y. Zhang, H. Wei, L. Han and W.-G. Ma, *Mod. Phys. Lett. A*29 (2014) 1450029, [arXiv:1401.4266](#).
- [540] X.-P. Li, L. Guo, W.-G. Ma, R.-Y. Zhang, L. Han and M. Song, *Phys. Rev. D*88 (2013) 014023, [arXiv:1307.2308](#).
- [541] J. A. Evans and D. Mckeen, “The Light Gluino Gap,” 2018. [arXiv:1803.01880](#).
- [542] D. Curtin, K. Deshpande, O. Fischer and J. Zurita, *Phys. Rev. D*99 (2019) 055011, [arXiv:1812.01568](#).
- [543] S. Antusch and O. Fischer, *JHEP* 05 (2015) 053, [arXiv:1502.05915](#).
- [544] S. Antusch, E. Cazzato and O. Fischer, *Int. J. Mod. Phys. A*32 (2017) 1750078, [arXiv:1612.02728](#).
- [545] S. Antusch, O. Fischer and A. Hammad, [arXiv:1908.02852](#).
- [546] A. Das, S. Jana, S. Mandal and S. Nandi, *Phys. Rev. D*99 (2019) 055030, [arXiv:1811.04291](#).
- [547] ATLAS Collaboration, G. Aad *et al.*, [arXiv:1905.09787](#).
- [548] S. Antusch, E. Cazzato and O. Fischer, *Phys. Lett. B*774 (2017) 114–118, [arXiv:1706.05990](#).
- [549] DELPHI Collaboration, P. Abreu *et al.*, *Z. Phys. C*74 (1997) 57–71. [Erratum: *Z. Phys.*C75,580(1997)].
- [550] MEG Collaboration, J. Adam *et al.*, *Phys. Rev. Lett.* 110 (2013) 201801, [arXiv:1303.0754](#).
- [551] S. Jana, N. Okada and D. Raut, [arXiv:1911.09037](#).
- [552] L. Duarte, G. A. González-Sprinberg and O. A. Sampayo, *Phys. Rev. D*91 (2015) 053007, [arXiv:1412.1433](#).
- [553] L. Duarte, G. Zapata and O. A. Sampayo, *Eur. Phys. J. C*78 (2018) 352, [arXiv:1802.07620](#).
- [554] S. Mondal and S. K. Rai, *Phys. Rev. D*93 (2016) 011702, [arXiv:1510.08632](#).
- [555] M. Lindner, F. S. Queiroz, W. Rodejohann and C. E. Yaguna, *JHEP* 06 (2016) 140, [arXiv:1604.08596](#).
- [556] S. Mondal and S. K. Rai, *Phys. Rev. D*94 (2016) 033008, [arXiv:1605.04508](#).
- [557] B. Holdom, *Phys. Lett.* 166B (1986) 196–198.
- [558] M. D’Onofrio, O. Fischer and Z. S. Wang, “Searching for Dark Photons at the LHeC and FCC-he,” 2019. [arXiv:1909.02312](#).
- [559] LHCb Collaboration, R. Aaij *et al.*, *Phys. Rev. Lett.* 120 (2018) 061801, [arXiv:1710.02867](#).
- [560] S. Heeba and F. Kahlhoefer, “Probing the freeze-in mechanism in dark matter models with $U(1)'$ gauge extensions,” 2019. [arXiv:1908.09834](#).
- [561] C.-X. Yue, M.-Z. Liu and Y.-C. Guo, *Phys. Rev. D*100 (2019) 015020, [arXiv:1904.10657](#).
- [562] HFLAV Collaboration, Y. S. Amhis *et al.*, [arXiv:1909.12524](#).
- [563] J. C. Pati and A. Salam, *Phys. Rev. D*10 (1974) 275–289. [Erratum: *Phys. Rev.*D11,703(1975)].
- [564] W. Buchmuller, R. Ruckl and D. Wyler, *Phys. Lett. B*191 (1987) 442–448. [Erratum: *Phys. Lett.*B448,320(1999)].
- [565] I. Doršner, S. Fajfer, A. Greljo, J. F. Kamenik and N. Košnik, *Phys. Rept.* 641 (2016) 1–68, [arXiv:1603.04993](#).
- [566] ATLAS Collaboration, “ATLAS Exotics Searches,”. https://atlas.web.cern.ch/Atlas/GROUPS/PHYSICS/CombinedSummaryPlots/EXOTICS/ATLAS_Exotics_Summary/ATLAS_Exotics_Summary.pdf.
- [567] CMS Collaboration, “Overview of CMS Exo Results,”. https://twiki.cern.ch/twiki/pub/CMSPublic/SummaryPlotsEX013TeV/EX0_barchart_Jan19.svg.
- [568] J. Zhang, C.-X. Yue and Z.-C. Liu, *Mod. Phys. Lett. A*33 (2018) 1850039.
- [569] I. Doršner and A. Greljo, *JHEP* 05 (2018) 126, [arXiv:1801.07641](#).

- [570] M. Bahr *et al.*, *Eur. Phys. J. C* 58 (2008) 639–707, [arXiv:0803.0883](#).
- [571] J. Bellm *et al.*, *Eur. Phys. J. C* 76 (2016) 196, [arXiv:1512.01178](#).
- [572] S. Mandal, M. Mitra and N. Sinha, *Phys. Rev. D* 98 (2018) 095004, [arXiv:1807.06455](#).
- [573] R. Padhan, S. Mandal, M. Mitra and N. Sinha, [arXiv:1912.07236](#).
- [574] Y.-J. Zhang, L. Han and Y.-B. Liu, *Phys. Lett. B* 768 (2017) 241–247.
- [575] Y.-B. Liu, *Nucl. Phys. B* 923 (2017) 312–323, [arXiv:1704.02059](#).
- [576] L. Han, Y.-J. Zhang and Y.-B. Liu, *Phys. Lett. B* 771 (2017) 106–112.
- [577] A. Ozansoy, V. Ar? and V. Çetinkaya, *Adv. High Energy Phys.* 2016 (2016) 1739027, [arXiv:1607.04437](#).
- [578] A. Caliskan, *Adv. High Energy Phys.* 2017 (2017) 4726050, [arXiv:1706.09797](#).
- [579] A. Caliskan and S. O. Kara, *Int. J. Mod. Phys. A* 33 (2018) 1850141, [arXiv:1806.02037](#).
- [580] Y. O. Günayd?n, M. Sahin and S. Sultansoy, *Acta Phys. Polon. B* 49 (2018) 1763, [arXiv:1707.00056](#).
- [581] M. Sahin, *Acta Phys. Polon. B* 45 (2014) 1811, [arXiv:1302.5747](#).
- [582] Y. C. Acar, U. Kaya, B. B. Oner and S. Sultansoy, *J. Phys. G* 44 (2017) 045005, [arXiv:1605.08028](#).
- [583] P. C. M. Yock, *Int. J. Theor. Phys.* 2 (1969) 247–254.
- [584] J. S. Schwinger, *Science* 165 (1969) 757–761.
- [585] ATLAS Collaboration, G. Aad *et al.*, *Phys. Rev. Lett.* 124 (2020) 031802, [arXiv:1905.10130](#).
- [586] P. C. M. Yock, *Submitted to: Phys. Lett. B* (2001) , [arXiv:hep-ph/0103146](#).
- [587] H1 Collaboration, C. Adloff *et al.*, *Z. Phys. C* 74 (1997) 191–206, [arXiv:hep-ex/9702012](#).
- [588] ZEUS Collaboration, J. Breitweg *et al.*, *Z. Phys. C* 74 (1997) 207–220, [arXiv:hep-ex/9702015](#).
- [589] ZEUS Collaboration, H. Abramowicz *et al.*, *Phys. Lett. B* 757 (2016) 468–472, [arXiv:1604.01280](#).
- [590] R. Hofstadter, *Rev. Mod. Phys.* 28 (1956) 214–254.
- [591] A. Michel and M. Sher, *Phys. Rev. D* 100 (2019) 095011, [arXiv:1909.10627](#).
- [592] G. R. Boroun, *Chin. Phys. C* 41 (2017) 013104, [arXiv:1510.02914](#).
- [593] G. R. Boroun, B. Rezaei and S. Heidari, *Int. J. Mod. Phys. A* 32 (2017) 1750197, [arXiv:1606.02864](#).
- [594] H.-Y. Bi, R.-Y. Zhang, H.-Y. Han, Y. Jiang and X.-G. Wu, *Phys. Rev. D* 95 (2017) 034019, [arXiv:1612.07990](#).
- [595] K. He, H.-Y. Bi, R.-Y. Zhang, X.-Z. Li and W.-G. Ma, *J. Phys. G* 45 (2018) 055005, [arXiv:1710.11508](#).
- [596] H.-Y. Bi, R.-Y. Zhang, X.-G. Wu, W.-G. Ma, X.-Z. Li and S. Owusu, *Phys. Rev. D* 95 (2017) 074020, [arXiv:1702.07181](#).
- [597] ATLAS Collaboration Collaboration, “Prospect for a measurement of the Weak Mixing Angle in $pp \rightarrow Z/\gamma^* \rightarrow e^+e^-$ events with the ATLAS detector at the High Luminosity Large Hadron Collider,” ATL-PHYS-PUB-2018-037, CERN, Geneva, Nov 2018. <https://cds.cern.ch/record/2649330>.
- [598] CMS Collaboration Collaboration, “A proposal for the measurement of the weak mixing angle at the HL-LHC,” CMS-PAS-FTR-17-001, CERN, Geneva, 2017. <https://cds.cern.ch/record/2294888>.
- [599] W. J. Barter, “Prospects for measurement of the weak mixing angle at LHCb,” LHCb-PUB-2018-013, CERN-LHCb-PUB-2018-013, CERN, Geneva, Nov 2018. <https://cds.cern.ch/record/2647836>.
- [600] L. A. Harland-Lang, A. D. Martin, P. Motylinski and R. S. Thorne, *Eur. Phys. J. C* 75 (2015) 204, [arXiv:1412.3989](#).
- [601] S. Dulat *et al.*, *Phys. Rev. D* 93 (2016) 033006, [arXiv:1506.07443](#).
- [602] M. Klein and V. Radescu, “Partons from the LHeC,” CERN-LHeC-Note-2013-002, Jul 2013.
- [603] ATLAS Collaboration, G. Aad *et al.*, *JHEP* 09 (2015) 049, [arXiv:1503.03709](#).
- [604] ATLAS Collaboration Collaboration, “Prospects for the measurement of the W-boson mass at the HL- and HE-LHC,” ATL-PHYS-PUB-2018-026, CERN, Geneva, Oct 2018. <http://cds.cern.ch/record/2645431>.
- [605] F. Zimmermann, *ICFA Beam Dynamics Newsletter* 72 (2017) 138.
- [606] M. E. Peskin and T. Takeuchi, *Phys. Rev. D* 46 (1992) 381–409.
- [607] J. De Blas *et al.*, [arXiv:1910.14012](#).
- [608] M. Cepeda *et al.*, *CERN Yellow Rep. Monogr.* 7 (2019) 221, [arXiv:1902.00134](#).
- [609] J. Campbell and T. Neumann, *JHEP* 12 (2019) 034, [arXiv:1909.09117](#).

- [610] B. Mistlberger, *JHEP* 05 (2018) 028, [arXiv:1802.00833](#).
- [611] F. Dulat, A. Lazopoulos and B. Mistlberger, *Comput. Phys. Commun.* 233 (2018) 243, [arXiv:1802.00827](#).
- [612] LHC Higgs Cross Section Working Group Collaboration, A. David *et al.*, “LHC HXSWG interim recommendations to explore the coupling structure of a Higgs-like particle,” 2012. [arXiv:1209.0040](#).
- [613] ATLAS Collaboration, G. Aad *et al.*, *Phys. Rev. D* 101 (2020) 012002, [arXiv:1909.02845](#).
- [614] J. de Blas *et al.*, “Higgs Boson Studies at Future Particle Colliders,” 2019. [arXiv:1905.03764](#).
- [615] ATLAS Collaboration, “Study of correlation of PDF uncertainty in single top and top pair production at the LHC,” ATL-PHYS-PUB-2015-010, Geneva, May 2015.
- [616] CMS Collaboration, V. Khachatryan *et al.*, *Phys. Rev. D* 94 (2016) 072002, [arXiv:1605.00116](#).
- [617] CDF and D0 Collaborations, T. E. W. Group and T. Aaltonen, [arXiv:1608.01881](#).
- [618] CMS Collaboration, V. Khachatryan *et al.*, *Phys. Rev. D* 93 (2016) 072004, [arXiv:1509.04044](#).
- [619] ATLAS Collaboration, M. Aaboud *et al.*, *Phys. Lett. B* 761 (2016) 350–371, [arXiv:1606.02179](#).
- [620] CMS Collaboration, A. M. Sirunyan *et al.*, *Eur. Phys. J. C* 77 (2017) 354, [arXiv:1703.02530](#).
- [621] CMS Collaboration, A. M. Sirunyan *et al.*, *Eur. Phys. J. C* 78 (2018) 891, [arXiv:1805.01428](#).
- [622] ATLAS Collaboration, “Prospects for measurement of the top quark mass using $t\bar{t}$ events with $J/\psi \rightarrow \mu^+\mu^-$ decays with the upgraded ATLAS detector at the High Luminosity LHC.” Dec 2018.
- [623] D. Britzger, K. Rabbertz, D. Savoie, G. Sieber and M. Wobisch, *Eur. Phys. J. C* 79 (2019) 68, [arXiv:1712.00480](#).
- [624] ATLAS Collaboration, M. Aaboud *et al.*, *Phys. Rev. D* 98 (2018) 092004, [arXiv:1805.04691](#).
- [625] ATLAS Collaboration, M. Aaboud *et al.*, *Eur. Phys. J. C* 77 (2017) 872, [arXiv:1707.02562](#).
- [626] M. Johnson and D. Maître, *Phys. Rev. D* 97 (2018) 054013, [arXiv:1711.01408](#).
- [627] T. Klijnsma, S. Bethke, G. Dissertori and G. P. Salam, *Eur. Phys. J. C* 77 (2017) 778, [arXiv:1708.07495](#).
- [628] CMS Collaboration, A. M. Sirunyan *et al.*, *Submitted to: Eur. Phys. J.* (2019) , [arXiv:1904.05237](#).
- [629] CMS Collaboration, A. M. Sirunyan *et al.*, “Determination of the strong coupling constant $\alpha_s(m_Z)$ from measurements of inclusive W^\pm and Z boson production cross sections in proton-proton collisions at $\sqrt{s} = 7$ and 8 TeV,” 2019. [arXiv:1912.04387](#).
- [630] D. d’Enterria and A. Poldaru, “Strong coupling $\alpha_s(m_Z)$ extraction from a combined NNLO analysis of inclusive electroweak boson cross sections at hadron colliders,” 2019. [arXiv:1912.11733](#).
- [631] B. Bouzid, F. Iddir and L. Semlala, [arXiv:1703.03959](#).
- [632] M. Grazzini, S. Kallweit, D. Rathlev and M. Wiesemann, *Phys. Lett. B* 761 (2016) 179–183, [arXiv:1604.08576](#).
- [633] M. Grazzini, S. Kallweit and M. Wiesemann, *Eur. Phys. J. C* 78 (2018) 537, [arXiv:1711.06631](#).
- [634] ATLAS Collaboration, M. Aaboud *et al.*, *Eur. Phys. J. C* 79 (2019) 535, [arXiv:1902.05759](#). Auxiliary figure.
- [635] CMS Collaboration, A. M. Sirunyan *et al.*, *JHEP* 04 (2019) 122, [arXiv:1901.03428](#).
- [636] X. Cid Vidal *et al.*, *CERN Yellow Rep. Monogr.* 7 (2019) 585–865, [arXiv:1812.07831](#).
- [637] ATLAS Collaboration, M. Aaboud *et al.*, *Phys. Rev. D* 97 (2018) 112001, [arXiv:1712.02332](#).
- [638] CMS Collaboration, A. M. Sirunyan *et al.*, *JHEP* 05 (2018) 025, [arXiv:1802.02110](#).
- [639] ATLAS Collaboration, M. Aaboud *et al.*, *JHEP* 10 (2017) 182, [arXiv:1707.02424](#).
- [640] CMS Collaboration, A. M. Sirunyan *et al.*, *JHEP* 04 (2019) 114, [arXiv:1812.10443](#).
- [641] NNPDF Collaboration, R. D. Ball *et al.*, *JHEP* 04 (2015) 040, [arXiv:1410.8849](#).
- [642] N. Armesto and E. Scomparin, *Eur. Phys. J. Plus* 131 (2016) 52, [arXiv:1511.02151](#).
- [643] W. Busza, K. Rajagopal and W. van der Schee, *Ann. Rev. Nucl. Part. Sci.* 68 (2018) 339, [arXiv:1802.04801](#).
- [644] P. Romatschke and U. Romatschke, *Relativistic Fluid Dynamics In and Out of Equilibrium*. Cambridge Monographs on Mathematical Physics. Cambridge University Press, 2019. [arXiv:1712.05815](#).
- [645] Y. Mehtar-Tani, J. G. Milhano and K. Tywoniuk, *Int. J. Mod. Phys. A* 28 (2013) 1340013, [arXiv:1302.2579](#).
- [646] A. Andronic *et al.*, *Eur. Phys. J. C* 76 (2016) 107, [arXiv:1506.03981](#).

- [647] “Proceedings, 9th International Conference on Hard and Electromagnetic Probes of High-Energy Nuclear Collisions: Hard Probes 2018 (HP2018),” SISSA, 2018. <https://pos.sissa.it/345>.
- [648] H. A. Andrews *et al.*, [arXiv:1808.03689](https://arxiv.org/abs/1808.03689).
- [649] ALICE Collaboration, B. B. Abelev *et al.*, *Phys. Lett. B* **734** (2014) 314, [arXiv:1311.0214](https://arxiv.org/abs/1311.0214).
- [650] H. Song, S. A. Bass, U. Heinz, T. Hirano and C. Shen, *Phys. Rev. Lett.* **106** (2011) 192301, [arXiv:1011.2783](https://arxiv.org/abs/1011.2783). [Erratum: *Phys. Rev. Lett.* **109**,139904(2012)].
- [651] H. Niemi, K. J. Eskola and R. Paatelainen, *Phys. Rev. C* **93** (2016) 024907, [arXiv:1505.02677](https://arxiv.org/abs/1505.02677).
- [652] J. Liu, C. Shen and U. Heinz, *Phys. Rev. C* **91** (2015) 064906, [arXiv:1504.02160](https://arxiv.org/abs/1504.02160). [Erratum: *Phys. Rev. C* **92**,no.4,049904(2015)].
- [653] B. Schenke, P. Tribedy and R. Venugopalan, *Phys. Rev. Lett.* **108** (2012) 252301, [arXiv:1202.6646](https://arxiv.org/abs/1202.6646).
- [654] J.-Y. Ollitrault, A. M. Poskanzer and S. A. Voloshin, *Phys. Rev. C* **80** (2009) 014904, [arXiv:0904.2315](https://arxiv.org/abs/0904.2315).
- [655] STAR Collaboration, J. Adams *et al.*, *Phys. Rev. C* **72** (2005) 014904, [arXiv:nuc1-ex/0409033](https://arxiv.org/abs/nuc1-ex/0409033).
- [656] STAR Collaboration, B. I. Abelev *et al.*, *Phys. Rev. C* **79** (2009) 034909, [arXiv:0808.2041](https://arxiv.org/abs/0808.2041).
- [657] CMS Collaboration, A. M. Sirunyan *et al.*, [arXiv:1905.01486](https://arxiv.org/abs/1905.01486).
- [658] V. Guzey and M. Zhalov, *JHEP* **10** (2013) 207, [arXiv:1307.4526](https://arxiv.org/abs/1307.4526).
- [659] J. G. Contreras, *Phys. Rev. C* **96** (2017) 015203, [arXiv:1610.03350](https://arxiv.org/abs/1610.03350).
- [660] V. Guzey and M. Klasen, *Eur. Phys. J. C* **79** (2019) 396, [arXiv:1902.05126](https://arxiv.org/abs/1902.05126).
- [661] ATLAS Collaboration, M. Aaboud *et al.*, *Phys. Rev. Lett.* **121** (2018) 212301, [arXiv:1806.08708](https://arxiv.org/abs/1806.08708).
- [662] ATLAS Collaboration, M. Aaboud *et al.*, *Phys. Rev. C* **100** (2019) 034903, [arXiv:1901.10440](https://arxiv.org/abs/1901.10440).
- [663] R. Aaij *et al.*, “Expression of Interest for a Phase-II LHCb Upgrade: Opportunities in flavour physics, and beyond, in the HL-LHC era,” CERN-LHCC-2017-003, CERN, Geneva, Feb 2017.
- [664] O. Brüning, “Accelerator design.” Presented at the lhec workshop, June 2015.
- [665] D. Brandt, H. Burkhardt, M. Lamont, S. Myers and J. Wenninger, *Rept. Prog. Phys.* **63** (2000) 939.
- [666] D. S. D. Pellegrini, A. Latina and S. Bogacz, *Phys. Rev. ST-AB* **12**1004 (2015) .
- [667] S. A. Bogacz *et al.*, *ICFA Beam Dynamics Newsletter* **71** (2017) 135.
- [668] 12 GeV CEBAF Upgrade, Reference Design: www.jlab.org/physics/GeV/accelerator (2012).
- [669] G. Hoffstaetter and I. Bazarov, *Phys. Rev. ST-AB* **7** (2004) .
- [670] J. S. Schwinger, *Phys. Rev.* **70** (1946) 798.
- [671] D. Pellegrini, *Ph.D. Thesis, EPFL, Switzerland* (2016) .
- [672] J. Jowett *et al.*, “The 2018 heavy-ion run of the LHC,” in *Proceedings, 10th International Particle Accelerator Conference (IPAC2019): Melbourne, Australia, May 19-24, 2019*, 2019.
- [673] T. Argyropoulos, T. Bohl, A. Lasheen, G. Papotti, D. Quartullo and E. Shaposhnikova, “Momentum slip-stacking in CERN SPS for the ion beams,” in *Proceedings, 10th International Particle Accelerator Conference (IPAC2019): Melbourne, Australia, May 19-24, 2019*, 2019.
- [674] M. Schaumann, *Phys. Rev. ST Accel. Beams* **18** (2015) 091002, [arXiv:1503.09107](https://arxiv.org/abs/1503.09107).
- [675] O. Brüning *et al.*, *ICFA Beam Dynamics Newsletter* **68** (2015) 46.
- [676] A. Milanese, *Talk presented at the LHeC workshop at CERN* (2014) .
- [677] R. Calaga and E. Jensen, “A Proposal for an ERL Test Facility at CERN,” in *Proceedings, 4th International Particle Accelerator Conference (IPAC 2013): Shanghai, China, May 12-17, 2013*, 2013. <http://JACoW.org/IPAC2013/papers/wepwo049.pdf>.
- [678] F. Marhauser, “Cost Rationales for an SRF Proton Linac,” in *Proceedings, 5th International Particle Accelerator Conference (IPAC 2014): Dresden, Germany, June 15-20, 2014*, 2014.
- [679] F. Marhauser, “Recent results on a multi-cell 802 mhz bulk nb cavity.” Presented at fcc week 2018, https://indico.cern.ch/event/656491/contributions/2932251/attachments/1629681/2597650/5_cell_Cavity_Marhauser.pdf, 2018.
- [680] W. Schneider, I. Campisi, E. Daly, T. Hiatt, J. Hogan, P. Kneisel, D. Machie, J. Preble, C. Rode, T. Whitlatch *et al.*, “Design of the sns cryomodule,” in *Proceedings, the 2001 Particle Accelerator Conference (PACS2001)*, 2001.
- [681] V. Parma *et al.*, “Conceptual design of the superconducting proton linac short cryo-module,” in *Proceedings of the SRF2011, Chicago, July, 2011*.

- [682] G. Olivier, J. Thermeau and P. Bosland, “Ess cryomodules for elliptical cavities,” in *Proceedings of the 2013 Superconducting Radio Frequency Conference*, 2013.
- [683] H. Bluem, D. Dowell, A. Todd and L. Young, “High Brightness Thermionic Electron Gun Performance,” in *Procings, 50th Advanced ICFA Beam Dynamics Workshop on Energy Recovery Linacs (ERL’11)*, Tsukuba, Japan, Oct. 2011, 2011.
- [684] F. Sannibale *et al.*, “The VHF-Gun, the LBNL High-Brightness Electron Photo-Injector for MHz-Class Repetition-Rate Applications,” in *High-Brightness Sources and Light-Driven Interactions*, Optical Society of America, 2016.
- [685] Z. Wang, Q. Gu, G. Wang and M. Zhao, “Injector Physics Design at SHINE,” in *Proceedings, 10th International Particle Accelerator Conference (IPAC’19)*, Melbourne, Australia, 19-24 May 2019, JACoW Publishing, Geneva, Switzerland, Jun. 2019.
- [686] G. Shu, Y. Chen, S. Lal, H. Qian, H. Shaker and F. Stephan, “FIRST DESIGN STUDIES OF A NC CW RF GUN FOR EUROPEAN XFEL,” in *Proceedings, 10th International Particle Accelerator Conference (IPAC’19)*, Melbourne, Australia, 19-24 May 2019, JACoW Publishing, Geneva, Switzerland, Jun. 2019.
- [687] J. Teichert *et al.*, *Nuclear Instruments and Methods in Physics Research Section A: Accelerators, Spectrometers, Detectors and Associated Equipment* 743 (2014) 114.
- [688] J. Bisognano *et al.*, “Wisconsin srf electron gun commissioning,” in *Proceedings, North American Particle Accelerator Conf. (NAPAC’13)*, Pasadena, CA, USA, Sep.-Oct. 2013, 09 2013.
<http://accelconf.web.cern.ch/AccelConf/PAC2013/papers/tupma19.pdf>.
- [689] E. Vogel *et al.*, “SRF Gun Development at DESY,” JACoW, Geneva, Sep 2018.
- [690] A. Neumann, and others, “Status of SRF Gun for bERLinPro,” in *Proceedings, ERL’19, Berlin, Germany, Sept. 2019*, 2019.
- [691] Belomestnykh, S.A. and others, “Commissioning of the 112 MHz SRF Gun,” in *Proceedings, 17th Int. Conf. RF Superconductivity, Whistler, Canada, Sep. 2015*, 2015.
- [692] Hernandez-Garcia, C. and others, “JLab FEL DC Gun,” in *Proceedings, 45th ICFA Advanced Beam Dynamics Workshop on Energy Recovery LINAC Workshop (ERL’09)*, Ithaca, NY, USA, June 2009 , 2009.
- [693] L. B. Jones, J. W. McKenzie, K. J. Middleman, B. L. Militsyn, Y. M. Saveliev and S. L. Smith, *Journal of Physics: Conference Series* 298 (2011) 012007.
- [694] R. Kato, Y. Honda, H. Kawata, T. Miyajima, N. Nakamura, H. Sakai, M. Shimada, Y. Tanimoto, K. Tsuchiya, “Ir-fel project at the cerl and future euv-fel lithography,” in *Presented at the 39th Int. Free Electron Laser Conf. (FEL’19)*, Hamburg, Germany, Aug. 2019, 2019.
- [695] Hoffstaetter, G.H. and others, “CBETA: The Cornell/BNL 4-turn ERL with FFAG Return Arcs for eRHIC Prototyping,” in *Proceedings, 28th Linear Accelerator Conf. (LINAC’16)*, East Lansing, MI, USA, 2016.
- [696] B. Hounsell, W. Kaabi, M. Klein, B. Militsyn and C. Welsch, “Optimisation of the PERLE injector,” in *Proceedings, ERL’19, Berlin, Germany, Sept. 2019*, 2019.
- [697] R. Suleiman, P. Adderley, J. Grames, J. Hansknecht, M. Poelker and M. Stutzman, *AIP Conference Proceedings* 1970 (2018) 050007, <https://aip.scitation.org/doi/pdf/10.1063/1.504022>.
- [698] C. K. Sinclair *et al.*, “Performance of a very high voltage photoemission electron gun for a high brightness, high average current ERL injector,” in *Proceedings, 22nd Particle Accelerator Conf. (PAC’07)*, Albuquerque, NM, USA, 2007.
- [699] N. Nishimori, R. Nagai, S. Matsuba, R. Hajima, M. Yamamoto, T. Miyajima, Y. Honda, H. Iijima, M. Kuriki and M. Kuwahara, *Applied Physics Letters* 102 (2013) 234103.
- [700] N. Nishimori, R. Nagai, R. Hajima, M. Yamamoto, Y. Honda, T. Miyajima and T. Uchiyama, *Phys. Rev. Accel. Beams* 22 (2019) 053402.
- [701] W. Liu, Y. Chen, W. Lu, A. Moy, M. Poelker, M. Stutzman and S. Zhang, *Applied Physics Letters* 109 (2016) 252104, <https://doi.org/10.1063/1.4972180>.
- [702] E. Wang, *AIP Conference Proceedings* 1970 (2018) 050008, <https://aip.scitation.org/doi/pdf/10.1063/1.5040227>.
- [703] A. Zaltsman and R. Lambiase, *Proceedings of the 24-th Particle Accelerator Conference, PAC-2011, TUP125* (2011) .
- [704] B. Parker, “Latest Developments and Progress on the IR magnet design.” presented at the LHeC and FCC-eh Workshop, Sept 2017.

- [705] B. Parker, “Superconducting Magnet Concepts for Electron Hadron Collider IRs.” Presented at the electrons for the lhc - lhec/fcch and perle workshop, Sept 2018.
- [706] E. Cruz-Alaniz, D. Newton, R. Tomás and M. Korostelev, *Phys. Rev. ST Accel. Beams* **18** (2015) 111001.
- [707] R. Martin and R. Tomás Garcia, “Length optimization of the detector region dipoles in LHeC and FCC-eh,” CERN-ACC-2018-0042, CERN, Geneva, Oct 2018. <http://cds.cern.ch/record/2644892>.
- [708] S. Fartoukh, *Phys. Rev. ST Accel. Beams* **16** (2013) 111002.
- [709] “Lattice repository.” <https://gitlab.cern.ch/lhec-optics/lhec-lattice>, 2019.
- [710] A. Gaddi, “Installation Issues of eh Detectors (LHC and FCC),” Talk presented at the LHeC and FCC-eh Workshop, CERN, Sept 2017.
- [711] A. Gaddi. Private communication, Jan 2019.
- [712] R. Bruce, C. Bracco, R. De Maria, M. Giovannozzi, S. Redaelli, R. Tomás Garcia, F. M. Velotti and J. Wenninger, “Updated parameters for HL-LHC aperture calculations for proton beams,” CERN-ACC-2017-0051, CERN, Geneva, Jul 2017. <https://cds.cern.ch/record/2274330>.
- [713] R. De Maria *et al.*, “HLLHCv1.3 Optics repository.” <http://lhc-optics.web.cern.ch/lhc-optics/HLLHCv1.3/>.
- [714] E. Cruz-Alaniz, R. Martin and R. Tomás, “LHeC optics with $\beta^* = 10$ cm and $L^* = 15$ m,” CERN-XXX-2019-XXX, CERN, Geneva, 2019.
- [715] Sixtrack web site: <http://sixtrack.web.cern.ch/SixTrack/>.
- [716] E. Cruz-Alaniz, J. L. Abelleira, L. van Riesen-Haupt, A. Seryi, R. Martin and R. Tomás, “Methods to increase the dynamic aperture of the fcc-hh lattice,” in *Proceedings. International Particle Accelerator Conference (IPAC’18), Vancouver, Canada, 2018*, JACoW, Geneva, Switzerland, May 2018.
- [717] F. Zimmermann *et al.*, “Interaction-Region Design Options for a Linac-Ring LHeC,” in *Proceedings, International Particle Accelerator Conference (IPAC’10), Kyoto, Japan, May 23-28, 2010*, JACoW, Geneva, Switzerland, May 2010.
- [718] J. L. Abelleira, H. Garcia, R. Tomás and F. Zimmermann, “Final-Focus Optics for the LHeC Electron Beam Line,” in *Proceedings, International Particle Accelerator Conference (IPAC’12), New Orleans, Louisiana, USA, May 20-25, 2012*, JACoW, Geneva, Switzerland, May 2012.
- [719] LHeC Study Group, FCC-eh Study Group, PERLE Collaboration, G. Arduini, O. Brüning and M. Klein, *PoS DIS2018* (2018) 183.
- [720] R. Tomás, “LHeC interaction region,” Talk presented at DIS 2012 Workshop, Bonn, 2012.
- [721] J. Parrell *et al.*, *IEEE Transactions on Applied Superconductivity* (2003) .
- [722] S. Russenschuck, *Field computation for accelerator magnets: analytical and numerical methods for electromagnetic design and optimization*. Wiley, Weinheim, 2010.
- [723] V. Fern, E.J.and Di Murro, K. Soga, Z. Li, L. Scibile and J. Osborne, (2018) . <https://doi.org/10.1016/j.tust.2018.04.003>.
- [724] C. Laughton, *International Journal of Mining and Geological Engineering* (1988) .
- [725] E. by M. Benedikt *et al.*, .
- [726] C. Tennant, “Energy Recovery Linacs,” in *Challenges and Goals for Accelerators in the XXI Century*, O. Brüning and S. Myers (eds.), World Scientific, 2016.
- [727] C. Tennant, “Progress at the Jefferson Laboratory FEL,” in *Particle accelerator. Proceedings, 23rd Conference, PAC’09, Vancouver, Canada, May 4-8, 2009*, 2010. http://www1.jlab.org/UL/publications/view_pub.cfm?pub_id=8641.
- [728] G. H. Hoffstaetter and I. V. Bazarov, *Phys. Rev. ST Accel. Beams* **7** (2004) 054401.
- [729] D. R. Douglas *et al.*, *Phys. Rev. ST Accel. Beams* **9** (2006) 064403.
- [730] S. Di Mitri, M. Cornacchia and S. Spampinati, *Phys. Rev. Lett.* **110** (2013) 014801.
- [731] M. G. Fedurin, D. Kayran, V. Yakimenko, A. V. Fedotov, V. Litvinenko and P. Muggli, *Conf. Proc. C110328* (2011) 1677.
- [732] S. Heifets, G. Stupakov and S. Krinsky, *Phys. Rev. ST Accel. Beams* **5** (2002) 064401.
- [733] Z. Huang and K.-J. Kim, *Phys. Rev. ST Accel. Beams* **5** (2002) 074401.
- [734] S. Di Mitri and M. Cornacchia, *EPL (Europhysics Letters)* **109** (2015) 62002.
- [735] C.-Y. Tsai, D. Douglas, R. Li and C. Tennant, *Phys. Rev. Accel. Beams* **19** (2016) 114401.

- [736] C.-Y. Tsai, S. Di Mitri, D. Douglas, R. Li and C. Tennant, *Phys. Rev. Accel. Beams* **20** (2017) 024401.
- [737] D. Douglas *et al.* Jefferson Laboratory Technical Note 12-017, 2012.
- [738] R. Alarcon *et al.*, *Phys. Rev. Lett.* **111** (2013) 164801.
- [739] T. Powers and C. Tennant, “Implications of incomplete energy recovery in srf-based energy recovery linacs,” in *Proceedings of the 2007 ICFA Workshop on Energy Recovery Linacs, Daresbury, UK*, 2007.
- [740] T. Powers, “Control of Microphonics for Narrow Control Bandwidth Cavities,” Talk presented at the 2017 International Conference on RF Superconductivity, Lanzhou, China, 2017.
- [741] S. Benson *et al.*, *Conf. Proc.* **C070625** (2007) 79.
- [742] T. Powers, “Optimization of SRF Linacs,” in *Proceedings of the 2013 International Conference on RF Superconductivity, Paris, France*, 2013.
- [743] P. Williams, “A Staged, Multi-User X-Ray Free Electron Laser and Nuclear Physics Facility based on a Multi-Pass Recirculating Superconducting CW Linac,” in *Proceedings, Future Light Sources 2018, Shanghai*, 2018.
- [744] S. Benson *et al.*, “Development of a Bunched-Beam Electron Cooler for the Jefferson Lab Electron-Ion Collider,” in *Proceedings, 9th International Particle Accelerator Conference (IPAC 2018), Vancouver, BC Canada*, 2018.
- [745] C. Tennant. <https://userweb.jlab.org/~tennant/>.
- [746] C. Tennant, “Analysis of the Baseline PERLE Lattice,” Jefferson Laboratory Technical Note 18-031, 2018.
- [747] D. Douglas *et al.*, ““Why PERLE?” Historical Context and Technological Motivation,” Jefferson Laboratory Technical Note 18-014, 2018.
- [748] G. H. Hoffstaetter *et al.*, “CBETA Design Report, Cornell-BNL ERL Test Accelerator,” 2017. [arXiv:1706.04245](https://arxiv.org/abs/1706.04245).
- [749] T. Satogata *et al.*, “ER@CEBAF: A test of 5-pass energy recovery at CEBAF,” Program Advisory Committee Proposal, June 2016.
- [750] M. Frank, F. Gaede, M. Petric and A. Sailer, “Aidasoft/dd4hep,” Oct. 2018.
- [751] CMS Collaboration, G. Bianchi, *JINST* **9** (2014) C03054.
- [752] GEANT4 Collaboration, S. Agostinelli *et al.*, *Nucl. Instrum. Meth.* **A506** (2003) 250.
- [753] M. Oreglia, *A Study of the Reactions $\psi' \rightarrow \gamma\gamma\psi$* . PhD thesis. <https://search.proquest.com/docview/303269954>.
- [754] J. E. Gaiser, *Charmonium Spectroscopy From Radiative Decays of the J/ψ and ψ'* . PhD thesis. <https://search.proquest.com/docview/303269954>.
- [755] T. Skwarnicki, *A study of the radiative CASCADE transitions between the Upsilon-Prime and Upsilon resonances*. PhD thesis, Cracow, INP, 1986. <http://www-library.desy.de/cgi-bin/showprep.pl?DESY-F31-86-02>.
- [756] ATLAS Collaborartion Collaboration, “Technical Design Report for the Phase-II Upgrade of the ATLAS Muon Spectrometer,” 2017.
- [757] CMS Collaborartion Collaboration, “The Phase-2 Upgrade of the CMS Muon Detectors,” 2017.
- [758] LHCf Collaboration, O. Adriani *et al.*, *Phys. Lett.* **B780** (2018) 233, [arXiv:1703.07678](https://arxiv.org/abs/1703.07678).